FRONTIERS IN PHYSICS - 2017 & 2018 EDITOR'S CHOICE

EDITED BY: Thomas Beyer, Ewald Moser, Dieter W. Heermann, Christian F. Klingenberg, James Sauls, José W. F. Valle, Jan de Boer, Emilio Elizalde, Dumitru Baleanu, Alex Hansen, Nicholas X. Fang, Lorenzo Pavesi, Bretislav Friedrich, Christine Charles, Matjaž Perc, Jasper Van Der Gucht, Rudolf von Steiger and Claudio Bogazzi

PUBLISHED IN: Frontiers in Physics

frontiers

frontiers

ISSN 2296-424X
ISBN 978-2-88945-804-2
DOI 10.3389/978-2-88945-804-2

About Frontiers

Frontiers is more than just an open-access publisher of scholarly articles: it is a pioneering approach to the world of academia, radically improving the way scholarly research is managed. The grand vision of Frontiers is a world where all people have an equal opportunity to seek, share and generate knowledge. Frontiers provides immediate and permanent online open access to all its publications, but this alone is not enough to realize our grand goals.

Frontiers Journal Series

The Frontiers Journal Series is a multi-tier and interdisciplinary set of open-access, online journals, promising a paradigm shift from the current review, selection and dissemination processes in academic publishing. All Frontiers journals are driven by researchers for researchers; therefore, they constitute a service to the scholarly community. At the same time, the Frontiers Journal Series operates on a revolutionary invention, the tiered publishing system, initially addressing specific communities of scholars, and gradually climbing up to broader public understanding, thus serving the interests of the lay society, too.

Dedication to Quality

Each Frontiers article is a landmark of the highest quality, thanks to genuinely collaborative interactions between authors and review editors, who include some of the world's best academicians. Research must be certified by peers before entering a stream of knowledge that may eventually reach the public - and shape society; therefore, Frontiers only applies the most rigorous and unbiased reviews.
Frontiers revolutionizes research publishing by freely delivering the most outstanding research, evaluated with no bias from both the academic and social point of view. By applying the most advanced information technologies, Frontiers is catapulting scholarly publishing into a new generation.

FRONTIERS IN PHYSICS - 2017 & 2018 EDITOR'S CHOICE

Launched in 2013, Frontiers in Physics consists of 18 specialties covering all areas of research in physics. With over 500 published manuscripts, the journal is now indexed in SCIE with the first impact factor coming in 2019. Frontiers in Physics aims to become the largest and most cited open access multidisciplinary physics journal.

This eBook collects what the Specialty Chief Editors of the journal believed were the most interesting manuscripts published over the past two years. It is a nice collection, which will offer the reader the chance to have a quick overview of the specialties of the journal and offer a glimpse into the state of the art of physics.

We must confess that it has been quite challenging to select only one article per specialty section given the many important manuscripts published by the journal in 2017 and 2018. We invite our reader to have a look at the journal homepage and browse what we have published so far. It includes articles on topics very different from each other, written by both early career scientists and well-known researchers, ranging from the indisputable advance of the field to the more bold.

We hope you enjoy reading our first edition of the Frontiers in Physics Editor's Choice eBook!

Professor Alex Hansen (Field Chief Editor) and Dr Claudio Bogazzi (Journal Manager)

Citation: Beyer, T., Moser, E., Heermann, D. W., Klingenberg, C. F., Sauls, J., Valle, J. W. F., de Boer, J., Elizalde, E., Baleanu, D., Hansen, A., Fang, N. X., Pavesi, L., Friedrich, B., Charles, C., Perc, M., Van Der Gucht, J., von Steiger, R., Bogazzi, C., eds. (2019). Frontiers in Physics - 2017 & 2018 Editor's Choice. Lausanne: Frontiers Media. doi: 10.3389/978-2-88945-804-2

Table of Contents

10. PLASMA PHYSICS

11. SOCIAL PHYSICS

12. SPACE PHYSICS

13. EDITORIAL OFFICE CHOICE

frontiers in Physics

REVIEW
published: 17 August 2017
doi: 10.3389/fphy.2017.00033

Ultra-High Field NMR and MRI—The Role of Magnet Technology to Increase Sensitivity and Specificity

Ewald Moser[1,2]*, *Elmar Laistler*[1,2], *Franz Schmitt*[3] and *Georg Kontaxis*[4]

[1] Center for Medical Physics and Biomedical Engineering, Medical University of Vienna, Vienna, Austria, [2] High-field MR Center, Medical University of Vienna, Vienna, Austria, [3] Lakeside Imaging/e, Quetzin, Plau am See, Germany, [4] Max F. Perutz Laboratories, Department of Structural and Computational Biology, Center for Molecular Biology, University of Vienna, Vienna, Austria

"History, of course, is difficult to write, if for no other reason, than that it has so many players and so many authors." – P. J. Keating (former Australian Prime Minister)

OPEN ACCESS

Edited by:
Evren Özarslan, Linköping University, Sweden

Reviewed by:
Alexander Rauscher, University of British Columbia, Canada
Pierre Pugnat, UPR3228 Laboratoire National des Champs Magnetiques Intenses (LNCMI), France

***Correspondence:**
Ewald Moser
ewald.moser@meduniwien.ac.at

Specialty section:
This article was submitted to Biomedical Physics, a section of the journal Frontiers in Physics

Received: *08 March 2017*
Accepted: *02 August 2017*
Published: *17 August 2017*

Citation:
Moser E, Laistler E, Schmitt F and Kontaxis G (2017) Ultra-High Field NMR and MRI—The Role of Magnet Technology to Increase Sensitivity and Specificity. Front. Phys. 5:33. doi: 10.3389/fphy.2017.00033

Starting with post-war developments in nuclear magnetic resonance (NMR) a race for stronger and stronger magnetic fields has begun in the 1950s to overcome the inherently low sensitivity of this promising method. Further challenges were larger magnet bores to accommodate small animals and eventually humans. Initially, resistive electromagnets with small pole distances, or sample volumes, and field strengths up to 2.35 T (or 100 MHz ^{1}H frequency) were used in applications in physics, chemistry, and material science. This was followed by stronger and more stable (Nb-Ti based) superconducting magnet technology typically implemented first for small-bore systems in analytical chemistry, biochemistry and structural biology, and eventually allowing larger horizontal-bore magnets with diameters large enough to fit small laboratory animals. By the end of the 1970s, first low-field resistive magnets big enough to accommodate humans were developed and superconducting whole-body systems followed. Currently, cutting-edge analytical NMR systems are available at proton frequencies up to 1 GHz (23.5 T) based on Nb_3Sn at 1.9 K. A new 1.2 GHz system (28 T) at 1.9 K, operating in persistent mode but using a combination of low and high temperature multi-filament superconductors is to be released. Preclinical instruments range from small-bore animal systems with typically 600–800 MHz (14.1–18.8 T) up to 900 MHz (21 T) at 1.9 K. Human whole-body MRI systems currently operate up to 10.5 T. Hybrid combined superconducting and resistive electromagnets with even higher field strength of 45 T dc and 100 T pulsed, are available for material research, of course with smaller free bore diameters. This rather costly development toward higher and higher field strength is a consequence of the inherently low and, thus, urgently needed sensitivity in all NMR experiments. This review particularly describes and compares the developments in superconducting magnet technology and, thus, sensitivity in three

fields of research: analytical NMR, biomedical and preclinical research, and human MRI and MRS, highlighting important steps and innovations. In addition, we summarize our knowledge on safety issues. An outlook into even stronger magnetic fields using different superconducting materials and/or hybrid magnet designs is presented.

Keywords: NMR, MRI, MRS, magnet technology, superconductors, gradients, sensitivity

BACKGROUND

Although there have been earlier attempts by physicists to measure the gyromagnetic ratio of various materials using nuclear magnetic resonance (NMR)[1], what we call NMR and later magnetic resonance spectroscopy (MRS) and imaging (MRI) today has been commercially available only from the 1950s on. This technology was based on simultaneous discoveries by Felix Bloch at Stanford and Edward Purcell at Harvard, who were jointly awarded the Nobel prize in physics already in 1952. In addition, a number of Nobel prizes related to NMR were given to physicists working in various related fields thereafter:

- A. Kastler (1966) for the "double resonance method,"
- J. H. van Vleck (1977) for a theory of dia- and paramagnetism,
- N. Bloembergen (1981) for relaxation, motion and the BPP theory of relaxation,
- H. G. Dehmelt (1989) for pure nuclear quadrupole resonance,
- N. F. Ramsey (1989) for the concept of chemical shift; spin inversion (180° pulse), and negative (spin) temperature.

Nobel prizes in Chemistry were subsequently awarded to

- R. R. Ernst (1991) for his contributions to the development of the methodology of high resolution nuclear magnetic resonance (NMR) spectroscopy,
- K. Wuethrich (2002, 50%) for his development of nuclear magnetic resonance spectroscopy for determining the three-dimensional structure of biological macromolecules in solution,

and, finally, the Nobel prize in Medicine or Physiology to

- P. C. Lauterbur and Sir P. Mansfield (jointly 2003) for their discoveries concerning magnetic resonance imaging.

Furthermore, other scientific achievements have been instrumental in the development of appropriate superconducting magnets, and were recognized by Nobel prizes in physics awarded to

- H. Kammerlingh Onnes (1913) for his investigations of the low-temperature behavior of matter, leading to a method to produce liquid Helium,
- J. Bardeen, L. N. Cooper, and J. R. Shrieffer (1972) for their development of the so-called BCS theory, the theory of the superconducting state,
- J. G. Bednorz and K. A. Mueller (1987) for their groundbreaking discovery of high-temperature (ceramic) superconductors,
- A. A. Abrikosov, V. L. Ginzburg, and A. L. Legget (2003) for pioneering contributions to the theory of superconductors and superfluids.

Historically, we may split the technological development, particularly of high and ultra-high field magnets, into four distinct periods:

A) Resistive electromagnets—with the design goals of increasing field strength, field stability improvement, and cutting operating costs
B) Permanent magnets (to be used at all times, without the need for an electrical power supply) providing low resolution at low cost
C) Superconducting electromagnets—the golden age of NMR, MRS, and MRI
D) Hybrid magnets—ever higher static magnetic fields causing stability and homogeneity problems again.

Based on the various (and sometimes conflicting) requirements and developments in magnet technology, including field stabilization, shimming, RF-coil design and field gradient coils, three distinct areas of research have branched out and have developed independently since:

1) Analytical NMR—determination of structure and dynamics of small organic molecules and large biological macromolecules using small vertical-bore (2–10 cm), ultra-high field magnets (currently up to 1.2 GHz/28.2 T)
2) Biomedical and preclinical MRI and MRS—animal research using horizontal medium bore size (10–40 cm), and ultra-high field magnets (currently up to 900 MHz/21.1 T)

Abbreviations: B_0, magnetic flux density (magnetic field strength); BPP, Bloembergen-Purcell-Pound theory of relaxation; CEST, Chemical Exchange Saturation Transfer; CRNM, European Center for High Field NMR; cw, continuous wave; dc, direct current; ECG, electro-cardiography; EPI, echo-planar imaging; FDA, Food and Drug Administration; fMRI, functional magnetic resonance imaging; γ, gyromagnetic ratio; G, gradient; GE, General Electric; GEMS, General Electric Medical Systems; GRAPPA, generalized autocalibrating partially parallel acquisitions; H_c, critical field; H_{c2}, upper critical field; HTS, high temperature superconductor; I_c, critical current; IGC, Intermagnetics General Corporation; MRI, magnetic resonance imaging; MRS, magnetic resonance spectroscopy; MRSI, magnetic resonance spectroscopic imaging; NIH, National Institute of Health; NMR, nuclear magnetic resonance; OI, Oxford Instruments; OMT, Oxford Magnet Technology; PNS, peripheral nerve stimulation; pTx, parallel transmission; RF, radio-frequency; SAR, specific absorption rate; sc, superconductor; SENSE, sensitivity encoding; SMT, Siemens Magnet Technology; SNR, signal-to-noise ratio; SR, slew rate; T_2, spin-spin relaxation time; T_c, critical temperature; UHF, ultra-high field.

[1]Due to the unfavorable political situation and war time, the Western scientific communities did not acknowledge that Lazarev and Schubnikov measured nuclear magnetism in solid hydrogen already in 1937 [1], and also discovered type 2 superconductors.

3) Human head only (60–70 cm bore) and whole-body (80–125 cm bore) MRI and MRS—in clinical diagnostics and research ranging between 0.2 T and 10.5 T.

The signal-to-noise ratio (SNR) of an NMR experiment depends strongly on the applied magnetic field B_0 and thus on the Larmor frequency $\omega = \gamma^* B_0$, where γ is the gyromagnetic ratio of the nucleus *excited (=detected)* by the pulse sequence applied. This is typically hydrogen in clinical MRI. In the case of heteronuclei, however, sensitivity can be greatly enhanced through polarization transfer methods, which is exploited to great advantage in spectroscopic techniques *in-vitro* (in chemical and bio-chemical applications) as well as *in-vivo*. In this case SNR prop. $n^*\gamma_e^*\mathrm{sqrt}(\gamma_d^{3*}B_0^{3*}t)$, where γ_e is the gyromagnetic ratio of the nucleus *excited* and γ_d of the nucleus *detected* by the pulse sequence applied. In any case, B_0 is the most essential parameter to boost SNR.

The achievable signal in an MR experiment is proportional to the equilibrium magnetization M_0 times the Larmor frequency ω_0, both of which are linearly proportional to the magnetic flux density B_0 (field strength), therefore leading to a dependence of the signal in ${B_0}^2$.

One main noise source is the RF system for the detection of the signal, showing a frequency dependence in $\omega_0^{1/2}$ and, hence, $B_0^{1/2}$ due to the skin depth effect. The other main noise source is the sample itself, exhibiting a dependence in ${B_0}^2$ due to induced eddy currents in the (conductive) tissue. Therefore, the SNR of the MR experiment is increasing with (i) the magnetic flux density B_0 (field strength), according to

$$\frac{signal}{\sqrt{noise}} \propto \frac{B_0^2}{\sqrt{\alpha B_0^{1/2} + \beta B_0^2}}, \tag{1}$$

scaling with B_0 for a lossless RF coil and a lossy conductive sample ($\alpha \rightarrow 0$), and with $B_0^{7/4}$ for a lossy coil and a lossless non-conductive sample ($\beta \rightarrow 0$).

Additionally, other parameters and factors contribute to the experiment's sensitivity as well. This includes (ii) RF coil design for improved coupling of the sample's spin system to the RF coil by sample-size- and shape-matched coil geometry (e.g., flexible coil arrays in human studies), as well as minimized losses in the RF coil, achieving sample-dominated noise through the choice of size and/or cooling of the coil, and sometimes also cooling of the preamplifier. Furthermore, the (iii) relaxation properties of the sample may be optimized to increase SNR or contrast. Also, (iv) RF-pulse sequences may be optimized for particular experiments, enabling faster scanning, higher spectral or spatial resolution, featuring particular contrast modules and thus improving specificity (most often at the cost of sensitivity). Enhanced (v) polarization of the spin system even beyond the natural Boltzmann distribution can be achieved via spin transfer from electrons to nearby nuclei, dynamic nuclear polarization, or application of polarized gases (*in vivo*). An interesting alternative (vi) to improve the detection sensitivity at very low field are quantum detectors such as SQUID (Superconducting Quantum Interference Device) [2, 3]. They work in the presence of metallic objects and makes imaging possible in the presence of large susceptibility. Though currently limited to ultra-low fields this technique may hold great potential for future interesting applications.

However, it is the magnetic flux density B_0 ("field strength"), that determines the initial Boltzmann population and the Larmor frequency of the nuclear spins, which are relevant in all fields and applications of NMR, and it is therefore the focus of this review.

Already, developments of ultra-high field hybrid MR systems (resistive and superconducting) are in progress [4, 5], providing up to 45 Tesla (with 3 cm bore size), and which are used in material research [6]. To employ such high fields for analytical NMR or animal studies would require further improvements in field stability and homogeneity for larger bore diameters, as well as a significant reduction in costs for the magnet itself, installation and running costs. Currently, a 14 T magnet (83 cm warm bore)[2] is designed for the German Cancer Centre, Heidelberg, Germany. Furthermore, a conceptual design for a 20 T human head magnet (68 cm warm bore, i.e., without gradient coil; homogeneity yet unknown) as well as a conceptual study toward a 60 T dc magnet (bore size and homogeneity yet unknown) is underway at the National High Magnetic Field Laboratory at Florida State University, Tallahassee, USA [6].

The dissipationless superconductivity only occurs below a certain critical current which is a function of the magnetic field and temperature, and this critical current is strongly dependent upon the metallurgical state of the superconducting material. It is important to note that a wire in the superconducting state can have a non-zero resistivity, and this dissipative state shall not be reached in a superconducting coil. If this occurs and the energy dissipation cannot be evacuated, the superconductor can quench, i.e., transiting to the normal state via a thermal runaway.

The superconducting parts of most current magnets are composed of type II superconductors like niobium-titanium (Nb-Ti). This material has a critical temperature of 10 K and can superconduct at up to about 15 T (upper critical field H_{c2}). More expensive magnets can be made of niobium-tin (Nb_3Sn). These have a T_c of 18 K. When operating at 4.2 K (the boiling point of liquid helium) they are able to withstand a much higher magnetic field strength, up to 20 T. Unfortunately, it is far more difficult to produce the required filaments from this material which is rather brittle. This is why sometimes a combination of Nb_3Sn for the high-field sections and Nb-Ti for the lower-field sections is used [7].

When the magnetic field is further increased, the critical temperature drops below 4.2 K and the boiling point of liquid Helium has to be lowered to ~1.9–2 K by reducing the pressure to 10–20 mbar. Through this technique the superconductivity of Nb_3Sn can be extended to around 23–25 T.

Only recently, hybrid magnets help to overcome this limit, by combining brittle superconductors like Nb_3Sn (for the outer magnet sections) and ceramic-based high temperature superconductors (HTS) for the inner parts [6]. Still, despite being HTS, the production of high fields with such superconducting materials requires to operate them at a temperature significantly

[2]200 tons unshielded, stored energy 660 MJ; courtesy M.E. Ladd and ASG Superconductors s.p.a., Genova, Italy.

lower than Tc and in general, the temperature of liquid helium is chosen. This may change with the development of dry cryogenics.

In **Figure 1**, the increase of magnetic flux density B_0 (in Tesla) over time is depicted for all types of commercially available magnets, i.e., in analytical NMR (left), preclinical MRI (middle), and human MRI (right) at their first commercial availability. Please note the rather similar time slopes for analytical and preclinical NMR, just shifted in time, due to the use of similar superconducting wire material, particularly Nb-Ti and Nb_3Sn, for the various NMR and MRI systems. Due to commercial and legal restraints, i.e., costs (magnet size) and safety issues, human MRI magnets show a somewhat lower slope.

In the following, we will be discussing critical steps and features in magnet and gradient development. In order to enable some transparency, we decided to list novel magnets (field strength and bore diameter) only in case they have been successfully applied in the field (or at the time of a first publication). In addition, we do not explicitly list further developments at the same field strength, e.g., actively shielded, or ultra-shielded refrigerated magnets, as they typically follow initial development within 3–10 years (depending on bore diameter).

RESISTIVE ELECTROMAGNETS, THE BEGINNING OF ANALYTICAL NMR

Early commercialization of NMR was initiated by R. Varian, based on F. Bloch's discovery of NMR in liquids [8], with the use of resistive electromagnets and employing continuous-wave (cw) sweep techniques [9, 10]. Varian Inc. provided commercial NMR instruments ranging from a proton resonance frequency of 30 MHz in 1952 to 100 MHz in 1962. *"The most successful Varian instruments, such as the HR30 (1952), HR40 (1955), HR60 (1958), and HR100 (1959), were all high resolution solution-state spectrometers that were based on continuous-wave (cw) sweep methods and on electromagnets."* [9] For routine chemical analyses at that time, the AR60 (60 MHz) was the workhorse, providing sufficient data quality and best value; as well as flexibility. In fact the famous imaging experiment designed by Lauterbur [11] was performed on such a system.

Despite the increases in flux density or field strength (and, thus, resonance frequency), overall sensitivity remained low due to the very slow cw measurement technique used at the time. Thus, stability, which was critically related to the stability of the electrical power supply, was a critical issue (**Figures 1**, **2**, bottom left).

Although the technique started maturing, and chemical shifts were experimentally discovered and (partially) theoretically understood, chemists were reluctant to move from already established analytical tools, based on optical spectroscopy (UV/Vis, IR) and X-ray absorption and diffraction methods, to NMR [9, 12].

Besides improving sensitivity and reducing measurement time, the increased flux density B_0 additionally increases spectral dispersion. Provided sufficient field stability during long experimental runs, more and more fine details in NMR spectra could be resolved with the advent of shim tools for creating homogeneous magnetic fields, enabling sub-Hertz spectral resolution.

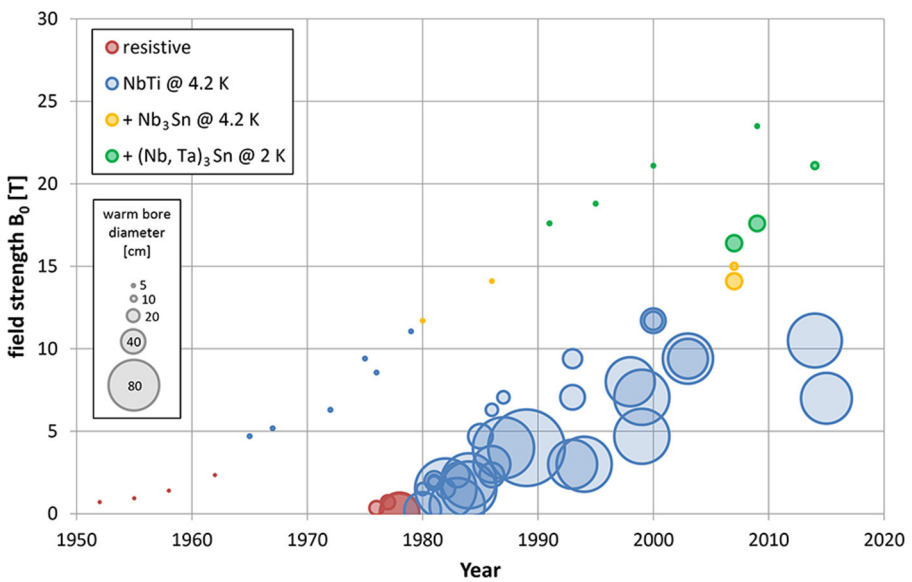

FIGURE 1 | Increase in field strength (and bore diameter) of commercially available NMR systems for analytical (points, left), biomedical and preclinical (small circles, middle), and human MRI and MRS (big circles, right). Please note the rather similar slopes of the analytical NMR and preclinical MR development, which are delayed in time by ~15 years. Both preclinical and human MR magnets started to evolve with the availability of reliable superconductor technology around the year 1980. The slope for human magnet development is less steep, likely due to costs (size of the magnet) and legal constraints (slowly increasing upper legal limits for field strength *in vivo*). References for all data points are given in the Supplementary Materials.

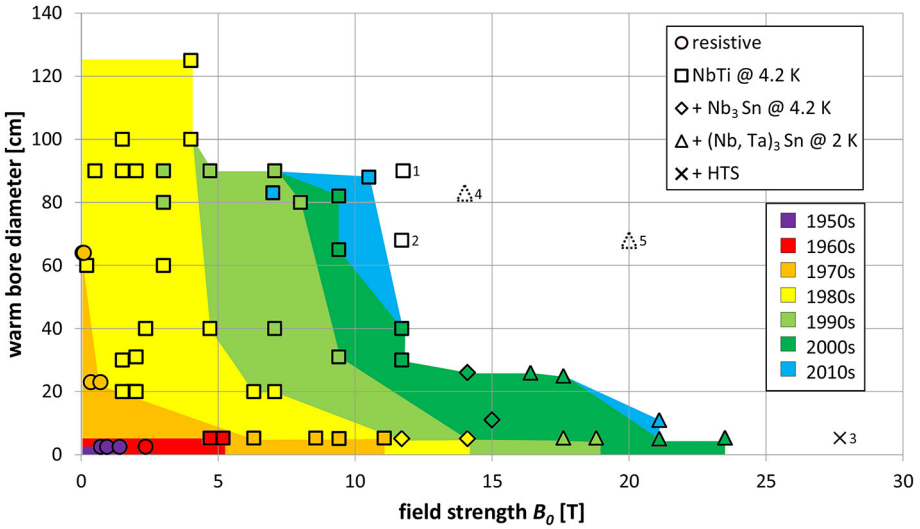

FIGURE 2 | Dependence of magnetic flux density (T) and bore size (cm) with color coding for the decade when the respective system was introduced. The shapes of the symbols represent the materials used for the magnet, as indicated in the legend. Magnets that have been successfully deployed in the field are shown with colored symbols. Symbols without color represent systems that have been installed, but are not yet fully functional (solid lines) or design studies (dotted lines). Details for these planned systems: (1) 11.75 T whole-body system CEA-Iseult, France, (2) 11.7 T head system, NIH, USA, (3) 28.2 T vertical bore system Garching, Germany, (4) Design study for 14 T whole-body system Heidelberg, Germany, (5) Design study for 20 T head system. Data and references for all data points are given in the Supplementary Materials. Fundamental limits due to the material are easily noticeable: in the lower left corner (i.e., low field strengths and small magnet bores) resistive magnets (copper wire) are clustered, with the superconducting magnets above (i.e., larger bores) and to the right (higher fields). Starting from ∼11 to 12 T, Nb_3Sn is used in addition to Nb-Ti; from ∼15 T, $(Nb,Ta)_3Sn$ is added. For the 28.2 T system, high-temperature superconductor is added.

Applications of *in vivo* systems started emerging, too. Already in 1965, proton NMR relaxation times of living frog muscle were published [13], and in 1968 the first whole-body spectrum of a rat was taken [14]. In the 1960s and 1970s a very large amount of work was published on relaxation, diffusion, and chemical exchange of water in cells and tissues of all sorts.

The highest field strength obtained with air cooled resistive electromagnets suitable for NMR, i.e., with an open gap of 2.5 cm, was first commercially achievable in 1962. In parallel, already starting in 1955, the first operational superconducting (sc) magnet based on Nb wire and operating at 0.7 T [15] was developed.

It was discovered at this early stage, that the critical current in a magnetic field could be increased by cold working of the wire (creating flux pins) and reduced by annealing. Obviously, this changes the critical current I_c and the upper critical field H_{2c}.

Several years later favorable sc properties of Nb-Ti alloys, i.e., high critical magnetic fields and high critical current densities, were discovered and paved the way for commercial use in high field magnets [16]. It took some more time to produce truly reliable superconducting wires based on Nb-Ti multifilaments embedded in a copper matrix, which could then be commercially used for large scale magnet production [7, 17]. The main reason for the long delay was flux jumping at increasing field strength, which strongly reduced the critical current and, thus, the achievable magnetic field strength [18]. Development was initially driven by requests from high energy physics, e.g., for particle accelerators, the production of superconducting magnets only became commercially viable around 1980 through the advent of large whole-body MRI magnets which by now is still, commercially speaking, the by far dominant application in terms of world sales of superconducting systems.

Bruker Spectrospin led by G. Laukien and T. Keller, and based on Trueb-Taeuber's expertise in high resolution NMR (supported by H. H. Guenthard and H. Primas from the University of Zurich), started later, however, turned out to be more innovative and flexible. In 1967 they built the first fully transistorized NMR spectrometer (HFX90) with three independent RF channels, for data acquisition, decoupling and spin-lock, allowing novel experiments and strongly simplifying routine experiments. In 1969, Bruker Inc. presented the first pulsed FT-NMR spectrometer based on Richard Ernst's Fourier transform technique [9, 19], which for the first time allowed the acquisition of excellent ^{13}C-spectra. Shortly thereafter, they presented the first high field NMR spectrometer built around a superconducting magnet (WH270), kicking-off the "arms race" for ever higher and higher field strengths in analytical NMR (**Figure 1**, left).

This made the technique more and more attractive for chemists, who took advantage of the increased sensitivity, which allowed the observation of low γ nuclei and increased spectral resolution.

On the other hand, technically this also made *in vivo* MRS and MRI possible [20, 21]—see also phase B. Direct *in vivo* ^{31}P NMR spectroscopy in living cells was first performed in Oxford from 1974 on, in the group of Rex E. Richards and George K. Radda.

On 2 September 1971, Paul C. Lauterbur, a professor of chemistry at the State University of New York at Stony Brook,

patented the idea of applying magnetic field gradients in all three dimensions to create NMR images [22]. Ideas spread quickly and first NMR images were already produced in the early 1970s [11], and human fingers and wrist were originally imaged in resistive, vertical NMR magnets operating at 0.35 T [23] and 0.7 T [24]. The first *in-vivo* whole-body scan was performed on Peter Mansfield's abdomen in 1978, still using resistive electromagnets, at ultra-low field strength—0.094 T [25, 26]. Early commercial MRI scanners prescribed for clinical diagnosis, e.g., Bruker's Tomikon, were also still based on resistive electromagnets with iron yokes, operating between 0.1 T and 0.28 T. Due to field stability limitations, counterbalanced by an iron-yoke and dedicated electronics, only T_2-weighted-imaging was feasible at sufficient quality and speed. The first large superconducting magnet was designed and built by Oxford Instruments (OI) around 1980, and the first prototype MRI system was installed at the Hammersmith Hospital, London (UK).

This phase has been highlighted by the two Nobel prizes in Chemistry for Richard R. Ernst (1991) and Kurt Wuethrich (2002), both from the ETH Zurich, and Paul C. Lauterbur and Peter Mansfield in Medicine (2003) but the full success in terms of applications only came during phase C—the Golden Age of NMR.

The upper limit for fully resistive magnets that have been reached so far are currently installed in Hefei, China (38.52 T in 32 mm), Nijmegen, The Netherlands (37.53 T in 32 mm), Tallahassee, USA, and Grenoble, Switzerland (36 T in 32 mm and 34 mm, respectively). However, they require electrical power typically in the range 24–30 MW. All resistive magnets except those from Grenoble are of Florida Bitter type.

PERMANENT MAGNETS, THE LOW COST ALTERNATIVE

In parallel, low-resolution NMR systems based on permanent magnets (typically $\leq$0.5 T or 20 MHz, using various rare earth materials) have been applied to measure relaxation times in fluids, cells and excised animal or human tissue. These systems provide a cost-effective and simple alternative to high-resolution systems required in analytical chemistry. This is mainly due to low electric power requirements, low stray fields, and, thus, low production and siting costs (even bench top systems are available).

Erik Odeblad, a gynecologist, after his stay at Stanford at about the time of Bloch's discovery, went back to Stockholm and, together with G. Lindstroem, built his own low-resolution NMR spectrometer. *Widely unnoticed by the scientific NMR community they found out, and already published in 1955* [27]*, that different tissues had distinct relaxation times, most likely due to different water content but also due to different compartmentalization and interections with lipids—a phenomenon that explains tissue contrast in MR imaging. Odeblad continued working on human fluids and tissues throughout the following decades and a large number of scientific papers on NMR relaxation in human tissues and secretions of mucous membranes followed until 1968* [22]. In 1975 Bruker presented the first commercial 20 MHz low-resolution spectrometer for industrial applications, like food quality control, also used to measure soft tissues and body fluids. A large number of studies between the 1960s and 1990s have been published by several research groups using low resolution ^{1}H-relaxometry to study relaxation time differences in different animal and human tissue *ex vivo*, at different field strength [28, 29] and under different storage conditions [30, 31]. Low-resolution, low-cost NMR is still in use today (e.g., Bruker's Minispec product line), particularly for quality control in the food industry and for well logging [32].

For historical purpose we should mention that for a certain period of time scaled-up permanent magnets were used for human MRI (e.g., FONAR Corp. 1980), however, they were severely limited by their weight (up to 300 t), cost and low field homogeneity. In addition, FONAR announced the first vertical MRI in 1996 and upright human MRI in 1999, enabling dynamic weight-bearing multi-position MRI at 0.6 T [33], potentially useful for claustrophobic patients.

Today, cost effective and custom made, small-size permanent magnets (0.3 T–0.4 T) can already be home made in a 3D-printer in all kinds of shapes and field profiles using polymer-bonded magnetic material [34].

SUPERCONDUCTING ELECTROMAGNETS, THE GOLDEN AGE OF NMR

All superconducting magnets developed so far for analytical NMR, and preclinical or human MRI and MRS, employ Nb-Ti or Nb_3Sn as the superconducting material and copper as stabilizer and enforcement material. This works up to a certain field strength and bore diameter as the hoop stress $F/S = a\ J\ B\ R$ (with a a geometrical factor, J the current density, B the flux density proportional to J, R the radius) increases quadratically with the current density J. This sets an upper limit for the use of Nb-Ti/Nb_3Sn and copper [4, 6]. Using Nb_3Sn is more expensive, because the material is rather brittle, and e.g., for field strengths higher than 12 T for a large bore magnet would therefore require high temperature superconductors (HTS) and steel enforcement as well [6].

The stored energy in the magnet coil $E = L\,x\,I^2/2$ (with L being the self-inductance of the coil and I the current) is plotted against the magnetic flux F in **Figure 3**, empirically showing a quadratic dependence.

Analytical NMR

The reason for the success of NMR in chemistry is that it does not require extensive sample preparation (e.g., crystallization), studies molecules in solution in their natural environment and can identify topological relationships between nuclei through their scalar coupling and dipolar interactions. Moving from organic chemistry to structural biology allows studies of the structure, dynamics and function of larger and more complex biological macromolecules [35].

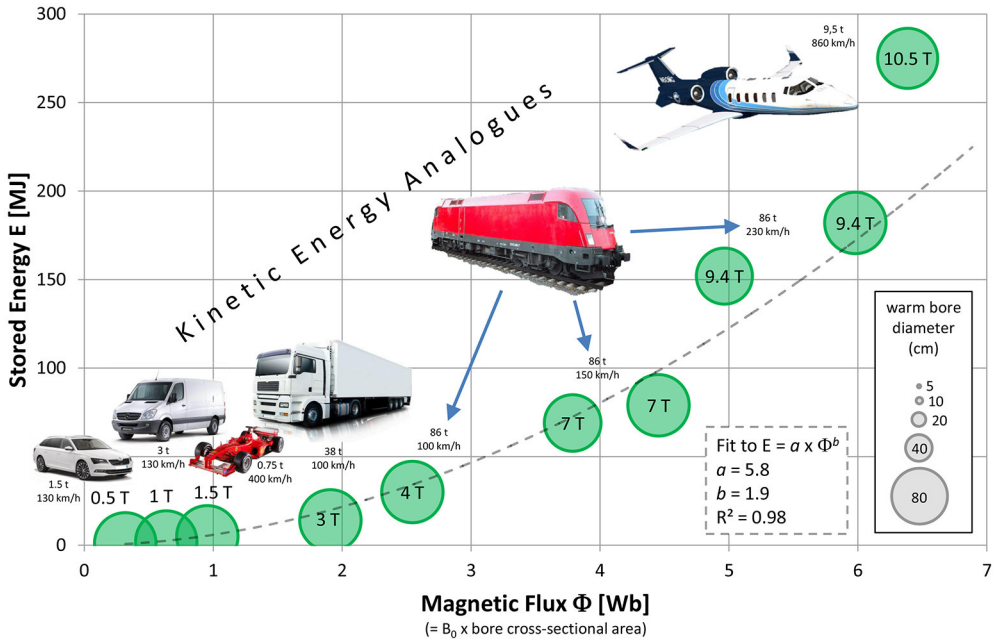

FIGURE 3 | Amount of energy stored in the magnet vs. magnetic flux (calculated from the warm bore diameter), showing an empirical trend of quadratic increase (dotted line). For illustration, everyday analogs in the form of vehicles with kinetic energy similar to the stored energies are depicted with their respective masses and velocities. Data and references for all data points are given in the Supplementary Materials. Please note that more precisely, the diameter of the magnet coils instead of the warm bore diameter should have been used for the calculation of magnetic flux; unfortunately this data could not be retrieved. However, when adding a constant offset in the range of 5–15 cm to the bore diameters for all data points, the fit still yields the quadratic dependence and only differs in its steepness *a*.

However, the extension to higher molecular mass also requires higher magnetic fields. In addition, more complex multidimensional experiments are employed and concentrations of interesting molecule are low (<1 mM). Furthermore, higher throughput in commercial applications requires shorter experiment times. Altogether, this requires higher and higher field strengths. Thus, the driving force in NMR has been the scientific quest to study more complex molecules and interactions leading to a field increase over the last 40 or so years of about 20 MHz (or 0.5 T) per year on average (**Figure 1**, left). As spectral resolution increases linearly with B_0 and the sensitivity in small, non-conducting samples with ${B_0}^{7/4}$, the acquisition time can be reduced by almost $1/{B_0}^3$. Thus, nothing other than economical aspects will slow down the quest for ever higher magnetic fields in NMR. **Figure 1** (left) visualizes this success story of the past 65 years, moving from 30 to 100 MHz using resistive, air-cooled electromagnets, to Nb-Ti single- and multifilament sc magnets up to 400 MHz (9.4 T) and using combined Nb-Ti and Nb_3Sn multifilament wires up to 600 MHz (14.1 T) at boiling He temperature (4.2 K). Above 15 T sc-wires are manufactured from (Nb, Ta)$_3$Sn, Nb_3Sn and Nb-Ti, and to further increase the current density wires are now square shaped and can operate up to 800 MHz (18.8 T) at 4.2 K and up to 1,000 MHz (23.5 T), if cooled to 2 K. All magnets in NMR are vertical, narrow (50–54 mm) or wide (89–110 mm) bore. To improve NMR safety and siting requirements, actively shielded high-field NMR magnets have been developed starting in 1995. As a downside, magnet costs and weight increases due to a 30% loss in B_0 and increased amount of sc wire for the active shielding.

The strongest commercially available magnet currently used in the field operates at 23.5 T, weighs 12 tons and is 4.5 m tall. It was first installed at the European Center for High Field NMR (CRNM) in Lyon, France, in 2009 at the cost of € 11.7 million. Subsequently, a new generation 1 GHz system, this time including active shielding and Helium refrigeration and recovery was installed at the University of Bayreuth, Germany, between 2015/2016. At 1 GHz new horizons open in structural biology, metabolomics and material science. Although the increase in field strength is only about 11% over previously available 900 MHz spectrometers, there is a significant increase in speed and sensitivity for low concentration samples [36].

Naturally, not every university or research center will be able to install such a system, the CRNM—funded also via the EU—is a resource for the whole NMR research community. Along this avenue, several universities world-wide already ordered a next generation 1.2 GHz spectrometer from Bruker; expected delivery time is 2017/18. Technically, the 1.2 GHz and higher systems depend on further progress in HTS conductor developments and HTS-based NMR magnet technology, including superconducting joints, switches and cables. Application wise, such systems will open up a broad range of interdisciplinary research applications in structural biology, catalysis, sustainable energy development as well as biomedical applications, to name just a few [35, 37].

Biomedical and Preclinical MRI and MRS Research

After early attempts on whole animals [14], numerous studies of live, intact animals took place in the 1970s to investigate anatomy, biochemistry, and physiology *in vivo* [38–41], also using perfused organs (e.g., [42–44]). In 1979, Britton Chance at University of Pennsylvania (PA, USA), contacted OI (UK) to design and build the first horizontal 1.5 T/20 cm magnet for metabolic research. This MRS system had no shimming capabilities and no gradients, thus could be used only for ^{31}P-MRS with small local Tx/Rx (transmit/receive)-coils. It was used to study human arm muscle as well as small animals. A similar magnet was delivered to Harvard University (MA, USA) in 1980 and, subsequently, the first magnet, which was a commercial product (1.5 T/30 cm) was delivered to G. K. Radda at Oxford University by OI [38]. Magnetic field strength for preclinical MRI and MRS scanners always followed in between the development for analytical NMR and human scanners (**Figure 1**, middle), just varying with bore diameter (i.e., about 10–20 cm for mice and rats and up to 40 cm for larger animals). Nowadays, high-field, small bore (horizontal) MRI and MRS scanners have been installed in most biomedical research institutions and research driven medical universities. Although various types of animals are being studied, the main targets still are rats and mice due to availability, cost, and the possibility to create genetically modified knock-out strains. As particularly large numbers of specifically modified mice are available today, noninvasive imaging is very attractive for mice phenotyping. Therefore, dedicated mouse imaging centers have been established and are frequently used to study genetic defects and to develop novel pharmaceuticals [45]. In parallel, substantial progress in the diversification and innovation of MR methods and increased sensitivity due to improving hardware and, particularly ultra-high-field magnets, provided a strong impetus to multi-parametric MRI and MRS of (small) laboratory animals [45, 46].

To further enhance sensitivity, without the need for increased magnetic field strength, cryo-cooled (20-25K) RF coils have been developed [47]. This drastically reduces the thermal noise and is a rather cost effective way to substantially improve sensitivity and still work at well established field strengths and frequencies between 7 T (300 MHz) and 11.7 T (500 MHz). However, at higher frequencies this approach becomes less effective because already for small coil (element) diameters the noise becomes sample-dominated. Although even stronger magnets are available for MRI of mice, i.e., up to 21.1 T, both costs and requirement for installation and operation of such systems limit their widespread use. Furthermore, physiological effects may limit studies on awake, behaving animals at 14 T or higher [48]. Whether or not this may also affect functional and metabolic studies in anesthetized animals yet has to be shown.

Clinical MRI and MR Research Using Whole-Body Superconductors

First images of human finger and wrist were taken at Nottingham still using vertical bore, resistive magnets (0.35 T and 0.7 T, respectively) in 1977 [23, 24, 26]. Human whole-body MRI prototype scanners have been co-developed by OI and installed during the late 1970s, employing resistive electromagnets operating at 0.05 T in Aberdeen and 0.094 T at Nottingham [20, 21, 25, 26, 49]. Homogeneity over a sufficiently large volume as well as long-term field stability (temperature dependent) was critical though. The first MRI scanner installed at a private radiology unit was probably Bruker's Tomikon using resistive electromagnets at 0.1 T and up to 0.23 T.

In parallel to proton MR imaging, metabolic research using ^{31}P MRS was performed mainly by research groups in the UK and USA. There the focus was on cerebral metabolism in newborns [50, 51] and adult muscle metabolism [52, 53]. Due to the limited sensitivity for low-γ nuclei and high requirements on technical and biochemical expertise, however, this application was less successful in a clinical setting despite high expectations [54].

High-quality clinical MRI became commercially available only in the mid 1980s, after superconductors (using Nb-Ti filaments in a copper matrix) could be employed successfully for whole-body magnets. Already in 1985 the first 10 commercial "high-field" (= 1.5 T) MRI systems have been installed, although the majority of the clinical MRI systems at that time operated at <1 T (in the early days of MRI there have been intense discussions about the optimum field strength, i.e., sensitivity/image SNR vs. specificity/tissue contrast). The total numbers installed increased steadily until 1992 where about 1250 units have been sold world-wide. In 1997 it became obvious that the low field systems are on a decline and 1.5 T became the "standard" clinical field strength. Due to the increased sensitivity, not only via B_0 but RF-coil design, contrast agents and fast imaging protocols, speed and contrast could be improved significantly. By 2003 about 65% of all MRI systems installed operated at 1.5 T (this very year already about 2,750 units have been sold). Research at 3 T started in the late 1980s (3T/80 cm, Detroit), on passively shielded prototype systems with fast gradients and local transmit-receive coils. Today, MRI is widely used for non-invasive imaging of internal body structures, providing high soft tissues contrast, at field strengths up to 3 T for clinical routine and 7 T, 9.4 T and 10.5 T (a 11.7 T for head only MRI scanner was designed, however, at the time of writing this magnet was out of order due to magnet quench) for research only [55–63].

Supporting particularly the booming field of functional MRI including BOLD-based contrast, started in the early 1990s, 3 T systems with strong and fast gradient coils have been developed in parallel and the first "high end" routine MRI systems operating at that field strength became commercially available in 2000. Together with "parallel imaging," i.e., array coils and SENSE [64]/GRAPPA [65] techniques, this move turned out to be extremely successful and quickly, i.e., within 10 years, 20% of all MRI sales are 3 T. BOLD-based fmri, greatly benefitting from the increased B_0 and faster/stronger gradients, was the driving force for developments and sales of 3 T systems. The following decade in clinical routine and research was characterized by a plateau in terms of newly installed systems (about 3,000 units p.a.), where 3 T systems started replacing the lower field units. Robust and strong/fast gradient

coils and efficient phased-array RF-coils (requiring multi-channel receive electronics) helped to constantly improve (fast) imaging performance. Again, the higher sensitivity achievable could be used for speed and increasing specificity, now also via multi-parametric imaging, e.g., combining structural and functional MRI, resulting in exam times still well tolerated by patients. For high resolution, localized MR spectroscopy of non-proton nuclei (e.g., ^{31}P, ^{13}C), the sensitivity was still too low to incorporate such a protocol into clinical routine. By 2015, about 60 % of all clinical MRI volume sales were achieved for 1.5 T, 34% for 3 T systems (slowly replacing current 1.5 T scanners), and a rather stable 6 % for low field scanners (<0.5 T). Although a few 4 T and 4.7 T prototype magnets have been installed since 1988, stronger magnets have been operating at 7 T for UHF research only [57, 58, 61, 66, 67]. Thus, 7 T human whole body scanners are currently only being installed in selected high end (clinical) research units (with about 70 systems installed so far). Currently, FDA approval has been obtained only for Siemens' 7 T Terra system, centered around an active shielded compact magnet and standard operating software/console.

A first 8 T Magnex prototype UHF magnet was installed at Ohio State University (1998) and has been operating for some time [59]

Shortly before he died in January of 1988, physicist I.I. Rabi was scanned in an MRI machine. When looking at his MR image he said "I never thought my work would come to this." (adopted from [68]).

This phase was essential for the Nobel Prize in Medicine or Physiology, awarded to Paul C. Lauterbur (Illinois, USA) and Sir Peter Mansfield (Nottingham, UK) in 2003, although their relevant scientific work started much earlier using resistive electromagnets but strongly stimulated the rapid development of human MRI—using whole-body, high-field superconducting magnets—and a wide range of still vivid methodological research and, subsequently, clinical applications.

HYBRID MAGNETS, BACK TO THE FUTURE

In order to be able to further increase the (persistent) static (dc) magnetic field, i.e., sensitivity in NMR, hybrid magnet concepts have been pursued for some time [5, 6]. Combining superconductors and resistive electromagnets, hybrid magnets allowed engineers to create a dc magnetic field of about 45 T, where the outer superconducting coil consists of three grades of Nb_3Sn CICC and the resistive coil insert consists of four nested Florida-Bitter coils [6]. However, the free inner bore is only 54 mm (unshimmed 50 ppm), intended to provide 1 ppm homogeneity and stability over a 1 cm diameter spherical volume. Nevertheless, in depth studies have started to design a 60 T dc magnet at the National High Magnetic Field Laboratory in Florida, using also HTS cables [6]. In addition to known problems of field stability and homogeneity, the energy stored and mechanical forces will dramatically increase (**Figure 3**), requiring novel concepts like steel enforcement and superconducting cables. Last but not least, extremely high costs currently prevent commercialization of these designs.

Innovation and Commercialization

The NMR/MRI market has always been dominated by a limited number of companies. Very early on Varian Inc., an innovation leader, developed a dominant position in the NMR market. In the late 1960s a young, entrepreneurial European company (Bruker Inc.) gained on the change in technology, i.e., from resistive to superconducting magnets and from CW to FT experiments, and built a strong position in analytical NMR and, later, biomedical and preclinical MRS and MRI. Nevertheless, Varian, taken over by Agilent in 2008, still was a strong player in the field until 2013. Obviously, a series of management decisions (e.g., to stop producing UHF NMR magnets beyond 200 MHz), and relying on third party magnet manufacturers instead, as well as an overgrown bureaucracy led to an unfavorable end of a once famous company [69].

Intermagnetics General Corporation (IGC), founded 1971 as a spin-off of General Electric (GE), was an early provider of (superconducting) wire and magnets. In 1974 IGC became independent of GE and had its initial public offering in 1981. In the early 1980s, for most clinical MRI systems (e.g., Picker, Diasonics, Technicare as well as GE, Siemens, and Philips) superconducting magnets were provided either by IGC or OI and later Oxford Magnet Technology (OMT), a subsidary of OI (1989 a joint venture between OI/OMT and Siemens was signed and OMT fully taken over by Siemens in 2003 and renamed SMT). Philips Medical Systems ordered their magnets mostly from IGC and finally acquired IGC in 2006. General Electric Medical Systems (GEMS) first ordered magnets also from IGC and later developed their own magnets in a facility in Florence, SC (South Carolina). Magnex Scientific Ltd. (MAGNEX) was founded in 1982 and delivered 0.5 T and 1.5 T magnets for Elscint starting 1983. In 1988 MAGNEX developed the first shielded 3 T MRI magnet (80 cm WB) for the Henry Ford Hospital (Detroit, USA). After a strategic partnership of MAGNEX and GEMS in 1996 the clinical business of MAGNEX was sold to GEMS in 2000 (for the only purpose to have 3 T technology available). Eventually, all clinical MRI manufacturers, including also Hitachi and Toshiba, had their own magnet production secured in order to be able to control quality and costs. In 1998 MAGNEX developed the first 8 T whole-body research magnet for Ohio State University and in 1999 the first 7 T clinical research magnet for University of Minnesota. GEMS, however, decided very early on to stop their activities in UHF magnets manufacturing for humans, which was based on MAGNEX technology, they rather invested in the application of hyperpolarized gases to increase much needed sensitivity. The research division of MAGNEX supplied MRS products and was transferred to Varian Inc. starting 2002, and Varian Inc. acquired Magnex Scientific Ltd. in 2004. Tesla Inc. was founded in 2014 in the UK after Agilent/Varian announced closure of the production of specialty UHF magnets for human MRI and MRS research. The near future will show whether magnet concepts developed for accelerators in high energy physics and for fusion reactors such as ITER, i.e.,

high field, low He use, may be transferred to perform in UHF human MRI.

Safety Issues Due to Static Magnetic Fields

Finally, we should not miss to summarize our current knowledge of safety issues concerning static magnetic fields and safety precautions in case of a magnet quench [70]. Empirically, most people experience some physiological sensations when moving their head in/into a 3 T magnet or even more so in a stronger magnetic field, like a certain metallic taste, dizziness, or short flashes of light (i.e., phosphenes) even when eyes are closed. When they stop moving or get out of the magnet these sensations disappear. As early as 1986 the Oxford group led by Radda (at 1.6 T) and in 1999 the Ohio group led by Robitaille performed studies on swine and humans in order to elucidate potential side effects of strong static magnetic fields on physiological or cognitive functions. The latter study of 10 healthy human subjects provided no evidence of measurable changes in body temperature, heart rate, respiratory rate, systolic pressure, or diastolic blood pressure after 1 h of exposure at 8 T [71]. Furthermore, no cognitive changes were noticeable. However, significant ECG changes have been noted which were related both to the position of the subject in the magnet and to the strength of the static magnetic field. Thus, the common ECG tracing was no longer diagnostically useful when performed at 8 T. Nevertheless, all (healthy) subjects showed normal ECG readings before and after the exposure to the 8 T static magnetic field. In addition, cardiac function was examined in some detail in an anesthetized swine. No significant changes in *"body temperature, heart rate, left ventricular pressure, left ventricular end diastolic pressure, time rate of change of left ventricular pressure, myocardial stiffness index, cardiac output, systolic volume, troponin, and potassium levels could be detected following 3 h of exposure to a field strength of 8.0 tesla. It is concluded that no short term cardiac or cognitive effects are observed following significant exposure to a magnetic field of up to 8.0 tesla."* Following up on this and due to the increase in UHF magnets installed world-wide a special issue on *Effects of static* magnetic *fields relevant to human health* appeared in the journal Progress in Biophysics and Molecular Biology in 2005 (Volume 87). Again, it was concluded that *"no permanent adverse effect on human subjects when exposed to static magnetic fields in strengths of up to 8 T could be detected. Also, there is no evidence of any clinically relevant alteration in human neuro-cognitive function related to static magnetic field exposure. Results suggest that the cognitive–motor (eye–hand coordination) and the sensory (near-visual contrast sensitivity) function are negatively influenced by exposure to magnetic fields as low as 700 mT. Although these effects are undesirable in interventional MRI procedures (and potentially affect functional MRI studies), it is not clear how these transient effects relate to actual performance in a clinical setting. The risks related to the interaction of a static magnetic field and magnetic or electrical hardware are much greater than the apparent biological interaction risks to human subjects alone."* [72].

However, an epidemiological review by Feychting [73] within the same journal/issue concludes that "the available evidence from epidemiological studies is not sufficient to draw any conclusions about potential health effects of static magnetic field exposure." Nevertheless, counting on numerous staff working at various field strength over decades, it seems unlikely that typical exposure to static magnetic fields of a few hours per day in the fringe field (i.e., below about 1 T at a clinical 3 T MRI system or below 2 T at a 7 T UHF MR system) will cause severe long term health problems (Personal Note: all authors had been exposed to strong static magnetic fields for decades without any adverse effects so far besides the dizziness effects while entering the magnet bore).

On the other hand, implanted ferromagnetic devices within patients (e.g., life supporting pace makers, passive hip or knee implants are less affected) and physical interactions between external magnetic material (like coins, working tools or medical equipment not checked for UHF compatibility) pose substantial hazards and represent a severe source of risk. Therefore, *it seems imperative that vigilance be maintained at ever higher field strengths to ensure that the high degree of patient and staff safety so far associated with clinical MRI and high field research is maintained* [74]. Especially, due to the shorter wavelength of the radio frequency fields at higher static field conductive implants and other metallic objects must be treated with caution, e.g., by accurate electromagnetic simulation, or, in doubt, excluded from MR examinations to minimize the risk of burn injuries. This becomes even more complicated by parallel transmission technology.

Based on empirical evidence, revealing uncomfortable physiological sensations in some of the volunteer studied in UHF MRI, several systematic studies have been performed [75–77] and the basic mechanisms of vertigo in high magnetic fields described [76, 78]. Despite the low magnetic susceptibility of human tissues and the lack of any substantial amount of ferromagnetic material typically occurring in healthy subjects, experimental evidence supports the hypothesis that magnetic-field related vertigo results from both magnetic susceptibility differences between vestibular organs and surrounding fluid, and induced currents acting on the vestibular hair cells. Both mechanisms are consistent with theoretical predictions [76]. This may cause a limit for routine clinical examinations at 7 T or higher [48, 79], as up to 12 % of healthy subjects experience such a brain exam as unpleasant. However, it should also be noted that subjective perception of metallic taste, vertigo and nausea may vary widely and that there exists a drug to prevent or reduce vertigo and nausea [80].

Future Directions in Human MRI and MRS

Analytical NMR

It seems obvious that the magnet development in analytical NMR is approaching technical limits. First, frequencies of 1,200 MHz and above cause technical problems in coil/probe manufacturing. Second, RF-penetration limits further frequency increase (unless sample size/volume is reduced, which again reduces sensitivity), and, third,

economics. Most routine applications in NMR work efficiently and cost effectively at 400–600 MHz, with special research applications at 800–1,200 MHz. Therefore, strategies to improve SNR even at lower field are requested and may be preferred as cost saving alternatives for routine analytical NMR [37].

Preclinical MRI and MRS

In preclinical MRI and MRS most labs work at field strength between 7 T (where the clear magnet bore allows application to rats), actually the bulk of preclinical research is performed at this field, and 11.7 T (at which available magnet bore diameter limits application to mice). To further increase sensitivity, either cryo-cooled probeheads and coils can be used for another $\sim$ >2-fold gain in sensitivity, which is much more cost effective than doubling the field strength [47]. Furthermore, physiological effects experienced by awake laboratory animals might limit the upper static field to about 14 T [48] and the same might apply to human subjects as well. In this regime shear forces acting in the vestibular system and between gray and white matter might be an issue [78], as well as cognitive function (e.g., in fMRI experiments). On the other hand, anesthetized animals will not be affected to the same extend.

Ultra-High Field Human MRI and MRS

Concerning ultra-high field human MRI and MRS we need to further increase sensitivity and/or speed to enable full multiparametric diagnosis within still comfortable total measurement time for patients. Also, we may trade (e.g., in fMRI/parenchyma) sensitivity for specificity (resolution vs. partial volume) if SNR is sufficient. Susceptibility based contrast in (functional) MRI benefits particularly from higher field strength, thus methods increasing specificity like spin-echo based fMRI vs. gradient-echo based fMRI may be more viable. On the other hand, we must not risk any short or long term hazard to the patient and personnel (for more details see also above), or increase discomfort due to (reversible) physiological sensations and, thus, damage the reputation and non-invasive status of the MR methods altogether [70, 74, 76, 78, 81]. In addition, a recent paper describes that one third of the patient scanned at 3 T *and* 7 T noticed stronger vertigo and nausea at the higher field strength [79].

Routine Clinical MRI and MRS

In routine clinical MRI and MRS, after about 35 years, the race for higher field strength would seem to be settled by the market already:

At the time being, about 33% of MRI sales volume per annum are 3 T, while 60 % still are 1.5 T and 6% are below 1.5 T. Thus, 1.5 T is the bread and butter field strength, covering the majority of clinical applications, and is providing the best possible compromise between sensitivity, speed, and imaging specificity (including prescription of contrast agents), and cost. This, of course, includes form and organ fitted phased-array RF-coils (enabling parallel imaging), as well as optimized MR-sequences and image reconstruction. Gradient strength achievable (45 mT/m and 200 mT/m/ms slew rate), without disturbing Peripheral Nerve Stimulation (PNS) or else seems optimal also at 1.5 T.

3 T MRIs are high-end clinical systems, particularly valuable in Neuroradiology, muscular-skeletal MRI, and clinical MRS [82].

For very specific clinical applications and research in high resolution, metabolic imaging like CEST and multi-nuclear, localized spectroscopy, 7 T is extremely useful [57, 58, 63, 66]. However, 7 T systems are more expensive and demanding in terms of siting and personnel required. Although imaging with CP transmit coils is sufficiently good for head and joints (in particular knee), parallel transmit excitation (pTx) is required to manage other organs. SAR limits are independent of field strength, but their supervision is drastically more complicated for multiple RF transmit channels with independent time-varying amplitudes and phases, especially due to a stronger dependence on the individual patient anatomy. Solution strategies have been proposed, but have not been implemented broadly in the field yet.

On the receive side, starting from 1.5 T and higher, the use of phased array receive coils has been proven advantageous. Their main benefits are the acceleration of the acquisition, shortening of TE, and/or better SNR in more superficial regions closer to the coil elements. Phased array coils are used in almost all current clinical MRI applications and are also benefitting hetero-nuclear MRS and MRSI.

Gradients, for signal localization, on the other hand are more or less independent of the field strength used, although it is also advantageous to increase gradient performance when increasing the field strength. **Figure 4A** shows the increase in peak gradient strength (mT/m) and slew rate (SR; T/m/s) of human MRI scanners over time. Clinical MRI scanners at 1.5 T nowadays use up to 45 mT/m at a slew rate (SR) of 200 T/s/m. At 3 T the high-end performance is now 80 mT/m but SR is still at 200 T/m/s due to PNS. While 7 T gradients are now in the range of 70–80 mT/m it is often desirable to go higher, but some adverse effects need to be considered, such as acoustic noise and mechanical vibrations. As it is known, the driving force behind mechanical vibration and acoustic noise is the Lorentz force, which is proportional to the field strength B_0 and the gradient strength, too. This is causing some limitations for the peak gradient strength. Slew rate on the other hand is limited by PNS, which are entirely independent of the magnetic field strength. The current limit for whole body gradients thus is SR 200 T/m/s. To get beyond this limit, one needs to either use head gradient inserts (obviously limiting the use to the head or foot) or one may relax the linearity of the gradient field and gain better performance with respect to PNS and peak gradient fields, as being done for the NIH Connectome project [83]. For that particular purpose, two dedicated gradient systems have been designed, built and installed [84] allowing either 100 mT/m peak gradients at SR 200 (installed at the Mallinckrot Institute in St. Louis, MS) or 300 mT/m at SR 200 (installed

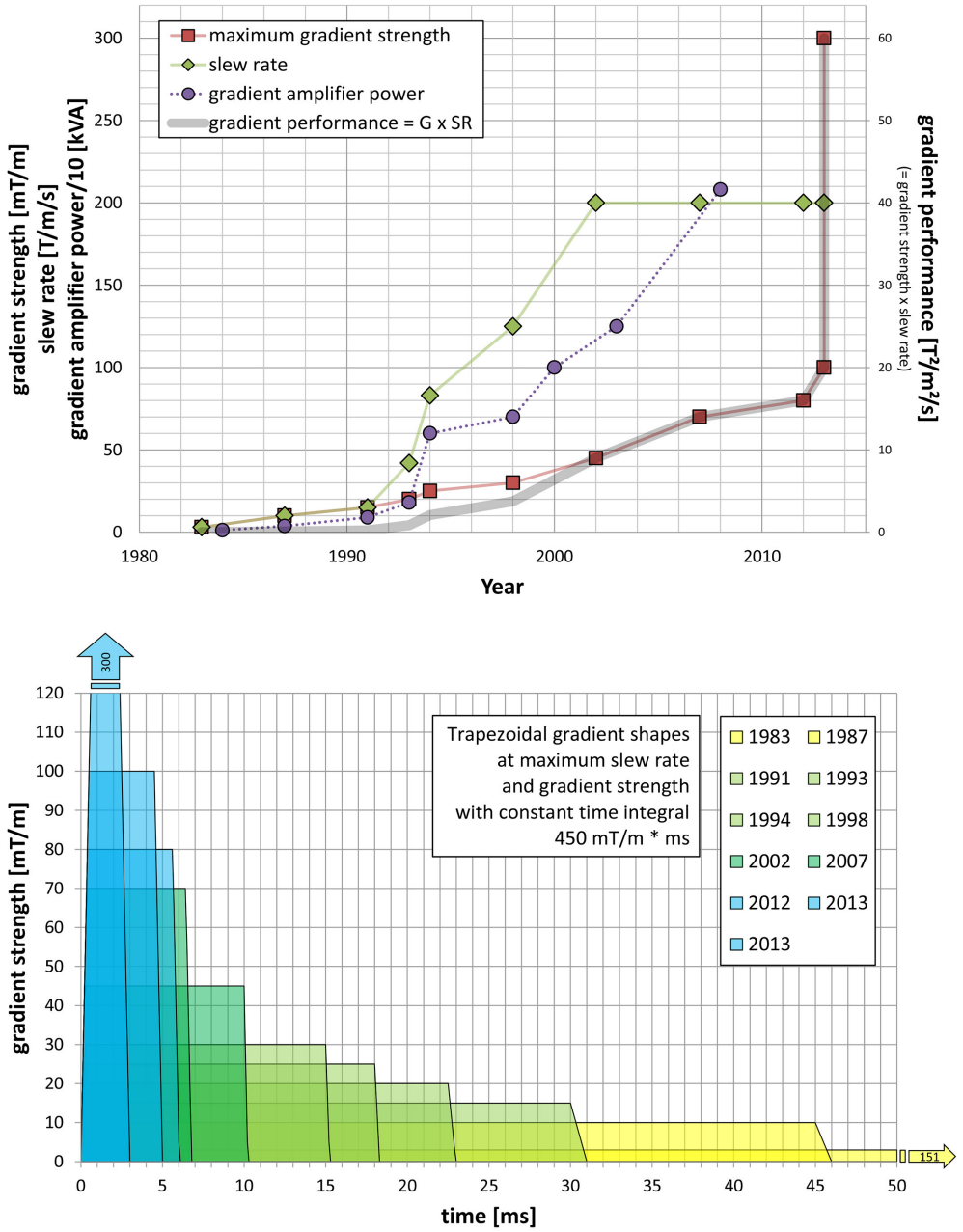

FIGURE 4 | (A) Shows the development of gradient coils for human MRS and MRI research and clinical diagnostics in terms of maximum gradient strength (mT/m, red) and slew rate (T/m/s, green), as well as gradient amplifier power development (left y-axis, purple). The product of maximum gradient strength and slew rate is the gradient performance (right y-axis, thick gray line). **(B)** Development of trapezoidal gradient shapes at maximum slew rate and gradient strength with constant time integral of 450 mT/m*ms, plus equivalent triangular gradient shape, i.e., without plateau time at the maximum gradient strength, for the strongest gradient available at a certain time.

at the A.A. Martinos Center in Charlestown, MA, USA). These strong gradients are particularly used in diffusion-weighted MRI research, revealing e.g., structure and distortions of white matter tracts in the brain [85]. When looking back at the development of gradient performance over the years, it is quite remarkable what has been achieved, i.e., an improvement better than Moore's law as can be seen in **Figure 4**, also including dedicated research systems like the Connectome scanners. Nevertheless, due to human physiology (PNS) no further increase in SR is possible for whole-body MRI (**Figure 4B**).

CONCLUSION

To summarize, for basic research in all three fields, and money not being a severe limitation, i.e., NMR, preclinical and human

MRI and MRS, higher B_0 are advantageous for research (up to known physiological limits) but not routinely required. In terms of human MRI and MRS, based on current sc-materials, technology and costs, it might be feasible to build a 14 T/83 cm magnet. As we cannot expect to further increase slew rates, also gradient coils for human use are operating at a limit. Thus, it would be best to put scientific effort into the development and optimization of novel rf-coils and phased-arrays also reducing noise sources to further push net SNR gain.

At the end of this review, we would like to modify a question posed by Nobel laureate Richard R. Ernst, one of the most proliferate contributors to the success of NMR and MRI: "Why just NMR?—"Why all the fuzz?"

Why just NMR?—*Because there is hardly another technique that is so informative for so many different types of applications, and because there is no other technique that provides so much fun.* [86]

Why all the fuzz?—Because NMR research over more than 90 years has clearly demonstrated that scientific challenges drive technology, drives research.

In this particular case, due to the persisting quest of ingenious scientists and engineers, we got an extremely versatile tool at hand, providing physicists, chemists, biochemists, researchers in life sciences and medicine, clinicians, but also nutritional chemists and well loggers, with multi-parametric information obtainable non-invasively about water and fat content, molecular motion, structure, dynamics, flow, perfusion, blood oxygenation, diffusion, susceptibility, various metabolites, from atoms and molecules to man—and down to molecular structure and dynamics in liquids, semi-solids (e.g., living tissue), and even solids.

Since ancient times physicists and engineers helped to develop novel methods and technologies to support medical diagnosis and therapy [87].

Keep going and enjoy—for more than another decade!

AUTHOR CONTRIBUTIONS

EM conceived the topic, collected the data and prepared the original manuscript. EL helped preparing the manuscript and prepared the figures. FS collected data and helped preparing the manuscript. GK critically revised the manuscript. All authors participated in manuscript review.

ACKNOWLEDGMENTS

As all history has no clear cut beginning and no end to be seen in the mist of time, we should be aware that an attempt to pick out a few aspects is prone to error. This being said, we would like to thank the many colleagues and friends who helped with additional information. However, all errors or omissions are due to our own limitations. Particularly, we would like to thank M. D. Bird (Tallahassee, FL, USA), C. Boesch (Bern, CH), A. Heerschap (Nijmegen, NL), P.R. Luijten (Utrecht, NL), M. Ilg, C. Oerther, P. Wikus, and G. Roth (Ettlingen, DE), P. A. Rinck (Sophia Antipolis, F), L. Soellner and M. Blasche (Erlangen, DE), S. Pittard, D. L. Rayner, and R. Warner (Oxford, UK). EM dedicates this review to the memory of his mentors, Britton Chance and John S. "Jack" Leigh (Philadelphia, PA, USA). Partly supported by the Austrian BMWFJ FFG Project 832107 Research Studio for Ultra-High Field MR Applications; EM acknowledges an unrestricted research grant by Siemens Healthineers (Erlangen, Germany). The funding sources had no influence on the scientific scope nor the outcome of this study.

SUPPLEMENTARY MATERIAL

The Supplementary Material for this article can be found online at: http://journal.frontiersin.org/article/10.3389/fphy.2017.00033/full#supplementary-material

REFERENCES

1. Lazarev B, Schubnikov LV. Magnetic moment of a proton. *Phys Zeitsch der Sow* (1937) **11**:445–57.
2. Espy M, Matlashov A, Volegov P. SQUID-detected ultra-low field MRI. *J Magn Reson.* (2013) **229**:127–41. doi: 10.1016/j.jmr.2013.02.009
3. Lee SK, Mößle M, Myers W, Kelso N, Trabesinger AH, Pines A, et al. SQUID-detected MRI at 132 μT with T1-weighted contrast established at 10 μT-300 mT. *Magn Reson Med.* (2005) **53**:9–14. doi: 10.1002/mrm.20316
4. Schneider-Muntau HJ. High field NMR magnets. *Solid State Nucl Magn Reson.* (1997) **9**:61–71. doi: 10.1016/S0926-2040(97)00044-1
5. Gan Z, Kwak H-T, Bird M, Cross T, Gor'kov P, Brey W, et al. High-field NMR using resistive and hybrid magnets. *J Magn Reson.* (2008) **191**:135–40. doi: 10.1016/j.jmr.2007.12.008
6. Bird MD, Dixon IR, Toth J. Large, high-field magnet projects at the NHMFL. *IEEE Trans Appl Supercond.* (2015) **25**:1–6. doi: 10.1109/TASC.2014.2367470
7. Wilson MN. *Superconducting Magnets*. Oxford, UK: Clarendon (1983).
8. Bloch F, Hansen WW, Packard M. Nuclear induction. *Phys Rev.* (1946) **69**:127. doi: 10.1103/PhysRev.69.127
9. Ernst RR. Zurich's contributions to 50 years development of bruker. *Angew Chemie Int Ed.* (2010) **49**:8310–5. doi: 10.1002/anie.201005067
10. Freeman R, Morris GA. The varian story. *J Magn Reson.* (2015) **250**:80–4.
11. Lauterbur PC. Image formation by induced local interactions. Examples employing nuclear magnetic resonance. *Nature* (1973) **242**:190–1.
12. Becker ED. A brief history of nuclear magnetic resonance. *Anal Chem.* (1993) **65**:295A–302A. doi: 10.1021/ac00054a001
13. Bratton CB, Hopkins AL, Weinberg JW. Nuclear magnetic resonance studies of living muscle. *Science* (1965) **147**:738–9. doi: 10.1126/science.147.3659.738
14. Jackson JA, Langham WH. Whole-body NMR spectrometer. *Rev Sci Instrum.* (1968) **39**:510–3.
15. Yntema GB. Superconducting winding for electromagnets. *Phys Rev.* (1955) **98**:1197.
16. Berlincourt TG, Hake RR. Pulsed-magnetic-field studies of superconducting transition metal alloys at high and low current densities. *Bull Am Phys Soc.* (1962) **II**:408.
17. Cheng-ren L, Xiao-zu W, Nong Z. Nb-Ti superconducting composite with high critical current density. *IEEE Trans Magn.* (1983) **19**:284–7. doi: 10.1109/TMAG.1983.1062365
18. Wilson MN. A century of superconducting technology. *AIP Conf Proc 1435* (2012) **11**:11–35. doi: 10.1063/1.4712077
19. Ernst RR, Anderson WA. Application of Fourier transform spectroscopy to magnetic resonance. *Rev Sci Instrum.* (1966) **37**:93–102. doi: 10.1063/1.1719961

20. Ernst RR. The advent of NMR in the light of Sir Peter Mansfield's innovations. *MAGMA* (1999). **9**:97–99.
21. Hahn EL, Mansfield P. NMR and MRI in Retrospect [and Discussion]. *Philos Trans R Soc A Math Phys Eng Sci*. (1990) **333**:403–11. doi: 10.1098/rsta.1990.0168
22. Rinck PA. *Magnetic Resonance in Medicine. The Basic Textbook of the European Magnetic Resonance Forum, 11th Edn*. E-version 11.1 beta. (2017).
23. Hinshaw WS, Bottomley PA, Holland GN. Radiographic thin-section image of the human wrist by nuclear magnetic resonance. *Nature* (1977) **270**:722–3. doi: 10.1038/270722a0
24. Mansfield P, Maudsley AA. Medical imaging by NMR. *Br J Radiol*. (1977) **50**:188–94. doi: 10.1259/0007-1285-50-591-188
25. Mansfield P, Pykett IL, Morris PG, Coupland RE. Human whole body line-scan imaging by NMR. *Br J Radiol*. (1978) **51**:921–2. doi: 10.1259/0007-1285-51-611-921
26. Morris P. Morris, Peter: whole-body MRI in nottingham: the first steps. In: Grant DM, Harris RK editors. *Encyclopedia of Magnetic Resonance*. Chichester: John Wiley & Sons, Ltd. (2012). p. 1–6.
27. Odeblad E, Lindström G. Some preliminary observations on the proton magnetic resonance in biologic samples. *Acta Radiol*. (2008) **49**:57–61. doi: 10.1080/02841850802133337
28. Rooney WD, Johnson G, Li X, Cohen ER, Kim SG, Ugurbil K, et al. Magnetic field and tissue dependencies of human brain longitudinal 1H2O relaxation *in vivo*. *Magn Reson Med*. (2007) **57**:308–18. doi: 10.1002/mrm.21122
29. Koenig SH, Brown RD. Relaxometry of tissue. In: Grant DM, Harris RK editors. *Encyclopedia of Magnetic Resonance*. Chichester: John Wiley & Sons, Ltd. (2007). doi: 10.1002/9780470034590.emrstm0466
30. Holzmueller P, Reckendorfer H, Burgmann H, Moser E. Viability testing of transplantation donor liver by1H NMR relaxometry. *Magn Reson Med*. (1990) **16**:173–8. doi: 10.1002/mrm.1910160117
31. Moser E, Holzmueller P, Reckendorfer H, Burgmann H. Cold-preserved rat liver viability testing by proton nuclear magnetic resonance relaxometry. *Transplantation* (1992) **53**:536–9.
32. Kleinberg RL, Jackson JA. An introduction to the history of NMR well logging. *Concepts Magn Reson*. (2001) **13**:340–2. doi: 10.1002/cmr.1018
33. Damadian RV, Chu D. The possible role of cranio-cervical trauma and abnormal CSF hydrodynamics in the genesis of multiple sclerosis. *Physiol Chem Phys Med NMR* (2011) **41**:1–17.
34. Huber C, Abert C, Bruckner F, Groenefeld M, Muthsam O, Schuschnigg S, et al. 3D print of polymer bonded rare-earth magnets, and 3D magnetic field scanning with an end-user 3D printer. *Appl Phys Lett*. (2016) **109**:162401. doi: 10.1063/1.4964856
35. Fan TW-M, Lane AN. Applications of NMR spectroscopy to systems biochemistry. *Prog Nucl Magn Reson Spectr*. (2016) **92–3**:18–53. doi: 10.1016/j.pnmrs.2016.01.005
36. Bhattacharya A. Breaking the billion-hertz barrier. *Nat News Featur*. (2010) **463**:605–6. doi: 10.1038/463605a.
37. Ardenkjaer-Larsen J-H, Boebinger GS, Comment A, Duckett S, Edison AS, Engelke F, et al. Facing and overcoming sensitivity challenges in biomolecular NMR spectroscopy. *Angew Chemie Int Ed*. (2015) **54**:9162–5. doi: 10.1002/anie.201410653
38. Gordon RE, Hanley PE, Shaw D, Gadian DG, Radda GK, Styles P, et al. Localization of metabolites in animals using 31P topical magnetic resonance. *Nature* (1980) **287**:736–8.
39. Bottomley PA, Kogure K, Namon R, Alonso OF. Cerebral energy metabolism in rats studied by phosphorus nuclear magnetic resonance using surface coils. *Magn Reson Imaging* (1982) **1**:81–5.
40. Koretsky AP, Wang S, Murphy-Boesch J, Klein MP, James TL, Weiner MW. 31P NMR spectroscopy of rat organs, *in situ*, using chronically implanted radiofrequency coils. *Proc Natl Acad Sci USA* (1983) **80**:7491–5.
41. Evanochko WT, Ng TC, Glickson JD. Application of *in vivo* NMR spectroscopy to cancer. *Magn Reson Med*. (1984) **1**:508–34.
42. Balaban RS, Gadian DG, Radda GK. Phosphorus nuclear magnetic resonance study of the rat kidney *in vivo*. *Kidney Int*. (1981) **20**:575–9. doi: 10.1038/ki.1981.179
43. Iles RA, Griffiths JR. Hepatic metabolism by 31P NMR. *Biosci Rep*. (1982) **2**:735–42. doi: 10.1007/BF01114837
44. Ingwall JS. Phosphorus nuclear magnetic resonance spectroscopy of cardiac and skeletal muscles. *Am J Physiol*. (1982) **242**:H729–44.
45. Heerschap A, Sommers MG, Zandt HJA, Renema WKJ, Veltien AA, Klomp DWJ. Nuclear magnetic resonance in laboratory animals. In: Conn PM editor. *Methods in Enzymology, Vol. 385*. Cambridge, MA: Elsevier (2004). p. 41–63.
46. Marzola P, Osculati F, Sbarbati A. High field MRI in preclinical research. *Eur J Radiol*. (2003) **48**:165–70. doi: 10.1016/j.ejrad.2003.08.007
47. Darrasse L, Ginefri J-C. Perspectives with cryogenic RF probes in biomedical MRI. *Biochimie* (2003) **85**:915–37. doi: 10.1016/j.biochi.2003.09.016
48. Houpt TA, Cassell JA, Riccardi C, DenBleyker MD, Hood A, Smith JC. Rats avoid high magnetic fields: dependence on an intact vestibular system. *Physiol Behav*. (2007) **92**:741–7. doi: 10.1016/j.physbeh.2007.05.062
49. Wells PN. Physics and engineering: milestones in medicine. *Med Eng Phys*. (2001) **23**:147–53. doi: 10.1016/S1350-4533(01)00042-X
50. Cady EB, Joan Dawson M, Hope PL, Tofts PS, De L. Costello AM, et al. Non-invasive investigation of cerebral metabolism in newborn infants by phosphorus nuclear magnetic resonance spectroscopy. *Lancet* (1983) **321**:1059–62. doi: 10.1016/S0140-6736(83)91906-2
51. Hope PL. Cerebral energy metabolism studied with phosphorus NMR spectroscopy in normal and birth-asphyxiated infants. *Lancet* (1984) **324**:366–70. doi: 10.1016/S0140-6736(84)90539-7
52. Chance B, Eleff S, Leigh JS, Sokolow D, Sapega A. Mitochondrial regulation of phosphocreatine/inorganic phosphate ratios in exercising human muscle: a gated 31P NMR study. *Proc Natl Acad Sci USA*. (1981) **78**:6714–8.
53. Radda GK, Bore PJ, Gadian DG, Ross BD, Styles P, Taylor DJ, Morgan-Hughes J. 31P NMR examination of two patients with NADH-CoQ reductase deficiency. *Nature* (1982) **295**:608–9. doi: 10.1038/295608a0
54. Radda G. The use of NMR spectroscopy for the understanding of disease. *Science* (1986) **233**:640–5. doi: 10.1126/science.3726553
55. Ertürk MA, Wu X, Eryaman Y, Van de Moortele PF, Auerbach EJ, Lagore RL, et al. Toward imaging the body at 10.5 tesla. *Magn Reson Med*. (2017) **77**:434–43. doi: 10.1002/mrm.26487
56. Lvovsky Y, Stautner EW, Zhang T. Novel technologies and configurations of superconducting magnets for MRI. *Supercond Sci Technol*. (2013) **26**:93001. doi: 10.1088/0953-2048/26/9/093001
57. Moser E. Ultra-high-field magnetic resonance: why and when? *World J Radiol*. (2010) **2**:37–40. doi: 10.4329/wjr.v2.i1.37
58. Moser E, Stahlberg F, Ladd ME, Trattnig S. 7T MR - from research to clinical applications? *NMR Biomed*. (2012) **25**:695–716. doi: 10.1002/nbm.1794
59. Robitaille PM, Warner R, Jagadeesh J, Abduljalil AM, Kangarlu A, Burgess RE, et al. Design and assembly of an 8 tesla whole-body MR scanner. *J Comput Assist Tomogr*. (1999) **23**:808–20.
60. Vaughan JT, Garwood M, Collins CM, Liu W, DelaBarre L, Adriany G, et al. 7T vs. 4T: RF power, homogeneity, and signal-to-noise comparison in head images. *Magn Reson Med*. (2001) **46**:24–30. doi: 10.1002/mrm.1156
61. Warner R. Ultra-high field magnets for whole-body MRI. *Supercond Sci Technol*. (2016) **29**:94006. doi: 10.1088/0953-2048/29/9/094006
62. Webb AG, Van de Moortele PF. The technological future of 7 T MRI hardware. *NMR Biomed*. (2016) **29**:1305–15. doi: 10.1002/nbm.3315
63. Zwanenburg JJM, van der Kolk AG, Luijten PR. Ultra-high-field MR imaging. *PET Clin*. (2013) **8**:311–28. doi: 10.1016/j.cpet.2013.03.004
64. Pruessmann KP, Weiger M, Scheidegger MB, Boesiger P. SENSE: sensitivity encoding for fast MRI. *Magn Reson Med*. (1999) **42**:952–62.
65. Griswold MA, Jakob PM, Heidemann RM, Nittka M, Jellus V, Wang J, et al. Generalized autocalibrating partially parallel acquisitions (GRAPPA). *Magn Reson Med*. (2002) **47**:1202–10. doi: 10.1002/mrm.10171
66. Ugurbil K, Adriany G, Andersen P, Chen W, Garwood M, Gruetter R, et al. Ultrahigh field magnetic resonance imaging and spectroscopy. *Magn Reson Imaging* (2003) **21**:1263–81. doi: 10.1016/j.mri.2003.08.027
67. Duyn JH. The future of ultra-high field MRI and fMRI for study of the human brain. *Neuroimage* (2012) **62**:1241–8. doi: 10.1016/j.neuroimage.2011.10.065
68. Tretkoff E. This Month in Physics History. July, 1977: MRI uses fundamental physics for clinical diagnosis. *Am Phys Soc News* (2006) **15**. Available online at: http://www.aps.org/publications/apsnews/200607/history.cfm
69. Freeman R, Morris GA. The Varian story. *J Magn Reson* (2015) **250**:80–4. doi: 10.1016/j.jmr.2014.12.001
70. Budinger TF. MR safety: past, present, and future from a historical perspective. *Magn Reson Imaging Clin N Am*. (1998) **6**:701–14.

71. Kangarlu A, Burgess RE, Zhu H, Nakayama T, Hamlin RL, Abduljalil AM, et al. Cognitive, cardiac, and physiological safety studies in ultra high field magnetic resonance imaging. *Magn Reson Imaging* (1999) **17**:1407–16. doi: 10.1016/S0730-725X(99)00086-7
72. Chakeres DW, de Vocht F. Static magnetic field effects on human subjects related to magnetic resonance imaging systems. *Prog Biophys Mol Biol*. (2005) **87**:255–65. doi: 10.1016/j.pbiomolbio.2004.08.012
73. Feychting M. Health effects of static magnetic fields—a review of the epidemiological evidence. *Prog Biophys Mol Biol*. (2005) **87**:241–6. doi: 10.1016/j.pbiomolbio.2004.08.007
74. Schenck JF. Physical interactions of static magnetic fields with living tissues. *Prog Biophys Mol Biol*. (2005) **87**:185–204. doi: 10.1016/j.pbiomolbio.2004.08.009
75. Cavin ID, Glover PM, Bowtell RW, Gowland PA. Thresholds for perceiving metallic taste at high magnetic field. *J Magn Reson Imaging* (2007) **26**:1357–61. doi: 10.1002/jmri.21153
76. Glover PM, Cavin I, Qian W, Bowtell R, Gowland PA. Magnetic-field-induced vertigo: a theoretical and experimental investigation. *Bioelectromagnetics* (2007) **28**:349–61. doi: 10.1002/bem.20316
77. Heilmaier C, Theysohn JM, Maderwald S, Kraff O, Ladd ME, Ladd SC. A large-scale study on subjective perception of discomfort during 7 and 1.5 T MRI examinations. *Bioelectromagnetics* (2011) **32**:610–9. doi: 10.1002/bem.20680
78. Roberts DC, Marcelli V, Gillen JS, Carey JP, Della Santina CC, Zee DS, et al. MRI magnetic field stimulates rotational sensors of the brain. *Curr Biol*. (2011) **21**:1635–40. doi: 10.1016/j.cub.2011.08.029
79. Springer E, Dymerska B, Cardoso PL, Robinson SD, Weisstanner C, Wiest R, et al. Comparison of routine brain imaging at 3 T and 7 T. *Invest Radiol*. (2016) **51**:469–82. doi: 10.1097/RLI.0000000000000256
80. Thormann M, Amthauer H, Adolf D, Wollrab A, Ricke J, Speck O. Efficacy of diphenhydramine in the prevention of vertigo and nausea at 7T MRI. *Eur J Radiol*. (2013) **82**:768–72. doi: 10.1016/j.ejrad.2011.08.001
81. Schenck JF, Dumoulin CL, Redington RW, Kressel HY, Elliott RT, McDougall IL. Human exposure to 4.0-Tesla magnetic fields in a whole-body scanner. *Med Phys*. (1992) **19**:1089–98. doi: 10.1118/1.596827
82. Wijnen JP, Klomp DWJ. Advances in magnetic resonance spectroscopy. *PET Clin*. (2013) **8**:237–44. doi: 10.1016/j.cpet.2013.03.001
83. Van Essen DC, Ugurbil K, Auerbach E, Barch D, Behrens TE, Bucholz R, et al. The human connectome project: a data acquisition perspective. *Neuroimage* (2012) **62**:2222–31. doi: 10.1016/j.neuroimage.2012.02.018
84. Kimmlingen R, Eberlein E, Dietz P, Kreher S, Schuster J, Riegler J. et al. Concept and realization of high strength gradients for the Human Connectome Project. *Proc Intl Soc Mag Reson Med*. (2012) **11**:63194.
85. Van Essen DC, Smith SM, Barch DM, Behrens TEJ, Yacoub E, Ugurbil K. The WU-Minn human connectome project: an overview. *Neuroimage* (2013) **80**:62–79. doi: 10.1016/j.neuroimage.2013.05.041
86. Ernst RR. Why just NMR? *Isr J Chem*. (1992) **32**:135–6. doi: 10.1002/ijch.199200019
87. Keevil SF, Duke T, Nunes A, Parisi A. Physics and medicine: a historical perspective. *Lancet* (2012) **379**:1517–24. doi: 10.1016/S0140-6736(11)60282-1

Conflict of Interest Statement: FS is a retired employee of Siemens Healthcare. All other authors declare no conflict of interest.

frontiers in Physics

ORIGINAL RESEARCH
published: 23 June 2017
doi: 10.3389/fphy.2017.00025

Stochastic Model of Acidification, Activation of Hemagglutinin and Escape of Influenza Viruses from an Endosome

Thibault Lagache[1†], *Christian Sieben*[2†], *Tim Meyer*[3], *Andreas Herrmann*[2] and *David Holcman*[1,4*]

[1] Applied Mathematics and Computational Biology, Ecole Normale Supérieure, Paris, France, [2] Department of Biology, Molecular Biophysics, IRI Life Sciences, Humboldt-Universität zu Berlin, Berlin, Germany, [3] Institute of Chemistry and Biochemistry, Free University Berlin, Berlin, Germany, [4] Newton Institute and Department of Applied Mathematics and Thearetical Physics (DAMTP), Cambridge, United Kingdom

OPEN ACCESS

Edited by:
Mario Nicodemi,
Universita' di Napoli "Federico II", Italy

Reviewed by:
Luis Diambra,
National University of La Plata, Argentina
Haiguang Liu,
Beijing Computational Science Research Center, China

***Correspondence:**
David Holcman
david.holcman@ens.fr

†Present Address:
Thibault Lagache,
Department of Biological Sciences, Columbia University, New York, NY, United States
Christian Sieben,
School of Basic Sciences, École Polytechnique Fédérale de Lausanne, Lausanne, Switzerland

Specialty section:
This article was submitted to Biophysics, a section of the journal Frontiers in Physics

Received: 30 March 2017
Accepted: 06 June 2017
Published: 23 June 2017

Citation:
Lagache T, Sieben C, Meyer T, Herrmann A and Holcman D (2017) Stochastic Model of Acidification, Activation of Hemagglutinin and Escape of Influenza Viruses from an Endosome. Front. Phys. 5:25. doi: 10.3389/fphy.2017.00025

Influenza viruses enter the cell inside an endosome. During the endosomal journey, acidification triggers a conformational change of the virus spike protein hemagglutinin (HA) that results in escape of the viral genome from the endosome into the cytoplasm. It is still unclear how the interplay between acidification and HA conformation changes affects the kinetics of the viral endosomal escape. We develop here a stochastic model to estimate the change of conformation of HAs inside the endosome nanodomain. Using a Markov process, we model the arrival of protons to HA binding sites and compute the kinetics of their accumulation. We compute the Mean First Passage Time (MFPT) of the number of HA bound sites to a threshold, which is used to estimate the HA activation rate for a given pH (i.e. proton concentration). The present analysis reveals that HA proton binding sites possess a high chemical barrier, ensuring a stability of the spike protein at sub-acidic pH. We predict that activating more than 3 adjacent HAs is necessary to trigger endosomal fusion and this configuration prevents premature release of viruses from early endosomes.

Keywords: modeling, first passage time, asymptotic analysis, conformational change, endosomal acidification, influenza virus, trafficking, Kramers-Moyal approximation

1. INTRODUCTION

For most viruses, the initial step of infection starts when the viral particles bind to specific receptors and enter the cell through the membrane, inside an endosomal compartment (**Figure 1**). Viral particles are then transported inside the endosome, from the cell periphery towards the nucleus. Several modeling approaches, including kinetics rate equations [1], stochastic modeling [2, 3] and mechanics of molecular binding [4] have been developed to describe how membrane receptors are activated and engaged into endosomal pathways. However, little attention has been devoted to study viral trafficking inside an endosome, which is a critical and limiting step in replication and more generally to gene delivery [5–8].

Cytoskeleton retrograde flow plays a key role for the Influenza virus transport inside the endosome toward the cell nucleus and to ensure a safe delivery of its genome near the nucleus, before replication [9, 10]. During this transport, the endosome can fuse with lysosomes, leading in that case to viral degradation. Thus, escaping the endosome at the right time must be

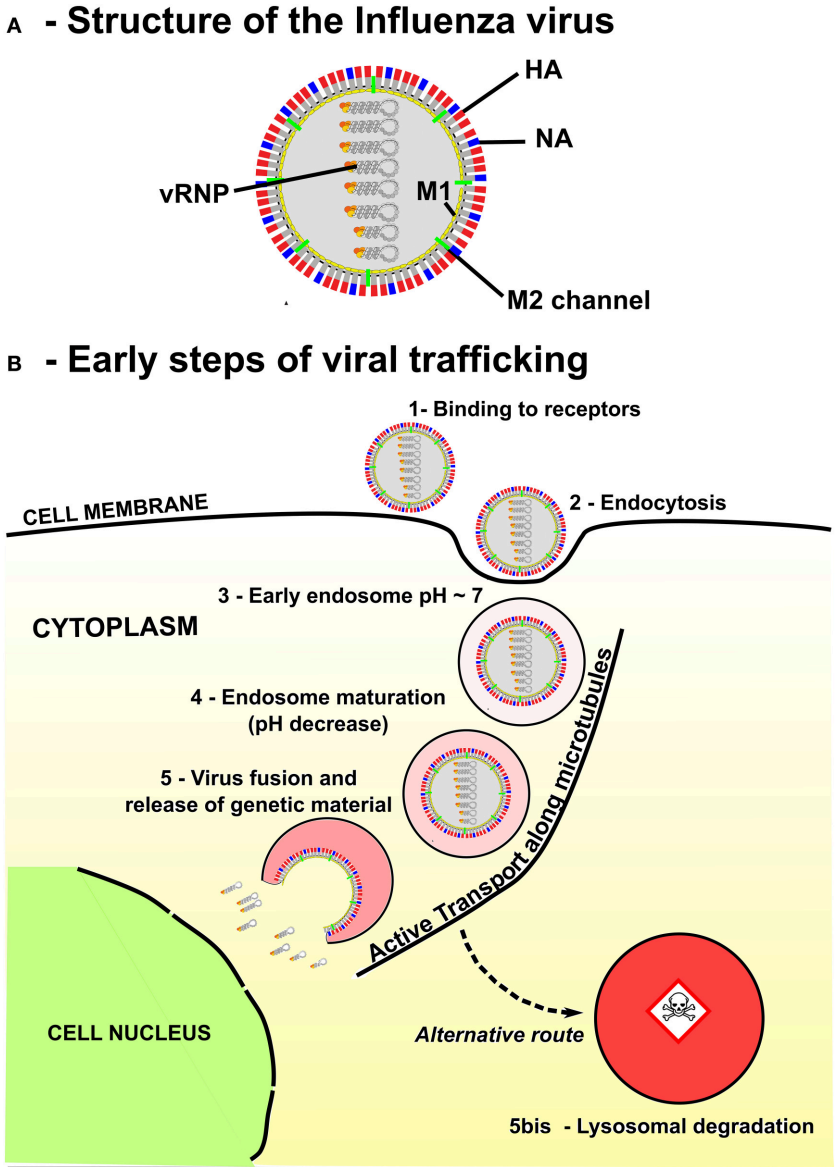

FIGURE 1 | Structure and endosomal trafficking of the Influenza virus. **(A)** Influenza is an enveloped virus. Main spike proteins anchored in the envelope are the neuraminidase (NA) and the Hemagglutinin (HA). Protons can access the core of the virus through M2 channels. Main matrix protein is M1 protein. Viral genome of the virus is composed by eight viral ribonucleoproteins (vRNPs). **(B)** Influenza virus enters the cell via receptor-mediated endocytosis and progress rapidly toward an early endosome. Then, maturation is associated with an acidification of the endosome lumen and a retrograde transport of the endosome along the microtubules toward the nucleus, the destination of vRNPS for virus replication. The final destination of many endosomes is the degradative lysosomes. Thus, the timing of Influenza virus escape has to be tightly regulated to avoid degradation in lysosomes while delivering the genetic material close to the nucleus.

tightly regulated to ensure that genes are released as close as possible from the nucleus, while avoiding degradation. Our goal here is to develop a first-principles model and the associated stochastic analysis to study this optimal escape time, and how it is controlled by acidification and conformational changes of viral proteins. The stochastic model developed in Lagache et al. [11] is inappropriate to compute the viral escape time based on the activation of a single molecule, and we develop here a different approach based on the mass-action equation for acidification.

The genome of Influenza virus is encoded by viral ribonucleoproteins (vRNPs) enveloped in a membrane. These vRNPs must translocate into the nucleus [12] (**Figure 1**) for reproduction. Endosomal escape is ensured by fusion between the endosomal and Influenza virus membrane. This fusion is mediated by a low pH conformational change of the viral glycoprotein hemagglutinin (HA) (**Figure 1A**). We account here for the detailed properties of the glycoprotein HA, composed of two linked subunits HA1 and HA2, the latter anchoring HA

to the viral envelope. At neutral pH, HA is not active (in a non-fusogenic state), but as the pH decreases due to acidification (proton entry into the endosome), a partial dissociation of the HA1 subunit results in a spring-loaded conformational change of HA2 into an active (fusogenic) state [13]. Consequently, the residence time of the Influenza virus genome within an endosome before fusion depends on the kinetics of endosome acidification. Yet, the absence of direct *in vivo* measurements of these parameters makes the endosomal step of virus infection difficult to analyze both theoretically and experimentally. To estimate the timing of the pH-driven fusion of Influenza viruses, the model we develop here accounts for the main kinetic parameters of the fusion process: endosomal acidification, binding of protons to HAs and independent activation of multiple HA neighbors, leading to membrane fusion and release of the genome into the cytoplasm.

The manuscript is organized as follow: Section 2.1 presents the kinetic model for endosomal acidification, calibrated to experimental data (Figures in the SI). The model depends on the buffering capacity of the endosome, membrane leakage and proton pumping rate that controls proton fluxes inside the endosome. In Section 2.2, we model the discrete and cumulative binding of protons to HAs using a Markov jump process [14]. We find an analytical expression for the kinetics of HA conformational change at a fixed proton concentration, by analyzing the mean first passage time (MFPT) equation for the number of bound protons to a given threshold. In our previous work [11], we developed a jump model for the conformational change of active proteins for the escape of non-enveloped Adeno-Associated Viruses (AAV) from a vesicle. Contrary to the assumptions of [11], the binding rates of protons to HAs are non-linear [15] and thus we obtain here a different analytical expressions for the MFPT of bound protons to the critical threshold. Finally, in Section 2.3, we combine the kinetic models of acidification and HA conformational change and estimate the rate of HAs' activation inside the endosome. While the conformational change of a single protein for AAV is sufficient to lyse the endosome and release genes in cytoplasm, the Influenza virus is covered by 400 HAs and several adjacent HAs seems required for fusion.

We predict here the mean number of fusogenic HAs in the endosome and use Monte-Carlo simulations to compute the time needed for neighboring HAs to change conformation in the contact zone between the viral and endosomal membrane: we find that at least three adjacent activated HAs are necessary to trigger membrane fusion [16, 17], a cooperativity process that should prevent premature fusion. Some predictions are tested experimentally using co-labeling viruses and endosomal markers, confirming that intracellular fusion of viruses mainly occur in maturing endosomes (ME).

2. RESULTS

2.1. Kinetic Model of Endosomal Acidification

The present model of endosomal acidification is based on computing the free number of protons $P_e(t)$ at time t in the endosomal compartment. The protons enter with an entry rate $\lambda(t)S$ through the V-ATPase proton pumps (S is the endosomal surface area and the rate $\lambda(t)$ is associated with the proton pumps activity) and can escape with a leakage rate $L_{ext}(t)$, but can also bind to endosomal buffers.

The proton pump rate $\lambda(t)$ is mainly determined by the membrane potential $\Psi(t)$ (Figure 11 in Grabe et al. [18]), which depends on the endosomal concentrations of several cations ($H^+, K^+, Na^+ \ldots$) and ($Cl^- \ldots$). The ionic concentrations inside endosome are tightly regulated by channels, exchangers and leak and in particular, by raising the interior-positive membrane potential, Na-K ATPase exchangers have been proposed to limit the acidification of early compared to late endosomes [19].

2.1.1. Mass Action Law for Free Protons

To derive the time-dependent equations for the free protons, we use the balance of fluxes: the fast equilibrium between fluxes determines the number of protons $\Delta P_e(t)$ entering the endosome during the time step Δt

$$\Delta P_e = \left(\lambda(t)S - L_{ext}(t)\right)\Delta t. \tag{1}$$

Entering protons are rapidly bound to endosomal buffers that we model using an ensemble of acid-base reactions [20]:

$$P_e + B_1 \underset{k_1^{(-1)}}{\overset{k_1}{\rightleftharpoons}} P_e\text{-}B_1\,, P_e + B_2 \underset{k_2^{(-1)}}{\overset{k_2}{\rightleftharpoons}} P_e\text{-}B_2 \ldots, P_e + B_n \underset{k_n^{(-1)}}{\overset{k_n}{\rightleftharpoons}} P_e\text{-}B_n, \tag{2}$$

where k_i (resp. $k_i^{(-1)}$) are binding (resp. unbinding) rate constants of protons to weak bases B_i, for $1 \leq i \leq n$. The binding rates of entering protons to the endosomal basis can be reduced to a single constant that we call the effective buffering capacity β_e^0 of the endosome. The kinetics equation for the number of free protons $P_e(t)$ inside an endosome is (Section 4)

$$\frac{dP_e(t)}{dt} = \left(\lambda - L\frac{P_e(t)}{N_A V_e}\right)\frac{S\log(10)P_e(t)}{N_A V_e \beta_e^0}. \tag{3}$$

When the proton leakage is counterbalanced by the pump activity, after a time long enough, the pH reaches an asymptotic value pH_∞, where the endosome cannot be further acidified. This value is given by

$$P_e(\infty) = N_A V_e 10^{-\mathrm{pH}_\infty}, \tag{4}$$

Consequently, the rate λ depends on pH_∞ with

$$\lambda = L10^{-\mathrm{pH}_\infty}, \tag{5}$$

and Equation (3) can be rewritten as

$$\frac{dP_e(t)}{dt} = \left(10^{-\mathrm{pH}_\infty} - \frac{P_e(t)}{N_A V_e}\right)\frac{LS\log(10)P_e(t)}{N_A V_e \beta_e^0}. \tag{6}$$

To conclude, we derived here a first order kinetic model (Equation 32) for the endosome acidification, based on the rapid equilibration of protons with buffer (see Equation 36). However, Equation (6) alone is not sufficient to account for endosomal maturation, because the final pH_∞ [12] and the permeability L decreases with the endosomal maturation [19] as they depend on time, as we analyse below.

2.1.2. Modeling pH Change and Acidification of an Endosome

Acidification in live cell imaging and the transition from an early endosome (EE) to a late endosome (LE) is monitored by a gradual exchange of Rab5/Rab7 proteins [21]. We approximate here the kinetics of the ratio Rab5/Rab7 (Figure 4C in Rink et al. [21]) by a sigmoidal function

$$\frac{\text{Rab7(t)}}{\text{Rab5(t)}+\text{Rab7(t)}}=\frac{1}{1+e^{-(t-t_{1/2})/\tau_c}}, \tag{7}$$

with the two free parameters: the half-maturation $t_{1/2}$ and Rab conversion τ_c times. The steady-state $\text{pH}_\infty(t)$ relative to the amount of Rab7 is given by

$$\text{pH}_\infty(t)=\text{pH}_\infty^{\text{early}}+\left(\text{pH}_\infty^{\text{late}}-\text{pH}_\infty^{\text{early}}\right)\frac{\text{Rab7(t)}}{\text{Rab5(t)}+\text{Rab7(t)}}. \tag{8}$$

Thus we propose that the permeability rate follows the Equation

$$\text{L}(t)=L^{\text{early}}+\left(L^{\text{late}}-L^{\text{early}}\right)\frac{\text{Rab7(t)}}{\text{Rab5(t)}+\text{Rab7(t)}}. \tag{9}$$

2.1.3. Acidification Model Calibrated from Live Cell Imaging Kinetics

We now explain the calibration of the acidification model to experimental data: First, we fitted Equation (7) to the experimental data (Figure 4C of Rink et al. [21]) where the lag time between initiation and termination of the Rab5/Rab7 permutation is estimated to 10 min., leading to a time constant for $\tau_c = 100s$.

We use data from endosomal acidification in MDCK cells where the pH inside endosomes decreases very quickly within the first 10–15 min (**Figure 2**) to reach a steady-state pH around 5.5 after 20 min, in agreement with [22]. The steady-state pH is $\text{pH}_\infty^{\text{early}} = 6.0$ and $\text{pH}_\infty^{\text{late}} = 5.5$ for early and late endosomes respectively [23]. Thus, we calibrated the permeability constant L and Rab conversion kinetics by solving numerically Equation 6 and fitting the experimental acidification curve (**Figure 2**). We found that the permeabilities of early and late endosomes are $L^{\text{early}} = 3.5\,10^{-3} N_A \text{cm s}^{-1}$ and $L^{\text{late}} = 0.1 N_A \text{cm s}^{-1}$, respectively, and the half-maturation time is $t_{1/2} = 10$ min.

2.1.4. Proton Influx Inside the Viral Core and Buffering

The last step of the kinetic model includes the buffering of protons to viral core components, defining the buffer capacity. Indeed, protein buffering capacity, influx of protons through M2-channels inside the viral core (**Figure 1A**) and the presence of viruses inside endosomes influences the overall buffering capacity of the endosome and acidification. To compute the influx through each viral M2 channel, we use a first order kinetics [24], summarized in the chemical equation

$$P_e + M2 \underset{k_e^{-1}}{\overset{k_e}{\rightleftharpoons}} M2\text{-}P \underset{k_v}{\overset{k_v^{-1}}{\rightleftharpoons}} P_v + M2. \tag{10}$$

When a proton P_e binds a free $M2$ protein channel with rates k_e(binding) and k_e^{-1} (unbinding), it is transported inside the virus core with a rate k_v^{-1}, while exit occurs with a rate k_v. At steady state, the inward flux in a single virus is computed from Equation (10) (see [24])

$$j_{M2}(P_e,P_v)=\frac{n_{M2}}{1+\alpha(P_e,P_v)}\left(k_e^{-1}-\frac{k_e P_e \alpha(P_e,P_v)}{N_A V_e}\right), \tag{11}$$

where n_{M2} is the number of M2 channels per viral particle, P_v is the number of free protons inside the viral core and

$$\alpha(P_e,P_v)=\frac{k_e^{-1}+k_v^{-1}}{k_e\left(\frac{P_e}{N_A V_e}+\frac{k_v^{-1}P_v}{k_e^{-1}N_A V_v}\right)}, \tag{12}$$

To extract the buffer capacity of a virus, we accounted for the viral genome, the internal viral proteins and unspecific buffers that can be reached through the M2 channels [24]. The most abundant internal proteins are M1 (3,000 copies per virus) and the nucleoproteins (NP, 330 copies per virus) [25] (**Figure 1A**). Proton binding sites of viral proteins are the ionogenic groups in their amino acid side chains [26], and the main ionogenic buffers in the endosome pH range are the aspartic acid (Asp, pKa = 3.9), the glutamic acid (Glu, pKa = 4.32) and the histidine (His, pKa = 6.04) [26]. Closely related binding sites can have strong influences on each other due to electrostatic interactions. In addition, the three-dimensional protein folding can hinder the accessibility of some residues to the solvent and protons.

Consequently, calculations based on the three-dimensional structure of the protein are necessary to determine the buffering capacity to pH. Using the spatial organization (crystal structure) of viral proteins, the overall buffering capacity β_i of the viral core is given by

$$\beta_i=\beta_v^0+\beta_v^{M1}+\beta_v^{NP}+\beta_v^{RNA}, \tag{13}$$

where β_v^0 is the buffering capacity of the lumen inside the virus, and β_v^{M1}, β_v^{NP} and β_v^{RNA} are the buffering capacity of M1 and NP proteins, and viral RNA (see Section 4).

Similar to the flux Equation (6), the number of free protons $P_v(t)$ contained in viral core at time t determines the influx of protons through M2 channels (Equation 11) and satisfies equation

$$\frac{dP_v(t)}{dt}=\frac{\log(10)}{N_A V_v\left(\beta_v^0+\beta_v^{M1}+\beta_v^{NP}+\beta_v^{RNA}\right)}P_v(t)j_{M2}\left(P_e(t),P_v(t)\right). \tag{14}$$

By solving numerically Equation (14) with the initial conditions $P_e(t=0) = 10^{-7.2} N_A V_e$ and $P_v(t=0) = 10^{-7.2} N_A V_v$, we estimate that $= 60,000$ protons enter the viral core during endosomal maturation. Using Equation (6) for the endosomal acidification kinetic, we find that more than 20,000,000 protons bind to the endosomal buffers during acidification of an endosome with a radius $r_e = 500$ nm (**Table 1**). Thus, the buffering capacity of a single virus should not influence the endosomal acidification. However, the number of protons that bind to endosomal buffers drastically decreases to 175,000 buffered protons when the endosomal radius is reduced $r_e =$ 100 nm. In addition viral particles may accumulate during

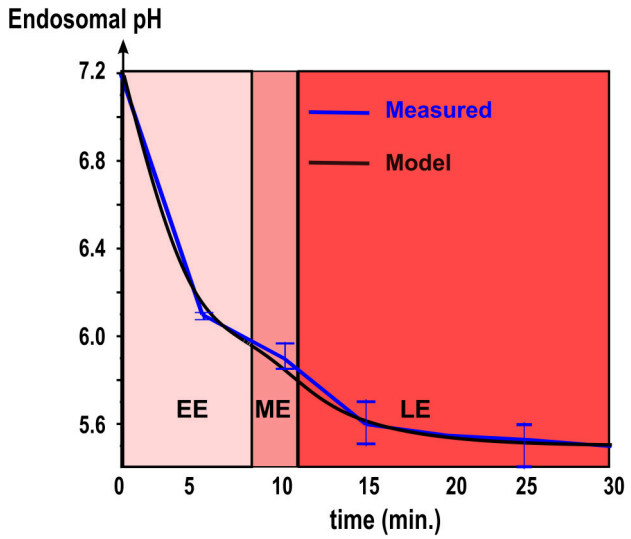

FIGURE 2 | Endosomal acidification. The kinetics of acidification obtained with intracellular fluorescence microscopy (red line. Mean ± SEM) is compared with coarse-grained modeling (Equation 6, black line. Model parameters are summarized in **Table 1**).

the endosomal journey [27]. Thus, for multiplicity of infection (MOI) and viral accumulation in endosomes, the viral buffering capacity may significantly affect the acidification kinetics of small and intermediate size endosomes.

2.2. Markov Jump Model of HA Conformational Change

Although the number of protons entering in the endosome is quite huge, as discussed in the previous section, the actual number of free protons defining endosomal pH is surprisingly low ($\sim$ 300 at pH 6 in an endosome with a radius of $r_e = 500$ nm). In addition, there are few proton binding sites on a single HA that trigger a conformational change [15], which is the event of interest. This change of scale between many entering protons and few free protons and HA binding sites requires a different description than the previous continuous model.

To compute the mean time for HA conformation to change as the pH drops, we first extracted the forward and backward proton binding rates by converting the HA conformational change kinetics, obtained from experimental data at various pH [28] into rate constants.

At temperature $T = 300K$, when the pH decreases from 7 to 4, the number of protons bound to HA1 increases approximatively from 123 to 132 (Figure 3 in Huang et al. [15]), suggesting that the number of available number of binding site is $n_s = 9$ at acidic pH. The Influenza virus carries $n_{HA} = 400$ HA trimers [17] (**Figure 3A**) and thus there are exactly $n_{HA}n_s$ sites that can competitively bind protons. In this section, we compute the mean time that a threshold n_T of bound protons to HA1 is reached, which is a model of fusogenic state, where proteins engage into the generation of a fusion pore with the endosomal membrane.

2.2.1. Modeling HA Conformational Change

To analyse the conformational change of a single HA trimer, we follow the occupied proton sites $X(t, c)$ at time t, for a fix proton concentration c. During time t and $t + \Delta t$, the number of specific bound sites can either increase with a probability $r(X, c)\Delta t$, when a proton arrives to a free site or decreases with probability $l(X, c)\Delta t$ when a proton unbinds or remains unchanged with probability $1 - l(X, c)\Delta t - r(X, c)\Delta t$ (**Figure 3A**).

We estimate hereafter the rates $l(X, c)$ and $r(X, c)$ and the critical threshold n_T, by approximating the number of bound protons $\tilde{X}_0(c)$ with the proton concentration c variable, by a linear function (Figure 3 in Huang et al. [15])

$$\tilde{X}_0(c) = \tilde{X}_0\left(10^{-7} mol.L^{-1}\right) + X_0(c) = \tilde{X}_0\left(10^{-7} mol.L^{-1}\right) + \left(\frac{7}{3} + \frac{\log(c)}{3\log 10}\right) n_s, \quad (15)$$

where $\tilde{X}_0\left(10^{-7} mol.L^{-1}\right)$ is the mean number of bound protons at pH = 7 and

$$X_0(c) = \left(\frac{7}{3} + \frac{\log(c)}{3\log 10}\right) n_s \quad (16)$$

is the mean number of HA1 sites that are additionally protonated for a proton concentration $c > 10^{-7}$mol. L^{-1}. Recently, we also used a similar jump model [11] to study the conformational change of active proteins for the escape of non-enveloped viruses, based on the assumption that proton binding and unbinding rates were linear functions of the proton concentration. Here however, the mean number of bound sites depends linearly on the endosomal pH (log of the proton concentration) (Equation 16), confirming the non-linear binding and unbinding rates of protons to HA.

To account for the non-linearity of the mean number of bound protons (Equation 16), we derived the expressions of the binding r and unbinding l rates of protons to HA binding sites. First, we assume that the binding rate $r(X, c)$ depends on both the proton concentration c and the number of free binding sites X, whereas the unbinding rate $l(X)$ depends only on X. Indeed, an increased concentration of protons inside the endosome favors the encounter and binding between protons and HA sites, but do not influence the unbinding rate of bound protons. Moreover, we assume that the binding rate $r(X, c)$ depends linearly on the proton concentration c and the number of free sites $n_s - X$ of the HA trimer leading to

$$r(X, c) = Kc(n_s - X), \quad (17)$$

where K is the forward binding rate of a proton to a binding site.

To determine the non-linear proton unbinding rate $l(X, c)$, we use the mean number of protons bound to HA at different pHs (Equation 16). Using at equilibrium the concentration $c(X) = 10^{\frac{3X}{n_s}-7}$ for which $X_0(c(X)) = X$, the mass-action law leads to $\frac{l(X_0(c),c)}{r(X_0(c),c)} = 1$ or equivalently $\frac{l(X)}{Kc(X)(n_s-X)} = 1$, and we get

$$l(X) = K(n_s - X)10^{\frac{3X}{n_s}-7}. \quad (18)$$

TABLE 1 | Parameters of the endosome acidification model.

Parameters	Description	Value
r_e	Radius of the endosome	$r_e = 500$ nm [21]
V_e	Volume of the endosome	$V_e = \frac{4}{3}\pi r_e^3 = 5.22\ 10^{-16}$L
r_v	Radius of the Influenza virus	$r_v = 60$ nm [42]
V_v	Volume of the viral internal lumen	$V_v = \frac{4}{3}\pi r_v^3 = 9\ 10^{-19}$L
N_A	Avogadro constant	$N_A = 6.02\ 10^{23}$ mol^{-1}
β_e^0	Buffering capacity of the endosomal lumen	$\beta_e^0 = 40$ mM/pH [40]
β_v^0	Buffering capacity of the viral lumen	$\beta_v^0 = \beta_e^0 = 40$ mM/pH (this study)
β_v^{M1}	Buffering capacity of viral M1s	$\beta_v^{M1} = \frac{10,500}{N_A V_v}$ mM/pH (this study)
β_v^{NP}	Buffering capacity of viral NPs	$\beta_v^{NP} = \frac{3,000}{N_A V_v}$ mM/pH (this study)
β_v^{RNA}	Buffering capacity of viral RNA	$\beta_v^{RNA} = \frac{1,200}{N_A V_v}$ mM/pH (Figure 3D in Stoyanov and Righetti [26])
L^{early}	Permeability constant of early endosomes	$L^{\text{early}} = 3.5\ 10^{-3}\, N_A$ cm s^{-1} (this study)
L^{late}	Permeability constant of late endosomes	$L^{\text{late}} = 3.5\ 10^{-4}\, N_A$ cm s^{-1} (this study)
$\text{pH}_\infty^{\text{early}}$	Steady state pH of early endosomes	$\text{pH}_\infty^{\text{early}} = 6.0$ [23]
$\text{pH}_\infty^{\text{late}}$	Steady state pH of late endosomes	$\text{pH}_\infty^{\text{late}} = 5.5$ [23]
$t_{1/2}$	Half maturation time of endosomes	$t_{1/2} = 10$ min. (this study)
τ_C	Rab5/Rab7 mean conversion time	$\tau_C = 100$ s (Figure 4C in Rink et al. [21])

TABLE 2 | Parameters of the HA's change of conformation model.

Parameters	Description	Value
$r(x, c)$	Proton binding rate	$r(x, c) = Kcn_S(1-x)$ (this study)
$l(x)$	Proton unbinding rate	$l(x) = Kn_S(1-x)10^{-(3(1-x)+4)}$ [15]
n_T	Critical threshold for the number of HA1 proton bound sites	$n_T = 6$ (this study)
K	Binding rate of a proton to a free HA1 proton binding site	$K = 7,500$ L.mol^{-1} s^{-1} (this study)
$n_S = 1/\epsilon$	Number of HA1 proton binding sites	$n_S = 9$ [15]
n_{HA}	Number of HAs	$n_{HA} = 400$ [17]

In summary, the binding and unbinding rates r and l are given by

$$r(X, c) = Kc(n_s - X), \text{ and } l(X, c) = l(X) = K(n_s - X)10^{\frac{3X}{n_s}-7}. \tag{19}$$

2.2.2. Rate of HA Conformational Change

To compute the mean time that exactly n_T protons are bound to a single HA, we use a Markov jump process for the number of protonated sites $X(t, c)$ among the $n_s = 9$ HA1 proton binding sites available. Following a similar approach as used in Lagache et al. [11] for non-enveloped viruses, we scale the variable

$$x(t, c) = \epsilon X(t, c), \tag{20}$$

where $\epsilon = 1/n_s$ and we use the Wentzel-Kramers-Brillouin (WKB) expansion of the mean first passage time (MFPT) $\tau(c)$ of the scaled number of protonated sites $x(t, c)$ to the (unknown) critical threshold $0 < x_T = \epsilon n_T < \epsilon n_s$ [11, 14, 29–31]

$$\tau(c) \approx \frac{1}{r\left(x_0(c), c\right)} \frac{\sqrt{\frac{2\pi}{\epsilon \frac{d}{dx}\left(\frac{l}{r}\right)(x_0(c), c)}}}{\phi(x_T, c)}, \tag{21}$$

where $x_0(c)$ is the mean number of HA1 sites that are additionally protonated for a concentration $c > 10^{-7}$mol.L^{-1} (Equation 16). The function $\phi(x, c)$ is given by

$$\phi(x, c) = \frac{\exp\left(-\frac{1}{\epsilon}\int_{x_0(c)}^{x} \log\left(\frac{l(s,c)}{r(s,c)}\right) ds\right)}{\sqrt{\frac{l(x,c)}{r(x,c)}}} \left(\frac{l(x, c)}{r(x, c)} - 1\right). \tag{22}$$

Replacing the transition rates $r(x, c)$ and $l(x)$ by their expressions (19) in Equation (22), we obtain that (see Section 4)

$$\tau(c) = \frac{\sqrt{6\pi}\exp\left(n_s\left(F\left(n_T/n_s\right) - F\left(7/3 + \frac{\log(c)}{3\log(10)}\right)\right)\right)}{K\sqrt{cn_s\log(10)}\left(4 + \frac{\log(c)}{\log(10)}\right)\left(c10^{7/2-3n_T/(2n_s)} - 10^{3n_T/(2n_s)-7/2}\right)}, \tag{23}$$

where $F(x) = \frac{3}{2}\log(10)x^2 - \log(10^7 c)x$.

To conclude, the expression for the MFPT (23) differs from the one computed in Lagache et al. [11] (Equation 5) derived for a linear unbinding rate $l(x, c) = k_{-1}xn_s$. Equation (23) links the affinities between the ligand (concentration c) and the binding sites of a trimer to the conformational change mean time $\tau(c)$ of the trimer. The two unknown parameters of the conformational MFPT (Equation 23) are the binding rate K of protons to HA sites and the number n_T of sites that have to be protonated (among the $n_s = 9$ total sites) to trigger the HA change of conformation.

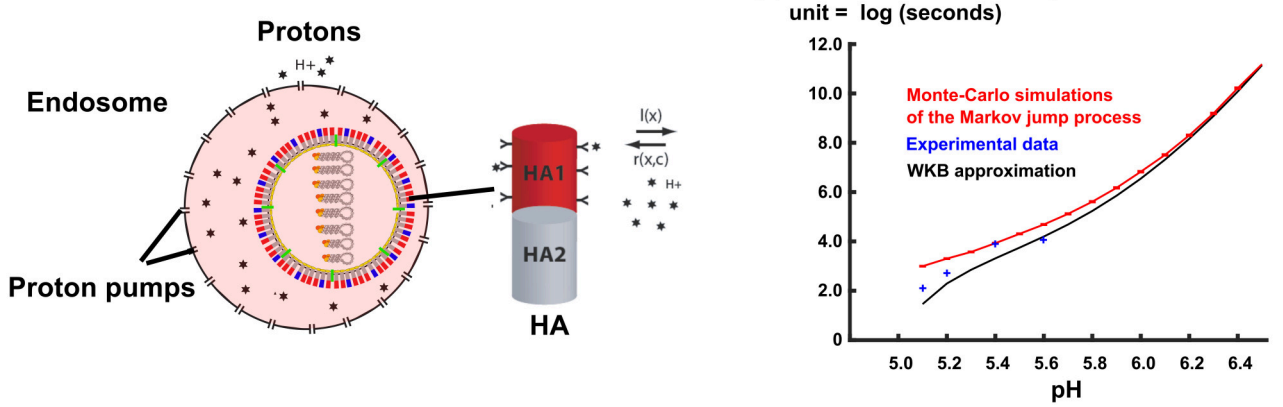

FIGURE 3 | Free protons in the endosome triggers HA conformational change. **(A)** The right-hand side shows a scheme of an isolated HA trimer. Free protons in the endosome can bind to HA trimers. The protons binding rates $r(X, c)$ and $l(X)$ depend on the number of occupied sites X and on the concentration c of free protons in the endosome. When the number of bound protons reaches a given threshold, the HA trimer changes conformation into a fusogenic state. **(B)** MFPT of a discrete Markov jump process with transition rates $r(X, c)$ and $l(X)$ to a critical threshold $n_T = 6$ is estimated with Monte-Carlo simulations ($N = 1000$) (solid red line), and compared with WKB approximation (solid black line) and experimental data points [28].

The reciprocal of the mean time $\frac{1}{\tau(c)}$ has been measured for various pH values [28]: $\left(\tau(pH = 4.9)\right)^{-1} = 5.78s^{-1}$, $\left(\tau(pH = 5.1)\right)^{-1} = 0.12s^{-1}$,..., $\left(\tau(pH = 5.6)\right)^{-1} = 0.017s^{-1}$. To estimate the unknown K and n_T, we thus use formula (23) to fit these data by a least square optimization procedure, and obtain that

$$n_T \approx 6 \tag{24}$$

and the forward rate

$$K \approx 7.5 \;\; 10^3 L.mol^{-1}s^{-1}. \tag{25}$$

These two estimations are the predictions of the present model. We reported here a good agreement between the WKB approximation (Equation 23) with the Monte-Carlo simulations of the Markov jump process, with the transition rates $r(X, c)$ and $l(X)$ given by Equation (19), and the experimental values of [28] (**Figure 3B**, model parameters are summarized in **Table 2**). The WKB solution is very close to the Markov jump simulations, especially for pH values $\geq$ 5.8, where the fusion takes place (Section 2.3 below). For lower values of the pH, the MFPT to threshold that triggers the conformational change of HA decreases drastically and a small discrepancy between discrete Monte-Carlo simulations and continuum WKB approximation can be seen. For these lower pH values, we observe that the WKB and the Monte-Carlo simulations agrees with the conformational change rates of HA, measured experimentally [28]. We highlight that the fitting of only two parameters K and n_T of the Markov model lead to a very good fit to all experimental data points, which indicates that the Markov jump approach with the WKB approximation is suitable to model the HA conformational changes.

2.2.3. A High Potential Barrier of HA Binding Sites Ensures HA Stability at Neutral pH

We have seen in Section 2.1 that during endosomal acidification, a huge number of protons enter the endosome (more than $20*10^6$ that bind mostly to endosome buffers, leaving very few free protons (around 300 at pH 6)). To test whether HAs buffer entering protons or interact with the remaining few free protons, we estimate the potential barrier generated at each HA binding site. For this purpose, we compare the reciprocal of the forward rate constant K (Equation 25), which is the mean time for a proton to bind a HA protein, with the free Brownian diffusion time scale. For a fixed proton concentration at a value c, the proton binding time is $\tau_{bind} = \frac{1}{Kc}$, while the mean time for a proton to diffuse to the same binding site is [32–35]

$$\tau_{diff} = \frac{V}{4\pi D_p \eta n(c)}. \tag{26}$$

The number of endosomal protons at concentration c is $n(c) = N_A cV$, while η is the interacting radius between a proton and a binding site and D_p the diffusion constant of a free proton ($D_p = 100\,\mu m^2\ s^{-1}$ measured in the cytoplasm [36]). For η =1 nm, we find a small ratio

$$\frac{\tau_{diff}}{\tau_{bind}} = \frac{K}{4\pi D_p \eta N_A} = 10^{-4}. \tag{27}$$

This result indicates that, on average, only 1 out of 10^4 encounters between a proton and a HA binding site lead to a binding event. Thus, the binding of protons to HA is strongly reaction-limited, dominated by a very high activation energy barrier at the HA binding sites. This high barrier prevents rapid proton binding and consequently, the buffering capacity of HAs can be neglected compared to the high capacity of other endosomal

buffers. In addition, the activation energy barrier of HA binding sites ensures a high stability of the protein at pH above 6, as previously characterized in Table 2 of Krumbiegel et al. [28] and confirmed in Figure S1.

To conclude, we found that the threshold for HA1 conformational change occurs when there are $n_T = 6$ bound proton in a total of $n_s = 9$ binding sites. The binding is characterized by a very high potential barrier. Thus, when protons enter an endosome, they will first be captured by endosomal buffers. The remaining free protons can bind to HA1 sites after passing across the high potential barrier to trigger HA conformational change.

2.3. A Closed Model of Virus-Endosome Fusion

Combining the kinetic model of endosome acidification with the Markov jump model of HA conformational change, we now derive a kinetic model of HAs conformational change inside an endosome. We account for the $n_T = 6$ protons activating a HA1 trigger leading to HA conformational change. We now estimate the numbers $HA_0(t), HA_1(t) \dots HA_6(t)$ of viral HAs that have $0, 1 \dots 6$ bound protons at time t, and compute the number of fusogenic (active) $HA_6(t)$, responsible for membrane fusion. From relation (17), the forward rate of a proton to a free HA1 binding site is

$$\tilde{r}(X) = r\left(X, P_e(t)\right)/P_e(t) = \frac{K(n_s - X)}{N_A V_e}. \tag{28}$$

and the backward rate $l(X)$ is given by relation 19, thus the chemical Equations for protons P_e and HA proteins are summarized by

$$\begin{aligned} HA_0 + P_e &\underset{l(1/n_s)}{\overset{\tilde{r}(0/n_s)}{\rightleftharpoons}} HA_1, \\ HA_1 + P_e &\underset{l(2/n_s)}{\overset{\tilde{r}(1/n_s)}{\rightleftharpoons}} HA_2, \\ &\dots \\ HA_5 + P_e &\xrightarrow{\tilde{r}(5/n_s)} HA_6, \end{aligned} \tag{29}$$

where the rate constant depends on each stage as given by relation 28. The stage HA_6 is irreversible and the kinetic rate equations are

$$\frac{dHA_0(t)}{dt} = -\tilde{r}\left(\frac{0}{n_s}\right) P_e(t) HA_0(t) + l\left(\frac{1}{n_s}\right) HA_1(t), \tag{30}$$

$$\begin{aligned} \frac{dHA_1(t)}{dt} &= \left(\tilde{r}\left(\frac{0}{n_s}\right) HA_0(t) - \tilde{r}\left(\frac{1}{n_s}\right) HA_1(t)\right) P_e(t) \\ &\quad + l\left(\frac{2}{n_s}\right) HA_2(t) - l\left(\frac{1}{n_s}\right) HA_1(t), \\ &\dots \\ \frac{dHA_6(t)}{dt} &= \tilde{r}\left(\frac{5}{n_s}\right) HA_5(t) P_e(t). \end{aligned} \tag{31}$$

Once the proton entry rate (Equation 6) is known, these equations can be solved numerically.

2.3.1. Modeling the Onset of Fusion between Virus and Endosome Membranes

Membrane fusion is triggered by the conformational change of multiple adjacent trimers located in the contact zone between the viral and endosomal membranes [16, 17]. However, the exact number of fusogenic HAs involved in formation and fusion pore enlargement is still unclear. To estimate this number, we model the contact zone between the virus and endosome membranes by 120 HAs among 400 covering the viral particle [17] (**Figure 4A**). Thus, each trimer in the contact zone possesses 6 adjacent neighbors.

We solved numerically Equation (31) and we chose the position of each new fusogenic HA (with $n_T = 6$ bound sites) randomly among the 400 HAs covering the virus envelope. For each simulation, we defined the onset of virus endosome fusion by the activation of Na adjacent HAs in the contact zone (**Figure 4A**). Using 1,000 Monte-Carlo simulations, we estimated the mean and confidence interval at 95% of the fusion onset time for different Na. We found that for $Na = 1 - 2$, most viruses fuse in EE, whereas for $Na = 3 - 4$, they fuse in ME. Finally, for $Na = 5$ or 6, viruses mostly fuse in LE (**Figures 4B,C**). To conclude, viruses shall fuse in ME [16, 17] and thus $Na = 3 - 4$.

2.3.2. Intracellular Localization of Fused Viral Particle with Live Cell Imaging

To experimentally determine the localization of virus fusion, we used the fluorescent endosomal markers Rab5 (EE) and Rab7 (LE) in combination with an intracellular fusion assay to detect virus-endosome fusion so that the localization to a specific compartment can be assigned. Single virus spots were analyzed, where fusion was indicated by a pronounced increase of spot signal (Figure S2). To determine the cellular localization of virus fusion, we analyse infected Rab5- and Rab7-expressing cells with R18-labeled viruses (**Figure 4D**). We classified single endosomes based on the presence of the two Rab proteins into three classes (Figure S3). Early endosomes (EE) do not show Rab7 association, such as late endosomes (LE) do not posses Rab5 signal. When endosomes possess both signals, they were counted as maturing endosomes (ME).

We observe a gradual increase of Rab7 along with a decrease of Rab5 (**Figure 4D**). After 5 min, we rarely observe fusion events in Rab5-only endosomes. The majority of fusion events (61%) are detected in maturing endosomes between 10 and 20 min post infection (**Figure 4E**). At later time points, the localization of fusion events shifted toward late endosomes. However, de-quenching kinetics show that fusion mostly occurs between 10 and 20 min (Figure S2).

We conclude that virual fusion was essentially associated with maturing endosomes confirming that the number of adjacent fusogenic HA required to mediate fusion are $Na = 3$ or 4.

3. DISCUSSION AND CONCLUSION

Influenza viruses are internalized into endosomes via receptor-mediated endocytosis. During their transport along microtubules, endosomes accumulate protons, which eventually

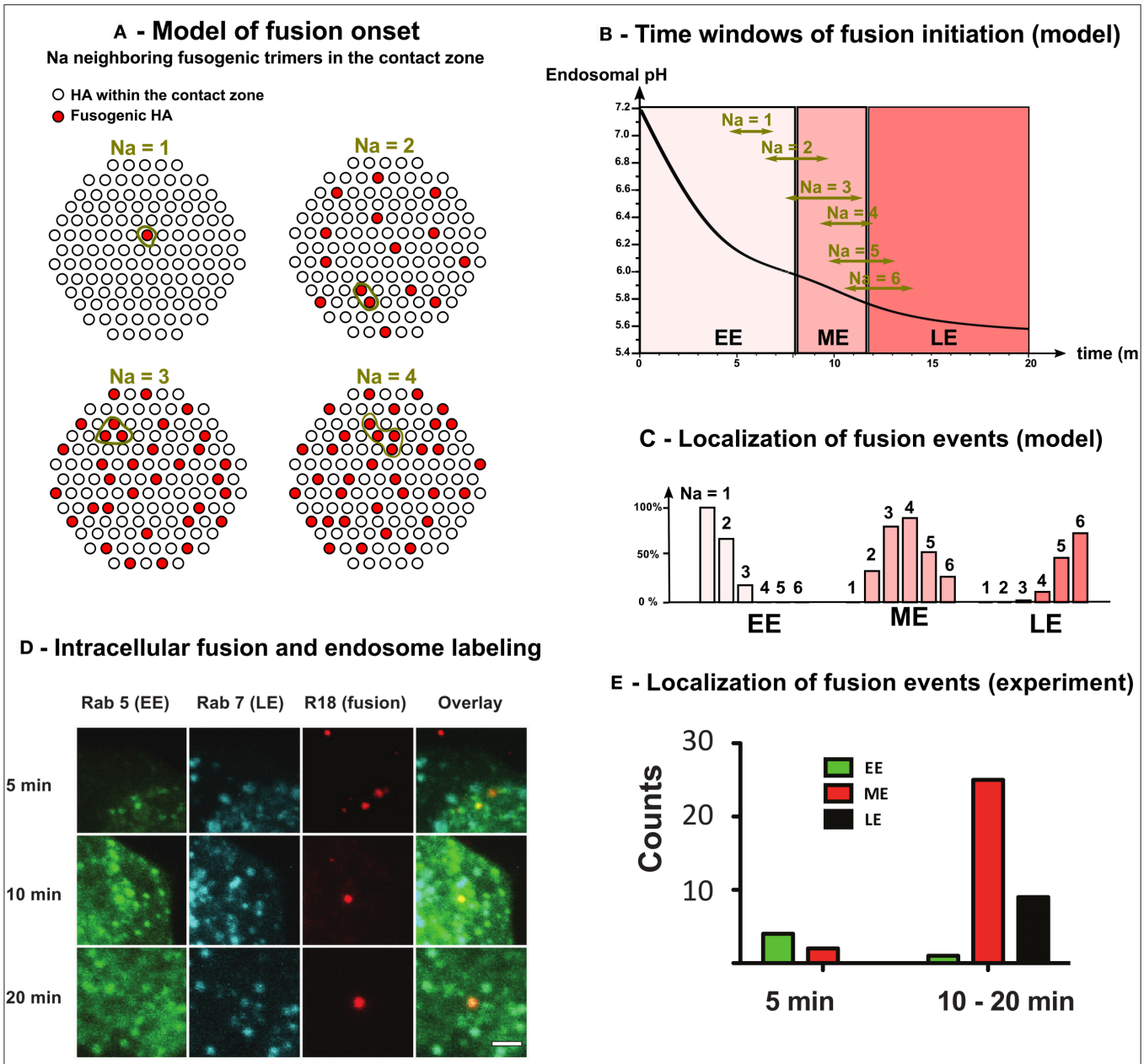

FIGURE 4 | Model and fluorescence experiments of the intracellular onset of virus-endosome fusion. **(A)** The fusion between virus and endosome membranes is triggered by the conformational change of *Na* adjacent HAs in the contact zone between virus and endosome (= 120 among the 400 HAs covering the virus envelope [17]). **(B)** Solving Equation (31) we estimated the time window (95% confidence interval) of intracellular fusion for $1 \leq Na \leq 6$. **(C)** Using time windows of fusion onset and endosome maturation kinetics (Equation 7), we estimated the localization (EE, ME, or LE) of fusion onset as function of the number *Na* of adjacent fusogenic HAs needed for the fusion onset.**(D)** MDCK cells expressing Rab5-CFP and Rab7-GFP were incubated with R18-labeled Influenza A viruses. Fusion was observed as a strong increase of R18 signal due to de-quenching after dilution. Scale bar = 1 μm **(E)** *In vivo* localization of fusion events. Fusion events were counted and categorized regarding their localization in early endosome (EE) (Rab5), ME (Rab5 + Rab7) or LE (Rab7).

enable virus-endosome fusion mediated by the influenza HA. This fusion mediates the release of the viral genome in the cell cytoplasm. The duration of endosomal transport as well as the localization of fusion critically depend on endosomal acidification and HA conformational change at low pH. Here we presented a new model to investigate the role of key parameters that shape the endosomal residence time of influenza viruses.

The Markov-jump process model of HA conformational change that we have developed here shows that 6 bound protons are enough to trigger conformational change for a total of 9 binding sites. The model also reveals that the HA activation is characterized by a high potential barrier with a forward rate constant $K = 7,500\,\mathrm{L.mol^{-1}s^{-1}}$. Interestingly the unbinding rate depends on the number of binding sites, suggesting a

modification that depends on history. This is in contrast with the large number of protons of the order of millions that enters and contributes to acidification. This confirms that buffers play a critical role to reduce this enormous quantity of protons into a countable number that will trigger HA activation. The multiscale process involved here is very different from the previous analysis and results [11] we found for the Adeno-associated virus .

Finally, associating the kinetic model of endosomal acidification with a Markov-jump process model of HA conformational change, we estimated how the number of fusogenic HAs evolved in time inside endosomes, and we modeled the onset of fusion with the stochastic activation of *Na* adjacent HAs. Using the model, we predict a high HA thermal stability at neutral pH due to a high activation barrier of proton binding sites. For $Na \geq 3$, we show that fusion should occur in ME, preventing a premature fusion in EE. Because endosomal maturation is associated with retrograde transport of endosomes along MTs, we conclude that mature virus should accumulate near the nuclear surface. Moreover, when an endosome contains multiple copies of Influenza viruses, we found that the cumulative buffering capacity of viruses might delay the acidification kinetics and viral escape into ME and LE.

4. MATERIALS AND METHODS

We describe here the experimental methods for extracting parameters used to validate the modeling approach. In the last section, we present the computation for the WKB computation for formula Equation (23).

4.1. Materials, Cell and Virus Culture

Madine Darby Canine Kidney (MDCK) cells were cultured in Dulbeccos Modified Eagles Medium (DMEM) without phenol red, supplemented with 1% penicillin/streptomycin and 10% fetal calf serum (FCS). The cells were passaged every 3–4 days. One day prior to the experiment, the cells were detached from the cell culture flask using 0.5 % Trypsin/EDTA for about 10 min. The cells were diluted in DMEM and 10–50 * 10^5 cells were seeded in 35 mm poly-L-lysine coated glass bottom petri dishes (MatTek Corp.). Influenza A (H3N2) X-31 was propagated in chicken eggs and A/Panama/2007/99 on MDCK cells. Prior to the experiment the virus was diluted to 1 mg/ml protein concentration. Octadecylrhodamine B (R18) was purchased from Molecular Probes (Life Technologies, USA). Phosphate buffered saline (PBS) was used for all dilutions during the experiments. Double labeled FITC/Rhodamine dextran was purchased from Life Technologies (USA). FITC-dextran was purchased from Sigma-Aldrich, Germany. Rab5-GFP (in pCDNA3) and Rab7-GFP (pEGFP-C1) were kindly provided by Volker Haucke (FMP, Berlin). Rab7 was then cloned into pECFP. MDCK cells were transfected using Turbofect (Fermentas, USA) according to the manufacturers manual. To disrupt microtubules, the cells were incubated with medium containing 50 μM nocodazole (Sigma Aldrich, Germany) for 30 min before experiments.

4.2. Immunostaining

MDCK were washed in PBS buffer and fixed in PBS containing 2% paraformaldehyde and 0.2 % glutaraldehyde for 20 min. The cells were permeabilized with PBS containing 0.2% Triton X-100 and 0.2 % BSA for 20 min, washed in PBS and incubated in anti-Nucleoprotein (Millipore, USA) antibody for 1 h. The cells were washed in PBS and incubated with the secondary anti-mouse Cy2 conjugate antibody for 1 h (Amersham, GE, USA). Finally, the cells were counterstained using PBS containing 0.2 μ g/ml DAPI for 10 min.

4.3. Fluorescence Microscopy

For fluorescence microscopy, we used an Olympus FV1000-MPE confocal microscope (Olympus, Japan) equipped with 405 nm (DAPI), 440 nm (CFP), 488 nm (GFP), 559 nm (R18) and 635 nm (A647) laser lines, an Olympus 60x/1.2 water UPlanSApo objective and 405-458/515/559/635 405/488/559/635 dichroic mirror filter sets.

4.4. Endosomal pH Determination

One day prior to the experiment, MDCK cells were seeded into 35 mm poly-L-lysine coated glass bottom petri dishes (MatTek Corp.). For dextran labeling, the cells were washed with PBS and incubated in serum free medium for 30 min at 37° C, followed by 5 min with 10 mg/ml dextran at 37° C (pulse). After the pulse, the cells were immediately washed and image acquisition was started. For plotting the pH evolution (experiments and model), we considered a time delay of 5 min due to technical limitations and set the starting point to pH 7.2.

4.5. Determination of a pH Standard Curve

The pH standard curve for intracellular pH measurements was done as previously described by others ([23]). In short, MDCK cells were detached from the culture dish, washed and pelleted with 2,000 g for 5 min. The cells were divided into eight fractions, pelleted again and resuspended pH standard buffer (obtained by mixing 50 mM HEPES buffer with 50 mM MES buffer (both containing 50 mM NaCl, 30 mM ammonium acetate, 40 mM sodium azide and 10 μM nigerizin). The samples were left on ice for 5 min and analyzed by flow cytometry.

4.6. Calculation of the Proton Binding Capacity of Viral Proteins

Proton binding and the total charge of the proteins was calculated as follows. First, the pKa values of all titrable residues in the proteins were determined with electrostatic energy calculations using the software Karlsberg+ [37]. The calculations are based on the crystal structures with PDB IDs 1hgg, 1hgd, 2bat and 2q06. All non-protein molecules were removed from the structures and therefore not considered in the calculations. Except for hydrogen atoms, all atomic coordinates were kept as found in the crystal structure in the Karlsberg+ calculations. If a titratable residue was missing in the structure, it was assumed that its pKa value equals the model pKa of this residue. The model pKa is the experimental pKa value of a residue in aqueous solution. The protonation state and therefore the charge of a residue at a certain pH value are determined by its pKa value. Here a residue is considered to be protonated if its pKa value is larger than the corresponding pH value. The number of bound protons at a given pH value was then obtained by counting the protonated

titratable residues in a protein, the total charge by summing up all individual residue charges.

4.7. Influenza Virus—Ghost Membrane Fusion Assay

To check that Influenza virus are fusion competent and calibrate intracellular fusion experiment we first performed an *in vitro* ghost-membrane assay [28]. We labeled Influenza viruses with lipophilic dye R18 and measured virus-membrane fusion by monitoring the fluorescence de-quenching (FDQ) of the lipid-like fluorophore R18 upon fusion of R18-labeled viruses with membranes. To this end, 10 µl of labeled virus suspension (1 mg/ml) were mixed with 40 µl ghost suspension ($\approx 2^*10^5$ cells) and incubated for 20 min at RT. Unbound virus was removed by centrifugation (5 min, 1,200 g). The virus-ghost suspension was transferred to a glass cuvette containing pre-warmed fusion buffer (pH 7.4), and the fluorescence was detected ($\lambda_{ex} = 560$ nm; $\lambda_{em} = 590$ nm) by using a Horiba Yobin Yvon FluoroMax spectrofluorometer. Fusion was triggered by the addition of citric acid (0.2 M). The suspension was stirred continuously with a 2 by 8 mm Teflon-coated magnetic stirring bar. After 600 s the fusion was stopped by adding Triton X-100 (50 µl, final concentration 0.5%) to obtain maximum R18 de-quenching. The final pH in the cuvette was measured using a standard pH meter. The percentage of FDQ was calculated as:

$$FDQ(\%) = \frac{F(t) - F(0)}{(F_{max} - F(0))} * 100$$

where F(0) and F(t) are the fluorescence intensity before starting fusion and at a given time (t), respectively. We observed that fusion starts around pH 6 as predicted by our model and already shown experimentally [38] (Figure S1).

4.8. Intracellular Fusion Assay

Influenza virus was diluted to a final concentration of 1 mg/ml in PBS and incubated with 20 mM R18 for 30 min at room temperature. Unbound R18 was removed by centrifugation at 25.000 g for 5 min or gel filtration (G25 sephadex in PBS). The virus was resuspended/eluted in PBS. Immediately before the experiment, the virus was diluted to 40 µg/ml and viral aggregates were removed with a 0.2 µm sterile filter. The virus was applied to the cells and allowed to bind for 10 min at 4°C. The temperature was elevated to 37°C and the R18 fluorescence was monitored by confocal microscopy.. 40 min after start of acquisition, the cells were fixed with PBS containing 2% paraformaldehyde and 0.2 % glutaraldehyde and the DNA was stained with Hoechst 33342 (Invitrogen, USA). The boundaries between cells were determined from the bright field image. Summed z-stacks were analyzed using an IDL-based particle identification software [39].

4.9. Derivation of the Acidification Kinetics Equation (3)

Protons that enter inside the endosome interact with endosomal buffers, and the number of free protons $P_e(t)$ inside an endosome is given by the mass-action law

$$\begin{aligned}\frac{dP_e(t)}{dt} &= \Delta P_e(t) + \sum_{i=1}^{n}\left(k_i^{(-1)}P_e\text{-}B_i(t) - \frac{k_i}{N_A V_e}P_e(t)B_i(t)\right)\\ &= \left(\lambda(t)S - L_{ext}(t)\right)\\ &+ \sum_{i=1}^{n}\left(k_i^{(-1)}P_e\text{-}B_i(t) - \frac{k_i}{N_A V_e}P_e(t)B_i(t)\right),\end{aligned} \tag{32}$$

where P_e-$B_i(t)$ and $B_i(t)$ are the number of weak acids and bases inside the endosome at time t, N_A is the Avogadro constant and V_e is the volume of the endosome. Assuming that the membrane potential $\Psi(t)$ reaches rapidly its steady state value $\Psi(\infty)$ compared to the acidification kinetics [18], we approximate the pumping rate $\lambda(t)S$ with its steady state value λ

$$\lambda(t)S = \lambda S. \tag{33}$$

where the parameter λ is related to the membrane potential $\Psi(\infty)$. In addition, the protons leak $L_{ext}(t)$ is proportional to the endosomal concentration and the endosomal surface [20]

$$L_{ext}(t) = LS\frac{P_e(t)}{N_A V_e}, \tag{34}$$

where L is a permeability constant. Consequently, using approximations 33 and 34 in Equation (32), we obtain the general dynamics of free protons:

$$\begin{aligned}\frac{dP_e(t)}{dt} &= \left(\lambda - L\frac{P_e(t)}{N_A V_e}\right)S\\ &+ \sum_{i=1}^{n}\left(k_i^{(-1)}P_e\text{-}B_i(t) - \frac{k_i}{N_A V_e}P_e(t)B_i(t),\right).\end{aligned} \tag{35}$$

When the protons enter the endosome they can interact with buffers which is much faster than acidification. Thus, we assume that $\Delta P_e(t)$ protons entering the endosome during dt bind instantaneously to bases, which leads to step decrease $-\Delta B_i(t)$ of the number of proton binding sites of each base $B_i(t)$:

$$\Delta P_e(t) = -\sum_{i=1}^{n}\Delta B_i(t). \tag{36}$$

To estimate the pH change $\Delta\text{pH}(t)$ associated with the entry $\Delta P_e(t)$ of protons and the corresponding decrease $-\Delta B_i(t)$ of each base, we use Equation (2) at equilibrium

$$k_i^{(-1)}P_e\text{-}B_i(t) = k_i\frac{P_e(t)B_i(t)}{N_A V_e}, \text{for all } 1 \le i \le n. \tag{37}$$

Thus,

$$\frac{P_e(t)}{N_A V_e} = K_i\frac{C_i - B_i(t)}{B_i(t)}, \text{for all } 1 \le i \le n, \tag{38}$$

where $K_i = \frac{k_i^{(-1)}}{k_i}$ and $C_i = P_e\text{-}B_i(0) + B_i(0)$ are constant. Consequently,

$$\text{pH}(t) = pK_i + \frac{1}{\log(10)}\log\left(\frac{B_i(t)}{\left(C_i - B_i(t)\right)}\right) \tag{39}$$

where $pK_i = -\log(K_i)/\log(10)$. By differentiating Equation (39) with respect to each $B_i(t)$, we obtain the infinitesimal variation $\Delta\text{pH}(t)$ of the endosomal pH at time t

$$\Delta\text{pH}(t) = \left(\frac{1}{\log(10)}\frac{C_i}{B_i(t)\left(C_i - B_i(t)\right)}\right)\Delta B_i(t). \quad (40)$$

Using Equation (38), we get

$$\Delta\text{pH}(t) = \left(\frac{1}{\log(10)}\frac{\left(N_A V_e K_i + P_e(t)\right)^2}{P_e(t) C_i N_A V_e K_i}\right)\Delta B_i(t), \quad (41)$$

leading to

$$\Delta B_i(t) = N_A V_e \beta_i\left(P_e(t)\right)\Delta\text{pH}(t), \quad (42)$$

where

$$\beta_i\left(P_e(t)\right) = \log(10) C_i \frac{P_e(t) K_i}{\left(P_e(t) + K_i N_A V_e\right)^2} \quad (43)$$

is the buffering capacity of the weak acid-base couple (P_e-B_i, B_i). Finally, using Equations (36) and (42), the infinitesimal change $\Delta\text{pH}(t)$ of the endosomal pH associated with the entry of $\Delta P_e(t)$ protons is

$$\Delta P_e(t) = -\sum_{i=1}^{n}\Delta B_i(t) = -N_A V_e\left(\sum_{i=1}^{n}\beta_i\left(P_e(t)\right)\right)\Delta\text{pH}(t), \quad (44)$$

that is

$$\Delta P_e(t) = -N_A V_e \beta_e^0\left(P_e(t)\right)\Delta\text{pH}, \quad (45)$$

where $\beta_e^0\left(P_e(t)\right) = \sum_{i=1}^{n}\beta_i\left(P_e(t)\right)$ is the total buffering capacity of the endosome, which is approximately constant $\beta_e^0\left(P_e(t)\right) = \beta_e^0 = 40 mM/pH$ [40]. Finally, using the proton extrusion and pumping rates (Equations 33 and 34), we obtain the kinetic Equation

$$\frac{d\text{pH}(t)}{dt} = \left(L\frac{P_e(t)}{N_A V_e} - \lambda\right)\frac{S}{N_A V_e \beta_e^0}. \quad (46)$$

The endosomal pH is related to the number of free protons $P_e(t)$ by

$$\text{pH(t)} = -\frac{1}{\log(10)}\log\left(\frac{P_e(t)}{N_A V}\right). \quad (47)$$

Thus

$$\frac{d\text{pH}(t)}{dt} = -\frac{1}{\log(10) P_e(t)}\frac{dP_e(t)}{dt}, \quad (48)$$

and replacing the pH derivative in Equation (46), we obtain that the accumulation of free protons $P_e(t)$ inside the ensosome during acidification is given by the kinetics Equation

$$\frac{dP_e(t)}{dt} = \left(\lambda - L\frac{P_e(t)}{N_A V_e}\right)\frac{S\log(10) P_e(t)}{N_A V_e \beta_e^0}. \quad (49)$$

4.10. Estimation of the Viral Buffering Capacity (Equation 13)

First, we estimated the buffering capacity of NP proteins [41] by computing the pKa values of all titratable residues in the proteins with electrostatic energy calculations using the software Karlsberg+ [37]. We then determined the mean number of protonated residues $n_P^{NP}(pH)$ of NP proteins and we found that $n_P^{NP}(pH)$ increases almost linearly with pH:

$$n_P^{NP}(pH) = n_P^{NP}(pH = 7) + 9\left(7 - pH\right), \quad (50)$$

indicating that the buffering capacity of NPs is approximatively constant between pH 7 and 5 (Equation 42)

$$\beta_v^{NP} = 9\frac{330}{N_A V_v} = \frac{3000}{N_A V_v} \quad (51)$$

where $V_v = \frac{4}{3}\pi r_v^3$ is the volume of the viral internal lumen, for a spherical viral particle with radius $r_v = 60$ nm [42]. The structure of the matrix M1 protein is unknown and consequently, we use the cumulative contributions of Asp, Glu and His residues to estimate the number of M1 proton binding sites. We thus estimate the fraction $P_i(pH)$ of occupied residues for a fixed pH using the equilibrium constant pKa_i for any residue i (Asp, Glu or His) to be

$$P_i(pH) = \left(10^{pH - pKa_i} + 1\right)^{-1}. \quad (52)$$

The mean number $n_P^{M1}(pH)$ of protonated site is then given by

$$n_P^{M1}(pH) = n_{Asp}^{M1}\left(10^{pH-3.9} + 1\right)^{-1} + n_{Glu}^{M1}\left(10^{pH-4.32} + 1\right)^{-1} + n_{His}^{M1}\left(10^{pH-6.04} + 1\right)^{-1}. \quad (53)$$

where the number of residue for each group is $n_{Asp}^{M1} = 12$, $n_{Glu}^{M1} = 12$ and $n_{His}^{M1} = 5$. Using Equation (53), we plotted $n_P^{M1}(pH)$as function of the pH and observed that $n_P^{M1}(pH)$ is almost a linear function

$$n_P^{M1}(pH) = n_P^{NP}(pH = 7) + 3.5\left(7 - pH\right), \quad (54)$$

and obtain that

$$\beta_v^{M1} = 3.5\frac{3,000}{N_A V_v} = \frac{10,500}{N_A V_v}. \quad (55)$$

Additionally to internal M1s and NPs proteins, protons entering the viral core through M2 channels can also bind to viral nucleic acids and in particular to basic groups in the guanine, adenine and cytosine nucleotides [26]. In particular, the buffering capacity β^{RNA} of oligonucleotides in solution, for a concentration $c_{monomers}$ of monomers, has been estimated to be $\beta^{RNA} = 0.1\, c_{monomers}$ in the pH range 5–7 (Figure 3D in Stoyanov and Righetti, [26]). Consequently the buffering capacity β_v^{RNA} of the $= 12,000$ viral nucleotides [43] is approximatively equal to

$$\beta_v^{RNA} = 0.1\frac{12,000}{N_A V_v} = \frac{1,200}{N_A V_v}. \quad (56)$$

Finally, the viral core lumen should also contain other unspecific buffers such as cytoplasmic buffers enclosed during the viral assembly, leading to an unspecific buffering capacity $\beta_v^0(pH)$

inside the viral lumen that has to be added to the buffering capacities β_v^{NP} and β_v^{M1} of internal proteins. Due to possible ionic exchange between viral and endosomal lumens, we approximate $\beta_v^0(pH)$ with the endosomal buffering capacity β_e^0, which is independent of the pH and has been estimated to be [40]

$$\beta_e^0 = 40\, mM/\text{pH}. \tag{57}$$

4.11. Derivation of Equation 23

Using the WKB approach [14], we obtain that the mean first passage time (MFPT) $\tau(c)$ of the scaled number of protonated sites $x(t,c)$ to the (unknown) critical threshold $0 < x_T = \epsilon n_T < \epsilon n_s$ is given by [11, 29–31]

$$\tau(c) \approx \frac{1}{r\left(x_0(c),c\right)} \frac{\sqrt{\frac{2\pi}{\epsilon \frac{d}{dx}\left(\frac{l}{r}\right)\left(x_0(c),c\right)}}}{\phi(x_T,c)},$$

where $x_0(c)$ is the mean number of HA1 sites that are additionally protonated for a concentration $c > 10^{-7} mol.L^{-1}$ (Equation 16) and $\phi(x,c)$ is given by

$$\phi(x,c) = \frac{\exp\left(-\frac{1}{\epsilon}\int_{x_0(c)}^{x} \log\left(\frac{l(s,c)}{r(s,c)}\right) ds\right)}{\sqrt{\frac{l(x,c)}{r(x,c)}}} \left(\frac{l(x,c)}{r(x,c)} - 1\right).$$

We first compute

$$\begin{aligned}\int_{x_0(c)}^{x_T} \log\left(\frac{l(s,c)}{r(s,c)}\right) ds &= \int_{x_0(c)}^{x_T} \left(\log\left(10^{3s-7}\right) - \log(c)\right) ds \\ &= \int_{x_0(c)}^{x_T} \left(3\log(10)s - \left(7\log(10) \right.\right. \\ &\quad \left.\left. + \log(c)\right)\right) ds,\end{aligned}$$

that is

$$\begin{aligned}\int_{x_0(c)}^{x_T} \log\left(\frac{l(s,c)}{r(s,c)}\right) ds &= \int_{x_0(c)}^{x_T} \left(3\log(10)s - \log(10^7 c)\right) ds \\ &= F\left(x_T\right) - F\left(x_0(c)\right),\end{aligned}$$

where

$$F(x) = \frac{3}{2}\log(10)x^2 - \log(10^7 c)x.$$

leading to

$$\phi(x_T,c) = \exp\left(-\frac{1}{\epsilon}\left(F\left(x_T\right) - F\left(x_0(c)\right)\right)\right) \frac{\frac{10^{3x_T-7}}{c} - 1}{\sqrt{\frac{10^{3x_T-7}}{c}}},$$

that is,

$$\begin{aligned}\phi(x_T,c) &= \exp\left(-\frac{1}{\epsilon}\left(F\left(x_T\right) - F\left(x_0(c)\right)\right)\right) \\ &\quad \left(\frac{10^{3x_T/2-7/2}}{\sqrt{c}} - \sqrt{c}10^{7/2-3x_T/2}\right).\end{aligned}$$

Using expressions for the binding and unbinding rates 19, we get

$$\begin{aligned}\frac{d}{dx}\left(\frac{l}{r}\right)\left(x_0(c),c\right) &= \frac{d}{dx}\left(\frac{10^{3x-7}}{c}\right)\left(x_0(c),c\right) \\ &= \frac{3\log(10)}{c} 10^{3x_0(c)-7},\end{aligned}$$

which reduces to

$$\frac{d}{dx}\left(\frac{l}{r}\right)\left(x_0(c),c\right) = 3\log(10).$$

Finally, re-injecting expression of potential $\phi(x_T,c)$ in the MFPT $\tau(c)$, we obtain that

$$\tau(c) = \frac{\epsilon}{-Kc\left(\frac{4}{3} + \frac{\log(c)}{3\log(10)}\right)} \frac{\sqrt{\frac{2\pi}{\epsilon 3\log(10)}} \exp\left(\frac{1}{\epsilon}\left(F\left(x_T\right) - F\left(7/3 + \frac{\log(c)}{3\log(10)}\right)\right)\right)}{\frac{10^{3x_T/2-7/2}}{\sqrt{c}} - \sqrt{c}10^{7/2-3x_T/2}}.$$

Using $\epsilon = 1/n_s$ and $x_T = n_T/n_s$, we get

$$\tau(c) = \frac{\sqrt{6\pi}\exp\left(n_s\left(F\left(n_T/n_s\right) - F\left(7/3 + \frac{\log(c)}{3\log(10)}\right)\right)\right)}{K\sqrt{cn_s\log(10)}\left(4 + \frac{\log(c)}{\log(10)}\right)\left(c10^{7/2-3n_T/(2n_s)} - 10^{3n_T/(2n_s)-7/2}\right)}.$$

AUTHOR CONTRIBUTIONS

TL, AH, and DH: Designed research. TL and CS: Performed experimental and simulations works. TM: Contributed analytic tools. TL, CS, and DH Analyzed data. TL, CS, AH, and DH: Wrote the paper.

ACKNOWLEDGMENTS

This research was supported by a Marie Curie grant (DH), by the Deutsche Forschungsgemeinschaft (HE 3763/15-1) (AH) and the Bundesministerium fur Bildung und Forschung (eBio: ViroSign) (CS and AH). TL is partially funded by a fellowship from the Fondation pour la Recherche Medicale and a grant from the Philippe Foundation.

SUPPLEMENTARY MATERIAL

The Supplementary Material for this article can be found online at: http://journal.frontiersin.org/article/10.3389/fphy.2017.00025/full#supplementary-material

REFERENCES

1. D'Orsogna MR, Chou T. Optimal cytoplasmic transport in viral infections. *PLoS ONE* (2009) **4**:e8165. doi: 10.1371/journal.pone.0008165
2. Gibbons MM, Chou T, D'orsogna MR. Diffusion-dependent mechanisms of receptor engagement and viral entry. *J Phys Chem B* (2010) **114**:15403–12. doi: 10.1021/jp1080725
3. Mistry B, D'Orsogna MR, Webb NE, Lee B, Chou T. Quantifying the Sensitivity of HIV-1 Viral Entry to Receptor and Coreceptor Expression. *J Phys Chem B* (2016) **120**:6189–99. doi: 10.1021/acs.jpcb.6b02102
4. Allard JF, Dushek O, Coombs D, Van Der Merwe PA. Mechanical modulation of receptor-ligand interactions at cell-cell interfaces. *Biophys J.* (2012) **102**:1265–73. doi: 10.1016/j.bpj.2012.02.006
5. Sodeik B. Mechanisms of viral transport in the cytoplasm. *Trends Microbiol.* (2000) **8**:465–72. doi: 10.1016/S0966-842X(00)01824-2
6. Imelli N, Meier O, Boucke K, Hemmi S, Greber UF. Cholesterol is required for endocytosis and endosomal escape of adenovirus type 2. *J Virol.* (2004) **78**:3089–98. doi: 10.1128/JVI.78.6.3089-3098.2004
7. Dauty E, Verkman AS. Actin cytoskeleton as the principal determinant of size-dependent DNA mobility in cytoplasm: a new barrier for non-viral gene delivery. *J Biol Chem.* (2005) **280**:7823–8. doi: 10.1074/jbc.M412374200
8. Xiao PJ, Samulski RJ. Cytoplasmic trafficking, endosomal escape, and perinuclear accumulation of adeno-associated virus type 2 particles are facilitated by microtubule network. *J Virol.* (2012) **86**:10462–73. doi: 10.1128/JVI.00935-12
9. Amoruso C, Lagache T, Holcman D. Modeling the early steps of cytoplasmic trafficking in viral infection and gene delivery. *Siam J Appl Math.* (2011) **71**:2334–58. doi: 10.1137/100816572
10. Schelker M, Mair CM, Jolmes F, Welke RW, Klipp E, Herrmann A, et al. Viral RNA Degradation and Diffusion Act as a Bottleneck for the Influenza A Virus Infection Efficiency. *PLoS Comput Biol.* (2016) **12**:e1005075. doi: 10.1371/journal.pcbi.1005075
11. Lagache T, Danos O, Holcman D. Modeling the step of endosomal escape during cell infection by a nonenveloped virus. *Biophys J.* (2012) **102**:980–9. doi: 10.1016/j.bpj.2011.12.037
12. Mercer J, Schelhaas M, Helenius A. Virus entry by endocytosis. *Annu Rev Biochem.* (2010) **79**:803–33. doi: 10.1146/annurev-biochem-060208-104626
13. Huang Q, Sivaramakrishna RP, Ludwig K, Korte T, Böttcher C, Herrmann A. Early steps of the conformational change of influenza virus hemagglutinin to a fusion active state: stability and energetics of the hemagglutinin. *Biochim Biophys Acta* (2003) **1614**:3–13. doi: 10.1016/S0005-2736(03)00158-5
14. Schuss Z. *Theory and Applications of Stochastic Processes.* New-York, NY: Springer (2010).
15. Huang Q, Opitz R, Knapp EW, Herrmann A. Protonation and stability of the globular domain of influenza virus hemagglutinin. *Biophys J.* (2002) **82**:1050–8. doi: 10.1016/S0006-3495(02)75464-7
16. Danieli T, Pelletier SL, Henis YI, White JM. Membrane fusion mediated by the influenza virus hemagglutinin requires the concerted action of at least three hemagglutinin trimers. *J Cell Biol.* (1996) **133**:559–69. doi: 10.1083/jcb.133.3.559
17. Ivanovic T, Choi JL, Whelan SP, van Oijen AM, Harrison SC. Influenza-virus membrane fusion by cooperative fold-back of stochastically induced hemagglutinin intermediates. *Elife* (2013) **2**:e00333. doi: 10.7554/eLife.00333
18. Grabe M, Wang H, Oster G. The mechanochemistry of V-ATPase proton pumps. *Biophys J.* (2000) **78**:2798–813. doi: 10.1016/S0006-3495(00)76823-8
19. Fuchs R, Schmid S, Mellman I. A possible role for Na^+,K^+-ATPase in regulating ATP-dependent endosome acidification. *Proc Natl Acad Sci USA.* (1989) **86**:539–43. doi: 10.1073/pnas.86.2.539
20. Grabe M, Oster G. Regulation of organelle acidity. *J Gen Physiol.* (2001) **117**:329–44. doi: 10.1085/jgp.117.4.329
21. Rink J, Ghigo E, Kalaidzidis Y, Zerial M. Rab conversion as a mechanism of progression from early to late endosomes. *Cell* (2005) **122**:735–49. doi: 10.1016/j.cell.2005.06.043
22. Zaraket H, Bridges OA, Duan S, Baranovich T, Yoon SW, Reed ML, et al. Increased acid stability of the hemagglutinin protein enhances H5N1 influenza virus growth in the upper respiratory tract but is insufficient for transmission in ferrets. *J Virol.* (2013) **87**:9911–22. doi: 10.1128/JVI.01175-13
23. Bayer N, Schober D, Prchla E, Murphy RF, Blaas D, Fuchs R. Effect of bafilomycin A1 and nocodazole on endocytic transport in HeLa cells: implications for viral uncoating and infection. *J Virol.* (1998) **72**:9645–55.
24. Leiding T, Wang J, Martinsson J, DeGrado WF, Arsköld SP. Proton and cation transport activity of the M2 proton channel from influenza A virus. *Proc Natl Acad Sci USA.* (2010) **107**:15409–14. doi: 10.1073/pnas.1009997107
25. Lamb R, Krug R. Orthomyxoviridae: The viruses and replication. In: Knipe D, Howley P, Griffin D, editors. *Fields Virology.* 4th Edn. Philadelphia, PA: Lippincott Wiliams and Wilkins (1996) 1487–1531.
26. Stoyanov AV, Righetti PG. Buffer properties of biopolymer solutions, as related to their behaviour in electrokinetic methodologies. *J Chromatogr A.* (1999) **838**:11–8. doi: 10.1016/S0021-9673(99)00090-4
27. Matlin KS, Reggio H, Helenius A, Simons K. Pathway of vesicular stomatitis virus entry leading to infection. *J Mol Biol.* (1982) **156**:609–31. doi: 10.1016/0022-2836(82)90269-8
28. Krumbiegel M, Herrmann A, Blumenthal R. Kinetics of the low pH-induced conformational changes and fusogenic activity of influenza hemagglutinin. *Biophys J.* (1994) **67**:2355–60. doi: 10.1016/S0006-3495(94)80721-0
29. Knessl C, Matkowsky B, Schuss Z, Tier C. An asymptotic theory of large deviations for Markov jump-processes. *Siam J Appl Math.* (1985) **45**:1006–28. doi: 10.1137/0145062
30. Matkowsky B, Schuss Z, Knessl C, Tier C, Mangel M. Asymptotic solution of the Kramers-Moyal equation and first-passage times for Markov jump processes. *Phys Rev A.* (1984) **29**:3359–69. doi: 10.1103/PhysRevA.29.3359
31. Knessl C, Mangel M, Matkowsky B, Schuss Z, Tier C. Solution of Kramers-Moyal equations for problems in chemical physics. *J Chem Phys.* (1984) **81**:1285–93. doi: 10.1063/1.447815
32. Ward M, Keller J. Strong localized perturbations of eigenvalue problems. *Siam J Appl Math.* (1993) **53**:770–98. doi: 10.1137/0153038
33. Singer A, Schuss Z, Holcman D. Narrow Escape, part III: Non-smooth domains and Riemann surfaces. *J Stat Phys.* (2006) **122**:491–509. doi: 10.1007/s10955-005-8028-4
34. Schuss Z, Singer A, Holcman D. The narrow escape problem for diffusion in cellular microdomains. *Proc Natl Acad Sci USA.* (2007) **104**:16098–103. doi: 10.1073/pnas.0706599104
35. Holcman D, Schuss Z. *Stochastic Narrow Escape in Molecular and Cellular Biology: Analysis and Applications.* New-York, NY: Springer (2015).
36. al Baldawi NF, Abercrombie RF. Cytoplasmic hydrogen ion diffusion coefficient. *Biophys J.* (1992) **61**:1470–9.
37. Kieseritzky G, Knapp EW. Optimizing pKA computation in proteins with pH adapted conformations. *Prot Struct Funct Bioinf.* (2008) **71**:1335–48. doi: 10.1002/prot.21820
38. Korte T, Ludwig K, Booy FP, Blumenthal R, Herrmann A. Conformational intermediates and fusion activity of influenza virus hemagglutinin. *J Virol.* (1999) **73**:4567–74.
39. Thompson RE, Larson DR, Webb WW. Precise nanometer localization analysis for individual fluorescent probes. *Biophys J.* (2002) **82**:2775–83. doi: 10.1016/S0006-3495(02)75618-X
40. Van Dyke RW, Belcher JD. Acidification of three types of liver endocytic vesicles: similarities and differences. *Am J Physiol.* (1994) **266**(1 Pt 1):C81–94.

41. Ng AKL, Zhang H, Tan K, Li Z, Liu Jh, Chan PKS, et al. Structure of the influenza virus A H5N1 nucleoprotein: implications for RNA binding, oligomerization, and vaccine design. *FASEB J.* (2008) **22**:3638–47. doi: 10.1096/fj.08-112110
42. Lamb RA, Choppin PW. The gene structure and replication of influenza virus. *Annu Rev Biochem.* (1983) **52**:467–506. doi: 10.1146/annurev.bi.52.070183.002343
43. Hutchinson EC, von Kirchbach JC, Gog JR, Digard P. Genome packaging in influenza A virus. *J Gen Virol.* (2010) **91**(Pt 2):313–28. doi: 10.1099/vir.0.017608-0

Conflict of Interest Statement: The authors declare that the research was conducted in the absence of any commercial or financial relationships that could be construed as a potential conflict of interest.

frontiers in Physics

ORIGINAL RESEARCH
published: 13 June 2018
doi: 10.3389/fphy.2018.00056

Stable and Efficient Time Integration of a Dynamic Pore Network Model for Two-Phase Flow in Porous Media

Magnus Aa. Gjennestad[1]*, *Morten Vassvik*[1], *Signe Kjelstrup*[2] and *Alex Hansen*[1]

[1] PoreLab, Department of Physics, Norwegian University of Science and Technology, Trondheim, Norway, [2] PoreLab, Department of Chemistry, Norwegian University of Science and Technology, Trondheim, Norway

We study three different time integration methods for a dynamic pore network model for immiscible two-phase flow in porous media. Considered are two explicit methods, the forward Euler and midpoint methods, and a new semi-implicit method developed herein. The explicit methods are known to suffer from numerical instabilities at low capillary numbers. A new time-step criterion is suggested in order to stabilize them. Numerical experiments, including a Haines jump case, are performed and these demonstrate that stabilization is achieved. Further, the results from the Haines jump case are consistent with experimental observations. A performance analysis reveals that the semi-implicit method is able to perform stable simulations with much less computational effort than the explicit methods at low capillary numbers. The relative benefit of using the semi-implicit method increases with decreasing capillary number Ca, and at Ca $\sim 10^{-8}$ the computational time needed is reduced by three orders of magnitude. This increased efficiency enables simulations in the low-capillary number regime that are unfeasible with explicit methods and the range of capillary numbers for which the pore network model is a tractable modeling alternative is thus greatly extended by the semi-implicit method.

Keywords: porous media, two-phase flow, pore network model, numerical methods, time integration, stability, low capillary number

OPEN ACCESS

Edited by:
Romain Teyssier,
Universität Zürich, Switzerland

Reviewed by:
Daniele Chiappini,
Università degli Studi Niccolò Cusano, Italy
Christian F. Klingenberg,
Universität Würzburg, Germany

***Correspondence:**
Magnus Aa. Gjennestad
magnus@aashammer.net

Specialty section:
This article was submitted to Computational Physics, a section of the journal Frontiers in Physics

Received: *19 January 2018*
Accepted: *17 May 2018*
Published: *13 June 2018*

Citation:
Gjennestad MA, Vassvik M, Kjelstrup S and Hansen A (2018) Stable and Efficient Time Integration of a Dynamic Pore Network Model for Two-Phase Flow in Porous Media. Front. Phys. 6:56. doi: 10.3389/fphy.2018.00056

1. INTRODUCTION

Different modeling approaches have been applied in order to increase understanding of immiscible two-phase flow in porous media. On the pore scale, direct numerical simulation approaches using e.g. the volume of fluid method [1] or the level-set method [2, 3] to keep track of the fluid interface locations, have been used. The lattice-Boltzmann method is another popular choice, see e.g. Ramstad et al. [4]. These methods can provide detailed information on the flow in each pore. They are, however, computationally intensive and this restricts their use to relatively small systems.

Pore network models have proven to be useful in order to reduce the computational cost [5], or enable the study of larger systems, while still retaining some pore-level detail. In these models, the pore space is partitioned into volume elements that are typically the size of a single pore or throat. The average flow properties in these elements are then considered, without taking into account the variation in flow properties within each element.

Pore network models are typically classified as either quasi-static or dynamic. The quasi-static models are intended for situations where flow rates are low, and viscous pressure drops are

neglected on the grounds that capillary forces are assumed to dominate at all times. In the quasi-static models by Lenormand et al. [6], Willemsen [7], and Blunt [8], the displacement of one fluid by the other proceeds by the filling of one pore at the time, and the sequence of pore filling is determined by the capillary entry pressure alone.

The dynamic models, on the other hand, account for the viscous pressure drops and thus capture the interaction between viscous and capillary forces. As three examples of such models, we mention those by Hammond and Unsal [5], Joekar-Niasar et al. [9], and Aker et al. [10]. A thorough review of dynamic pore network models was performed by Joekar-Niasar and Hassanizadeh [11].

The pore network model we consider here is of the dynamic type that was first presented by Aker et al. [10]. Since the first model was introduced, it has been improved upon several times. Notably, it was extended to include film and corner flow by Tørå et al. [12]. The model considered here does not contain this extension. This class of models, which we call the Aker-type models, is different from the majority of other pore network models [5, 9] in that both the pore body and pore throat volumes are assigned to the links, and no volume is assigned to the nodes. Fluid interface locations are tracked explicitly as they move continuously through the pore space. This is in contrast to the model by Hammond and Unsal [5], where interfaces are moved through whole volume elements at each time step, and to the model of Joekar-Niasar et al. [9], where interface locations are only implicitly available through the volume element saturation. One of the advantages of the Aker-type model is that a detailed picture of the fluid configuration is provided at any time during a simulation. Dynamic phenomena, such as the retraction of the invasion front after a Haines jump [13–16], are thus easily resolved.

Since 1985, numerical instabilities at low capillary numbers have been known to occur for various types of dynamic pore network models [17]. A whole section is devoted to the topic in the review by Joekar-Niasar and Hassanizadeh [11]. It is important to address such stability problems rigorously, as many of the practical applications of two-phase porous media flow are in the low capillary number regime. Examples include most parts of the reservoir rock during CO_2 sequestration, flow of liquid water in fuel cell gas diffusion layers and studies of Haines jump dynamics, see e.g. Armstrong and Berg [15].

When Aker-type pore network models are used, the numerical instabilities are observed as oscillations in the positions of the fluid interfaces. Some efforts to avoid these oscillations have been made by introduction of modifications to the model. Medici and Allen [18] used a scheme where water was allowed to flow in the forward direction only in order to study water invasion in fuel cell gas diffusion layers. While this approach led to interesting results, it has some downsides. First, the interface movement is artificially restricted, and certain dynamic effects can not be resolved. This includes e.g. invasion front retraction after a Haines jump. Second, the method can only be used in cases with transient invasion. Studies of steady-state flow, such as those performed by Knudsen et al. [21] and Savani et al. [19], are not possible.

Because the oscillations originate in the numerical methods, rigorous attempts to remove them should focus on these methods rather than the models themselves. Joekar-Niasar et al. [9] followed this avenue and achieved stabilization using a linearized semi-implicit method. Their work, however, concerned a different type of pore network model than that considered here.

In this work, we present three numerical methods that can be utilized to perform stable simulations of two-phase flow in porous media with pore network models of the Aker type. The stability problems previously observed are thus solved without the need to resort to model modifications that restrict interface movement or preclude steady-state flow simulations. Two explicit methods are discussed, the forward Euler method and the midpoint method. These are stabilized by a new time step criterion derived herein. The third method is a new semi-implicit method. Thorough verifications of all methods are performed, confirming correct convergence properties and stability. Finally, we compare the methods in terms of performance.

The rest of this paper is structured as follows. Section 2 contains background information on the pore network model. Section 3 presents briefly the nomenclature, used in subsequent sections to describe the time integration methods. In section 4, we recapitulate how the forward Euler method is used to integrate the model and we present a new time step criterion that stabilizes both forward Euler and the midpoint method at low capillary numbers. We briefly review the midpoint method in section 5. The new semi-implicit method is described in detail in section 6. Some remarks about the numerical implementation are made in section 7. Section 8 contains a description of the cases simulated. Numerical experiments, including a Haines jump case, that show convergence and stability are given in section 9 and a comparison of the method performances are made in section 10. Section 11 summarizes and concludes the paper.

2. PORE NETWORK MODEL

We consider incompressible flow of two immiscible fluids in a porous medium, where one fluid is more wetting toward the pore walls than the other. We call the less wetting fluid non-wetting (n) and the more wetting fluid we call wetting (w). The porous medium is represented in the model by a network of N nodes connected by M links. Each node is given an index $i \in [0, N-1]$, and each link is identified by the indices of the two nodes it connects. An example pore network is shown in **Figure 1**. The nodes are points that have no volume and, consequently, all fluid is contained in the links. The links therefore represent both the pore and the throat volumes of the physical porous medium. In this respect, the pore network model studied here differ from most other pore network models [11]. Each fluid is assumed to fill

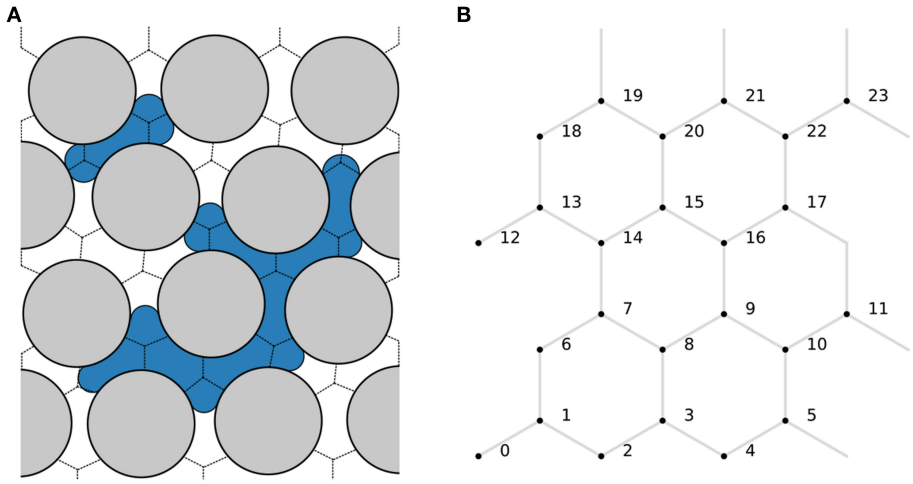

FIGURE 1 | Illustration of **(A)** a physical pore network with wetting (white) and non-wetting fluid (blue) and **(B)** its representation in the pore network model. The void space volumes separated by dashed lines in **(A)** are each represented as one link in **(B)**. The node points in the model representation **(B)** is assumed to be located at the intersection points of the dashed lines in **(A)**. Each fluid is assumed to fill the entire link cross section. The interface positions are therefore each represented in the model by a single number, giving its location along the link length.

the entire link cross section. The interface positions are therefore each represented in the model by a single number, giving its location along the link length.

The flow in each link is treated in a one-dimensional manner, where the flow is averaged over the link cross section. As we consider flow in relatively small cross sections only, we neglect any inertial effects and the volume flow rate ($m^3\ s^{-1}$) from node j to node i through the link connecting then is given by Washburn [20]

$$q_{ij} = -g_{ij}\left(\mathbf{z}_{ij}\right)\left\{p_i - p_j - c_{ij}\left(\mathbf{z}_{ij}\right)\right\}. \tag{1}$$

Herein, p_i (Pa) is the pressure in node i, g_{ij} ($m^3\ s^{-1}\ Pa^{-1}$) is the link mobility, c_{ij} (Pa) is the link capillary pressure and $\mathbf{z}_{ij}$ (m) is a vector containing the positions of any fluid interfaces present in the link. Both the link mobility and the capillary pressure depend on the fluid interface positions in the link. If two nodes i and j are *not* connected by a link, then $g_{ij} = 0$. Due to mass conservation, the net flow rate into every node i is zero

$$\sum_j q_{ij} = 0. \tag{2}$$

While the mobilities are symmetric with respect to permutation of the indices, the capillary pressures are anti-symmetric,

$$g_{ij} = g_{ji}, \tag{3}$$
$$c_{ij} = -c_{ji}. \tag{4}$$

Introducing this into Equation (1), we obtain the immediately intuitive result

$$q_{ij} = -q_{ji}. \tag{5}$$

The cross-sectional area of link ij is denoted a_{ij} (m^2). Interface positions are advected with the flow according to

$$\frac{\mathrm{d}}{\mathrm{d}t}\mathbf{z}_{ij} = \frac{q_{ij}}{a_{ij}}, \tag{6}$$

when they are sufficiently far away from the nodes. Near the nodes, however, the interfaces are subject to additional modeling to account for interface interactions in the pores. This is discussed further in section 2.3.

The form of the expressions for the mobilities and capillary pressures depends on the shape of the links, and many different choices and modeling approaches are possible. Here, we will use models similar to those previously presented and used by e.g. Knudsen et al. [21] and Aker et al. [10]. However, the treated time integration methods are more general and can be applied to other models as well.

2.1. Link Mobility Model

We apply a cylindrical link model when computing the mobilities, so that

$$g_{ij}(\mathbf{z}_{ij}) = \frac{\pi r_{ij}^4}{8 L_{ij}\mu_{ij}\left(\mathbf{z}_{ij}\right)}. \tag{7}$$

Here, r_{ij} (m) is the link radius and L_{ij} (m) is the link length. The viscosity μ_{ij} (Pa s) is the volume-weighted average of the fluid viscosities and can be computed from the wetting and non-wetting fluid viscosities μ_w and μ_n and the wetting fluid saturation s_{ij},

$$\mu_{ij}\left(\mathbf{z}_{ij}\right) = \mu_w s_{ij}\left(\mathbf{z}_{ij}\right) + \mu_n\left\{1 - s_{ij}\left(\mathbf{z}_{ij}\right)\right\}. \tag{8}$$

2.2. Capillary Pressure Model

In each link ij, there may be zero, one or more interfaces present. These are located at the positions specified in $\mathbf{z}_{ij}$. As the interfaces may be curved, there may be a discontinuity in pressure at these interface locations. The capillary pressure c_{ij} is the sum of interfacial pressure discontinuities in the link ij. When computing the capillary pressures, we assume that the links are wide near each end, and therefore that interfaces located near a link end have negligible curvature and no pressure discontinuity, while the links have narrow throats in the middle. The link capillary pressures are thus modeled as

$$c_{ij}\left(\mathbf{z}_{ij}\right) = \frac{2\sigma_{\mathrm{wn}}}{r_{ij}} \sum_{z \in \mathbf{z}_{ij}} (\pm 1) \left\{1 - \cos\left(2\pi\, \chi_{ij}\left(z\right)\right)\right\}. \tag{9}$$

The interfacial tension between the fluids is denoted σ_{wn} (N m^{-1}) and

$$\chi_{ij}\left(z\right) = \begin{cases} 0 & z < \alpha r_{ij}, \\ \frac{z - \alpha r_{ij}}{L_{ij} - 2\alpha r_{ij}} & \alpha r_{ij} < z < L_{ij} - \alpha r_{ij}, \\ 1 & z > L_{ij} - \alpha r_{ij}. \end{cases} \tag{10}$$

The χ_{ij}-function ensures zones of length αr_{ij} at both ends of each link with zero capillary pressure across any interface located there. Choosing $\alpha = 0$ is equivalent to replacing χ_{ij} with z/L_{ij} in (9).

2.3. Fluid Interface Interaction Models

The equations discussed so far in this section describe how the fluids and the fluid interfaces move through the links. In addition, we rely on models for how they behave close to the nodes. The purpose of these are to emulate interface interactions in the pore spaces.

The following is assumed about the fluid behavior near the nodes and is accounted for by the fluid interface interaction models.

- The mass of each fluid is conserved at every node. This means that at all times, all wetting and non-wetting fluid flowing into a node from one subset of its neighboring links must flow out into another disjoint subset of its neighboring links.
- The network nodes in the model have no volume. However, due to the finite size of the physical pore void spaces, wetting fluid flowing into a pore space must be able to flow freely past any non-wetting fluid occupying the node point if the non-wetting fluid does not extend far enough into the pore void space cut the wetting fluid off. An example is illustrated in **Figure 2**. We consider a link ij to be cut off from free outflow of wetting fluid if the non-wetting fluid continuously extends a length at least αr_{ij} into the link. Non-wetting fluid may freely flow past wetting fluid, or not, the same manner.
- In each link ij, interfacial tension will prevent droplets with length smaller than αr_{ij} from forming by separation from larger droplets. An example is illustrated in **Figure 3**.

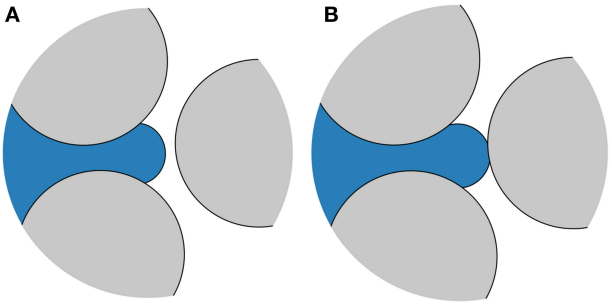

FIGURE 2 | Network node connected to three links. The node point, located near the middle of the pore space, is occupied by non-wetting fluid (blue). **(A)** The non-wetting fluid extends only a short distance into the links containing wetting fluid (white). The wetting fluid therefore remains connected and may flow freely through the pore space. **(B)** Non-wetting fluid protrudes far enough into all links to block the pore space for wetting fluid. The wetting fluid must now displace the non-wetting fluid in order to flow through.

2.4. Boundary Conditions

We consider only networks where the nodes and links can be laid out in the two-dimensional x-y plane. These networks will be periodic in both the x- and y-direction. However, the model is also applicable to networks that extend in three dimensions [22], and the presented numerical methods are also compatible both with networks in three dimensions and with other, non-periodic boundary conditions [23].

We will here apply two types of boundary conditions to the flow. With the first type, a specified pressure difference ΔP (Pa) will be applied across the network in the y-direction. This pressure difference will be equal to the sum of all link pressure differences in any path spanning the network once in the y-direction, ending up in the same node as it started. With the other type of boundary condition, we specify a total flow rate Q (m^3 s^{-1}) across the network. This flow rate will be equal to the sum of link flow rates flowing through any plane drawn through the network normal to the y-axis.

3. TEMPORAL DISCRETIZATION

In the following three sections, we describe the different time integration methods considered. These methods are applied to Equation (6), where evaluation of the right hand side involves simultaneously solving the mass conservation equation (2) and the constitutive equation (1) to obtain all unknown link flow rates and node pressures.

The discretized times (s) are denoted with a superscript where n is the time step number,

$$t^{(n)} = t^{(0)} + \sum_{i=0}^{n-1} \Delta t^{(i)}. \tag{11}$$

The time step $\Delta t^{(i)}$ is the difference between $t^{(i+1)}$ and $t^{(i)}$ and the time $t^{(0)}$ is the initial time in a simulation. Similarly,

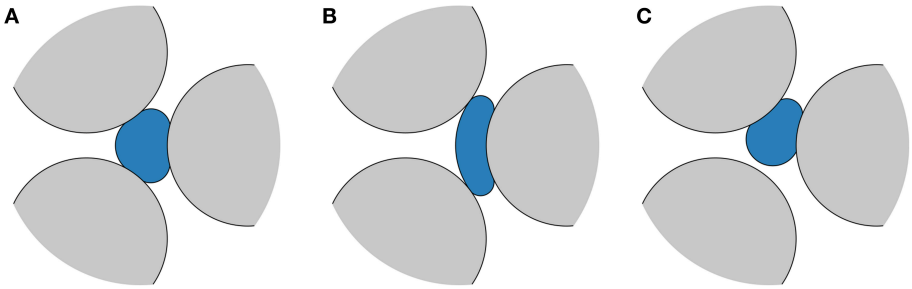

FIGURE 3 | (A) Small non-wetting bubble (blue) whose volume is small compared to the link volumes and is prevented from splitting by interfacial tension. This limits the minimum size of non-wetting bubbles, which will either **(B)** be stuck or **(C)** move through one of the links without splitting.

quantities evaluated at the discrete times are denoted with time step superscripts, e.g.

$$q_{ij}^{(n)} = q_{ij}\left(t^{(n)}\right). \tag{12}$$

Mobilities and capillary pressures with superscripts are evaluated using the interface positions at the indicated time step,

$$g_{ij}^{(n)} = g_{ij}\left(\mathbf{z}_{ij}^{(n)}\right), \tag{13}$$

$$c_{ij}^{(n)} = c_{ij}\left(\mathbf{z}_{ij}^{(n)}\right). \tag{14}$$

4. FORWARD EULER METHOD

The forward Euler method is the simplest of the time integration methods considered here and is the one used most frequently in previous works, see e.g. Knudsen et al. [21] and Sinha and Hansen [24]. We include its description here for completeness and to provide context for the proposed new capillary time step criterion that is introduced to stabilize the method at low capillary numbers.

The ordinary differential equation (ODE) (6) is discretized in a straightforward manner for each link ij using forward Euler,

$$\mathbf{z}_{ij}^{(n+1)} = \mathbf{z}_{ij}^{(n)} + \Delta t^{(n)} \frac{q_{ij}^{(n)}}{a_{ij}}. \tag{15}$$

The flow rates are calculated by inserting Equation (1), evaluated with the current known interface positions,

$$q_{ij}^{(n)} = -g_{ij}^{(n)}\left\{p_i^{(n)} - p_j^{(n)} - c_{ij}^{(n)}\right\}, \tag{16}$$

into the mass conservation equation (2). This results in the a system of linear equations consisting of one equation,

$$\sum_j g_{ij}^{(n)} p_j^{(n)} - p_i^{(n)} \sum_j g_{ij}^{(n)} = -\sum_j g_{ij}^{(n)} c_{ij}^{(n)}, \tag{17}$$

for each node i with unknown pressure. This linear system can be cast into matrix form,

$$\mathbf{A} \cdot \mathbf{x} = \mathbf{b}, \tag{18}$$

where the vector $\mathbf{x}$ contains the unknown node pressures, e.g.

$$\mathbf{x} = \begin{bmatrix} p_0^{(n)} \\ p_1^{(n)} \\ \vdots \\ p_{N-1}^{(n)} \end{bmatrix}. \tag{19}$$

The matrix elements are

$$A_{ij} = \left\{1 - \delta_{ij}\right\} g_{ij}^{(n)} - \delta_{ij} \sum_k g_{ik}^{(n)}, \tag{20}$$

and the elements of the constant vector are

$$b_i = -\sum_k g_{ik}^{(n)} c_{ik}^{(n)}. \tag{21}$$

The node pressures are obtained by solving this linear equation system. The flow rates are subsequently evaluated using Equation (16) and the interface positions are then updated using Equation (15) and the interface interaction models.

4.1. Time Step Restrictions

In previous works [10, 21], the time step length was chosen from a purely advective criterion,

$$\Delta t_{\mathrm{a}}^{(n)} = C_{\mathrm{a}} \min_{ij}\left(\frac{a_{ij} L_{ij}}{q_{ij}^{(n)}}\right). \tag{22}$$

The parameter C_{a} corresponds to the maximum fraction of a link length any fluid interface is allowed to move in a single forward Euler time step. The value of C_{a} must be chosen based on the level of accuracy desired from the simulation.

However, selecting the time step based on the advective criterion only, often results in numerical instabilities at low capillary numbers, where viscous forces are small relative to the capillary forces. This is demonstrated in section 9.2. The origins of the numerical instabilities can be identified by performing analysis on a linearized version of the governing equations. This is done in Appendix A. This analysis also leads to a new time step criterion, whereby the time step length is restricted by the

sensitivity of the capillary forces to perturbations in the current interface positions,

$$\Delta t_{\mathrm{c}}^{(n)} = C_{\mathrm{c}} \min_{ij} \left(\frac{2a_{ij}}{g_{ij}^{(n)} \left| \sum_{z \in \mathbf{z}_{ij}^{(n)}} \frac{\partial c_{ij}}{\partial z} \right|} \right). \tag{23}$$

For the particular choice of capillary pressure model given by (9), we obtain

$$\Delta t_{\mathrm{c}}^{(n)} = C_{\mathrm{c}} \min_{ij} \left(\frac{a_{ij} r_{ij} L_{ij}}{2\pi g_{ij}^{(n)} \sigma_{\mathrm{wn}} \left| \sum_{z \in \mathbf{z}_{ij}^{(n)}} (\pm 1) \sin\left(2\pi \chi_{ij}(z)\right) \frac{\mathrm{d}\chi_{ij}}{\mathrm{d}z} \right|} \right). \tag{24}$$

According to the linear analysis, numerical instabilities are avoided if the parameter C_{c} is chosen such that $0 < C_{\mathrm{c}} < 1$. However, we must regard (23) as an approximation when we apply it to the full non-linear model in simulations and, consequently, we may have to chose C_{c} conservatively to ensure stability for all cases.

At each step in the simulation, the time step used is then taken as

$$\Delta t^{(n)} = \min\left(\Delta t_{\mathrm{c}}^{(n)}, \Delta t_{\mathrm{a}}^{(n)}\right), \tag{25}$$

to comply with both the advective and the capillary time step criteria. The capillary time step restriction (23) is independent of flow rate. It therefore becomes quite severe, demanding relatively fine time steps, when flow rates are low.

4.2. Boundary Conditions

The periodic boundary conditions, specifying a total pressure difference ΔP across the network, can be incorporated directly into the linear equation system (18). For each node i, a term $g_{ij}^{(n)} \Delta P$ is added to or subtracted from b_i for any link ij that crosses the periodic boundary.

With the specified ΔP condition implemented, we can use it to obtain the node pressures and link flow rates corresponding to a specified total flow rate Q. Due to the linear nature of the model, the total flow rate is linear in ΔP [10], so that

$$Q = C_1 \Delta P + C_2, \tag{26}$$

for some unknown coefficients C_1 and C_2, that are particular to the current fluid configuration.

We choose two different, but otherwise arbitrary, pressure drop values ΔP_1 and ΔP_2 and, using the above procedure, we solve the network model once for each pressure difference and calculate the corresponding total flow rates Q_1 and Q_2. The coefficients C_1 and C_2 are then determined by,

$$C_1 = \frac{Q_2 - Q_1}{\Delta P_2 - \Delta P_1}, \tag{27}$$

$$C_2 = \frac{Q_2 \Delta P_1 - Q_1 \Delta P_2}{\Delta P_1 - \Delta P_2}. \tag{28}$$

The pressure difference ΔP required to obtain the specified flow rate Q is determined by solving Equation (26) for ΔP. Subsequently, the network model is solved a third time with pressure drop ΔP to obtain the desired node pressures and link flow rates.

5. MIDPOINT METHOD

The forward Euler method is first-order accurate in time. To obtain smaller numerical errors, methods of higher order are desirable. We therefore include in our discussion the second-order midpoint method. This method is identical to that used by Aker et al. [10], except with respect to choice of time step length.

The ODE (6) is discretized as

$$\mathbf{z}_{ij}^{(n+1)} = \mathbf{z}_{ij}^{(n)} + \Delta t^{(n)} \frac{q_{ij}^{(n+1/2)}}{a_{ij}}, \tag{29}$$

where $q_{ij}^{(n+1/2)}$ is the flow rate at the midpoint in time between point n and $n+1$. This flow rate is calculated in the same manner as described in section 4. The interface positions at $n + 1/2$ are obtained by taking a forward Euler step with half the length of the whole time step,

$$\mathbf{z}_{ij}^{(n+1/2)} = \mathbf{z}_{ij}^{(n)} + \frac{1}{2} \Delta t^{(n)} \frac{q_{ij}^{(n)}}{a_{ij}}. \tag{30}$$

5.1. Time Step Restrictions

Since the forward Euler stability region is contained within the stability region for the midpoint method, we use the same time step restrictions for the midpoint method as for forward Euler, see section 4.1.

5.2. Boundary Conditions

Both the specified ΔP and the specified Q boundary conditions are incorporated into the midpoint method by applying the procedures described in section 4.2 for each evaluation of the right hand side of Equation (6).

6. SEMI-IMPLICIT METHOD

To avoid both the numerical instabilities and the time step restriction (23), which becomes quite severe at low flow rates, we here develop a new semi-implicit time stepping method. Simulation results indicate that this method is stable with time steps determined by the advective criterion (22) only, and much longer time steps are therefore possible than with the forward Euler and midpoint methods at low capillary numbers.

The ODE (6) is now discretized according to

$$\mathbf{z}_{ij}^{(n+1)} = \mathbf{z}_{ij}^{(n)} + \Delta t^{(n)} \frac{q_{ij}^{(n+1)}}{a_{ij}}. \tag{31}$$

The semi-implicit nature of this discretization comes from the flow rate used,

$$q_{ij}^{(n+1)} = -g_{ij}^{(n)} \left\{ p_i^{(n+1)} - p_j^{(n+1)} - c_{ij}^{(n+1)} \right\}. \tag{32}$$

Herein, the link mobility is evaluated at time step n, while the node pressures and the capillary pressure are evaluated time step $n+1$.

The link mobilities could of course also have been evaluated at time step $n+1$, thus creating a fully implicit backward Euler scheme. As is shown in Appendix A, we may expect backward Euler to be stable with any positive $\Delta t^{(n)}$. The backward Euler scheme may therefore seem like a natural choice for performing stable simulations with long time steps. However, to evaluate the mobilities at time step $n+1$ complicates the integration procedure and was found to be unnecessary in practice. A semi-implicit alternative is therefore preferred.

To obtain the node pressures, we solve the mass conservation equations,

$$F_i = \sum_k q_{ik}^{(n+1)} = 0. \tag{33}$$

Again, we have one equation for each node i with unknown pressure. However, because the capillary pressures now depend on the flow rates,

$$c_{ij}^{(n+1)} = c_{ij}\left(\mathbf{z}_{ij}^{(n)} + \Delta t^{(n)}\frac{q_{ij}^{(n+1)}}{a_{ij}}\right), \tag{34}$$

the mass conservation equations are now a system of non-linear equations, rather than a system of linear equations. This system can be cast in the form

$$\mathbf{F}(\mathbf{x}) = \mathbf{0}, \tag{35}$$

where $\mathbf{x}$ contains the unknown pressures, e.g.

$$\mathbf{x} = \begin{bmatrix} p_0^{(n+1)} \\ p_1^{(n+1)} \\ \vdots \\ p_{N-1}^{(n+1)} \end{bmatrix}. \tag{36}$$

In order to solve Equation (35) using the numerical method described in section 7, it is necessary to have the Jacobian matrix of $\mathbf{F}$. Details on how the Jacobian matrix is calculated are given in Appendix B.

The calculation of link flow rates from node pressures, and thus every evaluation of $\mathbf{F}$ and its Jacobian, involves solving one non-linear equation for each link flow rate,

$$G_{ij}\left(q_{ij}^{(n+1)}\right) = q_{ij}^{(n+1)} + g_{ij}^{(n)}\left\{p_i^{(n+1)} - p_j^{(n+1)} - c_{ij}^{(n+1)}\right\} = 0. \tag{37}$$

The derivative of G_{ij} with respect to $q_{ij}^{(n+1)}$ is

$$\frac{\mathrm{d}G_{ij}}{\mathrm{d}q_{ij}^{(n+1)}} = 1 - g_{ij}^{(n)}\frac{\mathrm{d}c_{ij}^{(n+1)}}{\mathrm{d}q_{ij}^{(n+1)}}. \tag{38}$$

The procedure for updating the interface positions with the semi-implicit method may be summarized as follows. The non-linear equation system (35) is solved to obtain the unknown node pressures. In every iteration of the solution procedure, the flow rates are evaluated by solving Equation (37) for each link. When a solution to Equation (35) is obtained, the interface positions are updated using Equation (31) and the interface interaction models.

6.1. Time Step Restrictions

We aim to select the time steps such that

$$\Delta t^{(n)} = \Delta t_{\mathrm{a}}^{(n+1)}. \tag{39}$$

However, to solve the non-linear system (35) is challenging in practice and requires initial guess values for the link flow rates and node pressures that lie sufficiently close to the solution. For this purpose, we here use values from the previous time step. This turns out to be a sufficiently good choice for most time steps, but our numerical solution procedure does not always succeed. As the link flow rates and node pressures at two consecutive points in time become increasingly similar as the time interval between them is reduced, we may expect the guess values to lie closer to the solution if we reduce the time step. Thus, if our solution procedure is unable to succeed, our remedy is to shorten $\Delta t^{(n)}$. This will sometimes lead to time steps shorter than $\Delta t_{\mathrm{a}}^{(n+1)}$. If, for a given time step, $\Delta t^{(n)}$ must be reduced to less than twice the time step length allowed by the explicit methods, we revert to forward Euler for that particular step. As we demonstrate in section 10, however, this does not prevent the semi-implicit method from being much more efficient than the explicit methods at low capillary numbers.

6.2. Boundary Conditions

As with the explicit methods, the specified ΔP boundary condition can be incorporated directly into the mass balance equation system, in this case Equation (35). This is done by adding to or subtracting from the right hand sides of Equation (32) and Equation (37) a term $g_{ij}^{(n)}\Delta P$ for each link ij crossing the periodic boundary.

The specified flow rate boundary condition is incorporated by including ΔP as an additional unknown and adding an additional equation

$$F_m = \left\{\sum_{ij\in\Omega} q_{ij}^{(n+1)}\right\} - Q = 0, \tag{40}$$

to the non-linear equation system (35). Herein, Ω is the set of links crossing the periodic boundary, with i being the node on the downstream side and j being the node on the upstream side. Thus, Equation (40) is satisfied when the total flow rate through the network is equal to Q.

7. IMPLEMENTATION

The non-linear equation system (35) is solved using a Newton-type solution method that guarantees convergence to a local

minimum of $\mathbf{F} \cdot \mathbf{F}$, see Press et al. [25, p. 477]. However, a local minimum of $\mathbf{F} \cdot \mathbf{F}$ is not necessarily a solution to Equation (35), and good initial guess values for the node pressures and link flow rates are therefore crucial. For this purpose, we use the values from the previous time step and reduce the length of the current time step if the solution method fails, as discussed in section 6.1.

Solving Equation (37) is done using a standard Newton solver [26]. For robustness, a bisection solver [26] is used if the Newton solver fails.

The Newton-type solver for non-linear systems and the explicit time integration methods require methods for solving linear systems of equations. We use the conjugate gradient method in combination with the LU preconditioner implemented in the PETSc library, see Balay et al. [27]. An introduction to solving systems of Kirchhoff-type equations numerically can be found in Batrouni and Hansen [28].

8. CASE DESCRIPTIONS

In this section, we describe the two simulated cases. One is a test case where a single bubble is contained in a network consisting of links connected in series, while the other is designed to capture a single Haines jump in a small network where fluids flow at a specified rate.

8.1. Links-in-Series Test Case

The verification will include comparison of results from the various numerical methods applied to a test case. The test case is chosen such that it can be set up as a single ODE with a closed expression for the right-hand side. An accurate reference solution can thus be easily obtained using a high-order Runge–Kutta method. As our test case, we consider a network consisting of $M = 3$ identical links connected in series. The network contains a single bubble of length ℓ (m) with center position z (m). In the capillary pressure model, we choose $\alpha = 0$. The ODE (6) can then be restated as an equivalent equation for the bubble position,

$$\frac{\mathrm{d}z}{\mathrm{d}t} = \frac{Q}{a}, \tag{41}$$

where Q is the flow through the network and a is the link cross-sectional area. The model equations can be reduced to the following expression for flow rate.

$$Q = -\frac{g}{M}\left\{\Delta P + \frac{4\sigma_{\mathrm{wn}}}{r}\sin\left(\frac{\pi\ell}{L}\right)\sin\left(\frac{2\pi z}{L}\right)\right\} \tag{42}$$

Here, g is the mobility of a single link, $L = 1.0 \cdot 10^{-3}$ m is the length of a single link and $r = 1.0 \cdot 10^{-4}$ m is the link radius. The bubble has length $\ell = 4.8 \cdot 10^{-4}$ m and is initially located at $z = 2.4 \cdot 10^{-4}$ m. The fluid parameters used in all simulations are given in **Table 1**. The pressure difference ΔP will be stated for each simulation.

8.2. Haines Jump Case

The Haines jump was first reported almost 90 years ago [13]. It refers to the sudden drops in driving pressure observed in drainage experiments when non-wetting fluid breaks through a throat and invades new pores. This process was studied experimentally and numerically by Måløy et al. [16] and, more recently, it was imaged directly and analyzed in detail by Armstrong and Berg [15] for flow in a micromodel and by Berg et al. [14] for flow in a sample of Berea sandstone. The Haines jump case simulated here captures one such break-through and subsequent pressure drop.

TABLE 1 | Fluid properties corresponding to water (w) and decane (n) at atmospheric pressure and 298 K.

Parameter	Value	Unit	References
μ_{w}	$8.9 \cdot 10^{-4}$	Pa s	[29]
μ_{n}	$8.5 \cdot 10^{-4}$	Pa s	[29]
σ_{wn}	$5.2 \cdot 10^{-2}$	$\mathrm{N\,m^{-1}}$	[30]

Among the findings in the study by Måløy et al. [16] was that pore drainage is a non-local event, meaning that as one pore is drained, imbibition occurs in nearby neck regions. This was also observed by Armstrong and Berg [15], and was explained as follows. When the imposed flow rates are low, the non-wetting fluid that fills the newly invaded pores needs to be supplied from nearby locations rather than the external feed. Armstrong and Berg [15] also found, for their range of investigated parameters, that pore drainage occurred on the same time-scale, regardless of the externally imposed flow rate.

We consider a hexagonal network consisting $N = 24$ nodes and $M = 36$ links. All links have length $1.0 \cdot 10^{-3}$ m, while the link radii are drawn randomly from a uniform distribution between 0.1 and 0.4 link lengths. In the capillary pressure model, we choose $\alpha = 1$. The fluid parameters μ_{w}, μ_{n} and σ_{wn} are the same as in the links-in-series test case, see **Table 1**. With these fluid parameters and network length scales, the case mimics the flow of water (w) and decane (n) in a Hele-Shaw cell filled with glass beads similar to those used in e.g. Måløy et al. [16, 31] and Tallakstad et al. [32]. The linear dimensions are ~ 10 times bigger in this network compared to the micromodel of Armstrong and Berg [15]. Initially, the fluids are distributed in the network as shown in **Figure 4**, with the non-wetting fluid in a single connected ganglion.

Simulations are run at different specified flow rates Q until a net fluid volume equivalent to 5% of the total pore volume has flowed through the network. The flow dynamics will, of course, depend upon the specified flow rate. At low flow rates, however, the flow will exhibit some relatively fast fluid redistribution events and one relatively slow pressure build-up and subsequent Haines jump event. The Haines jump will occur as the non-wetting fluid breaks through the link connecting nodes 9 and 16 and invades node 16, see **Figure 4**.

It was mentioned by Armstrong and Berg [15] that the large local flow velocities that they observed as a pore was filled with non-wetting fluid during a Haines jump has implications for how such processes must be numerically simulated. Specifically, the time resolution of the simulation needs to be fine enough during these events to capture them. This poses a challenge when externally applied flow rates are low and there is thus a large difference in the large time

scale that governs the overall flow of the system and the small time scale than governs the local flow during Haines jumps.

9. VERIFICATION

In this section, we verify that the time integration methods presented correctly solve the pore network model equations and that the time step criteria presented give stable solutions.

9.1. Convergence Tests

All time integration methods presented should, of course, give the same solution for vanishingly small time steps. Furthermore, the difference between the solution obtained with a given finite time step and the fully converged solution should decrease as the time steps are refined, and should do so at a rate that is consistent with the order of the method. In this section, we verify that all three time integration methods give solutions that converge to the reference solution for the links-in-series test case and thus that the methods correctly solve the model equations for this case.

We choose the pressure difference to be $\Delta P = -3200\,\text{Pa}$. This value is large enough to overcome the capillary forces and push the non-wetting bubble through the links. We therefore expect a flow rate Q that varies in time, but is always positive.

As measures of the numerical error, we consider both the relative error in the flow rate Q and the relative error in bubble position z between the numerical solutions and reference solutions at the end of the simulation. Time integration is performed from $t = 0\,\text{s}$ to $t = 0.001\,44\,\text{s}$. To have control over the time step lengths, we ignore all time step criteria for now and instead set a constant Δt for each simulation.

In **Figure 5**, flow rates are plotted for each of the time integration methods. Results using a coarse time step, $\Delta t = 4 \cdot 10^{-5}\,\text{s}$, and a fine time step, $\Delta t = 1 \cdot 10^{-5}\,\text{s}$, are shown along with the reference solution.

For the forward Euler and the semi-implicit method, there is considerable discrepancy between the numerical and the reference solution with the coarse time step. The flow rate obtained from forward Euler lags behind the reference solution, while that from the semi-implicit method lies ahead of it. This may be expected, however, since forward Euler at each time step uses current information in the right hand side evaluation, whereas the semi-implicit method uses a combination of current and future information. With the fine time step, there is less difference between the reference and the numerical solutions.

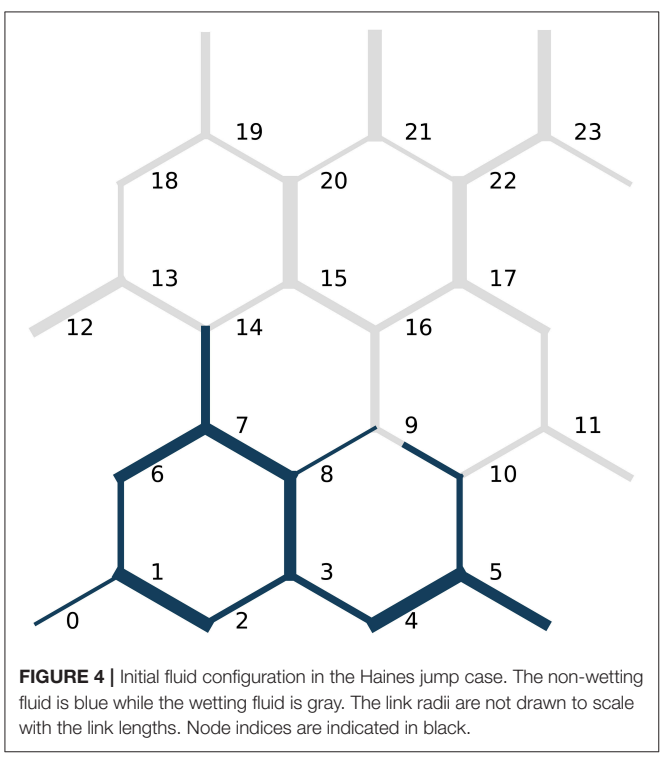

FIGURE 4 | Initial fluid configuration in the Haines jump case. The non-wetting fluid is blue while the wetting fluid is gray. The link radii are not drawn to scale with the link lengths. Node indices are indicated in black.

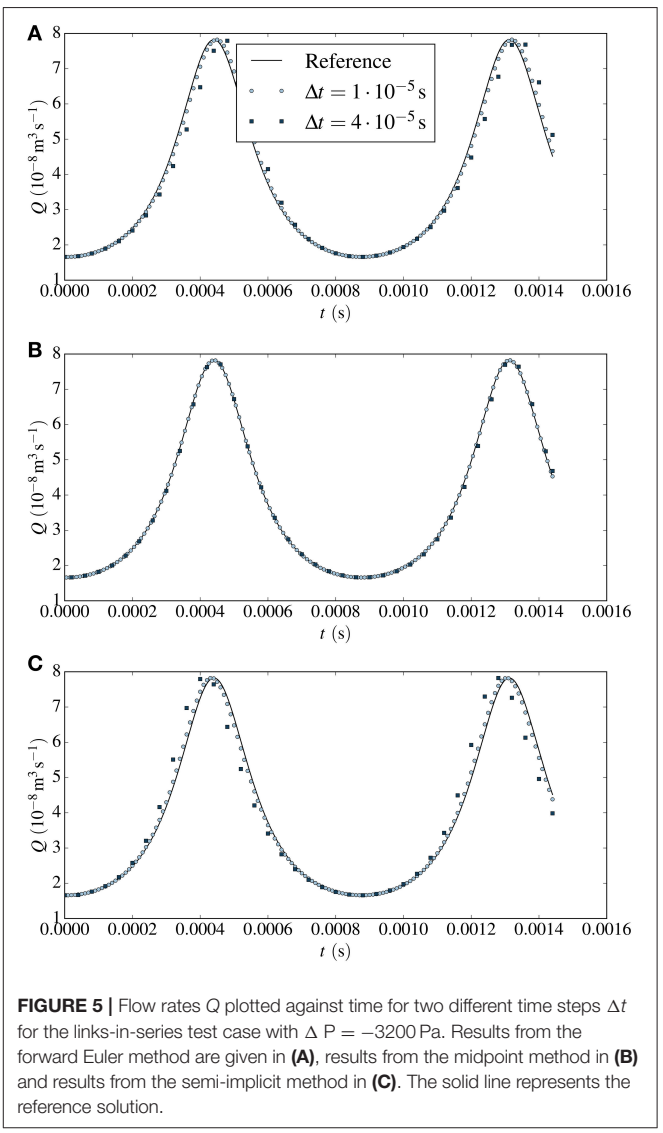

FIGURE 5 | Flow rates Q plotted against time for two different time steps Δt for the links-in-series test case with $\Delta P = -3200\,\text{Pa}$. Results from the forward Euler method are given in **(A)**, results from the midpoint method in **(B)** and results from the semi-implicit method in **(C)**. The solid line represents the reference solution.

With the more accurate midpoint method, the coarse-stepped numerical solution lies only marginally ahead of the reference solution while there is no difference between the fine-stepped numerical solution and the reference solution at the scale of representation.

The convergence of the numerical solutions to the reference solution upon time step refinement is quantified in **Tables 2–4**. Herein, the numerical errors and estimated convergence orders are given for the forward Euler, midpoint and semi-implicit method, respectively. For all methods considered, the numerical errors decrease when the time step is refined and do so at the rate that is expected. The forward Euler and the semi-implicit method exhibit first-order convergence, while the midpoint method shows second-order convergence. We note that the errors in both z and Q are similar in magnitude for the forward Euler and the semi-implicit method. The errors obtained with the midpoint method are smaller. The difference is one order of magnitude for $\Delta t = 1 \cdot 10^{-5}$ s.

In summary, we have verified that the presented time integration methods correctly solve the pore network model equations for the links-in-series test case and that the numerical errors decrease upon time step refinement at the rate that is consistent with the expected order of the methods.

TABLE 2 | Relative errors in bubble position z and flow rate Q at $t = 0.001\,44$ s and estimated convergence orders for the links-in-series test case computed with the forward Euler method.

Δt (s)	z-error	z-order	Q-error	Q-order
$4 \cdot 10^{-5}$	$1.55 \cdot 10^{-2}$		$1.33 \cdot 10^{-1}$	
$2 \cdot 10^{-5}$	$7.44 \cdot 10^{-3}$	1.06	$6.41 \cdot 10^{-2}$	1.06
$1 \cdot 10^{-5}$	$3.66 \cdot 10^{-3}$	1.02	$3.15 \cdot 10^{-2}$	1.02
$5 \cdot 10^{-5}$	$1.82 \cdot 10^{-3}$	1.01	$1.57 \cdot 10^{-2}$	1.01

TABLE 3 | Relative errors in bubble position z and flow rate Q at $t = 0.001\,44$ s and estimated convergence orders for the links-in-series test case computed with the midpoint method.

Δt (s)	z-error	z-order	Q-error	Q-order
$8 \cdot 10^{-5}$	$1.67 \cdot 10^{-2}$		$1.44 \cdot 10^{-1}$	
$4 \cdot 10^{-5}$	$4.24 \cdot 10^{-3}$	1.98	$3.65 \cdot 10^{-3}$	1.98
$2 \cdot 10^{-5}$	$1.08 \cdot 10^{-3}$	1.97	$9.33 \cdot 10^{-3}$	1.97
$1 \cdot 10^{-5}$	$2.86 \cdot 10^{-4}$	1.92	$2.46 \cdot 10^{-3}$	1.92

TABLE 4 | Relative errors in bubble position z and flow rate Q at $t = 0.001\,44$ s and estimated convergence orders for the links-in-series test case computed with the semi-implicit method.

Δt (s)	z-error	z-order	Q-error	Q-order
$4 \cdot 10^{-5}$	$1.39 \cdot 10^{-2}$		$1.18 \cdot 10^{-1}$	
$2 \cdot 10^{-5}$	$6.98 \cdot 10^{-3}$	0.99	$5.97 \cdot 10^{-2}$	0.98
$1 \cdot 10^{-5}$	$3.51 \cdot 10^{-3}$	0.99	$3.01 \cdot 10^{-2}$	0.99
$5 \cdot 10^{-5}$	$1.76 \cdot 10^{-3}$	1.00	$1.5 \cdot 10^{-2}$	1.00

9.2. Stability Tests

In this section, we demonstrate that the proposed capillary time step criterion (23) stabilizes the forward Euler method and the midpoint method at low flow rates. We simulated two different cases and varied C_c. Simulations run with low C_c turned out to be free of spurious oscillations, indicating that the proposed criterion stabilizes the methods, while simulations run with C_c significantly larger than unity produced oscillations, indicating that the proposed criterion is not unnecessarily strict.

First, consider the links-in-series test case with $\Delta P = 0$ Pa. With no applied pressure difference, the flow is driven purely by the imbalance of capillary forces on the non-wetting bubble. Therefore, there should only be flow initially and the bubble should eventually reach an equilibrium position where both interfaces experience the same capillary force and the flow rate is zero. Simulations were run with $C_a = 0.1$ and C_c equal to 2.0, 1.0, and 0.5. Results from forward Euler are shown in **Figure 6A** and results from the midpoint method are shown in **Figure 6B**. In both figures, the reference solution is also shown.

The forward Euler results are stable and qualitatively similar to the reference solution with $C_c = 0.5$. With $C_c = 1.0$, there are some oscillations initially that are dampened and eventually vanish. From comparison with the reference solution, it is clear that such oscillations have no origin in the model equations and are artifacts of the numerical method. With $C_c = 2.0$, the oscillations are severe and do not appear to be dampened by the method. Instead the non-wetting bubble keeps oscillating around its equilibrium position in a manner that is clearly unphysical.

The results from the midpoint method in **Figure 6B** follow a qualitatively similar trend as those from forward Euler with regard to stability. Results computed with $C_c = 0.5$ are stable and results with $C_c = 2.0$ exhibit severe oscillations. Still, the results from the midpoint method lie much closer to the reference solution than the results from the forward Euler method, as we would expect since the midpoint method is second-order. Both methods are, however, unstable with $C_c = 2.0$, indicating that the while the midpoint method has improved accuracy over forward Euler, it is unable to take significantly longer time steps without introducing oscillations. This is consistent with the analysis in Appendix A, since the two methods have identical stability regions in real space.

Next, consider the Haines jump case with $Q = 10^{-9}\,\mathrm{m^3\,s^{-1}}$, corresponding to $\mathrm{Ca} = 1.2 \cdot 10^{-5}$. This case was run using the forward Euler method, $C_a = 0.1$ and three different values of C_c, equal to 4.0, 2.0, and 1.0. The required pressure difference to drive the flow at the specified rate is shown in **Figure 7A**. **Figure 7B** shows the pressure from **Figure 7A** in greater detail.

For all three values of C_c, the main qualitative features of the flow are captured. We observe short transient pressure drops at $t \approx 0.08$ s and $t \approx 0.20$ s. These correspond to fluid redistribution events on the upstream side of the non-wetting ganglion, where the fluid rearranges itself to a more stable configuration with little change to the interface positions on the downstream side. The event at $t \approx 0.20$ s is illustrated in **Figure 8**. The fluid redistribution is driven by capillary forces and less external

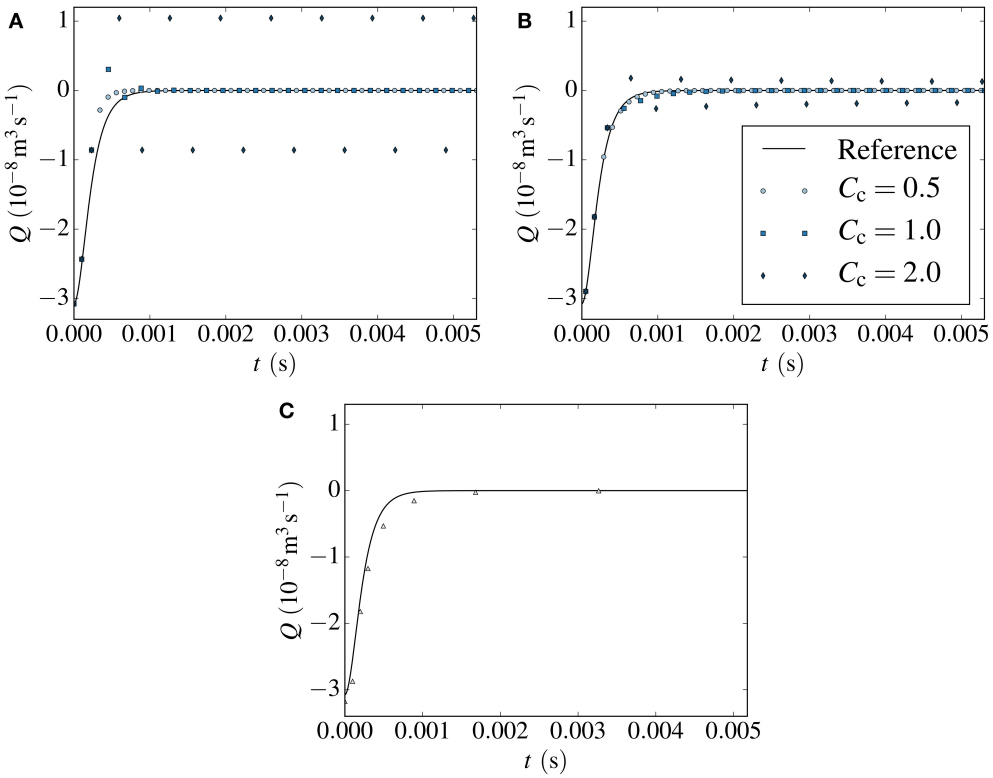

FIGURE 6 | Flow rate plotted against time in the link-in-series test case with $\Delta P = 0$ Pa. Results from the forward Euler method **(A)** and the midpoint method **(B)** are shown for different values of C_c. Severe numerical instabilities arise when $C_c = 2.0$. Results from the semi-implicit method are shown are shown in **(C)**. These are stable, even if the capillary time step criterion is not used. The solid black line represents a reference solution.

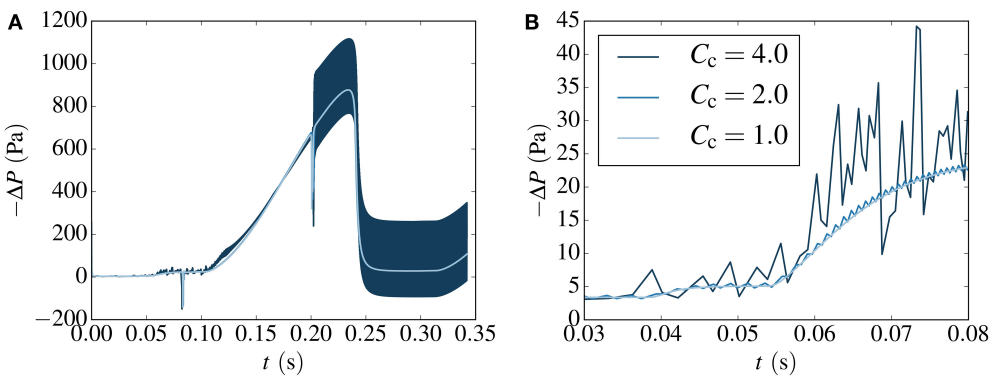

FIGURE 7 | Pressure difference required to drive the flow in the Haines jump case at a rate of $Q = 10^{-9}$ m^3 s^{-1}, corresponding to Ca $= 1.2 \cdot 10^{-5}$. In **(B)**, the results from **(A)** are shown in greater detail. Results are computed with the forward Euler method for different values of the capillary time step restriction parameter C_c. Numerical instabilities are seen to occur for $C_c > 1$.

pressure is therefore required to drive the flow during these events.

We also observe the slow pressure build-up from $t \approx 0.10$ s to $t \approx 0.23$ s, when the driving pressure becomes large enough to overcome the capillary forces and cause break-through of non-wetting fluid in the link connecting nodes 9 and 16, and we observe the subsequent Haines jump. The fluid configurations before and after the Haines jump are shown in **Figure 9**. Notice also that non-wetting fluid at the downstream end of the moving ganglion retracts during the Haines jump in links near to where the break-through occurs. This is seen e.g. in the links downstream of nodes 10 and 14. That such local imbibition occurs near the drained pore is in agreement with the observations of

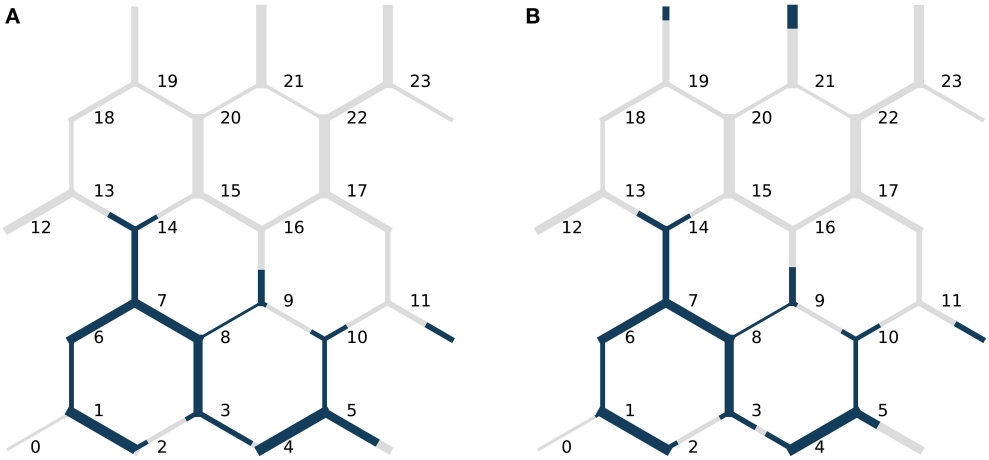

FIGURE 8 | Fluid distribution in the Haines jump case, **(A)** at $t = 0.19\,\mathrm{s}$ and **(B)** at $t = 0.21\,\mathrm{s}$, before and after the fluid redistribution event at $t \approx 0.20\,\mathrm{s}$. The link radii are not drawn to scale with the link lengths. Node indices are indicated in black.

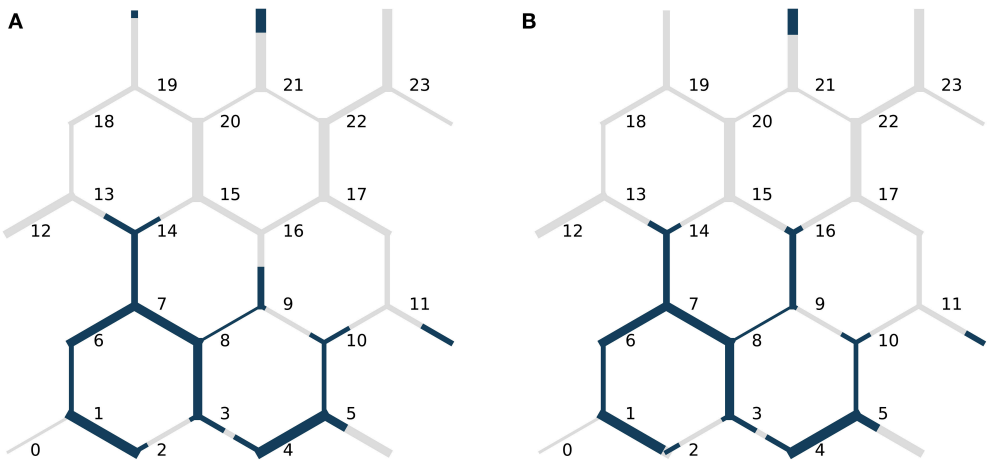

FIGURE 9 | Fluid distribution in the Haines jump case **(A)** at $t = 0.23\,\mathrm{s}$ and **(B)** at $t = 0.27\,\mathrm{s}$, before and after the Haines jump. During the jump, non-wetting fluid breaks-through the link connecting nodes 9 and 16 and invades node 16. Also, non-wetting fluid in other links at the downstream end of the moving ganglion retracts. This is seen e.g. in the links downstream of nodes 10 and 14. The link radii are not drawn to scale with the link lengths. Node indices are indicated in black.

Armstrong and Berg [15], and shows that the model is able to capture the non-local nature of pore drainage events in a numerically stable manner when the new numerical methods are used.

As in the links-in-series case, the solution exhibits oscillations for the values of C_c that are larger than unity. With $C_c = 1.0$, the results are free from oscillations and appear stable. This indicates that the stability criterion (23) is valid and not unnecessarily strict also for a network configuration that is much more complex than links in series.

Both the links-in-series case and the Haines jump case were simulated with the semi-implicit method and produced stable results with the advective time step criterion (22) only. The results from the links-in-series test case are shown in **Figure 6C**. For brevity, the results from the Haines jump case are omitted here. The reader is referred to **Figure 10A** in section 10, where stable results are shown for a lower flow rate.

To summarize, both the forward Euler and midpoint methods produce stable results for the cases considered when the capillary time step criterion (23) is used in addition to Equation (22) to select the time step lengths. By running simulations with different C_c, we have observed a transition from stable to unstable results for values of C_c near 1, in order of magnitude. In the Haines jump case, all methods presented are able to capture both the fast capillary-driven fluid redistribution events, and the slow pressure build-up before a Haines jump.

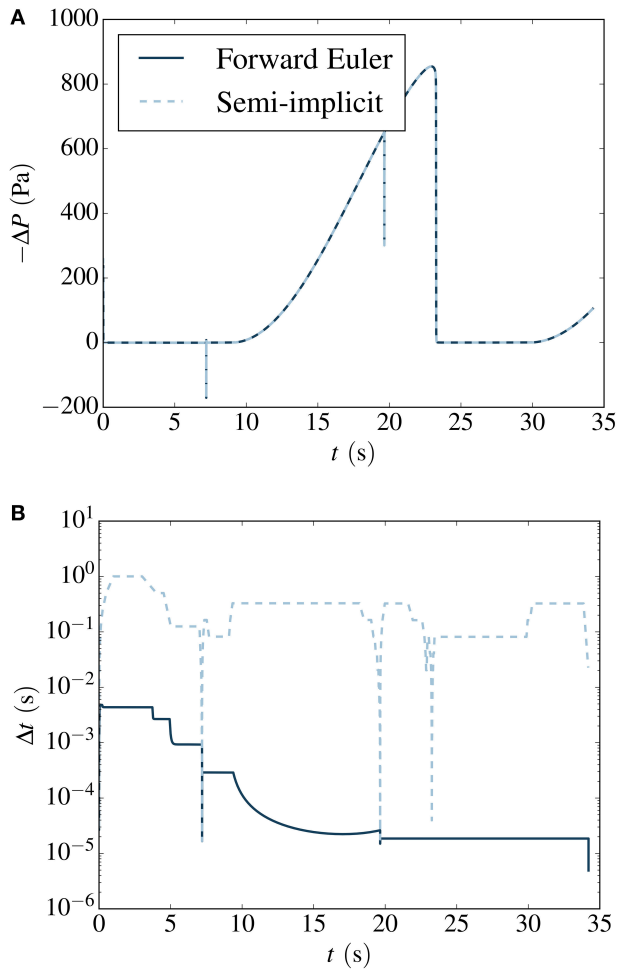

FIGURE 10 | (A) Pressure difference required to drive the flow at $Q = 10^{-11}$ m^3 s^{-1}, corresponding to Ca $= 1.2 \cdot 10^{-7}$, in the Haines jump case. Results are plotted for the forward Euler method (solid dark blue) and the semi-implicit method (dashed light blue). These lines coincide at the scale of representation. The time steps lengths used by each method are plotted in **(B)**.

10. PERFORMANCE ANALYSIS

In this section, we analyze and compare the performance of the time integration methods. In doing so, we consider the number of time steps and the wall clock time required to perform stable simulations of the Haines jump case with each of the methods at different specified flow rates Q. The flow rates simulated were 10^{-7} m^3 s^{-1}, 10^{-8} m^3 s^{-1}, 10^{-9} m^3 s^{-1}, 10^{-10} m^3 s^{-1}, 10^{-11} m^3 s^{-1}, and 10^{-12} m^3 s^{-1}. The accuracy of the methods was studied Section 9.1, and will not be part of the performance analysis. Instead, stable simulations are considered sufficiently accurate.

First, we look more closely at the results for $Q = 10^{-11}$ m^3 s^{-1}, corresponding to Ca $= 1.2 \cdot 10^{-7}$. The pressure difference required to drive the flow is shown in **Figure 10A**, and the time step lengths used are shown in **Figure 10B**. From the latter Figure, we see that the semi-implicit method is able to take longer time steps than forward Euler for most of the simulation. During the pressure build-up phase, the difference is four orders of magnitude. During the fast capillary-driven fluid redistribution events, however, the length of the semi-implicit time steps drop to the level of those used by forward Euler. This is because we here have relatively large flow rates in some links, even though Q is low, and the advective time step criterion (22) becomes limiting for both the semi-implicit method and forward Euler.

It was mentioned by Armstrong and Berg [15] that any accurate numerical simulation on the pore scale must have a time resolution fine enough to capture the fast events. The semi-implicit method accomplishes this by providing a highly dynamic time resolution, which is refined during the fast events. The method is therefore able to resolve these events, while time resolution can be coarsened when flow is governed by the slow externally applied flow rate, saving computational effort.

The time duration of the Haines jump pressure drops for all except the two largest externally applied flow rates were around 10 ms. This is in qualitative agreement with the results presented by Armstrong and Berg [15]. They found that, for their investigated range of parameters, pores were drained on the millisecond time scale regardless of externally applied flow rate. However, we stress that although we consider the same fluids, the pore network used here was approximately one order of magnitude larger in the linear dimensions than that of Armstrong and Berg [15].

The number of time steps and wall clock time required to simulate the Haines jump case at different specified flow rates Q are shown in **Figures 11A,B**, respectively.

For the explicit methods, both the number of time steps and the wall time are proportional to Ca^{-1} at low capillary numbers. This is because the capillary time step criterion (23) dictates the time step at low capillary numbers (except during fast fluid redistribution events). The criterion depends on the fluid configuration, while it is independent of the flow rate. At low enough flow rates, the system will pass through roughly the same fluid configurations during the simulation, regardless of the applied Q. The speed at which the system passes through these configurations, however, will be inversely proportional to Q and therefore, so will the required wall time and number of time steps. As the forward Euler and the midpoint method are subject to the same time step criteria, these require roughly the same number of time steps at all considered flow rates. However, since the midpoint method is a two-step method, the wall time it requires is longer and approaches twice that required by the forward Euler for long wall times.

For the semi-implicit method, on the other hand, the number of time steps required to do the simulation becomes effectively independent of the specified flow rate at capillary numbers smaller than approximately 10^{-4}. The result is that low-capillary number simulations can be done much more efficiently than with the explicit methods, in terms of wall time required to perform stable simulations. This is seen in **Figure 11B**. At Ca $\sim 10^{-5}$, the computational time needed by all three methods are similar in magnitude. The relative benefit of using the semi-implicit method increases at lower capillary numbers. For the lowest capillary number considered, the difference in wall time between

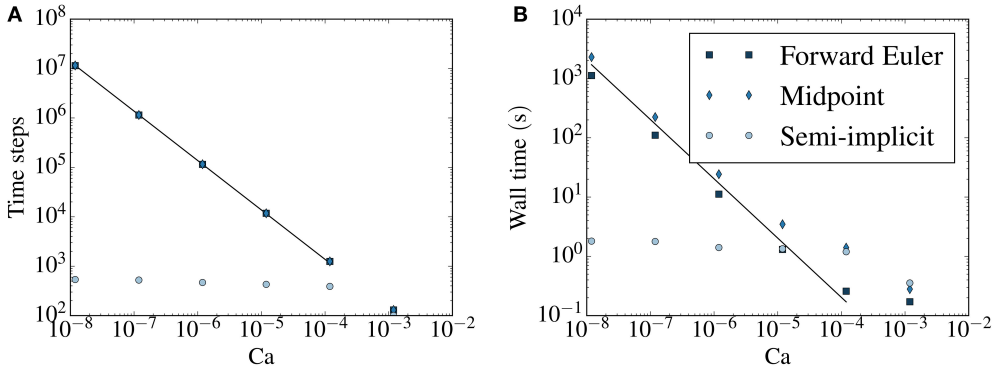

FIGURE 11 | (A) Number of time steps and **(B)** wall clock time required to simulate the Haines jump case at at different specified flow rates. In each simulation, the same volume of fluid (5% of the pore volume) flows through a network. Results from the forward Euler method (squares), the midpoint method (diamonds) and the semi-implicit method (circles) are shown. In **(A,B)**, the black lines are inversely proportional to Ca.

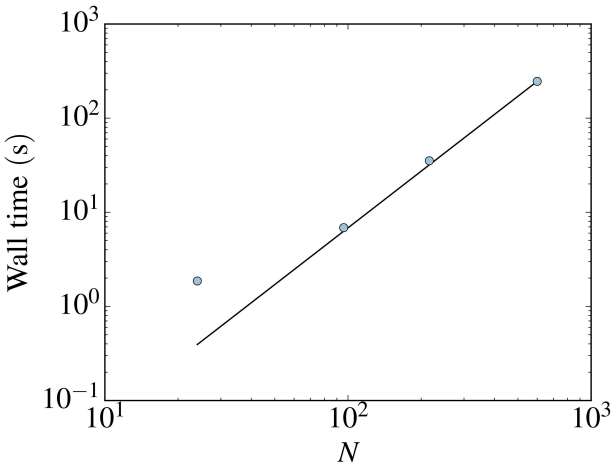

FIGURE 12 | Wall clock time time required to simulate the Haines jump case with the semi-implicit method for different network sizes. All simulations were run at Ca $\sim = 10^{-7}$ and N denotes the number of nodes in the network. The wall time is seen to increase proportionally to N^2 for the three largest networks.

the explicit methods and the semi-implicit is three orders of magnitude.

The increased efficiency of the semi-implicit method over explicit methods at low capillary numbers means that one can use the semi-implicit method to perform simulations in the low capillary number regime that are unfeasible with explicit methods. Thus, the range of capillary numbers for which the pore network model is a tractable modeling alternative is extended to much lower capillary numbers. This includes e.g. simulations of water flow in fuel cell gas diffusion layers, where capillary numbers are can be 10^{-8} [33].

Finally, to study the effect of an increase in network size on the wall time required by the semi-implicit method, the Haines jump case was run on three scaled-up versions of the network with $N = 24$ nodes considered so far, illustrated in **Figure 4**. All simulations were run at Ca $\sim 10^{-7}$. In **Figure 12** the wall clock time time required is plotted against the number of nodes N for the different networks. The wall time is seen to increase proportionally to N^2.

11. CONCLUSION

We have studied three different time integration methods for a pore network model for immiscible two-phase flow in porous media. Two explicit methods, the forward Euler and midpoint methods, and a new semi-implicit method were considered. The explicit methods have been presented and used in other works [10, 21, 24], and were reviewed here for completeness. The semi-implicit method was presented here for the first time, and therefore in detail.

The explicit methods have previously suffered from numerical instabilities at low capillary numbers. Here, a new time-step criterion was suggested in order to stabilize them and numerical experiments were performed demonstrating that stabilization was achieved.

It was verified that all three methods converged to a reference solution to a selected test case upon time step refinement. The forward Euler and semi-implicit methods exhibited first-order convergence and the midpoint method showed second-order convergence.

Simulations of a single Haines jump were performed. These showed that the all three methods were able to resolve both pressure build-up events and fluid redistribution events, including interfacial retraction after a Haines jump, which may occur at vastly different time scales when capillary numbers are low. The results from the Haines jump case were consistent with experimental observations made by Armstrong and Berg [15]. Fluid redistribution events cannot be properly captured when using solution methods that have previously been used at low capillary numbers that e.g. do not allow backflow [18].

A performance analysis revealed that the semi-implicit method was able to perform stable simulations with much less

computational effort than the explicit methods at low capillary numbers. For the case considered, the computational time needed was approximately the same for all three methods at Ca $\sim 10^{-5}$. At lower capillary numbers, the computational time needed by the explicit methods increased inversely proportional to the capillary number, while the time needed by the semi-implicit method was effectively constant. At Ca $\sim 10^{-8}$, the computational time needed by the semi-implicit methods was therefore three orders of magnitude smaller than those needed by the explicit methods.

The superior efficiency of the new semi-implicit method over the explicit methods at low capillary numbers enables simulations in this regime that are unfeasible with explicit methods. Thus, the range of capillary numbers for which the pore network model is a tractable modeling alternative is extended to much lower capillary numbers. This includes e.g. simulations of water flow in fuel cell gas diffusion layers, where capillary numbers are can be 10^{-8} [33].

In summary, use of Aker-type pore network models were previously restricted to relatively high capillary numbers due to numerical instabilities in the explicit methods used to solve them. With the new time step criterion presented here, these stability problems are removed. However, simulations at low capillary numbers still take a long time and the computational time needed increases inversely proportional to the capillary number. This problem is solved by the new semi-implicit method. With this method, the computational time needed becomes effectively independent of the capillary number, when capillary numbers are low.

AUTHOR CONTRIBUTIONS

To pursue low capillary number simulations with Aker-type pore network models was proposed by SK, MG, and AH in collaboration. MV developed the particular variation of the pore network model used. MG developed the new numerical methods and performed the simulations. MG wrote the manuscript, aided by comments and suggestions from MV, SK, and AH.

ACKNOWLEDGMENTS

The authors would like to thank Dick Bedeaux, Santanu Sinha, and Knut Jørgen Måløy for fruitful discussions. Special thanks are also given to Jon Pharoah for inspiring discussions and comments. This work was partly supported by the Research Council of Norway through its Centres of Excellence funding scheme, project number 262644.

SUPPLEMENTARY MATERIAL

The Supplementary Material for this article can be found online at: https://www.frontiersin.org/articles/10.3389/fphy.2018.00056/full#supplementary-material

REFERENCES

1. Raeini AQ, Blunt MJ, Bijeljic B. Modelling two-phase flow in porous media at the pore scale using the volume-of-fluid method. *J Comput Phys.* (2012) **231**:5653–68. doi: 10.1016/j.jcp.2012.04.011
2. Jettestuen E, Helland JO, Prodanović M. A level set method for simulating capillary-controlled displacements at the pore scale with nonzero contact angles. *Water Resour Res.* (2013) **49**:4645–61. doi: 10.1002/wrcr.20334
3. Gjennestad MA, Munkejord ST. Modelling of heat transport in two-phase flow and of mass transfer between phases using the level-set method. *Energy Proc.* (2015) **64**:53–62. doi: 10.1016/j.egypro.2015.01.008
4. Ramstad T, Øren PE, Bakke S. Simulation of two-phase flow in reservoir rocks using a lattice Boltzmann method. *SPE J.* (2010) **15**:917–27. doi: 10.2118/124617-PA
5. Hammond PS, Unsal E. A dynamic pore network model for oil displacement by wettability-altering surfactant solution. *Transport Porous Media* (2012) **92**:789–817. doi: 10.1007/s11242-011-9933-4
6. Lenormand R, Touboul E, Zarcone C. Numerical models and experiments on immiscible displacements in porous media. *J Fluid Mech.* (1988) **189**:165–87. doi: 10.1017/S0022112088000953
7. Wilkinson D, Willemsen JF. Invasion percolation: a new form of percolation theory. *J Phys A Math Gen.* (1983) **16**:3365. doi: 10.1088/0305-4470/16/14/028
8. Blunt MJ. Physically-based network modeling of multiphase flow in intermediate-wet porous media. *J Petroleum Sci Eng.* (1998) **20**:117–25. doi: 10.1016/S0920-4105(98)00010-2
9. Joekar-Niasar V, Hassanizadeh SM, Dahle H. Non-equilibrium effects in capillarity and interfacial area in two-phase flow: dynamic pore-network modelling. *J Fluid Mech.* (2010) **655**:38–71. doi: 10.1017/S0022112010000704
10. Aker E, Måløy KJ, Hansen A, Batrouni GG. A two-dimensional network simulator for two-phase flow in porous media. *Transport Porous Media* (1998) **32**:163–86. doi: 10.1023/A:1006510106194
11. Joekar-Niasar V, Hassanizadeh S. Analysis of fundamentals of two-phase flow in porous media using dynamic pore-network models: a review. *Crit Rev Environ Sci Technol.* (2012) **42**:1895–976. doi: 10.1080/10643389.2011.574101
12. Tørå G, Øren PE, Hansen A. A dynamic network model for two-phase flow in porous media. *Transport Porous Media* (2012) **92**:145–64. doi: 10.1007/s11242-011-9895-6
13. Haines WB. Studies in the physical properties of soil. v. the hysteresis effect in capillary properties, and the modes of moisture distribution associated therewith. *J Agric Sci.* (1930) **20**:97–116. doi: 10.1017/S002185960008864X
14. Berg S, Ott H, Klapp SA, Schwing A, Neiteler R, Brussee N, et al. Real-time 3D imaging of Haines jumps in porous media flow. *Proc Natl Acad Sci USA* (2013) **110**:3755–9. doi: 10.1073/pnas.1221373110
15. Armstrong RT, Berg S. Interfacial velocities and capillary pressure gradients during haines jumps. *Phys Rev E* (2013) **88**:043010. doi: 10.1103/PhysRevE.88.043010
16. Måløy KJ, Furuberg L, Feder J, Jøssang T. Dynamics of slow drainage in porous media. *Phys Rev Lett.* (1992) **68**:2161. doi: 10.1103/PhysRevLett.68.2161
17. Koplik J, Lasseter T. Two-phase flow in random network models of porous media. *Soc Petrol Eng J.* (1985) **25**:89–100. doi: 10.2118/11014-PA
18. Medici E, Allen J. The effects of morphological and wetting properties of porous transport layers on water movement in PEM fuel cells. *J Electrochem Soc.* (2010) **157**:B1505–14. doi: 10.1149/1.3474958
19. Savani I, Sinha S, Hansen A, Bedeaux D, Kjelstrup S, Vassvik M. A Monte Carlo algorithm for immiscible two-phase flow in porous media. *Transport Porous Media* (2017) **116**:869–88. doi: 10.1007/s11242-016-0804-x
20. Washburn EW. The dynamics of capillary flow. *Phys Rev.* (1921) **17**:273. doi: 10.1103/PhysRev.17.273
21. Knudsen HA, Aker E, Hansen A. Bulk flow regimes and fractional flow in 2D porous media by numerical simulations. *Transport Porous Media* (2002) **47**:99–121. doi: 10.1023/A:1015039503551

22. Sinha S, Bender AT, Danczyk M, Keepseagle K, Prather CA, Bray JM, et al. Effective rheology of two-phase flow in three-dimensional porous media: experiment and simulation. *Transport Porous Media* (2017) **119**:77–94. doi: 10.1007/s11242-017-0874-4
23. Erpelding M, Sinha S, Tallakstad KT, Hansen A, Flekkøy EG, Måløy KJ. History independence of steady state in simultaneous two-phase flow through two-dimensional porous media. *Phys Rev E* (2013) **88**:053004. doi: 10.1103/PhysRevE.88.053004
24. Sinha S, Hansen A. Effective rheology of immiscible two-phase flow in porous media. *Europhys Lett.* (2012) **99**:44004. doi: 10.1209/0295-5075/99/44004
25. Press WH, Flannery BP, Teukolsky SA, Vetterling WT. *Numerical Recipes: The Art of Scientific Computing, 3rd Edn*. New York, NY: Cambridge University Press (2007).
26. Süli E, Mayers D. *An Introduction to Numerical Analysis*. Cambridge: Cambridge University Press (2006).
27. Balay S, Abhyankar S, Adams MF, Brown J, Brune P, Buschelman K, et al. *PETSc Web Page* (2016). Available online at: http://www.mcs.anl.gov/petsc
28. Batrouni GG, Hansen A. Fourier acceleration of iterative processes in disordered systems. *J Stat Phys.* (1988) **52**:747–73. doi: 10.1007/BF01019728
29. Linstrom P, Mallard W, (eds.). *NIST Chemistry WebBook, NIST Standard Reference Database Number 69*. Gaithersburg, MD: National Institute of Standards and Technology (2017).
30. Zeppieri S, Rodríguez J, López de Ramos A. Interfacial tension of alkane + water systems. *J Chem Eng Data* (2001) **46**:1086–8. doi: 10.1021/je000245r
31. Måløy KJ, Feder J, Jøssang T. Viscous fingering fractals in porous media. *Phys Rev Lett.* (1985) **55**:2688. doi: 10.1103/PhysRevLett.55.2688
32. Tallakstad KT, Knudsen HA, Ramstad T, Løvoll G, Måløy KJ, Toussaint R, et al. Steady-state two-phase flow in porous media: statistics and transport properties. *Phys Rev Lett.* (2009) **102**:074502. doi: 10.1103/PhysRevLett.102.074502
33. Sinha PK, Wang CY. Pore-network modeling of liquid water transport in gas diffusion layer of a polymer electrolyte fuel cell. *Electrochim Acta* (2007) **52**:7936–45. doi: 10.1016/j.electacta.2007.06.061

Conflict of Interest Statement: The authors declare that the research was conducted in the absence of any commercial or financial relationships that could be construed as a potential conflict of interest.

frontiers in Physics

MINI REVIEW
published: 27 September 2018
doi: 10.3389/fphy.2018.00098

Skyrmions and Antiskyrmions in Quasi-Two-Dimensional Magnets

Alexey A. Kovalev and Shane Sandhoefner*

Department of Physics and Astronomy, Nebraska Center for Materials and Nanoscience, University of Nebraska, Lincoln, NE, United States

A stable skyrmion, representing the smallest realizable magnetic texture, could be an ideal element for ultra-dense magnetic memories. Here, we review recent progress in the field of skyrmionics, which is concerned with studies of tiny whirls of magnetic configurations for novel memory and logic applications, with a particular emphasis on antiskyrmions. Magnetic antiskyrmions represent analogs of skyrmions with opposite topological charge. Just like skyrmions, antiskyrmions can be stabilized by the Dzyaloshinskii-Moriya interaction, as has been demonstrated in a recent experiment. Here, we emphasize differences between skyrmions and antiskyrmions, e.g., in the context of the topological Hall effect, skyrmion Hall effect, as well as nucleation and stability. Recent progress suggests that antiskyrmions can be potentially useful for many device applications. Antiskyrmions offer advantages over skyrmions as they can be driven without the Hall-like motion, offer increased stability due to dipolar interactions, and can be realized above room temperature.

Keywords: Dzyaloshinskii Moriya interaction, chiral spin textures, race-track memory, topological transport, magnetic skyrmion, antiskyrmion, skyrmion Hall effect, skyrmion stability

OPEN ACCESS

Edited by:
Jamal Berakdar, Martin Luther University of Halle-Wittenberg, Germany

Reviewed by:
Asle Sudbø, Norwegian University of Science and Technology, Norway
Atsufumi Hirohata, University of York, United Kingdom
Vitalii Dugaev, Rzeszów University of Technology, Poland

****Correspondence:***
Alexey A. Kovalev
alexey.kovalev@unl.edu

Specialty section:
This article was submitted to Condensed Matter Physics, a section of the journal Frontiers in Physics

Received: *31 May 2018*
Accepted: *22 August 2018*
Published: *27 September 2018*

Citation:
Kovalev AA and Sandhoefner S (2018) Skyrmions and Antiskyrmions in Quasi-Two-Dimensional Magnets. Front. Phys. 6:98. doi: 10.3389/fphy.2018.00098

1. INTRODUCTION

A magnetic skyrmion is a non-collinear configuration of magnetic moments with a whirling magnetic structure (see **Figure 1**). Magnetic skyrmions represent a (2+1)-dimensional analog of the Skyrme model [1], which is a (3+1)-dimensional theory. Thus, magnetic skyrmions are often referred to as baby-skyrmions. From a topological point of view, a magnetic skyrmion is described by an integer invariant, referred to as topological charge, that arises in the map from the physical two-dimensional space to the target space S_2. The formula for topological charge is:

$$Q = \frac{1}{4\pi} \int d^2 r (\partial_x \boldsymbol{m} \times \partial_y \boldsymbol{m}) \cdot \boldsymbol{m}, \tag{1}$$

where $\boldsymbol{m}$ is a unit vector pointing in the direction of the magnetization. The topological charge describes how many times magnetic moments wrap around a unit sphere in the mapping (see **Figure 1**). Erasing a skyrmion requires globally modifying the system and, as a result, skyrmions possess topological protection. Initially, magnetic skyrmions of Bloch type (see **Figure 1**) [2–5] were discovered in chiral B20 compounds such as MnSi, FeGe, and $Fe_{1-x}Co_xSi$ in which spin-orbit interactions and the absence of the center of inversion lead to appearance of the Dzyaloshinskii-Moriya interaction (DMI) [6, 7]. Sufficiently strong DMI can then lead to the formation of isolated skyrmions or even skyrmion lattices.

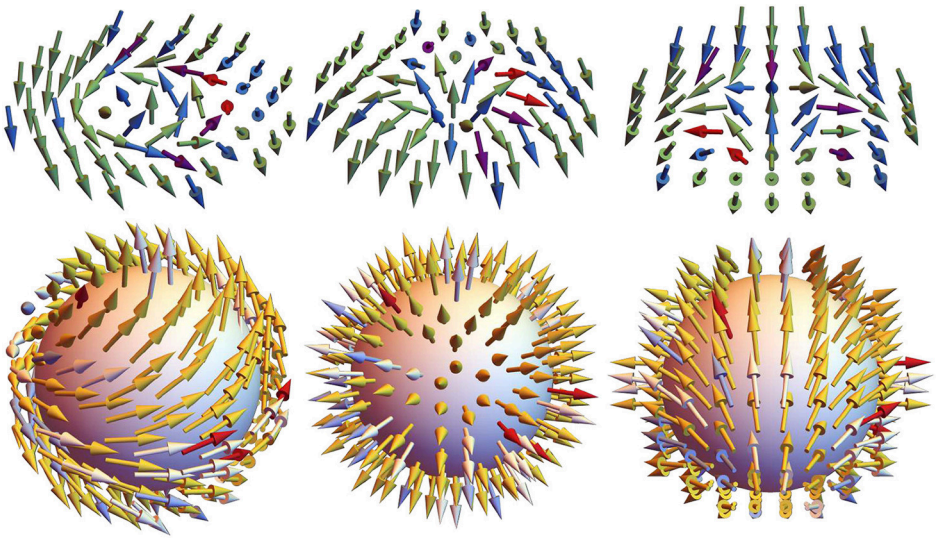

FIGURE 1 | (Top) Bloch (left) and Néel (middle) skyrmions with topological charge $Q = 1$ and polarity $p = 1$. Antiskyrmion (right) with topological charge $Q = -1$ and $p = 1$. **(Bottom)** For Néel skyrmion (left), Bloch skyrmion (middle), and antiskyrmion (right) the moments wrap around a unit sphere upon application of stereographic projection.

Skyrmions stabilized by DMI are commonly referred to as Bloch- and Néel-type skyrmions (see **Figure 1**). Helicity and polarity are also used to describe skyrmions. Helicity can be defined as the angle of the global rotation around the z-axis that relates various skyrmions to the Néel skyrmion. For the Néel skyrmion, helicity is zero. Polarity describes whether the magnetization points in the positive ($p = 1$) or negative ($p = -1$) z-direction at the center of the skyrmion [8]. For Bloch and Néel skyrmions, the topological charge and polarity are equal ($Q = p$). The difference in helicity distinguishes Bloch and Néel skyrmions from one another. On the other hand, magnetic textures stabilized by DMI can also have opposite topological charge and polarity ($Q = -p$). Such magnetic textures are referred to as *antiskyrmions*. Antiskyrmions (see **Figure 1**) can be stabilized by bulk DMI with lower symmetry as was first predicted [9, 10] and later realized experimentally at room temperatures in Heusler compounds with D_{2d} symmetry [11]. It has also been predicted that interfacial DMI with C_{2v} symmetry can lead to formation of antiskyrmions in ultrathin magnetic films [12, 13]. In general, various types of skyrmions and antiskyrmions, as shown in **Figure 3**, can be stabilized by changing the form of DMI tensor [12]. Anisotropic interfacial DMI with C_{2v} symmetry has recently been realized in epitaxial Au/Co/W magnetic films [14].

Microscopically, DMI arises when the interaction of two magnetic atoms is mediated by a non-magnetic atom via the superexchange or double-exchange mechanisms (see **Figure 2**). In the absence of an inversion center, a non-collinear configuration of magnetic moments is preferred by DMI energy:

$$H_{DMI} = \boldsymbol{\mathcal{D}}_{12} \cdot (\boldsymbol{S}_1 \times \boldsymbol{S}_2), \tag{2}$$

where $\boldsymbol{S}_1$ and $\boldsymbol{S}_2$ describe the spins and the DMI vector $\boldsymbol{\mathcal{D}}_{12} \propto \boldsymbol{r}_1 \times \boldsymbol{r}_2$ (see **Figure 2**). The strength of DMI is proportional to the strength of the spin-orbit interaction, which is expected to scale with the fourth power of the atomic number. However, in some cases the particular form of the band structure and/or effects related to charge transfer can influence the strength of the spin-orbit interaction. Particularly strong spin-orbit interaction and DMI can arise at interfaces between magnetic films and non-magnetic metals where the 3*d* orbitals of magnetic atoms interact with 5*d* orbitals of the heavy metal [15]. Néel type-skyrmions stabilized by interfacial DMI have been obtained at low temperatures in epitaxially grown Fe and PdFe magnetic layers on Ir [16, 17]. Another approach is to stack magnetic and non-magnetic layers in such a way that additive interfacial DMI leads to the formation of Néel skyrmions. Such an approach leads to the formation of room temperature skyrmions in magnetic layers (e.g., Co) sandwiched between two different non-magnetic layers (e.g., Ir and Pt) [18–21].

Non-collinear magnetic textures can also arise due to dipolar interactions in the form of magnetic bubbles. Compared to skyrmions, magnetic bubbles have larger size and no definite chirality. Thus, antiskyrmions can be realized in systems with dipolar interactions [22]. Magnetic skyrmion bubbles are similar to magnetic bubbles but have definite chirality induced by DMI [23–25]. Skyrmion-like structures can be also realized in systems without DMI [26–28], e.g., it has been predicted that skyrmions of both chiralities can be stabilized in lattices with frustrated exchange interactions [29–31].

2. DESCRIPTION OF SKYRMIONS AND ANTISKYRMIONS

Magnetic skyrmions in thin magnetic films can be well-understood by considering a continuous model with the free energy density written for a two-dimensional ferromagnet

well below the Curie temperature:

$$\mathcal{F} = A\,(\partial_i \boldsymbol{m})^2 - K m_z^2 - H m_z + \boldsymbol{D}_j \cdot (\partial_j \boldsymbol{m} \times \boldsymbol{m}), \qquad (3)$$

where the free energy is $F = \int d^2 r \mathcal{F}$, we assume summation over repeated index i, $j = x, y$, and $\boldsymbol{m}$ is a unit vector along the magnetization direction. The first term in Equation (3) describes isotropic exchange with exchange stiffness A, the second term describes uniaxial anisotropy with strength K, the third term describes the Zeeman energy due to the external magnetic field H_e, $H \equiv \mu_0 H_e M$ where M is the magnetization, and the last term corresponds to DMI described by a general tensor $D_{ij} = (\boldsymbol{D}_j)_i$ [12], where for a two-dimensional magnet j is limited to x and y. DMI is the most important term in Equation (3) for the formation of magnetic skyrmions. Modest DMI strength favors isolated metastable skyrmions [32], while strong DMI leads to condensation into a skyrmion lattice [33] (see discussion around Equation 5).

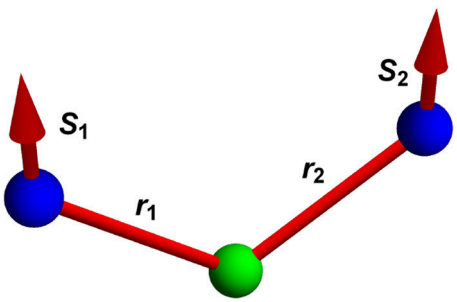

FIGURE 2 | Interaction between two neighboring spins is mediated by the non-magnetic atom. The direction of DMI vector resulting from such interaction is defined by the bond vectors, i.e., $\boldsymbol{\mathcal{D}}_{12} \propto \boldsymbol{r}_1 \times \boldsymbol{r}_2$.

The form of the DMI tensor D_{ij} is determined by the crystallographic symmetry of the system [12]. In particular, non-zero elements of the DMI tensor are determined by relations:

$$D_{ij} = (\det \boldsymbol{R}^{(\alpha)}) R_{il}^{(\alpha)} R_{jm}^{(\alpha)} D_{lm}, \qquad (4)$$

where $\boldsymbol{R}^{(\alpha)}$ are generators of the point group corresponding to the crystallographic symmetry, $\alpha = 1, 2, \ldots$, and the summation over repeated indices l and m is assumed. Note that the constraints on the DMI tensor in Equation (4) can be equivalently expressed via Lifshitz invariants [9, 34, 35].

A system invariant under $SO(3)$ rotations then results in $D_{ij} = D\delta_{ij}$, where δ_{ij} is the Kronecker delta. Such DMI

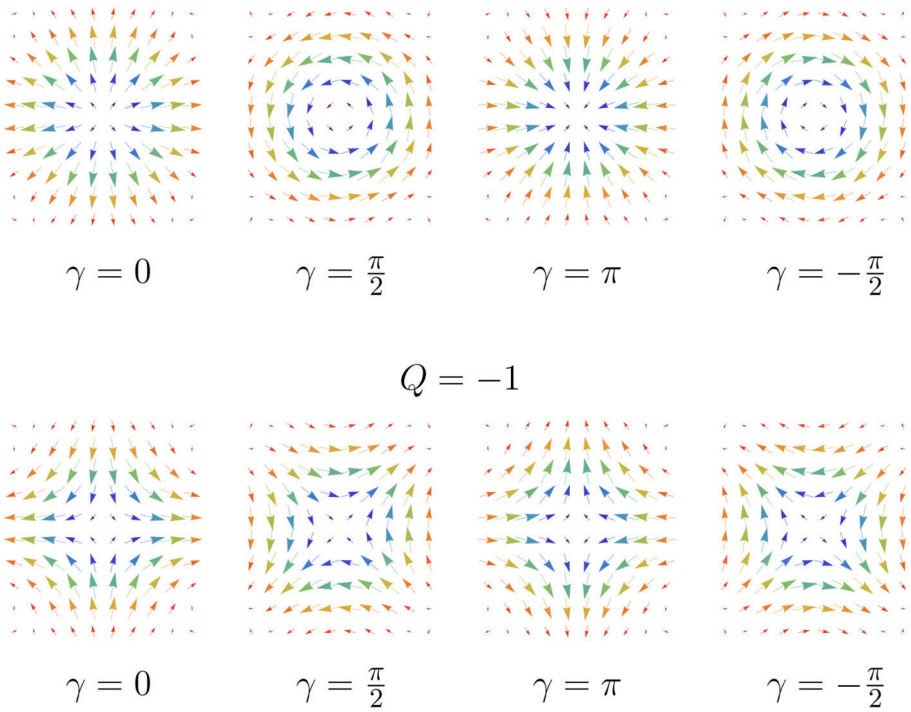

FIGURE 3 | Magnetization configuration of skyrmions ($Q = 1$) and antiskyrmions ($Q = -1$) with fixed polarity ($p = 1$) and varying helicity. The length and direction of the arrows represent the in-plane component of $\boldsymbol{m}$, and the color indicates m_z. A Néel skyrmion with $Q = 1$ and helicity $\gamma = 0$ corresponds to DMI with $C_{\infty v}$ symmetry. A Bloch skyrmion with $Q = 1$ and helicity $\gamma = \pi/2$ corresponds to DMI with $SO(3)$ symmetry. Antiskyrmion with $Q = -1$ and helicity $\gamma = 0$ corresponds to DMI with D_{2d} symmetry. An arbitrary helicity γ can be obtained via the global rotation arounds the z-axis by an angle γ. Antiskyrmions can be obtained from skyrmions by a reflection with respect to a plane perpendicular to the plane of the magnet. Figure is adapted with permission from Güngördu et al. [12].

stabilizes Bloch-type skyrmions (see **Figure 1**). A system with $C_{\infty v}$ symmetry is invariant under proper and improper rotations around the z axis and allows only two non-zero tensor coefficients $D_{12} = -D_{21} = D$. Such DMI stabilizes Néel-type skyrmions (see **Figure 1**). Another important example arises for a system invariant under D_{2d} symmetry, for which again only two non-zero tensor coefficients are allowed, i.e., $D_{12} = D_{21} = D$. The latter case realizes a system with *antiskyrmions* (see **Figure 1**). Within a simple model given by Equation (3), all three examples given above are mathematically equivalent as they can be mapped to each other by a global spin rotation/reflection accompanied by an appropriate transformation of the DMI tensor [12]. Since the free energy does not change in such a mapping, one can expect that the same stability diagram will describe the above skyrmions and antiskyrmions (other examples of equivalent skyrmions and antiskyrmions are shown in **Figure 3**) [12]. This equivalence is no longer valid in the presence of dipolar interactions [36] or more complicated magnetocrystalline anisotropy. In fact, antiskyrmions offer increased stability due to the presence of dipolar interactions [36].

The parameters A, K, H, and D in the above examples enter the free energy density (3), and they determine whether magnetic skyrmions or antiskyrmions can be present in a system. Minimization of the free energy corresponding to Equation (3) leads to the phase diagram shown in **Figure 4**, where the phase boundaries separate the cycloid or spiral phase (SP), the hexagonal skyrmion lattice (SkX), the square cell skyrmion lattice (SC), and the ferromagnetic phase (FM) [12]. It is convenient to introduce a critical DMI:

$$D_c = 4(AK)^{1/2}/\pi, \tag{5}$$

corresponding to the strength of DMI at which the formation of Dzyaloshinskii domain walls becomes energetically favorable [37]. In an infinite sample, the transition from isolated skyrmions to a skyrmion lattice or cycloid phase happens in the vicinity of this critical DMI strength [12, 33, 38] (see **Figure 4**). The magnetic skyrmion size changes substantially as one varies the strength of DMI. At $D < D_c$, the skyrmion size has been calculated analytically, $R_s \approx \Delta/\sqrt{2(1-D/D_c)}$, where $\Delta = \sqrt{A/K}$ [37]. The effects related to finite temperature and dipolar interactions modify this behavior, especially close to the divergence when $R_s \to \infty$ at $D = D_c$ [20]. At $D > D_c$, inside the skyrmion lattice phase the skyrmion lattice period can be estimated by the period of the equilibrium helix, $L_D = 4\pi A/D$ [12, 33, 39]. Note that the ballpark value for the critical DMI is $D_c \sim 4$ mJ/m^2 (we use parameters for Co/Pt multilayer [40]). Comparable DMI can be realized in magnetic layers sandwiched between non-magnetic layers. The skyrmion size can range from 8 nm at low temperatures (<30K) [41] to 50 nm at room temperature [18–20].

In principle, the stability of a skyrmion can be hindered by finite temperature. In studies of magnetic memories, this question is usually answered by studying the Arrhenius law of escape from a particular state [42]. Recent studies based on harmonic transition state theory confirm that the life-time of isolated skyrmions is sufficient for realizations of magnetic memories [43].

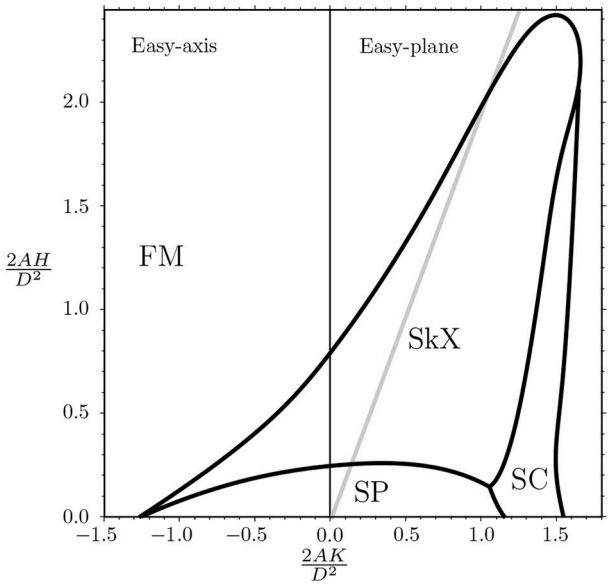

FIGURE 4 | Zero temperature phase diagram for the three cases corresponding to $SO(3)$, $C_{\infty v}$, and D_{2d} symmetries is obtained by numerically solving the LLG equation. The axes correspond to the dimensionless magnetic field and dimensionless uniaxial anisotropy parameter (see Equation 3). The gray line separates the aligned and the tilted regions of the FM phase. This phase is taken over by the hexagonal skyrmion lattcie (SkX), spiral (SP), and the square cell skyrmion lattice (SC) phases in the regions defined by the bold lines. Figure is adapted with permission from Güngördu et al. [12].

3. DYNAMICS OF SKYRMIONS AND ANTISKYRMIONS

A design of skyrmion-based memory device [15] closely resembles the race-track memory [44]. One of the challenges is to achieve efficient control of the skyrmion dynamics. Skyrmion dynamics can be induced by spin transfer torques (STT) [45–48], spin-orbit torques (SOT) (often referred to as spin Hall effect torques) [47, 49], voltage-controlled magnetic anisotropy [50], surface acoustic waves [51], temperature gradients [52–55], and other mechanisms.

Here, we discuss (anti)skyrmion dynamics due to STT and SOT induced by in-plane charge currents [31, 56]. These two mechanisms differ as the former vanishes in the absence of magnetic textures while the latter does not. Both mechanisms can be included in the Landau-Lifshitz-Gilbert equation:

$$s(1-\alpha\boldsymbol{m}\times)\dot{\boldsymbol{m}} = \boldsymbol{H}_{\text{eff}}\times\boldsymbol{m} - (1-\beta\boldsymbol{m}\times)(\boldsymbol{j}_s\cdot\nabla)\boldsymbol{m} + \boldsymbol{\tau}_{so}, \tag{6}$$

where $s = M_s/\gamma$ is the spin density, M_s is the saturation magnetization, γ is (minus) the gyromagnetic ratio ($\gamma > 0$ for electrons), α is the Gilbert damping, $H_{\text{eff}} = -\delta F/\delta\boldsymbol{m}$ is the effective field, β is the factor describing non-adiabaticity, $\boldsymbol{j}_s$ is the in-plane spin current proportional to the charge current $\boldsymbol{j}$, and $\boldsymbol{\tau}_{so}$

is the spin-orbit torque [57]. For the spin Hall contribution, $\boldsymbol{\tau}_{so} = (\hbar\theta_{SH}/2et_f)\boldsymbol{m} \times [\boldsymbol{m} \times (\hat{z} \times \boldsymbol{j})]$, where θ_{SH} is the spin Hall angle, e is the electron charge, and t_f is the thickness of the ferromagnetic layer. The Thiele approach [58] applied to Equation (6) leads to equations of motion describing (anti)skyrmion dynamics:

$$(Q\hat{z} \times +\alpha\hat{\eta})\boldsymbol{v} = \boldsymbol{F}, \tag{7}$$

where $\hat{\eta}$ is the damping dyadic tensor and $\boldsymbol{F} = \boldsymbol{F}_{so} + \boldsymbol{F}_{st}$ is the total force acting on the (anti)skyrmion due to SOT and STT. The SOT contribution is $\boldsymbol{F}_{so} = \hat{\mathcal{B}} \cdot \boldsymbol{j}$ where the tensor $\hat{\mathcal{B}}$ is proportional to the spin Hall angle and is determined by the configuration of the (anti)skyrmion [56, 59]. The STT contribution is $\boldsymbol{F}_{st} = (Q\hat{z} \times +\beta\hat{\eta})\boldsymbol{j}_s$ [48]. We obtain the (anti)skyrmion velocity in an infinite sample:

$$v_x = \frac{F_y Q + F_x \alpha\eta}{Q^2 + \alpha^2\eta^2}, \quad v_y = \frac{-F_x Q + F_y \alpha\eta}{Q^2 + \alpha^2\eta^2}, \tag{8}$$

where for typical (anti)skyrmions η is of the order of 1. The velocity in Equation (8) scales as $1/Q$. An interesting situation happens in a nanotrack geometry close to the edge. Due to the edge repulsion, an additional force term appears in Equation (8), $v_y = 0$, and the (anti)skyrmion velocity becomes $v_x = F_x/(\alpha\eta)$. As a result, a large (anti)skyrmion velocity is possible close to the edge due to SOT in systems with low Gilbert damping [47, 60].

From Equation (8), it is clear that (anti)skyrmions will move along a current with an additional side motion, resulting in the (anti)skyrmion Hall effect with the Hall angle $\theta_H = \tan^{-1}(v_y/v_x)$. Antiskyrmions exhibit an anisotropic Hall angle dependent on the current direction due to SOT, as the tensor $\hat{\mathcal{B}}$ becomes anisotropic for an antiskyrmion profile. This is in contrast to the isotropic behavior of skyrmions (the principal values are given by $\mathcal{B}_{xx} = -\mathcal{B}_{yy}$ for antiskyrmions with $\gamma = 0$ in **Figure 3**, and $\mathcal{B}_{xx} = \mathcal{B}_{yy}$ for Néel skyrmions) [56]. It is also possible to completely suppress the antiskyrmion Hall effect by properly choosing the direction of the charge current or by coupling skyrmions and antiskyrmions in a multilayer stack [56]. Note that antiferromagnetic skyrmions [61] or synthetic antiferromagnetic skyrmions in antiferromagnetically coupled layers [62, 63] also exhibit a vanishing Hall angle. This behavior can be useful for realizations of magnetic memories.

Skyrmion dynamics consistent with Equation (8) have been observed in magnetic multilayers, e.g., in Pt/Co/Ta [19], Ta/CoFeB/TaO_x [23, 24], $(Pt/CoFeB/MgO)_{15}$ [64], and $(Pt/Co/Ir)_{10}$ [65]. SOT and STT contribute to Equation (7) differently. The major component of SOT force pushes skyrmion in the direction of the current flow while the major component of STT pushes skyrmion in the transverse direction. It follows from Equation (8) that in the presence of the edge repulsion the velocity due to SOT, $v_x \propto F_{SOT}/\alpha$, is expected to be larger than the velocity due to STT, $v_x \propto F_{STT}$. Theoretical modeling [47] predicts that the velocity due to SOT is 60 m/s for the current $2 \times 10^{11}\,\mathrm{Am}^{-2}$. Similar modeling of the motion induced by STT results in much smaller velocity of 8 m/s for the same current. It has also been confirmed experimentally that in a sufficiently large sample the sign of the transverse response is determined by the sign of the spin Hall angle and the topological charge. Some aspects of skyrmion dynamics are still puzzling, i.e., the dependence of the skyrmion Hall angle on the velocity and the dependence of the velocity on the skyrmion size. Variations in the skyrmion Hall angle have been attributed to the presence of pinning sites [66]. In principle, the presence of pinning sites could be problematic for realizations of magnetic memories [67]. Nevertheless, the presence of the skyrmion Magnus force induced by pinning sites results in significant reduction of the depinning threshold current density [66, 68], e.g., by several orders of magnitude if compared to domain wall dynamics. Experimentally, the depinning threshold current density can be as low as $10^6\,\mathrm{Am}^{-2}$ [46].

4. WRITING, ERASING, AND DETECTING

Interfacial skyrmions in Fe on Ir have been controllably written and erased by STT induced by an STM tip at 4.2 K in the presence of high magnetic fields [17]. For practical applications it is necessary to write and erase skyrmions at room temperature in the presence of weak or, preferably, no magnetic fields. STT has been demonstrated to generate skyrmions in a confined geometry of a Pt/Co nanodot [47]. A SOT mechanism in which a pair of domain walls is converted into a skyrmion has been demonstrated numerically to require relatively large current densities [69]. At room temperature, SOT has been used to create elongated chiral domains that, under application of inhomogeneous current, break into skyrmion bubbles [23]. In this experiment, the inhomogeneous current of relatively low magnitude, $5 \times 10^8\ \mathrm{Am}^{-2}$, blows chiral domains into bubbles in analogy with how the Rayleigh-Plateau instabilities lead to formation of bubbles in fluid flows. This process has been reproduced by micromagnetic simulations [70]. Detailed analysis of topological charge density revealed that in the process of creating a skyrmion by SOT an unstable antiskyrmion can also be created for a period of time comparable to 0.5 ns [71]. As an antiskyrmion is not stable in the presence of interfacial DMI ($C_{\infty v}$ case), it eventually annihilates due to the presence of the Gilbert damping [72]. Thus, detailed studies of antiskyrmions can help in realizing new ways of writing and erasing skyrmions. Generation of skyrmions by charge currents has also been demonstrated for magnetic multilayer stacks [65], as well as for symmetric bilayers hosting pairs of skyrmions with opposite chirality [60]. Other approaches include laser-induced generation of topological defects [73, 74]. The feasibility of such an approach has been confirmed theoretically [75–78].

For device application, it is preferable to detect the presence of a skyrmion electrically. Several transport techniques have been suggested. Non-collinear magnetoresistance can be used to detect a skyrmion where changes in the band structure induced by non-collinear moments are detected by STM [79]. However, only non-collinearity is being detected and no information about the topological structure of a skyrmion is obtained. Measuring the z-component of magnetization is possible by employing the anomalous Hall effect [80]. This technique has been used to

detect a single skyrmion [81]. Measurement of the topological Hall effect can directly reveal the topological nature of a skyrmion as the effect originates in the fictitious magnetic field proportional to the topological charge. The presence of skyrmions has been detected by measurements of the topological Hall effect in non-centrosymmetric bulk materials in the B20 group [82, 83]. In principle, antiskyrmions [11] should also exhibit the topological Hall effect but with the reversed sign due to the opposite topological charge. On the other hand, in magnetic multilayers the topological Hall effect is expected to be much smaller than the anomalous Hall contribution [81].

5. CONCLUSIONS AND OUTLOOK

In this article, we review recent progress in the field of skyrmionics—a field concerned with studies of tiny whirls of magnetic configurations for novel memory and logic applications. A particular emphasis has been given to antiskyrmions. These, similar to skyrmions, are particle-like structures with topological protection. Compared to skyrmions, antiskyrmions have opposite topological charge and are anisotropic. Recent experimental observation of antiskyrmions at room temperature [11] encourages further studies of transport and dynamical properties such as the topological Hall effect, antiskyrmion Hall effect, antiskyrmion nucleation and stability, and others. On the other hand, realization of antiskyrmions requires careful material engineering which should also be addressed in future studies. All in all, antiskyrmions offer some advantages over skyrmions as they can be driven without the Hall-like motion, offer increased stability due to dipolar interactions, and can be realized above room temperature. A possibility to annihilate a skyrmion-antiskyrmion pair can lead to new concepts of logic devices [84]. Reservoir computing is another application in which skyrmions could prove highly useful. The anisotropic magnetoresistance (AMR) and the motion and deformation of magnetic texture caused by the interaction of a voltage-induced electric current and a single skyrmion can provide a non-linear relationship between voltage and current, which is a key ingredient for reservoir computing [85]. Skyrmion fabrics, which may include skyrmions, antiskyrmions, skyrmion crystal structure, and domain walls, represent a potential way to implement skyrmion-based reservoir computing since they fulfill the requirements of an Echo State Network (ESN) [86]. It is expected that, similar to skyrmions, antiskyrmions can potentially result in new device concepts for memory and neuromorphic computing applications [85].

AUTHOR CONTRIBUTIONS

AK conceived the project presented in this mini review article. AK and SS prepared the manuscript.

FUNDING

This work was supported by the DOE Early Career Award DE-SC0014189.

ACKNOWLEDGMENTS

The topic editors are acknowledged for supporting this open-access publication.

REFERENCES

1. Skyrme THR. A non-linear field theory. *Proc R Soc Lond.* (1961) **260**:127–38.
2. Bogdanov A, Hubert A. Thermodynamically stable magnetic vortex states in magnetic crystals. *J Magn Magn Mater*. (1994) **138**:255–69.
3. Rößler UK, Bogdanov AN, Pfleiderer C. Spontaneous skyrmion ground states in magnetic metals. *Nature* (2006) **442**:797–801. doi: 10.1038/nature05056
4. Mühlbauer S, Binz B, Jonietz F, Pfleiderer C, Rosch A, Neubauer A, et al. Skyrmion Lattice in a Chiral Magnet. *Science* (2009) **323**:915. doi: 10.1126/science.1166767
5. Yu XZ, Onose Y, Kanazawa N, Park JH, Han JH, Matsui Y, et al. Real-space observation of a two-dimensional skyrmion crystal. *Nature* (2010) **465**:901–4. doi: 10.1038/nature09124
6. Dzyaloshinsky I. A thermodynamic theory of "weak" ferromagnetism of antiferromagnetics. *J Phys Chem Solids* (1958) **4**:241–55.
7. Moriya T. Anisotropic superexchange interaction and weak ferromagnetism. *Phys Rev*. (1960) **120**:91–8.
8. Zheng F, Li H, Wang S, Song D, Jin C, Wei W, et al. Direct imaging of a zero-field target skyrmion and its polarity switch in a chiral magnetic nanodisk. *Phys Rev Lett.* (2017) **119**:197205. doi: 10.1103/PhysRevLett.119.197205
9. Bogdanov AN, Yablonskii D. Thermodynamically stable "vortices" in magnetically ordered crystals. the mixed state of magnets. *J Exp Theor Phys.* (1989) **95**:178.
10. Bogdanov AN, Rößler UK, Wolf M, Müller KH. Magnetic structures and reorientation transitions in noncentrosymmetric uniaxial antiferromagnets. *Phys Rev B* (2002) **66**:214410. doi: 10.1103/PhysRevB.66.214410
11. Nayak AK, Kumar V, Ma T, Werner P, Pippel E, Sahoo R, et al. Magnetic antiskyrmions above room temperature in tetragonal Heusler materials. *Nature* (2017) **548**:561–6. doi: 10.1038/nature23466
12. Güngördü U, Nepal R, Tretiakov OA, Belashchenko K, Kovalev AA. Stability of skyrmion lattices and symmetries of quasi-two-dimensional chiral magnets. *Phys Rev B* (2016) **93**:064428. doi: 10.1103/PhysRevB.93.064428
13. Hoffmann M, Zimmermann B, Müller GP, Schürhoff D, Kiselev NS, Melcher C, et al. Antiskyrmions stabilized at interfaces by anisotropic Dzyaloshinskii-Moriya interactions. *Nat Commun.* (2017) **8**:308. doi: 10.1038/s41467-017-00313-0
14. Camosi L, Rohart S, Fruchart O, Pizzini S, Belmeguenai M, Roussigné Y, et al. Anisotropic Dzyaloshinskii-Moriya interaction in ultrathin epitaxial Au/Co/W(110). *Phys Rev B* (2017) **95**:214422. doi: 10.1103/PhysRevB.95.214422
15. Fert A, Cros V, Sampaio J. Skyrmions on the track. *Nat Nanotechnol.* (2013) **8**:152–6. doi: 10.1038/nnano.2013.29
16. Heinze S, von Bergmann K, Menzel M, Brede J, Kubetzka A, Wiesendanger R, et al. Spontaneous atomic-scale magnetic skyrmion lattice in two dimensions. *Nat Phys.* (2011) **7**:713–8. doi: 10.1038/nphys2045
17. Romming N, Hanneken C, Menzel M, Bickel JE, Wolter B, von Bergmann K, et al. Writing and deleting single magnetic Skyrmions. *Science* (2013) **341**:636–9. doi: 10.1126/science.1240573
18. Moreau-Luchaire C, Moutafis C, Reyren N, Sampaio J, Vaz CAF, van Horne N, et al. Additive interfacial chiral interaction in multilayers for stabilization of small individual skyrmions at room temperature. *Nat Nanotechnol.* (2016) **11**:444–8. doi: 10.1038/nnano.2015.313

19. Woo S, Litzius K, Krüger B, Im MY, Caretta L, Richter K, et al. Observation of room-temperature magnetic skyrmions and their current-driven dynamics in ultrathin metallic ferromagnets. *Nat Mater.* (2016) **15**:501–6. doi: 10.1038/nmat4593
20. Boulle O, Vogel J, Yang H, Pizzini S, de Souza Chaves D, Locatelli A, et al. Room-temperature chiral magnetic skyrmions in ultrathin magnetic nanostructures. *Nat Nanotechnol.* (2016) **11**:449–54. doi: 10.1038/nnano.2015.315
21. Soumyanarayanan A, Raju M, Gonzalez Oyarce AL, Tan AKC, Im MY, Petrović AP, et al. Tunable room-temperature magnetic skyrmions in Ir/Fe/Co/Pt multilayers. *Nat Mater.* (2017) **16**:898–904. doi: 10.1038/nmat4934
22. Koshibae W, Nagaosa N. Theory of antiskyrmions in magnets. *Nat Commun.* (2016) **7**:10542. doi: 10.1038/ncomms10542
23. Jiang W, Upadhyaya P, Zhang W, Yu G, Jungfleisch MB, Fradin FY, et al. Blowing magnetic skyrmion bubbles. *Science* (2015) **349**:283–286. doi: 10.1126/science.aaa1442
24. Jiang W, Zhang X, Yu G, Zhang W, Wang X, Benjamin Jungfleisch M, et al. Direct observation of the skyrmion Hall effect. *Nat Phys.* (2017) **13**:162–9. doi: 10.1038/nphys3883
25. Yu G, Upadhyaya P, Shao Q, Wu H, Yin G, Li X, et al. Room-temperature skyrmion shift device for memory application. *Nano Lett.* (2017) **17**:261–8. doi: 10.1021/acs.nanolett.6b04010
26. Polyakov AM, Belavin AA. Metastable states of two-dimensional isotropic ferromagnets. *JETP Lett.* (1975) **22**:245–8.
27. Volovik G, Mineev V. Particle-like solitons in superfluid ^{3}He phases. *Sov Phys JETP* (1977) **45**:1186.
28. Dzyloshinskii I, Ivanov B. Localized topological solitons in a ferromagnet. *JETP Lett.* (1979) **29**:540.
29. Okubo T, Chung S, Kawamura H. Multiple-q states and the skyrmion lattice of the triangular-lattice heisenberg antiferromagnet under magnetic fields. *Phys Rev Lett.* (2012) **108**:017206. doi: 10.1103/PhysRevLett.108.017206
30. Leonov AO, Mostovoy M. Multiply periodic states and isolated skyrmions in an anisotropic frustrated magnet. *Nat Commun.* (2015) **6**:8275. doi: 10.1038/ncomms9275
31. Zhang X, Xia J, Zhou Y, Liu X, Zhang H, Ezawa M. Skyrmion dynamics in a frustrated ferromagnetic film and current-induced helicity locking-unlocking transition. *Nat Commun.* (2017) **8**:1717. doi: 10.1038/s41467-017-01785-w
32. Leonov AO, Monchesky TL, Romming N, Kubetzka A, Bogdanov AN, Wiesendanger R. The properties of isolated chiral skyrmions in thin magnetic films. *New J Phys.* (2016) **18**:065003. doi: 10.1088/1367-2630/18/6/065003
33. Banerjee S, Rowland J, Erten O, Randeria M. Enhanced stability of skyrmions in two-dimensional chiral magnets with Rashba spin-orbit coupling. *Phys Rev X* (2014) **4**:031045. doi: 10.1103/PhysRevX.4.031045
34. Dzyaloshinskii I. Theory of helicoidal structures in antiferromagnets. 1. Nonmetals. *Sov Phys JETP* (1964) **19**:17.
35. Bak P, Jensen MH. Theory of helical magnetic structures and phase transitions in MnSi and FeGe. *J Phys C Solid State Phys.* (1980) **13**:L881–5.
36. Camosi L, Rougemaille N, Fruchart O, Vogel J, Rohart S. Micromagnetics of antiskyrmions in ultrathin films. *Phys Rev B* (2018) **97**:134404. doi: 10.1103/PhysRevB.97.134404
37. Rohart S, Thiaville A. Skyrmion confinement in ultrathin film nanostructures in the presence of Dzyaloshinskii-Moriya interaction. *Phys Rev B* (2013) **88**:184422. doi: 10.1103/PhysRevB.88.184422
38. Siemens A, Zhang Y, Hagemeister J, Vedmedenko EY, Wiesendanger R. Minimal radius of magnetic skyrmions: statics and dynamics. *New J Phys.* (2016) **18**:045021. doi: 10.1088/1367-2630/18/4/045021
39. McGrouther D, Lamb RJ, Krajnak M, McFadzean S, McVitie S, Stamps RL, et al. Internal structure of hexagonal skyrmion lattices in cubic helimagnets. *New J Phys.* (2016) **18**:095004. doi: 10.1088/1367-2630/18/9/095004
40. Miron IM, Moore T, Szambolics H, Buda-Prejbeanu LD, Auffret S, Rodmacq B, et al. Fast current-induced domain-wall motion controlled by the Rashba effect. *Nat Mater.* (2011) **10**:419–23. doi: 10.1038/nmat3020
41. Bode M, Heide M, von Bergmann K, Ferriani P, Heinze S, Bihlmayer G, et al. Chiral magnetic order at surfaces driven by inversion asymmetry. *Nature* (2007) **447**:190–3. doi: 10.1038/nature05802
42. Langer JS. Statistical theory of the decay of metastable states. *Ann Phys.* (1969) **54**:258–75.
43. Bessarab PF, Müller GP, Lobanov IS, Rybakov FN, Kiselev NS, Jónsson H, et al. Lifetime of racetrack skyrmions. *Sci Rep.* (2018) **8**:3433. doi: 10.1038/s41598-018-21623-3
44. Hayashi M, Thomas L, Moriya R, Rettner C, Parkin SSP. Current-controlled magnetic domain-wall nanowire shift register. *Science* (2008) **320**:209. doi: 10.1126/science.1154587
45. Jonietz F, Mühlbauer S, Pfleiderer C, Neubauer A, Münzer W, Bauer A, et al. Spin transfer torques in MnSi at ultralow current densities. *Science* (2010) **330**:1648. doi: 10.1126/science.1195709
46. Yu XZ, Kanazawa N, Zhang WZ, Nagai T, Hara T, Kimoto K, et al. Skyrmion flow near room temperature in an ultralow current density. *Nat Commun.* (2012) **3**:988. doi: 10.1038/ncomms1990
47. Sampaio J, Cros V, Rohart S, Thiaville A, Fert A. Nucleation, stability and current-induced motion of isolated magnetic skyrmions in nanostructures. *Nat Nanotechnol.* (2013) **8**:839–44. doi: 10.1038/nnano.2013.210
48. Iwasaki J, Mochizuki M, Nagaosa N. Current-induced skyrmion dynamics in constricted geometries. *Nat Nanotechnol.* (2013) **8**:742–7. doi: 10.1038/nnano.2013.176
49. Woo S, Song KM, Han HS, Jung MS, Im MY, Lee KS, et al. Spin-orbit torque-driven skyrmion dynamics revealed by time-resolved X-ray microscopy. *Nat Commun.* (2017) **8**:15573. doi: 10.1038/ncomms15573
50. Kang W, Huang Y, Zheng C, Lv W, Lei N, Zhang Y, et al. Voltage controlled magnetic skyrmion motion for racetrack memory. *Sci Rep.* (2016) **6**:23164. doi: 10.1038/srep23164
51. Nepal R, Güngördü U, Kovalev AA. Magnetic skyrmion bubble motion driven by surface acoustic waves. *Appl Phys Lett.* (2018) **112**:112404. doi: 10.1063/1.5013620
52. Kong L, Zang J. Dynamics of an insulating skyrmion under a temperature gradient. *Phys Rev Lett.* (2013) **111**:067203. doi: 10.1103/PhysRevLett.111.067203
53. Lin SZ, Batista CD, Reichhardt C, Saxena A. ac current generation in chiral magnetic insulators and skyrmion motion induced by the spin seebeck effect. *Phys Rev Lett.* (2014) **112**:187203. doi: 10.1103/PhysRevLett.112.187203
54. Kovalev AA. Skyrmionic spin Seebeck effect via dissipative thermomagnonic torques. *Phys Rev B* (2014) **89**:241101. doi: 10.1103/PhysRevB.89.241101
55. Mochizuki M, Yu XZ, Seki S, Kanazawa N, Koshibae W, Zang J, et al. Thermally driven ratchet motion of a skyrmion microcrystal and topological magnon Hall effect. *Nat Mater.* (2014) **13**:241–6. doi: 10.1038/nmat3862
56. Huang S, Zhou C, Chen G, Shen H, Schmid AK, Liu K, et al. Stabilization and current-induced motion of antiskyrmion in the presence of anisotropic Dzyaloshinskii-Moriya interaction. *Phys Rev B* (2017) **96**:144412. doi: 10.1103/PhysRevB.96.144412
57. Brataas A, Kent AD, Ohno H. Current-induced torques in magnetic materials. *Nat Mater.* (2012) **11**:372–81. doi: 10.1038/nmat3311
58. Thiele AA. Steady-state motion of magnetic domains. *Phys Rev Lett.* (1973) **30**:230–3. doi: 10.1103/PhysRevLett.30.230
59. Tomasello R, Martinez E, Zivieri R, Torres L, Carpentieri M, Finocchio G. A strategy for the design of skyrmion racetrack memories. *Sci Rep.* (2014) **4**:6784. doi: 10.1038/srep06784
60. Hrabec A, Sampaio J, Belmeguenai M, Gross I, Weil R, Chérif SM, et al. Current-induced skyrmion generation and dynamics in symmetric bilayers. *Nat Commun.* (2017) **8**:15765. doi: 10.1038/ncomms15765
61. Barker J, Tretiakov OA. Static and dynamical properties of antiferromagnetic Skyrmions in the presence of applied current and temperature. *Phys Rev Lett.* (2016) **116**:147203. doi: 10.1103/PhysRevLett.116.147203
62. Zhang X, Ezawa M, Zhou Y. Thermally stable magnetic skyrmions in multilayer synthetic antiferromagnetic racetracks. *Phys Rev B* (2016) **94**:064406. doi: 10.1103/PhysRevB.94.064406
63. Woo S, Song KM, Zhang X, Zhou Y, Ezawa M, Liu X, et al. Current-driven dynamics and inhibition of the skyrmion Hall effect of ferrimagnetic skyrmions in GdFeCo films. *Nat Commun.* (2018) **9**:959. doi: 10.1038/s41467-018-03378-7
64. Litzius K, Lemesh I, Krüger B, Bassirian P, Caretta L, Richter K, et al. Skyrmion Hall effect revealed by direct time-resolved X-ray microscopy. *Nat Phys.* (2017) **13**:170–5. doi: 10.1038/nphys4000
65. Legrand W, Maccariello D, Reyren N, Garcia K, Moutafis C, Moreau-Luchaire C, et al. Room-temperature current-induced generation and

motion of sub-100 nm skyrmions. *Nano Lett.* (2017) **17**:2703–12. doi: 10.1021/acs.nanolett.7b00649
66. Reichhardt C, Ray D, Reichhardt CJO. Collective transport properties of driven skyrmions with random disorder. *Phys Rev Lett.* (2015) **114**:217202. doi: 10.1103/PhysRevLett.114.217202
67. Gross I, Akhtar W, Hrabec A, Sampaio J, Martínez LJ, Chouaieb S, et al. Skyrmion morphology in ultrathin magnetic films. *Phys Rev Mater.* 2018 **2**:024406. doi: 10.1103/PhysRevMaterials.2.024406
68. Lin SZ, Reichhardt C, Batista CD, Saxena A. Particle model for skyrmions in metallic chiral magnets: Dynamics, pinning, and creep. *Phys Rev B* (2013) **87**:214419. doi: 10.1103/PhysRevB.87.214419
69. Zhou Y, Ezawa M. A reversible conversion between a skyrmion and a domain-wall pair in a junction geometry. *Nat Commun.* (2014) **5**:4652. doi: 10.1038/ncomms5652
70. Lin SZ. Edge instability in a chiral stripe domain under an electric current and skyrmion generation. *Phys Rev B* (2016) **94**:020402. doi: 10.1103/PhysRevB.94.020402
71. Liu Y, Yan H, Jia M, Du H, Du A. Topological analysis of spin-torque driven magnetic skyrmion formation. *Appl Phys Lett.* (2016) **109**:102402. doi: 10.1063/1.4962452
72. Stier M, Häusler W, Posske T, Gurski G, Thorwart M. Skyrmion-anti-skyrmion pair creation by in-plane currents. *Phys Rev Lett.* (2017) **118**:267203. doi: 10.1103/PhysRevLett.118.267203
73. Finazzi M, Savoini M, Khorsand AR, Tsukamoto A, Itoh A, Duò L, et al. Laser-induced magnetic nanostructures with tunable topological properties. *Phys Rev Lett.* (2013) **110**:177205. doi: 10.1103/PhysRevLett.110.177205
74. Berruto G, Madan I, Murooka Y, Vanacore GM, Pomarico E, Rajeswari J, et al. Laser-induced skyrmion writing and erasing in an ultrafast cryo-lorentz transmission electron microscope. *Phys Rev Lett.* (2018) **120**:117201. doi: 10.1103/PhysRevLett.120.117201
75. Koshibae W, Nagaosa N. Creation of skyrmions and antiskyrmions by local heating. *Nat Commun.* (2014) **5**:5148. doi: 10.1038/ncomms6148
76. Fujita H, Sato M. Ultrafast generation of skyrmionic defects with vortex beams: Printing laser profiles on magnets. *Phys Rev B* (2017) **95**:054421. doi: 10.1103/PhysRevB.95.054421
77. Fujita H, Sato M. Encoding orbital angular momentum of light in magnets. *Phys Rev B* (2017) **96**:060407. doi: 10.1103/PhysRevB.96.060407
78. Yudin D, Gulevich DR, Titov M. Light-induced anisotropic skyrmion and stripe phases in a rashba ferromagnet. *Phys Rev Lett.* (2017) **119**:147202. doi: 10.1103/PhysRevLett.119.147202
79. Hanneken C, Otte F, Kubetzka A, Dupé B, Romming N, von Bergmann K, et al. Electrical detection of magnetic skyrmions by tunnelling non-collinear magnetoresistance. *Nat Nanotechnol.* (2015) **10**:1039–42. doi: 10.1038/nnano.2015.218
80. Nagaosa N, Sinova J, Onoda S, MacDonald AH, Ong NP. Anomalous hall effect. *Rev Mod Phys.* (2010) **82**:1539–92. doi: 10.1103/RevModPhys.82.1539
81. Maccariello D, Legrand W, Reyren N, Garcia K, Bouzehouane K, Collin S, et al. Electrical detection of single magnetic skyrmions in metallic multilayers at room temperature. *Nat Nanotechnol.* (2018) **13**:233–7. doi: 10.1038/s41565-017-0044-4
82. Lee M, Kang W, Onose Y, Tokura Y, Ong NP. Unusual hall effect anomaly in MnSi under pressure. *Phys Rev Lett.* (2009) **102**:186601. doi: 10.1103/PhysRevLett.102.186601
83. Neubauer A, Pfleiderer C, Binz B, Rosch A, Ritz R, Niklowitz PG, et al. Topological hall effect in the A phase of MnSi. *Phys Rev Lett.* (2009) **102**:186602. doi: 10.1103/PhysRevLett.102.186602
84. Zhang X, Ezawa M, Zhou Y. Magnetic skyrmion logic gates: conversion, duplication and merging of skyrmions. *Sci Rep.* (2015) **5**:9400. doi: 10.1038/srep09400
85. Prychynenko D, Sitte M, Litzius K, Krüger B, Bourianoff G, Kläui M, et al. Magnetic skyrmion as a nonlinear resistive element: a potential building block for reservoir computing. *Phys Rev Appl.* (2018) **9**:014034. doi: 10.1103/PhysRevApplied.9.014034
86. Bourianoff G, Pinna D, Sitte M, Everschor-Sitte K. Potential implementation of reservoir computing models based on magnetic skyrmions. *AIP Adv.* (2018) **8**:055602. doi: 10.1063/1.5006918

Conflict of Interest Statement: The authors declare that the research was conducted in the absence of any commercial or financial relationships that could be construed as a potential conflict of interest.

frontiers in Astronomy and Space Sciences

REVIEW
published: 09 October 2018
doi: 10.3389/fspas.2018.00036

Neutrino Mass Ordering From Oscillations and Beyond: 2018 Status and Future Prospects

Pablo F. de Salas, Stefano Gariazzo, Olga Mena, Christoph A. Ternes and Mariam Tórtola*

Instituto de Física Corpuscular, CSIC-Universitat de València, Valencia, Spain

The ordering of the neutrino masses is a crucial input for a deep understanding of flavor physics, and its determination may provide the key to establish the relationship among the lepton masses and mixings and their analogous properties in the quark sector. The extraction of the neutrino mass ordering is a data-driven field expected to evolve very rapidly in the next decade. In this review, we both analyse the present status and describe the physics of subsequent prospects. Firstly, the different current available tools to measure the neutrino mass ordering are described. Namely, reactor, long-baseline (accelerator and atmospheric) neutrino beams, laboratory searches for beta and neutrinoless double beta decays and observations of the cosmic background radiation and the large scale structure of the universe are carefully reviewed. Secondly, the results from an up-to-date comprehensive global fit are reported: the Bayesian analysis to the 2018 publicly available oscillation and cosmological data sets provides *strong* evidence for the normal neutrino mass ordering vs. the inverted scenario, with a significance of 3.5 standard deviations. This preference for the normal neutrino mass ordering is mostly due to neutrino oscillation measurements. Finally, we shall also emphasize the future perspectives for unveiling the neutrino mass ordering. In this regard, apart from describing the expectations from the aforementioned probes, we also focus on those arising from alternative and novel methods, as 21 cm cosmology, core-collapse supernova neutrinos and the direct detection of relic neutrinos.

Keywords: neutrino mass ordering, neutrino oscillations, neutrinoless double beta ($0\nu\beta\beta$) decay, large scale structure formation, cosmic microwave Background (CMB), neutrino masses and flavor mixing

OPEN ACCESS

Edited by:
Alberto Salvio,
European Organization for Nuclear Research (CERN), Switzerland

Reviewed by:
Thomas Schwetz,
Karlsruher Institut für Technologie (KIT), Germany
Orlando Luis Goulart Peres,
Universidade Estadual de Campinas, Brazil

****Correspondence:***
Olga Mena
omena@ific.uv.es

Specialty section:
This article was submitted to High-Energy and Astroparticle Physics, a section of the journal Frontiers in Astronomy and Space Sciences

Received: *28 July 2018*
Accepted: *12 September 2018*
Published: *09 October 2018*

Citation:
de Salas PF, Gariazzo S, Mena O, Ternes CA and Tórtola M (2018) Neutrino Mass Ordering From Oscillations and Beyond: 2018 Status and Future Prospects. Front. Astron. Space Sci. 5:36. doi: 10.3389/fspas.2018.00036

1. INTRODUCTION

The Royal Swedish Academy of Sciences decided to award the 2015 Nobel Prize in Physics to Takaaki Kajita and Arthur B. McDonald *"for the discovery of neutrino oscillations, which shows that neutrinos have mass. [...] New discoveries about the deepest neutrino secrets are expected to change our current understanding of the history, structure and future fate of the Universe"* (see Fukuda et al., 1998; Ahmad et al., 2001, 2002; Eguchi et al., 2003; Abe et al., 2011a; An et al., 2012) for essential publications. These discoveries robustly established that neutrinos are massive particles. However, neutrinos are massless particles in the Standard Model (SM) of particle physics: in the absence of any direct indication for their mass available at the time, they were introduced as fermions for which no gauge invariant renormalizable mass term can be constructed. As a consequence, in the SM there is neither mixing nor CP violation in the lepton sector. Therefore, neutrino oscillations and masses *imply the first known departure from the SM of particle physics*.

Despite the good precision that neutrino experiments have reached in the recent years, still many neutrino properties remain unknown. Among them, the neutrino character, Dirac vs. Majorana, the existence of CP violation in the leptonic sector, the absolute scale of neutrino masses, and the type of the neutrino mass spectrum. Future laboratory, accelerator and reactor, astrophysical and cosmological probes will address all these open questions, that may further reinforce the evidence for physics beyond the SM. The main focus of this review is, however, the last of the aforementioned unknowns. We will discuss what we know and how we could improve our current knowledge of the neutrino mass ordering.

Neutrino oscillation physics is only sensitive to the squared mass differences ($\Delta m^2_{ij} = m^2_i - m^2_j$). Current oscillation data can be remarkably well-fitted in terms of two squared mass differences, dubbed as the solar mass splitting ($\Delta m^2_{21} \simeq 7.6 \times 10^{-5}$ eV^2) and the atmospheric mass splitting ($|\Delta m^2_{31}| \simeq 2.5 \times 10^{-3}$ eV^2) (de Salas et al., 2018)[1]. Thanks to matter effects in the Sun, we know that $\Delta m^2_{21} > 0$[2]. Since the atmospheric mass splitting Δm^2_{31} is essentially measured only via neutrino oscillations in vacuum, which exclusively depend on its absolute value, its sign is unknown at the moment. As a consequence, we have two possibilities for the ordering of neutrino masses: *normal ordering* (NO, $\Delta m^2_{31} > 0$) or *inverted ordering* (IO, $\Delta m^2_{31} < 0$).

The situation for the mass ordering has changed a lot in the last few months. The 2017 analyses dealing with global oscillation neutrino data have only shown a mild preference for the normal ordering. Namely, the authors of Capozzi et al. (2017), by means of a frequentist analysis, found $\chi^2_{\rm IO} - \chi^2_{\rm NO} = 3.6$ from all the oscillation data considered in their analyses. Very similar results were reported in the first version of de Salas et al. (2018)[3], where a value of $\chi^2_{\rm IO} - \chi^2_{\rm NO} = 4.3$ was quoted[4] (nufit)[5] Furthermore, in Gariazzo et al. (2018a), the authors verified that the use of a Bayesian approach and the introduction of cosmological or neutrinoless double beta decay data did not alter the main result, which was a weak-to-moderate evidence for the normal neutrino mass ordering according to the Jeffreys' scale (see **Table 2**). The most recent global fit to neutrino oscillation data, however, reported a strengthened preference for normal ordering that is mainly due to the new data from the Super-Kamiokande Abe et al. (2018a), T2K Hartz (2017), and NOνA Radovic (2018) experiments. The inclusion of these new data in both the analyses of Capozzi et al. (2018a) and the 2018 update of de Salas et al. (2018)[1] increases the preference for normal ordering, which now lies mildly above the 3σ level. In this review we will comment these new results (see section 2) and use them to perform an updated global analysis, following the method of Gariazzo et al. (2018a) (see section 5).

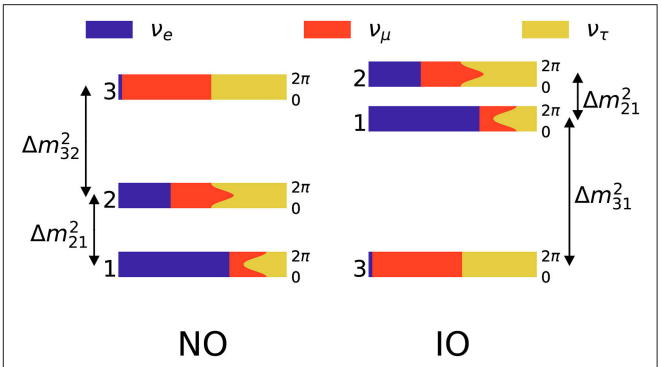

FIGURE 1 | Probability of finding the α neutrino flavor in the i-th neutrino mass eigenstate as the CP-violating phase, $\delta_{\rm CP}$, is varied. Inspired by Mena and Parke (2004).

The two possible hierarchical[6] neutrino mass scenarios are shown in **Figure 1**, inspired by Mena and Parke (2004), which provides a graphical representation of the neutrino flavor content of each of the neutrino mass eigenstates given the current preferred values of the oscillation parameters de Salas et al. (2018), see section 2. At present, even if the current preferred value of $\delta_{\rm CP}$ for both normal and inverted mass orderings lies close to $3\pi/2$ de Salas et al. (2018), the precise value of the CP violating phase in the leptonic sector remains unknown. Consequently, in **Figure 1**, we have varied $\delta_{\rm CP}$ within its entire range, ranging from 0 to 2π.

Given the two known mass splittings that oscillation experiments provide us, we are sure that at least two neutrinos have a mass above $\sqrt{\Delta m^2_{21}} \simeq 8$ meV and that at least one of these two neutrinos has a mass larger than $\sqrt{|\Delta m^2_{31}|} \simeq 50$ meV. For the same reason, we also know that there exists a lower bound on the sum of the three active neutrino masses ($\sum m_\nu = m_1 + m_2 + m_3$):

$$\sum m^{\rm NO}_\nu = m_1 + \sqrt{m_1^2 + \Delta m^2_{21}} + \sqrt{m_1^2 + \Delta m^2_{31}}\,, \qquad (1)$$
$$\sum m^{\rm IO}_\nu = m_3 + \sqrt{m_3^2 + |\Delta m^2_{31}|} + \sqrt{m_3^2 + |\Delta m^2_{31}| + \Delta m^2_{21}}\,,$$

where the lightest neutrino mass eigenstate corresponds to m_1 (m_3) in the normal (inverted) ordering. Using the best-fit values for the neutrino mass splittings in **Table 1** one finds that $\sum m_\nu \gtrsim 0.06$ eV in normal ordering, while $\sum m_\nu \gtrsim 0.10$ eV in inverted

[1] Valencia-Globalfit, 2018; Available online at: http://globalfit.astroparticles.es/.

[2] Note that the observation of matter effects in the Sun constrains the product $\Delta m^2_{21} \cos 2\theta_{12}$ to be positive. Therefore, depending on the convention chosen to describe solar neutrino oscillations, matter effects either fix the sign of the solar mass splitting Δm^2_{21} or the octant of the solar angle θ_{12}, with Δm^2_{21} positive by definition.

[3] See the "July 2017" version in[1].

[4] A somewhat milder preference in favor of normal mass ordering was obtained in the corresponding version of the analysis in Refs. Esteban et al. (2017)

[5] NuFIT v3.2, http://www.nu-fit.org/.

[6] A clarification about the use of "hierarchy" and "ordering" is mandatory. One talks about "hierarchy" when referring to the absolute scales of neutrino masses, in the sense that neutrino masses can be distinguished and ranked from lower to higher. This does not include the possibility that the lightest neutrino mass is much larger than the mass splittings obtained by neutrino oscillation measurements, since in this case the neutrino masses are degenerate. On the other hand, the mass "ordering" is basically defined by the sign of Δm^2_{31}, or by the fact that the lightest neutrino is the most (least) coupled to the electron neutrino flavor in the normal (inverted) case.

TABLE 1 | Neutrino oscillation parameters summary determined from the global analysis.

parameter	Best-fit ± 1σ	2σ range	3σ range
Δm^2_{21} [10^{-5}eV^2]	$7.55^{+0.20}_{-0.16}$	7.20–7.94	7.05–8.14
$\lvert\Delta m^2_{31}\rvert$ [10^{-3}eV^2] (NO)	2.50 ± 0.03	2.44–2.57	2.41–2.60
$\lvert\Delta m^2_{31}\rvert$ [10^{-3}eV^2] (IO)	$2.42^{+0.03}_{-0.04}$	2.34–2.47	2.31–2.51
$\sin^2\theta_{12}/10^{-1}$	$3.20^{+0.20}_{-0.16}$	2.89–3.59	2.73–3.79
$\sin^2\theta_{23}/10^{-1}$ (NO)	$5.47^{+0.20}_{-0.30}$	4.67–5.83	4.45–5.99
$\sin^2\theta_{23}/10^{-1}$ (IO)	$5.51^{+0.18}_{-0.30}$	4.91–5.84	4.53–5.98
$\sin^2\theta_{13}/10^{-2}$ (NO)	$2.160^{+0.083}_{-0.069}$	2.03–2.34	1.96–2.41
$\sin^2\theta_{13}/10^{-2}$ (IO)	$2.220^{+0.074}_{-0.076}$	2.07–2.36	1.99–2.44
δ_{CP}/π (NO)	$1.32^{+0.21}_{-0.15}$	1.01–1.75	0.87–1.94
δ_{CP}/π (IO)	$1.56^{+0.13}_{-0.15}$	1.27–1.82	1.12–1.94

The results for inverted mass ordering were calculated with respect to this mass ordering.

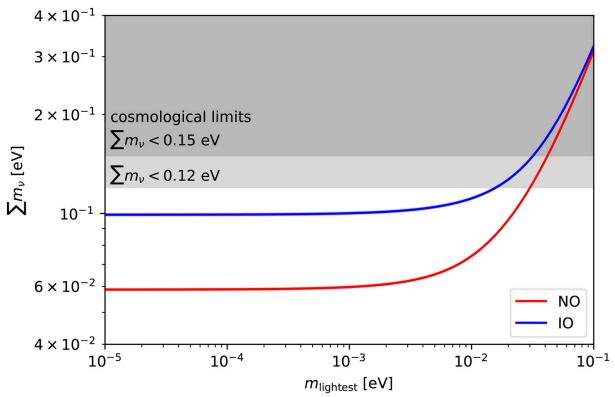

FIGURE 2 | The sum of the neutrino masses $\sum m_\nu$ as a function of the mass of the lightest neutrino, m_1 (m_3) for the normal (inverted) ordering, in red (blue) respectively. The (indistinguishable) width of the lines represents the present 3σ uncertainties in the neutrino mass splittings from the global fit to neutrino oscillation data (de Salas et al., 2018). The horizontal bands illustrate two distinct 95% Confidence Level (CL) limits on $\sum m_\nu$ from cosmology, see the text for details.

ordering. **Figure 2** illustrates the values of $\sum m_\nu$ as a function of the lightest neutrino mass for the two possible ordering schemes. We also show the two representative bounds on the sum of the neutrino masses from cosmology (discussed later in section 4) which is currently providing the strongest limits on $\sum m_\nu$ thanks to the fact that neutrinos affect both the evolution of the cosmological background and perturbation quantities (see e.g., the excellent detailed reviews of Lesgourgues and Pastor, 2006, 2012, 2014; Lesgourgues et al., 2013; Lattanzi and Gerbino, 2018).

The state-of-knowledge of cosmological observations Ade et al. (2016b) points to a flat Universe whose mass-energy density includes 5% of ordinary matter (baryons), 22% non-baryonic *dark matter*, and that is dominated by the *dark energy*, identified as the motor for the accelerated expansion. This is the so-called ΛCDM Universe, which fits extremely well the Cosmic Microwave Background (CMB) fluctuations, distant Supernovae Ia and galaxy clustering data.

Using the known neutrino oscillation parameters and the standard cosmological evolution, it is possible to compute the thermalization and the decoupling of neutrinos in the early universe (see e.g., Mangano et al., 2005; de Salas and Pastor, 2016). While neutrinos decoupled as ultra-relativistic particles, currently at least two out of the three neutrino mass eigenstates are non-relativistic. Neutrinos constitute the first and only known form of dark matter so far. Indeed, neutrinos behave as *hot* dark matter particles, possessing large thermal velocities, clustering only at scales below their free streaming scale, modifying the evolution of matter overdensities and suppressing structure formation at small scales. The CMB is also affected by the presence of massive neutrinos, as these particles may turn non-relativistic around the decoupling period. However, the strong degeneracy between the Hubble constant and the total neutrino mass requires additional constraints (from Baryon Acoustic Oscillations, Supernovae Ia luminosity distance data and/or direct measurements of the Hubble constant) to be added in the global analyses. In this regard, CMB lensing is also helpful and improves the CMB temperature and polarization constraints, as the presence of massive neutrinos modify the matter distribution along the line of sight through their free streaming nature, reducing clustering and, consequently, CMB lensing. The most constraining cosmological upper bounds to date on $\sum m_\nu$ can be obtained combining CMB with different large scale structure observations and range from $\sum m_\nu < 0.12$ eV to $\sum m_\nu < 0.15$ eV at 95% CL (Palanque-Delabrouille et al., 2015; Cuesta et al., 2016; Di Valentino et al., 2016c; Giusarma et al., 2016; Vagnozzi et al., 2017, 2018; Lattanzi and Gerbino, 2018), as illustrated in **Figure 2**.

If the massive neutrino spectrum does not lie in the degenerate region, the three distinct neutrino masses affect the cosmological observables in a different way. For instance, the transition to the non-relativistic period takes place at different cosmic times, and the associated free-streaming scale is different for each of the neutrino mass eigenstates. However, the effect on the power spectrum is very small (permille level) and therefore an extraction of the neutrino mass hierarchy via singling out each of the massive neutrino states seems a very futuristic challenge. This will be possibly attainable only via huge effective volume surveys, as those tracing the 21 cm spin-flip transition in neutral hydrogen, see sections 6.4 and 6.5. On the other hand, should the cosmological measurements of $\sum m_\nu$ be strong enough to rule out the $\sum m_\nu$ parameter space corresponding to the inverted ordering (i.e., strong enough to establish in a very significant way that $\sum m_\nu < 0.1$ eV), we would know that the neutrino mass ordering must be normal. A word of caution is needed here when dealing with Bayesian analyses, usually performed when dealing with cosmological data: a detection of the neutrino mass ordering could be driven by volume effects in the marginalization, and therefore the prior choice can make a huge difference, if data are not powerful enough (Schwetz et al., 2017).

Another way to probe the neutrino mass ordering, apart from direct determinations of the sign of the atmospheric mass splitting Δm^2_{31} in neutrino oscillation experiments and,

indirectly, from cosmological bounds on the sum of the neutrino masses, is *neutrinoless double β decay* (Rodejohann, 2011; Gomez-Cadenas et al., 2012; Vergados et al., 2012; Dell'Oro et al., 2016). This process is a spontaneous nuclear transition in which the charge of two isobaric nuclei would change by two units with the simultaneous emission of two electrons and without the emission of neutrinos. This process is only possible if the neutrino is a Majorana particle and an experimental signal of the existence of this process would constitute evidence of the putative Majorana neutrino character. The non-observation of the process provides bounds on the so-called *effective Majorana mass* $m_{\beta\beta}$, which is a combination of the (Majorana) neutrino masses weighted by the leptonic flavor mixing effects (see section 3). **Figure 3** illustrates the (Bayesian) 95.5% and 99.7% credible intervals for $m_{\beta\beta}$ as a function of the lightest neutrino mass in the case of three neutrino mixing, considering a logarithmic prior on the lightest neutrino mass. The picture differs from the plot that is usually shown, which features an open band toward increasingly smaller values of $m_{\beta\beta}$ for $m_{\rm lightest} \simeq 5$ meV, due to cancellations which depend on the values of the Majorana phases α_i (see section 3). In the Bayesian sense of credible intervals, the values of α_i which produce such a suppression of $m_{\beta\beta}$ represent an extremely small fraction of the parameter space, which is therefore not relevant when computing the 95.5% and 99.7% credible intervals. In other words, given our knowledge of the neutrino mixing parameters, having $m_{\beta\beta} \lesssim 2 \times 10^{-4}$ eV would require some amount of fine tuning in the Majorana phases. This figure is in perfect agreement with the results shown in Figure 1 of Agostini et al. (2017a), which shows that most of the allowed parameter space is not concentrated at small $m_{\beta\beta}$ if one considers a linear prior on the lightest neutrino mass. We also show the most conservative version of some of the most competitive current limits, as those from KamLAND-Zen ($m_{\beta\beta} < 61 - 165$ meV at 90% CL) Gando et al. (2016), GERDA Phase II ($m_{\beta\beta} < 120 - 260$ meV at 90% CL) Agostini et al. (2018) and CUORE ($m_{\beta\beta} < 110 - 520$ meV at 90% CL) Alduino et al. (2018a). Please note that a detection of the effective Majorana mass will not be sufficient to determine the mass ordering if the lightest neutrino mass is above ~ 40 meV: in this case, indeed, the normal and the inverted ordering become indistinguishable from the point of view of neutrinoless double beta decay. Similarly to the case of the cosmological bounds on the neutrino mass $\sum m_\nu$, in which only constraining $\sum m_\nu$ to be below 0.1 eV could be used to disfavor the inverted mass ordering, only a limit on $m_{\beta\beta}$ below ~ 10 meV could be used to rule out the inverted ordering scheme, and only assuming that neutrinos are Majorana particles.

Since neutrino oscillation measurements, cosmological observations and neutrinoless double beta decay experiments are cornering the inverted mass ordering region, it makes sense to combine their present results. Indeed, plenty of works have been recently devoted to test whether a preference for one mass ordering over the other exists, given current oscillation, neutrinoless double beta decay and cosmological data. A number of studies on the subject (Hannestad and Schwetz, 2016; Caldwell et al., 2017; Capozzi et al., 2017; Gerbino et al., 2017b; Wang and Xia, 2018) found that the preference for the normal vs. the inverted mass scenario is rather mild with current data, regardless the frequentist vs. Bayesian approach. In the latter case, however, the results may be subject-dependent, as a consequence of different possible choices of priors and parameterizations when describing the theoretical model, for example in the case of sampling over the three individual neutrino mass states. Therefore, one must be careful when playing with different priors, as recently shown in Gariazzo et al. (2018a). The current status of the preference of normal vs. inverted ordering will be further investigated carefully throughout this review. Furthermore, as it will be carefully detailed in section 5, the Bayesian global fit to the 2018 publicly available oscillation and cosmological data points to a strong preference (3.5 standard deviations) for the normal neutrino mass ordering vs. the inverted one.

To summarize and conclude this introductory part, we resume that the current available methods to determine the neutrino mass ordering can be grouped as:

a) neutrino oscillation facilities;
b) neutrinoless double beta decay experiments, with the caveat that the results will only apply in case neutrinos are Majorana fermions;
c) CMB and large scale structure surveys.

For each of these three categories we will review the current status and also analyse the future prospects, with a particular focus on the existing experiments which will be improved in the future and on new facilities which aim at determining the neutrino mass ordering in the next 22 years[7] In the second part of this review we will also focus on possible novel methods that in the future will enable us to determine the neutrino mass ordering, as for example future cosmological observations of the 21 cm line, the detection of neutrinos emitted by core-collapse supernovae, measurements of the electron spectrum of β-decaying nuclei and the direct detection of relic neutrinos.

We shall exploit the complementarity of both cosmology and particle physics approaches, profiting from the highly multidisciplinary character of the topic. We dedicate sections 2, 3, and 4 to explain the extraction of the neutrino mass ordering via neutrino oscillations, β and neutrinoless double β decays and cosmological observations, which will be combined in section 5 where we present the analysis of current data related to these three data sets. Future perspectives are described throughout section 6 and its subsections, while the final remarks will be outlined in section 7.

2. NEUTRINO OSCILLATIONS

Our current knowledge on the neutrino mass ordering comes mainly from the analysis of the available neutrino oscillation data. The sensitivity to the neutrino mass spectrum at oscillation experiments is mostly due to the presence of matter effects in the neutrino propagation. Therefore, one can expect that this sensitivity will increase with the size of matter effects, being larger for atmospheric neutrino experiments, where a fraction of

[7] See also the review Qian and Vogel (2015), focused mostly on neutrino oscillation perspectives.

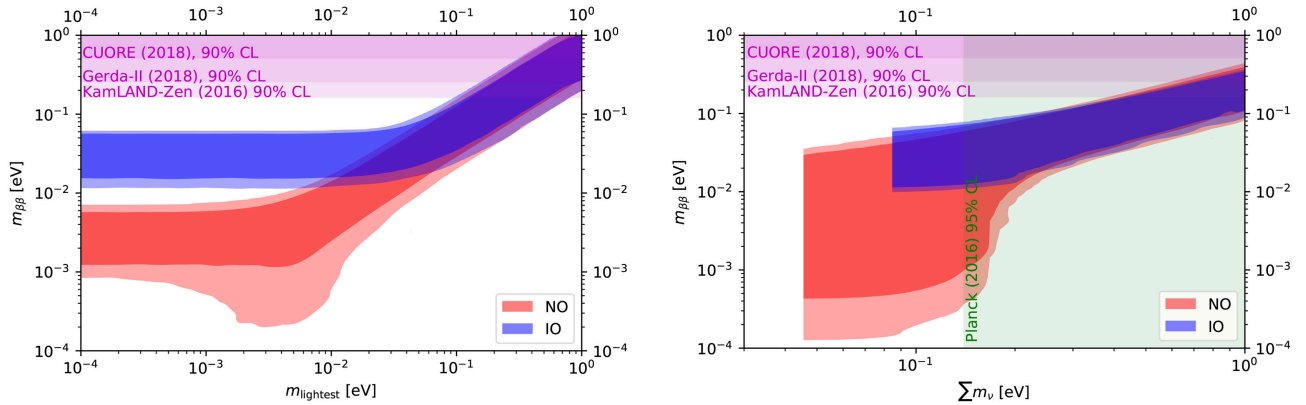

FIGURE 3 | 95.5 and 99.7% Bayesian credible intervals for the effective Majorana mass, $m_{\beta\beta}$, as a function of the lightest neutrino mass **(Left)** or of the sum of the neutrino masses $\sum m_\nu$ **(Right)**, taking into account the current uncertainties on the neutrino mixing parameters (angles and phases), when three neutrinos are considered. The horizontal bands indicate the most conservative version (obtained by each collaboration when assuming a disfavorable value for the nuclear matrix element of the process) of some of the most competitive upper bounds, as those reported by KamLAND-Zen Gando et al. (2016), GERDA Phase II Agostini et al. (2018) and CUORE Alduino et al. (2018a). The vertical band in the **Right** indicates the strongest limit reported by `Planck` Aghanim et al. (2016b), using the `Planck TT,TE,EE + SimLow + lensing` data combination.

neutrinos travel through the Earth. For long-baseline accelerator experiments, matter effects will increase with the baseline, while these effects will be negligible at short-baseline and medium-baseline experiments.

When neutrinos travel through the Earth, the effective matter potential due to the electron (anti)neutrino charged-current elastic scatterings with the electrons in the medium will modify the three-flavor mixing processes. The effect will strongly depend on the neutrino mass ordering: in the normal (inverted) mass ordering scenario, the neutrino flavor transition probabilities will get enhanced (suppressed). In the case of antineutrino propagation, instead, the flavor transition probabilities will get suppressed (enhanced) in the normal (inverted) mass ordering scenario. This is the Wolfenstein effect (Wolfenstein, 1978), later expanded by Mikheev and Smirnov Mikheev and Smirnov (1985, 1986), and commonly named as the Mikheev-Smirnov-Wolfenstein (MSW) effect (see e.g., Blennow and Smirnov, 2013 for a detailed description of neutrino oscillations in matter).

Matter effects in long-baseline accelerator or atmospheric neutrino oscillation experiments depend on the size of the effective mixing angle θ_{13} in matter, which leads the transitions $\nu_e \leftrightarrow \nu_{\mu,\tau}$ governed by the atmospheric mass-squared difference $\Delta_{31} = \Delta m^2_{31}/2E$. Within the simple two-flavor mixing framework, the effective θ_{13} angle in matter reads as

$$\sin^2 2\theta^{\rm m}_{13} = \frac{\sin^2 2\theta_{13}}{\sin^2 2\theta_{13} + \left(\cos 2\theta_{13} \mp \frac{\sqrt{2}G_F N_e}{\Delta_{31}}\right)^2}\,, \qquad (2)$$

where the minus (plus) sign refers to neutrinos (antineutrinos) and N_e is the electron number density in the Earth interior. The neutrino mass ordering fixes the sign of Δ_{31}, that is positive (negative) for normal (inverted) ordering: notice that, in the presence of matter effects, the neutrino (antineutrino) oscillation probability $P(\nu_\mu \to \nu_e)$ $[P(\bar\nu_\mu \to \bar\nu_e)]$ gets enhanced if the ordering is normal (inverted). Exploiting the different matter effects for neutrinos and antineutrinos provides therefore the ideal tool to unravel the mass ordering.

Matter effects are expected to be particularly relevant when the following resonance condition is satisfied:

$$\Delta m^2_{31} \cos 2\theta_{13} = 2\sqrt{2} G_F N_e E\,. \qquad (3)$$

The precise location of the resonance will depend on both the neutrino path and the neutrino energy. For instance, for $\Delta m^2_{31} \sim 2.5 \times 10^{-3}$ eV^2 and distances of several thousand kilometers, as it is the case of atmospheric neutrinos, the resonance effect is expected to happen for neutrino energies $\sim 3 - 8$ GeV.

In the case of muon disappearance experiments, in the $\sim$ GeV energy range relevant for long-baseline and atmospheric neutrino beams, the $P_{\mu\mu}$ survival probabilities are suppressed (enhanced) due to matter effects if the ordering is normal (inverted). If the matter density is constant, the $P_{\mu\mu}$ survival probability at terrestrial baselines[8] is given by

$$\begin{aligned} P_{\mu\mu} \;=\; & 1 - \cos^2\theta^{\rm m}_{13} \sin^2 2\theta_{23} \times \sin^2\left[1.27\left(\frac{\Delta m^2_{31} + A + (\Delta m^2_{31})^{\rm m}}{2}\right)\frac{L}{E}\right] \\ & - \sin^2\theta^{\rm m}_{13} \sin^2 2\theta_{23} \times \sin^2\left[1.27\left(\frac{\Delta m^2_{31} + A - (\Delta m^2_{31})^{\rm m}}{2}\right)\frac{L}{E}\right] \\ & - \sin^4\theta_{23} \sin^2 2\theta^{\rm m}_{13} \sin^2\left[1.27(\Delta m^2_{31})^{\rm m}\frac{L}{E}\right], \end{aligned} \qquad (4)$$

[8]For an expansion including also the solar mixing parameters, see Ref.Akhmedov et al. (2004).

where $A = 2\sqrt{2}G_F N_e E$, $\theta_{13}^{\rm m}$ is that of Equation (2) and

$$(\Delta m^2_{31})^{\rm m} = \Delta m^2_{31} \sqrt{\sin^2 2\theta_{13} + \left(\cos 2\theta_{13} \mp \frac{2\sqrt{2}G_F N_e E}{\Delta m^2_{31}}\right)^2}. \quad (5)$$

The dependence of the survival probability $P_{\mu\mu}$ on the neutrino energy E and the cosine of the zenith angle $\cos\theta_z$, related to the distance the atmospheric neutrinos travel inside the Earth before being detected at the experiments, is shown in **Figure 4** for normal **(Left)** and inverted **(Right)** ordering. There, we can see that reconstructing the oscillation pattern at different distances and energies allows to determine the neutrino mass ordering (see also section 6.1).

Until very recently, oscillation experiments were not showing a particular preference for any of the mass orderings, not even when combined in a global analysis (see for instance Forero et al., 2014). Lately, however, the most recent data releases from some of the experiments have become more sensitive to the ordering of the neutrino mass spectrum. In particular, the long-baseline experiments T2K and NOνA on their own obtain a slight preference in favor of normal mass ordering, with $\Delta\chi^2 \approx 4$ each (Hartz, 2017; Radovic, 2018). Note that these results have been obtained imposing a prior on the mixing angle θ_{13}, according to its most recent determination at reactor experiments. Relaxing the prior on the reactor angle results in a milder preference for normal over inverted mass ordering. The latest atmospheric neutrino results from Super-Kamiokande also show some sensitivity to the neutrino mass ordering. In this case, the collaboration obtains a preference for normal ordering with $\Delta\chi^2 \approx 3.5$, without any prior on the reactor angle. Constraining the value of θ_{13}, the preference for normal mass ordering increases up to $\Delta\chi^2 \approx 4.5$ Abe et al. (2018a).

The full sensitivity to the ordering of the neutrino mass spectrum from oscillations is obtained after combining the data samples described above with all the available experimental results in a global fit (de Salas et al., 2018). This type of analysis exploits the complementarity among the different results as well as the correlations among the oscillation parameters to obtain improved sensitivities on them. In the global analysis to neutrino oscillations, the parameters $\sin^2\theta_{12}$ and Δm^2_{21} are rather well measured by the solar experiments (Cleveland et al., 1998; Hosaka et al., 2006; Aharmim et al., 2008, 2010; Cravens et al., 2008; Abdurashitov et al., 2009; Kaether et al., 2010; Abe et al., 2011b; Bellini et al., 2014; Nakano, 2016) and the long-baseline reactor experiment KamLAND Gando et al. (2011). The short-baseline reactor neutrino experiments Daya Bay An et al. (2017), RENO Pac (2018) and Double Chooz Abe et al. (2014) are the most efficient ones in measuring the reactor angle θ_{13} and also measure very well the atmospheric mass splitting, Δm^2_{31}. Notice however that the atmospheric mass splitting is best measured by the combined data from MINOS (beam and atmospheric) and MINOS+, as shown in Adam (2018). This mass splitting is also measured, together with the atmospheric angle θ_{23}, by the atmospheric experiments IceCube-DeepCore Aartsen et al. (2015), ANTARES Adrian-Martinez et al. (2012) and Super-Kamiokande Abe et al. (2018a), where the latter shows some sensitivity to θ_{13} and $\delta_{\rm CP}$, too. The long-baseline accelerator experiments are also sensitive to these four parameters through their appearance and disappearance neutrino channels. Apart from the already mentioned T2K Hartz (2017) and NOνA Radovic (2018), the global fit also includes the previous experiments K2K Ahn et al. (2006) and MINOS Adamson et al. (2014).

The result of the global analysis is summarized in **Table 1** and **Figure 5**. Before discussing the sensitivity to the neutrino mass ordering, we shall briefly discuss some other features of this global fit. Notice first that now the best-fit value for the atmospheric mixing angle θ_{23} lies in the second octant, although values in the first octant are still allowed with $\Delta\chi^2 = 1.6$ (3.2) for normal (inverted) ordering. Therefore, the octant problem remains unsolved so far. Note also that, for the first time, the CP violating phase $\delta_{\rm CP}$ is determined with rather good accuracy. The best-fit values for this parameter lie close to maximal CP violation, being $\delta_{\rm CP} = 1.32\pi$ for normal ordering and $\delta_{\rm CP} = 1.56\pi$ for inverted ordering. As can be seen from the $\Delta\chi^2$ profile in **Figure 5**, values around $\delta_{\rm CP} \approx 0.5\pi$ are now highly disfavored by data. Indeed, only around 50% of the

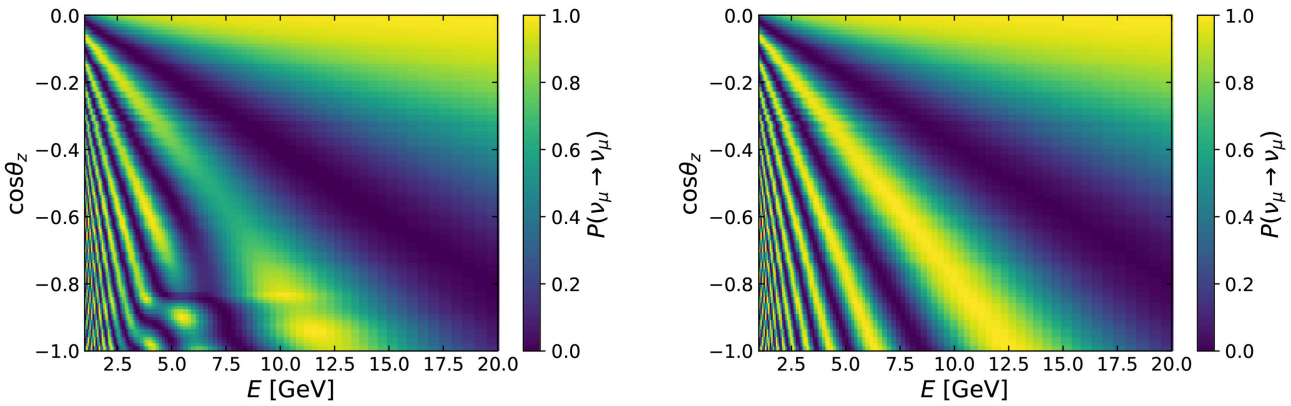

FIGURE 4 | Survival probability $P_{\mu\mu}$, as a function of the neutrino energy E and the cosine of the zenith angle $\cos\theta_z$, for normal (inverted) ordering in the **(Left, Right)**.

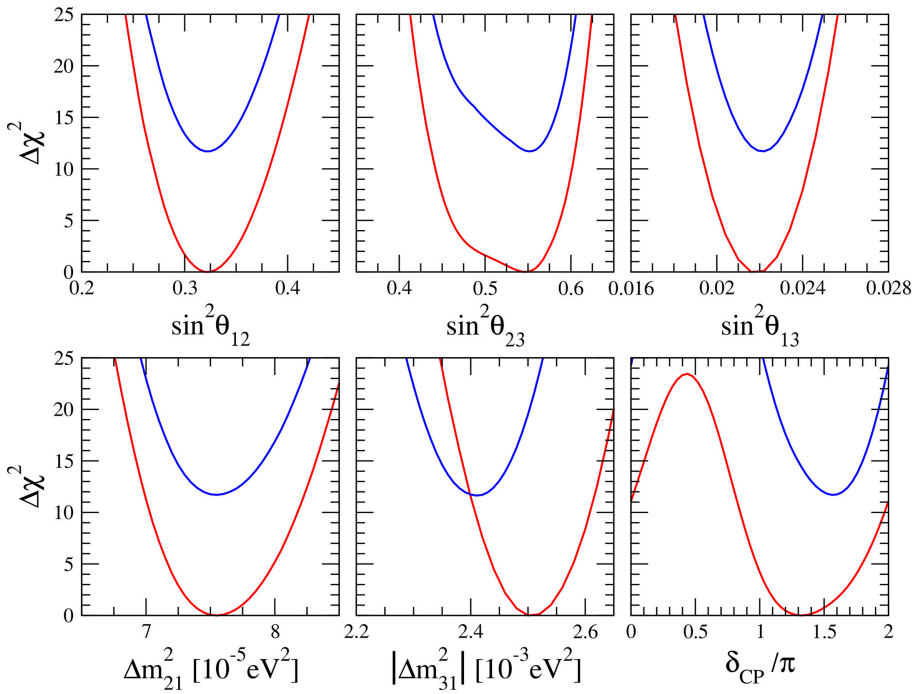

FIGURE 5 | Summary of neutrino oscillation parameters, 2018. Red (blue) lines correspond to normal ordering (inverted ordering). Notice that the $\Delta\chi^2$ profiles for inverted ordering are plotted with respect to the minimum for normal neutrino mass ordering.

parameter space remains allowed at the 3σ level, roughly the interval $[0.9\pi, 1.9\pi]$ for normal and $[1.1\pi, 1.9\pi]$ for inverted ordering. In the case of normal ordering, CP conservation remains allowed at 2σ, while it is slightly more disfavored for inverted ordering. For the remaining oscillation parameters, one clearly sees that neutrino oscillations are entering the precision era, with relative uncertainties on their determination of 5% or below. For a more detailed discussion about these parameters we refer the reader to de Salas et al. (2018) and[1].

Concerning the neutrino mass ordering, we obtain a global preference of 3.4σ ($\Delta\chi^2 = 11.7$) in favor of normal ordering. This result emerges from the combination of all the neutrino oscillation experiments, as we explain in the following. Starting with long-baseline data alone, the inverted mass ordering is disfavored with $\Delta\chi^2 = 2.0$, when no prior is considered on the value of θ_{13}. However, as explained above, the separate analysis of the latest T2K and NOνA data independently report a $\Delta\chi^2 \approx 4$ among the two possible mass orderings when a prior on the reactor angle is imposed. This comes from the mismatch between the value of θ_{13} preferred by short-baseline reactor and long-baseline accelerator experiments, which is more important for inverted ordering. Besides that, the combination of T2K and reactor data results in an additional tension relative to the preferred value of the atmospheric mass splitting Δm^2_{31}, which is again larger for the inverted mass ordering. This further discrepancy results in a preference for normal ordering with $\Delta\chi^2 = 5.3$ for the combination of "T2K plus reactors" and $\Delta\chi^2 = 3.7$ for the combination of "NOνA plus reactors". From the combined analysis of all long-baseline accelerator and short-baseline reactor data one obtains a $\Delta\chi^2 = 7.5$ between normal and inverted ordering, which corresponds to a preference of 2.7σ in favor of normal mass ordering. By adding the atmospheric data to the neutrino oscillations fit, we finally obtain $\Delta\chi^2 = 11.7$[9], indicating a global preference for normal ordering at the level of 3.4σ.

3. MASS ORDERING AND DECAY EXPERIMENTS

3.1. Mass Ordering Through β-Decay Experiments

The most reliable method to determine the absolute neutrino masses in a completely model independent way is to measure the spectrum of β-decay near the endpoint of the electron spectrum. The reason for this is related to the fact that, if neutrinos are massive, part of the released energy must go into the neutrino mass and the electron spectrum endpoint shifts to lower energies. When there are more than one massive neutrino, each of the separate mass eigenstates contributes to the suppression of the electron energy spectrum and it becomes possible to study the pattern of the neutrino masses. Nowadays none of the β-decay experiments can reach the energy resolution required to be able

[9]Note that this extra sensitivity comes essentially from Super-Kamiokande, since the effect of IceCube DeepCore and ANTARES is negligible in comparison.

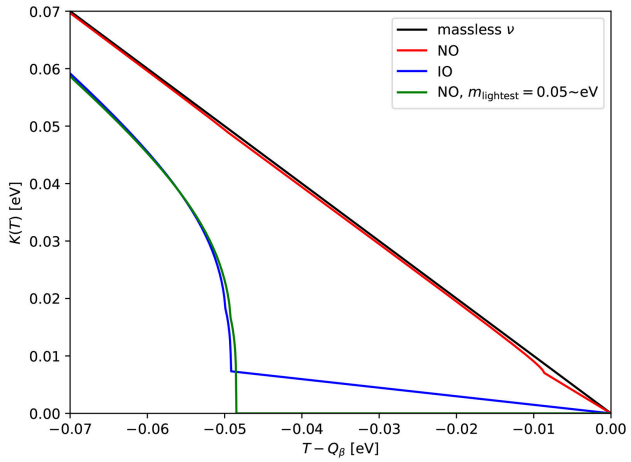

FIGURE 6 | Kurie function in β-decays. The red (blue) line indicates the normal (inverted) ordering case for a massless lightest neutrino, while the black line is for the case of three massless neutrinos. The green curve shows how the Kurie function of a normal ordering scenario with $m_{\rm lightest} \simeq \sqrt{\Delta m^2_{31}}$ can mimic the inverted ordering case.

to determine the mass hierarchy[10], but we will explain in the following how, in principle, future experiments may aim at such result.

The best way to depict the effects of the separate mass eigenstates is to compute the Kurie function for β-decay. The complete expression can be written as (see e.g., Giunti and Kim, 2007):

$$K(T) = \left[(Q_\beta - T) \sum_{i=1}^{N} |U_{ei}|^2 \sqrt{(Q_\beta - T)^2 - m_i^2}\ \Theta(Q_\beta - T - m_i) \right]^{1/2}, \quad (6)$$

where Q_β is the Q-value of the considered β-decay, T is the electron kinetic energy, Θ is the Heaviside step function and $|U_{ei}|^2$ is the mixing matrix element that defines the mixing between the electron neutrino flavor and the i-th mass eigenstate with a mass m_i. The standard scenario features $N = 3$, but the formula is valid also if a larger number of neutrinos exists (i.e., if there are sterile neutrinos, as explained for example in Gariazzo et al., 2016).

The Kurie function of Equation (6) is depicted in **Figure 6**, where we show in red (blue) the result obtained using a massless lightest neutrino and the current best-fit mixing angles and mass splittings for normal (inverted) ordering, as described in the previous section. As a reference, we also plot $K(T)$ for a case with massless neutrinos only (in black). Should we consider higher values for the lightest neutrino mass, the detection of the mass ordering would be increasingly more difficult, since the separation of the mass eigenstates would decrease, eventually becoming negligible in the degenerate case. For this reason we will only discuss the case of a massless lightest neutrino from the perspective of the β-decay experiments.

Given the unitarity of the mixing matrix ($\sum_{i=1}^{N} |U_{ei}|^2 = 1$), the normalization of the Kurie function is the same at $Q_\beta - T \gg m_i$. Since we are interested in the small differences which appear near the endpoint, the plot only focuses on the very end of the electron spectrum and the common normalization is not visible for the inverted ordering case. In the considered range, however, the effect of the different correspondence between the mass eigenstates and the mixing matrix elements introduces a difference which in principle would allow to determine the mass ordering through the observation of the β-decay spectrum. The observation of the kinks in the electron spectrum is very challenging, especially in the case of normal ordering, for which even the more pronounced kink (at $Q_\beta - T \simeq \sqrt{\Delta m^2_{21}} \simeq$ 8 meV) is barely visible in **Figure 6**. In the case of inverted ordering, since the mass difference between the two lightest mass eigenstates is the largest possible one ($\sqrt{\Delta m^2_{31}} \simeq 50$ meV), and the lightest neutrino is the one with the smallest mixing with the electron neutrino, the amplitude of the kink is much larger. As a consequence, an experiment with enough energy resolution to measure the spectrum in the relevant energy range can directly probe the mass ordering observing the presence of a kink. Note that this measurement can be obtained even without a detection of the lightest neutrino mass. As we show in **Figure 6**, however, it is crucial to have a non-zero observation of the electron spectrum between Q_β and $Q_\beta - \sqrt{\Delta m^2_{31}}$, otherwise one could confuse the inverted ordering spectrum with a normal ordering spectrum obtained with a larger lightest neutrino mass $m_{\rm lightest} \simeq \sqrt{\Delta m^2_{31}}$ (green curve).

Another consideration is due. One could think to probe the neutrino mass ordering just using the fact that the expected number of events is smaller in the inverted ordering than in the normal ordering case. As we discussed above, this could be possible only if some independent experiment would be able to determine the mass of the lightest neutrino, in order to break the possible degeneracy between $m_{\rm lightest}$ and the mass ordering depicted by the blue and green curves in **Figure 6**, otherwise the conditions required to observe the electron spectrum between Q_β and $Q_\beta - \sqrt{\Delta m^2_{31}}$ would be probably sufficient to guarantee a direct observation or exclusion of the kink. The best way to determine the neutrino mass ordering, however, may be to use an estimator which compares the binned spectra in the normal and inverted ordering cases, as proposed for example in Stanco et al. (2017) in the context of reactor neutrino experiments. The authors of the study, indeed, find that a dedicated estimator can enhance the detection significance with respect to a standard χ^2 comparison.

To conclude, today the status of β-decay experiments is far from the level of determining the mass ordering, since the energy resolution achieved in past and current measurements is not sufficient to guarantee a precise probe of the interesting part

[10]In the case of quasi-degenerate spectrum, the distortion of the spectrum will consist of just a bending and a shift of the end point, similar to the case of an electron neutrino with a given mass without mixing Farzan et al. (2001), and the ordering cannot be measured. Therefore, for future β-decay searches, measuring the neutrino mass *ordering* will be practically the same as measuring the neutrino mass *hierarchy*.

of the spectrum. KATRIN, for example, aims at a sensitivity of 0.2 eV on the effective electron neutrino mass (Angrik et al., 2004; Sejersen Riis et al., 2011), only sufficient to probe the fully degenerate region of the neutrino mass spectrum.

3.2. Mass Ordering From Neutrinoless Double Beta Decay

In the second part of this section we shall discuss instead the perspectives from the neutrinoless double beta decay (see e.g., the reviews Gomez-Cadenas et al., 2012; Dell'Oro et al., 2016 and also Pascoli and Petcov (2002)), a process allowed only if neutrinos are Majorana particles (Schechter and Valle, 1982), since it requires the lepton number to be violated by two units. Neutrinoless double beta decay experiments therefore aim at measuring the life time $T^{0\nu}_{1/2}$ of the decay, which can be written as:

$$\frac{1}{T^{0\nu}_{1/2}(\mathcal{N})} = G^{\mathcal{N}}_{0\nu} |\mathcal{M}^{0\nu}_{\mathcal{N}}|^2 \left(\frac{|m_{\beta\beta}|}{m_e}\right)^2 , \tag{7}$$

where m_e is the electron mass, $G^{\mathcal{N}}_{0\nu}$ is the phase space factor, $\mathcal{M}^{0\nu}_{\mathcal{N}}$ is the nuclear matrix element (NME) of the neutrinoless double beta decay process, $\mathcal{N}$ indicates the chemical element which is adopted to build the experiment and $m_{\beta\beta}$ is the effective Majorana mass, see below. In case no events are observed, a lower bound on $T^{0\nu}_{1/2}$ can be derived. Recent constraints on the neutrinoless double beta decay half-life come from the EXO−200 Albert et al. (2014), KamLAND−Zen Gando et al. (2016), CUORE Alduino et al. (2018a), Majorana Aalseth et al. (2018), CUPID−0 Azzolini et al. (2018), Gerda Agostini et al. (2018), and NEMO−3 Arnold et al. (2018) experiments. The strongest bounds to date on the half-life of the different isotopes are: $T^{0\nu}_{1/2}(^{76}\mathrm{Ge}) > 8.0 \times 10^{25}$ year from Gerda Agostini et al. (2018), $T^{0\nu}_{1/2}(^{82}\mathrm{Se}) > 2.4 \times 10^{24}$ year from CUPID−0 Azzolini et al. (2018), $T^{0\nu}_{1/2}(^{130}\mathrm{Te}) > 1.5 \times 10^{25}$ year from CUORE Alduino et al. (2018a) and $T^{0\nu}_{1/2}(^{136}\mathrm{Xe}) > 1.07 \times 10^{26}$ year from KamLAND−Zen, Gando et al. (2016).

The effective Majorana mass reads as:

$$m_{\beta\beta} = \sum_{k=1}^{N} e^{i\alpha_k} |U_{ek}|^2 m_k , \tag{8}$$

where N is the number of neutrino mass eigenstates, each with its mass m_k, α_k are the Majorana phases (one of which can be rotated away, so that there are $N-1$ independent phases), and U_{ek} represents the mixing between the electron flavor neutrino and the k-th mass eigenstate. Notice that the conversion between the half-life of the process and the effective Majorana mass depends on the NMEs (see e.g., Vergados et al., 2016; Engel and Menéndez, 2017), which are typically difficult to compute. Several methods can be employed and there is no full agreement between the results obtained with the different methods. As a consequence, the quoted limits on $T^{0\nu}_{1/2}$ can be translated into limits on $m_{\beta\beta}$ which depend on the NMEs. If the most conservative values for the NMEs are considered, none of the current constraints reaches the level required to start constraining the inverted ordering in the framework of three neutrinos, see **Figure 3**.

If we compute $m_{\beta\beta}$ as a function of the lightest neutrino mass with the current preferred values of the mixing parameters and in the context of three neutrinos, we discover that the value of $m_{\beta\beta}$ depends on the mass ordering only for $m_{\rm lightest} \lesssim 40$ meV, see **Figure 3**. For this reason, neutrinoless double beta experiments can aim to distinguish the mass ordering only for the smallest values of the lightest neutrino mass. Please note that this also means that if the lightest neutrino has a mass above ~ 40 meV, perfectly allowed by all the present constraints on the neutrino mass scale, the two mass orderings will never be distinguished in the context of neutrinoless double beta decay experiments.

When going to smaller $m_{\rm lightest}$, the situation changes, as $m_{\beta\beta}$ becomes independent of $m_{\rm lightest}$. In the region $m_{\rm lightest} \lesssim 10$ meV, a difference between the two mass orderings appears, since the effective Majorana mass is constrained by the mass splittings to be larger than ~ 10 meV for inverted ordering, while it must be below ~ 7 meV for normal ordering. This means that experiments which can test the region $m_{\beta\beta} < 10$ meV can rule out the inverted scenario. Note that a positive detection of $T^{0\nu}_{1/2}$ in the range that corresponds to $m_{\beta\beta} \gtrsim 10$ meV, on the other hand, would not give sufficient information to determine the mass ordering without an independent determination of $m_{\rm lightest}$. To resume, in the context of three neutrino mixing, neutrinoless double beta decay experiments alone will be able to determine the neutrino mass ordering only ruling out the inverted scheme, that is to say if the ordering is normal and $m_{\rm lightest} \lesssim 10$ meV.

In any case, we should remember that if no neutrinoless double beta decay candidate event will ever be observed we will not have determined the mass ordering univocally: Dirac neutrinos escape the constraints from this kind of process, so that it would be still perfectly allowed to have an inverted ordering scheme and no Majorana fermions in the neutrino sector. Due to the presence of the Majorana phases in Equation (8), unfortunately, there is a small window for $m_{\rm lightest}$ in normal ordering that can correspond to almost vanishing values of $m_{\beta\beta}$, which will possibly never be observable. As we show in **Figure 3**, however, the region of parameter space where this happens has a very small volume if one considers the phases to vary between 0 and 2π, so that the credible region for $m_{\beta\beta}$ in a Bayesian context shows that it is rather unlikely to have $m_{\beta\beta} \lesssim 2 \times 10^{-4}$ eV, as a significant amount of fine tuning would be needed in the (completely unknown) Majorana phases. Our statement, which arises from assuming a logarithmic prior on $m_{\rm lightest}$, is in perfect agreement with the results of Agostini et al. (2017a), where a linear prior on $m_{\rm lightest}$ is assumed.

Please note that the situation depicted in **Figure 3** is only valid if there are only three neutrinos. If, as the current DANSS Alekseev et al. (2018) and NEOS Ko et al. (2017) experiments may suggest, a sterile neutrino with a mass around 1 eV exists (see e.g., Dentler et al., 2017, 2018; Gariazzo et al., 2017, 2018b), the situation would be significantly different. The allowed bands for $m_{\beta\beta}$ as a function of the lightest neutrino mass when a light sterile neutrino is introduced are reported for example in Giunti and Zavanin (2015) (see also Gariazzo et al., 2016). In this three active plus one sterile neutrino case (3+1), the contribution of the

fourth neutrino mass eigenstate (mainly mixed with the sterile flavor) must be added in Equation (8), with the consequence that the allowed bands are located at higher $m_{\beta\beta}$. In **Figure 7**, adapted from Giunti (2017), we reproduce the dependence of the effective Majorana mass on the lightest neutrino mass when one assumes the 3+1 neutrino scenario, compared with the standard three neutrino case. As we can see, with the introduction of an extra sterile neutrino state, $m_{\beta\beta}$ is significantly increased for the normal ordering case, reaching the level of the inverted ordering bands, which are less shifted toward higher values of $m_{\beta\beta}$. Furthermore, in the 3+1 scenario, also in the inverted ordering case it is possible to have accidental cancellations due to the three independent Majorana phases in Equation (8) (see the detailed discussion of Giunti and Zavanin, 2015), so that a non-detection of the neutrinoless double beta decay process would never be sufficient to rule out the inverted ordering. The opposite situation may occur in case the lightest neutrino mass will be independently constrained to be below $\sim$ 10 meV while $m_{\beta\beta} \lesssim$ 10 meV: in this case, however, we would rule out normal ordering. Consequently, if a light sterile neutrino exists, neutrinoless double beta experiments will never be able to determine the mass ordering if the mass ordering is normal, while some possibility remains if the ordering of the three active neutrino masses is inverted, provided that the lightest neutrino is very light and the Majorana phases are tuned enough. The KamLAND−Zen, Gerda, and CUORE experiments, using three different materials, may very soon start probing the inverted ordering region in the case of 3+1 neutrino mixing for all the possible values of the NMEs, see **Figure 7**, where the current KamLAND−Zen Gando et al. (2016) constraints are reported.

To conclude and summarize the current status: neutrinoless double beta decay cannot yet provide constraints on the neutrino mass ordering. Depending on the lightest neutrino mass and on the existence of a fourth (sterile) neutrino, it would be possible that not even far-future experiments could be able to reach this goal.

4. RESULTS FROM COSMOLOGY

Massive neutrinos affect the cosmological observables in different ways, that we shall summarize in what follows. For a comprehensive review of the effects of neutrino masses in cosmology, we refer the reader to the recent work presented in Lattanzi and Gerbino (2018).

A very important epoch when discussing the impact of massive neutrinos in the cosmological expansion history and in the perturbation evolution is the redshift at which neutrinos become non-relativistic. This redshift is given by

$$1 + z_{\rm nr,i} \simeq 1890 \left(\frac{m_i}{1\,{\rm eV}}\right) , \qquad (9)$$

with m_i referring to the mass of each massive neutrino eigenstate. Current bounds on neutrino masses imply that at least two out of the three massive eigenstates became non-relativistic in the matter dominated period of the universe. As stated in the introductory section, and as we shall further illustrate along this section, cosmological measurements are currently unable to extract individually the masses of the neutrino eigenstates and the ordering of their mass spectrum and, therefore, concerning current cosmological data, all the limits on the neutrino mass ordering will come from the sensitivity to the total neutrino mass $\sum m_\nu$. Consequently, in what follows, we shall mainly concentrate on the effects on the cosmological observables of $\sum m_\nu$, providing additional insights on the sensitivity to the ordering of the individual mass eigenstates whenever relevant.

4.1. CMB

There are several imprints of neutrino masses on the CMB temperature fluctuations pattern once neutrinos become non-relativistic: a shift in the matter-radiation equality redshift or a change in the amount of non-relativistic energy density at late times, both induced by the evolution of the neutrino background, that will, respectively, affect the angular location of the acoustic peaks and the slope of the CMB tail, through the *Late Integrated Sachs Wolfe (ISW) effect*. The former will mostly modify Θ_s, i.e., the angular position of the CMB peaks, which is given by the ratio of the sound horizon and the angular diameter distance, both evaluated at the recombination epoch. Massive neutrinos enhance the Hubble expansion rate, with a consequent reduction of the angular diameter distance and an increase of Θ_s, which would correspond to a shift of the peaks toward larger (smaller) angular scales (multipoles). The latter, the Late ISW effect, is related to the fact that the gravitational potentials are constant in a matter-dominated universe. The inclusion of massive neutrinos will delay the dark energy dominated period and consequently reduce the time variation of the gravitational potential at late times, suppressing the photon temperature anisotropies in the multipole region $2 < \ell < 50$. A very similar effect occurs at early times through the so-called Early ISW effect, which governs the height of the first CMB peak. Light active neutrino species, indeed, reduce the time variations of the gravitational potential also around the recombination period, due to the different evolution of these potentials in radiation/matter dominated epochs, leaving a signature on the CMB photon fluctuations when they become non-relativistic. Massive neutrinos will therefore decrease the temperature anisotropies by $\Delta C_\ell/C_\ell \sim \left(m_{\nu,i}/0.1\ {\rm eV}\right)$ % in the multipole range $20 < \ell < 500$ (Lesgourgues and Pastor, 2012).

Unfortunately, the Late ISW effect affects the CMB spectrum in a region where cosmic variance does not allow for very accurate measurements. From what regards the other two effects, i.e., the shift in the location of the acoustic peaks and the Early ISW effect, they can both easily be compensated varying other parameters which govern the expansion of the universe. For example, within the minimal ΛCDM framework, the total amount of matter in the universe and the Hubble constant H_0 can be tuned in order to compensate the effects of massive neutrinos. Therefore, CMB primary anisotropies alone can not provide very tight bounds on the neutrino masses, due to the strong parameter degeneracies. This automatically implies that CMB measurements alone are unable to extract any information concerning the neutrino mass ordering, as shown in **Figure 8**, obtained by means of the publicly available Boltzmann solver

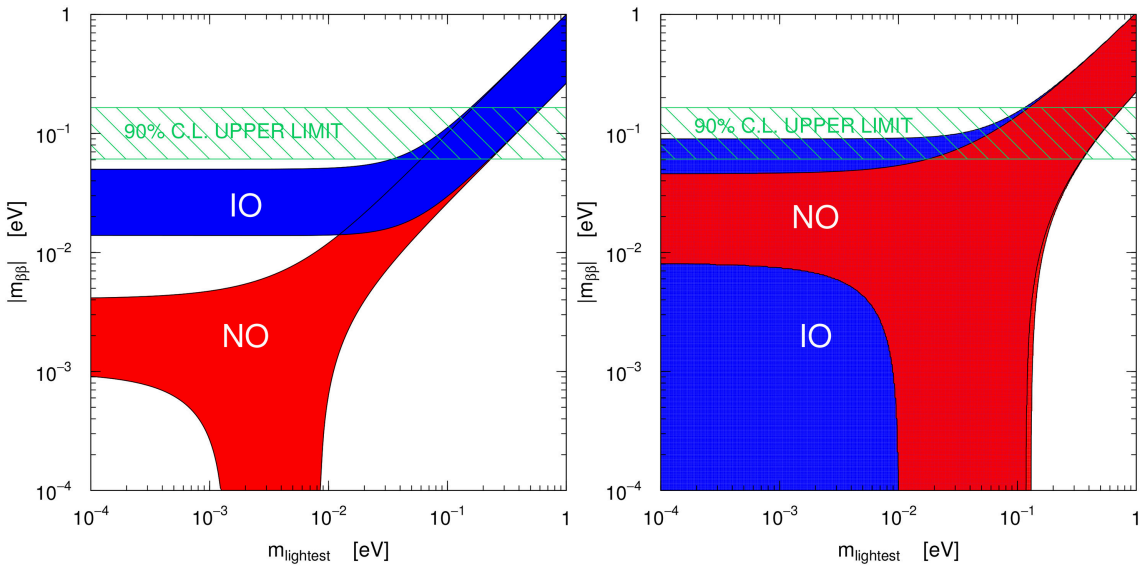

FIGURE 7 | Effective Majorana mass as a function of the lightest neutrino mass in the three neutrino **(Left)** and 3+1 neutrino **(Right)** scenarios, at 99.7% CL, comparing normal (red) and inverted (blue) ordering of the three active neutrinos. Adapted from Giunti (2017). The green band represents the 90% CL bounds from KamLAND-Zen Gando et al. (2016), given the uncertainty on the NME.

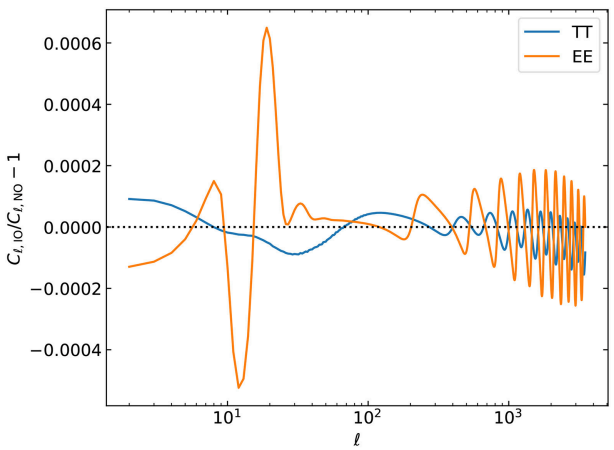

FIGURE 8 | Relative ratio of the temperature and polarization anisotropies for the inverted over the normal mass orderings, see the text for details.

Cosmic Linear Anisotropy Solving System (CLASS) (Blas et al., 2011; Lesgourgues, 2011a,b; Lesgourgues and Tram, 2014). In the figure we can notice that the difference between normal and inverted neutrino mass orderings, for $\sum m_\nu = 0.12$ eV[11] is almost negligible. Moreover, the largest differences appear in the multipole range where cosmic variance dominates.

[11]This is the most constraining 95% CL limit Palanque-Delabrouille et al. (2015) at present, excluding combinations of data sets that are in tension, and we have chosen it as the benchmark value in the following discussions throughout this review.

Among the secondary CMB anisotropies, i.e., those generated along the photon line of sight and not produced at recombination, there are two effects that can notably improve the sensitivity to the total neutrino mass $\sum m_\nu$ from CMB observations. One of them is CMB lensing, that is, a distortion of the photon paths because of the presence of matter inhomogeneities along the line of sight. Due to such distortion, the CMB acoustic oscillation features will be smeared out in a scale-dependent way, mostly due to matter overdensities at $z \lesssim 5$. By measuring the non-gaussianities of CMB polarization and temperature maps it is possible to extract the power spectrum of the lensing potential. This, in turn, contains very useful information on the integrated matter distribution along the line of sight. Since massive neutrinos behave differently from a pure cold dark matter component, characterized by zero velocities, the small-scale structure suppression induced by the non-negligible neutrino dispersion velocities will decrease the CMB lensing signal expected in the absence of neutrino masses (Kaplinghat et al., 2003; Song and Knox, 2004; Lesgourgues et al., 2006; Smith et al., 2006; de Putter et al., 2009; Allison et al., 2015), leaving unchanged the power spectrum of the lensing potential at large scales, and suppressing it at small scales. Furthermore, since CMB lensing involves high redshifts, non-linearities do not enter in the calculation of the matter density field. Therefore, CMB lensing enhances the capabilities to bound the neutrino masses using CMB data. In the future, this technique may even surpass weak lensing capabilities, based on statistical analyses of the ellipticity of remote galaxies, see below and section 6.4. Indeed, nowadays, measurements from the Planck satellite constrain the neutrino masses dominantly through CMB gravitational lensing. As stated in Ade et al. (2014), increasing the neutrino mass implies an increase on the expansion rate at redshifts $z \geq 1$,

corresponding to a suppression of clustering at scales below the size of the horizon at the non-relativistic transition. This effect leads to a decrease in CMB lensing that, at multipoles $\ell = 1,000$, is $\sim 10\%$ for $\sum m_\nu = 0.66$ eV.

On the other hand, we have the reionization process in the late universe, when the first generation of galaxies emitted ultraviolet (UV) photons that ionized the neutral hydrogen, leading to the end of the so-called *dark ages*. Reionization increases the number density of free electrons n_e which can scatter the CMB with a probability given by a quantity named *reionization optical depth*, τ, which can be computed as an integral over the line of sight of n_e. The consequence of an increase of τ on the CMB temperature fluctuations is the suppression of the acoustic peaks by a factor $\exp(-2\tau)$ at scales smaller than the Hubble horizon at the reionization epoch. Even if from the point of view of CMB temperature anisotropies this effect is highly degenerate with a change in the amplitude of the primordial power spectrum A_s, which governs the overall amplitude of the CMB spectra, reionization induces linear polarization on the CMB spectrum, leading to a "reionization bump" in the polarization spectra at large scales, which otherwise would vanish. Even if the reionization signal is rather weak, as it amounts to no more than $\sim 10\%$ of the primary polarization signal (Aghanim et al., 2008), very accurate measurements of the reionization optical depth τ sharpen considerably the CMB neutrino mass bounds (Vagnozzi et al., 2017), as they alleviate the degeneracy between A_s and τ and consequently the existing one between $\sum m_\nu$ and A_s.

4.2. Large Scale Structure of the Universe

The largest effect of neutrino masses on the cosmological observables is imprinted in the matter power spectrum (Bond et al., 1980; Hu et al., 1998). Neutrinos are *hot* dark matter particles and, therefore, due to the pressure gradient, at a given redshift z, the non-relativistic neutrino overdensities can only cluster at scales for which the wavenumber of perturbations is below the neutrino free streaming scale k_{f_s} (i.e., at scales $k < k_{f_s}$), with

$$k_{f_s}(z) = \frac{0.677}{(1+z)^{1/2}} \left(\frac{m_\nu}{1\ \text{eV}}\right) \sqrt{\Omega_m}\, h\ \text{Mpc}^{-1}\,, \qquad (10)$$

being Ω_m the ratio of the total matter energy density over the critical density at redshift zero. The free-streaming nature of the neutrino will be directly translated into a suppression of the growth of matter fluctuations at small scales. One could then conclude that extracting the neutrino relic masses and their ordering is a straightforward task, once that measurements of the matter power spectrum at the relevant scales are available at a different number of redshifts. The former statement is incorrect, not only because it does not consider the existence of degeneracies with the remaining cosmological parameters, but also because a number of subtleties must be taken into account, as we shall explain in what follows. The decrease of the matter power spectrum due to the total neutrino mass $\sum m_\nu$ is, in principle, currently measurable. Nonetheless, when fixing $\sum m_\nu$, the total mass could be splitted differently among the three neutrino mass eigenstates (i.e., m_1, m_2 and m_3), modifying slightly the relativistic to non-relativistic transition. This will affect both the background evolution and the perturbation observables (Lesgourgues et al., 2004): the different free-streaming scales associated to each of the three neutrino mass eigenstates will be imprinted in the matter power spectrum. **Figure 9** shows the ratios of the matter power spectrum for normal over degenerate, inverted over degenerate, and inverted over normal neutrino mass spectra for a total neutrino mass of 0.12 eV. We illustrate such ratios at different redshifts. Notice that the differences among the possible neutrino mass schemes are tiny, saturating at the 0.06% level at $k > 0.2h$ Mpc^{-1}. Therefore, only very futuristic means of measuring the matter power spectrum could be directly sensitive to the neutrino mass ordering, and, eventually, be able to isolate each of the free-streaming scales associated to each individual neutrino mass eigenstate. We shall comment on these future probes in section 6.5.

Since, at present, matter power spectrum data constrain exclusively $\sum m_\nu$, it is only via these bounds, combined with CMB or other external data sets, that nowadays a limit on the neutrino mass ordering can be obtained, see section 4.3. Nevertheless, and as aforementioned, there are a number of problems which may interfere with a proper understanding of the scale-dependent neutrino mass suppression of clustering. The first of them is due to the fact that observations measure the spatial distributions (or their Fourier transforms, the power spectra) of galaxies, clusters, or quasars, e.g., of given tracers, mapping the large scale structure of the Universe at a number of redshifts, by measuring the growth of fluctuations at different scales. However, the matter distribution is not directly measured, i.e., it needs to be inferred from the tracers observed. A simple model of structure formation suggests that at large scales and, therefore, when the perturbation evolution is still in the linear regime, the galaxy power spectrum is related to the matter one by a constant named b, the light-to-mass bias (Desjacques et al., 2018). The galaxy bias can be determined either separately by independent methods or to be considered as an additional free parameter to be measured together with the neutrino mass $\sum m_\nu$. This approach has been followed in many studies in the past (Cuesta et al., 2016; Giusarma et al., 2016; Vagnozzi et al., 2017). However, when dealing with neutrino masses, the relationship between the tracers and the underlying matter field may be more complicated, as neutrinos themselves may induce scale-dependent features in the bias (Castorina et al., 2014; LoVerde and Zaldarriaga, 2014; Muñoz and Dvorkin, 2018) due to their free-streaming nature (see also the recent work of Giusarma et al., 2018 for a new method to extract a scale-dependent bias, based on the cross-correlation of CMB lensing maps and galaxy samples).

Another additional complication when extracting the neutrino mass from clustering observations arises from to the presence of non-linearities at scales $k \gtrsim k^0_{\rm NL} \equiv 0.1 - 0.2\, h\,\text{Mpc}^{-1}$ at $z = 0$. The effect of neutrino masses is very-well understood on linear scales, i.e., scales below $k_{\rm NL}$ at $z = 0$ (or located at slightly larger values of k but at higher redshifts). Massive neutrinos induce a suppression in the linear matter power spectrum below their free streaming scale $\Delta P/P \propto -8 f_\nu$, with f_ν the fraction of matter in the form of massive neutrinos (Hu et al., 1998).

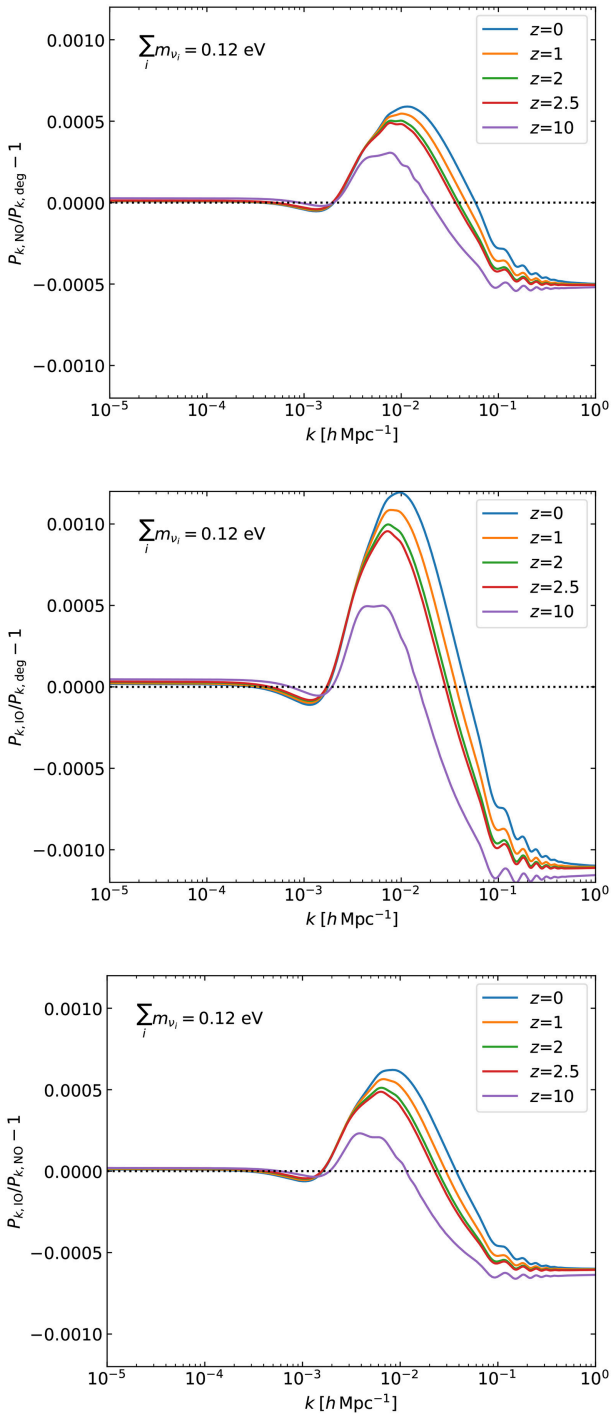

FIGURE 9 | The **Top (Middle)** shows the ratios of the matter power spectrum of normal (inverted) ordering over the degenerate case. The **Bottom** shows the ratio of the matter power spectra for the normal and inverted mass orderings. See the text for details.

Accurate descriptions of the matter power spectrum in the non-linear regime are therefore mandatory in order to be sensitive to the full neutrino mass signature. This is particularly important in the case of galaxy surveys, in which the information depends on the number of independent modes available, and where going to smaller scales (i.e., larger values of k) has a profound impact on the sensitivity to neutrino masses. Several approaches have been followed in the literature to account for the effect of massive neutrinos in the non-linear regime, most of them relying on N-body cosmological simulations, which have been upgraded to include the effects of neutrino clustering in the evolution of the cosmological structures. Methods range from perturbative attempts (Saito et al., 2008; Brandbyge and Hannestad, 2009; Shoji and Komatsu, 2010; Ali-Haimoud and Bird, 2012; Archidiacono and Hannestad, 2016; Upadhye et al., 2016; Dakin et al., 2017; Senatore and Zaldarriaga, 2017) to the fully non-linear inclusion (Villaescusa-Navarro et al., 2014a; Inman et al., 2015; Banerjee and Dalal, 2016; Dakin et al., 2017; Banerjee et al., 2018; Liu et al., 2018) of neutrinos as an extra set of particles. A conservative alternative consists on using exclusively power spectrum measurements within the linear regime (i.e., $k < 0.1\ h\ \mathrm{Mpc}^{-1}$). Some of the cosmological constraints have also been obtained using the mildly non-linear regime ($k < 0.2\ h\ \mathrm{Mpc}^{-1}$) by means of the so-called Halofit formalism (Smith et al., 2003; Takahashi et al., 2012). The Halofit prescription models the non-linear matter power spectrum, and it has been calibrated against a wide range of CDM simulations. It has also been extended for massive neutrino cosmologies (Bird et al., 2012). Other predictions for the non-linear matter power spectrum include the Coyote emulator (Heitmann et al., 2014), which is based on a set of high-accuracy N-body simulations.

However, there is also another avenue to use large scale structure information, the *geometrical* approach, which exploits the so-called Baryon Acoustic Oscillations (BAO) rather than the measurements of the broad-band *shape* of the galaxy power spectrum. The BAO signal appears as a peak in the two-point mass correlation function corresponding to the distance a sound wave can travel in the photon-baryon fluid from very early in the universe until the drag epoch, when the baryon optical depth equals one. The BAO signature provides a standard ruler to measure the distance to various redshifts, and it can be measured either *along the line of sight*, in which the radial distance is inversely proportional to the Hubble expansion rate $H(z)$, or *across the line of sight*, in which case the angular distance is proportional to an integral of $H(z)$, the angular diameter distance $d_A(z)$. To use the BAO method, one must, therefore, extract the acoustic scale from the clustering of some tracer of the baryon distribution (galaxies, quasars). This is typically done statistically using the two-point correlation function of the spatial distribution of tracers, or from its Fourier transform, the power spectrum. From these functions, it is possible to measure two different quantities corresponding to the oscillations parallel and perpendicular to the line of sight, that is $r_s H(z)$ and $d_A(z)/r_s$, with r_s the sound horizon at the drag epoch. Many of the BAO analyses to date have used spherically averaged clustering statistics, measuring an effective distance $D_V \equiv (z d_A(z)^2/H(z))^{\frac{1}{3}}$, which is the volume-averaged distance. Some of the most recent BAO extractions by the Sloan Digital Sky Survey III (SDSS-III) (Eisenstein et al., 2011) Baryon Oscillation Spectroscopic Survey (BOSS) (Dawson et al., 2013)

have achieved, by measuring the clustering of 1.2 million galaxies with redshifts $0.2 < z < 0.75$, 1.8% precision on the radial BAO distance and 1.1% precision on the transverse distance in the $z < 0.75$ redshift region (Beutler et al., 2017b; Ross et al., 2017; Vargas-Magaña et al., 2018). These results improve former determinations from previous data releases of BOSS and SDSS (Eisenstein et al., 2005; Anderson et al., 2013, 2014; Tojeiro et al., 2014; Ross et al., 2015) or other galaxy surveys (Percival et al., 2001; Cole et al., 2005; Beutler et al., 2011; Blake et al., 2011; Kazin et al., 2014), see also the recent works of Bautista et al. (2017b) for a 2.6% measurement of D_V at 2.8σ significance with the extended Baryon Oscillation Spectroscopic Survey (eBOSS) from SDSS−IV Dawson et al. (2016). The Dark Energy Survey (DES) has also achieved a 4.4% accuracy on the measurement of $d_A(z)/r_s$ at $z = 0.81$ Abbott et al. (2017).

Galaxy clustering measurements can also be exploited to constrain, at a number of redshifts, the product of the linear growth rate $f \times \sigma_8$[12], by means of the so-called redshift space distortions, caused by galaxy peculiar velocities, see the recent analyses of Beutler et al. (2017a), Satpathy et al. (2016), and Sanchez et al. (2017).

Apart from the spatial distribution of galaxies, there are also other ways of mapping the large scale structure of the universe at different cosmic times. The Lyman-α forest power spectrum from distant quasars plays a major role for constraining the neutrino masses, as it is sensitive to smaller scales, where the effect of neutrino masses is more pronounced. We refer the reader to the seminal works of Croft et al. (1999), Seljak et al. (2005), Goobar et al. (2006), Seljak et al. (2006), Gratton et al. (2008), Fogli et al. (2008), and Viel et al. (2010). In addition, since the redshifts at which Lyman-α forest probes are sensitive to are higher than those corresponding to galaxy surveys, a fixed scale k will be closer to the linear regime in the Lyman-α case. An additional benefit of going to higher redshifts is that uncertainties related to the evolution of the dark energy fluid will be sub-dominant, as dark energy effects are expected to be more prominent at very low redshifts. However, modeling the neutrino mass effect in the Lyman-α forest power spectrum is highly non-trivial as it may strongly rely on hydrodynamical simulations (Viel et al., 2010). These numerical calculations try to properly account for the late time non-linear evolution of the intergalactic medium (IGM), including reionization processes (Viel et al., 2010; Villaescusa-Navarro et al., 2013). The BAO signature can also be measured in the flux correlation function of the Lyman-α forest of quasars, first detected at a mean redshift $z = 2.3$ in Busca et al. (2013, see also Slosar et al., 2013; Font-Ribera et al., 2014a; Delubac et al., 2015; Bautista et al., 2017a; Bourboux et al., 2017 and Aubourg et al., 2015), in which joint constraints from the BAO signature from galaxies and quasars have been presented.

Galaxy clusters provide yet another test which allows us to trace the clustering of matter perturbations and, therefore, to test the suppression due to the presence of a non-zero $\sum m_\nu$. Galaxy clusters are, by far, the largest virialised objects in the universe, providing a measurement of the so-called cluster number count function dN/dz. This function gives the number of clusters of a certain mass M within a redshift interval (bin) $z + \delta z$ and, for a given survey:

$$\frac{dN}{dz}\Big|_{M>M_{\rm min}} = f_{\rm sky}\frac{dV(z)}{dz}\int_{M_{\rm min}}^{\infty} dM\,\frac{dn}{dM}(M,z)\,. \qquad (11)$$

The quantity $f_{\rm sky} = \Delta\Omega/4\pi$ refers to the fraction of sky covered by the survey and the unit volume is given by

$$\frac{dV(z)}{dz} = \frac{4\pi}{H(z)}\int_0^z dz'\frac{1}{H(z')^2}\,. \qquad (12)$$

While the redshift is relatively easy to measure, the main uncertainty of this method comes from the cluster mass estimates, determined through four main available methods: X-rays, velocity dispersion, Sunyaev-Zeldovich (SZ) effect[13] and weak lensing. The overall error in the cluster mass determination is usually around $\Delta M/M \sim 10\%$. Furthermore, in order to relate the cluster number count function to the underlying cosmological parameters, one needs as an input a mass function $dn(z,M)/dM$ describing the abundance of virialised objects at a given redshift, usually obtained by means of N-body simulations (Tinker et al., 2008; Costanzi et al., 2013). This mass function depends on both the matter mass-energy density and on the standard deviation (computed in linear perturbation theory) of the density perturbations:

$$\sigma^2 = \frac{1}{2\pi^2}\int_0^\infty dk k^2 P(k) W^2(kR)\,, \qquad (13)$$

where $P(k)$ is the matter power spectrum, $W(kR)$ is the top-hat window function, R is the comoving fluctuation size, related to the cluster mass M as $R = (3M/4\pi\rho_m)^{1/3}$, and

$$W(kR) = \frac{3\left(\sin(kR) - (kR)\cos(kR)\right)}{(kR)^3}\,. \qquad (14)$$

There are still some degeneracies in the cosmological parameters probed by cluster surveys, whose results are reported by means of a relationship between the matter clustering amplitude σ_8 (obtained from Equation 13), and the matter mass-energy density Ω_m parameters. More concretely, cluster catalogs measure the so-called cluster normalization condition, $\sigma_8\Omega_m^\gamma$, where $\gamma \sim 0.4$ (Allen et al., 2011; Weinberg et al., 2013). Current cluster catalogs include X ray clusters (see e.g., Hilton et al., 2018; Sohn et al., 2018 and references therein), the optically detected SDSS photometric redMaPPer cluster catalog (Rozo and Rykoff, 2014; Rykoff et al., 2014; Rozo et al., 2015) and the Planck SZ galaxy clusters (PSZ2) Ade et al. (2016a), which contains more than a thousand confirmed clusters. Other SZ cluster catalogs are those detected from the Atacama Cosmology Telescope (ACT) (Hilton et al., 2018) and from the South Pole Telescope (SPT) (de Haan et al., 2016).

[12]Here, σ_8 corresponds to the normalization of the matter power spectrum on scales of $8h^{-1}$ Mpc, see Equation (13).

[13]The thermal SZ thermal effect consists on a spectral distortion on CMB photons which arrive along the line of sight of a cluster.

Last but not least, weak lensing surveys are also an additional probe of the large scale structure effects of massive neutrinos (Cooray, 1999; Abazajian and Dodelson, 2003; Hannestad et al., 2006b; Kitching et al., 2008; De Bernardis et al., 2009; Ichiki et al., 2009; Tereno et al., 2009; Debono et al., 2010; Jimenez et al., 2010). Light rays from distant galaxies are bent by the matter density perturbations between the source galaxies and the observer, thereby inducing distortions in the observed images of the source galaxies (see the reviews Munshi et al., 2008; Kilbinger, 2015). Commonly, the deformations in the source galaxies are rather weak and to extract the lensing signature one needs a correlation among different galaxy images, the so-called shear-correlation functions. By measuring the angular correlation of these distortions, one can probe the clustering statistics of the intervening matter density field along the line of sight, without relying strongly on bias assumptions, setting therefore independent constraints on the neutrino masses. Weak lensing surveys usually report their cosmological constraints in terms of the clustering amplitude σ_8 and the current matter energy density Ω_m. More specifically, they make use of the combination $S \equiv \sigma_8\sqrt{\Omega_m}$ as an accurate description of the amplitude of structure growth in the universe. The most recent weak lensing cosmological analyses profiting of weak lensing data from DES and from the Kilo Degree Survey (KiDS), consisting of ~ 450 deg^2 of imaging data, are presented in Abbott et al. (2018), Hildebrandt et al. (2017),Joudaki et al. (2017), and Köhlinger et al. (2017), respectively.

4.3. Cosmological Bounds on Neutrino Masses and Their Ordering

In the following, we shall review the current cosmological bounds on neutrino masses and on their ordering, firstly in the standard ΛCDM scenario and then when considering extended cosmological models.

4.3.1. Constraints Within the ΛCDM Universe

Focusing on bounds exclusively from the Planck collaboration, making use of their CMB temperature anisotropies measurements in the multipole range $\ell \lesssim 2500$ (Planck TT) and of their low-multipole (up to $\ell = 29$) polarization data, lowP, a bound of $\sum m_\nu < 0.72$ eV at 95% CL Ade et al. (2016b) is reported. When high-multipole (i.e., small scale, $\ell > 30$) polarization measurements are included in the analyses (Planck TT,TE,EE + lowP), the quoted constraint is $\sum m_\nu < 0.49$ eV at 95% CL. As the Planck TT,TE,EE data combination may still have some systematics due to temperature-to-polarization leakage (Ade et al., 2016b), the bounds including these measurements provide the less conservative approach when exploiting CMB data. In 2016, the Planck collaboration presented a series of new results based on a new analysis, in which the modeling and removal of unexplained systematics in the large angular polarization data were accounted for Aghanim et al. (2016b). The value of the optical depth τ found in these refined analyses (using the SimLow likelihood) was smaller than that quoted in previous analyses (Ade et al., 2016b): while the lowP data was providing $\tau = 0.067 \pm 0.022$, the SimLow likelihood results in $\tau = 0.055 \pm 0.009$. The most important consequence of this lower value of τ on the CMB bounds on $\sum m_\nu$ is related to the degeneracy between the amplitude of the primordial power spectrum, A_s, and τ, as already introduced in section 4.1: a lower value of τ will imply a lower value of A_s, thus implying a lower overall normalization of the spectrum, leading therefore to tighter constraints on neutrino masses. The 95% CL limits of $\sum m_\nu < 0.72$ eV and $\sum m_\nu < 0.49$ eV, respectively from the Planck TT + lowP and Planck TT,TE,EE + lowP analyses, are updated to $\sum m_\nu < 0.59$ eV and $\sum m_\nu < 0.34$ eV when using Planck TT + SimLow and Planck TT,TE,EE + SimLow, respectively. These constraints are clearly located away from the region in which a preference for a given mass ordering (normal vs. inverted) may show up. Indeed, the CMB data alone were used by the authors of Gerbino et al. (2017b) which, by means of a novel approach to quantify the neutrino mass ordering, have shown that the odds favoring normal ordering vs. inverted ordering are 1 : 1 and 9 : 8 in the case of the Planck TT + lowP and Planck TT,TE,EE + lowP data combinations, respectively. These results point to an inconclusive strength of evidence, see **Table 2**. Based on a full Bayesian comparison analysis, Gariazzo et al. (2018a) has shown, using Planck TT,TE,EE + lowP measurements together with global neutrino oscillation data, that the Bayes factor for such a combination is $\log(B_{\rm NO,IO}) \simeq 2.5$ for almost all the possible parameterizations and prior choices considered. This valuev of the Bayes factor, which only points to weak preference for normal ordering, is entirely due to neutrino oscillation data, in agreement with the results of Caldwell et al. (2017). Therefore, Planck temperature and polarization measurements alone can not further improve our current knowledge of the neutrino mass ordering from global oscillation data.

The CMB limits on neutrino masses can also include the lensing likelihood, which leads to $\sum m_\nu < 0.59$ eV at 95% CL for the case of Planck TT,TE,EE + lowP + lensing measurements (Ade et al., 2016b). Notice that the bound with the lensing likelihood is less tight than that obtained without the lensing potential extraction ($\sum m_\nu < 0.49$ eV at 95% CL from Planck TT,TE,EE + lowP). The reason is related to the fact that, while the Planck CMB power spectra favor a larger lensing amplitude, the lensing potential reconstructions prefer

TABLE 2 | Jeffreys' scale Jeffreys (1961) for estimating the strength of the preference for one model over the other (adapted from Trotta (2008)) when performing Bayesian model comparison analysis.

$\lvert \ln B_{\rm NO,IO} \rvert$	Odds	Strength of evidence	$N\sigma$ for the mass ordering
< 1.0	$\lesssim 3:1$	inconclusive	$< 1.1\sigma$
$\in [1.0, 2.5]$	$(3-12):1$	weak	$1.1-1.7\sigma$
$\in [2.5, 5.0]$	$(12-150):1$	moderate	$1.7-2.7\sigma$
$\in [5.0, 10]$	$(150-2.2\times10^4):1$	strong	$2.7-4.1\sigma$
$\in [10, 15]$	$(2.2\times10^4-3.3\times10^6):1$	very strong	$4.1-5.1\sigma$
> 15	$> 3.3\times10^6:1$	decisive	$> 5.1\sigma$

The fourth column indicates the approximate correspondence between the quoted Bayes factor levels and the Nσ probabilities computed for a Gaussian variable.

a lower one. Since increasing the neutrino masses reduces the lensing amplitude, the one dimensional posterior distribution of $\sum m_\nu$ arising from the combination of CMB temperature, polarization and lensing data sets shifts the neutrino mass constraints away from zero, so that less posterior volume is found near zero than when constraining $\sum m_\nu$ only with CMB temperature and polarization data.

A significant strengthening on the aforementioned limits can be obtained by means of additional data sets, which help enormously in breaking the degeneracies which are allowed when only CMB data are considered. Among them, the one existing between $\sum m_\nu$ and the Hubble constant H_0 (see e.g Giusarma et al. (2013b)). Large scale structure data from galaxy clustering are of great help in breaking degeneracies. When exploited in the geometrical (BAO) form, the Planck collaboration quotes 95% CL limits of $\sum m_\nu < 0.17$ eV from the combination Planck TT,TE,EE + SimLow + lensing + BAO data Aghanim et al. (2016b)[14]. Concerning the neutrino mass ordering, the addition of BAO measurements to CMB Planck measurements leads to odds for the normal vs. the inverted ordering of 4 : 3 and of 3 : 2, in the case of the Planck TT + lowP + BAO and Planck TT,TE,EE + lowP + BAO respectively, suggesting only very mild evidence for the normal ordering case Gerbino et al. (2017b). These results confirmed the previous findings obtained in Hannestad and Schwetz (2016). The authors of Vagnozzi et al. (2017) reported odds for the normal vs. the inverted ordering of 2.4 : 1 from the combination of Planck TT,TE,EE + BAO plus the SimLow prior on the reionization optical depth, i.e., $\tau = 0.05 \pm 0.009$. Notice that if data are not informative enough, the choice of prior on $m_{\rm lightest}$ will make a difference in the odds ratio[15].

Another possible avenue to exploit galaxy clustering data is to use the information contained in the full-shape of the galaxy power spectrum (see e.g., Allen et al., 2003; Elgaroy and Lahav, 2003; Hannestad, 2003; Spergel et al., 2003; Barger et al., 2004; Crotty et al., 2004; Hannestad and Raffelt, 2004; Tegmark et al., 2004, 2006; Fogli et al., 2007, 2008; Hamann et al., 2007b, 2008, 2010a; de Putter et al., 2012, 2014; Riemer-Sorensen et al., 2012, 2014; Giusarma et al., 2013a, 2016; Zhao et al., 2013; Cuesta et al., 2016; Vagnozzi et al., 2017). Notice however that using BAO is currently a more robust method, as the effects of the galaxy bias and non-linearities are not as severe as in the *shape* approach. In the minimal ΛCDM scenario, the BAO *geometrical* approach can supersede the neutrino mass constraints obtained from the *shape* one (see e.g., Hamann et al., 2010a; Giusarma et al., 2013b). Indeed, a dedicated analysis has been devoted in Vagnozzi et al. (2017) to compare the constraining power of these two different approaches to large scale structure data with the SDSS-III BOSS measurements. The conclusions are that, even if the latest measurements of the galaxy power spectrum map a large volume of our universe, the geometric approach is still more powerful, at least within the minimal ΛCDM + $\sum m_\nu$ cosmology. The better performance of BAO measurements is partly due to the upper cutoff applied in the scale k of the power spectrum when dealing with shape analyses (mandatory to avoid non-linearities), and partly due to the fact that two additional nuisance parameters are further required to relate the galaxy power spectrum to the matter power one[16]. As an example, the 95% CL bound of $\sum m_\nu < 0.118$ eV obtained with Planck TT,TE,EE + BAO plus SimLow is degraded to $\sum m_\nu < 0.177$ eV when replacing part of the BAO data [more concretely, the high redshift BOSS CMASS Data Release 11 (DR11) sample by the full-shape power spectrum measurements from the BOSS CMASS Data Release 12 (DR12)].

An alternative tracer to map out the large scale structure in our universe and improve the CMB-only bounds on the sum of the three active neutrinos is the Lyman-α forest, leading to neutrino mass bounds which turn out to be among the most constraining ones. By means of the one-dimensional Lyman-α forest power spectrum extracted by Palanque-Delabrouille et al. (2013) and combining these measurements with Planck TT,TE,EE + lowP + BAO, the authors of Palanque-Delabrouille et al. (2015) find a 95% CL upper limit of $\sum m_\nu < 0.12$ eV. It is also remarkable the fact that, even without the addition of CMB data, the combination of the Lyman-α forest power spectrum of Palanque-Delabrouille et al. (2013), together with those from the XQ-100 quasars at $z \simeq 3.5 - 4.5$ and the high-resolution HIRES/MIKE spectrographs at $z = 4.2$ and $z = 4.6$ (Viel et al., 2013), is already able to provide a limit of $\sum m_\nu < 0.8$ eV (Yeche et al., 2017), showing clearly the enormous potential of small-scale probes to extract the neutrino masses.

The degeneracies among $\sum m_\nu$ and the other cosmological parameters that appear when considering CMB data only can also be strongly alleviated by the addition of Supernova Ia luminosity distance data and/or local measurements of the Hubble parameter[17]. Concerning Supernovae Ia data, the most complete photometric redshift calibrated sample joins the SuperNova Legacy Survey (SNLS) and SDSS supernova catalogs. This Joint Light-Curve Analysis (JLA) catalog (Betoule et al., 2013, 2014; Mosher et al., 2014) has been used by the Planck collaboration and by other analyses to improve the constraints on $\sum m_\nu$, being its impact particularly crucial in non-minimal cosmologies (Vagnozzi et al., 2018), as we shall explain toward the end of this section. Concerning the value of H_0, as there exists a strong anti-correlation between the Hubble constant and $\sum m_\nu$ when considering CMB measurements, larger mean values of H_0 will lead to tighter constraints on the neutrino mass and consequently on the inverted mass ordering. When performing combined analyses of CMB and H_0 data, the

[14]The BAO measurements exploited by the Planck collaboration include the 6dF Galaxy Survey (6dFGS) Beutler et al. (2011), the BOSS LOWZ BAO extraction of the spherical averaged D_v/r_s (Anderson et al., 2014; Ross et al., 2015) and the BOSS CMASS-DR11 data of Anderson et al. (2014).

[15]See e.g., the work of the authors of Simpson et al. (2017) and the explanation of their results in Schwetz et al. (2017) andGariazzo et al. (2018a). See also Long et al. (2018), Heavens and Sellentin (2018), Handley and Millea (2018) for useful discussions concerning the prior choice on the neutrino mass ordering extraction.

[16]As stated in Vagnozzi et al. (2017), in the future, a deeper understanding of the non-linear regime of the galaxy power spectrum with massive neutrinos included, plus a better understanding of the galaxy bias could change the constraining power of full-shape analyses vs. BAO ones.

[17]See Jackson (2007) and Freedman and Madore (2010) for dedicated reviews concerning the different possible local measurements of H_0. Among them, the one based on Cepheid variables.

2015 Planck release relies on the reanalysis Efstathiou (2014) of a former H_0 measurement based on the Hubble Space Telescope (HST) ($H_0 = (73.8 \pm 2.4)$ km s^{-1} Mpc^{-1};Riess et al., 2011), which was in mild (2.5σ) tension with the value of the Hubble parameter derived from 2013 Planck CMB data Ade et al. (2014). This reanalysis (Efstathiou, 2014) considers the original Cepheid data of Riess et al. (2011) and uses a new geometric maser distance estimate to the active galaxy NGC 4,258 (Humphreys et al., 2013), which is used as a distance anchor to find a value of the Hubble constant $H_0 = (70.6 \pm 3.3)$ km s^{-1} Mpc^{-1}[18]. The limit on the sum of the three active neutrino masses reported by the Planck collaboration using this value of H_0 is $\sum m_\nu < 0.23$ eV at 95% CL, when combined with Planck TT + lowP + lensing + BAO + SNIa data. Other estimates of the Hubble constant, however, exist. The 2.4% determination of Riess et al. (2016) profits from new, near-infrared observations of Cepheid variables, and it provides the value $H_0 = (73.02 \pm 1.79)$ km s^{-1} Mpc^{-1} Riess et al. (2016). As the former mean H_0 value is higher than the one considered by the Planck collaboration, it will lead to tighter limits on $\sum m_\nu$. Indeed, the work of Vagnozzi et al. (2017) quotes the 95% CL bounds of $\sum m_\nu < 0.196$ eV and $\sum m_\nu < 0.132$ eV when combining with external data sets using the priors $H_0 = (70.6 \pm 3.3)$ km s^{-1} Mpc^{-1} and $H_0 = (73.02 \pm 1.79)$ km s^{-1} Mpc^{-1}, respectively. Focusing on the less conservative choice $H_0 = (73.02 \pm 1.79)$ km s^{-1} Mpc^{-1}, odds for the normal vs. the inverted neutrino mass ordering of 3.3 : 1 were found for both the Planck TT,TE,EE + BAO + SimLow + H_0 and the Planck TT,TE,EE + BAO + SimLow + H_0 + Planck SZ data sets (Vagnozzi et al., 2017). The 95% CL upper bounds on the neutrino mass for these two combinations are $\sum m_\nu < 0.094$ eV and $\sum m_\nu < 0.093$ eV, respectively. These results indicate, once again, very mild evidence for the normal mass ordering, even within these more aggressive and less conservative scenarios, in which the very tight limit on $\sum m_\nu$ is mostly due to the tension between CMB and direct measurements of the Hubble constant H_0, together with the strong degeneracy between $\sum m_\nu$ and H_0. Using these results, we stress that having an upper bound $\sum m_\nu \lesssim 0.1$ eV at 95% CL is not equivalent to having a 95% CL preference for normal ordering: the probabilities for normal ordering and inverted ordering, as computed from the odds 3.3 : 1, are approximately 77 and 23% (see also section 5.1).

In general, the combination of data sets that are inconsistent is potentially dangerous. Apart from the constraining effect on the neutrino mass limits when considering a particular prior on the Hubble constant H_0, there have been also other related cases in which the neutrino masses were a tool to accommodate tensions among different data sets. For instance, in the case of galaxy cluster counts, a larger neutrino mass could in principle fit both CMB and low-redshift universe constraints on the power spectrum normalization σ_8 Allen et al. (2003). The effect of combining CMB and BAO observations with clusters and/or shear data is presented in Costanzi et al. (2014), where it is shown that the inclusion of either cluster or shear measurements in the Planck + BAO joint analysis indicates a preference for $\sum m_\nu > 0$ at more than 2σ. However, the authors clearly state that these results can not be interpreted as a claim for a cosmological detection of the neutrino mass, but rather as a remedy to palliate the existing tension between clusters/shear data and Planck/BAO observations.

Finally, weak lensing constraints from the Dark Energy Survey Year 1 results Abbott et al. (2018) (DES Y1), have also recently provided bounds on the sum of the total neutrino mass. Based on 1321 deg^2 imaging data, DES Y1 analyses exploit the galaxy correlation function (from 650.000 luminous red galaxies divided into five redshift bins) and the shear correlation function (from twenty-six million source galaxies from four different redshift bins) as well as the galaxy-shear cross-correlation. The 95% CL upper bound reported on the neutrino mass after combining their measurements with Planck TT,TE,EE + lowP + BAO +JLA is $\sum m_\nu < 0.29$ eV, $\sim$ 20% higher than without DES measurements. The reason for this higher value of $\sum m_\nu$ is that the clustering amplitude in the case of DES Y1 is mildly below the one preferred by Planck measurements. Since larger values of the neutrino mass will decrease the value of the clustering amplitude, the upper limit on the total neutrino mass is loosened by $\sim$ 20% after the DES results are also considered.

4.3.2. Extensions to the Minimal ΛCDM Universe

So far we have discussed the neutrino mass and neutrino mass ordering sensitivities within the minimal ΛCDM universe. However, these limits will change when additional parameters are introduced in the analyses.

The first and most obvious scenario one can consider is to test the stability of the neutrino mass limits when new physics is added in the neutrino sector. As already mentioned in section 3.2, short baseline neutrino experiments indicate that a light sterile neutrino at the eV scale may exist. These extra sterile species will contribute to the effective number of relativistic degrees of freedom, $N_{\rm eff}$, defined by

$$\rho_{\rm rad} = \left(1 + \frac{7}{8}\left(\frac{4}{11}\right)^{4/3} N_{\rm eff}\right)\rho_\gamma \,, \qquad (15)$$

where $\rho_{\rm rad}$ (ρ_γ) is the total radiation (CMB photons) energy density. In the standard picture $N_{\rm eff} = 3.046$ (Mangano et al., 2005; de Salas and Pastor, 2016). This number accounts for the three active neutrino contribution and considers effects related to non-instantaneous neutrino decoupling and QED finite temperature corrections to the plasma evolution[19]. Variations in $N_{\rm eff}$, apart from the light sterile neutrino, may be related to the existence of additional relativistic particles, as thermally-produced axions (see below). Analyses in which both the active neutrino masses and the number of additional massless or

[18]The final result of Efstathiou (2014) is however $H_0 = (72.5 \pm 2.5)$ km s^{-1} Mpc^{-1}, when the combination of the H_0 results obtained with three different distance estimators is performed. The value $H_0 = (70.6 \pm 3.3)$ km s^{-1} Mpc^{-1} is the only one of the three which shows a milder tension with the H_0 estimate from Planck.

[19]The work of de Salas and Pastor (2016), including three-flavor neutrino oscillations, has revisited previous calculations including all the proper collision integrals for both diagonal and off-diagonal elements in the neutrino density matrix and quotes the value of $N_{\rm eff} = 3.045$.

massive species are varied simultaneously have been extensively carried out in the literature (Hamann et al., 2007a, 2010b, 2011; Giusarma et al., 2011, 2013b; Archidiacono et al., 2013a,b; Di Valentino et al., 2013; Riemer-Sorensen et al., 2013), showing that the bounds on the active neutrino mass are relaxed when additional sterile species are added to the fermion content of the SM of particle physics. The constraints on the total neutrino mass $\sum m_\nu$ are less stringent than in the standard three neutrino case due to the large degeneracy between $\sum m_\nu$ and $N_{\rm eff}$, which arises from the fact that a number of massless or sub-eV sterile neutrino species contributing to the radiation content of the universe will shift both the matter-radiation equality era and the location of the CMB acoustic peaks. This effect could be compensated by enlarging the matter content of the universe, implying therefore that larger values for the neutrino masses could be allowed. Consequently, a priori, the constraints on $\sum m_\nu$ when $N_{\rm eff}$ is also a free parameter in the analyses are not very competitive. Fortunately, CMB measurements from the Planck collaboration help enormously in sharpening the measurement of $N_{\rm eff}$, especially when considering polarization measurements at small scales: including data at high multipoles, one obtains $\Delta N_{\rm eff} < 1$ at more than 4σ significance from Planck CMB observations alone. Indeed, the limit on the sum of the three active neutrino species considering also additional radiation neutrino species (i.e., massless sterile neutrino species) is $\sum m_\nu < 0.178$ eV at 95% CL from Planck TT,TE,EE + lowP + BAO data, very similar to the bound $\sum m_\nu < 0.168$ eV at 95% CL arising from the very same dataset within the minimal ΛCDM scenario with three active massive neutrinos. Another possible way of relaxing (or even avoiding) the cosmological neutrino mass limits is via the addition of non-standard interactions in the active neutrino sector (Beacom et al., 2004; Fardon et al., 2004; Afshordi et al., 2005; Hannestad, 2005b; Bell et al., 2006; Brookfield et al., 2006a,b; Bjaelde et al., 2008; Ichiki and Keum, 2008; Mota et al., 2008; Boehm et al., 2012; Archidiacono and Hannestad, 2014; Dvali and Funcke, 2016; Di Valentino et al., 2018b).

Furthermore, additional relics different from sterile neutrinos, as thermal axions (Peccei and Quinn, 1977a,b; Weinberg, 1978; Wilczek, 1978), contributing to both $N_{\rm eff}$ at early times and to the hot dark matter component in the late-time universe, suppress small-scale structure formation and show effects very similar to those induced by the (active) three massive neutrino species. Therefore, the cosmological bounds on the three active neutrino masses are modified in scenarios with thermal axions (see Hannestad et al., 2007, 2008, 2010; Melchiorri et al., 2007; Archidiacono et al., 2013c; Giusarma et al., 2014; Di Valentino et al., 2015, 2016a,b), as these two species have to share the allowed amount of dark matter. Nonetheless, there are non-negligible differences among neutrinos and thermal axions: *(a)* axions are colder than neutrinos, as they decouple earlier; *(b)* since the axion is a scalar particle, an axion mass larger than the neutrino one is required in order to make identical contributions to the current mass-energy density of the universe; *(c)* in the case of axions, the contribution to $N_{\rm eff}$ is related to their mass, while for neutrinos this is usually not true. Consequently, the bounds on the axion mass are always less constraining than for the neutrino, and $\sum m_\nu$ is slightly more constrained in scenarios in which thermal axions are also present. For instance, Di Valentino et al. (2016c) quotes $\sum m_\nu < 0.175$ eV at 95% CL from the Planck TT,TE,EE + lowP + BAO data combinations when considering only neutrinos, while the analyses in Di Valentino et al. (2016b), including massive axions, find $\sum m_\nu < 0.159$ eV and $m_a < 0.763$ eV, both at 95% CL, for the very same data combination.

There are also other ways of relaxing the cosmological neutrino mass bounds, related either to the early or the late-time accelerating periods in the universe. In the former case one can play with inflationary processes. There have been a number of studies devoted to explore their degeneracies with the neutrino sector(see the recent works of Hamann et al., 2007b; Archidiacono et al., 2013b; Joudaki, 2013; de Putter et al., 2014; Canac et al., 2016; Di Valentino et al., 2016a; Gerbino et al., 2017a). The authors of Di Valentino et al. (2016a) have considered a non-standard and parametric form for the primordial power spectrum, parameterized with the PCHIP (piecewise cubic Hermite interpolating polynomial) formalism with twelve nodes between $k_1 = 5 \times 10^{-6}$ Mpc^{-1} and $k_2 = 10$ Mpc^{-1} and derived the neutrino mass constraints within this more general scenario. When only Planck TT + lowP measurements were considered, the 95% CL mass bound of $\sum m_\nu < 0.75$ eV obtained with the usual power-law description of the primordial power spectrum was relaxed to $\sum m_\nu < 2.16$ eV. This large value is explained in terms of the strong degeneracy between $\sum m_\nu$ and the PCHIP nodes corresponding to the wave-numbers where the contribution of the Early ISW effect is located, in such a way that the effect induced by a non-zero neutrino mass is easily compensated by an increase of the primordial power spectrum at these scales only. BAO information improves considerably the limits in the PCHIP prescription, but it is the addition of high-ℓ polarization data what further constrains the effect. The 95% CL upper limit in the PCHIP scenario from the Planck TT,TE,EE + lowP + BAO data combination is $\sum m_\nu < 0.218$ eV, quite close to the bound found when the usual power-law description is applied ($\sum m_\nu < 0.175$ eV). Reference Gerbino et al. (2017a) deals instead with the robustness of the constraints on the scalar spectral index n_s under several neutrino physics scenarios. The authors have explored the shifts induced in the inflationary parameters for different choices of the neutrino mass ordering, comparing the approximate massive neutrino case (one massive eigenstate plus two massless species when the total mass is close to the minimum allowed value by oscillation data, and three degenerate massive neutrinos otherwise) vs. the exact case (normal or inverted mass orderings). While the mass-ordering assumptions are not very significant when $\sum m_\nu$ is fixed to its minimum value, there is a shift in n_s when $\sum m_\nu$ is a free parameter, inherited from the strong degeneracies in the $\sum m_\nu$, H_0 and $\Omega_m h^2$ parameter space. Fortunately, BAO measurements revert the $\sum m_\nu$-n_s anti-correlation present with CMB data only, and the shift in the spectral index turns out to be negligible.

The other possibility is to play with the late-time acceleration period and study how the neutrino mass bounds change. The current accelerated expansion of the universe, explained in terms

of a cosmological constant in the minimal ΛCDM scenario, may be due to a dynamical dark energy fluid with a constant equation of state $w \neq -1$ or a time-dependent $w(z)$ (Chevallier and Polarski, 2001; Linder, 2003), or to quintessence models, based on the existence of a cosmic scalar field (Peebles and Ratra, 1988; Ratra and Peebles, 1988; Wetterich, 1995; Caldwell et al., 1998; Zlatev et al., 1999; Wang et al., 2000), which provide a dynamical alternative to the cosmological constant scenario with $w = -1$. It is naturally expected that the neutrino mass bounds will increase when enlarging the parameter space. Indeed, when the dark energy equation of state is allowed to vary within the phantom region $w < -1$, there is a very well-known degeneracy between the dark energy equation of state w and the sum of the three active neutrino masses, as first noticed in Hannestad (2005a) (see also La Vacca and Kristiansen, 2009; Archidiacono et al., 2013b; Joudaki, 2013; Lorenz et al., 2017; Sutherland, 2018; Vagnozzi et al., 2018)[20]. It has been pointed out that for very high neutrino masses only dark energy models lying within the phantom region will be allowed. The reason for that is the following: a larger $\sum m_\nu$ can be compensated by a larger Ω_m, which in turn can be compensated by a smaller equation of state of the dark energy component, i.e., $w < -1$. Interestingly, the recent work of Vagnozzi et al. (2018) shows that the cosmological bounds on $\sum m_\nu$ become more restrictive in the case of a dynamical dark energy component with $w(z) \geq -1$. Following the usual dynamical dark energy description, whose redshift dependence is described by the standard Chevallier-Polarski-Linder (CPL) parametrization (Chevallier and Polarski, 2001; Linder, 2003), the authors of Vagnozzi et al. (2018) have shown that the combination of `Planck TT,TE,EE` + BAO + `JLA` plus the `SimLow` prior on the reionization optical depth provides, at 95% CL, $\sum m_\nu < 0.11$ eV in the CPL case when restricting $w(z) \geq -1$ (within the physical, non-phantom region), while $\sum m_\nu < 0.13$ eV in the ΛCDM case. When $w(z)$ is also allowed to be in the phantom region ($w(z) < -1$) within the CPL parameterization, the resulting 95% CL constraint on the three active neutrino masses is $\sum m_\nu < 0.37$ eV. These results have a direct impact on the cosmological preference for a given neutrino mass ordering. Following Hannestad and Schwetz (2016) and Vagnozzi et al. (2017), it is found that the normal ordering is mildly preferred over the inverted one, with posterior odds 3 : 1 for the data combination quoted above when $w(z) \geq -1$. On the contrary, if there is no such a restriction and $w(z)$ can also take values in the phantom region, the odds are 1 : 1. The odds in the non-phantom dynamical dark energy case show a mild preference for normal ordering. Therefore, if neutrino oscillation experiments or neutrinoless double beta decay searches find that the neutrino mass ordering is the inverted one, if the current cosmic acceleration is due to a dynamical dark energy component, one would require this component to be phantom.

As a final point in this section, we would like to note that also in scenarios in which the current accelerated expansion is explained by means of modifications of gravity at ultra-large length scales, the cosmological limits on neutrino masses will differ from those in the standard ΛCDM model (see e.g., Huterer and Linder (2007), Baldi et al. (2014), Hu et al. (2015), Shim et al. (2014), Barreira et al. (2014), Bellomo et al. (2017), Peirone et al. (2018), Renk et al. (2017), and Dirian (2017).

5. GLOBAL 2018 DATA ANALYSIS

In this section we shall combine the available measurements that allow us to constrain the neutrino mass ordering, updating the results presented in Gariazzo et al. (2018a).

5.1. Bayesian Model Comparison

Before performing the analysis, we will briefly summarize the method we will adopt to compare the two possible orderings.

We will follow a Bayesian approach to model comparison (see previous work suggesting the Bayesian method as the most suited one for the mass ordering extraction in Qian et al., 2012 and Blennow, 2014)[21], which makes use of the Bayesian evidence Z. This quantity, which is also known as the marginal likelihood, is defined as the integral over the entire parameter space $\Omega_\mathcal{M}$ of the prior $\pi(\theta) \equiv p(\theta|\mathcal{M})$ times the likelihood $\mathcal{L}(\theta) \equiv p(d|\theta, \mathcal{M})$, where θ is the set of parameters that describe the model $\mathcal{M}$ and d represents the available data:

$$Z_\mathcal{M} = \int_{\Omega_\mathcal{M}} \mathcal{L}(\theta)\, \pi(\theta)\, d\theta\,. \tag{16}$$

The posterior probability of the model $\mathcal{M}$ can be written in terms of its prior probability $\pi(\mathcal{M})$ times the Bayesian evidence $Z_\mathcal{M}$:

$$p(\mathcal{M}|d) \propto Z_\mathcal{M}\, \pi(\mathcal{M})\,, \tag{17}$$

where the proportionality constant depends only on the data. In our case we will be interested in comparing normal ordering (NO) and inverted ordering (IO), which can be considered as two different competing models $\mathcal{M}_1 \equiv$ NO and $\mathcal{M}_2 \equiv$ IO. The ratio of the posterior probabilities of the two models can be written as

$$\frac{p(\mathrm{NO}|d)}{p(\mathrm{IO}|d)} = B_{\mathrm{NO,IO}}\, \frac{\pi(\mathrm{NO})}{\pi(\mathrm{IO})}\,, \tag{18}$$

having defined the Bayes factor as

$$B_{\mathrm{NO,IO}} = Z_\mathrm{NO}/Z_\mathrm{IO}\,. \tag{19}$$

Assuming the same prior probabilities for normal and inverted ordering, the Bayes factor is what determines the odds in favor of one of the competing models. In particular we will indicate the results in terms of its natural logarithm $\ln B_{\mathrm{NO,IO}}$, which will be positive when data will prefer normal ordering and negative otherwise. Quantitatively, the preference is given in terms of posterior odds, which are always $|B_{\mathrm{NO,IO}}| : 1$ in favor of the preferred model. The strength of the preference can be

[20]Interacting dark energy models can also change the neutrino mass constraints (see e.g., Gavela et al., 2009; La Vacca et al., 2009; Lopez Honorez and Mena, 2010; Reid et al., 2010; Guo et al., 2018).

[21]We also refer the reader to Blennow et al. (2014), which provides a comprehensive study of the sensitivity reach to the mass ordering in the context of the frequentist approach.

also translated into an empirical scale, which in our case is summarized in the third column of **Table 2**.

Let us briefly discuss the correspondence of the quoted levels that classify the strength of the preference in favor of one of the competing models. In the case of the neutrino mass ordering, we have only two possibilities (normal or inverted), so that $p(\mathrm{NO}|d) + p(\mathrm{IO}|d) = \pi(\mathrm{NO}) + \pi(\mathrm{IO}) = 1$. If we assign the same prior probability to the two cases, $\pi(\mathrm{NO}) = \pi(\mathrm{IO}) = 1/2$, it is easy to compute the posterior probability for each of the two cases, which will be

$$p(\mathrm{NO}|d) = B_{\mathrm{NO,IO}}/(B_{\mathrm{NO,IO}} + 1)\,, \tag{20}$$

$$p(\mathrm{IO}|d) = 1/(B_{\mathrm{NO,IO}} + 1)\,, \tag{21}$$

having used Equations (18, 19). The confidence levels for the rejection of the disfavored (e.g., inverted) mass ordering will then be $x = 100 \times (1 - |B_{\mathrm{NO,IO}}|^{-1})\,\%$. For example, a Bayes factor $B_{\mathrm{NO,IO}} = 10$ corresponds to a rejection of the inverted ordering at 90% CL. If, instead, we want to reproduce the probability levels $P = \mathrm{erf}(\mathrm{N}/\sqrt{2})$ that are usually associated to the classical $N\sigma$ levels for a Gaussian measurement, being erf the error function and considering, for example, $N \in (1, 2, 3, 4, 5)$, the corresponding Bayes factors B can be computed to be $B = P/(1 - P)$, which gives us $\ln B_{N\sigma} \simeq 0.77, 3, 5.9, 9.7, 14.37$. Therefore, our "strong", "very strong" and "decisive" levels roughly correspond to the $> 3\sigma$, $> 4\sigma$ and $> 5\sigma$ probabilities, as indicated in the fourth column of **Table 2**.

5.2. Parameterization and Data

Our two competing models are described by the same number of parameters, listed with their priors in **Table 3**: the three neutrino mixing angles ($\sin^2\theta_{12}$, $\sin^2\theta_{13}$, $\sin^2\theta_{23}$), the CP violating phase δ_{CP} and the parameters associated with neutrino masses, neutrinoless double beta decay ($0\nu\beta\beta$) and cosmology, as we shall describe now.

We consider in our analysis the parameterization that uses the two mass splittings (Δm^2_{21} and Δm^2_{31}) and the lightest neutrino mass m_{lightest} with logarithmic priors. This parameterization, strongly motivated by the physical observables, was shown to provide the optimal strategy to successfully explore the neutrino parameter space (see Gariazzo et al., 2018a)[22]. Within the other possible choice, that is, within the parametrization that uses the three neutrino masses as free parameters, most of the parameter space at high neutrino masses is useless for the data fit. Therefore, this second possibility is penalized by the Occam's razor and we shall not explore it here.

The neutrino mixing parameters are constrained using the same data we described in section 2. The complete oscillation data set is indicated with the label "OSC" in the following.

For the cosmological part, we will describe the universe using the ΛCDM model and its six parameters: the baryon and cold dark matter densities, $\Omega_b h^2$ and $\Omega_c h^2$; the optical depth to reionization, τ; the angular scale of the acoustic peaks through Θ_s and the amplitude $\log(10^{10}A_s)$ and tilt n_s of the power spectrum of initial curvature perturbations. In addition, we add the effect of the three massive neutrinos computing the evolution of the cosmological observables assuming three independent mass eigenstates, which, in terms of the parameters involved in our analyses, read as $m_1 = m_{\mathrm{lightest}}$ $\left(m_1 = \sqrt{m^2_{\mathrm{lightest}} + |\Delta m^2_{31}|}\right)$, $m_2 = \sqrt{m^2_{\mathrm{lightest}} + \Delta m^2_{21}}$ $\left(m_2 = \sqrt{m^2_{\mathrm{lightest}} + |\Delta m^2_{31}| + \Delta m^2_{21}}\right)$ and $m_3 = \sqrt{m^2_{\mathrm{lightest}} + \Delta m^2_{31}}$ $\left(m_3 = m_{\mathrm{lightest}}\right)$ for normal (inverted) neutrino mass orderings.

When considering cosmological data, we will focus on the `Planck` measurements of the CMB spectrum and on the most recent results from BAO observations. For the former we consider the 2015 `Planck` release (Adam et al., 2016; Ade et al., 2016b) of the high-ℓ likelihood (Aghanim et al., 2016a), together with a prior on τ as obtained in the 2016 intermediate results (Aghanim et al., 2016b). For the purposes of our analyses, this will be sufficient to mimic the final `Planck` release which is expected within the next few months. Complementary to the CMB, we include in our calculations the final constraints from the `SDSS BOSS` experiment, the `DR12` release, in the form denoted as "final consensus" Alam et al. (2017), which provides constraints from observing 1.2 million massive galaxies in three separate bands at effective redshifts 0.38, 0.51, and 0.61, plus results from the `6DF` survey at $z = 0.106$ (Beutler et al., 2011) and from the `SDSS DR7 MGS` survey at $z = 0.15$ (Ross et al., 2015). The combined dataset including the mentioned CMB and BAO data will be denoted as "Cosmo."

In addition, we shall impose a prior on the Hubble parameter as obtained in the recent results from Riess et al. (2016): $H_0 = (73.24 \pm 1.74)\,\mathrm{km\,s^{-1}\,Mpc^{-1}}$. We will denote the data combinations including this prior with the label "H_0."

Finally, concerning neutrinoless double beta decay, we vary the two Majorana phases in the entire available range (0–2π) and the NMEs according to the range allowed by recent theoretical calculations. We revised the NME ranges adopted in Gariazzo et al. (2018a), which were the ones suggested in Giuliani and Poves (2012). Here we use these new ranges: [3.3 – 5.7] for ^{76}Ge and [1.5 – 3.7] for ^{136}Xe, following the 1σ range proposed in Vergados et al. (2016).

We use $0\nu\beta\beta$ data from the ^{136}Xe experiments `KamLAND-Zen` Gando et al. (2016) and `EXO-200` Albert et al. (2014) and from the ^{76}Ge experiment `Gerda`, for which we use the results in Agostini et al. (2017b), since the latest publication Agostini et al. (2018) does not contain enough information that allows us to parameterize a likelihood function. The most stringent bounds, anyways, still come from `KamLAND-Zen`, so that not including the new `Gerda` results does not affect significantly our results. For the very same reason we do not include the results of `CUORE` Alduino et al. (2018a), for which the uncertainty on the NME of ^{130}Te is very large and the constraints corresponding to most of the values of $\mathcal{M}^{0\nu}_{^{130}\mathrm{Te}}$ are much looser than the ones from `KamLAND-Zen`, and of `CUPID-0` Azzolini et al. (2018), which establishes a much less

[22] As we are making use of logarithmic priors here, we shall not report the upper limits we obtain on the sum of the neutrino masses, as they will be much smaller than the usually quoted results due to the volume effects associated with the use of the logarithmic prior, that naturally leads to a preference for small neutrino masses.

TABLE 3 | Neutrino, cosmological and $0\nu\beta\beta$ parameters used in the analysis, with the adopted priors.

Neutrino mixing and masses		Cosmological		$0\nu\beta\beta$	
Parameter	**Prior**	**Parameter**	**Prior**	**Parameter**	**Prior**
$\sin^2\theta_{12}$	0.1 – 0.6	$\Omega_b h^2$	0.019 – 0.025	α_2	$0 - 2\pi$
$\sin^2\theta_{13}$	0.00 – 0.06	$\Omega_c h^2$	0.095 – 0.145	α_3	$0 - 2\pi$
$\sin^2\theta_{23}$	0.25 – 0.75	Θ_S	1.03 – 1.05	$\mathcal{M}^{0\nu}_{^{76}\mathrm{Ge}}$	3.3 – 5.7
δ_{CP}/π	0 –2	τ	0.01 – 0.4	$\mathcal{M}^{0\nu}_{^{136}\mathrm{Xe}}$	1.5 – 3.7
$\Delta m^2_{21}/\mathrm{eV}^2$	$5\times10^{-5} - 10^{-4}$	n_S	0.885 – 1.04		
$\Delta m^2_{31}/\mathrm{eV}^2$	$1.5\times10^{-3} - 3.5\times10^{-3}$	$\log(10^{10}A_S)$	2.5 – 3.7		
$\log_{10}(m_{\mathrm{lightest}}/\mathrm{eV})$	−5 – 0				

All the priors are linear in the corresponding quantity.

stringent limit on the ^{82}Se half-life. The complete neutrinoless double beta set of data will be denoted as "$0\nu\beta\beta$."

All the previously listed data are coded as likelihood terms in a full Bayesian analysis. We compute the cosmological quantities using the Boltzmann solver `CAMB` Lewis et al. (2000), the likelihoods using the interface provided by `CosmoMC` Lewis and Bridle (2002), modified in order to take into account the oscillation and neutrinoless double beta decay data, while the calculation of the Bayesian evidence is committed to `PolyChord` Handley et al. (2015a,b).

5.3. Constraints on the Mass Orderings

The main results are depicted in **Figure 10**. The first data point corresponds to the Bayesian evidence from oscillation data only. Notice that the Bayes factor [$\ln(B_{\mathrm{NO,IO}}) = 6.5 \pm 0.2$ for concreteness] indicates *strong* evidence for the normal mass ordering *from oscillation data only*. This Bayes factor is translated into a $\sim 3.2\sigma$ evidence favoring normal mass ordering. This result was expected in light of the results presented in section 2, arising from the frequentist joint analysis. There it was reported a $\Delta\chi^2 = 11.7$ in favor of the normal mass ordering from the combination of all long baseline, reactor and atmospheric data, which corresponds, roughly, to $\sim 3.4\sigma$. Adding information from neutrinoless double beta decay searches does not affect the Bayesian analysis, as shown by the second data point in **Figure 10**, and as expected from previous work Gariazzo et al. (2018a).

Once CMB and BAO measurements are also added in the Bayesian analysis, $\ln(B_{\mathrm{NO,IO}}) = 7.4 \pm 0.3$ is obtained (see the third point in **Figure 10**), improving the significance of the preference for normal ordering from $\sim 3.2\sigma$ to $\sim 3.4\sigma$. Notice that, even if the preference for the normal neutrino mass ordering is mostly driven by oscillation data, the information provided by cosmological observations is more powerful than that in the analysis carried out in Gariazzo et al. (2018a), as the Bayesian analyses here also include BAO measurements, together with CMB data. Indeed, from the two Bayes factors obtained considering oscillation data only [$\ln(B_{\mathrm{NO,IO}}) = 6.5 \pm 0.2$] and oscillation plus cosmological measurements [$\ln(B_{\mathrm{NO,IO}}) = 7.4 \pm 0.3$], it is straightforward to infer the probability odds for normal ordering arising exclusively from cosmology. By doing so, one obtains odds of 2.7 : 1 for the normal ordering against the inverted one, in perfect agreement with the analyses of Vagnozzi et al. (2017), where odds of 2.4 : 1 with cosmological data only were reported when considering the very same data sets adopted here (albeit the odds were derived with an alternative method).

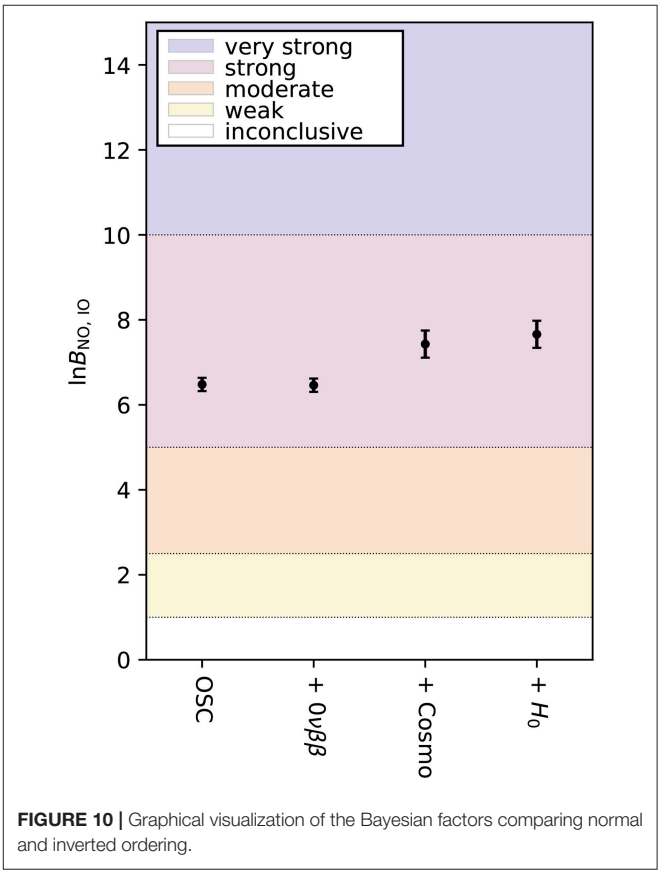

FIGURE 10 | Graphical visualization of the Bayesian factors comparing normal and inverted ordering.

Finally, the addition of the prior on the Hubble constant raises the evidence for the normal ordering to $\ln(B_{\mathrm{NO,IO}}) = 7.7 \pm 0.3$ (i.e., $\sim 3.5\sigma$). This improvement is expected, as previously explained in section 4, since a prior on the Hubble constant breaks the degeneracy between $\sum m_\nu$ and H_0 and, therefore, sharpens the neutrino mass bounds from cosmology. By performing a similar exercise to the one previously quoted,

one finds that the odds for normal vs. inverted ordering from cosmology data only are 3.3 : 1 for the combination of CMB, BAO plus the H_0 prior, again in excellent agreement with the results obtained in Vagnozzi et al. (2017).

6. FUTURE PROSPECTS

In this last section, we will explore the future prospects for the detection of the neutrino mass ordering. Let us clarify that many of the proposed methods are much less robust than the ones involving neutrino oscillations through matter (see section 6.1), and will likely give their first results much after the first experimental 5σ determinations which are likely to be reached in the next $5-10$ years. Many of the discussed methods, indeed, will give constraints on the neutrino mass ordering only as a secondary product of their operation and not as a main result, hence they are not optimized nor mainly focused on the mass ordering determination. Nevertheless, it is interesting to discuss these additional methods for different reasons. First of all, independent tests of the neutrino mass ordering from different methods are surely welcome to have more robust results. Secondly, the different methods can provide complementary information: if some inconsistencies or anomalies will appear, we will have new hints for our quest toward new physics beyond our current knowledge. In conclusion, even if the question regarding the neutrino mass ordering will be solved within the next few years by the currently running experiments or their immediate extensions, its study through the other methods we discuss here will be useful to shed more light on the topic and provide more interesting information on neutrino physics and beyond. This is why we do not focus only on neutrino oscillation experiments (section 6.1), which will probably provide the first and strongest results, but also on more exotic cases as determinations from decay experiments (sections 6.2 and 6.3) cosmological constraints (section 6.4), measurements from the 21 cm surveys (section 6.5), and probes which involve neutrinos emitted by core-collapse supernova explosions (section 6.6) or relic neutrinos from the early Universe (section 6.7).

6.1. Prospects From Oscillations

As we have seen in section 2, the combination of all current neutrino experiments leads to a preference for normal ordering of 3.4σ, within the context of the latest frequentists global data analyses. The Bayesian analysis described in the previous section confirms these results, as we have reported a 3.2σ evidence for normal mass ordering. In principle, one may expect to achieve further sensitivity on the neutrino mass ordering from more precise data by the current long-baseline and atmospheric neutrino experiments, since these experiments will still run for some time before the new experiments will take over. However, it is not easy to predict the final results of current experiments, since the sensitivity to the mass ordering is highly correlated to the true value of the CP phase $\delta_{\rm CP}$. The NOνA experiment alone expects a 3σ sensitivity for 30–50% of the values of $\delta_{\rm CP}$ by 2,024 Himmel (2018). If $\delta_{\rm CP} = 3\pi/2$, the expected sensitivity would be higher than that and, then, a very strong result could be obtained by 2,024 Himmel (2018). Note, however, that the NOνA sensitivity analysis considers a fixed value of θ_{13} and does not marginalize over Δm^2_{31}. Upgrading T2K to T2K-II will improve the sensitivity substantially, since the experiment should gather around 20×10^{21} POT by 2026, which would be roughly 6 times the current amount of data[23]. Combining beam data from T2K with atmospheric data from SK can improve the sensitivity even further, as shown in Abe et al. (2018a). Performing a combined fit of T2K, NOνA and eventually SK could bring the sensitivity to the 5σ level within a few years. In any case, apart from the combinations of different experiments, a very robust determination of the neutrino mass ordering from a single current experiment seems rather unlikely. Indeed, one of the main goals of the next-generation neutrino oscillation experiments, including new long-baseline, reactor, and atmospheric neutrino detectors, will be to perform the determination of the mass ordering by a single experiment. The upcoming facilities will be able to measure the neutrino mass ordering with astonishing precision. In this section we briefly discuss some of the proposed projects and their physics potential.

Long-Baseline Experiments

The Deep Underground Neutrino Experiment (DUNE) (Acciarri et al., 2015, 2016a,b; Strait et al., 2016) will be a new long-baseline accelerator experiment, with a small near detector and a huge far detector with a fiducial mass of 40 kton located 1,300 km away from the neutrino source at Fermilab. With its powerful 1.1 MW beam, it will be exposed to around 15×10^{20} POTs (protons on target) per year, which will lead to a huge number of events and therefore to high precision measurements of the neutrino oscillation parameters. As explained in section 2, the presence of matter affects differently the neutrino appearance probabilities for normal and inverted mass orderings. DUNE, with the longest baseline ever for an accelerator neutrino experiment, will be able to measure the neutrino mass ordering with a significance above 5σ for any set of the oscillation parameters $(\theta_{23}, \delta_{\rm CP})$ after 7 years of data taking. Note that this sensitivity could be further increased by using an improved energy reconstruction method, as shown in De Romeri et al. (2016). On the other hand, the sensitivities could also be biased by the potential presence of new physics beyond the SM, such as non-standard neutrino interactions (Miranda et al., 2006; Coloma, 2016; Coloma and Schwetz, 2016; de Gouvêa and Kelly, 2016; Forero and Huber, 2016; Masud and Mehta, 2016; Bakhti and Khan, 2017; Coloma et al., 2017; Deepthi et al., 2017; Forero and Huang, 2017; Farzan and Tortola, 2018), deviations from unitarity Blennow et al. (2017); Dutta et al. (2017); Escrihuela et al. (2017) or the presence of light-sterile neutrinos (Berryman et al., 2015, 2016; Agarwalla et al., 2016; Coloma et al., 2018). Indeed, besides providing very precise information about the neutrino oscillation mechanism, the DUNE experiment will also be very useful to test different models for neutrino masses and mixings (Chatterjee et al., 2017a,b; Pasquini et al., 2017; Agarwalla et al., 2018b; Chakraborty et al., 2018; Srivastava et al., 2018a,b) as well as to check for various effects of new physics such as the

[23] We are not aware of any study showing the T2K or SK expectations to the mass ordering in the next few years.

ones mentioned above, neutrino decay scenarios (Coloma and Peres, 2017; Ascencio-Sosa et al., 2018; Choubey et al., 2018c), quantum decoherence Balieiro Gomes et al. (2018) or even CPT invariance (de Gouvêa and Kelly, 2017; Barenboim et al., 2018b,c) and Lorentz invariance (Barenboim et al., 2018a; Jurkovich et al., 2018).

There are also plans to build a larger version of the Super–Kamiokande detector, Hyper–Kamiokande Abe et al. (2018b), that will be very similar to its predecessor but with a fiducial mass of 560 kton, 25 times larger than Super–Kamiokande. The Hyper–Kamiokande detector will be a requirement for the upgrade of T2K, the T2HK (Tokai-to-Hyper-Kamiokande) experiment (Abe et al., 2015). The very massive detector together with the upgraded neutrino beam from J-PARC will guarantee a huge number of neutrino events and therefore larger statistics. As a consequence, T2HK will be able to determine the neutrino mass ordering after few years of running time with very high significance, as well as to explore new physics scenarios (see for instance Abe et al., 2017, 2018b; Agarwalla et al., 2018a). In combination with atmospheric data from Hyper–Kamiokande, a 3σ rejection of the wrong mass ordering would be expected after 5 years of data taking. A third project has been proposed as an extension of T2HK to Korea, the T2HKK (Tokai-to-Hyper-Kamiokande-and-Korea) experiment (Abe et al., 2018c). This proposal includes a second far detector facility for the J-PARC neutrino beam, located at 1,000–1,300 km from the source. The longer path traveled within the Earth by the neutrinos detected in T2HKK will result in an enhanced sensitivity to the neutrino mass ordering if compared to T2HK alone.

The synergies and complementarities among the three long-baseline proposals above, DUNE, T2HK and T2HKK, have been discussed in Ballett et al. (2017). It is found that the combination of their experimental results may significantly mitigate the limitations of a given experiment, improving the precision in both the determination of the mass ordering and the measurement of CP violation.

Note that, although here we have focused on the long-baseline side of DUNE and Hyper–Kamiokande, they are actually designed as multi-purpose experiments, with a rich physics program aiming to study the neutrino oscillations with accelerator, atmospheric and solar neutrinos as well as to detect neutrinos from astrophysical sources and proton decay.

Atmospheric Experiments

In atmospheric neutrino experiments, the sensitivity to the mass ordering comes from the matter effects that distort the pattern of neutrino oscillations inside Earth, see Equation (4). Based on the oscillatory pattern that depends on the reconstructed neutrino energy and zenith angle, an ideal experiment would observe a given number of events in each energy and zenith angle bin as shown in **Figure 11**. Comparing the observed two-dimensional histograms with the theoretical ones for normal **(Left)** or inverted ordering **(Right)** allows to determine the true mass ordering that is realized in nature. In the following we list some of the future projects with this aim.

The Oscillation Research with Cosmics in the Abyss (ORCA) experiment Adrian-Martinez et al. (2016) will be a large neutrino telescope placed deep inside the Mediterranean sea. It will detect the Cherenkov light emitted by the muons and electrons created by the interactions of atmospheric neutrinos in the sea and that propagate into water. Unlike its precursor, ANTARES, with 12 lines and a separation of 70 meters between neighboring optical modules, ORCA will have 60 lines with modules separated by 9 m. Due to the matter effects on the propagation of atmospheric neutrinos, the ORCA experiment will be able to measure the neutrino mass ordering with very good precision. In particular, a 3σ determination of the mass ordering can be expected after only 3 years of data taking, with even higher significance for the case in which nature has chosen normal ordering and the upper octant for the atmospheric mixing angle. Several studies have been performed in order to analyze the sensitivity of ORCA to the standard oscillation parameters (Ribordy and Smirnov, 2013; Yañez and Kouchner, 2015). Its potential to determine the Earth matter density through neutrino oscillation tomography Winter (2016) or to test new physics scenarios (Ge et al., 2017; Capozzi et al., 2018b) have also been extensively discussed.

PINGU (Precision IceCube Next Generation Upgrade) (Aartsen and Adelaide, 2014) is a planned upgrade of the IceCube DeepCore detector, an ice-Cherenkov neutrino telescope which uses the antarctic ice as a detection medium. The IceCube design aims at the detection of very high energy neutrinos, with an energy threshold above the relevant energy range for neutrino oscillations. However, the denser instrumented region DeepCore allows IceCube to decrease its energy threshold down to $E_{\rm th} = 6.3$ GeV. A further improvement with an even denser zone, PINGU, could lower $E_{\rm th}$ to only a few GeV. With this very low-energy threshold, one of the main purposes of PINGU is the determination of the neutrino mass ordering, with expected sensitivities similar to the ORCA experiment[24]. Besides that, PINGU is expected to have the best sensitivity to ν_τ appearance and to determine accurately the octant of the atmospheric mixing angle. The PINGU capabilities to detect high-energy supernova neutrinos (Murase, 2018), and to investigate scenarios beyond the Standard Model, such as non-standard interactions (Choubey and Ohlsson, 2014) or dark matter self-interactions (Chen et al., 2014; Robertson and Albuquerque, 2018) have been also analyzed in the literature.

The India-based Neutrino Observatory (INO) is a very ambitious project, aiming to detect atmospheric neutrinos with a 50 kton magnetized iron calorimeter (ICAL) (Ahmed et al., 2017). The most outstanding feature of the INO experiment will be its capability to distinguish neutrinos from antineutrinos in an event by event basis. As a result, the identification of the matter effects in the neutrino and antineutrino propagation will be much cleaner in comparison with the sea water/ice Cherenkov detectors. Indeed, one of the main scientific goals of INO will be the determination of the neutrino mass ordering (Ghosh

[24]The effect of statistic and systematic uncertainties on the PINGU sensitivity to the mass ordering has been presented in Capozzi et al. (2015).

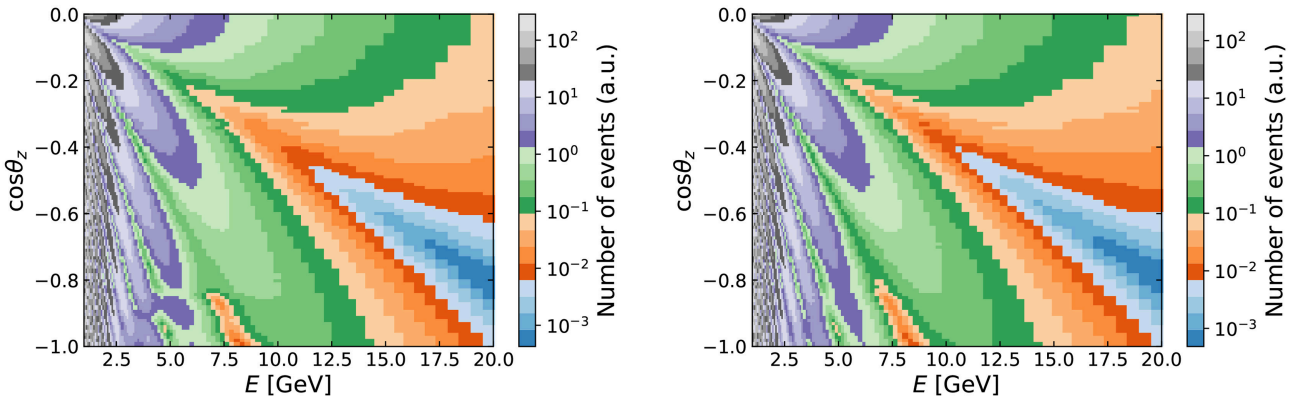

FIGURE 11 | Expected number of events (arbitrary units) for an hypothetical atmospheric neutrino detector with perfect energy resolution as a function of the reconstructed neutrino energy E and the cosine of the zenith angle $\cos\theta_Z$, for normal **(Left)** and inverted **(Right)** ordering.

et al., 2013). According to the Physics White Paper of the ICAL (INO) Collaboration Ahmed et al. (2017), after 10 years run, INO will be able to identify the correct neutrino mass ordering with a significance larger than 3σ. As the experiments discussed above, the atmospheric neutrino results from INO can also be used to test the presence of new physics beyond the SM, such as CPT- or Lorentz violation (Chatterjee et al., 2014), sterile neutrinos (Behera et al., 2017; Thakore et al., 2018), dark matter related studies Dash et al. (2016); Choubey et al. (2018a), non-standard neutrino interactions Choubey et al. (2015) or decaying neutrinos (Choubey et al., 2018b).

Medium-Baseline Reactor Experiments

We have focused so far on extracting the neutrino mass ordering from matter effects in the neutrino propagation through the Earth interior. An alternative technique is that provided by medium-baseline reactor neutrino experiments Petcov and Piai (2002). For baselines of the order of 50 km, the survival probability for reactor antineutrinos exhibits a pattern that may allow the discrimination between normal and inverted mass orderings. Indeed, for such distances, the electron antineutrino survival probability is given by the following expression:

$$\begin{aligned} P_{\bar{\nu}_e \to \bar{\nu}_e} \;=\; & 1 - \cos^4\theta_{13}\sin^2 2\theta_{12}\sin^2\Delta_{21} \\ & - \sin^2 2\theta_{13}\left[\sin^2\Delta_{31} + \sin^2\theta_{12}\sin^2\Delta_{21}\cos 2\Delta_{31}\right. \\ & \left. \mp \frac{\sin^2\theta_{12}}{2}\sin 2\Delta_{21}\sin 2|\Delta_{31}|\right], \end{aligned} \tag{22}$$

where $\Delta_{ij} = \frac{\Delta m^2_{ij} L}{4E}$ and the minus (plus) sign in the last term corresponds to normal (inverted) mass ordering. This probability contains a main oscillatory term with a frequency given by the solar neutrino mass splitting Δm^2_{21}, plus an additional term whose frequency depends on the sign of the atmospheric splitting Δm^2_{31}, i.e., on the neutrino mass ordering. The effect of the ordering over the neutrino survival probability in a medium-baseline reactor experiment is illustrated in **Figure 12**. There, we depict in black the oscillatory term corresponding to the solar splitting frequency. The red (blue) line corresponds to the full neutrino survival probability for normal (inverted) mass ordering. Note that this plot was obtained using the best-fit values from **Table 1** for each ordering.

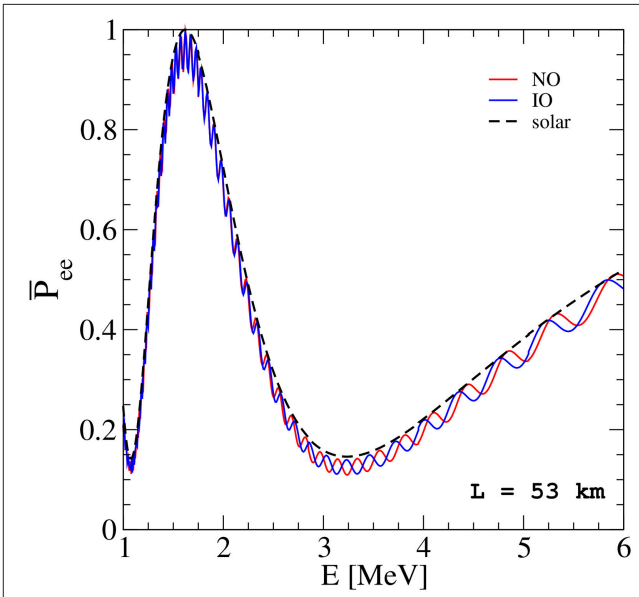

FIGURE 12 | Electron antineutrino survival probabilities in a medium-baseline reactor experiment with $L = 53$ km. The red (blue) line corresponds to normal (inverted) mass ordering using the best-fit values from **Table 2**, while the black line contains the main term in the survival probability, given by the solar mass splitting frequency by setting $\Delta m^2_{31} = 0$.

The Jiangmen Underground Neutrino Observatory (JUNO) An et al. (2016) is a 20 kton multi-purpose underground liquid scintillator detector. The site of the experiment, located 53 km away from the Yangjiang and Taishan nuclear power plants in China, was chosen to optimize its sensitivity to the neutrino mass ordering, one of its main physics goals. Like any other reactor neutrino experiment, JUNO will be sensitive to the disappearance of electron antineutrinos, with about 10^5 events

expected after 6 years of run time. From this high-statistics data sample, JUNO will try to reconstruct with extremely good precision the neutrino oscillation spectrum and to discriminate the different high-frequency behavior for normal and inverted mass ordering, as illustrated in Equation (22) and **Figure 12**. For a projected energy resolution of 3% at 1 MeV, JUNO will be able to establish the neutrino mass ordering at the level of 3-4σ in 6 years. Its combination with the PINGU facility could lead to a high significance improvement of the individual capabilities of these two experiments (see Blennow and Schwetz, 2013).

Apart from the mass ordering, JUNO will also provide precision measurements of the solar oscillation parameters, θ_{12} and Δm^2_{21}, with an accuracy of around 1%. In this sense, JUNO might help to solve the observed disagreement between the mass splitting measured at solar experiments and at the reactor experiment KamLAND. If the discrepancy persists after new measurements by JUNO and future solar results by Super-Kamiokande, it could be considered as an indication of new physics Farzan and Tortola (2018). Moreover, JUNO will be sensitive to different types of new physics scenarios beyond the SM, as studied in Khan et al. (2013), Bakhti and Farzan (2014), Girardi et al. (2014), Li and Zhao (2014), Ohlsson et al. (2014), Abrahão et al. (2015), Liao et al. (2017), Zhao et al. (2017), and Krnjaic et al. (2018) .

In parallel to JUNO, there is a proposal to extend the already existing experiment RENO with a third medium-baseline detector located at a distance of 47 km. This new project is known as RENO-50 Kim (2015), given its location, at approximately 50 km from the Hanbit power plant, in South Korea. The detector would consist of a 18 kton ultra-low-radioactive liquid scintillator instrumented with 15,000 high quantum efficiency photomultiplier tubes. Using the same technique described above, RENO-50 will be able to determine the neutrino mass ordering as well as the solar oscillation parameters with extremely good precision. Conceived as multi-purpose detectors, JUNO and RENO-50 will have a wide physics program, including not only the observation of reactor and solar neutrinos, but also neutrinos from supernova bursts, the diffuse supernova neutrino background, atmospheric neutrinos and geoneutrinos.

6.2. Prospects From Beta-Decay Experiments

As already mentioned in section 3, the determination of the mass ordering through the observation of the energy spectrum near the endpoint of β-decay or similar will be extremely challenging, because an impressive energy resolution is required to distinguish the kink due to the second and third mass eigenstates in the spectrum. We list here the main projects that aim at detecting the neutrino mass in the future and comment their perspectives for the mass ordering determination.

The first experiment we will comment on is KATRIN, which has recently started operations and aims at a detection of the effective electron antineutrino mass with a sensitivity of 0.2 eV (Angrik et al., 2004; Sejersen Riis et al., 2011). The first results from KATRIN are expected in early 2019, but the final target statistics will be reached after 3 year of data taking. Thanks to the detailed study of the detector systematics which has been carried out, it is possible that the final mass determination will reach a better sensitivity than the nominal one of 0.2 eV, eventually reaching something closer to 0.1 eV (Parno, 2018). Even with the more optimistic sensitivity, however, it will be impossible for KATRIN to determine the mass ordering.

Other tritium experiments exploiting different technologies include the Project-8 (Doe et al., 2013; Asner et al., 2015; Esfahani et al., 2017) experiment, which will use the Cyclotron Radiation Emission Spectroscopy (CRES) in order to determine the mass of the electron antineutrino. The technique consists in measuring the frequency of cyclotron radiation emitted by the electrons released during tritium decay and spiraling into a magnetic field. The frequency can then be related with the electron energy and consequently the energy spectrum can be determined. At the moment, Project-8 is in the calibration phase (phase-II) (Rybka, 2018) for a small prototype which will not have enough sensitivity to be competitive in the determination of the neutrino mass. Next phases include a large volume system using molecular tritium (phase-III), starting in 2020, which will be competitive in determining the neutrino mass and will serve as an intermediate step before moving to phase-IV, which will use atomic tritium, required in order to avoid uncertainties related to the existence of excited molecular tritium states. Project-8 in its atomic tritium phase is expected to reach the sensitivity $m_{\bar{\nu}_e} \lesssim 40$ meV with an exposure of $10 - 100$ m^3 year, sufficient to probe the values of $m_{\bar{\nu}_e}$ allowed in the context of inverted ordering (Esfahani et al., 2017), so that in case of no observation we will know that the ordering of neutrino masses must be normal.

Another interesting class of the experiments includes the HOLMES (Alpert et al., 2015; Giachero et al., 2017) and ECHo (Eliseev et al., 2015) experiments, which both aim at the determination of the electron neutrino mass through observations of the endpoint of the electron capture decay of ^{163}Ho, which practically proceeds through the measurement of de-excitation transitions of the Dy atoms, which are produced in the process $^{163}\mathrm{Ho} + e^- \rightarrow {}^{163}\mathrm{Dy}^* + \nu_e$ (De Rujula and Lusignoli, 1982). As for the tritium β-decay, also the endpoint of the ^{163}Ho electron capture spectrum depends on the value of the neutrino masses and, in principle, it would be possible to determine the mass ordering in this way. Besides the experimental and theoretical problems that the HOLMES and ECHo collaborations must face, however, it seems that the current technology is not yet at the level of precision required for the mass ordering determination. The HOLMES demonstrator, currently running, should reach a sensitivity of $m_{\nu_e} \lesssim 10$ eV by the end of 2018, while the full-scale experiment, possibly starting in 2019, has a target sensitivity of $m_{\nu_e} \lesssim 1$ eV (Gastaldo, 2018). ECHo, on the other hand, is running a first phase (ECHo-1k) which has also a target of $m_{\nu_e} \lesssim 10$ eV in 1 year, while the full scale ECHo-100k will reach $m_{\nu_e} \lesssim 1.5$ eV in 3 year of data taking, expected to start in 2019 (Gastaldo, 2018). Both results are impressive when compared with the current upper limit on the electron neutrino mass using the same isotope, which is 225 eV (Springer et al., 1987), more than two orders of magnitude larger.

Finally, to conclude this subsection we want to mention that the PTOLEMY proposal (Betts et al., 2013; Baracchini et al., 2018), aiming at the detection of the relic neutrino background and recently approved by the Scientific Committee of the Laboratori Nazionali del Gran Sasso (LNGS), will be able to study and possibly determine the mass ordering through the observation of the β-spectrum of tritium decay. PTOLEMY will be discussed later in section 6.7.

6.3. Prospects From Neutrinoless Double Beta Decay

We list here the future perspectives for neutrinoless double beta decay experiments in terms of sensitivity to the half-life for the processes of interest (where possible). As we already commented in section 3.2, the conversion between the half-life $T^{0\nu}_{1/2}$ and the effective Majorana mass $m_{\beta\beta}$ depends on the NME and the phase space factor of the process of interest, see Equation (7). In order to exclude the inverted ordering allowed range for $m_{\beta\beta}$ (in case there is no sterile neutrino), one would need to constrain $m_{\beta\beta} \lesssim$ 10 meV, which corresponds to $T^{0\nu}_{1/2} \simeq 1 \times 10^{28}$ year, with some dependence on the material (phase space and NME). This means that none of the current generation experiments will be able to reach the required sensitivity, and we will have to wait for next-generation upgrades and new projects. Many of the information listed in the following has been taken from Agostini et al. (2017a) and Giuliani (2018).

Current Generation Experiments

Let us firstly address the current generation of experiments, which at most will be able to start exploring the three-neutrino inverted mass ordering regime or to probe the upper range for $m_{\beta\beta}$ allowed within the 3+1 neutrino scenario. The experiments will be listed in alphabetical order.

AMoRE Alenkov et al. (2015) is an experiment devoted to determine the life-time of ^{100}Mo. After a first pilot run, the current status (AMoRE-I) is to test the technology with a ^{100}Mo mass of 5-6 kg, in order to demonstrate the scalability before moving to the full scale (AMoRE-II) detector, which will use 200 kg of material and is expected to start around 2020, with a final target sensitivity of $T^{0\nu}_{1/2} \simeq 5 \times 10^{26}$ year.

CUORE Artusa et al. (2015) and Alduino et al. (2016, 2018b), already mentioned in section 3.2, works with ^{130}Te and is already taking data with the full scale detector, which will have as ultimate sensitivity $T^{0\nu}_{1/2} \simeq 9 \times 10^{25}$ year after 5 year of data taking (Adams et al., 2018; Ouellet, 2018).

The KamLAND-Zen experiment (Gando et al., 2016; Gando, 2018), after the previous successful data taking period, is now upgrading the detector for a new observation run with approximately 750 kg of ^{136}Xe and a new balloon inside the KamLAND detector. The target sensitivity for the upcoming phase is around $T^{0\nu}_{1/2} \simeq 5 \times 10^{26}$ year, a factor of five larger than the current limit (Gando et al., 2016).

A smaller experiment is NEXT (Martín-Albo et al., 2016), which is running background studies in the Canfranc laboratories in Spain. NEXT will use high pressure ^{136}Xe TPCs, which will allow an impressive tracking of the emitted particles through scintillation and electroluminescence. A prototype with 10 kg of natural Xenon will start data taking this year to demonstrate that the expected background control and particle tracking have been achieved. In 2019 NEXT is expected to start a new phase with 100 kg of ^{136}Xe, which will reach $T^{0\nu}_{1/2} \simeq 1 \times 10^{26}$ year with 5 year of data.

A similar project is called Panda-X-III (Chen et al., 2017), which is based in the Jinping underground laboratories in China. Panda-X-III will run the first phase using 200 kg of ^{136}Xe to reach $T^{0\nu}_{1/2} \simeq 1 \times 10^{26}$ year in 3 year.

Going to a different concept, SNO+ (Andringa et al., 2016) will feature a detector of 760 ton of ultra-pure liquid scintillator. SNO+ will be a multipurpose detector, as it will be capable of studying reactor, solar, supernova and geoneutrinos, and also to probe proton decay (Orebi Gann, 2018). After the background studies will be completed, a 0.5% loading will be performed, inserting ^{130}Te in the detector to measure double beta decay processes. The target sensitivity after 5 year is $T^{0\nu}_{1/2} \simeq 2 \times 10^{26}$ year. Future plans for the SNO+ experiment include the further ^{130}Te loading to 1%, or even more, of the detector mass, with the advantage that increasing the ^{130}Te amount will not influence the backgrounds but only the signal. The final target for this second phase is to reach $T^{0\nu}_{1/2} \simeq 1 \times 10^{27}$ year, thus starting to cover the inverted ordering allowed range.

Let us finally comment the SuperNEMO experiment (Arnold et al., 2010; Patrick and Xie, 2017), which uses ^{82}Se for its study. SuperNEMO is particularly interesting because it will be able to perform a full topological reconstruction of the events, which is extremely important in case of detection because it opens the possibility to directly test the mechanism that underlies neutrinoless double beta decay and, in principle, to determine the lepton-number violating process. A first demonstrator of about 7 kg is expected to start in 2018 and to reach $T^{0\nu}_{1/2} \simeq 6 \times 10^{24}$ year with 2.5 year of data. The subsequent plans include an extension with a $\sim$ 100 kg scale detector with 20 modules, which will be able to probe $T^{0\nu}_{1/2}$ up to 1×10^{26} year, and the possibility to use the ^{150}Nd isotope, for two reasons: to have a more favorable phase space when converting $T^{0\nu}_{1/2}$ to $m_{\beta\beta}$ and to get rid of the Rn background which affects the ^{82}Se measurements (Giuliani, 2018).

As a summary, some of the current generation experiments will be able to probe the inverted ordering range of $m_{\beta\beta}$ within the standard three neutrino framework and assuming an exchange of light Majorana neutrinos. However, none of them will be able to rule out completely the inverted mass ordering, because of the uncertainty related to the NMEs.

Next Generation Experiments

The situation will be different for the following generation of experiments, which are mostly the natural evolution of current experiments to the ton-scale of decaying material. With the increased amount of material, a larger statistics will be achieved and stronger bounds, of the order of $T^{0\nu}_{1/2} \simeq 1 \times 10^{28}$ year, will be feasible. We briefly discuss here the main current proposals for the next 10–20 years. The time schedules for these projects will be necessarily vague, as they will depend on the results of the present ones.

Let us start with CUPID (CUORE Upgrade with Particle ID) (Wang et al., 2015; Azzolini et al., 2018), which will be the evolution of the previously discussed CUORE experiment. The goal of CUPID is to use particle tracking in order to have a better discrimination of background and ultimately allow a background-free experiment: the target is < 0.1 counts/(ton year) (Ouellet, 2018). A first demonstrator, named CUPID-0 (Azzolini et al., 2018), is already running with about 5 kg of ^{82}Se, and already obtained the strongest-to-date constraint on the life-time on this isotope. In order to reach the target sensitivity $T^{0\nu}_{1/2} \gtrsim 1 \times 10^{27}$ year, however, further improvement in the crystals quality and radio-purity is required. A full development plan for CUPID is currently under discussion.

Although not specifically designed for neutrinoless double beta decay searches, the DARWIN (DARk matter WImp search with liquid xenoN) experiment (Aalbers et al., 2016) will have sensitivity to a number of rare decay phenomena. The primary target of DARWIN is to perform direct detection of dark matter in a wide mass-range of the experimentally accessible parameter space for Weakly Interacting Massive Particles (WIMPs), to the level at which neutrino interactions with the target become an irreducible background (the so-called neutrino floor). The core of the detector will be a multi-ton liquid xenon time projection chamber. Having a large mass, low-energy threshold and ultra-low background level, DARWIN will also search for solar axions or galactic axion-like particles, measure the low-energy solar neutrino flux with $< 1\%$ precision, observe coherent neutrino-nucleus interactions, detect galactic supernovae neutrinos and study the double beta decay of ^{136}Xe (Aalbers et al., 2016). Even if it will be build using natural Xenon without isotope enrichment, DARWIN will contain 3.5 t of ^{136}Xe. If the target energy resolution of $1-2\%$ at 2.5 MeV will be achieved, the sensitivity of DARWIN will be $T^{0\nu}_{1/2} \simeq 5.6 \times 10^{26}$ year with an exposure of 30 t yr (Aalbers et al., 2016). The estimated ultimate sensitivity, which will be achieved only with a complete mitigation of the material background and 140 t year of exposure, is claimed to be $T^{0\nu}_{1/2} \simeq 8.5 \times 10^{27}$ year (Aalbers et al., 2016).

The successor of KamLAND-Zen, KamLAND2-Zen (Shirai, 2017; Gando, 2018; Giuliani, 2018) will benefit the upgrades of KamLAND into KamLAND2, including the improved light collection and better energy resolution guaranteed by the new photomultipliers, together with an increased amount of ^{136}Xe, to reach at least 1 ton of material. These upgrades will be performed after the completion of KamLAND-Zen 800, expected to start this year. The target sensitivity after 5 year will be $m_{\beta\beta} \lesssim 20$ meV[25], sufficient for "fully covering the inverted ordering region" (Shirai, 2017). Future studies will also test the possibility to accommodate scintillating crystals inside the detector and run a multi-isotope experiment.

Back to ^{76}Ge-based experiments, the efforts of the Gerda and Majorana collaborations will join to work on the LEGEND (Large Enriched Germanium Experiment for Neutrinoless Double beta decay) experiment. Learning from both its precursors, LEGEND will need further background rejection and will be built in different phases. The first module, LEGEND-200, made of 200 kg of Germanium and expected to start in 2021, will be built on top of the existing Gerda infrastructures and will have a target sensitivity $T^{0\nu}_{1/2} \simeq 1 \times 10^{27}$ year in 5 year. The full scale detector, LEGEND-1000, consisting in several modules summing up to a total of 1 ton of material, will have as an ultimate goal $T^{0\nu}_{1/2} \simeq 1 \times 10^{28}$ year in 10 year (Abgrall et al., 2017), giving a full coverage of the inverted mass ordering region.

Even larger in size, nEXO (Albert et al., 2018; Kharusi et al., 2018) will replace the EXO-200 experiment after its completion, expected this year. The new detector will use 5 ton of Xenon in order to reach $T^{0\nu}_{1/2} \simeq 1 \times 10^{27}$ year with just 1 year of data and $T^{0\nu}_{1/2} \simeq 1 \times 10^{28}$ year with the full statistics, after 10 year.

After the completion of the upcoming phase, NEXT-100 will be possibly upgraded into NEXT 2.0, which will need a 1.5 ton of Xenon to obtain the statistics for achieving $T^{0\nu}_{1/2} \simeq 1 \times 10^{27}$ year after 5 year of running (Agostini et al., 2017a; Giuliani, 2018).

In the same way, the Panda-X-III collaboration is also planning a 1 ton scale phase II with a target of $T^{0\nu}_{1/2} \simeq 1 \times 10^{27}$ year (Chen et al., 2017).

The last comment regards another interesting possibility related to the SNO+ experiment. The THEIA proposal (Orebi Gann, 2015) is a concept study for a gigantic detector of something around 30–100 kton of target material which will use water-based liquid scintillator. Such target allows to track both Cherenkov and delayed scintillation light, thus enabling high light yield and low-threshold detection with attenuation close to that of pure water. The result is that such a detector would be able to achieve excellent background rejection thanks to directionality, event topology, and particle ID, with very large statistics. Loading of metallic ions which can undergo neutrinoless double beta decay would enable to use the THEIA detector for studying the Dirac/Majorana nature of neutrinos. Given the size of the detector, a 0.5% loading will allow to store several tons of decaying material, which naturally result in huge statistics when compared with current experiments. A 3% loading with natural (not enriched) Tellurium will be sufficient to reach, assuming $m_{\beta\beta} \simeq 15$ meV, a 3σ discovery in 10 year (Alonso et al., 2014; Giuliani, 2018).

6.4. Prospects From Cosmology

There are a number of studies in the literature focused on forecasting the expected sensitivity from both future CMB and large scale structure surveys to the total neutrino mass $\sum m_\nu$ (de Putter et al., 2009; Abazajian et al., 2011; Carbone et al., 2011, 2012; Hamann et al., 2012; Basse et al., 2014; Font-Ribera et al., 2014b; Allison et al., 2015; Archidiacono et al., 2017; Amendola et al., 2018; Di Valentino et al., 2018a; Sprenger et al., 2018).

Awaiting for very futuristic measurements which may allow for the extraction of each of the individual masses associated to the neutrino mass eigenstates (see section 4), the extraction of the neutrino mass ordering strongly relies on the error achieved on $\sum m_\nu$ for a chosen *fiducial* value of the neutrino mass.

[25]The collaboration does not report the sensitivity in terms of the half-life of the decay.

A complete, updated and useful summary is provided in Table II of (Lattanzi and Gerbino, 2018), which shows the expected sensitivity $[\sigma(\sum m_\nu)]$ from different future cosmological probes, assuming the fiducial value $\sum m_\nu = 0.06$ eV. Nevertheless, the authors of Gerbino et al. (2017b) considered different fiducial values for the total neutrino mass and computed the odds for the normal vs. the inverted ordering for possible combinations of future cosmological probes including the current information from oscillation experiments. We shall comment on these results toward the end of this section.

6.4.1. CMB Prospects

Two main missions are expected to lead the next decade generation of CMB experiments, albeit a number of other experiments are in progress between now and then. The latter list includes ground-based observatories as the ACT (Atacama Cosmology Telescope) (De Bernardis et al., 2016), the SPT-3G (South Pole Telescope-3G) (Benson et al., 2014), the Simons Array (Suzuki et al., 2016), CLASS (Essinger-Hileman et al., 2014), BICEP3 (Ahmed et al., 2014), and the Simons Observatory[26]. The two main missions are expected to be the CMB-Stage IV project (Abazajian et al., 2016) and CORE (Cosmic Origin Explorer) (Delabrouille et al., 2018). The former, the CMB-Stage IV project (Abazajian et al., 2016), expected to be *the definitive ground-based CMB experiment*, aims at 250000 detectors operating for 4 years, covering a 40% fraction of the sky. Depending on the beam size and on the effective noise temperature, CMB Stage IV could reach sensitivities of $\sigma(\sum m_\nu) = 0.073 - 0.11$ eV, assuming $\sum m_\nu = 0.058$ eV as the fiducial model and an external prior on the reionization optical depth of $\tau = 0.06 \pm 0.01$, see (Abazajian et al., 2016) for the precise configuration details. The latter, CORE, a medium-size space mission proposed to the European Space Agency (ESA) (Delabrouille et al., 2018), is expected to have an one order of magnitude larger number of frequency channels and a twice better angular resolution than Planck. With these improved capabilities, CORE could achieve a sensitivity of $\sigma(\sum m_\nu) = 0.044$ eV (Di Valentino et al., 2018a; Lattanzi and Gerbino, 2018), for a fiducial total neutrino mass of 0.06 eV. As it is evident from these estimates, future CMB experiments alone will not be able to determine the neutrino mass ordering.

6.4.2. Large Scale Structure Prospects

From the large scale structure perspective, in analogy to the future CMB probes, there are also two main surveys, DESI (Dark Energy Spectroscopic Instrument) (Levi et al., 2013; Aghamousa et al., 2016), a ground-based telescope which will improve the SDSS-III and IV legacies (BOSS Dawson et al., 2013 and eBOSS galaxy surveys Dawson et al., 2016), and the Euclid space mission (Amendola et al., 2018). The baseline design of DESI assumes that it will run over 5 years, covering 14000 deg^2 of the sky targeting four different tracers: Bright, Luminous Red and Emission Line Galaxies plus quasars in the redshift interval ($0.05 < z < 1.85$), and a Lyman-α survey in the $1.9 < z < 4$ redshift interval. The expected error in $\sum m_\nu$ from DESI and Planck data is 0.02 eV. This number corresponds, approximately, to a 2σ determination of the neutrino mass ordering in case neutrinos have the minimal mass within the normal ordering scenario (Aghamousa et al., 2016). The authors of (Font-Ribera et al., 2014b) have also explored a number of possible combinations of DESI with other surveys. Namely, combining DESI measurements with the final results from DES, an error of 0.017 eV in $\sum m_\nu$ could be achieved. Their most constraining result, $\sigma(\sum m_\nu) = 0.011$ eV, however, arises from an extension of the DESI survey, together with data from Euclid and LSST (Large Synoptic Survey Telescope) (Ivezic et al., 2008; Abell et al., 2009) (see below). In case this small error is achieved, the neutrino mass ordering can be determined with a high accuracy, again assuming a massless lightest neutrino and normal ordering. Other analyses have also reduced the nominal $\sigma(\sum m_\nu) = 0.02$ eV expected from the DESI survey replacing the Planck CMB information with that expected from the future CMB Stage IV (Abazajian et al., 2016) or CORE (Di Valentino et al., 2018a) probes.

Euclid, an ESA mission expected to be launched early in the upcoming decade, mapping $\sim 15,000$ deg^2 of the sky, has also been shown to provide excellent capabilities to test the neutrino properties (Amendola et al., 2018). Euclid will focus on both galaxy clustering and weak lensing measurements, which, combined with Planck CMB data, will provide errors on the sum of the neutrino masses of $\sigma(\sum m_\nu) = 0.04$ eV (Carbone et al., 2011) and $\sigma(\sum m_\nu) = 0.05$ eV (Kitching et al., 2008), respectively, albeit exploiting the mildly non-linear regime could highly reduce these errors (Audren et al., 2013). While these errors are large to extract useful information concerning the neutrino mass ordering, the weak gravitational lensing abilities from Euclid have also been considered to extract the neutrino mass ordering when it lies far enough from the degenerate region (see e.g., Amendola et al., 2018). The addition of future CMB measurements, as those from CORE, could notably improve the expected Euclid sensitivity. The authors of Archidiacono et al. (2017) have shown that CMB measurements from CORE, combined with full shape measurements of the galaxy power spectrum and weak lensing data from Euclid, could reach $\sigma(\sum m_\nu) = 0.014$ eV. This result clearly states the complementarity of cosmic shear and galaxy clustering probes, crucial to test the neutrino mass ordering. Further improved measurements of the reionization optical depth τ could strengthen this bound and consequently the sensitivity to the ordering of the neutrino masses (Liu et al., 2016; Archidiacono et al., 2017; Sprenger et al., 2018), see the following section. Other future large scale structure surveys are the aforementioned LSST and WFIRST (Spergel et al., 2013, 2015), that will lead as well to accurate measurements of the total neutrino mass. Their combination with e.g., Euclid could provide an error of a few meV on the total neutrino mass, $\sigma(\sum m_\nu) \lesssim 0.008$ eV (Jain et al., 2015).

[26] For a detailed study on the prospects from pre- and post-2020 CMB experiments on the extraction of cosmological parameters, including the total neutrino mass $\sum m_\nu$, see also (Errard et al., 2016).

The above neutrino mass (neutrino mass ordering) projected errors (sensitivities), even if strongly constraining, are highly dependent on the fiducial value of $\sum m_\nu$, in the sense that the majority of the forecasts *(a)* are usually carried out assuming the minimal neutrino mass allowed within the normal ordering scheme, i.e., $\sum m_\nu \simeq 0.06$ eV[27]; *(b)* the quoted sensitivities in the neutrino mass ordering are computed via an extrapolation of the error on the sum of neutrino masses rather than from proper Bayesian comparison tools. The authors of Gerbino et al. (2017b) found that a future CMB CORE-like satellite mission, even combined with a 1% measurement of the Hubble constant H_0 and with the future DESI survey (Font-Ribera et al., 2014b; Aghamousa et al., 2016) can not extract the ordering if nature has chosen a value for the neutrino masses of $\sum m_\nu = 0.1$ eV. Odds for the normal vs. the inverted ordering of 1 : 1 were reported (Gerbino et al., 2017b). When considering the minimum allowed value for the total neutrino mass set by neutrino oscillation experiments, i.e., $\sum m_\nu = 0.06$ eV, they quote odds of 3 : 2 (9 : 1) for the case in which CORE and the prior on H_0 without (with) DESI measurements are considered[28]. Therefore, the next generation of CMB and large scale structure surveys will be sensitive to the mass ordering only if it is normal and the lightest neutrino mass is close to zero. The significance of such a measurement will crucially depend on how far $\sum m_\nu$ lies from its minimum allowed value from oscillation probes.

6.5. Prospects From 21 cm Surveys

Cosmological measurements of the redshifted 21 cm hydrogen line provide a unique test of the Epoch of Reionization (EoR) and the "dark ages," the period before the first stars formed. The 21 cm line is due to spin-flip transitions in neutral hydrogen between the more energetic triplet state and the ground singlet state, and its intensity depends on the ratio of the populations of these two neutral hydrogen hyperfine levels. At a given observed frequency ν, the 21 cm signal can be measured in emission or in absorption against the CMB. The so-called differential brightness temperature δT_b therefore refers to the contrast between the temperature of the hydrogen clouds and that of the CMB, which, for small frequencies and up to first order in perturbation theory, reads as Madau et al. (1997); Furlanetto et al. (2006); Pritchard and Loeb (2012); Furlanetto (2015)

$$\delta T_b(\nu) \simeq 27\, x_{\rm HI}\,(1+\delta_b)\left(1-\frac{T_{\rm CMB}}{T_S}\right)\left(\frac{1}{1+H^{-1}\partial v_r/\partial r}\right) \left(\frac{1+z}{10}\right)^{1/2}\left(\frac{0.15}{\Omega_m h^2}\right)^{1/2}\left(\frac{\Omega_b h^2}{0.023}\right) {\rm mK}\,, \qquad (23)$$

where $x_{\rm HI}$ is the fraction of neutral hydrogen, δ_b is the baryon overdensity, $\Omega_b h^2$ and $\Omega_m h^2$ the present baryon and matter contributions to the mass-energy budget of the Universe, $H(z)$ the Hubble parameter and $\partial v_r/\partial r$ the comoving peculiar velocity gradient along the line of sight. Therefore, 21 cm cosmology aims to trace the baryon overdensities via transitions in neutral hydrogen.

There are a number of current and future experimental setups devoted to detect the 21 cm global signal averaged over all directions in the sky, as EDGES (Experiment to Detect the Reionization Step) (Bowman and Rogers, 2010), the future LEDA (Large Aperture Experiment to Detect the Dark Ages) (Greenhill and Bernardi, 2012) or DARE (Moon space observatory Dark Ages Radio Experiment) (Burns et al., 2012). The EDGES experiment has quoted the observation of an absorption profile located at a frequency of 78 ± 1 MHz, corresponding to a redshift of $z \sim 17$, with an amplitude of about a factor of two larger than the maximum expected in the canonical ΛCDM framework (Bowman et al., 2018). This recent claim has led to a number of studies aiming either to explain the effect or to constrain some non-standard scenarios (Barkana, 2018; Barkana et al., 2018; Berlin et al., 2018; Cheung et al., 2018; Clark et al., 2018; Costa et al., 2018; D'Amico et al., 2018; Ewall-Wice et al., 2018; Falkowski and Petraki, 2018; Feng and Holder, 2018; Fialkov et al., 2018; Fraser et al., 2018; Hektor et al., 2018; Hill and Baxter, 2018; Hirano and Bromm, 2018; Kang, 2018; Liu and Slatyer, 2018; Mahdawi and Farrar, 2018; McGaugh, 2018; Mitridate and Podo, 2018; Muñoz and Loeb, 2018; Muñoz et al., 2018; Pospelov et al., 2018; Safarzadeh et al., 2018; Slatyer and Wu, 2018; Witte et al., 2018; Yang, 2018).

Fluctuations in the redshifted 21 cm signal can be used to compute the power spectrum of the differential brightness temperature. This is the major goal of experiments as GMRT (Giant Metrewave Radio Telescope) (Ananthakrishnan, 1995; Paciga et al., 2011), LOFAR (LOw Frequency ARray) (van Haarlem et al., 2013), MWA (Murchison Widefield Array) (Tingay et al., 2013) and PAPER (Precision Array for Probing the Epoch of Reionization) (Parsons et al., 2010; Ali et al., 2015; Pober et al., 2015), targeting statistical power-spectrum measurements of the 21 cm signal employing large radio interferometers. Even if current experiments have not yet detected the 21 cm cosmological signature, the PAPER collaboration has recently improved the previous upper limits at $z = 8.4$ (Ali et al., 2015). Next decade, high-redshift 21 cm experiments include the SKA (Square Kilometre Array) (Mellema et al., 2013) and HERA (Hydrogen Epoch of Reionization Array) (Beardsley et al., 2015). A three-dimensional map of the 21 cm signal could also be obtained by means of the so-called intensity mapping technique, which measures the collective emission from neutral hydrogen in dense clumps, targeting large regions without resolving individual galaxies in the post-reionization era ($z \lesssim 3$) (Chang et al., 2008; Loeb and Wyithe, 2008; Wyithe et al., 2008; Villaescusa-Navarro et al., 2014b). The experimental efforts for this technique include the GBT−HIM project, with the GBT (Green Bank Telescope) (Chang et al., 2016), CHIME (Canadian Hydrogen Intensity Mapping Experiment) (Newburgh et al., 2014), the Tianlai project (Chen and Xu, 2016) and SKA−mid frequency (Dewdney et al., 2015)(see e.g., Bull et al., 2015).

Despite the fact that the primary task of future 21 cm experiments is to improve our current knowledge of the reionization history, they provide as well an additional tool for

[27] The authors of Amendola et al. (2018) have nonetheless presented constraints for different fiducial models.

[28] For the CORE CMB mission, data were generated following Refs (Bond et al., 1997, 2000). For DESI, mock $r_s H(z)$ and $d_A(z)/r_s$ data were generated for the three DESI tracers in the $0.15 < z < 1.85$ redshift range, accordingly to Font-Ribera et al. (2014b).

fundamental cosmology (Scott and Rees, 1990; Tozzi et al., 2000; Iliev et al., 2002; Barkana and Loeb, 2005a,b; McQuinn et al., 2006; Santos and Cooray, 2006; Bowman et al., 2007; Mao et al., 2008; Visbal et al., 2009; Clesse et al., 2012; Liu and Parsons, 2016; Liu et al., 2016), complementary to CMB missions and galaxy surveys. Indeed, 21 cm cosmological observations will play a very important role concerning neutrino physics. As previously stated, there are two types of experiments. First of all, we will have observations focused on the pre-reionization and EoR periods, that can probe very large volumes (where the non-linear scale is small). Remember that the largest signal from relic neutrino masses and their ordering appears at scales which, at the redshifts attainable at galaxy clustering surveys, lie within the mildly non-linear regime. Therefore, one needs to rely on either N-body simulations or on analytical approximations for the matter power spectrum to simulate the massive neutrino signature. EoR 21 cm experiments will achieve the scales required to observe the neutrino signature within the linear regime, avoiding the simulation problems described in section 4.2. In this regard, these probes may widely surpass the constraints on neutrino masses expected from even very large galaxy surveys (McQuinn et al., 2006; Mao et al., 2008; Pritchard and Pierpaoli, 2008; Tegmark and Zaldarriaga, 2009; Abazajian et al., 2011; Oyama et al., 2013, 2016; Shimabukuro et al., 2014). Furthermore, the neutrino constraints will be largely independent of the uncertainties in the dark energy fluid, which, as we have seen in section 4.3.2, have instead a non-negligible impact in lower redshift, galaxy survey measurements. This is a byproduct of using the 21 cm line to trace the matter overdensities: at redshifts $z \lesssim 2$, the universe starts to be dominated by the dark energy fluid and the growth of matter perturbations is modified depending on the dark energy equation of state $w(z)$, whose precise time-evolution remains unknown. Consequently, for a given perturbation in the matter fluid, a suppression in its structure growth could be either due to the presence of massive neutrinos or to an evolving dark energy fluid. Focusing at higher redshifts, the neutrino mass constraints from 21 cm probes will be largely independent of the uncertainties in the dark energy fluid properties.

Expectations from MWA, SKA and FFTT (Fast Fourier Transform Telescope) (Tegmark and Zaldarriaga, 2009) were considered in Mao et al. (2008). Focusing on 4000 h of observations of two areas in the sky in a range of $z = 6.8 - 8.2$ (divided into three redshift bins) and a value of $k_{\rm max} = 2\ {\rm Mpc}^{-1}$, the reported errors on $\sum m_\nu$ are 0.19 (0.027), 0.056 (0.017), 0.007 (0.003) for MWA, SKA and FFTT, respectively, in their middle (optimistic) scenarios[29], when combined with Planck measurements. These forecasts were performed for a fiducial $\Omega_\nu h^2 = 0.0875$, which corresponds to a quite high value for the neutrino mass, lying in the fully degenerate neutrino mass spectrum.

The authors of Oyama et al. (2013) devoted a dedicated analysis to establish the potential for extracting the neutrino mass ordering combining the FFTT capabilities with future CMB polarization measurements. Based exclusively on the induced effect of the neutrino mass ordering on the cosmic expansion rate, a robust 90% CL neutrino mass ordering extraction was reported if $\sum m_\nu < 0.1$ eV, regardless the underlying true ordering (i.e., normal or inverted). In Oyama et al. (2016), the authors propose to combine ground-based CMB polarization observations, SKA Phase 2 and BAO measurements from DESI. With these data sets, a 2σ extraction of the neutrino mass ordering seems feasible, unless the neutrino spectrum is degenerate. Notice that these results arise from the signature induced by the neutrino mass ordering in the cosmic expansion rate, as the minimum cutoff of the wavenumber in the 21 cm observations is $k_{\rm min} = 0.06h\ {\rm Mpc}^{-1}$, while the wavenumber corresponding to the neutrino free-streaming scale is $k_{\rm min} \simeq 0.02h\ {\rm Mpc}^{-1}$ for a 0.05 eV massive neutrino.

More futuristic 21 cm experiments, as FFTT, may open the possibility of going beyond measurements of the total neutrino mass $\sum m_\nu$ and measure the individual neutrino masses, revealing the uniqueness of such experiments for constraining the neutrino properties. As shown in **Figure 9** in section 4, the differences in the power spectra for the two possible mass orderings are tiny. Therefore, exquisite precision measurements are required to identify such signatures. Galaxy surveys, already discussed in the previous section, are limited by two facts. The first one is related to non-linearities, which will not allow for a measurement of the power spectrum at scales $k > 0.2h\ {\rm Mpc}^{-1}$ at small redshifts, see section 4.2. Since the non-linear scale at $z = 8$ is $k \simeq 3h\ {\rm Mpc}^{-1}$, both SKA and FFTT can measure the entire linear region and be more sensitive to the scale-dependent suppression, which is different in the two neutrino mass orderings. The second one is related to the fact that a galaxy survey requires a large number density of tracers to ensure a good sensitivity at small scales, while for 21 cm surveys, tracing the ubiquitous permeating hydrogen, a high-density antennae distribution will already warrant excellent small-scale sensitivities. One drawback of 21 cm probes are foregrounds, which should be kept under control.

The authors of Pritchard and Pierpaoli (2008) have studied the perspectives for extracting the individual neutrino masses with SKA and FFTT, finding that FFTT could be able to distinguish all the three neutrino masses from zero at the 3σ level, due to its enormous effective volume (see Figure 3 of Pritchard and Pierpaoli, 2008). Extracting the neutrino mass ordering directly from the individual masses, however, was shown to be a very difficult achievement. Our calculations show that, for the total neutrino mass we use here as a reference, $\sum m_\nu = 0.12$ eV, the differences among the lightest (l), medium (m) and heaviest (h) neutrino mass eigenstates between the normal and inverted orderings are $(|\Delta m_l|,\ |\Delta m_m|,\ |\Delta m_h|) = (0.015, 0.0209, 0.0059)$ eV, which, especially for the case of $|\Delta m_h| = 0.0059$ eV, are tiny and very difficult to resolve, even with very futuristic 21 cm measurements. While increasing the exposure of FFTT may improve its capabilities for this purpose (the error in the most optimistic FFTT scenario of Mao et al. (2008) is 0.003 eV), it seems an extremely challenging task. **Figure 13** depicts the differences in the values of the three neutrino masses as a function of the total neutrino mass between

[29]These scenarios differ in the assumptions concerning the power modeling, the prior on the reionization history and the residual foregrounds cutoff scale, among other factors (see Tegmark and Zaldarriaga, 2009).

inverted and normal orderings. We show with a dashed vertical line our representative case $\sum m_\nu = 0.12$ eV (the present most constraining 95% CL upper limit) and another one for $\sum m_\nu = 0.34$ eV (the most recent 95% CL bound from the Planck collaboration after the removal of systematics in their polarization data at high angular scales Aghanim et al., 2016b). Notice that, as expected, the differences between the values of the three neutrino masses decrease with the total neutrino mass. In this regard, the lower the neutrino mass, the easier it could be to single out the three neutrino mass eigenstates, because they are more separated. However, an extraction of the mass ordering in the non-degenerate region via the values of the individual neutrino masses seems very difficult. Indeed, **Figure 13** illustrates the values of the individual neutrino masses for the heaviest, medium and lightest states for the normal and inverted orderings as a function of the total neutrino mass. The bands, from **Top to Bottom** , depict the errors $\sigma(m_i) = 0.02$ eV and $\sigma(m_i) = 0.01$ eV, together with the very futuristic FFTT one, $\sigma(m_i) = 0.005$ eV. For an error of $\sigma(m_i) = 0.02$ eV, there is no hope to disentangle the individual neutrino masses, as the error bands overlap for the heaviest, medium and lightest masses in all the parameter space. If instead one could achieve $\sigma(m_i) = 0.01$ eV, a measurement of the individual neutrino masses in the non-degenerate region could be possible at the $1-2\sigma$ level, but in order to unravel the ordering one would need very extreme conditions as, for instance, a value of $\sum m_\nu$ very close to 0.1 eV independently determined with very small errors. The bottom plot in **Figure 14** shows the results if we assume the futuristic value of $\sigma(m_i) = 0.005$, expected to be achieved by FFTT. In this case, a measurement of the three neutrino masses will be achieved. Furthermore, in this (very optimistic) situation, the error bars will be, in principle, sufficiently small to detect the presence (or the lack) of two massive neutrino states with masses in the 0.02–0.03 eV range, required if the ordering is normal to explain $\sum m_\nu \simeq 0.1$ eV, which would strongly confirm the normal (or inverted) neutrino mass ordering. If $\sigma(m_i) = 0.005$, the detection of the mass ordering will still be possible even if $\sum m_\nu \lesssim 0.1$ eV, since the error on $\sum m_\nu$ will allow to exclude the inverted ordering with great accuracy.

As already mentioned, another possibility is the so-called 21 cm intensity mapping, which will focus on low redshifts $z \lesssim 3$ and will measure, with low angular resolution, the integrated 21 cm flux emitted from unresolved sources observing large patches of the sky. The lack of high angular resolution will result in a less precise measurement of non-linear scales. On the other hand, low angular resolution will imply a much faster survey. Future planned intensity mapping surveys are developed within the Phase 1 of the SKA experiment, which will include a wide and deep survey at low redshifts ($z \lesssim 3$, the SKA1–MID array) and a narrow and deep survey at higher redshift ($3 \lesssim z \lesssim 6$, the SKA1–LOW array), and within the Phase 2 of SKA (SKA2). Since, in some sense, these intensity mapping probes will be complementary to future planned optical surveys, as DESI or Euclid, it makes sense to combine their expected results. The intensity mapping technique, as galaxy clustering, is also affected by bias uncertainties and non-linearities at small scales.

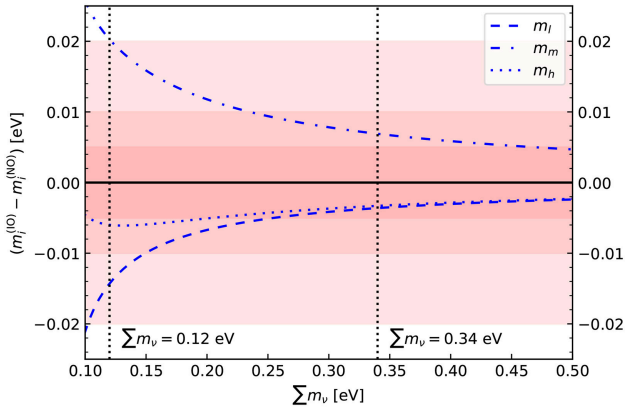

FIGURE 13 | Differences in the masses for three neutrino mass eigenstates as a function of the total neutrino mass between inverted and normal orderings. The vertical dashed lines depict the value $\sum m_\nu = 0.12$ eV and $\sum m_\nu = 0.34$ eV, which are the present most constraining 95% CL limit on $\sum m_\nu$ Palanque-Delabrouille et al. (2015) and the latest 95% CL bound quoted by the Planck collaboration (Aghanim et al., 2016b), respectively. Different shades of colored bands indicate the possible errors which could be achieved by future cosmological experiments on the determination of single neutrino masses: 0.02 eV, 0.01 eV or 0.005 eV.

Several studies have been carried out in the literature to unravel the perspectives of the intensity mapping technique in unveiling the neutrino properties. Some of them include the combination of the expectations from future large scale structure and intensity mapping surveys (Loeb and Wyithe, 2008; Visbal et al., 2009; Abazajian et al., 2011; Villaescusa-Navarro et al., 2015; Archidiacono et al., 2017; Sprenger et al., 2018). Notice that all these studies rely on different assumptions on the cosmological parameters, on the foregrounds and on the systematic uncertainties, therefore we can not do comparisons among them. Instead, we quote the most recent findings and the impact for an eventual future detection of the neutrino mass ordering.

The authors of Villaescusa-Navarro et al. (2015) found that, by combining SKA1–LOW with Planck measurements, the 95% CL error on $\sum m_\nu$ could be ~ 0.089 eV. It is remarkable that such a combination could potentially rule out the inverted ordering scenario, assuming that normal ordering is realized in nature. These authors also find that, under identical assumptions in the forecasted analyses, their combination of intensity mapping surveys (SKA1–LOW and MID) should be regarded as competitive with future spectroscopic surveys concerning neutrino mass properties. The authors of Archidiacono et al. (2017) showed that constraints of the future CORE CMB mission and galaxy redshift/weak lensing large scale structure surveys (as Euclid) on the neutrino mass can be improved if a prior on the reionization optical depth from 21 cm probes as HERA or SKA is also included. A prior of $\sigma(\tau) = 0.001$ will reduce the freedom in the amplitude of the primordial power spectrum A_s, as CMB measurements mostly constrain the combination $A_s \exp(-2\tau)$, see section 4.1. Therefore, the direct correlation between $\sum m_\nu$ and A_s, both modifying the amplitude of the

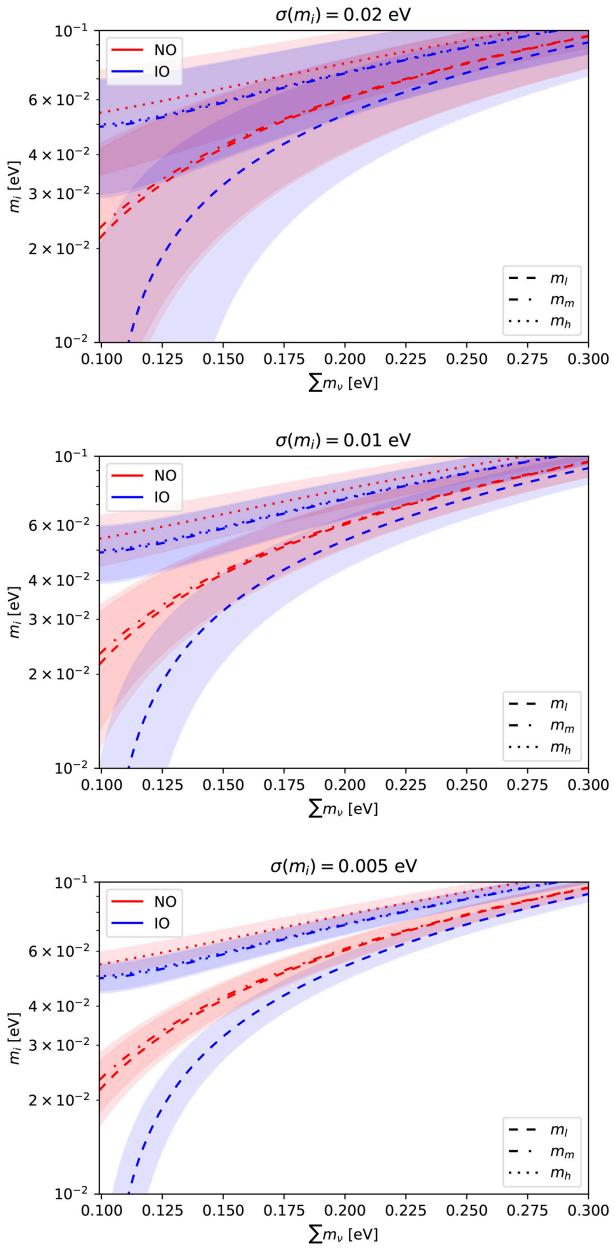

FIGURE 14 | Values of the individual neutrino masses for the heaviest, medium and lightest mass eigenstates for the normal and inverted orderings as a function of the total neutrino mass. The panels, from **Top to Bottom**, depict the error bands $\sigma(m_i) = 0.02$ eV, $\sigma(m_i) = 0.01$ eV and $\sigma(m_i) = 0.005$ eV.

matter power spectrum (although the change induced by $\sum m_\nu$ is, obviously, scale dependent), is largely affected by the presence of a precise determination of τ. The 1σ sensitivity they find for the combination of CORE, Euclid plus the prior on the optical depth from future 21 cm observations is $\sigma(\sum m_\nu) = 0.012$ eV[30].

[30]More recently, this very important synergy between Euclid and future 21 cm surveys, concretely with the intensity mapping survey SKA1, has been further assessed in Sprenger et al. (2018).

Nevertheless, as carefully detailed above, even if these tiny errors on $\sum m_\nu$ will be reached and extrapolated to an error on the individual neutrino mass eigenstates, the possibility of extracting the neutrino mass ordering via singling out the neutrino mass eigenstates with cosmological observables remains unfeasible, unless very visionary scenarios, as FFTT under the most optimistic assumptions, are envisaged.

6.6. Prospects From Core-Collapse Supernova

Neutrinos from core-collapse supernovae offer an independent and complementary way to test neutrino physics. The existence of these neutrinos was robustly confirmed by the detection of 25 events from Supernova 1987A in the Large Magellanic Cloud (Alekseev et al., 1987; Bionta et al., 1987; Hirata et al., 1987), located at $\sim$ 50 kpc from our Milky Way galaxy. Such a detection allowed to set very compelling bounds on a number of neutrino properties (Schramm and Truran, 1990; Raffelt, 1999). Even if laboratory experiments have surpassed some of these limits, the eventual detection of supernovae neutrinos will still provide precious information about the details of the explosion process (see e.g., Janka, 2012; Mirizzi et al., 2016; Scholberg, 2018 and references therein), and also of neutrino mixing effects in dense media, see also Horiuchi and Kneller (2018).

Neutrino production in core-collapse supernovae occurs in a number of different stages. The first one is the *infall*, in which electron neutrinos are produced, confined, as a result of the process $e^- + p \rightarrow n + \nu_e$. When electrons are converted, the outwards pressure they generate disappears and the gravity forces are no more balanced: the core will start to collapse until its density reaches that of matter inside atomic nuclei, i.e., nuclear densities. Once these densities are reached, matter becomes incompressible, and a hydrodynamic shock is formed. As this shock wave propagates outwards, it heats up the nuclei and disintegrates them, releasing neutrinos. This initial neutrino release is commonly known as *neutronization burst*, and it is mainly composed of ν_e and may last for a few tens of milliseconds. After the neutronization burst, the remnant proto-neutron star may evolve into a neutron star or collapse to a black hole, depending on the mass of the progenitor star. During this phase of *explosion and accretion*, which lasts for 1–2 s, the ν_e contribution is still the dominant one, albeit there is also a contribution from other (anti)neutrino flavors, in particular $\bar{\nu}_e$. The neutrinos produced in the *cooling* stage give the main contribution to the total flux, as it is in this phase when the supernova releases its energy via all-flavor neutrino-antineutrino pair production, reaching its final cold state. This process lasts for about tens of seconds. The differences in the mean temperature of the neutrino fluxes of ν_e, $\bar{\nu}_e$ and ν_x ($\bar{\nu}_x$) are due to the different medium opacity of each species. The larger the opacity, the lower the temperature that the (anti)neutrino will have at decoupling. The neutrino fluxes read as Scholberg (2018)

$$\phi(E_\nu) = N_0 \frac{(\alpha+1)^{(\alpha+1)}}{\langle E_\nu \rangle \Gamma(\alpha+1)} \left(\frac{E_\nu}{\langle E_\nu \rangle}\right)^\alpha \exp\left(-(\alpha+1)\frac{E_\nu}{\langle E_\nu \rangle}\right), \quad (24)$$

where N_0 is the total number of emitted neutrinos, and both α and the mean energy $\langle E_\nu \rangle$ are flavor dependent. The supernova neutrino energy spectra peaks around the $10-20$ MeV region.

The most popular process for supernova neutrino detection is inverse beta decay on protons ($\bar{\nu}_e + p \rightarrow n + e^+$). Other possibilities include elastic scattering on electrons ($\nu + e^- \rightarrow \nu + e^-$), whose kinematics may provide information on the supernova location. Supernova neutrinos can also interact with nuclei via charged current or neutral current interactions, giving rise to charged leptons and/or excited nuclei which may provide flavor tagging. A very important process on argon nuclei is $\nu_e + ^{40}\text{Ar} \rightarrow e^- + ^{40}\text{K}^*$, which allows for electron neutrino tagging. In practice, water Cherenkov and scintillator detectors are mostly sensitive to electron antineutrinos via inverse beta decay, while the liquid argon technique mainly detects electron neutrinos. While other flavors may also be detected, the two processes above are the dominant ones. Large detector volumes (dozens of kilotons) are required to detect neutrinos from core-collapse supernovae located at $\sim \mathcal{O}(10)$ kpc. A convenient way to scale the total number of supernova neutrino events in a detector of given effective mass is Beacom and Vogel (1998); Mena et al. (2007)

$$N = N_0 \left(\frac{E_{\rm B}}{3 \times 10^{53}\ {\rm erg}} \right) \left(\frac{10\ {\rm kpc}}{D_{\rm OS}} \right)^2 . \qquad (25)$$

In the expression above, $E_{\rm B}$ is the gravitational binding energy of the collapsing star and $D_{\rm OS}$ the distance between the observer and the supernova. Assuming sensitivity to all reactions, the reference rate is $N_0 = \mathcal{O}(10^4)$ for the Super–Kamiokande water Cherenkov detector with 32 kton and 5 MeV energy detection threshold. (Scholberg, 2012, 2018) give an estimate of the number of neutrino events for a number of ongoing and future facilities, based on different detection techniques: water Cherenkov (including also those with long string photosensors in ice, as Icecube and PINGU), liquid argon time projection chambers, and liquid scintillators. Upcoming neutrino detectors, already described in section 6.1 and crucial for oscillation physics measurements, such as the JUNO liquid scintillator (An et al., 2016), the liquid argon DUNE (Acciarri et al., 2015, 2016a,b; Strait et al., 2016) and the water Cherenkov Hyper–Kamiokande (Abe et al., 2015) can lead to a number of 6000, 3000 and 75000 supernova neutrino events respectively, assuming that the explosion occurs at 10 kpc from our position.

Flavor transitions inside a supernova have been carefully reviewed in Refs. Mirizzi et al. (2016); Scholberg (2018) (see also Lunardini and Smirnov, 2001a,b, 2003, 2004; Akhmedov et al., 2002). Here we summarize the most relevant results. As we have seen in section 2, when neutrinos propagate through matter their mixing effects undergo the so-called MSW mechanism, feeling a matter potential which is proportional to the electron number density N_e. If the supernova matter density has a profile which varies slowly, the neutrino matter eigenstates will propagate adiabatically and their final flavor composition will depend on the neutrino mass ordering, which will establish whether or not resonant transitions associated to each neutrino mass squared difference (solar and atmospheric) take place[31]. In the normal ordering case, the neutrino fluxes will have a significantly transformed spectrum, while the electron antineutrino one will only be partially transformed ($F^{\rm final}_{\nu_e} = F^{\rm initial}_{\nu_x}$ and $F^{\rm final}_{\bar{\nu}_e} = \cos^2\theta_{12} F^{\rm initial}_{\bar{\nu}_e} + \sin^2\theta_{12} F^{\rm initial}_{\bar{\nu}_x}$). In the inverted ordering case, the effects on the electron neutrino and antineutrino fluxes will be approximately the opposite ones ($F^{\rm final}_{\nu_e} = \sin^2\theta_{12} F^{\rm initial}_{\nu_e} + \cos^2\theta_{12} F^{\rm initial}_{\nu_x}$ and $F^{\rm final}_{\bar{\nu}_e} = F^{\rm initial}_{\bar{\nu}_x}$). Once neutrinos exit from supernovae, they can still undergo flavor transitions if they traverse the Earth. Their final flavor composition at the detector location will again depend on the neutrino mass ordering, as matter effects in Earth depend on it (see e.g., Scholberg, 2018) and references therein.

Furthermore, *collective effects* from neutrino self-interactions, due to $\nu_e + \bar{\nu}_e \rightarrow \nu_x + \bar{\nu}_x$ flavor processes, can lead to departures from the above summarized three-flavor oscillation picture (Hannestad et al., 2006a; Duan et al., 2007, 2010; Esteban-Pretel et al., 2007, 2008; Raffelt and Sigl, 2007; Mirizzi et al., 2016). The effective potential, proportional to the difference between the electron antineutrino and the muon/tau antineutrino fluxes, and inversely proportional to the supernova radius, should dominate over the standard matter one, leading to *spectral swaps or splits* (Raffelt and Smirnov, 2007a,b; Dasgupta et al., 2009, 2010). In the early stages, these self-interacting effects are sub-leading for mass ordering signatures, albeit we shall comment on possible non-thermal features in the neutrino or antineutrino spectra which depend on the mass ordering (Choubey et al., 2010).

In the following, we shall summarize the most relevant available methods to extract the neutrino mass ordering using the mentioned fluxes. For a recent and thorough review of the mass ordering signatures from supernovae neutrinos, we refer the reader to Scholberg (2018). The electron neutrinos produced in the neutronization burst undergo the MSW effect being fully (only partially) transformed, i.e., $F^{\rm final}_{\nu_e} = F^{\rm initial}_{\nu_x}$ ($F^{\rm final}_{\nu_e} = \sin^2\theta_{12} F^{\rm initial}_{\nu_e} + \cos^2\theta_{12} F^{\rm initial}_{\nu_x}$) if the mass ordering is normal (inverted), respectively. Therefore, detectors with good ν_e tagging, such as liquid argon or water Cherenkov ones, will detect a neutronization burst only in the inverted neutrino mass ordering case. Concerning the accretion phase, and once electron antineutrinos are also produced, as they are almost unchanged in the MSW resonance, the largest signature is expected to occur for the normal ordering case for the three type of aforementioned detector types (liquid argon, water Cherenkov and scintillator), although the Icecube detector, with its excellent capabilities to reconstruct the time dependence of the signal, could also distinguish between the normal and inverted mass orderings (Ott et al., 2013). While a devoted study with precise and accurate mass ordering sensitivities attainable at these three detector types via supernova neutrinos is, to our knowledge, missing in the literature, we exploit the event rates during the accretion phase quoted for normal and inverted orderings in Scholberg (2018) for a supernova located at 10 kpc. For a 40 kton liquid argon detector,

[31] In case the matter potential inside the supernova suffers from discontinuities, the neutrino transitions will be non-adiabatic and the final flavor composition will depend on the precise matter profile.

374 kton water Cherenkov and 20 kton scintillator, the normal mass ordering could be extracted with $\sim 2, 6$ and $2\,\sigma$ significance, respectively, based on a pure statistical-error analysis.

On the other hand, collective effects, which lead to spectral swaps in the electron (anti)neutrino spectra, show very sharp features at fixed energy values which depend, among other factors, on the neutrino mass ordering. However, these signatures are not as robust as the ones existing in the neutronization and accretion phases. Finally, a very significant imprint of the neutrino mass ordering on the supernovae neutrino fluxes is that due to their propagation through the Earth interior, where the standard MSW effect will induce a few percent-level oscillatory pattern in the $10 - 60$ MeV energy range, in the electron (anti)neutrino spectra in case of (normal) inverted mass ordering. The detection of these wiggles requires however excellent energy resolution.

6.7. Prospects From Relic Neutrino Direct Detection

In the early Universe, neutrinos decoupled from the cosmic plasma during the cool down, in a process similar to the one leading to the formation of the CMB but at an earlier time, when the universe was seconds to minutes old. These neutrinos have been free-streaming for such a long time that they have decohered and are currently propagating as mass eigenstates. The decoupling of neutrinos occurred just before $e^{\pm}$ annihilated and reheated photons, leading to the following ratio between the photon (T_γ) and neutrino (T_ν) temperatures, see Equation (15):

$$\frac{T_\nu}{T_\gamma} = \left(\frac{4}{11}\right)^{1/3}. \tag{26}$$

Today, the temperature of the neutrino background is $T_\nu^0 \simeq 1.6 \times 10^{-4}$ eV. Their mean energy is $\langle E_\nu \rangle \simeq 3\, T_\nu \simeq 5 \times 10^{-4}$ eV, much smaller than the minimal mass of the second-to-lightest neutrino as required by flavor oscillations, so that at least two out of three neutrinos are non-relativistic today. The cosmic neutrino background (CνB) is the only known source of non-relativistic neutrinos and it has never been detected directly.

Apart from the imprints that relic neutrinos leave in the CMB (see section 4.1), which allow to have an indirect probe of their existence through the determination of $N_{\rm eff}$, the direct detection of the CνB would offer a good opportunity to test neutrino masses and their ordering. Capturing relic neutrinos is not only rewarding from the point of view of what we can learn about neutrino properties, but also because it would be a further confirmation of the standard Big Bang cosmological model. Different ideas on how to achieve such a detection have been proposed (Weinberg, 1962; Weiler, 1982, 1984; Duda et al., 2001; Eberle et al., 2004; Barenboim et al., 2005; Gelmini, 2005; Ringwald, 2005; Cocco et al., 2007; Li, 2015; Vogel, 2015; Domcke and Spinrath, 2017), ranging from absorption dips in the ultra-high-energy (UHE) neutrino fluxes due to their annihilation with relic neutrinos at the Z boson resonance, to forces generated by coherent scattering of the relic bath on a pendulum and measured by laser interferometers. Most of these proposed methods are impractical from the experimental point of view. The one exploiting UHE neutrinos Weiler (1982, 1984); Eberle et al. (2004); Barenboim et al. (2005) has two problems, one related with the fact that it is difficult to think about a source that produces such UHE neutrinos, of energies

$$E_\nu^{\rm res} = \frac{m_Z^2}{2m_i} \simeq 4 \cdot 10^{22} \left(\frac{0.1\,{\rm eV}}{m_i}\right) {\rm eV}, \tag{27}$$

and another one regarding the difficulties of detecting a large enough sample of UHE neutrinos in order to resolve the dips. The method based on interferometers (Domcke and Spinrath, 2017) is even more complicated to address. At interferometers, current sensitivities to accelerations are of the order of $a \simeq 10^{-16}\,{\rm cm/s^2}$, with an optimistic estimation of $a \simeq 3 \cdot 10^{-18}\,{\rm cm/s^2}$ (Domcke and Spinrath, 2017) for the incoming generation. However, expected accelerations due to relic neutrino interactions are of the order of $\left(10^{-27} - 10^{-33}\right)\,{\rm cm/s^2}$ (Duda et al., 2001; Domcke and Spinrath, 2017), many orders of magnitude below the sensitivity of the next-generation interferometers.

The most promising approach to detect relic neutrinos is to use neutrino capture in a β-decaying nucleus A

$$\overset{(-)}{\nu}_e + A \to e^{\pm} + A', \tag{28}$$

where the signal for a positive detection is a peak located about $2m_\nu$ above the true β-decay endpoint (see below). In particular, tritium is considered as the best candidate since it has a high neutrino capture cross section, low Q-value and it is long-lived (Cocco et al., 2007; Blennow, 2008; Lazauskas et al., 2008; Faessler et al., 2011; Long et al., 2014). The proposal for an experiment chasing this purpose was made in Cocco et al. (2007). Currently, efforts are put for such experiment, the PonTecorvo Observatory for Light Early-Universe Massive-Neutrino Yield (PTOLEMY) (Betts et al., 2013; Baracchini et al., 2018), to be built. The experiment has recently been approved by the Scientific Committee of the Italian National Laboratories of Gran Sasso and, in the following months, the existing prototypes for various components are expected to be moved from Princeton, where the R&D has been performed up to now, to Gran Sasso. The idea is to implant the tritium source on graphene layers, to avoid the problems related to a gaseous source, then collect and measure the energy of the emitted electrons using a combination of MAC-E filter, radio-frequency tracking and micro-calorimetry to obtain a determination of the β-decay and neutrino capture spectrum of tritium with an energy resolution of the order $\Delta \simeq 0.05 - 0.1$ eV.

The total expected event rate from relic neutrino capture for a PTOLEMY-like experiment, assuming the estimated tritium mass of 100 g, is

$$\Gamma_{\rm C\nu B} = \left[n_0(\nu_{h_R}) + n_0(\nu_{h_L})\right] N_T\, \bar{\sigma} \sum_{i=1}^{3} |U_{ei}|^2 f_c(m_i)\,, \tag{29}$$

where $n_0(\nu_{h_{R,L}})$ is the averaged number density of relic neutrinos with right (R) or left (L) helicity, $N_T = M_T/m(^3{\rm H})$ is the approximated number of tritium atoms in the source, $\bar{\sigma} \simeq 3.834 \times 10^{-45}\,{\rm cm}^2$ (Long et al., 2014), and $f_c(m_i)$ is a mass-dependent overdensity factor that accounts for the clustering of

relic neutrinos under the gravitational attraction of the matter potential (mostly from the dark matter halo) of our galaxy. This last factor was originally computed in Singh and Ma (2003) and Ringwald and Wong (2004) and later updated in de Salas et al. (2017) (see also Zhang and Zhang, 2018), where smaller masses were considered for the neutrinos, and the treatment of the matter potential of the Milky Way was improved. The values of $f_c(m_\nu)$ range from $1.1-1.2$ for a neutrino with $m_\nu = 60$ meV to $1.7-2.9$ for $m_\nu = 150$ meV (de Salas et al., 2017).

For unclustered neutrinos (i.e., $f_c = 1$) and 100 g of tritium, the expected number of events per year is Long et al. (2014)

$$\Gamma^{\rm D}_{\rm C\nu B} \simeq 4\,{\rm year}^{-1}, \qquad \Gamma^{\rm M}_{\rm C\nu B} = 2\Gamma^{\rm D}_{\rm C\nu B} \simeq 8\,{\rm year}^{-1}, \quad (30)$$

where the upperscripts D and M stand for the possible Dirac and Majorana neutrino character. If neutrinos are Majorana particles, the expected number of events is doubled with respect to the Dirac case. The reason is related to the fact that, during the transition from ultra-relativistic to non-relativistic particles, helicity is conserved, but not chirality. The population of relic neutrinos is then composed by left- and right-helical neutrinos in the Majorana case, and only left-helical neutrinos in the Dirac case. Since the neutrino capture can only occur for left-chiral electron neutrinos, the fact that in the Majorana case the right-handed neutrinos can have a left-chiral component leads to a doubled number of possible interactions. While this means that in principle it is possible to distinguish the Dirac or Majorana neutrino nature with a precise determination of the event rate, there are two problems. First of all, even without assuming new physics, the factor of two coming from the neutrino nature is degenerate with the clustering factor, see Equation (29), so that a precise calculation of f_c is required to determine if neutrinos are Dirac or Majorana particles through the direct detection of relic neutrinos (de Salas et al., 2017). Moreover, non-standard interactions can increase the event rate in the Dirac case by a factor larger than two, canceling the difference with Majorana neutrinos in some scenarios (Arteaga et al., 2017).

Let us come back to the PTOLEMY proposal. Instead of considering the total event rate, for this kind of experiment it is much better to study the energy spectrum, as the direct detection of relic neutrinos can only be possible if one can distinguish the signal events due to neutrino capture from the background events due to the β-decay of tritium. A crucial issue for such an experiment, actually more important than the event rate, is therefore the energy resolution. In order to distinguish the peak due to the captured relic neutrinos from the β-decay background, a full-width half maximum (FWHM) energy resolution $\Delta \lesssim 0.7 m_\nu$ is needed (Long et al., 2014). If neutrinos are non-degenerate in mass, the neutrino capture signal has a peak for each of the separate neutrino mass eigenstates. The full expression of the energy spectrum of neutrino capture, given an energy resolution $\sigma = \Delta/\sqrt{8\ln 2}$, can be written as:

$$\frac{d\widetilde{\Gamma}_{\rm CNB}}{dE_e}(E_e) = \frac{1}{\sqrt{2\pi}\sigma} n_0 N_T \bar{\sigma} \sum_{i=1}^{N_\nu} |U_{ei}|^2 f_{c,i} \times \exp\left\{-\frac{[E_e - (E_{\rm end} + m_i + m_{\rm lightest})]^2}{2\sigma^2}\right\}, \quad (31)$$

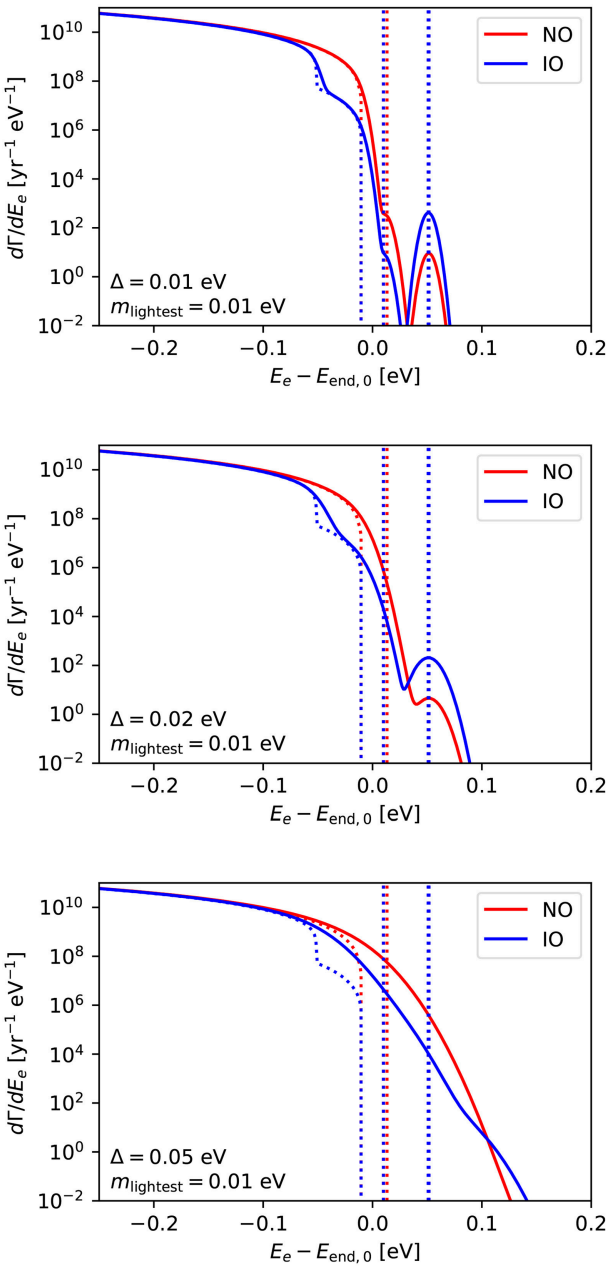

FIGURE 15 | Electron spectrum in a PTOLEMY-like experiment, comparing normal (red) and inverted ordering (blue) with $m_{\rm lightest} = 10$ meV and three different energy resolutions: $\Delta = 10$ meV **(Top)**, $\Delta = 20$ meV **(Middle)**, $\Delta = 50$ meV **(Bottom)**. Dashed lines indicate the spectrum as it would be measured by an experiment with perfect energy resolution.

where $E_{\rm end}$ is the energy of the β-decay endpoint, $E_{\rm end} = E_{\rm end,0} - m_{\rm lightest}$, being $E_{\rm end,0}$ the endpoint energy when $m_{\rm lightest} = 0$. If the energy resolution is good enough, the three peaks coming from the three neutrino mass eigenstates could be resolved, each of them with an expected number of events modulated by $|U_{ei}|^2$. This might lead to a positive detection of the neutrino mass ordering, since the electron-flavor component of ν_1 is

larger than the one of ν_2 and ν_3, and therefore the furthest peak from the β-decay endpoint (again if neutrinos are non-degenerate) is enhanced if the ordering of neutrino masses is inverted. This can be seen in the three panels of **Figure 15**, which also show the effect of changing the mass ordering on the β-decay spectrum. Dashed lines represent the spectrum which would be determined by an experiment capable of measuring the β spectrum with zero energy uncertainty, while solid lines represent the shape of the spectrum that one would observe in a real experiment. We plot in red (blue) the spectrum obtained using normal (inverted) ordering, a FWHM resolution Δ = 10 meV (top), Δ = 20 meV (middle), Δ = 50 meV (bottom) and a lightest neutrino mass $m_{\rm lightest}$ = 10 meV. As we can see from the figure, the kink commented in section 3 is clearly visible when one observes the huge number of events that come from the 100 g of decaying tritium with a sufficient energy resolution. While for distinguishing the relic neutrino events from the β-decay background and for having a direct detection of the CνB the energy resolution is a crucial requirement, in principle even a worse energy resolution may allow to determine the neutrino mass scale and the mass ordering, thanks to the fact that we expect less events near the endpoint when the ordering is inverted. A direct observation of the amplitude of all the CνB peaks, however, would give a much cleaner signal, because the peak corresponding to the heaviest neutrino would be always higher in the inverted ordering case, independently of any other factor.

In summary, the CνB capture event rate in a PTOLEMY-like experiment (Equation (31)), even within SM physics and without considering non-standard interactions, depends on several main unknowns: *i)* the absolute neutrino mass, *ii)* the matter distribution (especially that of dark matter) in our galaxy, *iii)* the nature of neutrino masses (whether neutrinos are Dirac or Majorana particles), and *iv)* the true mass ordering. This last dependence is encoded in the $|U_{ei}|^2$ factor in Equation (31) and it is only accessible if neutrinos are non-degenerate. A quantitative study on the PTOLEMY capabilities in determining the mass ordering has not been published yet, but a new Letter of Intent is in preparation (Baracchini et al., 2018)[32].

7. SUMMARY

Identifying the neutrino mass ordering is one of the major pending issues to complete our knowledge of masses and mixings in the lepton sector. The two possibilities, normal vs. inverted, may result from very different underlying symmetries and therefore to single out the one realized in nature is a mandatory step to solve the flavor puzzle, i.e., to ensure a full theoretical understanding of the origin of particle masses and mixings. We have presented a comprehensive review on the current status and on future prospects of extracting the neutrino mass ordering via a number of different ongoing and upcoming observations. Furthermore, the most updated and complete result on the preference for a given neutrino mass ordering from a Bayesian global fit to all 2018 publicly available neutrino data has also been presented.

Currently, among the three available methods to extract the neutrino mass ordering (oscillations, neutrinoless double beta decay searches and cosmological observations), the leading probe comes from oscillations in matter, measured at long-baseline accelerator or atmospheric neutrino beams in combination with reactor experiments. The latest frequentists global data analysis results in a preference for normal mass ordering with $\Delta\chi^2 = 11.7$ ($\sim 3.4\sigma$), mostly arising from the combination of the long-baseline T2K and NOνA data with reactor experiments (Daya Bay, RENO and Double Chooz), plus the latest atmospheric neutrino results from Super-Kamiokande. Similar results for the preference in favor of the normal mass ordering arise from other global fit analyses (Capozzi et al., 2018a).

Cosmological measurements are able to set indirect, albeit independent bounds on the neutrino mass ordering. Neutrinos affect Cosmic Microwave Background (CMB) primary anisotropies by changing the gravitational potential at the recombination period when they become non-relativistic. However, for sub-eV neutrino masses this effect is tiny and the most prominent effect on the CMB is via lensing, as neutrinos, having non-zero velocities, will reduce the lensing effect at small scales. Nevertheless, the largest impact of neutrinos in cosmology gets imprinted in the matter power spectrum. Once neutrinos become non-relativistic, their large velocity dispersions will prevent the clustering of matter inhomogeneities at all scales smaller than their free streaming length. At present, the cosmological constraints on the neutrino mass ordering come from the sensitivity to the total neutrino mass $\sum m_\nu$ and not via the effects induced in the CMB and matter power spectrum by each of the individual neutrino masses m_i. Within the context of the minimal ΛCDM model with massive neutrinos, current cosmological probes cannot provide odds stronger than $\sim 3:1$ in favor of normal ordering.

Neutrinoless double beta decay searches can also test the neutrino mass ordering if neutrinos are Majorana particles. However, present constraints on the so-called effective Majorana mass do not affect the overall Bayesian analyses.

All in all, the 2018 Bayesian global analysis, including all the neutrino oscillation data available before the Neutrino 2018 conference, results in a 3.2σ preference for the normal neutrino mass ordering which, in Bayesian words, implies a *strong* preference for such a scenario. One can then combine the oscillation data with $0\nu\beta\beta$ data from KamLAND-Zen, EXO-200 and Gerda and cosmological observations from Planck, SDSS BOSS, 6DF and SDSS DR7 MGS. Using this conservative cosmological data combination, the aforementioned preference becomes 3.4σ, which raises to 3.5σ if a prior on the Hubble parameter H_0 from local measurements is considered in addition. This clearly states the current power of oscillation results when dealing with neutrino mass ordering extractions.

While in the very near perspective an improved sensitivity (i.e., above the 3.5σ level) is expected mostly from more precise measurements of current long-baseline and atmospheric experiments, and, to a minor extent, from cosmological surveys

[32]We suggest the interested readers to look forward to the publication of this document, which will describe in more detail the physics reach and the technical characteristics of PTOLEMY.

(Planck, DES and eBOSS among others), there will be a number of planned experiments which will be crucial for extracting the neutrino mass ordering in the non-immediate future.

Of particular relevance are the upcoming neutrino oscillation facilities, as they will be able to measure the neutrino mass ordering with astonishing precision without relying on combinations of different data sets. Such is the case of the Deep Underground Neutrino Experiment (DUNE), that will be able to measure the neutrino mass ordering with a significance of 5σ with 7 years of data. Atmospheric neutrino observatories as PINGU or ORCA will also mainly focus on the mass ordering measurement. Some of these future devices could also identify the neutrino mass ordering via the detection of matter effects in the neutrino fluxes emitted at the eventual explosion of a supernova in our galaxy or in its neighborhood. On the other hand, medium baseline reactor neutrino detectors such as JUNO or RENO will also be able to extract the neutrino mass ordering despite matter effects are negligible for these two experiments. They will focus instead on an extremely accurate measurement of the survival electron antineutrino probability.

Improved masses and detection techniques in neutrinoless double beta decay future searches could go down the 10 meV region in the effective Majorana mass $m_{\beta\beta}$, and they could be able to discard at some significance level the inverted mass ordering scenario, in the absence of a positive signal. These limits, however, will apply only in case neutrinos have a Majorana nature. Moreover, the determination of the neutrino mass ordering may be complicated by the presence of a light sterile neutrino at the eV scale, as currently suggested by the NEOS and DANSS results.

Concerning future cosmological projects, the combination of different probes will still be required. Near-future CMB and large scale structure surveys will only be sensitive to the neutrino mass ordering via their achieved error on $\sum m_\nu$. Furthermore, the accuracy in the extraction of the neutrino mass ordering will strongly depend on how far $\sum m_\nu$ lies from the minimum allowed value from oscillation probes. The future CMB mission CORE plus the DESI galaxy survey could provide odds of $9:1$ for normal neutrino mass ordering assuming $\sum m_\nu = 0.056$ eV. Even if very futuristic surveys, based on the observation of the 21 cm redshifted line in neutral hydrogen, may be able to extract the individual values of the neutrino masses, their precision on the m_i values may not be enough to guarantee a direct determination of the neutrino mass ordering by these means, albeit they can achieve an accurate measurement of the ordering thanks to their unprecedented precision on $\sum m_\nu$.

Last, but not least, relic neutrino capture in tritium in a PTOLEMY-like experiment could also establish the neutrino mass ordering via an almost perfect energy reconstruction of the β-decay spectrum, ensured by the extremely large amount of tritium adopted. The detection is possible both from a kink in the β-decay spectrum which only appears if the ordering is inverted and from the peaks due to neutrino capture just above the endpoint.

All these future probes may either confirm or reject the current *strong* preference (3.5σ) in favor of the normal neutrino mass ordering. Such a preference has kept gaining significance in the recent years, thanks to the fact that current neutrino oscillation experiments have enormously improved our knowledge of neutrino flavor physics.

AUTHOR CONTRIBUTIONS

PFdS, CT, and MT have contributed mainly to review the current status of neutrino oscillations as well as to the summary of the prospects on the neutrino mass ordering from future neutrino oscillation experiments. SG has contributed to review beta and neutrinoless double beta decay current status and future prospects. SG has also led the 2018 Global Bayesian analysis results. PFdS and SG have also contributed to review the present and future cosmological bounds and have also reviewed the prospects from relic neutrino detection. OM has mainly contributed to review the cosmological bounds on the mass ordering and the perspectives from future 21 cm surveys and core-collapse supernovae.

ACKNOWLEDGMENTS

We thank C. Giunti for providing us the two panels constituting **Figure 7** and M. Hirsch for his suggestions on how to improve the first version of the manuscript. Work supported by the Spanish grants FPA2015-68783-REDT, FPA2017-90566-REDC (Red Consolider MultiDark), FPA2017-85216-P, FPA2017-85985-P and SEV-2014-0398 (AEI/FEDER, UE, MINECO), and PROMETEOII/2014/050, PROMETEO/2018/165 and GV2016-142 (Generalitat Valenciana). SG receives support from the European Union's Horizon 2020 research and innovation programme under the Marie Skłodowska-Curie individual grant agreement No. 796941. OM is also supported by the European Union's Horizon 2020 research and innovation program under the Marie Skłodowska-Curie grant agreements No. 690575 and 674896 and acknowledges the hospitality of the Fermilab Theoretical Physics Department. PFdS and CAT are also supported by the MINECO fellowships FPU13/03729 and BES-2015-073593, respectively. MT acknowledges financial support from MINECO through the Ramón y Cajal contract RYC-2013-12438 as well as from the L'Oréal-UNESCO *For Women in Science* initiative.

REFERENCES

Aalbers, J., Agostinib, F., Alfonsic, M., Amaror, F. D., Amslerd, C., Aprilee, E., et al. (2016). DARWIN: towards the ultimate dark matter detector. *JCAP* 11:017. doi: 10.1088/1475-7516/2016/11/017

Aalseth, C., Berkeley, U. C., and Richland, P. N. L. (2018). Search for Neutrinoless Double-β Decay in ^{76}Ge with the Majorana Demonstrator. *Phys. Rev. Lett.* 120:132502. doi: 10.1103/PhysRevLett.120.132502

Aartsen, M., and Adelaide U. (2014). Letter of intent: the precision iceCube next generation upgrade (PINGU). *arXiv:1401.2046*. 136.

Aartsen, M. G., Ackermann, M., Adams, J., Aguilar, J. A., Ahlers, M., Ahrens, M., et al. (2015). Determining neutrino oscillation parameters from atmospheric muon neutrino disappearance with three years of IceCube DeepCore data. *Phys. Rev. D* 91:072004. doi: 10.1103/PhysRevD.91.072004

Abazajian, K., Calabrese, E., Cooray, A., De Bernardis, F., Dodelson, S., Friedland, A., et al. (2011). Cosmological and astrophysical neutrino mass measurements. *Astropart. Phys.* 35, 177–184. doi: 10.1016/j.astropartphys.2011.07.002

Abazajian, K. N., Adshead, P., Ahmed, Z., Allen, S. W., Alonso, D., Arnold, K. S., et al. (2016). *CMB-S4 Science Book*, 1st Edn.

Abazajian, K. N., and Dodelson, S. (2003). Neutrino mass and dark energy from weak lensing. *Phys. Rev. Lett.* 91:041301. doi: 10.1103/PhysRevLett.91.041301

Abbott, T., Abdalla, F. B., Alarcon, A., Aleksić, J., Allam, S., Allen, S., et al. (2018). Dark energy survey year 1 results: cosmological constraints from galaxy clustering and weak lensing. *Phys. Rev. D* 98:043526. doi: 10.1103/PhysRevD.98.043526

Abbott, T., Abdalla, F. B., Alarcon, A., Allam, S., Andrade-Oliveira, F., Annis, J., et al. (2017). Dark energy survey year 1 results: measurement of the baryon acoustic oscillation Scale in the distribution of galaxies to redshift 1. *Mon. Not. R. Astron. Soc.* D98:043526.

Abdurashitov, J. N., Gavrin, V. N., Gorbachev, V. V., Gurkina, P. P., Ibragimova, T. V., Kalikhov, A. V. et al. (2009). Measurement of the solar neutrino capture rate with gallium metal. III: Results for the 2002–2007 data-taking period. *Phys. Rev. C* 80:015807. doi: 10.1103/PhysRevC.80.015807

Abe, K., Abe, Ke., Ahn, S. H., Aihara, H., Aimi, A., Akutsu, R., et al. (2018c). Physics potentials with the second hyper-kamiokande detector in Korea. *PTEP* 2018:063C01. doi: 10.1093/ptep/pty044

Abe, K., Abe, Ke., Aihara, H., Aimi, A., Akutsu, R., Andreopoulos, C., et al. (2018b). Hyper-kamiokande design report. *arXiv:1805.04163v1*.

Abe, K., Abgrall, N., Ajima, Y., Aihara, H., Albert, J. B., Andreopoulos, C., et al. (2011a). Indication of electron neutrino appearance from an accelerator-produced Off-axis muon neutrino beam. *Phys. Rev. Lett.* 107:041801. doi: 10.1103/PhysRevLett.107.041801

Abe, K., Aihara, H., Andreopoulos, C., Anghel, I., Ariga, A., Ariga, T., et al. (2015). Physics potential of a long-baseline neutrino oscillation experiment using a J-PARC neutrino beam and Hyper-Kamiokande. *Prog. Theor. Exp. Phys.* 2015:053C02. doi: 10.1093/ptep/ptv061

Abe, K., Bronner, C., Haga, Y., Hayato, Y., Ikeda, M., Iyogi, K., et al. (2018a). Atmospheric neutrino oscillation analysis with external constraints in Super-Kamiokande I-IV. *Phys. Rev. D* 97:072001. doi: 10.1103/PhysRevD.97.072001

Abe, K., Hayato, Y., Iida, T., Ikeda, M., Ishihara, C., Iyogi, K., et al. (2011b). Solar neutrino results in Super-Kamiokande-III. *Phys. Rev. D* 83:052010. doi: 10.1103/PhysRevD.83.052010

Abe, Y., Asano, Y., Haba, N., and Yamada, T. (2017). Heavy neutrino mixing in the T2HK, the T2HKK and an extension of the T2HK with a detector at Oki Islands. *Eur. Phys. J. C* 77:851. doi: 10.1140/epjc/s10052-017-5294-7

Abe, Y., dos Anjos, J. C., Barriere, J. C., Baussan, E., Bekman, I., Bergevin, M., et al. (2014). Improved measurements of the neutrino mixing angle θ_{13} with the Double Chooz detector. *JHEP* 10:086. doi: 10.1007/JHEP10(2014)086

Abell, P. A., Allison, J., Anderson, S. F., Andrew, J. R., Roger, J., Angel, P., et al. (2009). *LSST Science Book, Version 2.0*.

Abgrall, N., Abramov, A., Abrosimov, N., Abt, I., Agostini, M., Agartioglu, M., et al. (2017). The large enriched germanium experiment for neutrinoless double beta decay (LEGEND). *AIP Conf. Proc.* 1894:020027. doi: 10.1063/1.5007652

Abrahão, T., Minakata, H., Nunokawa, H., and Quiroga, A. A. (2015). Constraint on Neutrino Decay with Medium-Baseline Reactor Neutrino Oscillation Experiments. *J. High Energy Phys.* 11:001. doi: 10.1007/JHEP11(2015)001

Acciarri, R., Acero, M. A., Adamowski, M., Adams, C., Adamson, P., Adhikari, S., et al. (2016a). Long-baseline neutrino facility (LBNF) and deep underground neutrino experiment (DUNE) Volume 1. *arXiv:1601.05471v1*.

Acciarri, R., Acero, M. A., Adamowski, M., Adams, C., Adamson, P., Adhikari, S. et al., (2015). Long-Baseline Neutrino Facility (LBNF) and Deep Underground Neutrino Experiment (DUNE): Conceptual Design Report, Volume 2: The Physics Program for DUNE at LBNF. *arXiv:1512.06148*.

Acciarri, R., Acero, M. A., Adamowski, M., Adams, C., Adamson, P., Adhikari, S. et al., (2016b). Long-Baseline Neutrino Facility (LBNF) and Deep Underground Neutrino Experiment (DUNE) : Conceptual Design Report, Volume 4 The DUNE Detectors at LBNF. *arXiv:1601.02984*.

Adam, A. (2018). "Recent results from MINOS and MINOS+," in *XXVIII International Conference on Neutrino Physics and Astrophysics* (Heidelberg), Available online at: doi: 10.5281/zenodo.1286760

Adam, R., Ade, P. A. R., Aghanim, N., Akrami, Y., Alves, M. I. R., Arnaud, M., et al. (2016). Planck 2015 results. I. Overview of products and scientific results. *Astron. Astrophys.* 594:A1. doi: 10.1051/0004-6361/201527101

Adams, D., Adams, Q., Alduino, C., Alfonso, K., Avignone, F. T. III., Azzolini, O., et al. (2018). Update on the recent progress of the CUORE experiment. *arXiv:1808.10342v1*.

Adamson, P., Anghel, I., Aurisano, A., Barr, G., Bishai, M., Blake, A., et al. (2014). Combined analysis of ν_μ disappearance and $\nu_\mu \rightarrow \nu_e$ appearance in MINOS using accelerator and atmospheric neutrinos. *Phys. Rev. Lett.* 112:191801. doi: 10.1103/PhysRevLett.112.191801

Ade, P., Aghanim, N., Arnaud, M., Ashdown, M., Aumont, J., Baccigalupi, C., et al. (2016a). Planck 2015 results. XXVII. The Second Planck Catalogue of Sunyaev-Zeldovich Sources. *Astron. Astrophys.* 594:A27. doi: 10.1051/0004-6361/201525823

Ade, P. A. R., Aghanim, N., Armitage-Caplan, C., Arnaud, M., Ashdown, M., Atrio-Barandela, F., et al. (2014). Planck 2013 results. XVI. Cosmological parameters. *Astron. Astrophys.* 571:A16. doi: 10.1051/0004-6361/201321591

Ade, P. A. R., Aghanim, N., Arnaud, M., Ashdown, M., Aumont, J., Baccigalupi, C., et al. (2016b). Planck 2015 results. XIII. Cosmological parameters. *Astron. Astrophys.* 594:A13. doi: 10.1051/0004-6361/201525830

Adrian-Martinez, S., Ageron, M., Aharonian, F., Aiello, S., Albert, A., Ameli, F., et al. (2016). Letter of intent for KM3NeT 2.0. *J. Phys. G* 43, 084001. doi: 10.1088/0954-3899/43/8/084001

Adrian-Martinez, S., Al Samarai, I., Albert, A., Andre, M., Anghinolfi, M., Anton, G., et al. (2012). Measurement of atmospheric neutrino oscillations with the ANTARES neutrino telescope. *Phys. Lett.* B714, 224–230. doi: 10.1016/j.physletb.2012.07.002

Afshordi, N., Zaldarriaga, M., and Kohri, K. (2005). On the stability of dark energy with mass-varying neutrinos. *Phys. Rev. D* 72:065024. doi: 10.1103/PhysRevD.72.065024

Agarwalla, S. K., Chatterjee, S. S., and Palazzo, A. (2016). Physics Reach of DUNE with a Light Sterile Neutrino. *J. High Energy Phys.* 09:016. doi: 10.1007/JHEP09(2016)016

Agarwalla, S. K., Chatterjee, S. S., and Palazzo, A. (2018a). Signatures of a Light Sterile Neutrino in T2HK. *J. High Energy Phys.* 04:091. doi: 10.1007/JHEP04(2018)091

Agarwalla, S. K., Chatterjee, S. S., Petcov, S., and Titov, A. (2018b). Addressing Neutrino Mixing Models with DUNE and T2HK. *Eur. Phys. J. C* 78:286. doi: 10.1140/epjc/s10052-018-5772-6

Aghamousa, A. Aguilar, J., Ahlen, S., Alam, S., Allen, L. E., Prieto, C. A., et al et al. (2016). The DESI experiment part I: Science, targeting, and survey design. *arXiv:1611.00036v2*.

Aghanim, N., Arnaud, M., Ashdown, M., Aumont, J., Baccigalupi, C., Banday, A. J., et al. (2016a). Planck 2015 results. XI. CMB power spectra, likelihoods, and robustness of parameters. *Astron. Astrophys.* 594:A11. doi: 10.1051/0004-6361/201526926

Aghanim, N., Ashdown, M., Aumont, J., Baccigalupi, C., Ballardini, M., Banday, A. J., et al. (2016b). Planck intermediate results. XLVI. Reduction of large-scale systematic effects in HFI polarization maps and estimation of the reionization optical depth. *Astron. Astrophys.* 596:A107. doi: 10.1051/0004-6361/201628890

Aghanim, N., Majumdar, S., and Silk, J. (2008). Secondary anisotropies of the CMB. *Rept. Prog. Phys.* 71:066902. doi: 10.1088/0034-4885/71/6/066902

Agostini, M., Allardt, M., Bakalyarov, A. M., Balata, M., Barabanov, I., Baudis, L., et al. (2017b). Background-free search for neutrinoless double-β decay of ^{76}Ge with GERDA. *Nature* 544, 47–52. doi: 10.1038/nature21717

Agostini, M., Bakalyarov, A. M., Balata, M., Barabanov, I., Baudis, L., Bauer, C., et al. (2018). Improved Limit on Neutrinoless Double-β Decay of ^{76}Ge from GERDA Phase II. *Phys. Rev. Lett.* 120:132503. doi: 10.1103/PhysRevLett.120.132503

Agostini, M., Benato, G., and Detwiler, J. (2017a). Discovery probability of next-generation neutrinoless double-β decay experiments. *Phys. Rev. D* 96:053001. doi: 10.1103/PhysRevD.96.053001

Aharmim, B., Ahmed, S. N., Amsbaugh, J. F., Anthony, A. E., Banar, J., Barros, N., et al. (2008). An independent measurement of the total active B-8 solar neutrino flux using an array of He-3 proportional counters at the sudbury neutrino observatory. *Phys. Rev. Lett.* 101:111301. doi: 10.1103/PhysRevLett.101.111301

Aharmim, B., Ahmed, S. N., Anthony, A. E., Barros, N., Beier, E. W., Bellerive, A., et al. (2010). Low energy threshold analysis of the Phase I and Phase II data sets of the sudbury neutrino observatory. *Phys. Rev. C* 81:055504. doi: 10.1103/PhysRevC.81.055504

Ahmad, Q. R., Allen, R. C., Andersen, T. C., Anglin, J. D., Bühler, G., Barton, J. C., et al. (2001). Measurement of the rate of $\nu_e + d \rightarrow p + p + e^-$ interactions produced by ^8B solar neutrinos at the Sudbury Neutrino Observatory. *Phys. Rev. Lett.* 87:071301. doi: 10.1103/PhysRevLett.87.071301

Ahmad, Q. R., Allen, R. C., Andersen, T. C., Anglin, J. D., Bühler, G., Barton, J. C., et al. (2002). Direct evidence for neutrino flavor transformation from neutral current interactions in the Sudbury Neutrino Observatory. *Phys. Rev. Lett.* 89:011301. doi: 10.1103/PhysRevLett.89.011301

Ahmed, S., Sajjad Athar, M., Hasan, R., Salim, M., Singh, S. K., Inbanathan, S. S. R., et al. (2017). Physics Potential of the ICAL detector at the India-based Neutrino Observatory (INO). *Pramana* 88:79. doi: 10.1007/s12043-017-1373-4

Ahmed, Z., Amiri, M., Benton, S. J., Bock, J. J., Bowens-Rubin, R., Buder, I., et al. (2014). BICEP3: a 95GHz refracting telescope for degree-scale CMB polarization. 9153, 91531N. doi: 10.1117/12.2057224

Ahn, M. H., Aliu, E., Andringa, S., Aoki, S., Aoyama, Y., Argyriades, J., et al. (2006). Measurement of neutrino oscillation by the K2K experiment. *Phys. Rev. D* 74:072003. doi: 10.1103/PhysRevD.74.072003

Akhmedov, E. K., Johansson, R., Lindner, M., Ohlsson, T., and Schwetz, T. (2004). Series expansions for three flavor neutrino oscillation probabilities in matter. *J. High Energy Phys.* 04:078. doi: 10.1088/1126-6708/2004/04/078

Akhmedov, E. K., Lunardini, C., and Smirnov, A. Y. (2002). Supernova neutrinos: difference of muon-neutrino - tau-neutrino fluxes and conversion effects. *Nucl.Phys.* B643, 339–366. doi: 10.1016/S0550-3213(02)00692-2

Alam, S., Ata, M., Bailey, S., Beutler, F., Bizyaev, D., Blazek, J. A., et al. (2017). The clustering of galaxies in the completed SDSS-III Baryon Oscillation Spectroscopic Survey: cosmological analysis of the DR12 galaxy sample. *Mon. Not. Roy. Astron. Soc.* 470, 2617–2652. doi: 10.1093/mnras/stx721

Albert, J. B., Anton, G., Arnquist, I. J., Badhrees, I., Barbeau, P., Beck, D., et al. (2018). Sensitivity and discovery potential of nEXO to neutrinoless double beta decay. *Phys. Rev. C* 97:065503. doi: 10.1103/PhysRevC.97.065503

Albert, J. B., Auty, D. J., Barbeau, P. S., Beauchamp, E., Beck, D., Belov, V., Benitez-Medina, C., et al. (2014). Search for Majorana neutrinos with the first two years of EXO-200 data. *Nature* 510, 229–234. doi: 10.1038/nature13432

Alduino, C., Alfonso, K., Andreotti, E., Arnaboldi, C., Avignone, F. T. III., Azzolini, O., et al. (2018a). First results from CUORE: a search for lepton number violation via $0\nu\beta\beta$ Decay of ^{130}Te. *Phys. Rev. Lett.* 120:132501. doi: 10.1103/PhysRevLett.120.132501

Alduino, C., Alfonso, K., Artusa, D. R., Avignone, F. T. III., Azzolini, O., Balata, M., et al. (2016). CUORE-0 detector: design, construction and operation. *JINST* 11:P07009. doi: 10.1088/1748-0221/11/07/P07009

Alduino, C., Alfonso, K., Avignone, F. T. III., Azzolini, O., Bari, G., Bellini, F., et al. (2018b). Study of rare nuclear processes with CUORE. *Int. J. Mod. Phys.* A33:1843002. doi: 10.1142/S0217751X18430029

Alekseev, E., Alekseeva, L., Volchenko, V., and Krivosheina, I. (1987). Possible detection of a neutrino signal on 23 february 1987 at the baksan undergroundscintillation telescope of the institute of nuclear research. *JETP Lett.* 45, 589–592.

Alekseev, I., Belov, V., Brudanin, V., Danilov, M., Egorov, V., Filosofov, D., et al. (2018). Search for sterile neutrinos at the DANSS experiment. *High Energy Phys. Exp. arXiv:1804.04046v2.*

Alenkov, V., Aryal, P., Beyer, J., Boiko, R. S., Boonin, K., Buzanov, O., et al. (2015). Technical design report for the AMoRE $0\nu\beta\beta$ decay search experiment. *arXiv:1512.05957.*

Ali, Z. S., Parsons, A. R., Zheng, H., Pober, J. C., Liu, A., Aguirre, J. E., et al. (2015). PAPER-64 constraints on reionization: the 21cm power spectrum at z =8.4. *Astrophys. J.* 809:61. doi: 10.1088/0004-637X/809/1/61

Ali-Haimoud, Y., and Bird, S. (2012). An efficient implementation of massive neutrinos in non-linear structure formation simulations. *Mon. Not. R. Astron. Soc.* 428, 3375–3389. doi: 10.1093/mnras/sts286

Allen, S., Schmidt, R., and Bridle, S. (2003). A Preference for a non-zero neutrino mass from cosmological data. *Mon.Not.Roy.Astron.Soc.*, 346:593.

Allen, S. W., Evrard, A. E., and Mantz, A. B. (2011). Cosmological parameters from observations of galaxy clusters. *Ann. Rev. Astron. Astrophys.* 49, 409–470. doi: 10.1146/annurev-astro-081710-102514

Allison, R., Caucal, P., Calabrese, E., Dunkley, J., and Louis, T. (2015). Towards a cosmological neutrino mass detection. *Phys.Rev.D*, 92(12):123535.

Alonso, J., Barros, N., Bergevin, M., Bernstein, A., Bignell, L., Blucher, E., et al. (2014). Advanced scintillator detector concept (ASDC): a Concept Paper on the physics potential of water-based liquid scintillator. *e-Print: arXiv:1409.5864.*

Alpert, B., Balata, M., Bennett, D., Biasotti, M., Boragno, C., Brofferio, C., et al. (2015). HOLMES-The electron capture decay of ^{163}Ho to measure the electron neutrino mass with Sub-eV sensitivity. *Eur. Phys. J. C* 75:112. doi: 10.22323/1.244.0066

Amendola, L., Appleby, S., Bacon, D., Baker, T., Baldi, M., Bartolo, N., et al. (2018). Cosmology and fundamental physics with the euclid satellite. *Living Rev. Rel.* 21:2. doi: 10.1007/s41114-017-0010-3

An, F., An, G., An, Q., Antonelli, V., Baussan, E., Beacom, J., et al. (2016). Neutrino physics with JUNO. *J. Phys. G* 43:030401.

An, F. P., Bai, J. Z., Balantekin, A. B., Band, H. R., Beavis, D., Beriguete, W., et al. (2012). Observation of electron-antineutrino disappearance at Daya Bay. *Phys. Rev. Lett.* 108:171803. doi: 10.1103/PhysRevLett.108.171803

An, F. P., Balantekin, A. B., Band, H. R., Bishai, M., Blyth, S., Cao, D., et al. (2017). Measurement of electron antineutrino oscillation based on 1230 days of operation of the Daya Bay experiment. *Phys. Rev. D D* 95:072006. doi: 10.1103/PhysRevD.95.072006

Ananthakrishnan, S. (1995). The giant meterwave radio telescope/GMRT. *J. Astrophys. Astr. Suppl.* 16:427.

Anderson, L., Aubourg, E., Bailey, S., Beutler, F., Bhardwaj, V., Blanton, M., et al. (2014). The clustering of galaxies in the SDSS-III baryon oscillation spectroscopic survey: baryon acoustic oscillations in the Data Releases 10 and 11 Galaxy samples. *Mon. Not. R. Astron. Soc.*, 441, 24–62. doi: 10.1093/mnras/stu523

Anderson, L., Aubourg, E., Bailey, S., Bizyaev, D., Blanton, M., Bolton, A. S., et al. (2013). The clustering of galaxies in the SDSS-III baryon oscillation spectroscopic survey: baryon acoustic oscillations in the data release 9 spectroscopic galaxy sample. *Mon. Not. R. Astron. Soc.* 427, 3435–3467. doi: 10.1111/j.1365-2966.2012.22066.x

Andringa, S., Arushanova, E., Asahi, S., Askins, M., Auty, D. J., Back, A. R., et al. (2016). Current status and future prospects of the SNO+ experiment. *Adv. High Energy Phys.* 2016:6194250. doi: 10.1155/2016/6194250

Angrik, J., Armbrust, T., Beglarian, A., Besserer, U., Blumer, J., Bonn, J., et al. *KATRIN Design Report* (2004). Report NPI ASCR Řež, EXP-01/2005.

Archidiacono, M., Brinckmann, T., Lesgourgues, J., and Poulin, V. (2017). Physical effects involved in the measurements of neutrino masses with future cosmological data. *JCAP* 02:052. doi: 10.1088/1475-7516/2017/02/052

Archidiacono, M., Giusarma, E., Hannestad, S., and Mena, O. (2013a). Cosmic dark radiation and neutrinos. *Adv.High Energy Phys.*, 2013:191047.

Archidiacono, M., Giusarma, E., Melchiorri, A., and Mena, O. (2013b). Neutrino and dark radiation properties in light of recent CMB observations. *Phys.Rev.D*, 87(10):103519.

Archidiacono, M., and Hannestad, S. (2014). Updated constraints on non-standard neutrino interactions from Planck. *JCAP* 07:046. doi: 10.1088/1475-7516/2014/07/046

Archidiacono, M., and Hannestad, S. (2016). Efficient calculation of cosmological neutrino clustering in the non-linear regime. *JCAP* 06:018. doi: 10.1088/1475-7516/2016/06/018

Archidiacono, M., Hannestad, S., Mirizzi, A., Raffelt, G., and Wong, Y. Y. Y. (2013c). Axion hot dark matter bounds after Planck. *JCAP* 10:020. doi: 10.1088/1475-7516/2013/10/020

Arnold, R., Augier, C., Baker, J., Barabash, A. S., Basharina-Freshville, A., Bongrand, M., et al. (2010). Probing new physics models of neutrinoless double beta decay with superNEMO. *Eur. Phys. J. C* 70, 927–943. doi: 10.1140/epjc/s10052-010-1481-5

Arnold, R., Augier, C., Barabash, A. S., Basharina-Freshville, A., Blondel, S., Blot, S., et al. (2018). Final results on ^{82}Se double beta decay to the ground state of ^{82}Kr from the NEMO-3 experiment. *e-Print: arXiv:1806.05553.*

Arteaga, M., Bertuzzo, E., Perez-Gonzalez, Y. F., and Zukanovich Funchal, R. (2017). Impact of beyond the standard model physics in the detection of the cosmic neutrino background. *J. High Energy Phys.* 09:124. doi: 10.1007/JHEP09(2017)124

Artusa, D., Artusa, D. R., Avignone, F. T. III., Azzolini, O., Balata, M., Banks, T. I., et al. (2015). Searching for neutrinoless double-beta decay of ^{130}Te with CUORE. *Adv. High Energy Phys.* 2015:879871. doi: 10.1103/PhysRevLett.115.102502

Ascencio-Sosa, M., Calatayud-Cadenillas, A., Gago, A., and Jones-Pérez, J. (2018). Matter effects in neutrino visible decay at future long-baseline experiments. *J. High Energy Phys. arXiv:1805.03279.*

Asner, D. M., Bradley, R. F., de Viveiros, L., Doe, P. J., Fernandes, J. L., Fertl, M., et al. (2015). Single electron detection and spectroscopy via relativistic cyclotron radiation. *Phys. Rev. Lett.* 114:162501. doi: 10.1103/PhysRevLett.114.162501

Aubourg, E., Bailey, S., Bautista, J. E., Beutler, F., Bhardwaj, V., Bizyaev, D., et al. (2015). Cosmological implications of baryon acoustic oscillation measurements. *Phys. Rev. D* 92:123516. doi: 10.1103/PhysRevD.92.123516

Audren, B., Lesgourgues, J., Bird, S., Haehnelt, M. G., and Viel, M. (2013). Neutrino masses and cosmological parameters from a Euclid-like survey: markov chain monte carlo forecasts including theoretical errors. *JCAP* 01:026. doi: 10.1088/1475-7516/2013/01/026

Azzolini, O., Barrera, M. T., Beeman, J. W., Bellini, F., Beretta, M., Biassoni, M., et al. (2018). First result on the neutrinoless double beta decay of ^{82}Se with CUPID-0. *Phys. Rev. Lett.* 120:232502. doi: 10.1103/PhysRevLett.120.232502

Bakhti, P., and Farzan, Y. (2014). Shedding light on LMA-Dark solar neutrino solution by medium baseline reactor experiments: JUNO and RENO-50. *J. High Energy Phys.* 07:064. doi: 10.1007/JHEP07(2014)064

Bakhti, P., and Khan, A. N. (2017). Sensitivities to charged-current nonstandard neutrino interactions at DUNE. *J. Phys. G* 44:125001. doi: 10.1088/1361-6471/aa9098

Baldi, M., Villaescusa-Navarro, F., Viel, M., Puchwein, E., Springel, V., and Moscardini, L. (2014). Cosmic degeneracies – I. Joint N-body simulations of modified gravity and massive neutrinos. *Mon. Not. R. Astron. Soc.* 440, 75–88. doi: 10.1093/mnras/stu259

Balieiro Gomes, G., Forero, D., Guzzo, M., De Holanda, P., and Oliveira, R. N. (2018). Quantum decoherence effects in neutrino oscillations at DUNE. *High Energy Phys. arXiv:1805.09818.*

Ballett, P., King, S. F., Pascoli, S., Prouse, N. W., and Wang, T. (2017). Sensitivities and synergies of DUNE and T2HK. *Phys. Rev. D* 96:033003. doi: 10.1103/PhysRevD.96.033003

Banerjee, A., and Dalal, N. (2016). Simulating nonlinear cosmological structure formation with massive neutrinos. *JCAP* 11:015. doi: 10.1088/1475-7516/2016/11/015

Banerjee, A., Powell, D., Abel, T., and Villaescusa-Navarro, F. (2018). Reducing noise in cosmological N-body simulations with neutrinos. *JCAP arXiv:1801.03906.* doi: 10.1088/1475-7516/2018/09/028

Baracchini, E. et al. (2018). PTOLEMY: a proposal for thermal relic detection of massive neutrinos and directional detection of MeV dark matter. *Cosmol. Nongalact. Astrophys. arXiv:1808.01892.*

Barenboim, G., Masud, M., Ternes, C. A., and Tórtola, M. (2018a). Exploring the intrinsic Lorentz-violating parameters at DUNE. *High Energy Phys. arXiv:1805.11094.*

Barenboim, G., Mena Requejo, O., and Quigg, C. (2005). Diagnostic potential of cosmic-neutrino absorption spectroscopy. *Phys. Rev. D* 71:083002. doi: 10.1103/PhysRevD.71.083002

Barenboim, G., Ternes, C. A., and Tórtola, M. (2018b). Neutrinos, DUNE and the world best bound on CPT invariance. *Phys. Lett.* B780, 631–637. doi: 10.1016/j.physletb.2018.03.060

Barenboim, G., Ternes, C. A., and Tórtola, M. (2018c). New physics vs new paradigms: distinguishing CPT violation from NSI. *High Energy Phys. arXiv:1804.05842.*

Barger, V., Marfatia, D., and Tregre, A. (2004). Neutrino mass limits from SDSS, 2dFGRS and WMAP. *Phys. Lett.* B595, 55–59. doi: 10.1016/j.physletb.2004.06.049

Barkana, R. (2018). Possible interaction between baryons and dark-matter particles revealed by the first stars. *Nature* 555, 71–74. doi: 10.1038/nature25791

Barkana, R., and Loeb, A. (2005a). A Method for separating the physics from the astrophysics of high-redshift 21 cm fluctuations. *Astrophys. J.* 624, L65–L68. doi: 10.1086/430599

Barkana, R., and Loeb, A. (2005b). Probing the epoch of early baryonic infall through 21cm fluctuations. *Mon. Not. R. Astron. Soc.* 363, L36–L40. doi: 10.1111/j.1745-3933.2005.00079.x

Barkana, R., Outmezguine, N. J., Redigolo, D., and Volansky, T. (2018). Signs of Dark Matter at 21-cm? *Cosmol. Nongalact. Astrophy. arXiv:1803.03091.*

Barreira, A., Li, B., Baugh, C., and Pascoli, S. (2014). Modified gravity with massive neutrinos as a testable alternative cosmological model. *Phys. Rev. D* 90:023528. doi: 10.1103/PhysRevD.90.023528

Basse, T., Bjaelde, O. E., Hamann, J., Hannestad, S., and Wong, Y. Y. (2014). Dark energy properties from large future galaxy surveys. *JCAP* 05:021. doi: 10.1088/1475-7516/2014/05/021

Bautista, J. E., Busca, N. G., Guy, J., Rich, J., Blomqvist, M., Bourboux, H. d. M. d., et al. (2017a). Measurement of BAO correlations at $z = 2.3$ with SDSS DR12 Lyα-Forests. *Astron. Astrophys.* 603:A12. doi: 10.1051/0004-6361/201730533

Bautista, J. E., Vargas-Magaña, M., Dawson, K. S., Percival, W. J., Brinkmann, J., Brownstein, J., et al. (2017b). The SDSS-IV extended baryon oscillation spectroscopic survey: baryon acoustic oscillations at redshift of 0.72 with the DR14 luminous red galaxy sample. *Astrophys. J.* 863:110. doi: 10.3847/1538-4357/aacea5

Beacom, J. F., Bell, N. F., and Dodelson, S. (2004). Neutrinoless universe. *Phys. Rev. Lett.* 93:121302. doi: 10.1103/PhysRevLett.93.121302

Beacom, J. F., and Vogel, P. (1998). Mass signature of supernova muon-neutrino and tau-neutrino neutrinos in Super-Kamiokande. *Phys. Rev. D* 58:053010. doi: 10.1103/PhysRevD.58.053010

Beardsley, A. P., Morales, M. F., Lidz, A., Malloy, M., and Sutter, P. M. (2015). Adding context to james webb space telescope surveys with current and future 21cm radio observations. *Astrophys. J.* 800:128. doi: 10.1088/0004-637X/800/2/128

Behera, S. P., Ghosh, A., Choubey, S., Datar, V. M., Mishra, D. K., and Mohanty, A. K. (2017). Search for the sterile neutrino mixing with the ICAL detector at INO. *Eur. Phys. J. C* 77:307. doi: 10.1140/epjc/s10052-017-4851-4

Bell, N. F., Pierpaoli, E., and Sigurdson, K. (2006). Cosmological signatures of interacting neutrinos. *Phys. Rev. D* 73:063523. doi: 10.1103/PhysRevD.73.063523

Bellini, G., Benziger, J., Bick, D., Bonfini, G., Bravo, D., Avanzini, M. B., et al. (2014). Final results of Borexino Phase-I on low energy solar neutrino spectroscopy. *Phys. Rev. D*, 89:112007. doi: 10.1103/PhysRevD.89.112007

Bellomo, N., Bellini, E., Hu, B., Jimenez, R., Peña-Garay, C., and Verde, L. (2017). Hiding neutrino mass in modified gravity cosmologies. *JCAP* 02:043. doi: 10.1088/1475-7516/2017/02/043

Benson, B., Ade, P. A. R., Ahmed, Z., Allen, S. W., Arnold, K., Austermann, J. E., et al. (2014). "SPT-3G: a next-generation cosmic microwave background polarization experiment on the south pole telescope," *Proceedings Volume 9153, Millimeter, Submillimeter, and Far-Infrared Detectors and Instrumentation for Astronomy VII* (Montréal, QC).

Berlin, A., Hooper, D., Krnjaic, G., and McDermott, S. D. (2018). Severely constraining dark matter interpretations of the 21-cm anomaly. *Phys. Rev. Lett.* 121:011102. doi: 10.1103/PhysRevLett.121.011102

Berryman, J. M., de Gouvea, A., Kelly, K. J., and Kobach, A. (2015). Sterile neutrino at the deep underground neutrino experiment. *Phys. Rev. D* 92:073012. doi: 10.1103/PhysRevD.92.073012

Berryman, J. M., de Gouvea, A., Kelly, K. J., Peres, O. L. G., and Tabrizi, Z. (2016). Large, extra dimensions at the deep underground neutrino experiment. *Phys. Rev. D* 94:033006. doi: 10.1103/PhysRevD.94.033006

Betoule, M., Kessler, R., Guy, J., Mosher, J., Hardin, D., Biswas, R., et al. (2014). Improved cosmological constraints from a joint analysis of the SDSS-II and SNLS supernova samples. *Astron. Astrophys.* 568:A22. doi: 10.1051/0004-6361/201423413

Betoule, M., Marriner, J., Regnault, N., Cuillandre, J.-C., Astier, P., Guy, J., et al. (2013). Improved photometric calibration of the SNLS and the SDSS supernova surveys. *Astron. Astrophys.* 552:A124. doi: 10.1051/0004-6361/201220610

Betts, S., Blanchard, W. R., Carnevale, R. H., Chang, C., Chen, C., Chidzik, S., et al. (2013). "Development of a Relic Neutrino Detection Experiment at PTOLEMY: Princeton Tritium Observatory for Light, Early-Universe, Massive-Neutrino Yield." in *Proceedings, Community Summer Study 2013: Snowmass on the Mississippi (CSS2013)* (Minneapolis, MN).

Beutler, F., Blake, C., Colless, M., Jones, D. H., Staveley-Smith, L., Campbell, L., Parker, Q., Saunders, W., and Watson, F. (2011). The 6dF galaxy survey: baryon acoustic oscillations and the local hubble constant. *Mon. Not. Roy. Astron. Soc.* 416, 3017–3032. doi: 10.1111/j.1365-2966.2011.19250.x

Beutler, F., Seo, H.-J., Ross, A. J., McDonald, P., Saito, S., Bolton, A. S., et al. (2017b). The clustering of galaxies in the completed SDSS-III Baryon Oscillation spectroscopic survey: baryon acoustic oscillations in Fourier-space. *Mon. Not. R. Astron. Soc.* 464, 3409–3430. doi: 10.1093/mnras/stw2373

Beutler, F., Seo, H.-J., Saito, S., Chuang, C.-H., Cuesta, A. J., Eisenstein, D. J., et al. (2017a). The clustering of galaxies in the completed SDSS-III baryon oscillation spectroscopic survey: anisotropic galaxy clustering in Fourier-space. *Mon. Not. R. Astron. Soc.* 466, 2242–2260. doi: 10.1093/mnras/stw3298

Bionta, R., Blewitt, G., Bratton, C. B., Casper, D., Ciocio, A., Claus, R., Cortez, B., et al. (1987). Observation of a neutrino burst in coincidence with supernova SN 1987a in the large magellanic cloud. *Phys. Rev. Lett.* 58:1494. doi: 10.1103/PhysRevLett.58.1494

Bird, S., Viel, M., and Haehnelt, M. G. (2012). Massive Neutrinos and the Non-linear Matter Power Spectrum. *Mon. Not. R. Astron. Soc.* 420, 2551–2561. doi: 10.1111/j.1365-2966.2011.20222.x

Bjaelde, O. E. et al. (2008). Neutrino dark energy–revisiting the stability issue. *JCAP* 01:026. doi: 10.1088/1475-7516/2008/01/026

Blake, C., Kazin, E., Beutler, F., Davis, T., Parkinson, D., Brough, S., et al. (2011). The WiggleZ Dark Energy Survey: mapping the distance-redshift relation with baryon acoustic oscillations. *Mon. Not. R. Astron. Soc.* 418, 1707–1724. doi: 10.1111/j.1365-2966.2011.19592.x

Blas, D., Lesgourgues, J., and Tram, T. (2011). The cosmic linear anisotropy solving system (CLASS) II: approximation schemes. *JCAP* 07:034. doi: 10.1088/1475-7516/2011/07/034

Blennow, M. (2008). Prospects for cosmic neutrino detection in tritium experiments in the case of hierarchical neutrino masses. *Phys. Rev. D* 77:113014. doi: 10.1103/PhysRevD.77.113014

Blennow, M. (2014). On the Bayesian approach to neutrino mass ordering. *J. High Energy Phys.* 01:139. doi: 10.1007/JHEP01(2014)139

Blennow, M., Coloma, P., Fernandez-Martinez, E., Hernandez-Garcia, J., and Lopez-Pavon, J. (2017). Non-Unitarity, sterile neutrinos, and Non-Standard neutrino Interactions. *J. High Energy Phys.* 04:153. doi: 10.1007/JHEP04(2017)153

Blennow, M., Coloma, P., Huber, P., and Schwetz, T. (2014). Quantifying the sensitivity of oscillation experiments to the neutrino mass ordering. *J. High Energy Phys.* 03:028. doi: 10.1007/JHEP03(2014)028

Blennow, M., and Schwetz, T. (2013). Determination of the neutrino mass ordering by combining PINGU and Daya Bay II. *J. High Energy Phys.* 09:089. doi: 10.1007/JHEP09(2013)089

Blennow, M., and Smirnov, A. Y. (2013). Neutrino propagation in matter. *Adv. High Energy Phys.* 2013:972485. doi: 10.1155/2013/972485

Boehm, C., Dolan, M. J., and McCabe, C. (2012). Increasing Neff with particles in thermal equilibrium with neutrinos. *JCAP* 12:027. doi: 10.1088/1475-7516/2012/12/027

Bond, J., Efstathiou, G., and Tegmark, M. (1997). Forecasting cosmic parameter errors from microwave background anisotropy experiments. *Mon. Not. R. Astron. Soc.* 291, L33–L41. doi: 10.1093/mnras/291.1.L33

Bond, J., Jaffe, A. H., and Knox, L. (2000). Radical compression of cosmic microwave background data. *Astrophys. J.* 533:19. doi: 10.1086/308625

Bond, J. R., Efstathiou, G., and Silk, J. (1980). Massive neutrinos and the large scale structure of the universe. *Phys. Rev. Lett.* 45, 1980–1984. doi: 10.1103/PhysRevLett.45.1980

Bourboux, H. d. M. d., Le Goff, J.-M., Blomqvist, M., Busca, N. G., Guy, J., Rich, J., et al. (2017). Baryon acoustic oscillations from the complete SDSS-III Lyα-quasar cross-correlation function at $z = 2.4$. *Astron. Astrophys.* 608:A130. doi: 10.1051/0004-6361/201731731

Bowman, J. D., Morales, M. F., and Hewitt, J. N. (2007). Constraints on fundamental cosmological parameters with upcoming epoch of reionization observations. *Astrophys. J.* 661, 1–9. doi: 10.1086/516560

Bowman, J. D., and Rogers, A. E. (2010). A lower limit of dz $>$ 0.06 for the duration of the reionization epoch. *Nature* 468, 796–798. doi: 10.1038/nature09601

Bowman, J. D., Rogers, A. E. E., Monsalve, R. A., Mozdzen, T. J., and Mahesh, N. (2018). An absorption profile centred at 78 megahertz in the sky-averaged spectrum. *Nature* 555, 67–70. doi: 10.1038/nature25792

Brandbyge, J., and Hannestad, S. (2009). Grid based linear neutrino perturbations in cosmological N-body simulations. *JCAP* 05:002. doi: 10.1088/1475-7516/2009/05/002

Brookfield, A., van de Bruck, C., Mota, D., and Tocchini-Valentini, D. (2006a). Cosmology with massive neutrinos coupled to dark energy. *Phys. Rev. Lett.* 96:061301. doi: 10.1103/PhysRevLett.96.061301

Brookfield, A. W., van de Bruck, C., Mota, D., and Tocchini-Valentini, D. (2006b). Cosmology of mass-varying neutrinos driven by quintessence: theory and observations. *Phys. Rev. D* 73:083515. doi: 10.1103/PhysRevD.73.08351510.1103/PhysRevD.76.049901

Bull, P., Ferreira, P. G., Patel, P., and Santos, M. G. (2015). Late-time cosmology with 21cm intensity mapping experiments. *Astrophys. J.* 803:21. doi: 10.1088/0004-637X/803/1/21

Burns, J. O., Lazio, T. J. W., Bale, S. D., Bowman, J. D., Bradley, R. F., Carilli, C. L., et al. (2012). Probing the first stars and black holes in the early universe with the dark ages radio explorer (DARE). *Adv. Space Res.* 49, 433–450. doi: 10.1016/j.asr.2011.10.014

Busca, N. G., Delubac, T., Rich, J., Bailey, S., Font-Ribera, A., Kirkby, D., et al. (2013). Baryon acoustic oscillations in the Ly-α forest of BOSS quasars. *Astron. Astrophys.* 552:A96. doi: 10.1051/0004-6361/201220724

Caldwell, A., Merle, A., Schulz, O., and Totzauer, M. (2017). A global bayesian analysis of neutrino mass data. *Phys. Rev. D* 96:073001. doi: 10.1103/PhysRevD.96.073001

Caldwell, R., Dave, R., and Steinhardt, P. J. (1998). Cosmological imprint of an energy component with general equation of state. *Phys. Rev. Lett.* 80, 1582–1585. doi: 10.1103/PhysRevLett.80.1582

Canac, N., Aslanyan, G., Abazajian, K. N., Easther, R., and Price, L. C. (2016). Testing for new physics: neutrinos and the primordial power spectrum. *JCAP* 09:022. doi: 10.1088/1475-7516/2016/09/022

Capozzi, F., Di Valentino, E., Lisi, E., Marrone, A., Melchiorri, A., and Palazzo, A. (2017). Global constraints on absolute neutrino masses and their ordering. *Phys. Rev. D D* 95:096014. doi: 10.1103/PhysRevD.95.096014

Capozzi, F., Lisi, E., and Marrone, A. (2015). PINGU and the neutrino mass hierarchy: Statistical and systematic aspects. *Phys. Rev. D* 91:073011. doi: 10.1103/PhysRevD.91.073011

Capozzi, F., Lisi, E., Marrone, A., and Palazzo, A. (2018a). Current unknowns in the three neutrino framework. *Prog. Part. Nucl. Phys.* 102, 48–72. doi: 10.1016/j.ppnp.2018.05.005

Capozzi, F., Shoemaker, I. M., and Vecchi, L. (2018b). Neutrino oscillations in dark backgrounds. *JCAP* 07:004. doi: 10.1088/1475-7516/2018/07/004

Carbone, C., Fedeli, C., Moscardini, L., and Cimatti, A. (2012). Measuring the neutrino mass from future wide galaxy cluster catalogues. *JCAP* 03:023. doi: 10.1088/1475-7516/2012/03/023

Carbone, C., Verde, L., Wang, Y., and Cimatti, A. (2011). Neutrino constraints from future nearly all-sky spectroscopic galaxy surveys. *JCAP* 03:030. doi: 10.1088/1475-7516/2011/03/030

Castorina, E., Sefusatti, E., Sheth, R. K., Villaescusa-Navarro, F., and Viel, M. (2014). Cosmology with massive neutrinos II: on the universality of the halo mass function and bias. *JCAP* 02:049. doi: 10.1088/1475-7516/2014/02/049

Chakraborty, K., Deepthi, K., Goswami, S., Joshipura, A. S., and Nath, N. (2018). Partial μ-τ reflection symmetry and its verification at DUNE and hyper-kamiokande. *High Energy Phys. arXiv:1804.02022.*

Chang, C., Pujol, A., Gaztanaga, E., Amara, A., Refregier, A., Bacon, D., et al. (2016). Galaxy bias from the dark energy survey science verification data: combining galaxy density maps and weak lensing maps. *Mon. Not. R. Astron. Soc.* 459, 3203–3216. doi: 10.1093/mnras/stw861

Chang, T.-C., Pen, U.-L., Peterson, J. B., and McDonald, P. (2008). Baryon acoustic oscillation intensity mapping as a test of dark energy. *Phys. Rev. Lett.* 100:091303. doi: 10.1103/PhysRevLett.100.091303

Chatterjee, A., Gandhi, R., and Singh, J. (2014). Probing lorentz and CPT violation in a magnetized iron detector using atmospheric neutrinos. *J. High Energy Phys.* 06:045. doi: 10.1007/JHEP06(2014)045

Chatterjee, S. S., Masud, M., Pasquini, P., and Valle, J. (2017a). Cornering the revamped BMV model with neutrino oscillation data. *Phys. Lett.* B774, 179–182. doi: 10.1016/j.physletb.2017.09.052

Chatterjee, S. S., Pasquini, P., and Valle, J. W. F. (2017b). Probing atmospheric mixing and leptonic CP violation in current and future long baseline oscillation experiments. *Phys. Lett.* B771, 524–531. doi: 10.1016/j.physletb.2017.05.080

Chen, C.-S., Lee, F.-F., Lin, G.-L., and Lin, Y.-H. (2014). Probing dark matter self-interaction in the sun with iceCube-PINGU. *JCAP* 10:049. doi: 10.1088/1475-7516/2014/10/049

Chen, X. et al. (2017). PandaX-III: Searching for neutrinoless double beta decay with high pressure^{136}Xe gas time projection chambers. *Sci. China Phys. Mech. Astron.* 60:061011. doi: 10.1007/s11433-017-9028-0

Chen, Y., and Xu, L. (2016). Galaxy clustering, CMB and supernova data constraints on ϕ CDM model with massive neutrinos. *Phys. Lett.* B752, 66–75. doi: 10.1016/j.physletb.2015.11.022

Cheung, K., Kuo, J.-L., Ng, K.-W., and Tsai, Y.-L. S. (2018). The impact of EDGES 21-cm data on dark matter interactions. *arXiv:1803.09398.*

Chevallier, M., and Polarski, D. (2001). Accelerating universes with scaling dark matter. *Int. J. Mod. Phys.* D10, 213–224. doi: 10.1142/S0218271801000822

Choubey, S., Dasgupta, B., Dighe, A., and Mirizzi, A. (2010). Signatures of collective and matter effects on supernova neutrinos at large detectors. *arXiv:1008.0308.*

Choubey, S., Ghosh, A., Ohlsson, T., and Tiwari, D. (2015). Neutrino physics with non-standard interactions at INO. *J. High Energy Phys.* 12:126. doi: 10.1007/JHEP12(2015)126

Choubey, S., Ghosh, A., and Tiwari, D. (2018a). Prospects of Indirect Searches for Dark Matter at INO. *JCAP* 05:006. doi: 10.1088/1475-7516/2018/05/006

Choubey, S., Goswami, S., Gupta, C., Lakshmi, S., and Thakore, T. (2018b). Sensitivity to neutrino decay with atmospheric neutrinos at the INO-ICAL detector. *Phys. Rev. D* 97:033005. doi: 10.1103/PhysRevD.97.033005

Choubey, S., Goswami, S., and Pramanik, D. (2018c). A Study of Invisible Neutrino Decay at DUNE and its Effects on θ_{23} Measurement. *J High Energy Phys.* 02:055. doi: 10.1007/JHEP02(2018)055

Choubey, S., and Ohlsson, T. (2014). Bounds on non-standard neutrino interactions using PINGU. *Phys. Lett.* B739, 357–364. doi: 10.1016/j.physletb.2014.11.010

Clark, S., Dutta, B., Gao, Y., Ma, Y.-Z., and Strigari, L. E. (2018). 21cm limits on decaying dark matter and primordial black holes. *Phys. Rev. D* 98:043006. doi: 10.1103/PhysRevD.98.043006

Clesse, S., Lopez-Honorez, L., Ringeval, C., Tashiro, H., and Tytgat, M. H. (2012). Background reionization history from omniscopes. *Phys. Rev. D* 86:123506. doi: 10.1103/PhysRevD.86.123506

Cleveland, B., Daily, T., Davis, R. Jr., Distel1, J. R., Lande, K., Lee, C. K., et al. (1998). Measurement of the solar electron neutrino flux with the Homestake chlorine detector. *Astrophys. J.* 496, 505–526. doi: 10.1086/305343

Cocco, A. G., Mangano, G., and Messina, M. (2007). Probing low energy neutrino backgrounds with neutrino capture on beta decaying nuclei. *JCAP* 06:015. doi: 10.1088/1475-7516/2007/06/015

Cole, S., Percival, W. J., Peacock, J. A., Norberg, P., Baugh, C. M., Frenk, C. S., et al. (2005). The 2dF galaxy redshift survey: power-spectrum analysis of the final dataset and Cosmological Implications. *Mon. Not. R. Astron. Soc.* 362, 505–534. doi: 10.1111/j.1365-2966.2005.09318.x

Coloma, P. (2016). Non-standard interactions in propagation at the deep underground neutrino experiment. *J. High Energy Phys.* 03:016. doi: 10.1007/JHEP03(2016)016

Coloma, P., Denton, P. B., Gonzalez-Garcia, M. C., Maltoni, M., and Schwetz, T. (2017). Curtailing the dark side in non-standard neutrino interactions. *J. High Energy Phys.* 04:116. doi: 10.1007/JHEP04(2017)116

Coloma, P., Forero, D. V., and Parke, S. J. (2018). DUNE sensitivities to the mixing between sterile and tau neutrinos. *J. High Energ. Phys.* 07:079. doi: 10.1007/JHEP07(2018)079

Coloma, P., and Peres, O. L. G. (2017). Visible neutrino decay at DUNE. *J. High Energy Phys. arXiv:1705.03599.*

Coloma, P., and Schwetz, T. (2016). Generalized mass ordering degeneracy in neutrino oscillation experiments. *Phys. Rev. D* 94:055005. doi: 10.1103/PhysRevD.95.079903

Cooray, A. R. (1999). Weighing neutrinos: weak lensing approach. *Astron. Astrophys.* 348:31.

Costa, A. A., Landim, R. C., Wang, B., and Abdalla, E. (2018). Interacting dark energy: possible explanation for 21-cm absorption at cosmic dawn. *Eur. Phys. J. C* 78:746. doi: 10.1140/epjc/s10052-018-6237-7

Costanzi, M., Sartoris, B., Viel, M., and Borgani, S. (2014). Neutrino constraints: what large-scale structure and CMB data are telling us? *JCAP* 10:081. doi: 10.1088/1475-7516/2014/10/081

Costanzi, M., Villaescusa-Navarro, F., Viel, M., Xia, J.-Q., Borgani, S., Castorina, E., et al. (2013). Cosmology with massive neutrinos III: the halo mass function andan application to galaxy clusters. *JCAP* 12:012. doi: 10.1088/1475-7516/2013/12/012

Cravens, J. et al. (2008). Solar neutrino measurements in Super-Kamiokande-II. *Phys.Rev.D*, 78:032002.

Croft, R. A., Hu, W., and Dave, R. (1999). Cosmological Limits on the Neutrino Mass from the Lya Forest. *Phys. Rev. Lett.* 83, 1092–1095. doi: 10.1103/PhysRevLett.83.1092

Crotty, P., Lesgourgues, J., and Pastor, S. (2004). Current cosmological bounds on neutrino masses and relativistic relics. *Phys. Rev. D* 69:123007. doi: 10.1103/PhysRevD.69.123007

Cuesta, A. J., Niro, V., and Verde, L. (2016). Neutrino mass limits: robust information from the power spectrum of galaxy surveys. *Phys. Dark Univ.* 13, 77–86. doi: 10.1016/j.dark.2016.04.005

Dakin, J., Brandbyge, J., Hannestad, S., Haugbølle, T., and Tram, T. (2017). νCONCEPT: Cosmological neutrino simulations from the non-linear Boltzmann hierarchy. *arXiv:1712.03944.*

D'Amico, G., Panci, P., and Strumia, A. (2018). Bounds on dark matter annihilations from 21 cm data. *Phys. Rev. Lett.* 121:011103. doi: 10.1103/PhysRevLett.121.011103

Dasgupta, B., Dighe, A., Raffelt, G. G., and Smirnov, A. Y. (2009). Multiple spectral splits of supernova neutrinos. *Phys. Rev. Lett.* 103:051105. doi: 10.1103/PhysRevLett.103.051105

Dasgupta, B., Mirizzi, A., Tamborra, I., and Tomas, R. (2010). Neutrino mass hierarchy and three-flavor spectral splits of supernova neutrinos. *Phys. Rev. D* 81:093008. doi: 10.1103/PhysRevD.81.093008

Dash, N., Datar, V., and Majumder, G. (2016). Sensitivity for detection of decay of dark matter particle using ICAL at INO. *Pramana* 86, 927–937. doi: 10.1007/s12043-015-1094-5

Dawson, K. S., Kneib, J.-P., Percival, W. J., Alam, S., Albareti, F. D., Anderson, S. F., et al. (2016). The SDSS-IV extended baryon oscillation spectroscopic survey: overview and early data. *Astron. J.* 151:44. doi: 10.3847/0004-6256/151/2/44

Dawson, K. S., Schlegel, D. J., Ahn, C. P., Anderson, S. F., Aubourg, É., Bailey, S., et al. (2013). The baryon oscillation spectroscopic survey of SDSS-III. *Astron. J.* 145:10. doi: 10.1088/0004-6256/145/1/10

De Bernardis, F., Kitching, T. D., Heavens, A., and Melchiorri, A. (2009). Determining the neutrino mass hierarchy with cosmology. *Phys. Rev. D* 80:123509. doi: 10.1103/PhysRevD.80.123509

De Bernardis, F., Stevens, J. R., Hasselfield, M., Alonso, D., Bond, J. R., Calabrese, E., et al. (2016). "Survey strategy optimization for the atacama Cosmology telescope," in *Proceedings Volume 9910, Observatory Operations: Strategies, Processes, and Systems VI; 991014* (Edinburgh).

de Gouvêa, A., and Kelly, K. J. (2016). Non-standard neutrino interactions at DUNE. *Nucl. Phys.* B908, 318–335. doi: 10.1016/j.nuclphysb.2016.03.013

de Gouvêa, A. and Kelly, K. J. (2017). Neutrino vs. Antineutrino oscillation parameters at DUNE and hyper-kamiokande. *Phys. Rev. D* 96:095018. doi: 10.1103/PhysRevD.96.095018

de Haan, T., Benson, B. A., Bleem, L. E., Allen, S. W., Applegate, D. E., Ashby, M. L. N., et al. (2016). Cosmological constraints from galaxy clusters in the 2500 square-degree SPT-SZ survey. *Astrophys. J.* 832:95. doi: 10.3847/0004-637X/832/1/95

de Putter, R., Linder, E. V., and Mishra, A. (2014). Inflationary freedom and cosmological neutrino constraints. *Phys. Rev. D* 89:103502. doi: 10.1103/PhysRevD.89.103502

de Putter, R., Mena, O., Giusarma, E., Ho, S., Cuesta, A., Seo, H.-J., et al. (2012). New neutrino mass bounds from sloan digital sky survey

III data release 8 photometric luminous galaxies. *Astrophys. J.* 761:12. doi: 10.1088/0004-637X/761/1/12

de Putter, R., Zahn, O., and Linder, E. V. (2009). CMB lensing constraints on neutrinos and dark energy. *Phys. Rev. D* 79:065033. doi: 10.1103/PhysRevD.79.065033

De Romeri, V., Fernandez-Martinez, E., and Sorel, M. (2016). Neutrino oscillations at DUNE with improved energy reconstruction. *J. High Energy Phys.* 09:030. doi: 10.1007/JHEP09(2016)030

De Rujula, A., and Lusignoli, M. (1982). Calorimetric measurements of ^{163}Ho decay as tools to determine the electron neutrino mass. *Phys. Lett.* B118:429. doi: 10.1016/0370-2693(82)90218-0

de Salas, P., Forero, D., Ternes, C., Tórtola, M., and Valle, J. (2018). Status of neutrino oscillations 2018: 3 σ hint for normal mass ordering and improved CP sensitivity. *Phys. Lett.* B782, 633–640. doi: 10.1016/j.physletb.2018.06.019

de Salas, P. F., Gariazzo, S., Lesgourgues, J., and Pastor, S. (2017). Calculation of the local density of relic neutrinos. *JCAP* 09:034. doi: 10.1088/1475-7516/2017/09/034

de Salas, P. F., and Pastor, S. (2016). Relic neutrino decoupling with flavour oscillations revisited. *JCAP* 07:051. doi: 10.1088/1475-7516/2016/07/051

Debono, I., Rassat, A., Refregier, A., Amara, A., and Kitching, T. (2010). Weak lensing forecasts for dark energy, neutrinos and initial conditions. *Mon. Not. R. Astron. Soc.* 404, 110–119. doi: 10.1111/j.1365-2966.2010.16284.x

Deepthi, K. N., Goswami, S., and Nath, N. (2017). Nonstandard interactions jeopardizing the hierarchy sensitivity of DUNE. *Phys. Rev. D* 96:075023. doi: 10.1103/PhysRevD.96.075023

Delabrouille, J., de Bernardis, P., Bouchet, F. R., Achúcarro, A., Ade, P. A. R., Allison, R., et al. (2018). Exploring cosmic origins with CORE: survey requirements and mission design. *JCAP* 04:014. doi: 10.1088/1475-7516/2018/04/014

Dell'Oro, S., Marcocci, S., Viel, M., and Vissani, F. (2016). Neutrinoless double beta decay: 2015 review. *Adv. High Energy Phys.* 2016:2162659. doi: 10.1155/2016/2162659

Delubac, T., Bautista, J. E., Busca, N. G., Rich, J., Kirkby, D., Bailey, S., et al. (2015). Baryon acoustic oscillations in the Lyα forest of BOSS DR11 quasars. *Astron. Astrophys.* 574:A59. doi: 10.1051/0004-6361/201423969

Dentler, M., Hernández-Cabezudo, á., Kopp, J., Machado, P. A. N., Maltoni, M., Martinez-Soler, I., et al. (2018). Updated global analysis of neutrino oscillations in the presence of eV-scale sterile neutrinos. *J. High Energy Phys.* 08:010. doi: 10.1007/JHEP08(2018)010

Dentler, M., Hernández-Cabezudo, A., Kopp, J., Maltoni, M., and Schwetz, T. (2017). Sterile neutrinos or flux uncertainties?-status of the reactor anti-neutrino anomaly. *J. High Energy Phys.* 11:099. doi: 10.1007/JHEP11(2017)099

Desjacques, V., Jeong, D., and Schmidt, F. (2018). Large-scale galaxy bias. *Phys. Rept.* 733:1–193. doi: 10.1016/j.physrep.2017.12.002

Dewdney, P., Turner, W., Millenaar, R., McCool, R., Lazio, J., Cornwell, T. J., et al. (2015). *SKA Baseline Description*. Available online at: https://www.skatelescope.org/wp-content/uploads/2014/03/SKA-TEL-SKO-0000308_SKA1_System_Baseline_v2_DescriptionRev01-part-1-signed.pdf.

Di Valentino, E., Brinckmann, T., Gerbino, M., Poulin, V., Bouchet, F. R., Lesgourgues, J., et al. (2018a). Exploring cosmic origins with cORE: cosmological parameters. *JCAP* 04:017. doi: 10.1088/1475-7516/2018/04/017

Di Valentino, E., Gariazzo, S., Gerbino, M., Giusarma, E., and Mena, O. (2016a). Dark radiation and inflationary freedom after planck 2015. *Phys. Rev. D D* 93:083523. doi: 10.1103/PhysRevD.93.083523

Di Valentino, E., Gariazzo, S., Giusarma, E., and Mena, O. (2015). Robustness of cosmological axion mass limits. *Phys. Rev. D D* 91:123505. doi: 10.1103/PhysRevD.91.123505

Di Valentino, E., Giusarma, E., Lattanzi, M., Mena, O., Melchiorri, A., and Silk, J. (2016b). Cosmological Axion and neutrino mass constraints from Planck 2015 temperature and polarization data. *Phys. Lett.* B752, 182–185. doi: 10.1016/j.physletb.2015.11.025

Di Valentino, E., Giusarma, E., Mena, O., Melchiorri, A., and Silk, J. (2016c). Cosmological limits on neutrino unknowns versus low redshift priors. *Phys. Rev. D* 93:083527. doi: 10.1103/PhysRevD.93.083527

Di Valentino, E., hm, C. B. e., Hivon, E., and Bouchet, F. R. (2018b). Reducing the H_0 and σ_8 tensions with Dark Matter-neutrino interactions. *Phys. Rev. D* 97:043513. doi: 10.1103/PhysRevD.97.043513

Di Valentino, E., Melchiorri, A., and Mena, O. (2013). Dark radiation sterile neutrino candidates after Planck data. *JCAP* 11:018. doi: 10.1088/1475-7516/2013/11/018

Dirian, Y. (2017). Changing the prior: absolute neutrino mass constraints in nonlocal gravity. *Phys. Rev. D* 96:083513. doi: 10.1103/PhysRevD.96.083513

Doe, P., Kofron, J., McBride, E. L., Robertson, R. G. H., Rosenberg, L. J., Rybka, G., S. et al. (2013) Project 8: determining neutrino mass from tritium beta decay using a frequency-based method. *Nuclear Exp.* arXiv:1309.7093.

Domcke, V., and Spinrath, M. (2017). Detection prospects for the cosmic neutrino background using laser interferometers. *JCAP* 06:055. doi: 10.1088/1475-7516/2017/06/055

Duan, H., Fuller, G. M., Carlson, J., and Qian, Y.-Z. (2007). Neutrino mass hierarchy and stepwise spectral swapping of supernova neutrino flavors. *Phys. Rev. Lett.* 99:241802. doi: 10.1103/PhysRevLett.99.241802

Duan, H., Fuller, G. M., and Qian, Y.-Z. (2010). Collective neutrino oscillations. *Ann. Rev. Nucl. Part. Sci.* 60, 569–594. doi: 10.1146/annurev.nucl.012809.104524

Duda, G., Gelmini, G., and Nussinov, S. (2001). Expected signals in relic neutrino detectors. *Phys. Rev. D* 64:122001. doi: 10.1103/PhysRevD.64.122001

Dutta, D., Ghoshal, P., and Roy, S. (2017). Effect of non unitarity on neutrino mass hierarchy determination at DUNE, NOνA and T2K. *Nucl. Phys.* B920, 385–401. doi: 10.1016/j.nuclphysb.2017.04.018

Dvali, G., and Funcke, L. (2016). Small neutrino masses from gravitational θ-term. *Phys. Rev. D* 93:113002. doi: 10.1103/PhysRevD.93.113002

Eberle, B., Ringwald, A., Song, L., and Weiler, T. J. (2004). Relic neutrino absorption spectroscopy. *Phys. Rev. D* 70:023007. doi: 10.1103/PhysRevD.70.023007

Efstathiou, G. (2014). H0 revisited. *Mon. Not. R. Astron. Soc.* 440, 1138–1152. doi: 10.1093/mnras/stu278

Eguchi, K., Enomoto, S., Furuno, K., Goldman, J., Hanada, H., Ikeda, H. et al. (2003). First results from KamLAND: evidence for reactor anti-neutrino disappearance. *Phys. Rev. Lett.* 90:021802. doi: 10.1103/PhysRevLett.90.021802

Eisenstein, D. J., Weinberg, D. H., Agol, E., Aihara, H., Prieto, C. A., Anderson, S. F., et al. (2011). SDSS-III: massive spectroscopic surveys of the distant universe, the milky way galaxy, and extra-solar planetary systems. *Astron. J.* 142:72. doi: 10.1088/0004-6256/142/3/72

Eisenstein, D. J., Zehavi, I., Hogg, D. W., Scoccimarro, R., Blanton, M. R., Nichol, R. C., et al. (2005). Detection of the baryon acoustic peak in the large-scale correlation function of SDSS luminous red galaxies. *Astrophys. J.* 633, 560–574. doi: 10.1086/466512

Elgaroy, O., and Lahav, O. (2003). Upper limits on neutrino masses from the 2dFGRS and WMAP: the role of priors. *JCAP* 04:004. doi: 10.1088/1475-7516/2003/04/004

Eliseev, S., Blaum, K., Block, M., Chenmarev, S., Dorrer, H., Düllmann, C. E. et al. (2015). Direct measurement of the mass difference of ^{163}Ho and ^{163}Dy solves the *Q*-value puzzle for the neutrino mass determination. *Phys. Rev. Lett.* 115:062501. doi: 10.1103/PhysRevLett.115.062501

Engel, J., and Menéndez, J. (2017). Status and future of nuclear matrix elements for neutrinoless double-beta decay: a review. *Rept. Prog. Phys.* 80:046301.

Errard, J., Feeney, S. M., Peiris, H. V., and Jaffe, A. H. (2016). Robust forecasts on fundamental physics from the foreground-obscured, gravitationally-lensed CMB polarization. *JCAP* 03:052. doi: 10.1088/1475-7516/2016/03/052

Escrihuela, F. J., Forero, D. V., Miranda, O. G., Tortola, M., and Valle, J. W. F. (2017). Probing CP violation with non-unitary mixing in long-baseline neutrino oscillation experiments: DUNE as a case study. *New J. Phys.* 19:093005. doi: 10.1088/1367-2630/aa79ec

Esfahani, A. A., Asner, D. M., Böser, S., Cervantes, R., Claessens, C., de Viveiros, L., et al. (2017). Determining the neutrino mass with cyclotron radiation emission spectroscopy-Project 8. *J. Phys. G* 44:054004. doi: 10.1088/1361-6471/aa5b4f

Essinger-Hileman, T., Ali, A., Amiri, M., Appel, J. W., Araujo, D., Bennett, C. L., et al. (2014). "CLASS: the cosmology large angular scale surveyor," in *Proceedings Millimeter, Submillimeter, and Far-Infrared Detectors and Instrumentation for Astronomy VII* (Montréal, QC). doi: 10.1117/12.2056701

Esteban, I., Gonzalez-Garcia, M. C., Maltoni, M., Martinez-Soler, I., and Schwetz, T. (2017). Updated fit to three neutrino mixing: exploring the accelerator-reactor complementarity. *J. High Energy Phys.* 01:087. doi: 10.1007/JHEP01(2017)087

Esteban-Pretel, A., Mirizzi, A., Pastor, S., Tomas, R., Raffelt, G. G., Serpico, P. D., G., et al. (2008). Role of dense matter in collective supernova neutrino transformations. *Phys. Rev. D* 78:085012. doi: 10.1103/PhysRevD.78.085012

Esteban-Pretel, A., Pastor, S., Tomas, R., Raffelt, G. G., and Sigl, G. (2007). Decoherence in supernova neutrino transformations suppressed by deleptonization. *Phys. Rev. D* 76:125018. doi: 10.1103/PhysRevD.76.125018

Ewall-Wice, A., Chang, T., Lazio, J., Dore, O., Seiffert, M., and Monsalve, R. (2018). Modeling the radio background from the first black holes at cosmic Dawn: implications for the 21 cm absorption amplitude. *arXiv:1803.01815*.

Faessler, A., Hodak, R., Kovalenko, S., and Simkovic, F. (2011). Beta decaying nuclei as a probe of cosmic neutrino background. *J. High Energy Phys. arXiv:1102.1799*.

Falkowski, A., and Petraki, K. (2018). 21cm absorption signal from charge sequestration. *J. High Energy Phys. arXiv:1803.10096*.

Fardon, R., Nelson, A. E., and Weiner, N. (2004). Dark energy from mass varying neutrinos. *JCAP* 10:005. doi: 10.1088/1475-7516/2004/10/005

Farzan, Y., Peres, O., and Smirnov, A. (2001). Neutrino mass spectrum and future beta decay experiments. *Nucl. Phys.* B612, 59–97. doi: 10.1016/S0550-3213(01)00361-3

Farzan, Y., and Tortola, M. (2018). Neutrino oscillations and Non-Standard Interactions. *Front. Phys.* 6:10. doi: 10.3389/fphy.2018.00010

Feng, C., and Holder, G. (2018). Enhanced global signal of neutral hydrogen due to excess radiation at cosmic dawn. *Astrophys. J.* 858:L17. doi: 10.3847/2041-8213/aac0fe

Fialkov, A., Barkana, R., and Cohen, A. (2018). Constraining baryon–dark matter scattering with the cosmic dawn 21-cm signal. *Phys. Rev. Lett.* 121:011101. doi: 10.1103/PhysRevLett.121.011101

Fogli, G., Lisi, E., Marrone, A., Melchiorri, A., Palazzo, A., Serra, P., Silk, J., et al. (2007). Observables sensitive to absolute neutrino masses: a Reappraisal after WMAP-3y and first MINOS results. *Phys. Rev. D* 75:053001. doi: 10.1103/PhysRevD.75.053001

Fogli, G., Lisi, E., Marrone, A., Melchiorri, A., Palazzo, A., Serra, P., Silk, J., et al. (2008). Observables sensitive to absolute neutrino masses. 2. *Phys. Rev. D* 78:033010. doi: 10.1103/PhysRevD.78.033010

Font-Ribera, A., Kirkby, D., Busca, N., Miralda-Escudé, J., Ross, N. P., Slosar, A., et al. (2014a). Quasar-lyman α forest cross-correlation from bOSS DR11 : baryon acoustic oscillations. *JCAP* 05:027. doi: 10.1088/1475-7516/2014/05/027

Font-Ribera, A., McDonald, P., Mostek, N., Reid, B. A., Seo, H.-J., and Slosar, A. (2014b). DESI and other dark energy experiments in the era of neutrino mass measurements. *JCAP* 05:023. doi: 10.1088/1475-7516/2014/05/023

Forero, D. V. and Huang, W.-C. (2017). Sizable NSI from the $SU(2)_L$ scalar doublet-singlet mixing and the implications in DUNE. *J. High Energy Phys.* 03:018. doi: 10.1007/JHEP03(2017)018

Forero, D. V., and Huber, P. (2016). Hints for leptonic CP violation or New Physics? *Phys. Rev. Lett.* 117:031801. doi: 10.1103/PhysRevLett.117.031801

Forero, D. V., Tortola, M., and Valle, J. W. F. (2014). Neutrino oscillations refitted. *Phys. Rev. D* 90:093006. doi: 10.1103/PhysRevD.90.093006

Fraser, S., Hektor, A., Hütsi, G., Kannike, K., Marzo, C., Marzola, L., et al. (2018). The EDGES 21 cm anomaly and properties of dark matter. *Phys. Lett. B* 785, 159–164. doi: 10.1016/j.physletb.2018.08.035

Freedman, W. L., and Madore, B. F. (2010). The hubble constant. *Ann. Rev. Astron. Astrophys.* 48, 673–710. doi: 10.1146/annurev-astro-082708-101829

Fukuda, Y., Hayakawa, T., Ichihara, E., Inoue, K., Ishihara, K., Ishino, H., et al. (1998). Evidence for oscillation of atmospheric neutrinos. *Phys. Rev. Lett.* 81, 1562–1567. doi: 10.1103/PhysRevLett.81.1562

Furlanetto, S., Oh, S., and Briggs, F. (2006). Cosmology at low frequencies: the 21 cm transition and the high-redshift universe. *Phys. Rept.* 433, 181–301. doi: 10.1016/j.physrep.2006.08.002

Furlanetto, S. R. (2015). "The 21-cm line as a probe of reionization," in *UUnderstanding the Epoch of Cosmic Reionization. Astrophysics and Space Science Library*, Vol 423, ed A. Mesinger (Cham: Springer), 247–280.

Gando, A., Gando, Y., Ichimura, K., Ikeda, H., Kibe, Y., Kishimoto, Y., et al. (2011). Constraints on θ_{13} from a three-flavor oscillation analysis of reactor antineutrinos at KamLAND. *Phys. Rev. D* 83:052002. doi: 10.1103/PhysRevD.83.052002

Gando, A., Gando, Y., Ichimura, K., Ikeda, H., Kibe, Y., Kishimoto, Y., et al. (2016). Search for majorana neutrinos near the inverted mass hierarchy region with KamLAND-Zen. *Phys. Rev. Lett.* 117:082503. doi: 10.1103/PhysRevLett.117.082503

Gando, A. "KamLAND-Zen," in *XXVIII International Conference on Neutrino Physics and Astrophysics*, 4–9 June (2018), (Heidelberg). Available online at: URL: http://doi.org/10.5281/zenodo.1286895

Gariazzo, S., Archidiacono, M., de Salas, P. F., Mena, O., Ternes, C. A., and Tórtola, M. (2018a). Neutrino masses and their ordering: global data, priors and models. *JCAP* 03:011. doi: 10.1088/1475-7516/2018/03/011

Gariazzo, S., Giunti, C., Laveder, M., and Li, Y. F. (2017). Updated global 3+1 analysis of short-baseLine neutrino oscillations. *J. High Energy Phys.* 06:135. doi: 10.1007/JHEP06(2017)135

Gariazzo, S., Giunti, C., Laveder, M., and Li, Y. F. (2018b). Model-independent $\bar{\nu}_e$ short-baseline oscillations from reactor spectral ratios. *Phys. Lett.* B782, 13–21. doi: 10.1016/j.physletb.2018.04.057

Gariazzo, S., Giunti, C., Laveder, M., Li, Y. F., and Zavanin, E. M. (2016). Light sterile neutrinos. *J. Phys. G*, 43:033001.

Gastaldo, L. (2018) "Determining the electron neutrino mass with Ho-163," in *XXVIII International Conference on Neutrino Physics and Astrophysics* (Heidelberg). Available online at: https://doi.org/10.5281/zenodo.1286950

Gavela, M. B., Hernandez, D., Lopez Honorez, L., Mena, O., and Rigolin, S. (2009). Dark coupling. *JCAP* 07:034. doi: 10.1088/1475-7516/2009/07/034

Ge, S.-F., Lindner, M., and Rodejohann, W. (2017). New physics and atmospheric neutrino trident production with PINGU and ORCA. *Phys. Lett.* B772, 164–168. doi: 10.1016/j.physletb.2017.06.020

Gelmini, G. B. (2005). Prospect for relic neutrino searches. *Phys. Scripta* T121, 131–136. doi: 10.1088/0031-8949/2005/T121/019

Gerbino, M., Freese, K., Vagnozzi, S., Lattanzi, M., Mena, O., Giusarma, E., and Ho, S. (2017a). Impact of neutrino properties on the estimation of inflationary parameters from current and future observations. *Phys. Rev. D* 95:043512. doi: 10.1103/PhysRevD.95.043512

Gerbino, M., Lattanzi, M., Mena, O., and Freese, K. (2017b). A novel approach to quantifying the sensitivity of current and future cosmological datasets to the neutrino mass ordering through Bayesian hierarchical modeling. *Phys. Lett.* B775, 239–250. doi: 10.1016/j.physletb.2017.10.052

Ghosh, A., Thakore, T., and Choubey, S. (2013). Determining the neutrino mass hierarchy with INO, T2K, NOvA and reactor Experiments. *J. High Energy Phys.* 04:009. doi: 10.1007/JHEP04(2013)009

Giachero, A., Alpert, B., Becker, D., Bennett, D., Biasotti, M., Brofferio, C., et al. (2017). Measuring the electron neutrino mass with improved sensitivity: the HOLMES experiment. *JINST* 12:C02046. doi: 10.1088/1748-0221/12/02/C02046

Girardi, I., Meloni, D., Ohlsson, T., Zhang, H., and Zhou, S. (2014). Constraining sterile neutrinos using reactor neutrino experiments. *J. High Energy Phys.* 08:057. doi: 10.1007/JHEP08(2014)057

Giuliani, A. (2018) "The mid and long term future of neutrinoless double beta decay," in *XXVIII International Conference on Neutrino Physics and Astrophysics* (Heidelberg) Avaialable online at : http://doi.org/10.5281/zenodo.1286915

Giuliani, A., and Poves, A. (2012). Neutrinoless double-beta decay. *Adv. High Energy Phys.* 2012:857016.

Giunti, C. (2017). "Light sterile neutrinos and neutrinoless double-beta decay," in *Proceedings, Matrix Elements for the Double beta decay Experiments (MEDEX'17)* (Prague) Vol. 1894, 020009.

Giunti, C., and Kim, C. W. (2007). *Fundamentals of Neutrino Physics and Astrophysics*. Oxford: Oxford University Press.

Giunti, C., and Zavanin, E. M. (2015). Predictions for neutrinoless double-beta decay in the 3+1 sterile neutrino scenario. *J. High Energy Phys.* 07:171. doi: 10.1007/JHEP07(2015)171

Giusarma, E., Corsi, M., Archidiacono, M., de Putter, R., Melchiorri, A., Mena, O., et al. (2011). Constraints on massive sterile neutrino species from current and future cosmological data. *Phys. Rev. D* 83:115023. doi: 10.1103/PhysRevD.83.115023

Giusarma, E., de Putter, R., Ho, S., and Mena, O. (2013a). Constraints on neutrino masses from Planck and Galaxy Clustering data. *Phys. Rev. D* 88:063515. doi: 10.1103/PhysRevD.88.063515

Giusarma, E., De Putter, R., and Mena, O. (2013b). Testing standard and nonstandard neutrino physics with cosmological data. *Phys. Rev. D* 87:043515. doi: 10.1103/PhysRevD.87.043515

Giusarma, E., Di Valentino, E., Lattanzi, M., Melchiorri, A., and Mena, O. (2014). Relic neutrinos, thermal axions and cosmology in early 2014. *Phys. Rev. D* 90:043507. doi: 10.1103/PhysRevD.90.043507

Giusarma, E., Gerbino, M., Mena, O., Vagnozzi, S., Ho, S., and Freese, K. (2016). Improvement of cosmological neutrino mass bounds. *Phys. Rev. D* 94:083522. doi: 10.1103/PhysRevD.94.083522

Giusarma, E., Vagnozzi, S., Ho, S., Ferraro, S., Freese, K., Kamen-Rubio, R., et al. (2018). Scale-dependent galaxy bias, CMB lensing-galaxy cross-correlation, and neutrino masses. *arXiv:1802.08694*.

Gomez-Cadenas, J. J., Martin-Albo, J., Mezzetto, M., Monrabal, F., and Sorel, M. (2012). The Search for neutrinoless double beta decay. *Riv. Nuovo Cim.* 35, 29–98. doi: 10.1393/ncr/i2012-10074-9

Goobar, A., Hannestad, S., Mortsell, E., and Tu, H. (2006). A new bound on the neutrino mass from the sdss baryon acoustic peak. *JCAP* 06:019. doi: 10.1088/1475-7516/2006/06/019

Gratton, S., Lewis, A., and Efstathiou, G. (2008). Prospects for constraining neutrino mass using planck and lyman-alpha forest data. *Phys. Rev. D* 77:083507. doi: 10.1103/PhysRevD.77.083507

Greenhill, L., and Bernardi, G. (2012). HI epoch of reionization arrays. *arXiv:1201.1700*.

Guo, R.-Y., Zhang, J.-F., and Zhang, X. (2018). Exploring neutrino mass and mass hierarchy in the scenario of vacuum energy interacting with cold dark matter. *Chin. Phys. C* 42:095103. doi: 10.1088/1674-1137/42/9/095103

Hamann, J., Hannestad, S., Lesgourgues, J., Rampf, C., and Wong, Y. Y. Y. (2010a). Cosmological parameters from large scale structure - geometric versus shape information. *JCAP* 07:022. doi: 10.1088/1475-7516/2010/07/022

Hamann, J., Hannestad, S., Melchiorri, A., and Wong, Y. Y. (2008). Nonlinear corrections to the cosmological matter power spectrum and scale-dependent galaxy bias: implications for parameter estimation. *JCAP* 07:017. doi: 10.1088/1475-7516/2008/07/017

Hamann, J., Hannestad, S., Raffelt, G., and Wong, Y. Y. (2007a). Observational bounds on the cosmic radiation density. *JCAP* 08:021. doi: 10.1088/1475-7516/2007/08/021

Hamann, J., Hannestad, S., Raffelt, G. G., Tamborra, I., and Wong, Y. Y. (2010b). Cosmology seeking friendship with sterile neutrinos. *Phys. Rev. Lett.* 105:181301. doi: 10.1103/PhysRevLett.105.181301

Hamann, J., Hannestad, S., Raffelt, G. G., and Wong, Y. Y. Y. (2011). Sterile neutrinos with eV masses in cosmology: how disfavoured exactly? *JCAP* 09:034. doi: 10.1088/1475-7516/2011/09/034

Hamann, J., Hannestad, S., Sloth, M. S., and Wong, Y. Y. (2007b). How robust are inflation model and dark matter constraints from cosmological data? *Phys. Rev. D* 75:023522. doi: 10.1103/PhysRevD.75.023522

Hamann, J., Hannestad, S., and Wong, Y. Y. Y. (2012). Measuring neutrino masses with a future galaxy survey. *JCAP* 11:052. doi: 10.1088/1475-7516/2012/11/052

Handley, W., and Millea, M. (2018). Maximum entropy priors with derived parameters in a specified distribution. *e-Print: arXiv:1804.08143*.

Handley, W. J., Hobson, M. P., and Lasenby, A. N. (2015a). PolyChord: nested sampling for cosmology. *Mon. Not. R. Astron. Soc.* 450, L61–L65. doi: 10.1093/mnrasl/slv047

Handley, W. J., Hobson, M. P., and Lasenby, A. N. (2015b). PolyChord: next-generation nested sampling. *Mon. Not. R. Astron.Soc.* 453:4384. doi: 10.1093/mnras/stv1911

Hannestad, S. (2003). Neutrino masses and the number of neutrino species from WMAP and 2dFGRS. *JCAP* 05:004. doi: 10.1088/1475-7516/2003/05/004

Hannestad, S. (2005a). Neutrino masses and the dark energy equation of state - Relaxing the cosmological neutrino mass bound. *Phys. Rev. Lett.* 95:221301. doi: 10.1103/PhysRevLett.95.221301

Hannestad, S. (2005b). Structure formation with strongly interacting neutrinos - Implications for the cosmological neutrino mass bound. *JCAP* 02:011.

Hannestad, S., Mirizzi, A., Raffelt, G. G., and Wong, Y. Y. (2008). Cosmological constraints on neutrino plus axion hot dark matter: Update after WMAP-5. *JCAP* 04:019. doi: 10.1088/1475-7516/2008/04/019

Hannestad, S., Mirizzi, A., Raffelt, G. G., and Wong, Y. Y. Y. (2007). Cosmological constraints on neutrino plus axion hot dark matter. *JCAP* 08:015. doi: 10.1088/1475-7516/2007/08/015

Hannestad, S., Mirizzi, A., Raffelt, G. G., and Wong, Y. Y. Y. (2010). Neutrino and axion hot dark matter bounds after WMAP-7. *JCAP* 08:001. doi: 10.1088/1475-7516/2010/08/001

Hannestad, S., and Raffelt, G. (2004). Cosmological mass limits on neutrinos, axions, and other light particles. *JCAP* 04:008. doi: 10.1088/1475-7516/2004/04/008

Hannestad, S., Raffelt, G. G., Sigl, G., and Wong, Y. Y. (2006a). Self-induced conversion in dense neutrino gases: pendulum in flavour space. *Phys. Rev. D* 74:105010. doi: 10.1103/PhysRevD.76.029901

Hannestad, S., and Schwetz, T. (2016). Cosmology and the neutrino mass ordering. *JCAP* 11:035. doi: 10.1088/1475-7516/2016/11/035

Hannestad, S., Tu, H., and Wong, Y. Y. (2006b). Measuring neutrino masses and dark energy with weak lensing tomography. *JCAP* 06:025. doi: 10.1088/1475-7516/2006/06/025

Hartz, M. (2017). *T2K NEUTRINO OSCILLATION RESULTS WITH DATA UP TO 2017 SUMMER*. Available online at: http://www.t2k.org/docs/talk/282

Heavens, A. F., and Sellentin, E. (2018). Objective Bayesian analysis of neutrino masses and hierarchy. *JCAP* 04:047. doi: 10.1088/1475-7516/2018/04/047

Heitmann, K., Lawrence, E., Kwan, J., Habib, S., and Higdon, D. (2014). The coyote universe extended: precision emulation of the matter power spectrum. *Astrophys. J.*, 780:111. doi: 10.1088/0004-637X/780/1/111

Hektor, A., Hütsi, G., Marzola, L., Raidal, M., Vaskonen, V., and Veermäe, H. (2018). Constraining primordial black holes with the EDGES 21-cm absorption signal. *Phys. Rev. D* 98:023503. doi: 10.1103/PhysRevD.98.023503

Hildebrandt, H., Viola, M., Heymans, C., Joudaki, S., Kuijken, K., Blake, C., et al. (2017). KiDS-450: cosmological parameter constraints from tomographic weak gravitational lensing. *Mon. Not. R. Astron. Soc.* 465:1454. doi: 10.1093/mnras/stw2805

Hill, J. C., and Baxter, E. J. (2018). Can early dark energy explain EDGES? *JCAP* 08:037. doi: 10.1088/1475-7516/2018/08/037

Hilton, M., Hasselfield, M., Sifón, C., Battaglia, N., Aiola, S., Bharadwaj, V., et al. (2018). The atacama cosmology telescope: the two-season ACTPol Sunyaev-Zel'dovich effect selected cluster catalog. *Astrophys. J. Suppl.* 235:20. doi: 10.3847/1538-4365/aaa6cb

Himmel, A. (2018). *First Oscillation Results With Neutrino and Antineutrino Beams in NOvA*. Available online at: http://nova-docdb.fnal.gov/cgi-bin/ShowDocument?docid=30273

Hirano, S., and Bromm, V. (2018). Baryon-dark matter scattering and first star formation. *Mon. Not. R. Astron. Soc.* 480:L85. doi: 10.1093/mnrasl/sly132

Hirata, K., Kajita, T., Koshiba, M., Nakahata, M., Oyama, Y., Sato, N., et al. (1987). Observation of a Neutrino Burst from the Supernova SN 1987a. *Phys. Rev. Lett.* 58, 1490–1493. doi: 10.1103/PhysRevLett.58.1490

Horiuchi, S., and Kneller, J. P. (2018). What can be learned from a future supernova neutrino detection? *J. Phys. G* 45:043002. doi: 10.1088/1361-6471/aaa90a

Hosaka, J. et al. (2006). Solar neutrino measurements in super-Kamiokande-I. *Phys. Rev. D* 73:112001. doi: 10.1103/PhysRevD.73.112001

Hu, B., Raveri, M., Silvestri, A., and Frusciante, N. (2015). Exploring massive neutrinos in dark cosmologies with *EFTCAMB*/ EFTCosmoMC. *Phys. Rev. D* 91:063524. doi: 10.1103/PhysRevD.91.063524

Hu, W., Eisenstein, D. J., and Tegmark, M. (1998). Weighing neutrinos with galaxy surveys. *Phys. Rev. Lett.* 80, 5255–5258. doi: 10.1103/PhysRevLett.80.5255

Humphreys, E. M. L., Reid, M. J., Moran, J. M., Greenhill, L. J., and Argon, A. L. (2013). Toward a new geometric distance to the active galaxy NGC 4258. III. Final results and the hubble constant. *Astrophys. J.* 775:13. doi: 10.1088/0004-637X/775/1/13

Huterer, D., and Linder, E. V. (2007). Separating dark physics from physical darkness: minimalist modified gravity vs. dark energy. *Phys. Rev. D* 75:023519. doi: 10.1103/PhysRevD.75.023519

Ichiki, K., and Keum, Y.-Y. (2008). Neutrino masses from cosmological probes in interacting neutrino dark-energy models. *J. High Energy Phys.* 06:058. doi: 10.1088/1126-6708/2008/06/058

Ichiki, K., Takada, M., and Takahashi, T. (2009). Constraints on Neutrino Masses from Weak Lensing. *Phys. Rev. D* 79:023520. doi: 10.1103/PhysRevD.79.023520

Iliev, I. T., Shapiro, P. R., Ferrara, A., and Martel, H. (2002). On the direct detectability of the cosmic dark ages: 21-cm emission from minihalos. *Astrophys. J.* 572:123. doi: 10.1086/341869

Inman, D., Emberson, J. D., Pen, U.-L., Farchi, A., Yu, H.-R., and Harnois-Déraps, J. (2015). Precision reconstruction of the cold dark matter-neutrino relative velocity from *N*-body simulations. *Phys. Rev. D* 92:023502. doi: 10.1103/PhysRevD.92.023502

Ivezic, Z., Tyson, J., Allsman, R., Andrew, J., and Angel, R. (2008). LSST: from science drivers to reference design and anticipated data products. *Astrophysics arXiv:0805.2366*.

Jackson, N. (2007). The hubble constant. *Living Rev. Rel.* 10:4. doi: 10.12942/lrr-2007-4

Jain, B., Spergel, D., Bean, R., Connolly, A., Dell'antonio, I., Frieman, J., et al. (2015). The whole is greater than the sum of the parts: optimizing the joint science return from LSST, Euclid and WFIRST. *arXiv:1501.07897*.

Janka, H.-T. (2012). Explosion mechanisms of core-collapse supernovae. *Ann. Rev. Nucl. Part. Sci.* 62, 407–451. doi: 10.1146/annurev-nucl-102711-094901

Jeffreys, H. (1961). *Theory of Probability*. The International series of monographs on physics. Clarendon Press.

Jimenez, R., Kitching, T., Peña-Garay, C., and Verde, L. (2010). Can we measure the neutrino mass hierarchy in the sky? *JCAP* 05:035. doi: 10.1088/1475-7516/2010/05/035

Joudaki, S. (2013). Constraints on neutrino mass and light degrees of freedom in extended cosmological parameter spaces. *Phys. Rev. D* 87:083523. doi: 10.1103/PhysRevD.87.083523

Joudaki, S., Mead, A., Blake, C., Choi, A., de Jong, J., Erben, T., et al. (2017). KiDS-450: testing extensions to the standard cosmological model. *Mon. Not. R. Astron. Soc.* 471, 1259–1279. doi: 10.1093/mnras/stx998

Jurkovich, H., Ferreira, C., and Pasquini, P. (2018). Shadowing neutrino mass hierarchy with lorentz invariance violation *High Energy Phys. arXiv:1806.08752*.

Kaether, F., Hampel, W., Heusser, G., Kiko, J., and Kirsten, T. (2010). Reanalysis of the GALLEX solar neutrino flux and source experiments. *Phys. Lett.* B685, 47–54. doi: 10.1016/j.physletb.2010.01.030

Kang, Z. (2018). Post-recombination dark matter for the 21-cm signal. *arXiv:1803.04928*.

Kaplinghat, M., Knox, L., and Song, Y.-S. (2003). Determining neutrino mass from the CMB alone. *Phys. Rev. Lett.* 91:241301. doi: 10.1103/PhysRevLett.91.241301

Kazin, E. A., Koda, J., Blake, C., Padmanabhan, N., Brough, S., Colless, M., et al. (2014). The wiggleZ dark energy survey: improved distance measurements to z = 1 with reconstruction of the baryonic acoustic feature. *Mon. Not. R. Astron. Soc.* 441, 3524–3542. doi: 10.1093/mnras/stu778

Khan, A. N., McKay, D. W., and Tahir, F. (2013). Sensitivity of medium-baseline reactor neutrino mass-hierarchy experiments to nonstandard interactions. *Phys. Rev. D* 88:113006. doi: 10.1103/PhysRevD.88.113006

Kharusi, S. A., Alamre, A., Albert, J. B., Alfaris, M., Anton, G., Arnquist, I. J., et al. (2018). nEXO Pre-Conceptual Design Report. *arXiv:1805.11142*.

Kilbinger, M. (2015). Cosmology with cosmic shear observations: a review. *Rept. Prog. Phys.* 78:086901. doi: 10.1088/0034-4885/78/8/086901

Kim, S.-B. (2015). New results from RENO and prospects with RENO-50. *Nucl. Part. Phys. Proc.* 265–266, 93–98. doi: 10.1016/j.nuclphysbps.2015.06.024

Kitching, T., Heavens, A., Verde, L., Serra, P., and Melchiorri, A. (2008). Finding evidence for massive neutrinos using 3D weak lensing. *Phys. Rev. D* 77:103008. doi: 10.1103/PhysRevD.77.103008

Ko, Y. J., Kim, B. R., Kim, J. Y., Han, B. Y., Jang, C. H., Jeon, E. J., et al. (2017). Sterile neutrino search at the NEOS experiment. *Phys. Rev. Lett.* 118:121802. doi: 10.1103/PhysRevLett.118.121802

Köhlinger, F., Viola, M., Joachimi, B., Hoekstra, H., van Uitert, E., Hildebrandt, H., et al. (2017). KiDS-450: the tomographic weak lensing power spectrum and constraints on cosmological parameters. *Mon. Not. R. Astron. Soc.* 471:4412. doi: 10.1093/mnras/stx1820

Krnjaic, G., Machado, P. A. N., and Necib, L. (2018). Distorted neutrino oscillations from ultralight scalar dark matter. *Phys. Rev. D* 97:075017. doi: 10.1103/PhysRevD.97.075017

La Vacca, G., Bonometto, S., and Colombo, L. (2009). Higher neutrino mass allowed if DM and DE are coupled. *New Astron.* 14, 435–442. doi: 10.1016/j.newast.2008.12.004

La Vacca, G., and Kristiansen, J. (2009). Dynamical dark energy model parameters with or without massive neutrinos. *JCAP* 07:036. doi: 10.1088/1475-7516/2009/07/036

Lattanzi, M., and Gerbino, M. (2018). Status of neutrino properties and future prospects - Cosmological and astrophysical constraints. *Front. Phys.* 5:70. doi: 10.3389/fphy.2017.00070

Lazauskas, R., Vogel, P., and Volpe, C. (2008). Charged current cross section for massive cosmological neutrinos impinging on radioactive nuclei. *J. Phys. G* 35:025001. doi: 10.1088/0954-3899/35/2/025001

Lesgourgues, J. (2011a). The cosmic linear anisotropy solving system (CLASS) I: overview. *arXiv:1104.2932* .

Lesgourgues, J. (2011b). The cosmic linear anisotropy solving system (CLASS) III: comparision with CAMB for lambdaCDM. *arXiv:1104.2934*.

Lesgourgues, J., Mangano, G., Miele, G., and Pastor, S. (2013). *Neutrino Cosmology*. Cambridge, UK: Cambridge University Press. doi: 10.1017/CBO9781139012874

Lesgourgues, J., and Pastor, S. (2006). Massive neutrinos and cosmology. *Phys. Rept.* 429, 307–379. doi: 10.1016/j.physrep.2006.04.001

Lesgourgues, J., and Pastor, S. (2012). Neutrino mass from Cosmology. *Adv. High Energy Phys.* 2012:608515. doi: 10.1155/2012/608515

Lesgourgues, J., and Pastor, S. (2014). Neutrino cosmology and Planck. *New J. Phys.* 16:065002. doi: 10.1088/1367-2630/16/6/065002

Lesgourgues, J., Pastor, S., and Perotto, L. (2004). Probing neutrino masses with future galaxy redshift surveys. *Phys. Rev. D* 70:045016. doi: 10.1103/PhysRevD.70.045016

Lesgourgues, J., Perotto, L., Pastor, S., and Piat, M. (2006). Probing neutrino masses with cmb lensing extraction. *Phys. Rev. D*, 73:045021. doi: 10.1103/PhysRevD.73.045021

Lesgourgues, J., and Tram, T. (2014). Fast and accurate CMB computations in non-flat FLRW universes. *JCAP* 09, 032. doi: 10.1088/1475-7516/2014/09/032

Levi, M., Bebek, C., Beers, T., Blum, R., Cahn, R., Eisenstein, D., et al. (2013). The DESI experiment, a Whitepaper for snowmass 2013. *arXiv:1308.0847*.

Lewis, A., and Bridle, S. (2002). Cosmological parameters from CMB and other data: a monte carlo approach. *Phys. Rev. D* 66:103511. doi: 10.1103/PhysRevD.66.103511

Lewis, A., Challinor, A., and Lasenby, A. (2000). Efficient computation of CMB anisotropies in closed FRW models. *Astrophys. J.* 538, 473–476. doi: 10.1086/309179

Li, Y.-F. (2015). Detection prospects of the cosmic neutrino background. *Int. J. Mod. Phys.* A30:1530031. doi: 10.1142/9789814704779_0025

Li, Y.-F.m and Zhao, Z.-h. (2014). Tests of lorentz and CPT violation in the medium baseline reactor antineutrino experiment. *Phys. Rev. D* 90:113014. doi: 10.1103/PhysRevD.90.113014

Liao, J., Marfatia, D., and Whisnant, K. (2017). Nonstandard interactions in solar neutrino oscillations with Hyper-Kamiokande and JUNO. *Phys. Lett.* B771, 247–253. doi: 10.1016/j.physletb.2017.05.054

Linder, E. V. (2003). Exploring the expansion history of the universe. *Phys. Rev. Lett.* 90:091301. doi: 10.1103/PhysRevLett.90.091301

Liu, A., and Parsons, A. R. (2016). Constraining cosmology and ionization history with combined 21 cm power spectrum and global signal measurements. *Mon. Not. R. Astron. Soc.* 457, 1864–1877. doi: 10.1093/mnras/stw071

Liu, A., Pritchard, J. R., Allison, R., Parsons, A. R., Seljak, U., and Sherwin, B. D. (2016). Eliminating the optical depth nuisance from the CMB with 21 cm cosmology. *Phys. Rev. D* 93:043013. doi: 10.1103/PhysRevD.93.043013

Liu, H., and Slatyer, T. R. (2018). Too hot, too cold or just right? Implications of a 21-cm signal for dark matter annihilation and decay. *Phys. Rev. D* 98:023501. doi: 10.1103/PhysRevD.98.023501

Liu, J., Bird, S., Matilla, J. M. Z., Hill, J. C., Haiman, Z., Madhavacheril, M. S., et al. (2018). MassiveNuS: cosmological massive neutrino simulations. *JCAP* 03:049. doi: 10.1088/1475-7516/2018/03/049

Loeb, A., and Wyithe, S. (2008). Precise measurement of the cosmological power spectrum with a dedicated 21cm survey after reionization. *Phys. Rev. Lett.* 100:161301. doi: 10.1103/PhysRevLett.100.161301

Long, A. J., Lunardini, C., and Sabancilar, E. (2014). Detecting non-relativistic cosmic neutrinos by capture on tritium: phenomenology and physics potential. *JCAP* 08:038. doi: 10.1088/1475-7516/2014/08/038

Long, A. J., Raveri, M., Hu, W., and Dodelson, S. (2018). Neutrino mass priors for cosmology from random matrices. *Phys. Rev. D* 97:043510. doi: 10.1103/PhysRevD.97.043510

Lopez Honorez, L., and Mena, O. (2010). Instabilities in dark coupled models and constraints from cosmological data. *AIP Conf. Proc.* 1241, 1016–1024. doi: 10.1063/1.3462595

Lorenz, C. S., Calabrese, E., and Alonso, D. (2017). Distinguishing between Neutrinos and time-varying Dark Energy through Cosmic Time. *Phys. Rev. D* 96:043510. doi: 10.1103/PhysRevD.96.043510

LoVerde, M., and Zaldarriaga, M. (2014). Neutrino clustering around spherical dark matter halos. *Phys. Rev. D* 89:063502. doi: 10.1103/PhysRevD.89.063502

Lunardini, C., and Smirnov, A. (2001a). Neutrinos from SN1987A, earth matter effects and the LMA solution of the solar neutrino problem. *Phys. Rev. D* 63:073009. doi: 10.1103/PhysRevD.63.073009

Lunardini, C., and Smirnov, A. (2001b). Supernova neutrinos: earth matter effects and neutrino mass spectrum. *Nucl. Phys.* B616:307–348.

Lunardini, C., and Smirnov, A. Y. (2003). Probing the neutrino mass hierarchy and the 13 mixing with supernovae. *JCAP* 06:009. doi: 10.1088/1475-7516/2003/06/009

Lunardini, C. and Smirnov, A. Y. (2004). Neutrinos from SN1987A: flavor conversion and interpretation of results. *Astropart. Phys.* 21, 703–720. doi: 10.1016/j.astropartphys.2004.05.005

Madau, P., Meiksin, A., and Rees, M. J. (1997). 21-CM tomography of the intergalactic medium at high redshift. *Astrophys. J.* 475:429. doi: 10.1086/303549

Mahdawi, M. S., and Farrar, G. R. (2018). Constraints on dark matter with a moderately large and velocity-dependent DM-Nucleon cross-section. *arXiv:1804.03073*.

Mangano, G., Miele, G., Pastor, S., Pinto, T., Pisanti, O., and Serpico, P. D. (2005). Relic neutrino decoupling including flavor oscillations. *Nucl. Phys.* B729, 221–234. doi: 10.1016/j.nuclphysb.2005.09.041

Mao, Y., Tegmark, M., McQuinn, M., Zaldarriaga, M., and Zahn, O. (2008). How accurately can 21 cm tomography constrain cosmology? *Phys. Rev. D* 78:023529. doi: 10.1103/PhysRevD.78.023529

Martín-Albo, J., Muñoz Vidal, J., Ferrario, P., Nebot-Guinot, M., Gómez-Cadenas, J. J., Álvarez, V., et al. (2016). Sensitivity of NEXT-100 to neutrinoless double beta decay. *J. High Energy Phys.* 05:159. doi: 10.1007/JHEP05(2016)159

Masud, M., and Mehta, P. (2016). Nonstandard interactions and resolving the ordering of neutrino masses at DUNE and other long baseline experiments. *Phys. Rev. D* 94:053007. doi: 10.1103/PhysRevD.94.053007

McGaugh, S. (2018). Strong hydrogen absorption at cosmic Dawn: the signature of a baryonic universe. *Res. Notes AAS* 2:37. doi: 10.3847/2515-5172/aab497

McQuinn, M., Zahn, O., Zaldarriaga, M., Hernquist, L., and Furlanetto, S. R. (2006). Cosmological parameter estimation using 21 cm radiation from the epoch of reionization. *Astrophys. J.* 653, 815–830. doi: 10.1086/505167

Melchiorri, A., Mena, O., and Slosar, A. (2007). An improved cosmological bound on the thermal axion mass. *Phys. Rev. D* 76:041303. doi: 10.1103/PhysRevD.76.041303

Mellema, G., Koopmans, L., Abdalla, F., Bernardi, G., Ciardi, B., Daiboo, S., et al. (2013). Reionization and the cosmic dawn with the square kilometre array. *Exper. Astron.* 36, 235–318. doi: 10.1007/s10686-013-9334-5

Mena, O., Mocioiu, I., and Quigg, C. (2007). Gravitational lensing of supernova neutrinos. *Astropart. Phys.* 28, 348–356. doi: 10.1016/j.astropartphys.2007.07.002

Mena, O. and Parke, S. J. (2004). Unified graphical summary of neutrino mixing parameters. *Phys. Rev. D* 69:117301.

Mikheev, S. P., and Smirnov, A. Yu. (1985). Resonance amplification of oscillations in matter and spectroscopy of solar neutrinos. *Sov. J. Nucl. Phys.* 42:913–917. doi: 10.1103/PhysRevD.69.117301

Mikheev, S. P., and Smirnov, A. Yu. (1986). Resonant amplification of neutrino oscillations in matter and solar neutrino spectroscopy. *Nuovo Cim.* C9, 17–26. doi: 10.1007/BF02508049

Miranda, O., Tortola, M., and Valle, J. (2006). Are solar neutrino oscillations robust? *J. Health Energy Phys.* 10:008. doi: 10.1088/1126-6708/2006/10/008

Mirizzi, A., Tamborra, I., Janka, H.-T., Saviano, N., Scholberg, K., Bollig, R., et al. (2016). Supernova neutrinos: production, oscillations and detection. *Riv. Nuovo Cim.* 39, 1–112. doi: 10.1393/ncr/i2016-10120-8

Mitridate, A., and Podo, A. (2018). Bounds on dark matter decay from 21 cm line. *JCAP* 05:069. doi: 10.1088/1475-7516/2018/05/069

Mosher, J. et al. (2014). Cosmological parameter uncertainties from SALT-II type Ia supernova light curve models. *Astrophys. J.* 793:16. doi: 10.1088/0004-637X/793/1/16

Mota, D., Pettorino, V., Robbers, G., and Wetterich, C. (2008). Neutrino clustering in growing neutrino quintessence. *Phys. Lett.* B663:160–164. doi: 10.1016/j.physletb.2008.03.060

Muñoz, J. B., and Dvorkin, C. (2018). Efficient computation of galaxy bias with neutrinos and other relics. *Phys. Rev. D* 98:043503. doi: 10.1103/PhysRevD.98.043503

Muñoz, J. B., Dvorkin, C., and Loeb, A. (2018). 21-cm fluctuations from charged dark matter. *arXiv:1804.01092*.

Muñoz, J. B., and Loeb, A. (2018). A small amount of mini-charged dark matter could cool the baryons in the early Universe. *Nature* 557:684. doi: 10.1038/s41586-018-0151-x

Munshi, D., Valageas, P., Van Waerbeke, L., and Heavens, A. (2008). Cosmology with weak lensing surveys. *Phys. Rept.* 462, 67–121. doi: 10.1016/j.physrep.2008.02.003

Murase, K. (2018). New prospects for detecting high-energy neutrinos from nearby Supernovae. *Phys. Rev. D* 97:081301. doi: 10.1103/PhysRevD.97.081301

Nakano, Y. (2016). Ph.D. Thesis, University of Tokyo. Available online at: http://www-sk.icrr.u-tokyo.ac.jp/sk/_pdf/articles/2016/doc_thesis_naknao.pdf

Newburgh, L. B., Addison, G. E., Amiri, M., Bandura, K., Bond, J. R., Connor, L.,et al. (2014). Calibrating CHIME, a new radio interferometer to probe dark energy. *Proc. SPIE Int. Soc. Opt. Eng.* 9145: 4V. doi: 10.1117/12.2056962

Ohlsson, T., Zhang, H., and Zhou, S. (2014). Nonstandard interaction effects on neutrino parameters at medium-baseline reactor antineutrino experiments. *Phys. Lett.* B728, 148–155. doi: 10.1016/j.physletb.2013.11.052

Orebi Gann, G. (2018) "SNO+," in *XXVIII International Conference on Neutrino Physics and Astrophysics* (Heidelberg) Available online at: http://doi.org/10.5281/zenodo.1286908

Orebi Gann, G. D. (2015). Physics potential of an advanced scintillation detector: introducing THEIA *arXiv:1504.08284*.

Ott, C., O'Connor, E., Gossan, S., Abdikamalov, E., Gamma, U., and Drasco, S. (2013). Core-collapse supernovae, neutrinos, and gravitational waves. *Nuclear Phys. B* 235-236, 381–387. doi: 10.1016/j.nuclphysbps.2013.04.036

Ouellet, J. (2018) "Latest results from the CUORE experiment," in *XXVIII International Conference on Neutrino Physics and Astrophysics, 4–9 June 2018*, (Heidelberg) Available online at: URL: http://doi.org/10.5281/zenodo.1286904

Oyama, Y., Kohri, K., and Hazumi, M. (2016). Constraints on the neutrino parameters by future cosmological 21 cm line and precise CMB polarization observations. *JCAP* 02:008. doi: 10.1088/1475-7516/2016/02/008

Oyama, Y., Shimizu, A., and Kohri, K. (2013). Determination of neutrino mass hierarchy by 21 cm line and CMB B-mode polarization observations. *Phys. Lett.* B718, 1186–1193. doi: 10.1016/j.physletb.2012.12.053

Pac, M. Y. (2018). Recent results from RENO. *PoS* NuFact2017:038. doi: 10.22323/1.295.003

Paciga, G., Chang, T.-C., Gupta, Y., Nityanada, R., Odegova, J., Pen, U.-L., et al. (2011). The GMRT epoch of reionization experiment: a new upper limit on the neutral hydrogen power spectrum at z 8.6. *Mon. Not. R. Astron. Soc.* 413, 1174–1183. doi: 10.1111/j.1365-2966.2011.18208.x

Palanque-Delabrouille, N., Yeche, C., Baur, J., Magneville, C., Rossi, G., Lesgourgues, J., Arnaud Borde, et al. (2015). Neutrino masses and cosmology with Lyman-alpha forest power spectrum. *JCAP* 11:011. doi: 10.1088/1475-7516/2015/11/011

Palanque-Delabrouille, N., Yèche, C., Borde, A., Le Goff, J.-M., Rossi, G., Viel, M., et al. (2013). The one-dimensional Ly-alpha forest power spectrum from BOSS. *Astron. Astrophys.* 559:A85. doi: 10.1051/0004-6361/201322130

Parno, D. (2018) "KATRIN: toward a high-precision neutrino-mass determination with tritium," in *XXVIII International Conference on Neutrino Physics and*

Astrophysics, 4–9 June 2018, (Heidelberg). Available online at: http://doi.org/10.5281/zenodo.1287933

Parsons, A. R., Backer, D. C., Bradley, R. F., Aguirre, J. E., Benoit, E. E., Carilli, C. L., et al. (2010). The precision array for probing the epoch of reionization: 8 station results. *Astron. J.* 139:1468. doi: 10.1088/0004-6256/139/4/1468

Pascoli, S., and Petcov, S. (2002). The SNO solar neutrino data, neutrinoless double beta decay and neutrino mass spectrum. *Phys. Lett.* B544, 239–250. doi: 10.1016/S0370-2693(02)02510-8

Pasquini, P., Chulia, S. C., and Valle, J. W. F. (2017). Neutrino oscillations from warped flavor symmetry: predictions for long baseline experiments T2K, NOvA and DUNE. *Phys. Rev. D* 95:095030. doi: 10.1103/PhysRevD.95.095030

Patrick, C., and Xie, F. (2017). Status of the superNEMO $0\nu\beta\beta$ Experiment. *arXiv:1704.06670*.

Peccei, R. D., and Quinn, H. R. (1977a). Constraints imposed by CP conservation in the presence of instantons. *Phys. Rev. D* 16, 1791–1797.

Peccei, R. D., and Quinn, H. R. (1977b). CP Conservation in the Presence of Instantons. *Phys. Rev. Lett.* 38, 1440–1443.

Peebles, P., and Ratra, B. (1988). Cosmology with a Time Variable Cosmological Constant. *Astrophys. J.* 325:L17. doi: 10.1086/185100

Peirone, S., Frusciante, N., Hu, B., Raveri, M., and Silvestri, A. (2018). Do current cosmological observations rule out all Covariant Galileons? *Phys. Rev. D* 97:063518. doi: 10.1103/PhysRevD.97.063518

Percival, W. J., Baugh, C. M., Bland-Hawthorn, J., Bridges, T., Cannon, R., Cole, S., et al. (2001). The 2dF galaxy redshift survey: the power spectrum and the matter content of the Universe. *Mon. Not. R. Astron. Soc.* 327:1297. doi: 10.1046/j.1365-8711.2001.04827.x

Petcov, S., and Piai, M. (2002). The LMA MSW solution of the solar neutrino problem, inverted neutrino mass hierarchy and reactor neutrino experiments. *Phys. Lett.* B533, 94–106. doi: 10.1016/S0370-2693(02)01591-5

Pober, J. C., Ali, Z. S., Parsons, A. R., McQuinn, M., Aguirre, J. E., Bernardi, G., et al. (2015). PAPER-64 constraints on reionization II: the temperature of the $z = 8.4$ intergalactic medium. *Astrophys. J.* 809:62. doi: 10.1088/0004-637X/809/1/62

Pospelov, M., Pradler, J., Ruderman, J. T., and Urbano, A. (2018). Room for new physics in the rayleigh-jeans tail of the cosmic microwave background. *Phys. Rev. Lett.* 121:031103. doi: 10.1103/PhysRevLett.121.031103

Pritchard, J. R., and Loeb, A. (2012). 21-cm cosmology. *Rept. Prog. Phys.* 75:086901. doi: 10.1088/0034-4885/75/8/086901

Pritchard, J. R., and Pierpaoli, E. (2008). Constraining massive neutrinos using cosmological 21 cm observations. *Phys. Rev. D* 78:065009. doi: 10.1103/PhysRevD.78.065009

Qian, X., Tan, A., Wang, W., Ling, J., McKeown, R., and Zhang, C. (2012). Statistical evaluation of experimental determinations of neutrino mass hierarchy. *Phys. Rev. D* 86:113011. doi: 10.1103/PhysRevD.86.113011

Qian, X., and Vogel, P. (2015). Neutrino mass hierarchy. *Prog. Part. Nucl. Phys.* 83, 1–30. doi: 10.1016/j.ppnp.2015.05.002

Radovic, A. (2018). *JETP January 2018, NOvA Oscillation Results*. Available online at: http://nova-docdb.fnal.gov/cgi-bin/ShowDocument?docid=25938

Raffelt, G. (1999). Stars as particle-physics laboratories. *AIP Conf. Proc.* 490, 125–162.

Raffelt, G., and Sigl, G. (2007). Self-induced decoherence in dense neutrino gases. *Phys. Rev. D* 75:083002. doi: 10.1103/PhysRevD.75.083002

Raffelt, G. G., and Smirnov, A. Y. (2007a). Adiabaticity and spectral splits in collective neutrino transformations. *Phys. Rev. D* 76:125008. doi: 10.1103/PhysRevD.76.125008

Raffelt, G. G., and Smirnov, A. Y. (2007b). Self-induced spectral splits in supernova neutrino fluxes. *Phys. Rev. D* 76:081301. doi: 10.1103/PhysRevD.77.029903

Ratra, B., and Peebles, P. (1988). Cosmological consequences of a rolling homogeneous scalar field. *Phys. Rev. D* 37:3406.

Reid, B. A., Verde, L., Jimenez, R., and Mena, O. (2010). Robust neutrino constraints by combining low redshift observations with the CMB. *JCAP* 01:003. doi: 10.1088/1475-7516/2010/01/003

Renk, J., Zumalacárregui, M., Montanari, F., and Barreira, A. (2017). Galileon gravity in light of ISW, CMB, BAO and H_0 data. *JCAP* 10:020. doi: 10.1088/1475-7516/2017/10/020

Ribordy, M., and Smirnov, A. Y. (2013). Improving the neutrino mass hierarchy identification with inelasticity measurement in PINGU and ORCA. *Phys. Rev. D* 87:113007. doi: 10.1103/PhysRevD.87.113007

Riemer-Sorensen, S. et al. (2012). The wiggleZ dark energy survey: cosmological neutrino mass constraint from blue high-redshift galaxies. *Phys. Rev. D* 85:081101. doi: 10.1103/PhysRevD.85.081101

Riemer-Sorensen, S., Parkinson, D., and Davis, T. M. (2014). Combining Planck data with large scale structure information gives a strong neutrino mass constraint. *Phys. Rev. D* 89:103505. doi: 10.1103/PhysRevD.89.103505

Riemer-Sorensen, S., Parkinson, D., Davis, T. M., and Blake, C. (2013). Simultaneous constraints on the number and mass of relativistic species. *Astrophys. J.* 763:89. doi: 10.1088/0004-637X/763/2/89

Riess, A. G., Macri, L., Casertano, S., Lampeitl, H., Ferguson, H. C., Filippenko, A. V., et al. (2011). A 3% solution: determination of the hubble constant with the hubble space telescope and wide field camera 3. *Astrophys. J.* 730:119. doi: 10.1088/0004-637X/730/2/119

Riess, A. G., Macri, L. M., Hoffmann, S. L., Scolnic, D., Casertano, S., Filippenko, A. V., et al. (2016). A 2.4% determination of the local value of the hubble constant. *Astrophys. J.* 826:56. doi: 10.3847/0004-637X/826/1/56

Ringwald, A. (2005). How to detect big bang relic neutrinos? *High Energy Phys.* 473–491.

Ringwald, A. and Wong, Y. Y. Y. (2004). Gravitational clustering of relic neutrinos and implications for their detection. *JCAP* 12:005. doi: 10.1088/1475-7516/2004/12/005

Robertson, D. S., and Albuquerque, I. F. M. (2018). Probing velocity dependent self-interacting dark matter with neutrino telescopes. *JCAP* 02:056. doi: 10.1088/1475-7516/2018/02/056

Rodejohann, W. (2011). Neutrino-less double beta decay and particle physics. *Int. J. Mod. Phys.* E20, 1833–1930. doi: 10.1142/S0218301311020186

Ross, A. J., Beutler, F., Chuang, C.-H., Pellejero-Ibanez, M., Seo, H.-J., Vargas-Magana, M., et al. (2017). The clustering of galaxies in the completed SDSS-III Baryon Oscillation Spectroscopic Survey: observational systematics and baryon acoustic oscillations in the correlation function. *Mon. Not. R. Astron. Soc.* 464, 1168–1191. doi: 10.1093/mnras/stw2372

Ross, A. J., Samushia, L., Howlett, C., Percival, W. J., Burden, A., and Manera, M. (2015). The clustering of the SDSS DR7 main Galaxy sample - I. A 4 per cent distance measure at $z = 0.15$. *Mon. Not. R. Astron. Soc.* 449, 835–847. doi: 10.1093/mnras/stv154

Rozo, E., and Rykoff, E. S. (2014). redMaPPer II: X-ray and SZ performance benchmarks for the SDSS catalog. *Astrophys. J.*, 783:80. doi: 10.1088/0004-637X/783/2/80

Rozo, E., Rykoff, E. S., Bartlett, J. G., and Melin, J. B. (2015). redMaPPer – III. A detailed comparison of the Planck 2013 and SDSS DR8 redMaPPer cluster catalogues. *Mon. Not. R. Astron. Soc.* 450, 592–605. doi: 10.1093/mnras/stv605

Rybka, G. (2018). "Project 8: progress towards using cyclotron radiation emission spectroscopy on atomic tritium for a neutrino mass measurement, " in *XXVIII International Conference on Neutrino Physics and Astrophysics, 4–9 June 2018* (Heidelberg). Avilable online at: http://doi.org/10.5281/zenodo.1286954

Rykoff, E., Rozo, E., Busha, M. T., Cunha, C. E., Finoguenov, A., Evrard, A., et al. (2014). redMaPPer I: algorithm and SDSS DR8 catalog. *Astrophys. J.* 785, 104. doi: 10.1088/0004-637X/785/2/104

Safarzadeh, M., Scannapieco, E., and Babul, A. (2018). A limit on the warm dark matter particle mass from the redshifted 21 cm absorption line. *Astrophys. J.* 859:L18. doi: 10.3847/2041-8213/aac5e0

Saito, S., Takada, M., and Taruya, A. (2008). Impact of massive neutrinos on nonlinear matter power spectrum. *Phys. Rev. Lett.* 100:191301. doi: 10.1103/PhysRevLett.100.191301

Sanchez, A. G. et al. (2017). The clustering of galaxies in the completed SDSS-III Baryon oscillation spectroscopic survey: cosmological implications of the configuration-space clustering wedges. *Mon. Not. R. Astron. Soc.* 464, 1640–1658. doi: 10.1093/mnras/stw2443

Santos, M. G., and Cooray, A. (2006). Cosmological and astrophysical parameter measurements with 21-cm anisotropies during the era of reionization. *Phys. Rev. D* 74:083517. doi: 10.1103/PhysRevD.74.083517

Satpathy, S., Alam, S., Ho, S., White, M., Bahcall, N. A., Beutler, F., et al. (2016). BOSS DR12 combined galaxy sample: The clustering of galaxies in the completed SDSS-III Baryon Oscillation Spectroscopic Survey: On the

measurement of growth rate using galaxy correlation functions. *Mon. Not. R. Astron. Soc.* doi: 10.1093/mnras/stx883

Schechter, J., and Valle, J. W. F. (1982). Neutrinoless Double beta Decay in SU(2) x U(1) Theories. *Phys. Rev. D* 25:2951. doi: 10.1103/PhysRevD.25.2951

Scholberg, K. (2012). Supernova neutrino detection. *Ann. Rev. Nucl. Part. Sci.* 62, 81–103. doi: 10.1146/annurev-nucl-102711-095006

Scholberg, K. (2018). Supernova signatures of neutrino mass ordering. *J. Phys. G* 45:014002. doi: 10.1088/1361-6471/aa97be

Schramm, D., and Truran, J. (1990). New physics from supernova SN1987A. *Phys. Rept.* 189, 89–126. doi: 10.1016/0370-1573(90)90020-3

Schwetz, T., Freese, K., Gerbino, M., Giusarma, E., Hannestad, S., Lattanzi, M., et al. (2017). Comment on "strong evidence for the normal neutrino hierarchy". *arXiv:1703.04585*.

Scott, D., and Rees, M. J. (1990). The 21-cm line at high redshift: a diagnostic for the origin of large scale structure. *Mon. Not. R. Astron. Soc.* 247:510.

Sejersen Riis, A., Hannestad, S., and Weinheimer, C. (2011). Analysis of simulated data for the KArlsruhe TRItium Neutrino experiment using Bayesian inference. *Phys. Rev. C* 84:045503. doi: 10.1103/PhysRevC.84.045503

Seljak, U., Makarov, A., McDonald, P., Anderson, S., Bahcall, N., Brinkmann, J., et al. (2005). Cosmological parameter analysis including SDSS Ly-alpha forest and galaxy bias: Constraints on the primordial spectrum of fluctuations, neutrino mass, and dark energy. *Phys. Rev. D* 71:103515. doi: 10.1103/PhysRevD.71.103515

Seljak, U., Slosar, A., and McDonald, P. (2006). Cosmological parameters from combining the Lyman-alpha forest with CMB, galaxy clustering and SN constraints. *JCAP* 10:014. doi: 10.1088/1475-7516/2006/10/014

Senatore, L., and Zaldarriaga, M. (2017). The effective field theory of large-Scale structure in the presence of massive neutrinos. *arXiv:1707.04698*.

Shim, J., Lee, J., and Baldi, M. (2014). Breaking the cosmic degeneracy between modified gravity and massive neutrinos with the cosmic web. *arXiv:1404.3639*.

Shimabukuro, H., Ichiki, K., Inoue, S., and Yokoyama, S. (2014). Probing small-scale cosmological fluctuations with the 21 cm forest: Effects of neutrino mass, running spectral index, and warm dark matter. *Phys. Rev. D* 90:083003. doi: 10.1103/PhysRevD.90.083003

Shirai, J. (2017). Results and future plans for the KamLAND-Zen experiment. *J. Phys.* 888, 012031. doi: 10.1088/1742-6596/888/1/012031

Shoji, M., and Komatsu, E. (2010). Massive neutrinos in cosmology: analytic solutions and fluid approximation. *Phys. Rev. D* 81:123516. doi: 10.1103/PhysRevD.81.123516

Simpson, F., Jimenez, R., Peña-Garay, C., and Verde, L. (2017). Strong evidence for the normal neutrino hierarchy. *JCAP* 06:029. doi: 10.1088/1475-7516/2017/06/029

Singh, S., and Ma, C.-P. (2003). Neutrino clustering in cold dark matter halos : implications for ultrahigh-energy cosmic rays. *Phys. Rev. D* 67:023506. doi: 10.1103/PhysRevD.67.023506

Slatyer, T. R., and Wu, C.-L. (2018). Early-universe constraints on dark matter-baryon scattering and their implications for a global 21cm signal. *Phys. Rev. D* 98:023013. doi: 10.1103/PhysRevD.98.023013

Slosar, A., Iršič, V., Kirkby, D., Bailey, S., Busca, N. G., Delubac, T., et al. (2013). Measurement of baryon acoustic oscillations in the lyman-alpha forest fluctuations in boss data release 9. *JCAP* 04:026. doi: 10.1088/1475-7516/2013/04/026

Smith, K. M., Hu, W., and Kaplinghat, M. (2006). Cosmological Information from Lensed CMB Power Spectra. *Phys. Rev. D* 74:123002. doi: 10.1103/PhysRevD.74.123002

Smith, R. E., Peacock, J. A., Jenkins, A., White, S. D. M., Frenk, C. S., Pearce, F. R., et al. (2003). Stable clustering, the halo model and nonlinear cosmological power spectra. *Mon. Not. R. Astron. Soc.* 341:1311. doi: 10.1046/j.1365-8711.2003.06503.x

Sohn, J., Chon, G., Böhringer, H., Geller, M. J., Diaferio, A., Hwang, H. S., et al. (2018). The hectoMAP cluster survey - II. X-ray clusters. *Astrophys. J.* 855:100. doi: 10.3847/1538-4357/aaac7a

Song, Y.-S., and Knox, L. (2004). Determination of cosmological parameters from cosmic shear data. *Phys. Rev.D* 70:063510. doi: 10.1103/PhysRevD.70.063510

Spergel, D., Gehrels, N., Baltay, C., Bennett, D., Breckinridge, J., Donahue, M., et al. (2015). Wide-Field infrarRed Survey telescope-astrophysics focused telescope assets WFIRST-AFTA 2015 Report. *arXiv:1503.03757*.

Spergel, D., Gehrels, N., Breckinridge, J., Donahue, M., Dressler, A., Gaudi, B. S., et al. (2013). Wide-field infraRed survey telescope-astrophysics focused telescope assets WFIRST-AFTA Final Report. *arXiv:1305.5422*.

Spergel, D., Verde, L., Peiris, H. V., Komatsu, E., Nolta, M. R., Bennett, C. L., et al. (2003). First year wilkinson microwave anisotropy probe (WMAP) observations: determination of cosmological parameters. *Astrophys. J. Suppl.* 148, 175–194. doi: 10.1086/377226

Sprenger, T., Archidiacono, M., Brinckmann, T., Clesse, S., and Lesgourgues, J. (2018). Cosmology in the era of Euclid and the Square Kilometre Array. *arXiv:1801.08331*.

Springer, P., Bennett, C., and Baisden, P. (1987). Measurement of the neutrino mass using the Inner Bremsstrahlung Emitted in the Electron-Capture Decay og 163Ho. *Phys. Rev. A* 35, 679–689. doi: 10.1103/PhysRevA.35.679

Srivastava, R., Ternes, C. A., Tórtola, M., and Valle, J. W. F. (2018a). Testing a lepton quarticity flavor theory of neutrino oscillations with the DUNE experiment. *Phys. Lett.* B778, 459–463. doi: 10.1016/j.physletb.2018.01.014

Srivastava, R., Ternes, C. A., Tórtola, M., and Valle, J. W. F. (2018b). Zooming in on neutrino oscillations with DUNE. *Phys. Rev. D* 97:095025. doi: 10.1103/PhysRevD.97.095025

Stanco, L., Salamanna, G., Sawy, F., and Sirignano, C. (2017). A new way to determine the neutrino mass hierarchy at reactors. *arXiv:1707.07651*.

Strait, J. et al. (2016). Long-baseline neutrino facility (LBNF) and deep underground neutrino experiment (DUNE). *arXiv: 1601.05823*.

Sutherland, W. (2018). The CMB neutrino mass/vacuum energy degeneracy: a simple derivation of the degeneracy slopes. *Mon. Not. R. Astron. Soc.* 477, 1913–1920. doi: 10.1093/mnras/sty687

Suzuki, A. et al. (2016). The POLARBEAR-2 and the Simons Array Experiment. *J. Low. Temp. Phys.* 184, 805–810. doi: 10.1007/s10909-015-1425-4

Takahashi, R., Sato, M., Nishimichi, T., Taruya, A., and Oguri, M. (2012). Revising the halofit model for the nonlinear matter power spectrum. *Astrophys. J.* 761:152. doi: 10.1088/0004-637X/761/2/152

Tegmark, M., Eisenstein, D., Strauss, M., Weinberg, D., Blanton, M., Frieman, J., et al. (2006). Cosmological constraints from the SDSS luminous red galaxies. *Phys. Rev. D* 74:123507. doi: 10.1103/PhysRevD.74.123507

Tegmark, M., Strauss, M., Blanton, M., Abazajian, K., Dodelson, S., Sandvik, H., et al. (2004). Cosmological parameters from SDSS and WMAP. *Phys. Rev. D* 69:103501. doi: 10.1103/PhysRevD.69.103501

Tegmark, M., and Zaldarriaga, M. (2009). The fast fourier transform telescope. *Phys. Rev. D* 79:083530. doi: 10.1103/PhysRevD.79.083530

Tereno, I., Schimd, C., Uzan, J.-P., Kilbinger, M., Vincent, F. H., and Fu, L. (2009). CFHTLS weak-lensing constraints on the neutrino masses. *Astron. Astrophys.* 500, 657–665. doi: 10.1051/0004-6361/200811077

Thakore, T., Devi, M. M., Kumar Agarwalla, S., and Dighe, A. (2018). Active-sterile neutrino oscillations at INO-ICAL over a wide mass-squared range. *J. High Energy Phys.* 08:022. doi: 10.1007/JHEP08(2018)022

Tingay, S., Goeke, R., Bowman, J. D., Emrich, D., Ord, S. M., Mitchell, D. A., et al. (2013). The murchison widefield array: the square kilometre array precursor at low radio frequencies. *Publ. Astron. Soc. Austral.* 30:7. doi: 10.1017/pasa.2012.007

Tinker, J. L., Kravtsov, A. V., Klypin, A., Abazajian, K., Warren, M. S., Yepes, G., et al. (2008). Toward a halo mass function for precision cosmology: the Limits of universality. *Astrophys. J.* 688, 709–728. doi: 10.1086/591439

Tojeiro, R., Ross, A. J., Burden, A., Samushia, L., Manera, M., Percival, W. J., et al. (2014). The clustering of galaxies in the SDSS-III baryon oscillation spectroscopic survey: galaxy clustering measurements in the low redshift sample of data release 11. *Mon. Not. R. Astron. Soc.* 440, 2222–2237. doi: 10.1093/mnras/stu371

Tozzi, P., Madau, P., Meiksin, A., and Rees, M. J. (2000). Radio signatures of hi at high redshift: mapping the end of the "dark ages". *Astrophys. J.* 528:597. doi: 10.1086/308196

Trotta, R. (2008). Bayes in the sky: bayesian inference and model selection in cosmology. *Contemp. Phys.*, 49, 71–104. doi: 10.1080/00107510802066753

Upadhye, A., Kwan, J., Pope, A., Heitmann, K., Habib, S., Finkel, H., and Frontiere, N. (2016). Redshift-space distortions in massive neutrino and evolving dark energy cosmologies. *Phys. Rev. D* 93:063515. doi: 10.1103/PhysRevD.93.063515

Vagnozzi, S., Dhawan, S., Gerbino, M., Freese, K., Goobar, A., and Mena, O. (2018). Constraints on the sum of the neutrino masses in dynamical dark energy models with $w(z) \geq -1$ are tighter than those obtained in ΛCDM. *arXiv:1801.08553*.

Vagnozzi, S., Giusarma, E., Mena, O., Freese, K., Gerbino, M., Ho, S., and Lattanzi, M. (2017). Unveiling ν secrets with cosmological data: neutrino masses and mass hierarchy. *Phys. Rev. D* 96:123503. doi: 10.1103/PhysRevD.96.123503

van Haarlem, M., Wise, M. W., Gunst, A. W., Heald, G., McKean, J. P., Hessels, J. W. T., et al. (2013). LOFAR: the low-frequency ARray. *Astron. Astrophys.* 556:A2. doi: 10.1051/0004-6361/201220873

Vargas-Magaña, M. et al. (2018). The clustering of galaxies in the completed SDSS-III Baryon Oscillation Spectroscopic Survey: theoretical systematics and Baryon Acoustic Oscillations in the galaxy correlation function. *Mon. Not. R. Astron. Soc.* 477, 1153–1188. doi: 10.1093/mnras/sty571

Vergados, J., Ejiri, H., and Simkovic, F. (2012). Theory of neutrinoless double beta decay. *Rept. Prog. Phys.* 75:106301. doi: 10.1088/0034-4885/75/10/106301

Vergados, J., Ejiri, H., and Šimkovic, F. (2016). Neutrinoless double beta decay and neutrino mass. *Int. J. Mod. Phys.* E25:1630007. doi: 10.1142/S0218301316300071

Viel, M., Becker, G. D., Bolton, J. S., and Haehnelt, M. G. (2013). Warm dark matter as a solution to the small scale crisis: new constraints from high redshift Lyman-α forest data. *Phys. Rev. D* 88:043502. doi: 10.1103/PhysRevD.88.043502

Viel, M., Haehnelt, M. G., and Springel, V. (2010). The effect of neutrinos on the matter distribution as probed by the intergalactic medium. *JCAP* 06:015. doi: 10.1088/1475-7516/2010/06/015

Villaescusa-Navarro, F. et al. (2014a). Cosmology with massive neutrinos I: towards a realistic modeling of the relation between matter, haloes and galaxies. *JCAP* 03:011. doi: 10.1088/1475-7516/2014/03/011

Villaescusa-Navarro, F., Bull, P., and Viel, M. (2015). Weighing neutrinos with cosmic neutral hydrogen. *Astrophys. J.* 814:146. doi: 10.1088/0004-637X/814/2/146

Villaescusa-Navarro, F., Viel, M., Datta, K. K., and Choudhury, T. R. (2014b). Modeling the neutral hydrogen distribution in the post-reionization Universe: intensity mapping. *JCAP* 09:050. doi: 10.1088/1475-7516/2014/09/050

Villaescusa-Navarro, F., Vogelsberger, M., Viel, M., and Loeb, A. (2013). Neutrino signatures on the high transmission regions of the lyman-alpha forest. *Mon. Not. R. Astron. Soc.* 431:3670. doi: 10.1093/mnras/stt452

Visbal, E., Loeb, A., and Wyithe, J. B. (2009). Cosmological constraints from 21cm surveys after reionization. *JCAP* 10:030. doi: 10.1088/1475-7516/2009/10/030

Vogel, P. (2015). How difficult it would be to detect cosmic neutrino background? *AIP Conf. Proc.* 1666, 140003. doi: 10.1063/1.4915587

Wang, G., Chang, C. L., Yefremenko, V., Ding, J., Novosad, V., Bucci, C., et al. (2015). CUPID: CUORE (Cryogenic underground observatory for rare events) upgrade with particle IDentification. *arXiv:1504.03599*.

Wang, L.-M., Caldwell, R., Ostriker, J., and Steinhardt, P. J. (2000). Cosmic concordance and quintessence. *Astrophys. J.* 530, 17–35. doi: 10.1086/308331

Wang, S., and Xia, D.-M. (2018). Constraints on the sum of neutrino masses from Bayesian analysis of the latest cosmological data. *Chin. Phys. C* 42:065103.

Weiler, T. J. (1982). Resonant absorption of cosmic ray neutrinos by the relic neutrino background. *Phys. Rev. Lett.* 49:234. doi: 10.1103/PhysRevLett.49.234

Weiler, T. J. (1984). Big bang cosmology, relic neutrinos, and absorption of neutrino cosmic rays. *Astrophys. J.* 285:495. doi: 10.1086/162524

Weinberg, D. H., Mortonson, M. J., Eisenstein, D. J., Hirata, C., Riess, A. G., and Rozo, E. (2013). Observational probes of cosmic acceleration. *Phys. Rept.* 530, 87–255. doi: 10.1016/j.physrep.2013.05.001

Weinberg, S. (1962). Universal neutrino degeneracy. *Phys. Rev.* 128, 1457–1473. doi: 10.1103/PhysRev.128.1457

Weinberg, S. (1978). A new light boson? *Phys. Rev. Lett.* 40, 223–226. doi: 10.1103/PhysRevLett.40.223

Wetterich, C. (1995). The Cosmon model for an asymptotically vanishing time dependent cosmological 'constant'. *Astron.Astrophys.*, 301:321–328.

Wilczek, F. (1978). Problem of strong p and t invariance in the presence of instantons. *Phys. Rev. Lett.* 40, 279–282. doi: 10.1103/PhysRevLett.40.279

Winter, W. (2016). Atmospheric neutrino oscillations for earth tomography. *Nucl. Phys.* B908, 250–267. doi: 10.1016/j.nuclphysb.2016.03.033

Witte, S., Villanueva-Domingo, P., Gariazzo, S., Mena, O., and Palomares-Ruiz, S. (2018). EDGES result versus CMB and low-redshift constraints on ionization histories. *Phys. Rev. D*, 97:103533. doi: 10.1103/PhysRevD.97.103533

Wolfenstein, L. (1978). Neutrino oscillations in matter. *Phys. Rev. D* 17, 2369–2374. doi: 10.1103/PhysRevD.17.2369

Wyithe, S., Loeb, A., and Geil, P. (2008). Baryonic acoustic oscillations in 21cm emission: a probe of dark energy out to high redshifts. *Mon. Not. R. Astron. Soc.*, 383:1195. doi: 10.1111/j.1365-2966.2007.12631.x

Yañez, J., and Kouchner, A. (2015). Measurement of atmospheric neutrino oscillations with very large volume neutrino telescopes. *Adv. High Energy Phys.*, 2015:271968. doi: 10.1155/2015/271968

Yang, Y. (2018). The contributions of dark matter annihilation to the global 21cm spectrum observed by the EDGES experiment. *arXiv:1803.05803*.

Yeche, C., Palanque-Delabrouille, N., Baur, J. ., and BourBoux, H. d. M. d. (2017). Constraints on neutrino masses from Lyman-alpha forest power spectrum with bOSS and XQ-100. *JCAP* 06:047. doi: 10.1088/1475-7516/2017/06/047

Zhang, J., and Zhang, X. (2018). Gravitational clustering of cosmic relic neutrinos in the milky way. *Nat. Commun.* 9:1833. doi: 10.1038/s41467-018-04264-y

Zhao, G.-B., Saito, S., Percival, W. J., Ross, A. J., Montesano, F., Viel, M., et al. (2013). The clustering of galaxies in the SDSS-III Baryon Oscillation Spectroscopic Survey: weighing the neutrino mass using the galaxy power spectrum of the CMASS sample. *Mon. Not. R. Astron. Soc.* 436, 2038–2053. doi: 10.1093/mnras/stt1710

Zhao, J., Wen, L.-J., Wang, Y.-F., and Cao, J. (2017). Physics potential of searching for $0\nu\beta\beta$ decays in JUNO. *Chin. Phys. C* 41:053001. doi: 10.1088/1674-1137/41/5/053001

Zlatev, I., Wang, L.-M., and Steinhardt, P. J. (1999). Quintessence, cosmic coincidence, and the cosmological constant. *Phys. Rev. Lett.* 82, 896–899. doi: 10.1103/PhysRevLett.82.896

Conflict of Interest Statement: The authors declare that the research was conducted in the absence of any commercial or financial relationships that could be construed as a potential conflict of interest.

frontiers in Physics

ORIGINAL RESEARCH
published: 26 January 2017
doi: 10.3389/fphy.2016.00053

Toward a Quantum Theory of Humor

Liane Gabora[1]* *and Kirsty Kitto*[2]

[1] Department of Psychology, University of British Columbia, Kelowna, BC, Canada, [2] Department of Mathematical Sciences, Queensland University of Technology, Brisbane, QLD, Australia

This paper proposes that cognitive humor can be modeled using the mathematical framework of quantum theory. We begin with brief overviews of both research on humor, and the generalized quantum framework. We show how the bisociation of incongruous frames or word meanings in jokes can be modeled as a linear superposition of a set of basis states, or possible interpretations, in a complex Hilbert space. The choice of possible interpretations depends on the context provided by the set-up vs. the punchline of a joke. We apply the approach to a verbal pun, and consider how it might be extended to frame blending. An initial study of that made use of the Law of Total Probability, involving 85 participant responses to 35 jokes (as well as variants), suggests that the Quantum Theory of Humor (QTH) proposed here provides a viable new approach to modeling humor.

Keywords: bisociation, context, humor, incongruity, law of total probability, pun, quantum cognition, quantum interaction

OPEN ACCESS

Edited by:
Andrei Khrennikov,
Linnaeus University, Sweden

Reviewed by:
Haroldo Valentin Ribeiro,
Universidade Estadual de Maringá, Brazil
Raimundo Nogueira Costa Filho,
Federal University of Ceará, Brazil
Irina Basieva,
Graduate School for the Creation of New Photonics Industries, Russia

***Correspondence:**
Liane Gabora
liane.gabora@ubc.ca

Specialty section:
This article was submitted to Interdisciplinary Physics, a section of the journal Frontiers in Physics

Received: *01 September 2016*
Accepted: *21 December 2016*
Published: *26 January 2017*

Citation:
Gabora L and Kitto K (2017) Toward a Quantum Theory of Humor. Front. Phys. 4:53. doi: 10.3389/fphy.2016.00053

1. INTRODUCTION

Humor has been called the "killer app" of language [1]; it showcases the speed, playfulness, and flexibility of human cognition, and can instantaneously put people in a positive mood. For over a 100 years scholars have attempted to make sense of the seemingly nonsensical cognitive processes that underlie humor. Despite considerable progress with respect to categorizing different forms of humor (e.g., irony, jokes, cartoons, and slapstick) and understanding what people find funny, there has been little investigation of the question: What kind of formal theory do we need to model the cognitive representation of a joke as it is being understood?

This paper attempts to answer this question with a new model of humor that uses a generalization of the quantum formalism. The last two decades have witnessed an explosion of applications of quantum models to psychological phenomena that feature ambiguity and/or contextuality [2–4]. Many psychological phenomena have been studied using quantum models, including the combination of words and concepts [5–10], similarity and memory [11, 12], information retrieval [13, 14], decision making and probability judgment errors [15–19], vision [20, 21], sensation–perception [22], social science [23, 24], cultural evolution [25, 26], and creativity [27, 28]. These quantum inspired approaches make no assumption that phenomena at the quantum level affect the brain, but rather, draw solely on abstract formal structures that, as it happens, found their first application in quantum mechanics. They utilize the structurally different nature of quantum probability. While in classical probability theory events are drawn from a common sample space, quantum models define states and variables with reference to a context, represented using a basis in a Hilbert space. This results in phenomena such as interference, superposition and entanglement, and ambiguity with respect to the outcome is resolved with a quantum measurement and a collapse to a definite state.

This makes the quantum inspired approach an interesting new candidate for a theory of humor. Humor often involves ambiguity due to the presence of incongruous schemas: internally coherent but mutually incompatible ways of interpreting or understanding a statement or situation. As a simple example, consider the following pun:

"Time flies like an arrow. Fruit flies like a banana."

This joke hangs on the ambiguity of the phrase FRUIT FLIES, where the word FLIES can be either a verb or a noun. As a verb, FLIES means "to travel through the air." However, as a noun, FRUIT FLIES are "insects that eat fruit." Quantum formalisms are highly useful for describing cognitive states that entail this form of ambiguity. This paper will propose that the quantum approach enables us to naturally represent the process of "getting a joke."

We start by providing a brief overview of the relevant research on humor.

2. BRIEF BACKGROUND IN HUMOR RESEARCH

Even within psychology, humor is approached from multiple directions. Social psychologists investigate the role of humor in establishing, maintaining, and disrupting social cohesion and social status, developmental psychologists investigate how the ability to understand and generate humor changes over a lifetime, and health psychologists investigate possible therapeutic aspects of humor. This paper deals solely with the cognitive aspect of humor. Much cognitive theorizing about humor assumes that it is driven by the simultaneous perception [29, 30] or "bisociation" [31] of incongruent *schemas*. Schemas can be either static *frames*, as in a cartoon, or dynamically unfolding *scripts*, as in a pun. For example, in the "time flies" joke above, interpreting the phrase FRUIT FLIES as referring to the insect is incompatible with interpreting it as food traveling through the air. Incongruity is generally accompanied by the violation of expectations and feelings of surprise. While earlier approaches posited that humor comprehension involves the *resolution* of incongruous frames or scripts [32, 33], the notion of resolution often plays a minor role in contemporary theories, which tend to view the punchline as activating multiple schemas simultaneously and thereby underscoring ambiguity (e.g., 34, 35).

There are computational models of humor detection and understanding (e.g., 36), in which the interpretation of an ambiguous word or phrase changes as new surrounding contextual information is parsed. For example, in the "time flies" joke, this kind of model would shift from interpreting FLIES as a verb to interpreting it as a noun. There are also computational models of humor that generate jokes through lexical replacement; for example, by replacing a "taboo" word with a similar-sounding innocent word (e.g., [37, 38]). These computational approaches to humor are interesting, and occasionally generate jokes that are laugh-worthy. However, while they tell us something about humor, we claim that they do not provide an accurate model of the cognitive state of a human mind at the instant of perceiving a joke. As mentioned above, humor psychologists believe that humor often involves not just shifting from one interpretation of an ambiguous stimulus to another, but simultaneously holding in mind the interpretation that was perceived to be relevant during the set-up and the interpretation that is perceived to be relevant during the punchline. For this reason, we turned to the generalized quantum formalism as a possible approach for modeling the cognitive state of holding two schemas in mind simultaneously.

3. BRIEF BACKGROUND IN GENERALIZED QUANTUM MODELING

Classical probability describes events by considering subsets of a common sample space [39]. That is, considering a set of elementary events, we find that some event e occurred with probability p_e. Classical probability arises due to a lack of knowledge on the part of the modeler. The act of measurement merely reveals an existing state of affairs; it does not interfere with the results.

In contrast, quantum models use variables and spaces that are defined with respect to a particular context (although this is often done implicitly). Thus, in specifying that an electron has spin "up" or "down," we are referring to experimental scenarios (e.g., Stern-Gerlach arrangements and polarizers) that denote the context in which a measurement occurred. This is an important subtlety, as many experiments have shown that it is impossible to attribute a pre-existing reality to the state that is measured; measurement necessarily involves an interaction between a state and the context in which it is measured, and this is traditionally modeled in quantum theory using the notion of projection. The *state* $|\Psi\rangle$ representing some aspect of interest in our system is written as a linear superposition of a set of *basis states* $\{|\phi_i\rangle\}$ in a *Hilbert space*, denoted $\mathcal{H}$, which allows us to define notions such as distance and inner product. In creating this superposition we weight each basis state with an amplitude term, denoted a_i, which is a complex number representing the contribution of a component basis state $|\phi_i\rangle$ to the state $|\Psi\rangle$. Hence $|\Psi\rangle = \sum_i a_i|\phi_i\rangle$. The square of the absolute value of the amplitude equals the probability that the state changes to that particular basis state upon measurement. This non-unitary change of state is called *collapse*. The choice of basis states is determined by the *observable*, $\hat{O}$, to be measured, and its possible outcomes o_i. The basis states corresponding to an observable are referred to as *eigenstates*. Observables are represented by self-adjoint operators on the Hilbert space. Upon *measurement*, the state of the entity is projected onto one of the eigenstates.

It is also possible to describe combinations of two entities within this framework, and to learn about how they might influence one another, or not. Consider two entities A and B with Hilbert spaces $\mathcal{H}_\mathcal{A}$ and $\mathcal{H}_\mathcal{B}$. We may define a basis $|i\rangle_A$ for $\mathcal{H}_\mathcal{A}$ and a basis $|j\rangle_B$ for $\mathcal{H}_\mathcal{B}$, and denote the amplitudes associated with the first as a_i^A and the amplitudes associated with the second as a_j^B. The Hilbert space in which a composite of these entities exists is given by the tensor product $\mathcal{H}_\mathcal{A} \otimes \mathcal{H}_\mathcal{B}$. The most general state in $\mathcal{H}_\mathcal{A} \otimes \mathcal{H}_\mathcal{B}$ has the form

$$|\Psi\rangle_{AB} = \sum_{i,j} a_{ij} |i\rangle_A \otimes |j\rangle_B \quad (1)$$

This state is separable if $a_{ij} = a_i^A a_j^B$. It is inseparable, and therefore an entangled state, if $a_{ij} \neq a_i^A a_j^B$.

In some applications, the procedure for describing entanglement is more complicated than what is described here. For example, it has been argued that the quantum field theory procedure, which uses Fock space to describe multiple entities, gives a kind of internal structure that is superior to the tensor product for modeling concept combination [5]. Fock space is the direct sum of tensor products of Hilbert spaces, so it is also a Hilbert space. For simplicity, this initial application of the quantum formalsm to modeling humor will omit such refinements, but such a move may become necessary in further developments of the model.

Quantum models can be useful for describing situations involving *potentiality*, in which change of state is nondeterministic and contextual. The concept of potentiality has broad implications across the sciences; for example, every biological trait not only has direct implications for existing phenotypic properties such as fitness, but both enables and constrains potential future evolutionary changes for a given species. The quantum approach been used to model the biological phenomenon of *exaptation*—wherein a trait that originally evolved for one purpose is co-opted for another (possibly after some modification) [40]. The term *exaptation* was coined by Gould and Vrba [41] to denote what Darwin referred to as *preadaptation*[1]. Exaptation occurs when selective pressure causes this potentiality to be exploited. Like other kinds of evolutionary change, exaptation is observed across all levels of biological organization, i.e., at the level of genes, tissue, organs, limbs, and behavior. Quantum models have also been used to model the cultural analog of exaptation, wherein an idea that was originally developed to solve one problem is applied to a different problem [40]. For example, consider the invention of the tire swing. It came into existence when someone re-conceived of a tire as an object that could form the part of a swing that one sits on. This re-purposing of an object designed for one use for use in another context is referred to as *cultural exaptation*. Much as the current structural and material properties of an organ or appendage constrain possible re-uses of it, the current structural and material properties of a cultural artifact (or language, or art form, etc.) constrain possible re-uses of it. We suggest that incongruity humor constitutes another form of exaptation; an ambiguous word, phrase, or situation, that was initially interpreted one way is revealed to have a second, incongruous interpretation. Thus, it is perhaps unsurprising that, as with other forms of exaptation, a quantum model is explored.

4. A QUANTUM INSPIRED MODEL OF HUMOR

A quantum theory of humor (QTH) could potentially inherit several core concepts from previous cognitive theories of humor while providing a unified underlying model. Considering the past work discussed in Section 2, it seems reasonable to focus on the notion that cognitive humor involves an ambiguity brought on by the bisociation of internally consistent but mutually incongruous schemas. Thus, cognitive humor appears to arise from the double think that is brought about by being forced to reconsider some currently held interpretation of a joke in light of new information: a frame shift. Such an insight opens humor upto quantum-like models, as a frame shift of an ambiguous concept is well modeled by the notion of a quantum superposition described using two sets of incompatible basis states within some underlying Hilbert space structure.

In what follows we sketch out a preliminary quantum inspired model of humor and discuss what would be required for a full-fledged formal QTH. Next, we outline a study aimed at discovering whether humor behaves in a quantum-like manner. The last section discusses how the QTH opens up avenues for future investigation in a field that to date has not been well modeled.

4.1. The Mathematical Structure of QTH

We start our journey toward a QTH by building upon an existing model of conceptual combination [8]: the State–COntext–Property (SCOP) model. As per the standard approach used in most quantum-like models of cognition, $|\Psi\rangle$ represents the state of an ambiguous element, be it a word, phrase, object, or something else, and its different possible interpretations are represented by basis states. Core to the SCOP model is a treatment of the context in which every measurement of a state occurred, and the resultant property that was measured. These three variables are stored as a triple in a lattice.

4.1.1. The State Space

Following Aerts and Gabora [6], the set of all possible interpretation states for the ambiguous element of a joke is given by a state space Σ. Specific interpretations of a joke are denoted by $|p\rangle, |q\rangle, |r\rangle, \cdots \in \Sigma$ which form a basis in a complex Hilbert space $\mathcal{H}$. Before the ambiguous element of the joke is resolved, it is in a state of potentiality, represented by a superposition state of all possible interpretations. Each of these represents a possible understanding arising due to activation of a schema associated with a particular interpretation of an ambiguous word or situation. The interpretations that are most likely are most heavily weighted. The amplitude term associated with each basis state represented by a complex number coefficient a_i gives a measure of how likely an interpretation is given the current contextual information available to the listener. We assume that all basis states have unit length, are mutually orthogonal, and are complete, thus $\sum_i |a_i|^2 = 1$.

4.1.2. The Context

In the context of a traditional verbal joke, the context consists primarily of the setup, and the setup is the only contextual element considered in the study in Section 5. However, it should be kept in mind that several other contextual factors not considered in our analysis can affect perceived funniness. Prominent amongst these is the delivery; the way

[1]The terms *exaptation*, *preadaptation* and *co-option* are often used interchangeably.

in which a joke is delivered can be everything when it comes to whether or not it is deemed funny. Other factors include the surroundings, the person delivering the joke, the power relationships among different members of the audience, and so forth.

As a first step, we might represent the set of possible contexts for a given joke as $c_i \in \mathcal{C}$. Each possible interpretation of a joke comes with a set $f_i \in \mathcal{F}$ of properties (i.e., features or attributes), which may be weighted according to their relevance with respect to this contextual information. The *weight* (or renormalized applicability) of a certain property given a specific interpretation $|p\rangle$ in a specific context $c_i \in \mathcal{C}$ is given by ν. For example, $\nu(p, f_1)$ is the weight of feature f_i for state $|p\rangle$, which is determined by a function from the set $\Sigma \times \mathcal{F}$ to the interval $[0, 1]$. We write:

$$\begin{aligned} \nu : \Sigma \times \mathcal{F} &\rightarrow [0,1] \\ (p, f_i) &\mapsto \nu(p, f_i). \end{aligned} \tag{2}$$

4.1.3. Transition Probabilities

A second function μ describes the transition probability from one state to another under the influence of a particular context. For example, $\mu(q, e, p)$ is the probability that state $|p\rangle$ under the influence of context c_i changes to state $|q\rangle$. Mathematically, μ is a function from the set $\Sigma \times \mathcal{C} \times \Sigma$ to the interval $[0, 1]$, where $\mu(q, e, p)$ is the probability that state $|p\rangle$ under the influence of context $|e\rangle$ changes to state $|q\rangle$. We write:

$$\begin{aligned} \mu : \Sigma \times \mathcal{C} \times \Sigma &\rightarrow [0,1] \\ (q, e, p) &\mapsto \mu(q, e, p). \end{aligned} \tag{3}$$

Thus, a first step toward a full quantum model of humor consists of the 3-tuple $(\Sigma, \mathcal{C}, \mathcal{F})$, and the functions ν and μ. Next we address a key question that should be asked of any cognitive theory of humor: what is the underlying cognitive model of the funniness of a joke?

4.2. The Humor of a Joke

As the listener hears a joke, more context is provided, and in our model the listener's understanding evolves according to the transition probabilities associated with the cognitive state and the emerging context. When the listener hear the joke a bisociation of meaning is percieved; that is, the listener realizes that a second way of interpreting it is possible. A projective measurement onto a funniness frame is the mechanism that we use to model the likelihood that a given joke is considered funny.

Thus, in our model, funniness plays the role of a measurement operator, and it is affected by the shift that occurs in the understanding of a joke with respect to two possible framings: one created by the setup, and one by the punchline. The probability of a joke being regarded as funny or not is proportional to the projection of the individual's understanding of the joke ($|\Psi\rangle$) onto a basis representing funniness. This means that the probability of a joke being considered as funny, p_F is given by a projection onto the $|1\rangle$ axis in $\mathcal{H}_F^2$, a two-dimensional Hilbert sub-space where $|0\rangle$ represents "not funny" and $|1\rangle$ represents "funny."

$$p_F = ||1\rangle\langle 1|\Psi\rangle|^2 \tag{4}$$

Similarly, the probability of a joke being regarded as not funny is represented by

$$p_{\bar{F}} = ||0\rangle\langle 0|\Psi\rangle|^2. \tag{5}$$

Note that $|\Psi\rangle$ evolves as the initial conceptualization of the joke is reinterpreted with respect to the frame of the punchline. This is a difficult process to model, and we consider the work in this paper to be an early first step toward an eventually more comprehensive theory of humor that includes predictive models.

We now present two examples in which specific instances of humor are considered within the perspective of this basic quantum inspired model. First the approach is applied to a pun. Second, the approach is applied to a cartoon that is a frame blend. Both scenarios will help to deepen our understanding of the significant complexity of humor, and the difficulties associated with creating a mathematical model of this important human phenomenon.

4.3. Applying QTH to a Pun

Consider the pun: "Why was 6 afraid of 7? Because 789." The humor of this pun hinges on the fact that the pronunciation of the number EIGHT, a noun, is identical to that of the verb ATE. We refer to this ambiguous word, with its two possible meanings, as EYT. An individual's interpretation of the word EYT is represented by $|\Psi\rangle$, a vector of length equal to 1. This is a linear superposition of basis states in the semantic sub-space $\mathcal{H}_M^2$ which represents possible states (meanings) of the word EYT: EIGHT or ATE[2]. The interpretation of EYT as a noun, and specifically the number EIGHT, is denoted by the unit vector $|n\rangle$. The verb interpretation, ATE, is denoted by the unit vector $|v\rangle$. The set $\{|n\rangle, |v\rangle\}$ forms a basis in $\mathcal{H}_M^2$. Thus, we have now expanded our original two-dimensional funniness space with an additional two-dimensional semantic space, where the full space $\mathcal{H}^4 = \mathcal{H}_F^2 \otimes \mathcal{H}_M^2$. We note that these two spaces should not be considered as mutually orthogonal, but that they will overlap. If they were orthogonal then the funniness of a joke would be independent of the interpretation that a person attributes to it.

With this added mathematical structure, we can represent the interpretation of the joke as a superposition state in $\mathcal{H}_M^2$

$$|\Psi\rangle = a_n|n\rangle + a_v|v\rangle, \tag{6}$$

where a_n and a_v are amplitudes which, when squared, represent the probability of a listener interpreting the joke in a noun or a verb form ($|n\rangle$ and $|v\rangle$) respectively. This state is depicted in **Figure 1A**, which shows a superposition state in the semantic space. When given no context in the form of the actual presentation of the joke, these amplitudes represent the prior

[2]We acknowledge that other interpretations are possible, and so this is a simplified model. It is straightforward to extend the model into higher dimensions by adding further interpretations as basis states.

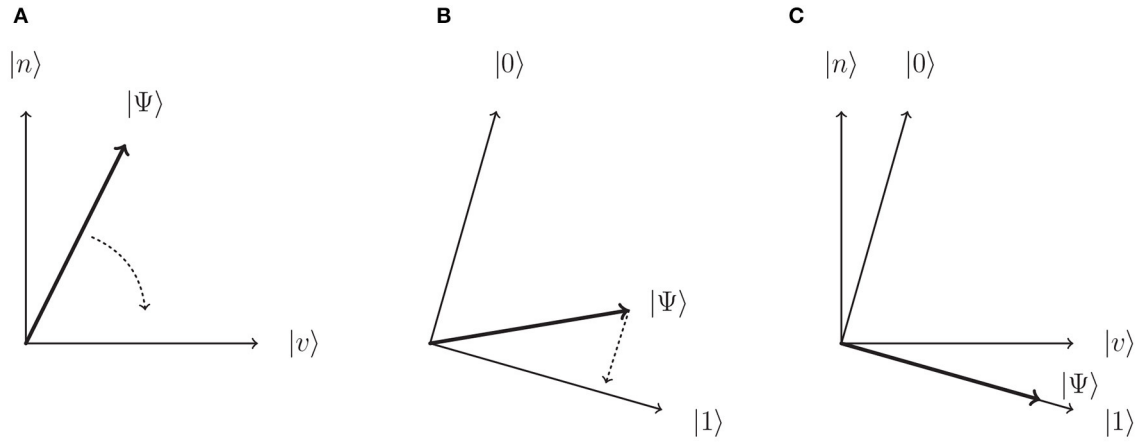

FIGURE 1 | The humor of a joke can be explained as arising from a measurement process that occurs with respect to two incompatible frames. Using the example of the pun, **(A)** the meaning of the set-up is reinterpreted with EYT updating toward the interpretations ATE. **(B)** Funniness is then treated as a measurement, with the probability of funniness being judged with respect to a projection on the $\{|0\rangle, |1\rangle\}$ basis. In this case there is a large probability of the joke being considered funny due to the dominant component of the projection of $|\Psi\rangle$ lying on the $|1\rangle$ axis. **(C)** The cognitive state of the subject then collapses to the observed state (i.e., funny or not).

likelihood of a listener interpreting the uncontextualized word (i.e., EYT) in either of the noun or verb senses (e.g., a free association probability; see [12] for a review). However, we would expect to see these probabilities evolving throughout the course of the pun as more and more context is provided (in the form of additional sentence structure). Throughout the course of the joke, the state vector $|\Psi\rangle$ therefore evolves to a new position in $\mathcal{H}^4$.

Since the set-up of the joke,"Why was 6 afraid of 7?," contains two numbers, it is likely that the numbers interpretation of EYT is activated (a situation represented in **Figure 1A**). The listener is biased toward an interpretation of EYT in this sense, and so we would expect that $a_n >> a_v$. However, a careful listener will feel confused upon considering this set-up because we do not think of numbers as beings that experience fear. This keeps the interpretation of EYT shifted away from an equivalence with the eigenvector $|n\rangle$. As the joke unfolds, the predator interpretation that was hinted at in the set-up by the word "afraid," and reinforced by "789," activates a more definite alternative meaning, ATE, represented by $|v\rangle$. This generates an alternative interpretation of the punchline: that the number 7 ate the number 9. The cognitive state $|\Psi\rangle$ has evolved to a new position in $\mathcal{H}^4$, a scenario that is represented in **Figure 1B**. At this point a measurement occurs: the individual either considers the joke as funny or not within the context represented by the funniness sub space $\mathcal{H}^2_F$, and a collapse to the relevant funniness basis state occurs (see **Figure 1C**). Note that this final state still contains a superposition within the meaning subspace H^2_M—the funniness judgment merely shifts the interpretation of the joke, it does not eliminate the bisociation. Rather, it depends upon it.

If we consider the set of properties associated with EYT then we would expect to see two very different prototypical characteristics associated with each interpretation. For example, the EIGHT interpretation is difficult to map into properties such as "food" denoted f_1, and "not living" denoted f_2 (since when something is eaten it is usually no longer alive). Because "food" and "not living" are not properties of EIGHT, $\nu(p,f_0) << \nu(n,f_0)$, and similarly $\nu(p,f_1) << \nu(n,f_1)$. However, "food" and "not living" are properties of EYT, $\nu(p,f_0) << \nu(v,f_0)$, and similarly $\nu(p,f_1) << \nu(v,f_1)$.

We can now start to construct a model of humor that could be correlated with data. If jokes satisfy the law of total probability (LTP) then their funniness should satisfy the distributive axiom, which states that the total probability of some observable should be equal to the sum of the probabilities of it under sets of more specific conditions. Thus, considering a funniness observable $\hat{O}_F$ (with eigenstates $\{|1\rangle, |0\rangle\}$ and the semantic observable $\hat{O}_M$ (with a simplified two eigenstate structure $\{|M\rangle, |\bar{M}\rangle\}$ representing two possible meanings that could be attributed to the joke). We can take the spectral decomposition of $\hat{O}_M = m|M\rangle\langle M| + \bar{m}|\bar{M}\rangle\langle\bar{M}|$, where $m, \bar{m}$ are eigenvalues of the two eigenstates $\{|M\rangle, |\bar{M}\rangle\}$. Doing this, we should find that if this system satisfies the LTP then the probability of the joke being judged as funny is equal to the sum of the probability of it being judged funny *g*iven either semantic interpretation

$$p(F) = p(|1\rangle) = p(M) \cdot p(F|M) + p(\bar{M}) \cdot p(F|\bar{M}). \qquad (7)$$

We can manipulate the interpretation that a participant is likely to attribute to a joke by changing the semantics of the joke itself. Thus, changing the joke should change the semantics, and so affect the humor that is attributed to the joke. We shall return to this idea in Section 5.

This section has demonstrated that a formal approach to concept interactions that has been previously shown to be consistent with human data [5] can be adapted to

the simultaneous perception of incongruous meanings of an ambiguous word or phrase in the understanding of a pun.

4.4. Applying QTH to a Frame Blend

Although our first example used a pun for simplicity, we believe that quantum inspired models may also be useful for more elaborate forms of humor, such as jokes and cartoons referred to as frame blends. A frame blend involves the merging of incongruous frames of reference [42]. A common example of a frame blend is a cartoon in which animals are engaged in some kind of human behavior (such as a cartoon of a cow with all her teats pierced saying "Just gotta be me"). In a frame blend rather than being led "down the garden path" by the setup and subsequent re-interpretation in light of the punchline, the humor results from the simultaneous presentation of seemingly incompatible frames. Using QTH, the two interpretations of the incongruous situation would be designated by the unit vectors $\{|d\rangle, |o\rangle\}$. The cognitive state of perceiving the blended frames is represented as a superposition of the two frames. As with phenomena such as conceptual combination, there are likely to be constraints on how frames can be successfully blended, and it will be necessary to consider this when constructing models of frame blends. We reserve further exploration of this interesting class of humor for future work.

5. PROBING THE STATE SPACE OF HUMOR

Returning to the question raised by Equation (7), a QTH should be justified by considering whether humor does indeed violate the Law of Total Probability (LTP) [3]. However, the complexity of language makes it difficult to test how humor might violate the LTP using a method similar to those followed for decision making [11]. Past work on humor is unlikely to yield the data required to perform tests such as this. For example, we currently have no experimental understanding of how the semantics of a joke interplays with its perceived funniness. It seems reasonable to suppose that the two are related, but how? We are not aware of any data that provide a way to evaluate this relationship. This is problematic, as there are a number of interdependencies in the framing of a joke that make it difficult to construct a model (even before considering factors such as the context in which the joke is made, and the socio-cultural background of the teller and the listener). In this section we present results from an exploratory study designed to start unpacking whether humor should indeed be considered within the framework of quantum cognition. As an illustrative example, consider the following joke:

> V_O: "Time flies like an arrow. Fruit flies like a banana."

As with the joke discussed in Section 4.3, the humor arises from the ambiguity of the words FRUIT and FLIES. The first frame ($F1$, the set-up), leads one to interpret FLIES as a verb and LIKE as a preposition, but the second frame ($F2$, the punchline), leads one to interpret FRUIT FLIES as a noun and LIKE as a verb. A QTH must be able to explain how the funniness of the joke depends upon a shift in the semantic understanding of the two frames, $F1$ and $F2$.

We now outline a preliminary study that has helped us to explore the state space of humor.

5.1. Stimuli

We collected a set of 35 jokes and for each joke we developed a set of joke variants. A V_S variant consisted of the set-up only for the original, V_O. Thus, the V_S variant of the V_O joke is

> V_S: "Time flies like an arrow."

A V_P variant consists of the original punchline only. Thus, the V_P variant of the V_O joke is

> V_P: "Fruit flies like a banana."

We then considered the notion of a congruent punchline as one that does not introduce a new interpretation or context for an ambiguous element of the set-up (or punchline). Congruence was achieved by modifying the set-up to make it congruent with the punchline, or by modifying the punchline to make it congruent with the set-up. Thus, if the original set-up makes use of a noun, then so does a congruent modification (and similarly for the punchline).

A CP variant consists of the original set-up followed a congruent version of the punchline. Thus, a CP variant of the O joke is:

> CP: "Time flies like an arrow; time flies like a bird."

A CS variant consists of the original punchline preceded by a congruent version of the set-up. Thus, a CS variant of the O' joke is

> CS: "Horses like carrots; fruit flies like a banana."

For some jokes we had a fifth kind of variant. A IS variant consists of the original set-up followed an incongruent version of the punchline that we believed was comparable in funniness to the original. Thus, considering the joke discussed in Section 4.3:

> O: "Why was 6 afraid of 7? Because 789."

A IS variant of this joke is:

> IS: "Why was 6 afraid of 7? Because 7 was a six offender."

Thus the stimuli consisted of a questionnaire containing original jokes, and the above variants presented in randomized order. The complete collection of jokes and their variants is presented in the Appendix (Supplementary Material).

5.2. Participants

The participants in this study were 85 first year undergraduate students enrolled in an introductory psychology course at the University of British Columbia (Okanagan campus). They received partial course credit for their participation.

5.3. Procedure

Participants signed up for the study using the SONA recruitment system, and subsequently responded at their convenience to an online questionnaire hosted by FluidSurveys. They were informed that the study was completely voluntary, and that they were free to withdraw at any point in time. They were also informed that the researcher would not have any knowledge of who participated in the study, and that their participation would not affect their standing in the psychology class or relationship with the university. Participants were told that the purpose of the study was to investigate humor, and to help contribute to a better understanding the cognitive process of "getting" a joke. Participants were asked to fill out consent forms. If they agreed to participate, they were provided a questionnaire consisting of a series of jokes and joke variants (as described above) and asked to rate the funniness of each using a Likert scale, from 1 (not funny) to 5 (hilarious). The questionnaire took approximately 25 min to complete. They received partial course credit for their participation.

5.4. Results

The mean funniness ratings across all participants for the entire collection of jokes and their variants (as well as the jokes and variants themselves) is provided in the Appendix (Supplementary Material). **Table 1** provides a summary of this information (the mean funniness rating of each kind of joke variant across all participants) aggregated across all joke sets. As expected, the original joke (O) was funniest (mean funniness = 2.70), followed by those jokes that had been intentionally modified to be funny: Incongruent Setup (IS) (mean funniness = 2.37) and Incongruent Punchline (IP) (mean funniness = 2.12). Next in funniness were the jokes that had been modified to eradicate the incongruency and thus the source of the humor: Congruent Setup (CS) (mean funniness = 1.41) and Congruent Punchline (CP) (mean funniness = 1.47). The joke fragments without a counterpart–i.e., either Setup (S) or Punchline (P) alone–were considered least funny of all (the mean funniness of both was 1.22). The dataset is entirely consistent with the view that the humor derives from incongruence due to bisociation.

5.5. Toward a Test of the QTH

Recall that the Law of Total Probability (LTP) as represented by Equation (7) suggests that the mean funniness of a joke should be equal to the sum of its funniness as judged under all possible semantic interpretations. This is not an equality that we can directly test given our current understanding of language and how it might interplay with humor. However, the dataset reported here gives us some initial ways to address this. With a methodology for converting the Likert scale ratings into projective measurements of a joke being funny or not, we can start to consider the relative frequency that an original joke is judged as funny and compare this result with the individual components.

We start by translating the Likert scale responses into a simplified measurement of funniness, by mapping the funniness ratings into a designation of funny or not. In order to run a quick comparison between the relative frequencies that participants decided the full joke (V_O) was funny when compared to the components of the joke (V_S and V_P), we took the mean value of the components for each subject. Given that puns are not generally considered particularly funny (a result backed up by our participant ratings) we used a fairly low threshold value of 2.5 (i.e., if the mean was less than 2.5 then the components were judged as unfunny, and vice versa). Exploring the results of this mapping gives us the data reported in **Figure 2** for the V_O, V_S and V_P variants of the jokes, listing the frequency at which participants judged the joke and subcomponents funny. A mean value for the joke fragments is also presented. All data uses confidence intervals at the 95% level.

We see a significant discrepancy between the funniness of the original and the combined funniness of its components. This is not a terribly surprising result; jokes are not funny when the set-up is not followed by the punchline, and participants usually rated V_S and V_P variants as unfunny (i.e., scoring them at 1). Table 2 in the Appendix (Supplementary Material) shows that in the participant pool of 85, the set-up and punchline variants of the joke rarely had a mean funniness rating above 1.5. However, to extract a violation of the LTP for this scenario, we would need to construct expressions such as the following

$$p(F) = p(EIGHT).p(F|EIGHT) + p(ATE).p(F|ATE). \quad (8)$$

How precisely could such a relationship be tested? Two forms of data are required to test whether the simple puns used in our experiment actually violate the LTP:

1. **Funniness ratings:** These are the probabilities regarding the probability that different components of the joke are considered funny (the whole joke ($p(F)$); just the setup ($p(F|EIGHT)$); and just the punchline ($p(F|ATE)$); and
2. **Semantic probabilities:** These list the probability of EYT being interpreted as EIGHT: $p(EIGHT)$, or ATE: $p(ATE)$, within the context of the specific joke fragment.

We have demonstrated a method for extracting the funniness ratings above. How might we obtain data for the semantic probabilities? We must consider the precise interpretation of what these probabilities might actually be. Firstly, we note that it seems likely participants will interpret just a set-up or a punchline in the sense that the fragment represents. The bisociation that humor relies upon is not present for a fragment, and so a person hearing a fragment will be primed by its surrounding context toward interpreting an ambiguous word in precisely the sense intended for that fragment. Indeed, the incongruity that results from having to readjust the interpretation of the joke, and the

TABLE 1 | The mean funniness ratings across all participants and all joke sets for each kind of joke variant.

Joke variant	O	S	P	CS	CP	IS	IP
Mean funniness	2.70	1.22	1.22	1.41	1.47	2.37	2.12

O, Original; S, Set-up only; P, Punchline only; CS, Congruent Set-up; CP, Congruent Punchline; IS, Incongruent Set-up; IP, Incongruent Punchline.

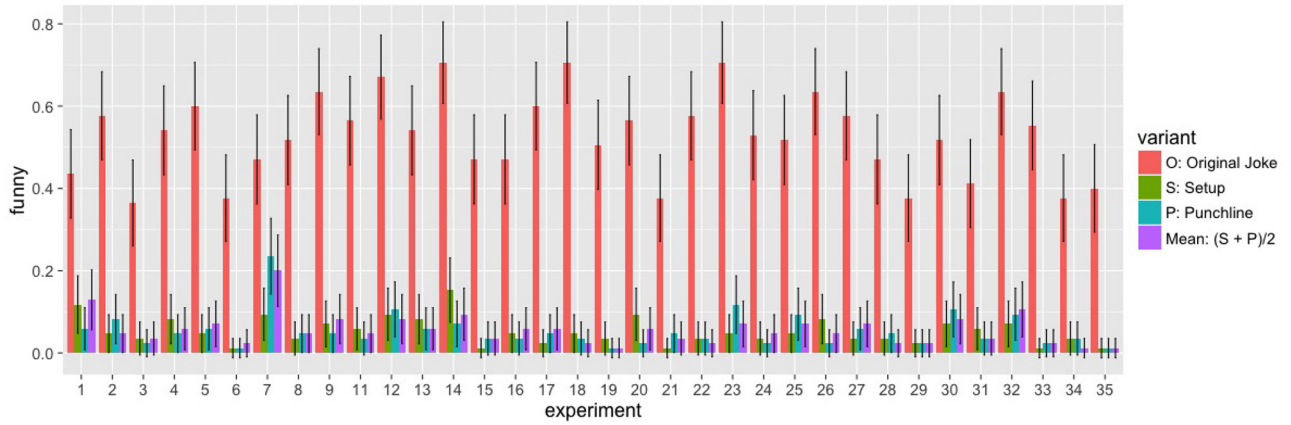

FIGURE 2 | A comparison of the frequency with which a specific joke and its fragments are considered funny for participants in the pilot trial (using a threshold value of 2.5, $n = 85$). A mean of the set-up and the punchline variants (V_S and V_P) is also given. Confidence intervals are set at 95%.

resulting bisociation, lies at the very base of the humor that arises. Free association probabilities will not give these values. To test the LTP, it would be necessary to extract information about how a participant is interpreting core terms in the joke as it progresses; some form of nondestructive measurement is required, and a new experimental protocol will have to be defined. We reserve this for future work.

However, the significant difference between the rated funniness of the fragments and that of the original joke allows us to formulate an alternative mechanism for testing equations of the form (7) and (8). We can do this by asking whether there is *any* way in which the semantic probabilities could have values that would satisfice the LTP? An examination of **Figure 2** for the setup and punchline variants of the jokes suggests that there is no way in which to chose semantic probabilities that will satisfy the LTP. Thus, we have preliminary evidence that humor should perhaps be treated using a quantum inspired model.

6. DISCUSSION

It would appear that there is some support for the hypothesis that the humor arising from bisociation can be modeled by a quantum inspired approach. Furthermore, the experimental results presented in section 5 suggest that this model might more appropriate than one grounded in classical probability. However, much work remains to be completed before we can consider these findings anything but preliminary.

Firstly, the model presented in Section 4 is simple, and will need to be extended. While an extension to more senses for an ambiguous element of a joke is straightforward with a move to higher dimensions, the model is currently not well suited to the set of variants discussed in Section 5.3. A model that can show how they interrelate, and how their underlying semantics affects the perceived humor in a joke is desirable. Furthermore, the funniness of the joke was simplistically represented by a projection onto the "funny"/"not funny" axis. A more theoretically grounded treatment of the Likert data is desirable. For example, the current threshold value of 2.5 was chosen somewhat arbitrarily [although could be justified by a consideration of the mean values for funniness scores reported in the Appendix (Supplementary Material)—see Table 2]. A more systematic way of considering the Likert scale measures to allow for a normalization of funniness ratings at the level of an individual is also desirable. As a highly subjective phenomenon, funniness is liable to be judged by different individuals inconsistently and so it will be important that we control for this effect in comparing Likert responses among individuals.

Considering experimental results, the sample size of the data set is somewhat small (85 participants), although our funniness ratings appear to be reasonably stable for this cohort. A more concerning problem revolves around the construction of a LTP relationship for our simple model. There are many alternative ways in which a LTP could be constructed for puns, and more sophisticated models need to be investigated before we can be confident that our results conclusively demonstrate that humor *must* be modeled using a quantum inspired approach. In particular, we require a more sophisticated method that facilitates the extraction of data about the semantics attributed by a participant to a joke. A two stage protocol may be the answer for obtaining the necessary semantic information for a more rigorously founded test of the violation of LTP. It would be useful to construct a systematic study of the manner in which adjusting the congruence of the set-ups and punchlines influences perception of the joke. The quantum inspired semantic space approaches of Van Rijsbergen [13] and Widdows [43] may prove fruitful in this regard, as they would facilitate the creation of similarity models such as those explored by Aerts et al. [44] and Pothos and Trueblood [45].

In summary, humor is complex, and it will take an ongoing program of research to understand the interplay between the semantics of a joke and its perceived funniness. However, at this point we might pause to consider the broader question of *why* humor might be better modeled by a quantum inspired approach than by one grounded in classical probability? To

this end we return to the discussion of Section 3. As we saw, the humor of a pun involves the bisociation of incongruent frames, i.e., re-viewing a setup frame in light of new contextual information provided by a punchline frame. Moreover, the broader contextuality of humor means that even the funniest of jokes can become markedly unfunny if delivered in the wrong way (e.g., a monotone voice), or in the wrong situation (e.g., after receiving very bad news). Funniness is not a pre-existing "element of reality" that can be measured; it emerges from an interaction between the underlying nature of the joke, the cognitive state of the listener, and other social and environmental factors. This makes the quantum formalism an excellent candidate for modeling humor, as this interaction is well described by the concept of a vector state embedded in a space which is represented using basis states that can be reoriented according to the framing of the joke. However, this paper only provides a preliminary indication that a QTH may indeed provide a good theoretical underpinning for this complex process. Much more work remains to be done.

7. CONCLUSIONS

This paper has provided a first step toward a quantum theory humor (QTH). We constructed a model where frame blends are represented in a Hilbert space spanned by two sets of basis states, one representing the ambiguous framing of a joke, and the other representing funniness. The process of "getting a joke" then consists of a dual stage scenario, where the cognitive state of a person evolves toward a re-interpretation of the meaning attributed to the joke, followed by a measurement of funniness. We conducted a study in which participants rated the funniness of jokes as well as the funniness of variants of those jokes consisting of setting or punchline by alone. The results demonstrate that the funniness of the jokes is significantly greater than that of their components, which is not particularly surprising, but does show that there is something cognitive taking place above and beyond the information content delivered in the joke. A preliminary test to see whether the humor in a joke violates the law of total probability appears to suggest that there is reason to suppose that a quantum inspired model is indeed appropriate.

Our QTH is not proposed as an all-encompassing theory of humor; for example, it cannot explain why laughter is contagious, or why children tease each other, or why people might find it funny when someone is hit in the face with a pie (and laugh even if they know it will happen in advance). It aims to model the cognitive aspect of humor only. Moreover, despite the intuitive appeal of the approach, it is still rudimentary, and more research is needed to determine to what extent it is consistent with empirical data. Nevertheless, we believe that the approach promises an exciting step toward a formal theory of humor. It is hoped that future research will build upon this modest beginning.

ETHICS STATEMENT

This research was approved by the Behavioral Research Ethics Board at the University of British Columbia (Okanagan Campus).

AUTHOR CONTRIBUTIONS

LG had the idea for the paper and designed and conducted the study. Both authors contributed equally to all other aspects of the research and the writing of the paper.

ACKNOWLEDGMENTS

This work was supported by a grant (62R06523) from the Natural Sciences and Engineering Research Council of Canada. We are grateful to Samantha Thomson who assisted with the development of the questionnaire and the collection of the data for the study reported here.

SUPPLEMENTARY MATERIAL

The Supplementary Material for this article can be found online at: http://journal.frontiersin.org/article/10.3389/fphy.2016.00053/full#supplementary-material

REFERENCES

1. Veale T, Brone G, Feyaerts K. Humour as the killer-app of language: a view from Cognitive Linguistics. In: Brone G, Feyaerts K, Veale T, editors. *Cognitive Linguistics and Humor Research*. Berlin; Boston, MA: De Gruyter (2015). p. 1–11. doi: 10.1515/9783110346343-001
2. Khrennikov AY. *Ubiquitous Quantum Structure: From Psychology to Finance*. Berlin; Heidelberg: Springer (2010). doi: 10.1007/978-3-642-05101-2
3. Busemeyer J, Bruza P. *Quantum Models of Cognition and Decision*. Cambridge: Cambridge University Press (2012). doi: 10.1017/CBO9780511997716
4. Asano M, Khrennikov A, Ohya M, Tanaka Y, Yamato I. *Quantum Adaptivity in Biology: From Genetics to Cognition*. Dordrecht: Springer (2015).
5. Aerts D. Quantum structure in cognition. *J Math Psychol.* (2009) **53**:314–48. doi: 10.1016/j.jmp.2009.04.005
6. Aerts D, Gabora L. A theory of concepts and their combinations I: the structure of the sets of contexts and properties. *Kybernetes* (2005) **34**:167–91. doi: 10.1108/03684920510575799
7. Aerts D, Gabora L. A theory of concepts and their combinations II: a Hilbert space representation. *Kybernetes* (2005) **34**:192–221. doi: 10.1108/03684920510575807
8. Gabora L, Aerts D. Contextualizing concepts using a mathematical generalization of the quantum formalism. *J Exp Theor Artif Intell.* (2002) **14**:327–58. doi: 10.1080/09528130210162253
9. Bruza P, Kitto K, Nelson D, McEvoy C. Is there something quantum-like about the human mental lexicon? *J Math Psychol.* (2009) **53**:362–77. doi: 10.1016/j.jmp.2009.04.004
10. Bruza P, Kitto K, Ramm B, Sitbon L. A probabilistic framework for analyzing the compositionality of conceptual combinations. *J Math Psychol.* (2015) **67**:26–38. doi: 10.1016/j.jmp.2015.06.002
11. Pothos EM, Busemeyer JR, Trueblood JS. A quantum geometric model of similarity. *Psychol Rev.* (2013) **120**:679–96. doi: 10.1037/a0033142
12. Nelson DL, Kitto K, Galea D, McEvoy CL, Bruza PD. How activation, entanglement, and search in semantic memory contribute to event memory. *Mem Cogn.* (2013) **41**:717–819. doi: 10.3758/s13421-013-0312-y

13. Van Rijsbergen. *The Geometry of Information Retrieval*. Cambridge: Cambridge University Press (2004).
14. Melucci M. A basis for information retrieval in context. *ACM Trans Inf Syst*. (2008) **26**:14:1–14:41. doi: 10.1145/1361684.1361687
15. Aerts D, Aerts S. Applications of quantum statistics in psychological studies of decision processes. *Found Sci*. (1994) **1**:85–97.
16. Busemeyer JR, Wang Z, Townsend JT. Quantum dynamics of human decision making. *J Math Psychol*. (2006) **50**:220–41. doi: 10.1016/j.jmp.2006.01.003
17. Busemeyer J, Pothos E, Franco R, Trueblood J. A quantum theoretical explanation for probability judgement errors. *Psychol Rev*. (2011) **118**:193–218. doi: 10.1037/a0022542
18. Mogiliansky AL, Zamir S, Zwirn H. Type indeterminacy: a model of the KT (Kahneman–Tversky)-man. *J Math Psychol*. (2009) **53**:349–61. doi: 10.1016/j.jmp.2009.01.001
19. Yukalov VI, Sornette D. Processing information in quantum decision theory. *Entropy* (2009) **11**:1073–120. doi: 10.3390/e11041073
20. Atmanspacher H, Filk T, Römer H. Quantum Zeno features of bistable perception. *Biol Cybern*. (2004) **90**:33–40. doi: 10.1007/s00422-003-0436-4
21. Atmanspacher H, Filk T. The Necker–Zeno model for bistable perception. *Top Cogn Sci*. (2013) **5**:800–17. doi: 10.1111/tops.12044
22. Khrennikov A. Quantum-like model of unconscious–conscious dynamics. *Front Psychol*. (2015) **6**:997. doi: 10.3389/fpsyg.2015.00997
23. Haven E, Khrennikov A. *Quantum Social Science*. Cambridge: Cambridge University Press (2013). doi: 10.1017/CBO9781139003261
24. Kitto K, Boschetti F. Attitudes, ideologies and self-organization: information load minimization in multi-agent decision making. *Adv Comp Syst*. (2013) **16**:1350029. doi: 10.1142/S021952591350029X
25. Gabora L. *Cognitive Mechanisms Underlying the Origin and Evolution of Culture. Doctoral Thesis*. Free University of Brussels (2001).
26. Gabora L, Aerts D. A model of the emergence and evolution of integrated worldviews. *J Math Psychol*. (2009) **53**:434–51. doi: 10.1016/j.jmp.2009.06.004
27. Gabora L, Kitto K. Concept combination and the origins of complex cognition. In: Swan E, editor. *Origins of Mind: Biosemiotics Series*, Vol. 8. Berlin: Springer (2013). p. 361–82. doi: 10.1007/978-94-007-5419-5_19
28. Gabora L, Carbert N. *A Study and Preliminary Model of Cross-domain Influences on Creativity*. Austin TX: Cognitive Science Society (2015).
29. Attardo S. *Linguistic Theories of Humor*. Berlin: Mouton de Gruyter (1994).
30. Raskin V. *Semantic Mechanisms of Humor*. Dordrecht: Reidel (1985).
31. Koestler A. *The Act of Creation*. New York, NY: Macmillan (1964).
32. Shultz TR. Order of cognitive processing in humour appreciation. *Can J Psychol*. (1974) **28**:409–20. doi: 10.1037/h0082006
33. Suls JM. A two stage model for appreciation ofjokes and cartoons: an information-processing analysis. In: Goldstein JH, McGhee PE, editors. *The Psychology of Humor: Theoretical Perspectives und Empirical Issues*. New York, NY: Academic Press (1972). p. 81–100. doi: 10.1016/B978-0-12-288950-9.50010-9
34. Martin RA. *The Psychology of Humor: An Integrative Approach*. Burlington, MA: Elsevier Academic Press (2007).
35. McGraw AP, Warren C. Benign violations: making immoral behavior funny. *Psychol Sci*. (2010) **21**:1141–9. doi: 10.1177/0956797610376073
36. Reyes A, Rosso P, Veale T. A multidimensional approach for detecting irony in Twitter. *Lang Resour Eval*. (2013) **47**:239–68. doi: 10.1007/s10579-012-9196-x
37. Binsted K, Pain H, Ritchie G. Childrens evaluation of computer-generated punning riddles. *Pragmat Cogn*. (1997) **5**:305–354. doi: 10.1075/pc.5.2.06bin
38. Valitutti A, Toivonen H, Doucet A, Toivanen JM. "Let everything turn well in your wife": generation of adult humor using lexical constraints. In: *Proceedings of the 51st Annual Meeting of the Association for Computational Linguistics. Association for Computational Linguistics* Sofia: Association for Computational Linguistics (2013). p. 243–8.
39. Isham CJ. *Lectures on Quantum Theory*. London: Imperial College Press (1995).
40. Gabora L, Eric S, Kauffman S. A quantum model of exaptation: incorporating potentiality into biological theory. *Prog Biophys Mol Biol*. (2013) **113**:108–116. doi: 10.1016/j.pbiomolbio.2013.03.012
41. Gould SJ, Vrba ES. Synopsis of a workshop on humor and cognition. *Paleobiology* (1982) **8**:4–15. doi: 10.1017/S0094837300004310
42. Hofstadter D, Gabora L. Synopsis of a workshop on humor and cognition. *Humor* (1989) **2**:417–40.
43. Widdows D. *Geometry and Meaning*. Stanford, CA: CSLI Publications (2004).
44. Aerts S, Kitto K, Sitbon L. Similarity metrics within a point of view. In: Song D, Melucci M, Frommholz, I, Zhang, P, Wang, L, Arafat, S, editors. *Quantum Interaction 5th International Symposium, QI 2011, June 26-29, 2011, Revised Selected Papers. Vol. 7052 of LNCS*. Aberdeen: Springer (2011). p. 13–24. doi: 10.1007/978-3-642-24971-6_3
45. Pothos EM, Trueblood JS. Structured representations in a quantum probability model of similarity. *J Math Psychol*. (2015) **64**:35–43. doi: 10.1016/j.jmp.2014.12.001

Conflict of Interest Statement: The authors declare that the research was conducted in the absence of any commercial or financial relationships that could be construed as a potential conflict of interest.

frontiers in Physics

ORIGINAL RESEARCH
published: 14 August 2018
doi: 10.3389/fphy.2018.00079

A Remark on the Fractional Integral Operators and the Image Formulas of Generalized Lommel–Wright Function

Ritu Agarwal[1]*, *Sonal Jain*[2], *Ravi P. Agarwal*[3] and *Dumitru Baleanu*[4,5]

[1] Department of Mathematics, Malaviya National Institute of Technology, Jaipur, India, [2] Department of Mathematics, Faculty of Applied Science, Madhav Institue of Technology & Sciences, Gwalior, India, [3] Department of Mathematics, Texas A&M University, Kingsville, TX, United States, [4] Department of Mathematics, Çankaya University, Ankara, Turkey, [5] Institute of Space Science, Bucharest, Romania

In this paper, the operators of fractional integration introduced by Marichev-Saigo-Maeda involving Appell's function $F_3(\cdot)$ are applied, and several new image formulas of generalized Lommel–Wright function are established. Also, by implementing some integral transforms on the resulting formulas, few more image formulas have been presented. We can conclude that all derived results in our work generalize numerous well-known results and are capable of yielding a number of applications in the theory of special functions.

OPEN ACCESS

Edited by:
Carla M. A. Pinto,
Instituto Superior de Engenharia do Porto (ISEP), Portugal

Reviewed by:
Bruce J. West,
United States Army Research Laboratory, United States
Carlo Cattani,
Università degli Studi della Tuscia, Italy

***Correspondence:**
Ritu Agarwal
ragarwal.maths@mnit.ac.in

Specialty section:
This article was submitted to Mathematical Physics, a section of the journal Frontiers in Physics

Received: 23 May 2018
Accepted: 05 July 2018
Published: 14 August 2018

Citation:
Agarwal R, Jain S, Agarwal RP and Baleanu D (2018) A Remark on the Fractional Integral Operators and the Image Formulas of Generalized Lommel–Wright Function. Front. Phys. 6:79. doi: 10.3389/fphy.2018.00079

Primary: 44A20 Transforms of special functions; 65R10 For numerical methods; 26A33 Fractional derivatives and integrals; Secondary: 33C20 Generalized hypergeometric series, pFq; 33E50 Special functions in characteristic p (gamma functions, etc.); 2010 AMS classification by MathSciNet

Keywords: Marichev-Saigo-Maeda fractional integral operators, generalized Lommel–Wright function, generalized Fox–Wright function, generalized hypergeometric series, integral transform

1. INTRODUCTION AND PRELIMINARIES

Fractional calculus (FC) represents a complex physical phenomenon in a more accurate and efficient way than classical calculus. In recent years, many researchers [1–7] have used fractional order integral models in real-world problems in various fields of science and technology. There exists several definitions of fractional order integrals in the literature that can be used to solve the fractional integral equations involving special functions. For an exhaustive literature review, one may refer to the paper by Srivastava and Saxena [8].

The generalized functions such as Bessel, Lommel, Struve, and Lommel–Wright functions have originated from concrete problems in applied fields of sciences viz mechanics, physics, engineering, astronomy, etc.

The *generalized Lommel–Wright function* $J^{\varphi,m}_{\omega,\vartheta}(z)$ is defined by de'Oteiza et al. [9] and is represented in the following manner:

$$\begin{aligned} J^{\varphi,m}_{\omega,\vartheta}(z) &= (z/2)^{\omega+2\vartheta}\sum_{k=0}^{\infty}\frac{(-1)^k(z/2)^{2k}}{(\Gamma(\vartheta+k+1))^m\Gamma(\omega+k\varphi+\vartheta+1)} \\ &= (z/2)^{\omega+2\vartheta}\,{}_1\psi_{m+1}[(1,1);\ \underbrace{(\vartheta+1,1),}_{m-times}\ (\omega+\vartheta+1,\varphi);-z^2/4] \\ z\in\mathbb{C}\backslash(-\infty,0],&\quad \varphi>0,\quad m\in\mathbb{N},\quad \omega,\vartheta\in\mathbb{C}, \end{aligned} \tag{1.1}$$

where ${}_p\psi_q$ denotes the Fox–Wright generalized hypergeometric function which is defined as given in Srivastava and Karlsson [10, p. 21] and Kilbas et al. [11, P. 56]

$$ {}_p\psi_q\left(\begin{matrix}(a_1,A_1),...(a_p,A_p);\\(b_1,B_1),...,(b_q,B_q);\end{matrix} z\right)=\sum_{n=0}^{\infty}\frac{\Pi_{j=1}^{p}\Gamma(a_j+nA_j)}{\Pi_{j=1}^{q}\Gamma(b_j+nB_j)}\frac{z^n}{n!}, \tag{1.2}$$

where $a_i, b_j \in \mathbb{C}$ and $A_i, B_j \in \mathbb{R} = (-\infty,\infty)$; $A_i, B_j \neq 0$, $i = 1,2,...,p, j = 1,2,...,q$, $\sum_{j=1}^{q} B_j - \sum_{j=1}^{p} A_j > -1$.

A useful generalization of the Lommel–Wright function and its special cases, $J_{\omega}^{\varphi}(z)J_{\omega,\vartheta}^{\varphi}(z)$, depending on the arbitrary fractional parameter $\varphi > 0$ presents a fractional order extension of the Bessel function $J_{\omega}(z)$.

Prieto et al. [12] studied some useful results in the theory of fractional calculus operators of generalized Lommel–Wright function. The convergence of series involving generalized Lommel–Wright function was studied by Konovska [13].

When $m = 1$, the following generalization of the Bessel function, introduced by Pathak [14] is obtained as a special case of generalized Lommel–Wright function (1.1) (see e.g., [15, p. 353]):

$$\begin{aligned} J_{\omega,\vartheta}^{\varphi}(z) &= J_{\omega,\vartheta}^{\varphi,1}(z)\\ &= \left(\frac{z}{2}\right)^{\omega+2\vartheta}\sum_{k=0}^{\infty}\frac{(-1)^k\left(\frac{z}{2}\right)^{2k}}{\Gamma(\vartheta+k+1)\Gamma(\omega+k\varphi+\vartheta+1)}, \\ & z\in\mathbb{C}\backslash(-\infty,0],\quad \varphi>0,\quad \omega,\vartheta\in\mathbb{C}. \end{aligned} \tag{1.3}$$

On taking $m = 1, \varphi = 1$, and $\vartheta = \frac{1}{2}$ in (1.1), we obtain the *Struve function* $H_{\omega}(\cdot)$ (see e.g., [16, p. 28, Equation (1.170)])

$$\begin{aligned} H_{\omega}(z) &= J_{\omega,1/2}^{1,1}\\ &= \left(\frac{z}{2}\right)^{\omega+1}\sum_{k=0}^{\infty}\frac{(-1)^k\left(\frac{z}{2}\right)^{2k}}{\Gamma(k+\frac{3}{2})\Gamma(k+\omega+\frac{3}{2})}z, \omega\in\mathbb{C}. \end{aligned} \tag{1.4}$$

If we take $m = 1, \varphi = 1$, and $\vartheta = 0$ in (1.1), it gives the relationship with the *Bessel function* as follows (see e.g., [16, p. 27, Equation (1.161)]):

$$\begin{aligned} J_{\omega}(z) = J_{\omega,0}^{1,1}(z) &= \sum_{k=0}^{\infty}\frac{(-1)^k(z/2)^{\omega+2k}}{\Gamma(\omega+k+1)k!} \\ & z,\omega\in\mathbb{C},\quad z\neq 0,\quad \Re(\omega)>-1. \end{aligned} \tag{1.5}$$

A generalization of the hypergeometric fractional integrals, including the Saigo operators [17, 18] has been introduced by Marichev [19]. The details of these fractional operators have been found in Samko et al. [5, p. 194, Equation (10.47)] and later extended and studied by Saigo and Maeda [20, p. 393, Equation (4.12) and Equation (4.13)] in terms of complex order Appell function $F_3(\cdot)$ of two variables (see [10, p. 23]) in the kernel

$$\begin{aligned} &F_3(\zeta,\zeta^{'},\varrho,\varrho^{'};\eta;x;y)\\ &=\sum_{m,n=0}^{\infty}\frac{(\zeta)_m(\zeta^{'})_n(\varrho)_m(\varrho^{'})_n}{(\eta)_{m+n}}\frac{x^m}{m!}\frac{y^n}{n!}, \quad (\max\{|x|,|y|\}<1). \end{aligned} \tag{1.6}$$

The Appell function F_3 reduces to the Gauss hypergeomatric function ${}_2F_1$ and satisfies the system of two linear partial differential equations of the second order as follows (see [10, p. 301, Equation 9.4]):

$$F_3(\zeta,\eta-\zeta,\varrho,\eta-\varrho;\eta;x;y) = {}_2F_1(\zeta,\varrho;\eta;x+y-xy). \tag{1.7}$$

Further, it is easy to see that

$$F_3(\zeta,0,\varrho,\varrho^{'},\eta;x,y) = {}_2F_1(\zeta,\varrho;\eta;x) \tag{1.8}$$

and

$$F_3(0,\zeta^{'},\varrho,\varrho^{'},\eta;x,y) = {}_2F_1(\zeta^{'},\varrho^{'};\eta;y). \tag{1.9}$$

In this paper, we develop and study the image formulas involving the generalized Lommel–Wright function using fractional calculus integral operators. We use the generalized Marichev-Saigo-Maeda fractional integral operators, involving the Appell function, defined as follows:

$$\begin{aligned} \left(I_{0+}^{\zeta,\zeta^{'},\varrho,\varrho^{'},\kappa}f\right)(x) &= \frac{x^{-\zeta}}{\Gamma\kappa}\int_0^x (x-t)^{\kappa-1}t^{-\zeta^{'}} \\ &\times F_3\left(\zeta,\zeta^{'},\varrho,\varrho';\kappa;1-\frac{t}{x},1-\frac{x}{t}\right)f(t)dt, \\ &\Re(\kappa)>0,\zeta,\zeta^{'},\varrho,\varrho',\kappa\in\mathbb{C},x>0 \end{aligned} \tag{1.10}$$

and

$$\begin{aligned} &\left(I_{0-}^{\zeta,\zeta^{'},\varrho,\varrho^{'},\kappa}f\right)(x)\\ &=\frac{x^{-\zeta}}{\Gamma\kappa}\int_x^{\infty}(t-x)^{\kappa-1}t^{-\zeta}F_3\left(\zeta,\zeta^{'},\varrho,\varrho';\kappa;1-\frac{x}{t},1-\frac{t}{x}\right)f(t)dt, \\ &\Re(\kappa)>0,\zeta,\zeta^{'},\varrho,\varrho',\kappa\in\mathbb{C},x>0. \end{aligned} \tag{1.11}$$

respectively.

The power functions of left-hand sided and right-hand sided Marichev-Saigo-Maeda fractional integral operators as given in the Equations (1.10) and (1.11) (see Saigo et al. [6, 20]) are given by

$$\begin{aligned} &\left(I_{0+}^{\zeta,\zeta^{'},\varrho,\varrho^{'},\kappa}t^{\chi-1}\right)(x)\\ &=\frac{\Gamma(\chi)\Gamma(\chi+\kappa-\zeta-\zeta^{'}-\varrho)\Gamma(\chi+\varrho^{'}-\zeta^{'})}{\Gamma(\chi+\varrho^{'})\Gamma(\chi+\kappa-\zeta-\zeta^{'})\Gamma(\chi+\kappa-\zeta^{'}-\varrho)}x^{\chi+\kappa-\zeta-\zeta^{'}-1}, \end{aligned} \tag{1.12}$$

where $\zeta,\zeta^{'},\varrho,\varrho',\kappa \in \mathbb{C}$, $x > 0$ and if $\Re(\kappa) > 0, \Re(\chi) > \max\{0, \Re(\zeta+\zeta^{'}+\varrho-\kappa), \Re(\zeta^{'}-\varrho^{'})\}$.

$$\begin{aligned} &\left(I_{0-}^{\zeta,\zeta^{'},\varrho,\varrho^{'},\kappa}t^{\chi-1}\right)(x)\\ &=\frac{\Gamma(1-\chi-\kappa+\zeta+\zeta^{'})\Gamma(1-\chi+\zeta+\varrho^{'}-\kappa)\Gamma(1-\chi-\varrho)}{\Gamma(1-\chi)\Gamma(1-\chi+\zeta+\zeta^{'}+\varrho+\varrho^{'}-\kappa)\Gamma(1-\chi+\zeta-\varrho)}\\ &\times x^{\chi-\zeta-\zeta^{'}+\kappa-1}, \end{aligned} \tag{1.13}$$

where $\zeta,\zeta^{'},\varrho,\varrho',\kappa \in \mathbb{C}$ are such that $\Re(\kappa) > 0$ and $\Re(\chi) < 1 + \min\{\Re(-\varrho), \Re(\zeta+\zeta^{'}-\kappa), \Re(\zeta+\varrho^{'}-\kappa)\}$.

1.1. Relation Among the Operators

In this section, we recall some relationships between the fractional integral operators.

If we set $\zeta^{'} = 0$ then in view of the formula (1.8), the relationship between Marichev-Saigo-Maeda and the Saigo fractional integral operators is found by Saxena and Saigo [6, p. 93, Equation (2.15)] as

$$\left(I_{0,x}^{\zeta,0,\varrho,\varrho^{'},\eta}f\right)(x) = \left(I_{0,x}^{\eta,\zeta-\eta,-\varrho}f\right)(x), \quad (\Re(\eta) > 0) \tag{1.14}$$

and

$$\left(I_{x,\infty}^{\zeta,0,\varrho,\varrho^{'},\eta}f\right)(x) = \left(I_{x,\infty}^{\eta,\zeta-\eta,-\varrho}f\right)(x), \quad (\Re(\eta) > 0), \tag{1.15}$$

where the general operators $I_{0,x}^{\zeta,0,\varrho,\varrho^{'},\eta}$ and $I_{0,x}^{\zeta,0,\varrho,\varrho^{'},\eta}$ reduce, respectively, to the Saigo operators $I_{0,x}^{\zeta,\varrho,\eta}$ and $I_{x,\infty}^{\zeta,\varrho,\eta}$ [17] defined as follows:

$$\begin{aligned}\left(I_{0,x}^{\zeta,\varrho,\eta}f\right)(x) &= \frac{x^{-\zeta-\varrho}}{\Gamma(\zeta)}\int_0^x (x-t)_2^{\zeta-1} \\ &\times F_1\left(\zeta+\varrho,-\eta;\zeta;1-\frac{t}{x}\right)f(t)dt, \quad (\Re(\zeta) > 0)\end{aligned} \tag{1.16}$$

and

$$\begin{aligned}\left(I_{x,\infty}^{\zeta,\varrho,\eta}f\right)(x) &= \int_x^\infty (t-x)^{\zeta-1}t^{-\zeta-\varrho}{}_2 \\ &\times F_1\left(\zeta+\varrho,-\eta;\zeta;1-\frac{x}{t}\right)f(t)dt, \quad (\Re(\zeta) > 0)\end{aligned} \tag{1.17}$$

where integrals in (1.16) and (1.17) exist.

Let $\zeta, \varrho, \eta, \chi \in \mathbb{C}$ with $\Re(\zeta) > 0$. Then the following power function formulas involving the Saigo operators hold true:

$$\left(I_{0,x}^{\zeta,\varrho,\eta}t^{\chi-1}\right)(x) = \frac{\Gamma(\chi)\Gamma(\chi+\eta-\varrho)}{\Gamma(\chi-\varrho)\Gamma(\chi+\eta+\zeta)}x^{\chi-\varrho-1}, \tag{1.18}$$

$$\Re(\chi) > \max\left\{0, \Re(\varrho-\eta)\right\}$$

and

$$\left(I_{x,\infty}^{\zeta,\varrho,\eta}t^{\chi-1}\right)(x) = \frac{\Gamma(1-\chi+\varrho)\Gamma(1-\chi+\eta)}{\Gamma(1-\chi)\Gamma(1-\chi+\zeta+\varrho+\eta)}x^{\chi-\varrho-1}, \tag{1.19}$$

$$(\Re(\chi) < 1 + \min\left\{\Re(\varrho), \Re(\eta)\right\}).$$

On replacing $\varrho = -\zeta$ in the operators $I_{0,x}^{\zeta,\varrho,\eta}(\cdot)$ and $I_{x,\infty}^{\zeta,\varrho,\eta}(\cdot)$, these reduce to the Riemann-Liouville and the Weyl fractional integral operators, respectively, by means of the following relationships (see Kilbas [11]):

$$\left(\mathcal{R}_{0,x}^{\zeta}f\right)(x) = \left(I_{0,x}^{\zeta,-\zeta,\eta}f\right)(x) \tag{1.20}$$

and

$$\left(\mathcal{W}_{x,\infty}^{\zeta}f\right)(x) = \left(I_{x,\infty}^{\zeta,-\zeta,\eta}f\right)(x). \tag{1.21}$$

The Riemann-Liouville fractional integral operator and the Weyl fractional integral operator are defined as follows (see e.g., [21]):

$$\left(\mathcal{R}_{0,x}^{\zeta}f\right)(x) = \frac{1}{\Gamma(\zeta)}\int_0^x (x-t)^{\zeta-1}f(t)dt, \quad (\Re(\zeta) > 0) \tag{1.22}$$

and

$$\left(\mathcal{W}_{x,\infty}^{\zeta}f\right)(x) = \frac{1}{\Gamma(\zeta)}\int_0^x (t-x)^{\zeta-1}f(t)dt, \quad (\Re(\zeta) > 0), \tag{1.23}$$

provided both the integrals converge.

The operators $I_{0,x}^{\zeta,\varrho,\eta}(\cdot)$ and $I_{x,\infty}^{\zeta,\varrho,\eta}(\cdot)$ reduce to Erdélyi–Kober fractional integral operators on setting $\varrho = 0$ as follows:

$$\left(\mathcal{E}_{0,x}^{\zeta,\eta}f\right)(x) = \left(I_{0,x}^{\zeta,0,\eta}f\right)(x), \tag{1.24}$$

and

$$\left(\mathcal{K}_{x,\infty}^{\zeta,\eta}f\right)(x) = \left(I_{0,x}^{\zeta,0,\eta}f\right)(x), \tag{1.25}$$

where the Erdélyi–Kober type fractional integral operators are defined as follows (see [22]):

$$\left(\mathcal{E}_{0,x}^{\zeta,\eta}f\right)(x) = \frac{x^{-\zeta-\eta}}{\Gamma(\zeta)}\int_0^x (x-t)^{\zeta-1}t^{\eta}f(t)dt, \quad (\Re(\zeta) > 0) \tag{1.26}$$

and

$$\left(\mathcal{K}_{x,\infty}^{\zeta,\eta}f\right)(x) = \frac{x^{\eta}}{\Gamma(\zeta)}\int_x^\infty (t-x)^{\zeta-1}t^{-\zeta-\eta}f(t)dt, \quad (\Re(\zeta) > 0), \tag{1.27}$$

The function $f(t)$ is constrained so that both the defining integrals (1.26) and (1.27) converge.

The *Beta transform* (see, e.g.[23]) of a complex valued function $f(t)$ of a real variable t is defined as follows:

$$\begin{aligned}B\{f(t):a,b\} &= \int_0^1 t^{a-1}(1-t)^{b-1}f(t)\,dt, \\ &\Re(t) > 0,\ \Re(a), \Re(b) > 0.\end{aligned} \tag{1.28}$$

Beta transform of the power function $t^{\chi-1}$ is given by:

$$\begin{aligned}B\left\{t^{\chi-1};a,b\right\} &= \int_0^1 t^{a+\chi-2}(1-t)^{b-1}dt \\ &= \frac{\Gamma(a+\chi-1)\Gamma(b)}{\Gamma(a+\chi+b-1)},\ \Re(t) > 0,\ \Re(a), \Re(b) > 0.\end{aligned} \tag{1.29}$$

The P_δ - *transform* of a complex valued function $f(t)$ of a real variable t denoted by $P_\delta[f(t);s]$ is a function $F(s)$ of a complex

variable s, valid under certain conditions on $f(t)$, (given below is defined as (see Kumar [24])

$$P_\delta[f(t);s] = F(s) = \int_0^\infty [1+(\delta-1)s]^{-\frac{t}{\delta-1}} f(t)dt, \quad \delta > 1. \tag{1.30}$$

Here $f(t)$ as a function is integrable over any finite interval (a,b), $0 < a < t < b$; there exists a real number c such that

(i) if $b > 0$ is arbitrary, then $\int_b^\Upsilon e^{-ct} f(t)dz$ tends to a finite limit as $\Upsilon \to \infty$

(ii) for arbitrary $a > 0$, $\int_\omega^a |f(t)dt|$ tends to a finite limit as $\omega \to 0+$, then the P_δ-transform $P_\delta[f(t);s]$ exists for $\Re\left(\frac{\ln[1+(\delta-1)s]}{\delta-1}\right) > c$ for $s \in \mathbb{C}$.

P_δ - transform of the power function $t^{\chi-1}$ is given by

$$P_\delta[z^{\chi-1};s] = \left\{\frac{\delta-1}{\ln[1+(\delta-1)s]}\right\}^\chi \Gamma(\chi), \quad \chi \in \mathbb{C}, \ \Re(\chi) > 0, \ \delta > 1. \tag{1.31}$$

P_δ-transform has found many applications. The pathway transforms are the paths going from the binomial form $\ln[1+(\delta-1)s]^{-\frac{t}{\delta-1}}$ to the exponential from e^{-st}. In P_δ-transform, the variable t is shifted from the binomial factor $\ln[1+(\delta-1)s]^{-\frac{t}{\delta-1}}$ to the exponent, Hence, this form is more suitable for obtaining translation, convolution, etc. Recently, Agarwal et al. [25] found the solution of non-homogeneous time fractional heat equation and fractional Volterra integral equation using integral transform of pathway type. Also, Srivastava et al. [26] and [27] found some results involving generalized hypergeometric function and generalized incomplete gamma function by using P_δ-transform.

If we take $\delta \to 1$ in Equation (1.30), the P_δ-transform reduces to *Laplace integral transform* (Sneddon [23]):

$$L\left[f(t);s\right] = \int_0^\infty e^{-ts} f(t)dz; , \qquad \Re(s) > 0. \tag{1.32}$$

The following relationship between the P_δ-transform is defined by (1.30) and the classical Laplace transform is defined by (1.32)

$$P_\delta[f(t):s] = L\left[f(t):\frac{\ln[1+(\delta-1)s]}{\delta-1}\right], \qquad (\delta > 1) \tag{1.33}$$

or, equivalently,

$$L[f(t):s] = P_\delta\left[f(t):\frac{e^{(\delta-1)s}-1}{\delta-1}\right], \qquad (\delta > 1), \tag{1.34}$$

which can be applied to convert the table of Laplace transforms into the corresponding table of P_δ-transforms and *vice versa*.

The following integral formula involving the Whittaker function (see Mathai et al. [16, p. 56]) is used in finding the image formula:

$$\int_0^\infty t^{\tau-1} e^{-\frac{t}{2}} W_{\sigma,\eta}(t)\, dt = \frac{\Gamma(\tau+\eta+\frac{1}{2})\Gamma(\tau-\eta+\frac{1}{2})}{\Gamma(\tau-\sigma+\frac{1}{2})}, \tag{1.35}$$

$$(\sigma \in \mathbb{C}, \ \Re(\tau \pm \eta) > -1/2).$$

The Whittaker function (see e.g., Mathai et al. [16, p. 22]) is defined by

$$\begin{aligned} W_{\sigma,\eta}(z) &= \frac{\Gamma(-2\eta)}{\Gamma(\frac{1}{2}-\sigma-\eta)} M_{\sigma,\eta}(z) + \frac{\Gamma(2\eta)}{\Gamma(\frac{1}{2}-\sigma+\eta)} M_{\sigma,-\eta}(z) \\ &= W_{\sigma,-\eta}(z), \end{aligned} \tag{1.36}$$

$$\sigma \in \mathbb{C}, \ \Re(1/2+\eta\pm\sigma) > 0$$

where

$$M_{\sigma,\eta}(z) = z^{\eta+\frac{1}{2}} e^{-\frac{z}{2}} {}_1F_1\left(\frac{1}{2}-\sigma+\eta; 2\eta+1; z\right), \quad \Re(1/2+\eta\pm\sigma) > 0, \quad |argz| < \pi. \tag{1.37}$$

2. IMAGE FORMULA ASSOCIATED WITH FRACTIONAL INTEGRAL OPERATORS

Here, we establish image formulas for the generalized Lommel–Wright function involving Saigo-Maeda fractional integral operators (1.10) and (1.11), in terms of the Fox–Wright function.

Theorem 2.1. *Let* $\zeta, \zeta', \varrho, \varrho', \kappa, \vartheta \in \mathbb{C}, m \in \mathbb{N}, \ \varphi > 0$ *and* $x > 0$ *be such that*

$$\Re(\kappa) > 0, \quad \Re(\omega) > -1, \quad \Re(\chi+\omega) > \max\{0, \Re(\zeta+\zeta'+\varrho-\kappa), \Re(\zeta'-\varrho')\} \tag{2.1}$$

then there holds the formula

$$I_{0+}^{\zeta,\zeta',\varrho,\varrho',\kappa}\left[t^{\chi-1} J_{\omega,\vartheta}^{\varphi,m}(tz)\right](x) = x^{A-\zeta-\zeta'+\kappa-1}\left(\frac{z}{2}\right)^{\omega+2\vartheta} {}_4\psi_{4+m}\left[\begin{matrix}(A,2),(A+\kappa-\zeta-\zeta'-\varrho,2),(A+\varrho'-\zeta',2),(1,1)\\ (A+\varrho',2),(A+\kappa-\zeta-\zeta',2),(A+\kappa-\zeta'-\varrho,2),(\omega+\vartheta+1,\varphi),\underbrace{(\vartheta+1,1)}_{m-times}\end{matrix}\ \middle|\ -\frac{(zx)^2}{4}\right] \tag{2.2}$$

where $A = \chi+\omega+2\vartheta$.

Proof: Under the conditions stated with the Theorem 2.1, by taking the fractional integral of (1.1) using the equation (1.10) therein and changing the order of integration and summation, we get

$$\begin{aligned} &I_{0+}^{\zeta,\zeta',\varrho,\varrho',\kappa}\left[t^{\chi-1} J_{\omega,\vartheta}^{\varphi,m}(tz)\right](x) \\ &= \sum_{k=0}^\infty \frac{(-1)^k (\frac{z}{2})^{\omega+2\vartheta+2k}\Gamma(k+1)}{(\Gamma(\vartheta+k+1))^m \Gamma(\omega+k\varphi+\vartheta+1)k!} \\ &\quad \times I_{0+}^{\zeta,\zeta',\varrho,\varrho',\kappa}\left(t^{\omega+2\vartheta+2k+\chi-1}\right)(x) \end{aligned} \tag{2.3}$$

Further, applying the result (1.12) with χ replaced by $\chi+\omega+2\vartheta+2k$, we obtain

$$I_{0+}^{\zeta,\zeta^{'},\varrho,\varrho',\kappa}\left[t^{\chi-1}J_{\omega,\vartheta}^{\varphi,m}(tz)\right](x)$$
$$=x^{A-\zeta-\zeta^{'}+\kappa-1}\left(\frac{z}{2}\right)^{\omega+2\vartheta}\sum_{k=0}^{\infty}\frac{(-1)^k\Gamma(A+2k)\Gamma(k+1)}{\Gamma(A+\varrho^{'}+2k)(\Gamma(\vartheta+1+k))^m}$$
$$\times\frac{\Gamma(A+\kappa-\zeta-\zeta^{'}-\varrho+2k)\Gamma(A+\varrho^{'}-\zeta^{'}+2k)}{\Gamma(A+\kappa-\zeta^{'}-\varrho+2k)\Gamma(\omega+\vartheta+1+\varphi k)\Gamma(A+\kappa-\zeta-\zeta^{'}+2k)}$$
$$\times\frac{(zx)^{2k}}{4^k k!} \tag{2.4}$$

Here $A=\chi+\omega+2\vartheta$.

Interpreting the right-hand side of the above equation, in view of the definition (1.2), we arrive at the result (2.2).

Theorem 2.2. *Let $\zeta,\zeta^{'},\varrho,\varrho',\kappa,\vartheta\in\mathbb{C}, m\in\mathbb{N},\ \varphi>0$ and $x>0$ be such that*

$$\Re(\kappa)>0,\ \ \Re(\omega)>-1,$$
$$\Re(\chi-\omega)>1+\min\{\Re(-\varrho),\Re(\zeta+\zeta^{'}-\kappa),\Re(\zeta+\varrho^{'}-\kappa)\} \tag{2.5}$$

then there holds the formula

$$I_{0-}^{\zeta,\zeta^{'},\varrho,\varrho',\kappa}\left[t^{\chi-1}J_{\omega,\vartheta}^{\varphi,m}(z/t)\right](x)=x^{\kappa-\zeta-\zeta^{'}-A}\left(\frac{z}{2}\right)^{\omega+2\vartheta}$$
$${}_4\psi_{4+m}\left[\begin{matrix}(A-\kappa+\zeta+\zeta^{'},2),(A+\zeta+\varrho^{'}-\kappa,2),\\(A-\varrho,2),(1,1)\\(A,2)(A+\zeta+\zeta^{'}+\varrho'-\kappa,2),(A+\zeta-\varrho,2),\\(\omega+\vartheta+1,\varphi),\underbrace{(\vartheta+1,1)}_{m-times}\end{matrix}\middle|-\frac{z^2}{4x^2}\right] \tag{2.6}$$

where $A=1-\chi+\omega+2\vartheta$.

Proof: Under the conditions stated with the Theorem 2.2, on making use of the definitions (1.11) and (1.1) and changing the order of integration and summation, we have

$$I_{0-}^{\zeta,\zeta^{'},\varrho,\varrho',\kappa}\left[t^{\chi-1}J_{\omega,\vartheta}^{\varphi,m}(z/t)\right](x)$$
$$=\sum_{k=0}^{\infty}\frac{(-1)^k(\frac{z}{2})^{\omega+2\vartheta+2k}\Gamma(k+1)}{(\Gamma(\vartheta+k+1))^m\Gamma(\omega+k\varphi+\vartheta+1)k!}$$
$$\times I_{0-}^{\zeta,\zeta^{'},\varrho,\varrho',\kappa}\left(t^{\chi-\omega-2\vartheta-2k-1}\right)(x) \tag{2.7}$$

Here, on applying the formula (1.13) with χ replaced by $\chi-\omega-2\vartheta-2k$, we obtain

$$I_{0-}^{\zeta,\zeta^{'},\varrho,\varrho',\kappa}\left[t^{\chi-1}J_{\omega,\vartheta}^{\varphi,m}(z/t)\right](x)$$
$$=x^{\kappa-\zeta-\zeta^{'}-A}\left(\frac{z}{2}\right)^{\omega+2\vartheta}\sum_{k=0}^{\infty}\frac{(-1)^k\Gamma(A-\varrho+2k)}{\Gamma(A+2k)(\Gamma(\vartheta+k+1))^m}$$
$$\times\frac{\Gamma(k+1)\Gamma(A-\kappa+\zeta+\zeta^{'}+2k)\Gamma(A+\zeta+\varrho^{'}-\kappa+2k)}{\Gamma(A+\zeta-\varrho+2k)\Gamma(\omega+k\varphi+\vartheta+1)\Gamma(A+\zeta+\zeta^{'}+\varrho'-\kappa+2k)}$$
$$\times\frac{(z)^{2k}}{(4x^2)^k k!} \tag{2.8}$$

where $A=1-\chi+\omega+2\vartheta$.

So in view of the definition of the generalized Lommel–Wright function given by (1.1), the Equation (2.8) leads to the result (2.6).

For $m=1$ and in the light of Equation (1.3), Theorem 2.1 leads to the following corollaries:

Corollary 2.1. *Under the conditions stated with the Equation (2.1), the following image formula*

$$I_{0+}^{\zeta,\zeta^{'},\varrho,\varrho',\kappa}\left[t^{\chi-1}J_{\omega,\vartheta}^{\varphi,1}(zt)\right](x)=x^{A-\zeta-\zeta^{'}+\kappa-1}\left(\frac{z}{2}\right)^{\omega+2\vartheta}$$
$$\times\,{}_4\psi_5\left[\begin{matrix}(A,2),(A+\kappa-\zeta-\zeta^{'}-\varrho,2),\\(A+\varrho^{'}-\zeta^{'},2),(1,1)\\(A+\varrho^{'},2),(A+\kappa-\zeta-\zeta^{'},2),(A+\kappa-\zeta^{'}-\varrho,2),\\(\omega+\vartheta+1,\varphi),(\vartheta+1,1)\end{matrix}\middle|-\frac{(zx)^2}{4}\right] \tag{2.9}$$

$A=\chi+\omega+2\vartheta$, for generalized Bessel function $J_{\omega,\vartheta}^{\varphi,1}(zt)$ holds true.

Corollary 2.2. *Under the conditions stated with the Equation (2.5), the image formula*

$$I_{0-}^{\zeta,\zeta^{'},\varrho,\varrho',\kappa}\left[t^{\chi-1}J_{\omega,\vartheta}^{\varphi,1}(z/t)\right](x)$$
$$=x^{\kappa-\zeta-\zeta^{'}-A}\left(\frac{z}{2}\right)^{\omega+2\vartheta}$$
$$\times\,{}_4\psi_5\left[\begin{matrix}(A-\kappa+\zeta+\zeta^{'},2),(A+\zeta+\varrho^{'}-\kappa,2),\\(A-\varrho,2),(1,1)\\(A,2)(A+\zeta+\zeta^{'}+\varrho'-\kappa,2),(A+\zeta-\varrho,2),\\(\omega+\vartheta+1,\varphi),(\vartheta+1,1)\end{matrix}\middle|-\frac{z^2}{4x^2}\right] \tag{2.10}$$

$A=1-\chi+\omega+2\vartheta$, for generalized Bessel function $J_{\omega,\vartheta}^{\varphi,1}(z/t)$ holds true.

If we take $m=1,\ \varphi=1$, and $\vartheta=\frac{1}{2}$ in (2.2), then we obtain the corresponding results for the Struve function $H_\omega(\cdot)$ [16] as

Corollary 2.3. *Under the conditions stated with the Equation (2.1), the following image formula*

$$I_{0+}^{\zeta,\zeta^{'},\varrho,\varrho',\kappa}\left[t^{\chi-1}H_{\omega}(zt)\right](x)$$
$$=x^{A-\zeta-\zeta^{'}+\kappa-1}\left(\frac{z}{2}\right)^{\omega+1}$$
$$\times\,{}_4\psi_5\left[\begin{matrix}(A,2),(A+\kappa-\zeta-\zeta^{'}-\varrho,2),\\(A+\varrho^{'}-\zeta^{'},2),(1,1)\\(A+\varrho^{'},2),(A+\kappa-\zeta-\zeta^{'},2),\\(A+\kappa-\zeta^{'}-\varrho,2),(\omega+\frac{3}{2},1),(\frac{3}{2},1)\end{matrix}\middle|-\frac{(zx)^2}{4}\right] \tag{2.11}$$

$A=\chi+\omega+1$, for Struve function $H_\omega(zt)$ holds true.

Corollary 2.4. *Under the conditions stated with the Equation (2.5), the following image formula*

$$I_{0-}^{\zeta,\zeta^{'},\varrho,\varrho^{'},\kappa}\left[t^{\chi-1}H_{\omega}(z/t)\right](x) = x^{\chi-\omega-\zeta-\zeta^{'}+\kappa-2}\left(\frac{z}{2}\right)^{\omega+1} \times {}_4\psi_5\left[\begin{matrix}(A-\kappa+\zeta+\zeta^{'},2),(A+\zeta+\varrho^{'}-\kappa,2),\\ (A-\varrho,2),(1,1)\\ (A,2)(A+\zeta+\zeta^{'}+\varrho^{'}-\kappa,2),(A+\zeta-\varrho,2),\\ (\omega+\frac{3}{2},1),(\frac{3}{2},1)\end{matrix}\middle|-\frac{z^2}{4x^2}\right] \tag{2.12}$$

where $A = 2-\chi+\omega$, for Struve function $H_{\omega}(z/t)$ holds true.

2.1. Special Cases

(1) On taking $\varphi = 1$, $m = 1$, $\vartheta = 0$, and $z = 1$ in Theorem 2.1, we obtain the image formula for the Bessel function considered by Purohit et al. [28, Theorem 1].

Corollary 2.5. *Under the conditions stated with the Equation (2.1), the following image formula*

$$I_{0+}^{\zeta,\zeta^{'},\varrho,\varrho^{'},\kappa}\left[t^{\chi-1}J_{\omega}(t)\right](x) = \frac{x^{\chi+\omega-\zeta-\zeta^{'}+\kappa-1}}{2^{\omega}} \times {}_3\psi_4\left[\begin{matrix}(\chi+\omega,2),(\chi+\omega+\kappa-\zeta-\zeta^{'}-\varrho,2),\\ (\chi+\omega+\varrho^{'}-\zeta^{'},2)\\ (\chi+\omega+\varrho^{'},2),(\chi+\omega+\kappa-\zeta-\zeta^{'},2),\\ (\chi+\omega+\kappa-\zeta^{'}-\varrho,2),(\omega+1,1)\end{matrix}\middle|-\frac{x^2}{4}\right] \tag{2.13}$$

for Bessel function $J_{\omega}(t)$ holds true.

(2) Further, on taking $\varphi = 1, m = 1$, and $\vartheta = 0$ in Theorem 2.2, we arrive the right-sided image formula for the Bessel function considered by Purohit et al. [28, Theorem 2].

Corollary 2.6. *Under the conditions stated with the Equation (2.5), the image formula*

$$I_{0-}^{\zeta,\zeta^{'},\varrho,\varrho^{'},\kappa}\left[t^{\chi-1}J_{\omega}(1/t)\right](x) = \frac{x^{\kappa-\zeta-\zeta^{'}-1+\chi-\omega}}{2^{\omega}} \times {}_3\psi_4\left[\begin{matrix}(1-\chi+\omega-\kappa+\zeta+\zeta^{'},2),(1-\chi+\omega+\zeta+\varrho^{'}-\kappa,2),(1-\chi+\omega-\varrho,2)\\ (1-\chi+\omega,2)(1-\chi+\omega+\zeta+\zeta^{'}+\varrho^{'}-\kappa,2),(1-\chi+\omega+\zeta-\varrho,2),(\omega+1,1)\end{matrix}\middle|-\frac{1}{4x^2}\right] \tag{2.14}$$

for Bessel function $J_{\omega}(1/t)$ holds true.

3. IMAGE FORMULAS ASSOCIATED WITH INTEGRAL TRANSFORMS

In this section, we obtain the theorem involving the results obtained in previous sections associated with the integral transforms such as Beta transform, pathway transform, Laplace transform, and Whittaker transform.

3.1. Image Formulas for Beta Transform

Theorem 3.1. *Let $\zeta, \zeta^{'}, \varrho, \varrho^{'}, \kappa, \vartheta \in \mathbb{C}, m \in \mathbb{N}$, $\varphi > 0$, and $x > 0$ be such that*

$$\begin{aligned}&\Re(l) > 0, \quad \Re(n) > 0 \quad \Re(\kappa) > 0, \quad \Re(\omega) > -1,\\ &\Re(\chi+\omega) > \max\{0, \Re(\zeta+\zeta^{'}+\varrho-\kappa), \Re(\zeta^{'}-\varrho^{'})\}\end{aligned} \tag{3.1}$$

then the following Beta transform formula holds:

$$B\left[I_{0+}^{\zeta,\zeta^{'},\varrho,\varrho^{'},\kappa}\left(t^{\chi-1}J_{\omega,\vartheta}^{\varphi,m}(tz)\right)(x) : l, n\right] = \frac{x^{A-\zeta-\zeta^{'}+\kappa-1}\Gamma(n)}{2^{\omega+2\vartheta}} {}_5\psi_{5+m}\left[\begin{matrix}(A,2),(A+\kappa-\zeta-\zeta^{'}-\varrho,2),\\ (A+\varrho^{'}-\zeta^{'},2),(C-n,2)(1,1)\\ (A+\varrho^{'},2),(A+\kappa-\zeta-\zeta^{'},2),(A+\kappa-\zeta^{'}-\varrho,2),\\ (\omega+\vartheta+1,\varphi),(C,2),\underbrace{(\vartheta+1,1)}_{m-times}\end{matrix}\middle|-\frac{x^2}{4}\right] \tag{3.2}$$

Here $A = \chi+\omega+2\vartheta$ and $C = l+\omega+2\vartheta+n$.

Proof: For our convenience, let the left-hand side of the formula (3.2) be denoted by ς. Applying (1.28) to Equation (3.2), we get

$$\varsigma = \int_0^1 z^{l-1}(1-z)^{n-1}\left[I_{0+}^{\zeta,\zeta^{'},\varrho,\varrho^{'},\kappa}\left(t^{\chi-1}J_{\omega,\vartheta}^{\varphi,m}(tz)\right)(x)\right]dz.$$

Here, applying Equation (2.2) to the integral, we obtain the following expression

$$\varsigma = \int_0^1 z^{l-1}(1-z)^{n-1}z^{\omega+2\vartheta}\frac{x^{A-\zeta-\zeta^{'}+\kappa-1}}{2^{\omega+2\vartheta}} \times \sum_{k=0}^{\infty}\frac{(-1)^k\Gamma(A+2k)\Gamma(k+1)}{\Gamma(A+\varrho^{'}+2k)\Gamma(A+\kappa-\zeta-\zeta^{'}+2k)} \times \frac{\Gamma(A+\varrho^{'}-\zeta^{'}+2k)\Gamma(A+\kappa-\zeta-\zeta^{'}-\varrho+2k)}{\Gamma(A+\kappa-\zeta^{'}-\varrho+2k)\Gamma(\omega+\vartheta+1+\varphi k)(\Gamma(\vartheta+1+k))^m} \times \frac{(zx^2)^k}{4^k k!}dz$$

Here $A = \chi+\omega+2\vartheta$.

Interchanging the order of integration and summation, we have

$$\begin{aligned}\varsigma &= \frac{x^{A-\zeta-\zeta^{'}+\kappa-1}}{2^{\omega+2\vartheta}}\sum_{k=0}^{\infty}\frac{\Gamma(A+2k)\Gamma(A+\kappa-\zeta-\zeta^{'}-\varrho+2k)}{\Gamma(A+\kappa-\zeta-\zeta^{'}+2k)\Gamma(A+\kappa-\zeta^{'}-\varrho+2k)}\\ &\times\frac{\Gamma(A+\varrho^{'}-\zeta^{'}+2k)\Gamma(k+1)(-1)^k}{\Gamma(A+\varrho^{'}+2k)\Gamma(\omega+\vartheta+1+\varphi k)(\Gamma(\vartheta+1+k))^m}\frac{(x^2)^k}{4^k k!}\times\int_0^1 z^{l+\omega+2\vartheta+2k-1}(1-z)^{n-1}dz\\ &= \frac{x^{A-\zeta-\zeta^{'}+\kappa-1}}{2^{\omega+2\vartheta}}\sum_{k=0}^{\infty}\frac{\Gamma(l+\omega+2\vartheta+2k)\Gamma(n)\Gamma(A+2k)\Gamma(A+\kappa-\zeta-\zeta^{'}-\varrho+2k)}{\Gamma(l+\omega+2\vartheta+2k+n)\Gamma(A+\varrho^{'}+2k)\Gamma(A+\kappa-\zeta-\zeta^{'}+2k)}\\ &\times\frac{\Gamma(A+\varrho^{'}-\zeta^{'}+2k)\Gamma(k+1)}{\Gamma(A+\kappa-\zeta^{'}-\varrho+2k)\Gamma(\omega+\vartheta+1+\varphi k)(\Gamma(\vartheta+1+k))^m}\times\frac{(-x^2)^k}{4^k k!}\end{aligned}\tag{3.3}$$

Interpreting the right-hand side of the above equation, in the view of the definition (1.2), we arrive at the required result (3.2).

Theorem 3.2. *Let* $\zeta,\zeta^{'},\varrho,\varrho',\kappa,\vartheta,\omega\in\mathbb{C},m\in\mathbb{N},\ \varphi>0$, *and* $x>0$ *be such that*

$$\begin{aligned}\Re(\kappa)>0,\quad \Re(\omega)>-1,\quad \Re(l)>0,\ \ \Re(n)>0,\\ \Re(\chi-\omega)>1+\min\{\Re(-\varrho),\Re(\zeta+\zeta^{'}-\kappa),\Re(\zeta+\varrho^{'}-\kappa)\}\end{aligned}\tag{3.4}$$

then the following Beta transform formula holds:

$$\begin{aligned}&B\left[I_{0-}^{\zeta,\zeta^{'},\varrho,\varrho',\kappa}\left(t^{\chi-1}J_{\omega,\vartheta}^{\varphi,m}(z/t)\right)(x):l,n\right\}\\ &=\frac{x^{\kappa-\zeta-\zeta^{'}-A}\Gamma(n)}{2^{\omega+2\vartheta}}\\ &\times{}_5\psi_{5+m}\left[\begin{matrix}(A-\kappa+\zeta+\zeta^{'},2),(A+\zeta+\varrho^{'}-\kappa,2),\\(A-\varrho,2),(C-n,2),(1,1)\\(A,2)(A+\zeta+\zeta^{'}+\varrho'-\kappa,2),(A+\zeta-\varrho,2),\\(\omega+\vartheta+1,\varphi),(C,2),\underbrace{(\vartheta+1,1)}_{m-times}\end{matrix}\right|-\frac{1}{4x^2}\Bigg]\end{aligned}\tag{3.5}$$

where $A=1-\chi+\omega+2\vartheta$ *and* $C=l+\omega+2\vartheta+n$.

Proof: The proof of the fractional integral formula (3.5) is similar to the proof of the formula (3.2) given in Theorem 3.1.

Remark 3.1.

(1) For $m=1$, *Theorem 3.1 and Theorem 3.2 leads to the corresponding results for fractional integral of generalized Bessel function defined by (1.3).*
(2) If we take $m=1,\ \varphi=1$, *and* $\vartheta=\frac{1}{2}$ *in (3.2) and (3.5), we get the corresponding results for fractional integral of Struve function defined in (1.4).*
(3) On taking $m=1,\varphi=1$, *and* $\vartheta=0$, *in (3.2) and (3.5), we get the results for fractional integral of Bessel function defined in (1.5).*

3.2. Image Formulas for P_δ-Transform

Theorem 3.3. *Let* $\zeta,\zeta^{'},\varrho,\varrho',\kappa,\chi,\vartheta\in\mathbb{C},m\in\mathbb{N},\ \varphi>0,\ \Re(\chi)>0,\ \Re(s)>0,\ \delta>1$, *and* $x>0$ *be such that*

$$\begin{aligned}\Re(\kappa)>0,\quad \Re(\omega)>-1,\quad \Re(s)>0,\\ \Re(\chi+\omega)>\max\{0,\Re(\zeta+\zeta^{'}+\varrho-\kappa),\Re(\zeta^{'}-\varrho^{'})\}\end{aligned}\tag{3.6}$$

then the following P_δ*-transform formula holds:*

$$\begin{aligned}&P_\delta\left[z^{l-1}\left(I_{0+}^{\zeta,\zeta^{'},\varrho,\varrho',\kappa}t^{\chi-1}J_{\omega,\vartheta}^{\varphi,m}(tz)\right)(x):s\right]\\ &=\left(\Lambda(\delta;s)\right)^{l+\omega+2\vartheta}\ \frac{x^{A-\zeta-\zeta^{'}+\kappa-1}}{2^{\omega+2\vartheta}}\\ &\times{}_5\psi_{4+m}\left[\begin{matrix}(A,2),(A+\kappa-\zeta-\zeta^{'}-\varrho,2),\\(A+\varrho^{'}-\zeta^{'},2),(l+\omega+2\vartheta,2),(1,1)\\(A+\varrho^{'},2),(A+\kappa-\zeta-\zeta^{'},2),\\(A+\kappa-\zeta^{'}-\varrho,2),\\(\omega+\vartheta+1,\varphi),\underbrace{(\vartheta+1,1)}_{m-times}\end{matrix}\right|-\frac{(\Lambda(\delta;s)x)^2}{4}\Bigg]\end{aligned}\tag{3.7}$$

where $A=\chi+\omega+2\vartheta$ *and* $\Lambda(\delta;s)=\left(\frac{\delta-1}{\ln[1+(\delta-1)s]}\right)$.

Proof: For our convenience, we let the left-hand side of the formula (3.7) be denoted as Ξ. Applying (1.30) to Equation (3.2) we get,

$$\Xi=\int_0^\infty[1+(\delta-1)s]^{-\frac{z}{\delta-1}}z^{l-1}I_{0+}^{\zeta,\zeta^{'},\varrho,\varrho',\kappa}\left(t^{\chi-1}J_{\omega,\vartheta}^{\varphi,m}(tz)\right)(x)dz$$

Here, applying Equation (2.4) to the integral, we obtain the following expression:

$$\begin{aligned}\Xi&=\frac{x^{A-\zeta-\zeta^{'}+\kappa-1}}{2^{\omega+2\vartheta}}\sum_{k=0}^{\infty}\frac{(-1)^k\Gamma(A+2k)\Gamma(A+\kappa-\zeta-\zeta^{'}-\varrho+2k)}{\Gamma(A+\varrho^{'}+2k)\Gamma(A+\kappa-\zeta-\zeta^{'}+2k)\Gamma(A+\kappa-\zeta^{'}-\varrho+2k)}\\ &\frac{\Gamma(A+\varrho^{'}-\zeta^{'}+2k)\Gamma(k+1)}{\Gamma(\omega+\vartheta+1+\varphi k)(\Gamma(\vartheta+1+k))^m}\frac{(x)^{2k}}{4^k k!}\times\int_0^\infty[1+(\delta-1)s]^{-\frac{z}{\delta-1}}z^{\omega+2\vartheta+2k+l-1}dz\end{aligned}$$

Here making use of the result (1.31) and interchanging the order of integration and summation, we obtain,

$$\Xi = \left(\Lambda(\delta;s)\right)^{l+\omega+2\vartheta}\ \frac{x^{A-\zeta-\zeta^{'}+\kappa-1}}{2^{\omega+2\vartheta}}\sum_{k=0}^{\infty}\frac{\Gamma(A+2k)\Gamma(A+\kappa-\zeta-\zeta^{'}-\varrho+2k)}{\Gamma(A+\varrho^{'}+2k)\Gamma(A+\kappa-\zeta-\zeta^{'}+2k)}$$
$$\times\frac{\Gamma(\omega+2\vartheta+2k+l)\Gamma(A+\varrho^{'}-\zeta^{'}+2k)\Gamma(k+1)(-1)^{k}}{\Gamma(A+\kappa-\zeta^{'}-\varrho+2k)\Gamma(\omega+\vartheta+1+\varphi k)(\Gamma(\vartheta+1+k))^{m}}\ \frac{\{\Lambda(\delta;s)x\}^{2k}}{4^{k}k!} \tag{3.8}$$

where $A=\chi+\omega+2\vartheta$ and $\Lambda(\delta;s)=\left(\frac{\delta-1}{\ln[1+(\delta-1)s]}\right)$.
In view of the definition (1.2), we arrive at the required result (3.7).

Theorem 3.4. *Let $\zeta,\zeta^{'},\varrho,\varrho^{'},\kappa,\vartheta\in\mathbb{C},m\in\mathbb{N},\ \varphi>0\ \Re(\chi)>0,\ \Re(s)>0,\ \delta>1$, and $x>0$ be such that*

$$\Re(\kappa)>0,\ \ \Re(\omega)>-1,\ \ \Re(s)>0,$$
$$\Re(\chi-\omega)>1+\min\{\Re(-\varrho),\Re(\zeta+\zeta^{'}-\kappa),\Re(\zeta+\varrho^{'}-\kappa)\} \tag{3.9}$$

then the following P_δ- transform formula holds:

$$P_\delta\left(z^{l-1}\left[I_{0-}^{\zeta,\zeta^{'},\varrho,\varrho^{'},\kappa}t^{\chi-1}J_{\omega,\vartheta}^{\varphi,m}(z/t)\right](x):s\right)$$
$$=\left(\Lambda(\delta;s)\right)^{l+\omega+2\vartheta}\ \frac{x^{\chi-\omega-2\vartheta-\zeta-\zeta^{'}+\kappa-1}}{2^{\omega+2\vartheta}}$$
$$\times\ {}_5\psi_{4+m}\left[\begin{matrix}(A-\kappa+\zeta+\zeta^{'},2),(A+\zeta+\varrho^{'}-\kappa,2),\\(A-\varrho,2),(l+\omega+2\vartheta,2),(1,1)\\(A,2)(A+\zeta+\zeta^{'}+\varrho^{'}-\kappa,2),(A+\zeta-\varrho,2),\\(\omega+\vartheta+1,\varphi),\underbrace{(\vartheta+1,1)}_{m-times}\end{matrix}\ \middle|\ -\frac{\{\Lambda(\delta;s)\}^{2}}{4x^{2}}\right] \tag{3.10}$$

where $A=1-\chi+\omega+2\vartheta$ and $\Lambda(\delta;s)=\left\{\frac{\delta-1}{\ln[1+(\delta-1)s]}\right\}$.

Proof: Our demonstration of the P_δ-transform of generalized Lommel–Wright function (3.10) is based upon the known result (2.6).

A limit case of the Theorems 3.3 and 3.4 when $\delta\to 1$ yields the following corollaries for the Laplace transform in view of the (1.32).

Corollary 3.1. *Under the conditions stated with the Equation (3.6), the following Laplace transform formula holds true:*

$$P_\delta\left(z^{l-1}\left(I_{0+}^{\zeta,\zeta^{'},\varrho,\varrho^{'},\kappa}t^{\chi-1}J_{\omega,\vartheta}^{\varphi,m}(tz)\right)(x):s\right)=\frac{x^{A-\zeta-\zeta^{'}+\kappa-1}}{s^{l}\ 2^{\omega+2\vartheta}}$$
$$\times\ {}_5\psi_{4+m}\left[\begin{matrix}(A,2),(A+\kappa-\zeta-\zeta^{'}-\varrho,2),(A+\varrho^{'}-\zeta^{'},2),\\(l+\omega+2\vartheta,2),(1,1)\\(A+\varrho^{'},2),(A+\kappa-\zeta-\zeta^{'},2),(A+\kappa-\zeta^{'}-\varrho,2),\\(\omega+\vartheta+1,\varphi),\underbrace{(\vartheta+1,1)}_{m-times}\end{matrix}\ \middle|\ -\frac{x^{2}}{s^{2l}4}\right] \tag{3.11}$$

where $A=\chi+\omega+2\vartheta$.

Corollary 3.2. *Under the conditions stated with the Equation (3.9), the following Laplace transform formula holds true:*

$$P_\delta\left(z^{l-1}\left[I_{0-}^{\zeta,\zeta^{'},\varrho,\varrho^{'},\kappa}t^{\chi-1}J_{\omega,\vartheta}^{\varphi,m}(z/t)\right](x):s\right)=\frac{x^{\chi-\omega-2\vartheta-\zeta-\zeta^{'}+\kappa-1}}{s^{l}\ 2^{\omega+2\vartheta}}$$
$$\times\ {}_5\psi_{4+m}\left[\begin{matrix}(A-\kappa+\zeta+\zeta^{'},2),(A+\zeta+\varrho^{'}-\kappa,2),\\(A-\varrho,2),(l+\omega+2\vartheta,2),(1,1)\\(A,2)(A+\zeta+\zeta^{'}+\varrho^{'}-\kappa,2),(A+\zeta-\varrho,2),\\(\omega+\vartheta+1,\varphi),\underbrace{(\vartheta+1,1)}_{m-times}\end{matrix}\ \middle|\ -\frac{1}{s^{2l}\ 4x^{2}}\right] \tag{3.12}$$

where $A=1-\chi+\omega+2\vartheta$.

Remark 3.2.

(1) *On taking $m=1$, Theorems 3.3 and 3.4 lead to the P_δ-transform formulas for fractional integrals of generalized Bessel function.*
(2) *A limit case of the Theorems 3.3 and 3.4, when $\delta\to 1$ and $m=1$, yields the Laplace transform formulas for fractional integrals of generalized Bessel function.*
(3) *On taking $m=1,\ \varphi=1$, and $\vartheta=\frac{1}{2}$, Theorems 3.3 and 3.4 yield the P_δ-transform formulas for fractional integrals of Struve function.*
(4) *A limit case of Theorem 3.3 and 3.4, when $\delta\to 1$ and $m=1,\ \varphi=1$, and $\vartheta=\frac{1}{2}$, yield the Laplace transform formulas for fractional integrals of Struve function.*
(5) *On taking $m=1,\ \varphi=1$, and $\vartheta=0$, Theorem 3.3 and 3.4 yield the corresponding results for fractional integrals of Bessel function.*
(6) *A limit case of Theorem 3.3 when $\delta\to 1$ and $m=1,\ \varphi=1$, and $\vartheta=0$ yield the corresponding Laplace transform formulas for fractional integrals of Bessel function.*

3.3. Image Formulas for Whittaker Transform

Theorem 3.5. *Let $\zeta,\zeta^{'},\varrho,\varrho^{'},\kappa,\vartheta,\eta,\sigma\in\mathbb{C},\ m\in\mathbb{N},\ \varphi>0$, and $x>0$ be such that*

$$\Re(\kappa)>0,\Re(\omega)>-1,\ \ \Re(\tau\pm\eta)>-1/2,$$
$$\Re(\chi+\omega)>\max\{0,\Re(\zeta+\zeta^{'}+\varrho-\kappa),\Re(\zeta^{'}-\varrho^{'})\} \tag{3.13}$$

then the following Whittaker transform formula holds:

$$\int_0^\infty z^{\sigma-1}e^{-z/2}\left[W_{\sigma,\eta}I_{0+}^{\zeta,\zeta^{'},\varrho,\varrho^{'},\kappa}\left(t^{\chi-1}J_{\omega,\vartheta}^{\varphi,m}(zt)\right)(x)\right]dz$$
$$=\frac{x^{A-\zeta-\zeta^{'}+\kappa-1}}{2^{\omega+2\vartheta}}$$
$$\times\ {}_6\psi_{5+m}\left[\begin{matrix}(A,2),(A+\kappa-\zeta-\zeta^{'}-\varrho,2),(A+\varrho^{'}-\zeta^{'},2),\\(E+\eta,2),(E-\eta,2),(1,1)\\(A+\varrho^{'},2),(A+\kappa-\zeta-\zeta^{'},2),(A+\kappa-\zeta^{'}-\varrho,2),\\(\omega+\vartheta+1,\varphi),(E-\sigma,2),\underbrace{(\vartheta+1,1)}_{m-times}\end{matrix}\ \middle|\ -\frac{x^{2}}{4}\right] \tag{3.14}$$

where $A = \chi + \omega + 2\vartheta$ *and* $E = \tau + \omega + 2\vartheta + 1/2$.

Proof: For simplicity, let ϖ be the left-hand side of the formula (3.14). Applying (1.35) to Equation (3.14), we have

$$\varpi = \int_0^\infty z^{\sigma-1} e^{-z/2} W_{\sigma,\eta}\left[I_{0+}^{\zeta,\zeta',\varrho,\varrho',\kappa}\left(t^{\chi-1} J_{\omega,\vartheta}^{\varphi,m}(zt)\right)(x)\right] dz. \tag{3.15}$$

Here, applying Equation (2.2) to the integral, we obtain the following expression:

$$\begin{aligned}\varpi = &\int_0^\infty z^{\sigma+\omega+2\vartheta-1} e^{-z/2} W_{\sigma,\eta} \\ &\left[\frac{x^{A-\zeta-\zeta'+\kappa-1}}{2^{\omega+2\vartheta}} \sum_{k=0}^{\infty} \frac{\Gamma(A+2k)\Gamma(A+\kappa-\zeta-\zeta'-\varrho+2k)}{\Gamma(A+\varrho'+2k)\Gamma(A+\kappa-\zeta-\zeta'+2k)}\right. \\ &\times \frac{\Gamma(A+\varrho'-\zeta'+2k)\Gamma(k+1)(-1)^k}{\Gamma(A+\kappa-\zeta'-\varrho+2k)\Gamma(\omega+\vartheta+1+\varphi k)(\Gamma(\vartheta+1+k))^m} \\ &\left.\times \frac{(zx)^{2k}}{4^k k!}\right] dz\end{aligned}$$

where $A = \chi+\omega+2\vartheta$. Interchanging the order of integration and summation, we have

$$\begin{aligned}\varpi = &\frac{x^{A-\zeta-\zeta'+\kappa-1}}{2^{\omega+2\vartheta}} \sum_{k=0}^{\infty} \frac{\Gamma(E+\eta+2k)\Gamma(E-\eta+2k)\Gamma(A+\kappa-\zeta-\zeta'-\varrho+2k)}{\Gamma(E-\sigma+2k)\Gamma(A+\kappa-\zeta'-\varrho+2k)} \\ &\times \frac{(-1)^k\Gamma(A+2k)\Gamma(A+\varrho'-\zeta'+2k)\Gamma(k+1)}{\Gamma(A+\varrho'+2k)\Gamma(A+\kappa-\zeta-\zeta'+2k)\Gamma(\omega+\vartheta+1+\varphi k)(\Gamma(\vartheta+1+k))^m} \frac{x^{2k}}{4^k k!}\end{aligned} \tag{3.16}$$

where $A = \chi + \omega + 2\vartheta$ and $E = \tau + \omega + 2\vartheta + 1/2$.
Interpreting the right-hand side of the above equation, in view of the definition (1.2), we arrive at the required result (3.14).

Theorem 3.6. *Let* $\zeta, \zeta', \varrho, \varrho', \kappa, \vartheta, \eta, \sigma \in \mathbb{C}, m \in \mathbb{N}$, $\varphi > 0$, *and* $x > 0$ *be such that*

$$\begin{aligned}&\Re(\kappa) > 0, \quad \Re(\omega) > -1, \quad \Re(\tau \pm n) > -1/2, \\ &\Re(\chi-\omega) > 1 + \min\{\Re(-\varrho), \Re(\zeta+\zeta'-\kappa), \Re(\zeta+\varrho'-\kappa)\}\end{aligned} \tag{3.17}$$

then there holds the formula

$$\begin{aligned}&\int_0^\infty z^{\sigma-1} e^{-z/2} W_{\sigma,\eta}\left[\left(I_{0-}^{\zeta,\zeta',\varrho,\varrho',\kappa} t^{\chi-1} J_{\omega,\vartheta}^{\varphi,m}(zt)\right)(x)\right] dz \\ &= \frac{x^{\chi-\omega-2\vartheta-\zeta-\zeta'+\kappa-1}}{2^{\omega+2\vartheta}} \\ &{}_6\psi_{5+m}\left[\begin{matrix} (A-\kappa+\zeta+\zeta',2), (A+\zeta+\varrho'-\kappa,2), \\ (A-\varrho,2), (E+\eta,2), (E-\eta,2), (1,1) \\ (A,2)(A+\zeta+\zeta'+\varrho'-\kappa,2), (A+\zeta-\varrho,2), \\ (\omega+\vartheta+1,\varphi), (E-\sigma,2), \underbrace{(\vartheta+1)}_{m-times} \end{matrix}\middle| -\frac{1}{4x^2}\right]\end{aligned} \tag{3.18}$$

where $A = 1-\chi+\omega+2\vartheta$ *and* $E = \tau+\omega+2\vartheta+1/2$.

Proof: We can establish the result given in Theorem 3.6 similar to the proof of Theorem 3.5.

Remark 3.3.

(1) *For* $m = 1$, *Theorems 3.5 and 3.6 lead to the corresponding results for fractional integral of generalized Bessel function defined in (1.3).*
(2) *If we take* $m = 1$, $\varphi = 1$, *and* $\vartheta = \frac{1}{2}$, *Theorems 3.5 and 3.6 yield the corresponding results for fractional integral of Struve function defined in (1.4).*
(3) *On taking* $m = 1$, $\varphi = 1$, *and* $\vartheta = 0$, *Theorems 3.5 and 3.6 yield the corresponding results for fractional integral of Bessel function defined in (1.5).*

4. SPECIAL CASES AND CONCLUDING REMARKS

In this section, we consider some special cases of our main results involved in Theorems 2.1–3.6 which can be obtained by setting $\zeta' = 0$. These interesting corollaries of our results involve the Saigo fractional integral operators $I_{0,x}^{\zeta,\varrho,\eta}$ and $I_{x,\infty}^{\zeta,\varrho,\eta}$ and can be deduced from the Theorems 2.1–3.6 by appropriately applying the relationships given in the definitions (1.16) and (1.17). If we set $\varrho = -\zeta$ in the Theorems 2.1–3.6, then from the relationships (1.20) and (1.21) we obtain the corresponding results for the Riemann–Liouville and the Weyl fractional integral operators, respectively. Again, if we put $\varrho = 0$ in the Theorems 2.1–3.6, then from the relationships (1.24) and (1.25) we obtain the analogous results for Erdélyi-Kober type fractional integral operators.

In our present investigation, we establish the relationship between well-known fractional integral operators with novel integral transforms. The results obtained here are useful in deriving at various image formulas. The results presented here are very generic and can be specialized to give further potentially interesting and useful formulas involving fractional integral operators.

AUTHOR CONTRIBUTIONS

RPA devised the problem and supervised the manuscript by adding various results to it. RA and SJ worked on the mathematics in the manuscript. DB provided guidance, checked all calculations, and suggested language modifications to the article paper.

REFERENCES

1. Atangana A, Jain S. A new numerical approximation of the fractal ordinary differential equation. *Eur Phys J Plus* (2018) **133**:37. doi: 10.1140/epjp/i2018-11895-1
2. Jain S. Numerical analysis for the fractional diffusion and fractional Buckmaster's equation by two step Adam- Bashforth method. *Eur Phys J Plus* (2018) **133**:19 doi: 10.1140/epjp/i2018-11854-x
3. Agarwal R, Jain S, Agarwal RP. Analytic solution of generalized space time advection-dispersion equation with fractional Laplace operator. *J Nonlinear Sci Appl.* (2016) **9**:3545–54. doi: 10.22436/jnsa.009.06.09
4. Agarwal R, Jain S, Agarwal RP. Analytic solution of generalized space time fractional fraction diffusion equation. *Fract Differ Calc.* (2017) **7**:169–84. doi: 10.7153/fdc-07-05
5. Samko SG, Kilbas AA, Marichev OI. *Fractional Integrals and Derivatives: Theory and Applications* New York, NY: Gordon & Breach Science Publishers Inc. (1993).
6. Saxena RK, Saigo M. Generalized fractional calculus of the H-function associated with the Appell function. *J Frac Calc.* (2001) **19**:89–104.
7. Srivastava HM, Tomovski Z. Fractional calculus with an integral operator containing a generalized Mittag-Leffler function in the kernel. *Appl Math Comput.* (2009) **211**:198–210. doi: 10.1016/j.amc.2009.01.055
8. Srivastava HM, Saxena RK. Operators of fractional integration and their applications. *Appl Math Comput.* (2001) **118**:1–52 doi: 10.1016/S0096-3003(99)00208-8
9. Oteiza MBM, de Kalla S, Conde S. Un estudio sobre la funcition Lommel-Maitland. *Rev Técnica Facult Ingenieria Univers Zulia* (1986) **9**:33–40.
10. Srivastava HM, Karlsson PW. *Multiple Gaussian Hypergeometric Series*. New York, NY; Chichester; Brisbane, QLD; Toronto, ON: Halsted Press; Ellis Horwood Limited; John Wiley and Sons (1985).
11. Kilbas AA, Srivastava HM, Trujillo JJ. *Theory and Applications of Fractional Differential Equations*. Amsterdem: Elsevier Science; North-Holland Mathematical Studies (2006).
12. Prieto AI, de Romero SS, Srivastava HM. Some fractional calculus results involving the generalized Lommel-Wright and related functions. *Appl Math Lett.* (2007) **20**:17–22. doi: 10.1016/j.aml.2006.02.018
13. Paneva-Konovska J. Theorems on the convergence of series in genearlized Lommel-Wright functions. *Frac Cal Appl Anal.* (2007) **10**:60–74.
14. Pathak RS. Certain convergence theorems and asymptotic properties of a generalization of Lommel and Maitland transformations. *Proc Nat Acad Sci USA.* (1966) **A-36**:81–6.
15. Kiryakova V. On two Saigo's fractional integral operators in the class of univalent functions. *Fract Calc Appl Anal.* (2006) **9**:159–76.
16. Mathai AM, Saxena RK, Haubold HJ. *The H-Function Theory and Applications*. New York, NY: Springer-Verlag (2010).
17. Saigo M. A remark on integral operators involving the Gauss hypergeometric functions. *Math Rep Kyushu Univ.* (1978) **11**:135–43.
18. Saigo M. A certain boundary value problem for the Euler-Darboux equation I. *Math Japonica* (1979) **24**:377–85.
19. Marichev OI. Volterra equation of Mellin convolution type with a Horn function in the kernel (In Russian). *Izv AN BSSR Ser Fiz -Mat Nauk* (1974) **1**:128–9.
20. Saigo M, Maeda N. More generalization of fractional calculus. In: *Transform Methods and Special Functions*. Varna: Bulgarian Academy of Science (1998).
21. Oldham KB, Spanier J. *The Fractional Calculus: Theory and Applications of Differentiation and Integration of Arbitrary Order* . New York, NY: Academic Press (1974).
22. Kober H. On fractional integrals and derivatives. *Quart J Math Oxford Ser.* (1940) **11**:193–212.
23. Sneddon IN. *The Use of Integral Transforms*. New Delhi: Tata McGraw-Hill (1979).
24. Kumar D. Solution of fractional kinetic equation by a class of integral transform of pathway type. *J Math Phys.* (2013) **54**:043509. doi: 10.1063/1.4800768
25. Agarwal R, Jain S, Agarwal RP. Solution of fractional Volterra integral equation and non-homogeneous time fractional heat equation using integral transform of pathway type. *Progr Fract Differ Appl.* (2015) **1**:145–55. doi: 10.12785/pfda/010301
26. Srivastava HM, Agarwal R, Jain S. Integral transform and fractional derivative formulas involving the extended generalized hypergeometric functions and probability distributions *Math Methods Appl Sci.* (2017) **40**:255–73. doi: 10.1002/mma.3986
27. Srivastava R, Agarwal R, Jain S. A family of the incomplete hypergeometric functions and associated integral transform and fractional derivative formulas. *Filomat* (2017) **31**:125–40. doi: 10.2298/FIL1701125S
28. Purohit SD, Suthar DL, Kalla SL. Marichev-Saigo-Maeda fractional integration operators of the Bessel functions. *Matematiche* (2012) **67**:21–32.

Conflict of Interest Statement: The authors declare that the research was conducted in the absence of any commercial or financial relationships that could be construed as a potential conflict of interest.

frontiers in Physics

ORIGINAL RESEARCH
published: 08 May 2018
doi: 10.3389/fphy.2018.00033

One-Dimensional Multi-Channel Photonic Crystal Resonators Based on Silicon-On-Insulator With High Quality Factor

Joaquin Faneca[1,2], *Tatiana S. Perova*[3,4]*, *Vladimir Tolmachev*[5] *and Anna Baldycheva*[1]*

[1] College of Engineering Mathematics and Physical Sciences, University of Exeter, Exeter, United Kingdom, [2] EPSRC Centre for Doctoral Training in Electromagnetic Metamaterials, University of Exeter, Exeter, United Kingdom, [3] Department of Electronic and Electrical Engineering, Trinity College Dublin, The University of Dublin, Dublin, Ireland, [4] International Research and Education Centre for Physics of Nanostructures, ITMO University, Saint Petersburg, Russia, [5] Division of Solid State Electronics, Ioffe Institute, Saint Petersburg, Russia

We have theoretically and experimentally demonstrated a Fabry-Pérot (FP) resonators based on a Si-air one-dimensional photonic crystal (1D PhC) with coupled triple-cavity modes (or defects). These defects are obtained by filling selected air channels in the 1D PhC with an actively reconfigurable fluid. Simulations of the optical properties of these FP resonators were performed in the wide infrared spectral range. It is shown that by changing the refractive index, n_C, of the fluid simultaneously in all three channels, a set of narrow triple resonance peaks can be obtained within wide stop-bands of different order in the infrared range. In addition, at certain values of n_C, splitting of the triple resonance peaks into a doublet and a single peak with a significantly larger quality factor, Q = 21,200, occurs. Prototype devices based on Silicon-On-Insulator platform were fabricated and characterized by electro-optical and spectroscopic measurements. The electro-optical measurements demonstrate the possibility of refractive index manipulation of the filler in the FP channels individually or simultaneously. Spectroscopic measurements performed in the range 1540–1630 nm using fiber-coupling confirm the presence of triple resonance peaks in the 3rd stop-band in the absence of an electric field applied to the FP channels. At an applied voltage of 10 V to the middle channel, an increase of Q to 3720 in the single peak is registered.

Keywords: one-dimensional Si photonic crystal, multiple Fabry-Perot resonators, tunable triple-cavity modes, stop-bands, high quality factor, refractive index sensing

OPEN ACCESS

Edited by:
Petra Granitzer,
University of Graz, Austria

Reviewed by:
Venu Gopal Achanta,
Tata Institute of Fundamental Research, India
Weiren Zhu,
Shanghai Jiao Tong University, China
Bernard Gelloz,
Nagoya University, Japan

***Correspondence:**
Tatiana S. Perova
perovat@tcd.ie
Anna Baldycheva
a.baldycheva@exeter.ac.uk

Specialty section:
This article was submitted to Optics and Photonics, a section of the journal Frontiers in Physics

Received: *03 January 2018*
Accepted: *27 March 2018*
Published: *08 May 2018*

Citation:
Faneca J, Perova TS, Tolmachev V and Baldycheva A (2018) One-Dimensional Multi-Channel Photonic Crystal Resonators Based on Silicon-On-Insulator With High Quality Factor. Front. Phys. 6:33. doi: 10.3389/fphy.2018.00033

INTRODUCTION

Modern Silicon fabrication technology has advanced remarkably over the last two decades, demonstrating an unprecedented level of photonic integration [1–7]. Particular attention is paid to different types of photonic devices based on one-dimensional, two-dimensional and three-dimensional photonic crystals with a consequent variation of layers of different refractive indices in these (various) directions [4–6]. Development of integrated compact multi-channel filters in particular, for applications including communication systems [8, 9], multifunctional sensing [10–12] and spectral imaging detection [13] is an active area of research in this field. Vertically etched

silicon one-dimensional photonic crystals (1D PhCs) have attracted particular interest, due to their easy fabrication and integration onto a chip with in-plane light propagation [14–16]. Other advantages of these structures are the possibility of tuning their optical properties [17–19], as well as their ease of adoption for micro/nano-fluidic devices [20–22].

These advantages have resulted in the development of a variety of opto-electronic devices, including multimode filters for wavelength division multiplexing (WDM) as well as opto-fluidic devices for biochemical and biomedical sensing. The desired characteristics for these devices are high quality factor (Q), large modulation depth, also known as extinction ratio (E.R), high selectivity, high out-of-band rejection, low power attenuation, low insertion losses and a small footprint, see, for example, Reed [6]. The use of vertical 1D PhCs for sensing is particularly important for the near- and mid-infrared regions and may be extended in future to the far-infrared and even the THz regions [1–3, 7, 23]. Another attraction of these structures is that the delivery of chemical or biological substances into the air gaps can be performed via standard "flow-over" (see, for example [24]) and "flow-through" approaches. The latter method is achieved by pumping through the channels as well as by capillary action [25–27]. Simulations of three vertical silicon/air 1D PhC Fabry-Perot resonant cavities with different architectures and fluidic functionalities were discussed in Surdo and Barillaro [28]. The impact of cavity order and 1D PhC micromirror reflectivity on their biosensing performance is analyzed. Results on the surface sensitivity, the limit of detection and the range of linearity of the devices are reported.

For effective frequency separation, multimode filters are used. These are fabricated by creating a cavity of extended size in a Fabry-Perot (FP) resonator, as well as by using cascaded and coupled resonators [17, 29–31]. These cascaded structures consist of separate FP filters connected in series. Changing the optical properties of individual filters does not affect the properties of the neighboring filters [29–31]. The use of PhC technology can remarkably improve the tuning capability of individual channels within these filters and optical switches for WDM optical interconnect applications. PhC technology can also reduce the footprint and provide an easier integration process [32]. Tunable multichannel PhC filters rely on the tuneability of the refractive index, *n*, of several periods within the periodic photonic structure, allowing the formation of coupled resonators, via thermotuning, electrotuning and a photorefractive effect [33–37]. These devices allow fine-tuning of individual channels in the filter system, by, for example, varying the temperature or applying an electric or magnetic field.

The development of integrated compact multi-channel optical filters is a rapidly developing area. Coupled microresonators are used in waveguide structures [38] and ring resonators [39], which can be tuned by injecting carriers with $\Delta n < 10^{-4}$, resulting in a relatively small tunable range. By using liquid crystals with a larger range of Δn, up to 0.4, tuning of the resonance modes has been significantly extended, for example, in a cascade resonator [29]. In Cos et al. [40] the design of an optical equalizer, or tunable filter, is proposed, with the possibility of changing the shape of the interference bands by changing *n* within different periods of the 1D PhC structure.

The optical properties of a system of two coupled Fabry-Perot microresonators were investigated theoretically in Kaliteevski [41], where the interaction of localized photon states is considered, leading to a splitting of the optical modes of the system. In this study, the coupling parameter, the reflection, *R*, of the common mirror, is identified, characterizing the interaction force between the modes. A decrease in *R* led to an increase in the splitting of the peaks in the spectrum. By using coupled FP resonators and exploiting the possibility of individual tuning of *n* in each resonator, a 1D PhC structure with two defects and various options to control the position of the doublet of resonance modes was investigated in Tolmachev et al. [42].

In this study, we propose a novel design for a multichannel integrated filters based on silicon-on-insulator (SOI) photonic crystal concepts and optofluidics technology. By infiltrating specific periods of a 1D PhC with a reconfigurable liquid filler, an efficiently coupled Fabry-Pérot micro-resonator (**Figure 1**) can be realized in which the wide stop band (SB) is used for frequency channel separation. Using a coupled triple-cavity 1D PhC filter operated using the third SBs, we have demonstrated refractive index control within individual cavities using a reconfigurable fluid, enabling independent fine tuning of each channel in the system by an applied voltage. By applying a voltage to one of the cavities, a triplet resonance is achieved with a significant increase in the *Q* factor for one of the resonance peaks.

SIMULATIONS

Coupled Fabry-Perot Resonators With Tunable Triple Mode Capability

In this section, we describe the optical properties of 1D PhCs based on a Si-air structure with three central air channels infiltrated with an LC of tunable refractive index, n_c. These structures form three coupled FP resonators with triple-defect modes within the photonic SBs. The optical properties of these structures were estimated using a transfer matrix method (TMM), see for details [26].

The introduction of 3 cavities, infiltrated with a filler of tunable n_c, to a 1D PhC, leads to the formation of triple conjugated FP resonators, **Figure 1A**. The transfer matrix for 3-coupled resonators (M_{3CR}) can be written as

$$M_{3CR} = H(LH)^{mBr}L_{c2}[(HL)^{mo}H]L_{c4}[(HL)^{mo}H]L_{c6}[(HL)(HL)^{mB}H, \quad (1)$$

where H – stands for the matrix of the high-refractive index component and L—the matrix of the low-refractive index component, c_2, c_4 and c_6—refer to the resonator cavities (2, 4, and 6), *mBr*—the number of periods for the Bragg mirror and *mo*—the number of periods for the internal mirror. The refractive index of the air is taken as $n_{air} = 1$, while the data for the dispersion of Si, n_{Si}(v), were taken from Salzberg and Villa [43]. For our calculations, we use various combinations of n_c in the FP-resonator cavities, with parallel or cross-tuning in the range 1.5–1.7. From the large range of possible n_c available, we selected

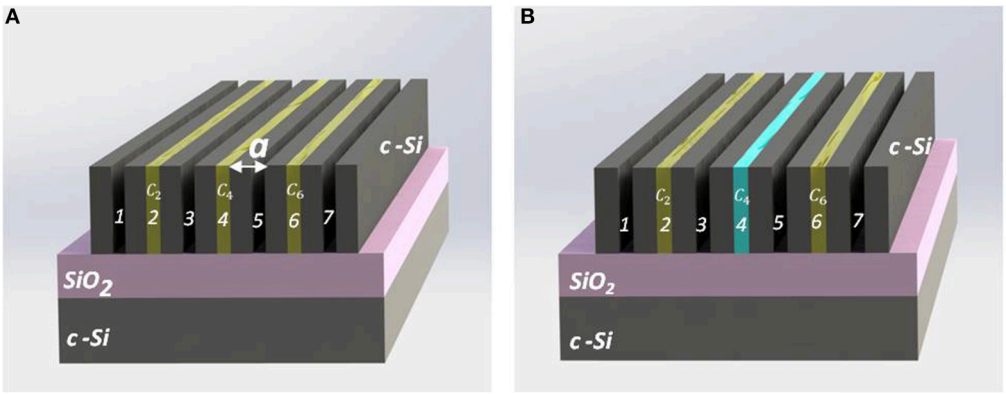

FIGURE 1 | (A) Schematic diagram of 1D PhC based on a Si-air structure with three central air channels (c2, c4, and c6) infiltrated with a nematic liquid crystal (LC) of tunable refractive index, n_C. **(B)** Schematic diagram of 1D PhC in which the refractive index of the central cavity n_{c4} is changed without changing n_C in the edge cavities, giving a new sequence of n_C. The notation a stands for the lattice constant of the 1D PhC and is equal to a sum of the thicknesses of crystalline Si (c-Si) rib, d_{Si}, and the air (or LC) channel, d_{air}.

four specific cases which may be of practical interest for different applications. The calculations were performed for the following geometrical parameters of a 1D PhC: $d_{Si} = 0.718\,\mu$m and $d_{air} = 2.5\,\mu$m (i.e., $a = 3.218\,\mu$m) and $mBr = mo = 1$.

Parallel Tuning of Triplet FP Resonator

In the initial state, when the filler in all three cavities of the resonator have $n_c = 1.585$ (**Figure 2a**), a triplet of defect modes appears in the spectrum of the 1st SB, **Figure 2c**—bottom spectrum. The distance between the peak positions in this triplet is $\Delta\nu \approx 40$ cm^{-1}, the linewidth, i.e., the full width at half-maximum, FWHM, for the edge and central peaks is = 2.5 and 5.5 cm^{-1} respectively, and the *Q*-factors for each peak are 420 and 190, respectively.

When n_c in all three cavities is decreased from 1.585 to 1.515 (**Figure 2b**), the triplet as a whole experiences a blue shift by $\Delta\nu = 30$ cm^{-1} (**Figure 2c**—top spectrum), or in relative units by $\Delta\nu/\Delta n_c = 429$ cm^{-1}/RIU, where RIU stands for refractive index unit. Taking into account the linewidth of the peaks and the distance between them, equal to $\Delta\nu \approx 40$ cm^{-1}, as well as the possibility of changing the values of n_c to a high degree of accuracy, it is possible to obtain other triplets occupying different positions in the spectrum. Thus, it is possible to achieve tuning of 4 triplets, with 12 resonant peaks in total, covering the range $\Delta\nu_{\text{total}} = 116$ cm^{-1} (**Figure 2d**).

The tuning effect can be increased by using higher order SBs. To obtain non-overlapping peaks, it is possible to use an almost full range of n_c variation in the range 1.5–1.7, **Figure 3A**. Calculations show that in the 3st SB the linewidth of the peaks remains the same as in the 1st SB, viz. 2.5 cm^{-1} for the edge peaks and 4.5 cm^{-1} for the central peak. The distance between the two nearest peaks is 40 cm^{-1} and the tuning range increased 5-fold from 30 to 167 cm^{-1}, **Figure 3B**. The relative tuning was $\Delta\nu/\Delta n_c$ = 835 cm^{-1}/RIU, a 2-fold increase. We note that 12 resonant peaks were obtained using only four possible values of n_c in the range 1.5–1.7, including the lowest and the highest n_c values. However, to obtain the maximum number of non-overlapping peaks, further fine tuning of the n_c values within this range is required.

The spectrum in **Figure 3B** (bottom spectrum) shows only one triplet for $n_c = 1.585$, whereas in all other spectra in this Figure, two triplets are shown for the larger and smaller values of n_c to save space. **Figure 3C** shows the positions of all 27 peaks in the range $\Delta\nu_{\text{total}} = 420$ cm^{-1}, exhibiting good resolution between the peaks. As in the case of double resonators [41, 42] the central position of the resonance peaks in the 3rd SB, with a linewidth of $w_{3SB} \approx 600$ cm^{-1}, made it possible to use over 2/3 of the SB to create a wide range of tunable resonances within it. In contrast, for the 1st SB, only 15% of the width of the band, $w_{1SB} \approx 770$ cm^{-1}, can be used in this manner.

Tuning of the Edge Peaks in the Triplet

Other options for triplet tuning are available. The initial state of the resonators is described by the following sequence of n_c: 1.515–1.515–1.515, **Figure 4a**. The calculated transmission spectrum, *T,* for the 1st SB is shown in **Figure 4d**. The n_c of the central cavity is changed to 1.585 without changing n_c in the edge cavities, giving a new sequence of n_c: 1.515–1.585–1.515 (**Figure 4b**) with the corresponding spectrum shown in **Figure 4e**.

Finally, by changing n_c in the central cavity to 1.7, **Figure 4c**, we obtain the spectrum shown in **Figure 4f**. The result of this tuning is a red shift of two edge defect modes at $\Delta\nu = 45$ cm^{-1}. In relative units, the shift is small, i.e., $\Delta\nu/\Delta n_c = 225$ cm^{-1}/RIU, and the central mode within the triplets remains stationary.

This is more clearly manifested in the 3rd SB shown in **Figures 4g–i**. Indeed, splitting of the triplet into a double peak (doublet) and a single peak (mono-peak) occurred, and, as seen in **Figure 4i**, both peaks in the doublet merge to form a single broadened peak, while the monopeak is narrowed greatly. Formation of the doublet structure is explained by the interaction between two resonators with identical resonant frequencies. These are the two extreme cavities, with $n_c = 1.515$, connected through a central resonator. Its resonant frequency,

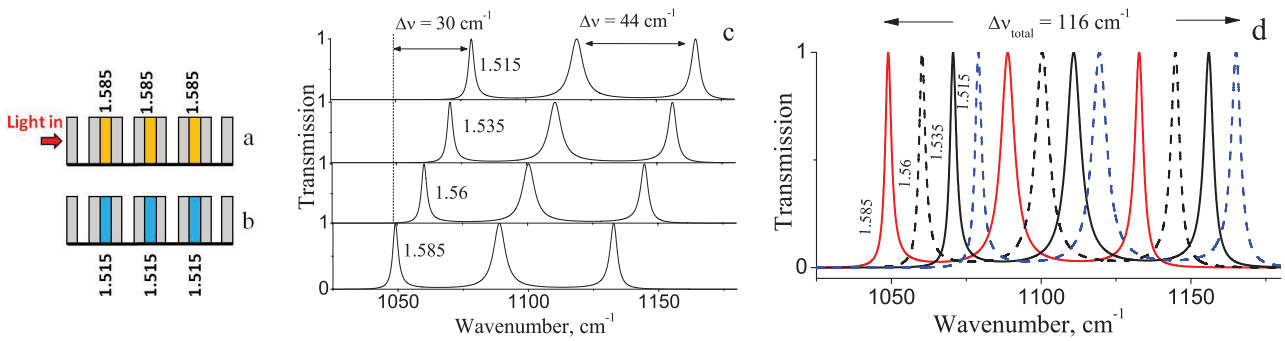

FIGURE 2 | Schematic diagram of three coupled resonators with tuning of n_C of the filler from **(a)** 1.585 to **(b)** 1.515; **(c)** parallel tuning of the triplet mode with $\Delta\nu = 30\ cm^{-1}$ for the 1st SB, **(d)** the full range of 12 resonance peaks with $\Delta\nu_{total} = 116\ cm^{-1}$. The numbers beside the peaks are the refractive indices, n_C, of the filler liquid in the resonator cavities.

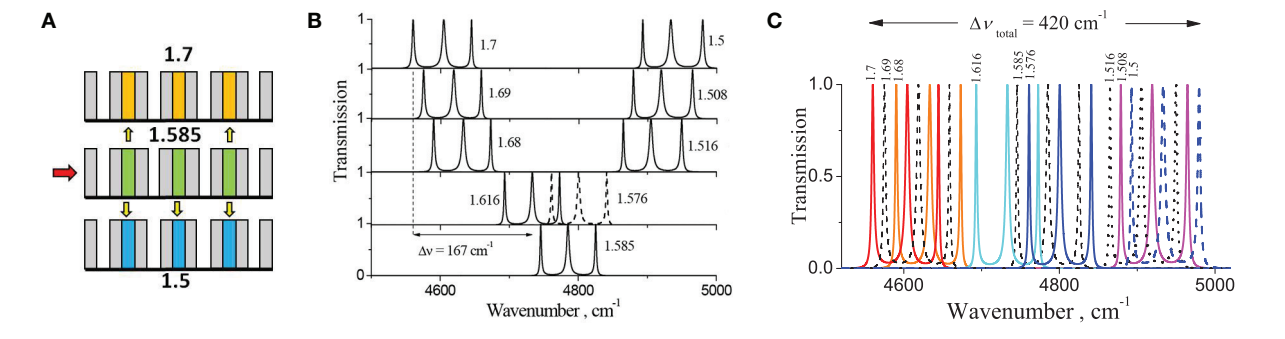

FIGURE 3 | (A) Schematic diagram illustrating n_C tuning in resonator cavities, **(B)** nine triple peaks in the spectra of the 3rd SB with parallel tuning of the n_C filler from 1.5 to 1.7, **(C)** the full range of 27 resonance peaks with $\Delta\nu_{total} = 420\ cm^{-1}$. Numbers beside the peaks correspond to the values of n_C for the fillers in all three cavities of the resonators.

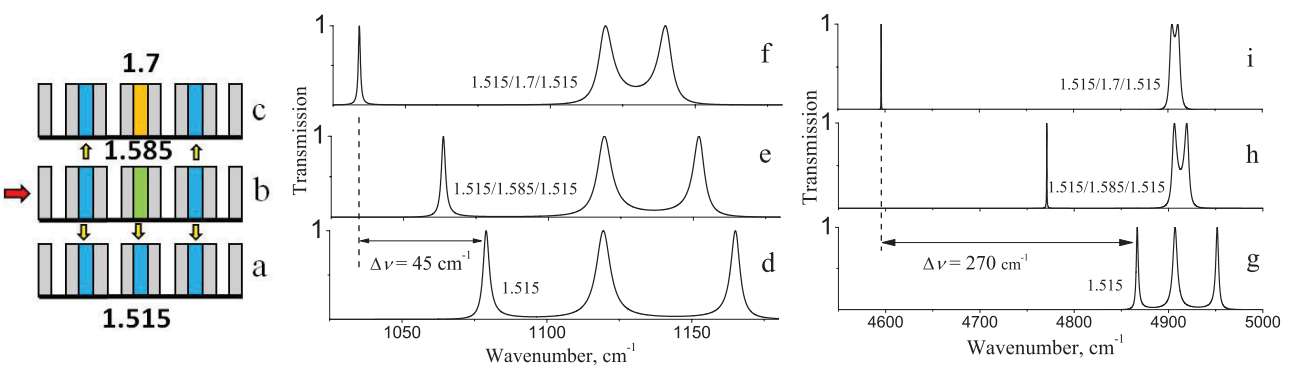

FIGURE 4 | (a–c) Schematic diagram illustrating tuning of n_C in one of the three cavities of the resonator. Triplet peaks with tuning of the n_C filler from 1.5 to 1.7 in the central cavity with splitting of the triplet into doublet and mono-peaks in the spectra of the 1st SB **(d–f)** and 3rd SB **(g–i)**. The numbers correspond to the value of n_C of the filler in the resonator cavities.

with a change of n_{c2} to 1.585 and then to 1.7, differs from the frequency of the resonators forming a doublet. For the initial state, the central resonator was in resonance with the edge cavities and it's intrinsic frequency begins to increase as n_c increases. This, in turn, reduces the interaction between the resonances in the edge cavities, due to the appearance of a reflector at their intrinsic frequency, ultimately greatly weakening their interaction, resulting in minimal peak splitting in the doublet (**Figure 4i**). From **Figures 4g–i**, the total shift as a result of the tuning is $\Delta\nu = 270\ cm^{-1}$, which is significant if expressed in relative units, viz. $\Delta\nu/\Delta n_c = 1{,}350\ cm^{-1}$/RIU. In addition, the quality factor, $Q = \nu_{res}/\Delta\nu$, where ν_{res} is the resonance peak position and $\Delta\nu$ is the linewidth, is significantly increased from 1,400 to 21,200 for the left peaks in **Figures 4g,i** respectively.

Let us now consider the following tuning option utilizing the 3rd SB: n_c in the edge cavities unchanged and equal to 1.6, while the n_c of the central cavity (n_{c2}) changes to a larger or smaller value from n_c, that is, $n_{c2} = \pm \Delta n$, where $\Delta n = 0.035$. A schematic of the n_c changes is shown in **Figures 5a–c**. **Figure 5d** shows the original triplet, obtained in the 3rd SB with splitting of the peaks by $\Delta\nu = 40$ cm^{-1} for the original state with $n_c = 1.6$ in all 3 cavities of the resonator. Furthermore, by increasing or decreasing n_c by $\Delta n = 0.006$, 0.017, and 0.035, different triplets were obtained, as presented in **Figures 5e–g**. As a result, the position of the central peak on the graphs remains unchanged while peak splitting is observed. With increased n_{c2} the edge peaks are red shifted, while with decreasing n_{c2} the peaks are blue shifted.

In addition, the nature of the peak splitting of the triplet changes. For example, increasing n_c to 1.635, the left peak splits more strongly ($\Delta\nu = 79$ cm^{-1}), while the right peak approaches the central peak ($\Delta\nu = 20$ cm^{-1}). This situation is analogous to the effect shown in **Figures 4g–i**, where splitting of the triplet into a doublet and a mono-peak was observed. This was explained by a weakening of the interaction of the coupled resonators caused by different n_c values within the cavities. Thus, by selecting a more appropriate combination of n_c values, (**Figures 5a–c**), it is possible to obtain well-separated transmission peaks in the interval $\Delta\nu_{total} = 157$ cm^{-1} as shown in **Figure 5h**. So, it is possible to tune 7 different peak pairs with one common unchanged transmission channel, that is, 15 channels in total.

Summarizing the results from the data shown in **Figures 4g–i**, **5d–h**, we conclude that changes in the triplet with increasing Δn between the cavities are more pronounced in the 3rd SB when compared with the 1st SB, allowing edge tuning to provide a larger range of transmission channels.

Tuning of the Central Peak in the Triplet

Another option for triplet tuning was investigated, that of changing n_c simultaneously in all 3 cavities. The variation of n_c was carried out according to the schematic shown in **Figures 6a–c**. For the initial state n_c in the cavities (1.6/1.6/1.6), the triplet in the 1st SB is shown in **Figure 6d**. A decrease of n_{c4} to 1.57 was made in the central cavity of the resonator, with a simultaneous increase of n_{c2} and n_{c6} to 1.625. This state (1.625 / 1.57 / 1.625) is depicted in **Figure 6b**. Since n_c in the resonators now changes in opposite directions, we refer to this situation as cross-tuning. The original triplet calculated is shown in **Figure 6d** with another triplet obtained using an intermediate value of n_c. Also included are triplets obtained by reverse tuning of n_c in the resonators, as shown in the schematic in **Figure 6c**.

From **Figure 6d**, the positions of the side peaks remain practically the same for the 5 triplets obtained, while the central peak experiences a red shift as the n_{c2} of the central cavity decreases. This is the opposite case to the tuning effect for a single peak in a classical FP resonator. In a single peak in a classical FP resonator, a decrease in the optical thickness of the cavity results in the resonance peak experiencing a blue shift. Examining this effect for the 3st SB in **Figures 6e–h**, it is apparent that as the cross-sectional change in n_c increases, resonance effects split the triplet into a doublet and a mono-peak, as observed earlier, see **Figure 4**. Indeed, the central peak of the triplet in this case experiences a red shift. Thus, for the 3rd SB, performing cross-tuning of n_c in the cavities enables control of the doublet structure, shifting it to the red. The edge cavities with the same refractive index are responsible for the appearance of the doublet structure. n_c in this case increases, leading to a redshift of the doublet, and the central peak responsible for its creation. This redshift is apparent in **Figures 6e–h**.

It should be noted that because of strong splitting due to cross-tuning of n_c in the cavities in the 3rd SB, the side peaks in the triplet cannot be fixed, as was possible in the 1st SB. Attempts to realize a similar resonator, i.e., fixed edge channels—tuning of the central channel, for the well-divided peaks in the 3rd SB failed, even when changing the values of n_c by small amounts.

The results of simulations demonstrating the tuning of triple FP resonances with suppression of the edge peaks are described in the Supplementary Materials section and shown in Supplementary Figure S1.

EXPERIMENT

Results and Discussions

Prototypes of integrated triple-cavity PhC filters were designed and fabricated on a Silicon-On-Insulator (SOI) platform. The triple-channel resonator device was fabricated on a <100> p-type SOI wafer with a silicon device layer thickness of 4.5 μm and a 1 μm thick buried oxide layer, Supplementary Figure S2 in Supplementary Material. Electron-Beam Lithography followed by plasma etching was used to fabricate the nano-scale structures with a lattice constant of 1600 nm and a Si wall thickness of 1040 nm. These design parameters for the 1D PhC structures were selected in order to create triple resonances in the telecommunication wavelength range after infiltration of the 2nd, 4th, and 6th grooves with a nematic liquid crystal filler E7, **Figure 7a**. This liquid crystal was chosen mainly because of its high birefringence, $n_e - n_o = 0.21$, where n_e and n_o correspond to the extraordinary and ordinary refractive indices respectively, as well as a wide nematic temperature range (from -10^oC to 59^oC). Electrical isolation of the 2nd, 4th, and 6th grooves of the 1D PhC was achieved by dry-etching the micro-channels across the chip, Supplementary Figure S3 in Supplementary Material. One cone-shape cavity is designed for the easy infiltration of these grooves with LC E7, **Figure 7a**. A 500 nm layer of aluminum was deposited by sputtering for the contact pads. Optical lithography followed by a wet etch process was used to define the contact pads, as shown in **Figure 7a**. Finally, U-grooves with a depth of 60 μm were etched from both sides of the nano-structure for easier integration of the optical fibers and direct coupling to the device (**Figures 7b,c**).

By applying a voltage to the aluminum contact pads, different orientations of the LC molecules were obtained in the individual grooves, allowing manipulation of the refractive index in the 2nd, 4th, and 6th grooves and, consequently, with the transmission channels as described earlier in the Simulations section. In **Figure 8**, the electro-optical effect obtained for three channels is demonstrated with crossed-polarized optical microscopy. The black stripes are silicon electrodes, orange lines are air

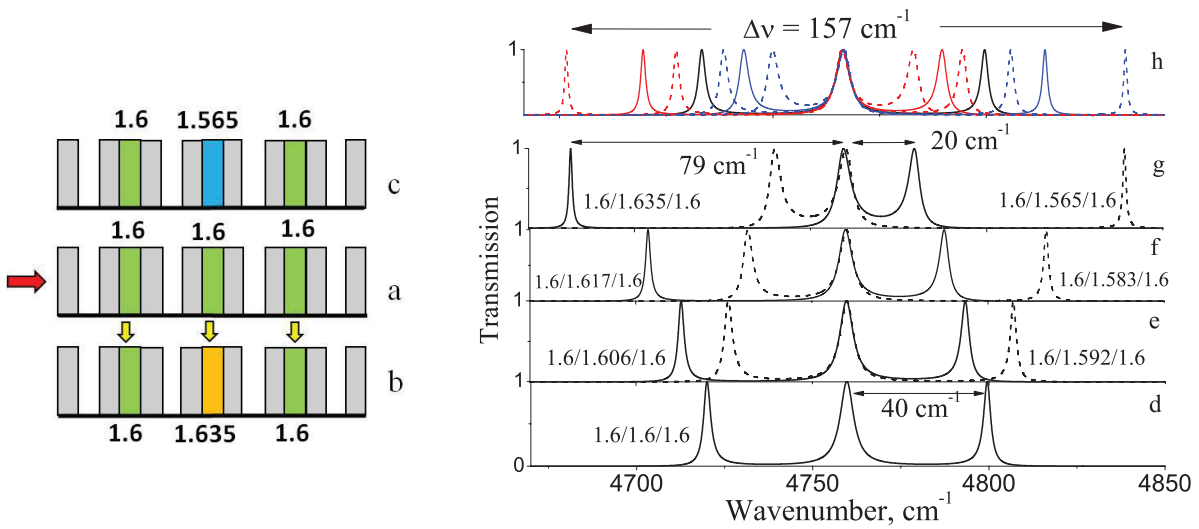

FIGURE 5 | (a–c) Tuning of the n_C filler in the central cavity only: **(d–g)** 7 triplets in the 3rd SB, realized with different n_{C2} (shown by numbers at the peaks) with a fixed central peak and tuned lateral (edge) resonances, **(h)** summing peaks for all states of n_C.

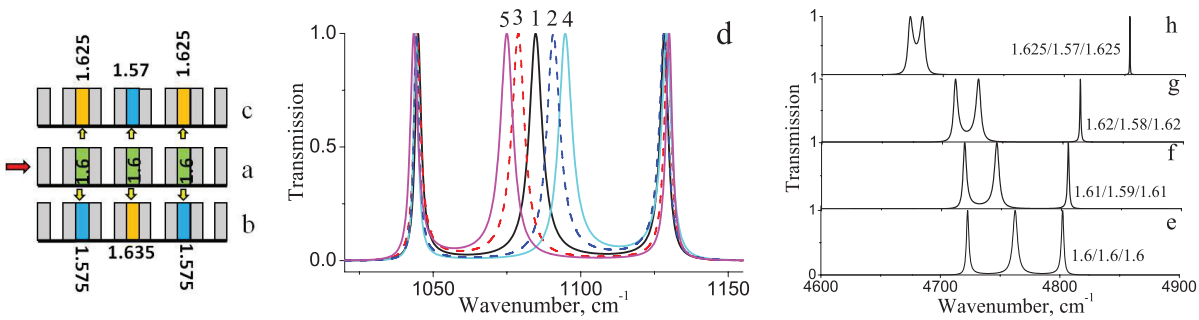

FIGURE 6 | (a–c) Schematic diagram illustrating cross-tuning of the n_C filler, **(d)** 5 triplets in the 1st SB with fixed edge peaks and a tunable central peak, **(e–h)** the original triplet and 3 triplets in the 3rd SB, demonstrating the split into a doublet and a mono-peak. Numbers at the peaks are the values of n_C for the fillers in the cavities of the resonators. In panel **(d)** the numbers beside the curves correspond to the following set of n_C: 1 – 1.6/1.6/1.6; 2 – 1.585/1.62/1.585; 3 – 1.615/1.58/1.615; 4 – 1.575/1.63/1.575; 5 – 1.625/1.57/1.625.

grooves and light stripes are grooves filled with a LC, **Figure 8**. A rectangular pulse train is applied to the three channels, alternating between 0 and 10 V, with a pulse duration of τ_p = 1 ms and a frequency of f_p = 100 Hz. The applied voltage causes the Fredericks transition to occur in the LC in the grooves, as demonstrated by the change in color of the groove stripes. The effect of the applied voltage on all three FP channels individually or simultaneously is demonstrated clearly in the video uploaded in the Supplementary Material section.

A demonstration of the appearance of the full set of resonance peaks within the 1st and 3rd SBs under applied voltage was not possible in this work due to limitations in the wavenumber range available for measurements in our fiber-coupling set-up. However, a shift of the resonance peak position by the applied electric field of different strength (and, therefore, by fine-tuning of n_c) was demonstrated by us earlier [44], see also a schematic illustration of this effect shown in Supplementary Figure S4 in Supplementary Material section. In Tolmachev et al. [44], we presented the results of TMM simulations for a single-cavity FP resonator, filled with LC E7, over a wide IR spectral range. The experimental verifications of these calculations were provided using FTIR microspectroscopy.

On-chip *in-situ* transmission testing of the device with an electric field applied to the micro-fluidic cavities was performed in the geometry demonstrated in **Figure 7c** (see also Supplementary Figure S5 in Supplementary Material). Light from the Yeniast Tunics T100S tunable laser source in the range 1,540–1,630 nm was coupled into the chip on the left-hand side. The transmitted signal was collected from the right-hand side, using standard optical fibers. Output power was measured using an optical spectrum analyser (OSA), Yenista Optics FP002417 OSA. The schematic of this set-up is shown in Supplementary Material section.

The device was electrically driven by terminating probes on the contact pads during the transmission measurements using a customized Microtech 2 probe coupler. Device transmission characteristics were initially assessed with no voltage applied to the channels, as in **Figure 8a**. In **Figure 9A** we demonstrate the realization of a triple resonance mode obtained with a spontaneously aligned LC in the grooves with an average

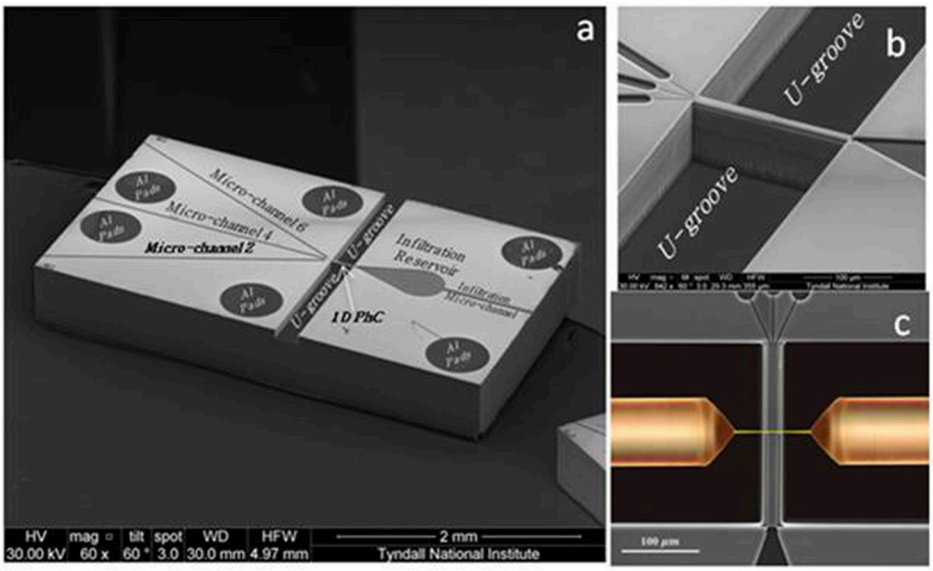

FIGURE 7 | SEM images of the fabricated **(a)** SOI-based chip with integrated triple-coupled defect photonic crystal filter with connected microfluidic channels to the 2nd, 4th, and 6th periods (clearly indicated beside the output channels) and metal contact pads (circles), and **(b)** closer view of the defect-free 1D PhC with three-channels connected to the 2nd, 4th, and 6th grooves for infiltration purposes. **(c)** Schematic representation of light coupling with optical fibers integrated on-chip using U-grooves from both sides of the PhC structure.

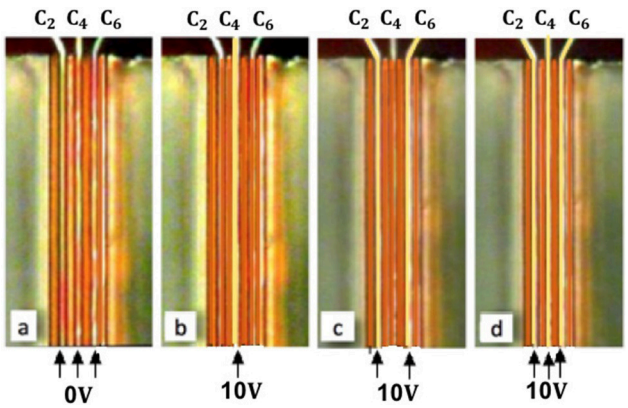

FIGURE 8 | Polarized Optical Microscope images showing a top view of the channels: **(a)** no applied electric field (0 V), **(b)** under applied electric field of 10 V to the 4th central channel, **(c)** under applied electric field of 10 V to the 2nd and the 6th channels and **(d)** under applied electric field of 10 V to all three channels. Note: Applied voltage indicated by numbers (0 and 10) in Volts.

refractive index of 1.68. The simulated resonance peaks obtained at 1,589.4, 1,608 and 1,629.6 nm demonstrate a Q factor of the order of 1,130 with a total resonance wavelength spacing of 40.2 nm. Under an applied AC voltage of 10V, the refractive index of c_4 channel is decreased to 1.458. This results in the formation of a doublet at 1,607.6 and 1,617 nm and a single resonance peak at 1,562.4 nm, with a significant increase of the Q factor to 3,720, see **Figure 9B** and Supplementary Figure S6 in Supplementary Material. Under applied voltage, this peak is shifted by 27 nm from its original position at 1,589.4 nm, as shown in **Figure 9A** with no voltage applied. The fitted n_c value corresponds to a homeotropic alignment of rod-like LC molecules perpendicular to the Si walls (see Supplementary Figure S4d in Supplementary Material), expected to occur with an applied electric field across the 1D PhC groove channels, see, for example, page 516 in Perova et al. [26] and Tolmachev et al. [44]. This experimental result demonstrates for the first time, electrically controllable, ultra-high sensitivity of a single resonance device based on the triple cavity Fabry-Pérot system. The LC filler in the 2nd and 6th cavities can be replaced by any other liquid filler analyte or gas with arbitrary refractive index, while the electrically tunable 4th central cavity can be used as a highly-sensitive reference liquid. The nematic LC E7 can demonstrate a relatively high-quality factor and sensitivity for high-order stop-bands in particular.

We note that for SOI electro-optical devices, that required a fast tuning of the refractive index of liquid crystal, the LC E7 is not very suitable, since its operation time is in the range of milliseconds. However, the other nematic LCs like, for example, 5CB and CCN-47 not only characterized by their high birefringence but also demonstrate an impressive electro-optical switching time in the range of 30–50 nanoseconds, as recently was demonstrated under specific experimental conditions in Geis et al. [45] and Borshch et al. [46]. In addition to that, it was shown during the last decade that some new type of liquid crystal molecules (for example, banana-shaped or bent-core LCs) can demonstrate also fast switching time at microseconds/nanoseconds level [47, 48].

CONCLUSIONS

In this paper, we propose a novel design for multichannel integrated devices based on SOI photonic crystal concepts and optofluidic technology. By infiltrating specific periods of a 1D

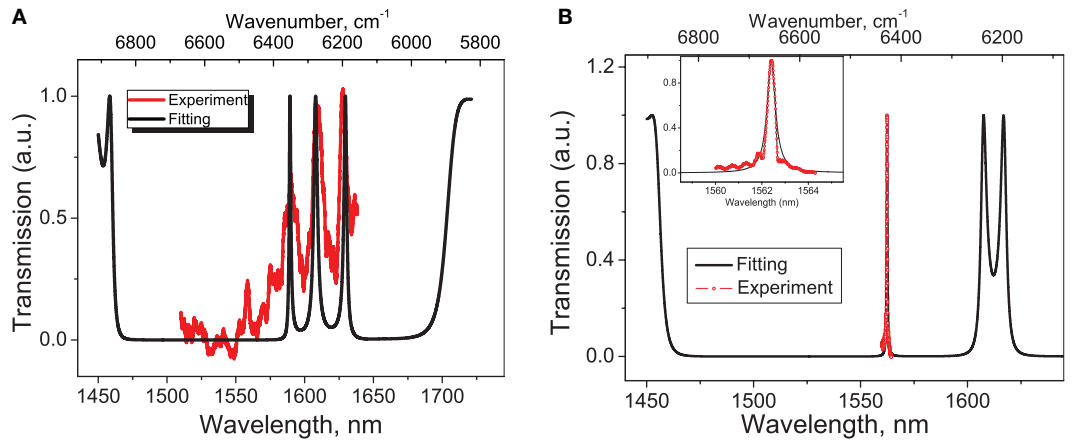

FIGURE 9 | Simulated (black) and experimental (red) transmission spectra of **(A)** triple resonance system with refractive index of LC filler of n_C =1.68 in 2nd, 4th, and 6th grooves and **(B)** single resonance system realized by application of 10V to the 4th groove and reduction of refractive index to n_C = 1.458. A magnified view of the single resonance peak can be found in the inset figure.

PhC with a reconfigurable liquid filler of different refractive indices, n_c, an efficiently coupled Fabry-Pérot micro-resonators can be realized. Various combinations of n_c in the cavities of the FP resonators with parallel and cross-tuning in the range 1.5–1.7 are investigated by simulations using the transfer matrix method. With parallel tuning of n_c in all three cavities, a large number of narrow triple resonance peaks can be obtained within the wide stop-bands of different order in the infrared range of spectra. Simulations of cross-tuning of n, reveal splitting of the triple resonance peaks into a doublet and a single peak with significantly enhanced quality factor, $Q = 21{,}200$.

Prototype devices were fabricated with three central cavities infiltrated with LC E7. Simulations of the electro-optical and optical properties of these devices were confirmed experimentally using polarized optical microscopy and spectroscopic measurements using fiber-coupling. Tuning of the refractive index of the filler in all three cavities simultaneously or individually was confirmed by electro-optical measurements. These structures may have application to WDM devices in the near IR to THz range, depending on the geometry. Spectroscopic measurements, performed over a limited near-IR spectral range, verified the presence of the triple resonance peaks within the 3rd stop-band in the absence of an applied electric field in the grooved channels. Application of an electric field to one of the three channels, using a voltage of 10 V, caused a shift of the low-frequency peak and a substantial increase of the quality factor to $Q = 3{,}720$. This suggests that these devices could form the basis of coupled FR resonators for application in refractive index sensing and for ultra-narrow optical filters in the infrared range.

AUTHOR CONTRIBUTIONS

TP, VT, and AB: conceived the idea; VT, AB, and JF: performed device design and simulation; TP and AB: participated in device fabrication; AB and JF: performed near-IR measurements; TP, VT, AB, and JF: wrote the manuscript. All authors were involved in the analysis of the results and revision of the manuscript.

ACKNOWLEDGMENTS

We acknowledge financial support from: The Engineering and Physical Sciences Research Council (EPSRC) of the United Kingdom via the EPSRC (Grant No. EP/L015331/1 and Grant No. EP/N035569/1) and the Royal Society International Exchange Grant 2015/R3. The microfluidic structures were fabricated at Tyndall National Institute under the Science Foundation Ireland NAP368 and NAP94 programs. The part of this research at the Ioffe Institute was supported by the Russian Federal Agency of Scientific Organizations.

SUPPLEMENTARY MATERIAL

The Supplementary Material for this article can be found online at: https://www.frontiersin.org/articles/10.3389/fphy.2018.00033/full#supplementary-material

REFERENCES

1. Soref R. The past, present, and future of silicon photonics. *IEEE J Sel Top Quantum Electron* (2006) **12**:1678–87. doi: 10.1109/JSTQE.2006.883151
2. Soref R. Mid-infrared photonics in silicon and germanium. *Nature Photon.* (2010) **4**:495–7. doi: 10.1038/nphoton.2010.171
3. Soref R. Group IV photonics for the mid infrared. *Proc SPIE* (2013) **8629**:862902. doi: 10.1117/12.2013769
4. Wehrspohn RB, Kitzerow HS, Busch K. *Nanophotonic Materials: Photonic Crystals, Plasmonics, and Metamaterials*. Weinheim: Wiley-VCH (2008).
5. Vivien L, Pavesi L. *Handbook of Silicon Photonics*. Boca Raton, FL: CRC Press (2013).
6. Reed GT. *Silicon Photonics: The State of the Art*. West Sussex: Wiley (2008).
7. Hu T, Dong B, Luo X, Liow TY, Song J. Silicon photonic platforms for mid-infrared applications. *Photon Res.* (2017) **5**:417. doi: 10.1364/PRJ.5.000417

8. Yariv A, Yeh P. *Photonics: Optical Electronics in Modern Communications*, Oxford: Oxford University Press (2007).
9. Li Q, Soltani M, Yegnanarayanan S, Adibi A. Design and demonstration of compact, wide bandwidth coupled-resonator filters on a silicon-insulator platform. *Opt Express* (2009) **17**:2247–54. doi: 10.1364/OE.17.002247
10. Shu X, Chisholm K, Felmeri I, Sugden K. Highly sensitive transverse load sensing with reversible sampled fiber Bragg gratings. *Appl Phys Lett.* (2003) **83**:3003–5. doi: 10.1063/1.1618367
11. Armani AM, Kulkarni RP, Fraser SE, Flagan RC, Vahala KJ. Label-free, single-molecule detection with optical microcavities. *Science* (2007) **317**:783–7. doi: 10.1126/science.1145002
12. Marquez S, Alvarez M, Plaza JA, Villanueva LG, Dominguez C, Lechuga LM. Asymmetrically coupled resonators for mass sensing. *J Appl Phys*. (2017) **111**:113101. doi: 10.1063/1.5003023
13. Lin J, Tong Q, Lei Y, Xin Z, Wei D, Zhang X, et al. Electrically tunable infrared filter based on a cascaded liquid-crystal Fabry–Perot for spectral imaging detection. *Appl Opt*. (2017) **56**:1925–9. doi: 10.1364/AO.56.001925
14. Tolmachev VA, Perova TS, Astrova EV, Volchek BZ, Vij JK. Vertically etched silicon as 1-D photonic crystal. *Phys Status Solidi A* (2003) **197**:544–8. doi: 10.1002/pssa.200306561
15. Barillaro G, Strambini LM, Annovazzi-Lodi V, Merlo S. Optical characterization of high-order 1-D silicon photonic crystals. *IEEE J Sel Top Quantum Electron* (2009) **15**:1359. doi: 10.1109/JSTQE.2009.2017278
16. St-Gelais R, Poulin A, Peter YA. Advances in modelling, design, and fabrication of deep-etched multilayer resonators. *J Lightwave Technol.* (2012) **30**:1900–8. doi: 10.1109/JLT.2012.2191136
17. Yi Y, Bermel P, Wada K, Duan X, Joannopoulos JD, Kimerling LC. Tunable multichannel optical filter based on silicon photonic band gap materials actuation. *Appl Phys Lett*. (2002) **81**:4112–4. doi: 10.1063/1.1525072
18. Lipson A, Yeatman EM. A 1-D photonic band gap tunable optical filter in (110) silicon. *J Microelectromech Syst.* (2007) **16**:521–7. doi: 10.1109/JMEMS.2007.892894
19. Masson J, St -Gelais R, Poulin A, Peter YA. Tunable fiber laser using a MEMS-based in plane Fabry-Perot filter. *IEEE J Quantum Electron.* (2010) **46**:1313–9. doi: 10.1109/JQE.2010.2050299
20. Zhao Y, Zhao X, Gu Z. Photonic crystals in bioassays. *Adv Funct Mater.* (2010) **20**:2970–88. doi: 10.1002/adfm.201000098
21. Surdo S, Merlo S, Carpignano F, Strambini LM, Trono C, Giannetti A, et al. Optofluidic microsystems with integrated vertical one-dimensional photonic crystals for chemical analysis. *Lab Chip* (2012) **12**:4403–15. doi: 10.1039/c2lc40613f
22. St-Gelais R, Masson J, Peter YA. All-silicon integrated Fabry-Perot cavity for volume refractive index measurements in microfluidic system. *Appl Phys Lett.* (2009) **94**:243905. doi: 10.1063/1.3152286
23. Lavchiev VM, Jakoby B. Photonics in the mid-infrared: challenges in single-chip integration and absorption sensing. *IEEE J Select Top Quantum Electron*. (2017) **23**:8200612. doi: 10.1109/JSTQE.2016.2619330
24. Mazzini G, Carpignano F, Surdo S, Aredia F, Panini N, Torchio M, et al. 3D Silicon microstructures: a new tool for evaluating biological aggressiveness of tumor cells. *IEEE Trans Nanobiosci*. (2015) **14**:797–805. doi: 10.1109/TNB.2015.2476351
25. Surdo S, Carpignano F, Strambini LM, Merlo S, Barillaro G. Capillarity-driven (self -powered) one-dimensional photonic crystals for refractometry and (bio)sensing applications. *RSC Adv*. (2014) **4**:51935–41. doi: 10.1039/C4RA09056J
26. Perova T, Tolmachev V, Berwick K. Chapter XI: Design of composite and multi-component one-dimensional photonic crystal structures based on silicon. In: Granitzer P, Rumpf K, editors. *Nanostructured Semiconductors: From Basic Research to Applications.* Singapore: Pan Stanford Publishing Pte. Ltd. (2014). 453–526.
27. Hogan BT, Dyakov S, Brennan LJ, Younesy S, Perova TS, Gun'ko YK, et al. Dynamic *in-situ* sensing of fluid-dispersed 2D materials integrated on microfluidic Si chip. *Sci Rep*. (2017) **7**:42120. doi: 10.1038/srep42120
28. Surdo S, Barillaro G. On the performance of label-free biosensors based on vertical one-dimensional photonic crystal resonant cavities. *Opt Express* (2015) **23**:9192–201. doi: 10.1364/OE.23.009192
29. Zheng Z, Yang G, Li H, Liu X. Three-stage Fabry–Perot liquid crystal tunable filter with extended spectral range. *Optics Express* (2011) **19**:2158–64. doi: 10.1364/OE.19.002158
30. Shabtay G, Eidinger E, Zalevsky Z, Mendlovic D, Marom E. Tunable birefringent filters – optimal iterative design. *Opt Express* (2002) **10**:1534–41. doi: 10.1364/OE.10.001534
31. Aharon O, Abdulhalim I. Tunable optical filter having a large dynamic range. *Opt Lett*. (2009) **34**:2114–6. doi: 10.1364/OL.34.002114.
32. Zhao X, Yang Y, Chen Z, Wang Y, Fei H, Deng X. Ultra-wide tuning single channel filter based on one-dimensional photonic crystal with an air cavity. *J Semicond.* (2017) **38**:023004. doi: 10.1088/1674-4926/38/2/023004
33. Hu X, Liu Z, Gong Q. Tunable multichannel filter in photonic crystal heterostructure containing permeability-negative materials. *Phys Lett A* (2008) **372**:333–9. doi: 10.1016/j.physleta.2007.07.029
34. Yun SS, Lee JH. A micromachined in-plane tunable optical filter using the thermo-optic effect of crystalline silicon. *J Micromech Microeng.* (2003) **13:**721–5. doi: 10.1088/0960-1317/13/5/326
35. Pruessner MW, Stievater TH, Rabinovich WS. In-plane microelectromechanical resonator with integrated Fabry–Pérot cavity. *Appl Phys Lett*. (2008) **92**:081101. doi: 10.1063/1.2883874
36. Barrios CA, Almeida VR, Panepucci RR, Schmidt BS, Lipson M. Compact silicon tunable fabry-perot resonator with low power consumption. *IEEE Photon Technol Lett*. (2004) **16**:506–8. doi: 10.1109/LPT.2003.822251
37. Baldycheva A, Tolmachev VA, Berwick K, Perova TS. Multi-channel Si-liquid crystal filter with fine tuning capability of individual channels for compensation of fabrication tolerances. *Nanosci Res Lett.* (2012) **7**:387. doi: 10.1186/1556-276X-7-387
38. O'Brien D, Settle MD, Karle T, Michaeli A, Salib M, Krauss TF. Coupled photonic crystal heterostructure nanocavities. *Opt Express* (2007) **15**:1228–33. doi: 10.1364/OE.15.001228
39. Vahala KJ. Optical microcavities. *Nature* (2003) **424**:839–46. doi: 10.1038/nature01939
40. Cos J, Ferre-Borrull J, Pallares J, Marsal LF. Tunable Fabry–Pérot filter based on one-dimensional photonic crystals with liquid crystal components. *Opt Commun.* (2009) **282**:1220–5. doi: 10.1016/j.optcom.2008.11.074
41. Kaliteevski MA. Optical properties of a system of two coupled vertical microcavities. *Technol Phys*. (1998) **43**:565–8.
42. Tolmachev VA, Baldycheva AV, Perova TS. Coupled microresonator structures. In: *Book of Abstracts of VII International Conference on Fundamental Problems in Optics.* St.-Petersburg: ITMO University (2012). p. 340–1.
43. Salzberg CD, Villa JJ. Infrared refractive indexes of silicon, germanium and modified selenium glass. *J Opt Soc Am*. (1957) **47**:244–6. doi: 10.1364/JOSA.47.000244
44. Tolmachev VA, Melnikov VA, Baldycheva AV, Berwick K, Perova TS. Electrically tunable Fabry-Pérot resonator based on microstrcutured Si containing liquid crystal. *Prog Electromagn Res.* (2012) **122**:293–309. doi: 10.2528/PIER11091506
45. Geis MW, Molnar RJ, Turner GW, Lyszczarz TM, Osgood RM, Kimball BR. 30 to 50 ns liquid-crystal optical switches. In: *Proceedings Volume 7618, Emerging Liquid Crystal Technologies V*. San Francisco, CA (2010).
46. Borshch V, Shiyanovskii S.V, Lavrentovich OD. Nanosecond electro-optic switching of a liquid crystal. *Phys Rev Lett.* (2013) **111**:1–5. doi: 10.1103/PhysRevLett.111.107802
47. Jakli AI. *Fast Switching Electro-Optical Devices Using Banana-Shaped Liquid Crystals*. US Patent 7782438 (2010).
48. Jakli AI. Liquid crystals of the twenty-first century – nematic phase of bent-core molecules. *Liquid Cryst Rev.* (2013) **1**:65–82. doi: 10.1080/21680396.2013.803701

Conflict of Interest Statement: The authors declare that the research was conducted in the absence of any commercial or financial relationships that could be construed as a potential conflict of interest.

frontiers in Physics

REVIEW
published: 19 March 2018
doi: 10.3389/fphy.2018.00025

Status of the Vibrational Theory of Olfaction

Ross D. Hoehn[1]*, *David E. Nichols*[2], *Hartmut Neven*[3] and *Sabre Kais*[1,4]*

[1] Departments of Chemistry and Physics, Purdue University, West Lafayette, IN, United States, [2] Department of Pharmacology, University of North Carolina, Chapel Hill, Chapel Hill, NC, United States, [3] Google Los Angeles, Venice, CA, United States, [4] Santa Fe Institute, Santa Fe, NM, United States

The vibrational theory of olfaction is an attempt to describe a possible mechanism for olfaction which is explanatory and provides researchers with a set of principles which permit predictions allowing for structure-odor relations. Similar theories have occurred several times throughout olfactory science; this theory has again recently come to prominence by Luca Turin, who suggested that inelastic electron tunneling is the method by which vibrations are detected by the olfactory receptors within the hose. This work is intended to convey to the reader an up-to-date account of the vibrational theory of olfaction, both the historical iterations as well as the present iteration. This text is designed to give a chronological account of both theoretical and experimental studies on the topic, while providing context, comments, and background where they were found to be needed.

Keywords: olfaction, biophyiscs, vibration detection, review literature as topic, GPCRs

OPEN ACCESS

Edited by:
Alkwin Slenczka,
University of Regensburg, Germany

Reviewed by:
Jens Riedel,
Bundesanstalt für Materialforschung und Prüfung (BAM), Germany
Luca Evangelisti,
Università di Bologna, Italy

***Correspondence:**
Ross D. Hoehn
rhoehn8701@gmail.com
Sabre Kais
kais@purdue.edu

Specialty section:
This article was submitted to Physical Chemistry and Chemical Physics, a section of the journal Frontiers in Physics

Received: *23 November 2017*
Accepted: *28 February 2018*
Published: *19 March 2018*

Citation:
Hoehn RD, Nichols DE, Neven H and Kais S (2018) Status of the Vibrational Theory of Olfaction. Front. Phys. 6:25. doi: 10.3389/fphy.2018.00025

1. INTRODUCTION

Olfaction is the oldest and most fundamental chemical sense by which lifeforms interpret their surroundings. This sense has always fascinated the sciences, delivering a great number of unique theories each divining the mechanism of this process. Richard Axel and Linda B. Buck published a landmark paper reporting their the discovery and cloning of the genetic code for several mammalian olfactory receptors (ORs) within a larger gene family [1]. Soon thereafter the first insect olfactory receptors were independently discovered by three research teams, all working on *Drosophila melanogaster* [2–4]. Olfaction within vertebrates and insects differs in the types of receptors used; in humans olfaction is performed via G-protein coupled receptors (GPCRs), whereas olfaction in insects primarily uses insect olfactory receptors (insect ORs). At present, the most accepted theory by which olfaction operates is based on the electrostatics and van der Waals surface of the odorant permitting binding to the receptor, after which the receptor undergoes a conformation change from its inactive state to its active state. The interplay between active and inactive conformations was validated as a likely description of activation in central nervous system (CNS) GPCRs through the analysis of the dynamics of the histidine and adenosine receptors [5–10].

Quantum effects in biology are a growing field of interest; this includes coherent energy transfer within photosynthetic bacteria proteins, mechanism of the avian magnetic compass and the possibility of inelastic electronic transfer (IET) occurring in olfactory receptors [11–15]. Considering the possible importance of quantum mechanics in biology, each suspected case of non-trivial quantum effects in biology should be examined skeptically [16]. Our intention in compiling this review is to present the vital findings and models used during the validation and examination of the contemporary Vibrational Theory of Olfaction (VTO), and to address an important question suggested by Barwich [17]: What, if anything, is so special about smell?

2. HISTORICAL VIBRATIONAL THEORIES

The present vibrational theory is an iteration in a historical movement within olfactory science to propose a relationship between molecular vibration and osmic properties. The proposition of vibrational modes controlling the osmic mechanism originates from the works of Malcolm Dyson [18, 19]. Coming off the contemporaneous development of Raman spectroscopy, Dyson believed that probing molecular vibrations of a molecule would elucidate correlations between these vibrations and the osmic properties of the odorant. The proposition was that the thermalized vibrations inherent to a molecule at a given (physiological) temperature would activate the receptor protein. Within his works he made it clear that the considerations of the vibrational components were independent of other properties necessary for odorant detections, such as the molecular volatility. Dyson continued to suggest that vibrational modes within the range of 1,400–3,500 cm^{-1} were responsible for the activation of olfactory receptor sites. Due to the contemporaneous nature of the application of Maxwell-Boltzmann statistics within his work, the ability of vibrational modes to be thermally excited at physiological temperatures was not addressed; a consideration later taken up by proponents of vibrational theories.

The VTO was revisited by Wright [20] who examined Dyson's model, noting that in higher energy regions vibrations correlate specifically with functional groups; therefore odor could equally be correlated to either vibrational frequency or functional groups. Additionally, the high energy ranges proposed by Dyson were found to have so small a population that it was unlikely that they could be responsible for a reliable olfactory sense. By considering this, Wright proposed that it was vibrations of $\sim$700 cm^{-1} or less that were responsible for any activation process. Additionally, Wright espoused that the modes below 700 cm^{-1} were both "more characteristic of the molecule as a whole" and less dependent on the particulars of specific functional groups. In a second work Lloyd [21] analyzed the low energy Raman spectral region of several almond odorants, finding that the collection of almond-odorants all possessed a similarly strong band within the 150–200 cm^{-1} range. They emphasized that the nose need not act as a Raman spectrographic device, but that the underlying molecular motion is detected through a mechanical—not spectroscopic—means by the receptor.

Contemporaneously, Amoore and Moncrieff independently published the basic concepts and arguments that formed a stereochemical/steric theory governing olfaction; an important theory whose aspects have remained with us to the present [22–26]. Later Wright and Michels completed a survey of 50 test odorants. First, using trained human subjects within two counter-ordered groups to place the odorants into one of nine training classes and then to use these data through a standard similarity matrix method to compare with the Raman spectra. Although the raw Raman data had a low correlation score, the rotationally oriented data (along several olfactory factors) were found to have a high significance factor, implying strong correlation [27].

Doolittle et al. completed a study of the olfactory responses of melon flies (*Bactrocera cucurbitae*) with deuterated variants of a known attractant. They concluded that there was no relationship between the low-energy infrared frequencies and the perceived effect on the behavior of the exposed melon flies [28, 29]. Blum et al. conducted a similar deuteration study with the Florida harvester ant (*Pogonomyrmex badius*). Ants were exposed to several ketones to determine which are capable of mimicking the natural alarm pheromone—4-mthyl-3-heptanone—and the successful candidates were then deuterated to test the VTO. They found no evidence supporting a molecular vibration related mechanism for olfaction. A brief report was published by Barker et al. [30] providing highly suggestive evidence that *Apis mellifera L.* are also incapable of discerning between deuterated variants of nitrobenzene. This paper prompted a response from Wright as the negative conclusion drawn did not include information concerning the infrared spectrum, explicitly lacking information concerning the low energy region. In 1977, Wright completed the basis of his—and several facets of the modern iteration VTO, asserting the feasibility of the theory within a biological context [31]. Subsequent studies were conducted on both the German and the American cockroaches with mixed results. Sugawara et al. [32] and Havens and Meloan [33] Hara contextualized his results as altered molecular motion—vis-á-vis Wright's theory—in his report finding that whitefish (*Coregonus clupeaformis*) are capable of discriminating between glycine and d_5-glycine in a behavioral study [34].

In 1978, Wright completed an information theory analysis that maintained the plausibility of the VTO in the context of a limiting number of receptor sites, and that the osmic spectrum could be feasibly detectable under his theory [35]. Wright attempted to justify the inclusion of his VTO within the context of enantiomeric osmic differences, by noting that the sterochemical aspect alone is insufficient to account for differences [36]. Eriksson et al. completed a study comparing the predictive nature of the contemporary olfactory theories on substituted pyridine and the perseverance of the pure pyridine odor; it was found that a particular out-of-plane collective vibration was present in all the osmically pyridine odorants. It was determined that vibrations were no more predictive than the molecular shape and space filling nature of the electron cloud; additionally, both examined properties were found to be necessary, but not essential properties [37]. Wright further attempted to provide a vibrational explanation for human perception of odor blending [38]. It was not long after these final works that it was clear that the VTO—as proposed by Wright—had no more predictive ability than considering facets of the odorant's structure alone [37, 39, 40].

3. REINCARNATION

A contemporary iteration of the VTO was introduced in an effort to generate a systematic approach to the olfactory process, as well as to forward better odorant classification, prediction, and molecular design [41, 42]. Here we will provide a brief description of aspects associated with the VTO as Turin presents it.

Beginning with the works of Dyson and Wright, Turin appends the general theory with a mechanism physically

capable of detecting vibrational modes feasibly within biological environments: IET. Many of the important early theoretical methods were devised by Lambe and Jaklevic [43], Kirtley et al. [44], Lambe and McCarthy [45], Khanna and Lambe [46], and Phillips and Adkins [47], while an excellent introductory overview of this spectroscopic method is available from Reed [48]. Speaking generally, this is a method capable of detecting the vibrational modes of a molecule. Importantly, as no light-matter interaction is involved, both IR and Raman active modes appear in IET spectra with roughly equal weight as no invocation of the dipole rule is required. Furthermore, this non-photon driven process would permit a larger range (0–4,000 cm^{-1}) of possible olfactory vibrations to be examined, rather than the highly truncated range (~0–500 cm^{-1}) attributable to a thermally driven process [40].

Specifically, within a laboratory environment, an analyte molecule is deposited upon a metal surface in close proximity to another metal surface, while a tunable electrostatic potential is generated across the insulating gap between the plates. This potential will drive electrons from one side of the gap to the other via evanescent tunneling. During the elastic tunneling processes, electrons are driven from the donor (D) to the acceptor (A) while obeying strict energy conservation; if this is the only process, the junction is Ohmic. This elastic process is shown in **Figure 1** as the red arrow; as electrons traversing the gap from the left (donor) are deposited in an energy level on the right (acceptor) with no change in energy. As we have deposited an analyte molecule on one surface, other processes may take place. The tunneling electron will be capable of donating a quantum of energy to the analyte before moving on to the acceptor; this process being termed first-order inelastic tunneling, shown as the green arrow within **Figure 1**. The electron leaves the donor energy level, and traverses the gap, falling into an energy level at the acceptor with less energy than initially, due to the electron having donated a quantum of energy to the "molecule" within the figure. Within the figure, the "molecule" is represented by a one-dimensional quantum harmonic oscillator, while in reality the molecule is comprised of anharmonic collective oscillations. Yet this distinction makes no difference in the physics as the important facets remain: the molecule retains the ability to resonantly absorb specific quanta of energy, absorption of off-resonant energy will result in emission, and highly local absorption/interaction can result in energy redistribution throughout the normal coordinates of a specific phase-consistent motion. Higher energy levels of a real molecule may undergo energetic shifts due to the incorporation of more anharmonic character, yet a system evolved to detect molecules in this fashion would likely (entirely hypothetically) have evolved with an "understanding" of the typical energy required to provide a quantum of energy to the molecule (on average) while it sits in a typical (most populated, average) vibrational energy distribution. Subsequently, the vibrational state population of the oscillator will increase from merely thermally activated (magenta shading) to a new distribution incorporating the additional excitation originating from the electron (green shading). This new pathway for electron transfer presents itself as a minute increase in the measured tunneling current across the gap: non-Ohmic behavior. These increases are typically small enough that plotting the second derivative of the IR curve with respect to V, $\frac{\delta^2 IR}{\delta V^2}$, is beneficial for their visualization. There are other processes involved, such as second-order elastic processes (where the electron donates and accepts quanta from the molecule), but such higher-order processes (not pictured in **Figure 1**) typically present diminishing contributions to the over-all current with an increase in order.

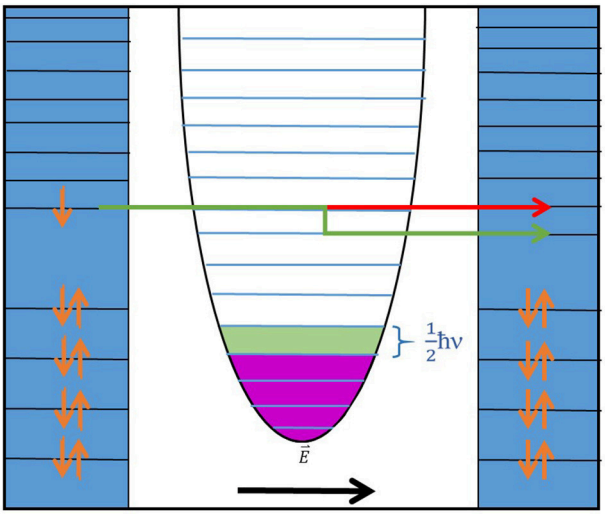

FIGURE 1 | A schematic representation of the electron-donor(left)-acceptor (right) system as is of concerning in IET. A full description is discussed within the main text.

Within the context of Turin's theory the odorant binding site of the OR acts as the tunneling junction. The electron donor and acceptor sites within the biological system have been suggested to be charged amino acid sidechains or, possibly, a redox ready metal. Odorants, in general, are not redox ready or charged; both of these traits would hinder the volatility of the odorant, detrimentally affecting the ability of the molecule to act as an odorant. As there is no continuum of unoccupied states within the likely biological acceptor, this biological tunneling gap is capable of electron transfer at a finite number of specific energy values; that carries two important implications: (1) The probability of a biological Ohmic junction is very low (and would be entirely undesirable for a spectroscopic junction, as non-Ohmic junctions would prevent constant misfiring of the receptor in the absence of an appropriately bound ligand). (2) Contrary to laboratory IET spectroscopy, the biological case is likely to be many single apparatuses (unique ORs) each operating at a single difference frequency. Also, the interaction between the electron and dipole is very close in proximity, thereby preventing the application of the dipole approximation, forcing one to employ the exact form of the interaction. This leads to an IETS intensity $\propto \sum_i x_i^2 q_i^2$, where x_i^2 and q_i^2 describe the displacement of the partial charge, q_i^2, along a single coordinate, x_i^2. This implies the sensitivity of the method to both partial charge and to displacement (from equilibrium position); it is for this reason

that the effects of large atom isotopic replacement would be smaller than that of hydrogen, as hydrogen displacements within normal mode coordinates are typically much larger.

Within the receptor environment, an electron will likely originate from an electron donor site—either the metal cofactor or an electron rich amino acid sidechain—and travel through or near the bound ligand to an electron acceptor site's energy level. Within Turin's original proposal, no concern was given to electron spin; this is likely due to his nearly direct application (and thereby close mirroring) of standard IETS theory, where electrons would originate from the electron sea of the donor and traverse toward a vacant conduction band at the acceptor. Under this situation, spin is able to be treated as an ergodic property in the system, as it lacks a dance partner. That stated, there is little present understanding of the exact (hypothetical) origin or destination of the ballistic electron; that is, there is no observation that the metal undergoes oxidation and no evidence of a charged side-chain (both suggested scenarios require a direct excitation as either oxidation or a charge side-chain would lose energy through donating its electron). Complicating the problem even further, Turin's proposal is an activation method for the protein, not a method of describing the totality of the events determining perception. This is more noteworthy as Turin's theory cannot describe any perireceptor events, aspects of intermolecular interactions during the docking of the ligand, nor consider any degree of complexity in the olfactory coding.

Finally, the standard laboratory procedure typically requires the IET spectroscopic junction to be cooled to cryogenic or near-cryogenic temperatures to reduce the effects of thermal broadening as the rotational states couple with the vibrations, or vibrations coupling with electronic states, where one performs IETS to activate electronic states. Thermal broadening cannot be eliminated in the biological environment, as the homeostatic temperature of the body (or near epidermal temperature for nasal olfactory receptors) is much higher than cryogenic temperatures. Yet, within the confines of the orthosteric binding site the ability of the ligand to freely rotate or translate is severely hindered, likely narrowing the Gaussian profile contribution for these motions. Competing with the aforementioned reduction, thermally active vibronic coupling between the ligand and protein environment will remain, and will increase the overall number of degrees of freedom. These effects were considered in a recent theoretical work to be discussed later [49].

The adaptation of the standard metal-electrode model mechanism of an IETS to an olfactory receptor is *ad hoc*; yet within his works, Turin provides a number of tertiary supporting facts. Foremost, electron transfer and tunneling mechanisms are prevalent throughout biological systems [50–53], whose early models were hypothesized by Marcus [54] and Siddarth and Marcus [55]. Secondly, he hypothesizes that there should be a redox-ready metal near the activation site to donate the electron necessary to the process. The possibility of a metal cofactor playing an important role in either binding or activation at GPCRs and other non-GPCR chemokine receptors is largely substantiated. It is known that divalent cations such as Mg(II) and Zn(II) are vital for both binding and the formation of activated complexes for opiate, MC1, MC4, and CXCR4 receptors [56–60]. Na^+ has been shown to allosterically modulate several GPCRs, including opiate and dopamine receptors via a specific binding site between helices 1, 2, and 7 [61]. Zn^0 nanopartiles, specific to oxidation and size, have been shown to enhance olfaction in rodents and canines [62–66] and have been shown to inhibit certain rodent ORs through competitive binding [67]; circumstantially, it should be noted that large concentrations of zinc have been found in specific areas of the brain [68–71]. Ionic copper has been shown to be vital for the robust activation of thiol-detecting olfactory receptors [72–74]. Ethylene hormone receptors of the *Arabidopsis* genus require a copper cofactor and specific mercury complexes have been known to inhibit the olfaction of *Heliothis virescens* [75, 76]. Finally, an extensive number studies (especially in rodents) have shown both the presence and the importance of metals/metal ions in olfaction [77–81].

4. EXPERIMENTS

The prior two decades have provided several experimental works concerning Turin's proposed mechanism. The works have taken place in vacillating waves of pro and con stances, and have utilized—for purpose of experimentation—both human and insect test subjects. We will now delineate these studies, addressing each article in chronological order of publication and illuminating the article both within the contest of the conflicting theories.

The earliest experimental work evaluating Turin's theory was performed by Haffenden et al. [82]. Those authors obtained several highly pure, commercially available labeled benzaldehydes; three isotope-substituted variants, as well as the natural abundance compound. Panelists were assigned to complete a series of three forced judgement, duo-trio tests [83, 84]. Unadjusted *P*-values suggested that the ^{13}C analogs were not discerned at statistically relevant rates, whereas the deuterated variant was. After further correcting the values for perceived sequence bias, it was found that after considering the 50% chance of guessing there existed a 47 $\pm$ 32% "actual true" detection rate of the deuterated compound, while neither ^{13}C-labeled compound was discernable. These findings were in line with the initial suggestions made by Turin that the difference in vibration-mode displacement of the carbon atoms is too small to perhaps be perceived, whereas deuteration causes a more appreciable response. Haffenden et al. argue that their findings—coupled with infrared spectrum studies—indicate that the 3,000–2,500 cm^{-1} range could play host to one of the bitter-almond bands. Although their finds provide some support for this region playing host to the cause of the bitter-almond scent, it should be further noted that this spectral region is characteristic of such a plethora of functional groups (including the saturated C-H, S-H, N-H salt, aldehyde and carboxylic acid stretching bands) that it is an entirely non-descript descriptor; especially, as any structural aspect (whichever in the list) causing this band would become the primary correlation between odorant and odor.

A series of experiments were conducted to test several claims put forth by Keller and Vosshall [85]. The first test examined the claim of odor blending originating from Wright [38]. The claim of odor blending appears twice in Turin's original paper [41], most notably the addition of guaiacol and ethylbenzaldehyde to replicate a vanilla note through the addition of spectral features. Keller and Voshall determined that at either of the concentrations presented of a 1:1 mixture of guaiacol:benzaldehyde panelists discerned no additional vanilla odor when compared to a respective concentration of either individual component. This is sensible as even under Turin's proposal, this was the least feasible assertion: that two molecules—which clearly would not occupy the same receptor—adding their individual spectra together (in uncorrelated and unrelated environments) to generate a third "ghost" odor, and without any foreknowledge of the structural olfactory code. Secondly, within Turin's original paper, it was claimed that for aldehydes of chain length C_8 through C_{12}, aldehydes with an even number of carbons are perceived to be fruity (citrusy) whereas those with an odd number of carbons are found to be floral (or waxy). Pairs of aldehydes—from a selection of unbranched aldehydes spanning butanal to dodecanal (L.B. Voshall, personal communication April 16-18, 2017)—with the same parity of carbons did not present with more dissimilar odors than those with different parity; in fact, the difference in perceived odor increased generally with an increase in carbon chain length. It should be noted that several of the aldehyde molecules examined by Keller and Vosshall fall outside the range of aldehyde chain lengths discussed in Turin's initial claim and thus may very well bias the statistics concerning the C_8-C_{10} range through out-of-scope sampling. Though, Turin himself likely determined the root cause of this odor difference, yet ascribed it to a IET-scattering mechanism rather than simple conformation space. It was found that the rotation of the aldehyde group was more hindered in the odd numbered chains; this fact would present any receptors able to encapsulate (in whole or par) the aldehyde to perceive a different free energy pathway toward the ground state of the complex, this additional hindrance to rotation (larger energy barrier to rotation) could negatively affect the receptor's ability to reach the active conformation. Finally, the claimed difference in odor between acetophenone and d_6-acetophenone was examined; the human panelists employed perceived no difference in odor between the compounds when they were presented via a triangle test. Secondary testing of those who perceived the odor differences returned statically average findings.

To test the VTO, Franco et al. [86]. employed several strains of (*Drosophila melanogaster*, which is commonly used in biological research. Untrained *Drosophila* were examined and found able to both recognize and react (attraction/aversion) to various levels of deuterated ACP during a simple T-maze test [87], and the aversion response roughly scaled with the level of deuteration. These flies were also trained to react to specific levels of deuterated vs. natural abundance species through application of negative electronic stimulus in a similar T-maze. A generalization experiment was also performed showing that *Drosophila* trained to avoid 1-octanol vs. d_{17}-1-octanol were able to generalize some characteristics and showed selective avoidance for ACP vs. d_5-ACP, thereby suggesting that there is a salient odor feature provided by deuteration that is generalizable across molecules. A group of mutated ansomic flies no longer displayed untrained avoidance of either d_8-ACP or d_{17}-1-octanol. The evidence provided by the anosmic flies is chiefly that the flies discerned these compounds through olfaction. The scaling of aversion response and trainability could likely have been due to (larger degrees of deuteration requiring) larger concentrations of a reactant/contaminant within the samples, where anosmic flies would detect neither the analyte nor any contaminant present.

Gane et al. [88, 89] examined the VTO through two tests employing both trained and untrained human subjects. Furthermore, great effort was expended to address the concern of impurities; assuring GC-level purities of all odorants, even those purchased at high purity. In a forced-choice same-difference test 5 panelists (3 perfumers, 2 untrained) were presented with GC purified, stored samples of commercially available 99% ACP and d_8-ACP. Agreement was reached with the findings of Keller and Vosshall [85]; explicitly, humans are not able to distinguish between these two isotopologues of ACP. The second test examined the human ability to discriminate deuterated variants of musk-class odorants, including: cyclopentadecanone, cyclopentadecanolide, 1,4-dioxa cyclohepta decane-5,17-dione, and 1-(3,5,5,6,8,8 - hexamethyl-6,7-dihydronaphthalen-2-yl) ethanone. This test was conceptualized by considering the larger ratio between carbons and hydrogens in the (typically saturated) musk compounds, and that this may generate a system where the possible isotopic characteristics may present the largest differences. Upon analysis of the data from 11 subjects, the *p*-values of the individual subjects ranged from 0.109 to $7.62 * 10^6$; the statistical chance of the aggregate trials (119 correct identifications during the aggregated 132 total trials) to have occurred accidentally was found to be $5.9 * 10^{-23}$. In brief, deuterated musk odorants were determined discernible from their non-deuterated counterparts by the study subjects. Gane et al. attribute the musk odor perception to be symptomatic of groups responsible for a strong absorption within the 1,380–1,550 cm^{-1} IR region. Yet a broader examination of the IR and Raman absorptions of musks, including popular nitro-musks, structurally similar non-musks, and recently examined silio-musks (see [90]), show no clean relationship between musk odor and any single spectral feature.

Gronenberg et al. examined the ability of the western honey bee (*Apis mellifera*) to discern between isotopomers [91]. Bees were tested with three chromatographically pure compounds ACP, BNZ, and OCT against their fully deuterated counterparts. Although the learning curve response was flatter than expected by the authors, it was clear that the bees were able to discriminate between these two related molecules. Discrimination testing over the deuterated and un-deuterated pairs revealed that the bees were able to differentiate between the two isotopomers; this effect was truly independent of whether the deuterated or natural analog was the "trained" stimulus. The authors did find it noteworthy that the deuterated odorants tended to confuse the bees more than the h-BNZ vs. h-ACP test—possibly alluding to a greater degree of difficulty in isotope discrimination compared to chemical discrimination. This confusion could also be a product

of unintended contamination of samples during the deuteration, minute amounts of solvent or reactant causing confusion as they present as accidentally introduced, untrained stimuli. A control experiment was also undertaken, generating mixtures (95:5) and pure samples of h-ACP and h-BZN. The addition of a minor component did not affect the bees' response compared to the pure training test. Gronenberg believes this shows that the bee's ability to respond to minor impurities within the samples is minimal. It should be noted that although the 95:5 mixture of h-ACP:h-BZN did not elicit a novel response, neither of the components were deuterated, and could have possibly lacked a systemic contaminant which elicited the trainable responses seen in the previous experiments.

Block et al. [92]—instead of providing another psychophysical experiment with either insects or humans—examined the theory at the receptor level [92]. Within the main paper, Block conducted three unique series of experiments: (i) Examination of receptor activation by isotopologues of Exaltone; (ii) Activation by isotopomers of acetopheonone and benzaldehyde; and (iii) Testing isotopomers of ten receptors and ten h/d ligand pairs. In the first series of experiments, a collection of 330 human ORs were screened with h-cyclopentadecanone (Exaltone, a musk odorant) and four deuterated variants (d_4, d_{24}, and d_{28}). A single OR, OR5AN1, was found to be a "bona fide" receptor for this musk. They reported no receptor responded to only one of the four compounds (a claim refuted by [93]), which would contest the possibility that different ORs respond to different isotopomers. EC_{50}'s and dose-response curves were found to be very similar for each of the 4 isotope-specific compounds. Secondly, Block and colleges tested acetophenone and benzaldehyde at various mouse ORs, and repeated this with isotopologues of these compounds. No significant differences were found between the activations of the receptors by the isotope-specific ligands. Finally, several ligands—most importantly MTMT and bis(methylthiomethyl) disulfide—were examined with their isotopomers. In none of the cases was a significant difference in activation found. MTMT and bis(methylthiomethyl) disulfide are known to require a copper cofactor in their overall activation scheme, most likely during binding; for this reason, Block et al. repeated the above series of tests while also introducing 30 μM of Cu^{+2}. Introduction of copper—to provoke a differential response due to increased cofactor concentration—provided no results divergent from the original conclusion.

Acknowledged by Block et al., differentiation of a pair of isotopomers does not necessarily prove an IET-esque mechanism of OR activation; nor does a collection of negative results absolutely disprove such a theory. (I speak here of proper evidence of absence, not absence of evidence!) A possible reason that previous behavioral studies (explicitly [41, 82]) that determined various abilities at discerning isotopologues—whereas the present study did not—are those events that occur before the activation of the receptor itself, perireceptor events. Three pertinent perireceptor events for behavioral studies conducted above would be (i) Enzymatic activity within the nasal mucosa converting chemical species or exchanging hydrogen [94, 95]. (ii) The action of odorant binding proteins within the nasal mucosa in transporting specific species through the hydrophobic environment. (iii) The ability of the nasal mucosa itself to act as a separatory media through differential diffusion or solubility [96, 97]. Alteration of protium to deuterium has other important effects on systems resembling the prescient solvated ligand-receptor system, e.g., isotopic alteration changes the zero point energy of the bond and will have an effect on intermolecular forces, for H/D this effect is manifest in hydrogen bonds. A possible IET-esque mechanism would be extremely sensitive to both geometry and orientation. The geometry of the bound ligand will differ greater from the gas phase geometry, affecting the vibrational modes. Also, orientation has been described to be so important in IETS that it is likened to a selection rule, and electron tunneling is known to be a very local process. We do not know the true crystal structure of an OR, it's ligand-bound structure, nor the possible donor or acceptor sites, thus we cannot possibly predict the appropriate IETS of any such system. It should also be noted that Block reported that d_4-muscone lacked activity in the IR region (1,380–1,550 cm^{-1}) that Gane et al. [88] had claimed should have an "intense" absorption to realize a musk odorant. One should recall that any electron tunneling mechanism would be evident in both Raman and IR spectra [44, 47], therefore solely examining the IR spectra will not elucidate the totality of possible vibrational modes.

To better address the conflicting accounts of odorant isotopologues sensitivity, two independent works revealed that insects can differentiate isotopologues of odorants. First, Paoli et al. [98] examined the local activity of specific odorants at the glomeruli of the honey bee. Four odorants (1-octanol, benzaldehyde, acetophenone, and isoamyl acetate) and a single deuterated variant of each (d_{17}, d_5, d_8, and d_3, respectively) were examined at 19 *Apis* glomeruli. Initially calcium flux was used to determine the activity of the glomeruli, and that was followed up by employing two-photon functional microscopy to assist in visualizing the local activity on the topography of the sensory organ. It was noted that several of the glomeruli displayed differential flux responses with respect to exposure to isotopologues of an odorant. When regional activity of the glomeruli were examined it was found that—although there was differential detection of isotopes—the ability of *Apis* to differentiate isotopologues is smaller than the ability to differentiate unique chemical species. Drimyli et al. [99] examined the ability of *drosophila* to differentiate isotopologues. Both behavioral (T-maze) and electroantennography (EAG) tests were conducted; the behavior tests were performed to corroborate that any differences found in the EAG were salient and perceived by the insects themselves. EAG revealed a differential response between deuterated and non-deuterated ligands. With forethought to possible criticisms and non-VTO explanations, Drimyli et al. conducted a preemptory discussion concerning purity, perireceptor events, and the extent to which size or number of deuteriums may affect the EAG. As there was no variation in the EAG rise times (the time at which a $^2/_3$'s maximal response was recorded [100]), Drimyli et al. argue that the effect of polarity difference between ^1H and ^2H has a minimal effect on the totality of perireceptor events [101], as well as the binding/activation steps. In a cross comparison of maximal

EAG response between each of the odorants, prodeutero-analogs and several non-prodeuterated versions it was found that the differential response to any deuteration was similar; implying that the detection ability is less sensitive to the extent of deuteration than the difference between deuterated and non-deuterated, implying that the insect detects deuterium or it does not. That does suggest—thought not conclusively—that the extent of isotopic exchange is unimportant, in opposition to the commentaries: [93, 102]. This dichotomy of detection also supports the hypothesis that the effect is caused by the presence of impurities, as unique impurities may likely be present in deuterated samples compared to the natural abundance sample.

Voshall [103] made two poignant observations: (1) Generally, psychological experiments are both poorly reproducible and have many (both obvious and obfuscating) variables that complicate the interpretation of results, and (2) The unlikelihood that a molecular-level mechanism could be clearly discerned through perception-based, *in vivo* psychological studies on humans. Therefore, the finding of humanity's ability to discern isotopologues of musk compounds is important; yet, it does not prove that an IET-esque mechanism—or any activation mechanism—is dependent on vibrations. Human subject examination—such as the Gane [88] or Haffenden [82] studies—are entirely *in vivo*; for this reason the examiner is provided no ability to attribute this isotope-sensitivity to events that occur in the nasal mucosa [94], with odorant binding proteins [104–106], at the antechamber of the receptor [10], during docking [107], or during activation itself.

Block et al. [92] provided an extensive discussion over their concerns about impurities in previous works, and various isotope effects within biology and the nasal passage. In a reexamination of an early experimental work, Turin determined that the ability of *D. melanogaster* to discriminate between acetophenone and d_5-acetophenone was very likely due to minute impurities within the commercially "pure" isotopologue samples; this finding does not invalidate the VTO, yet does remove one of the most important experimental findings in support of the theory, as well as calling into question several other studies where GC-levels of purity were not observed [108]. As an example, throughout Franco's experiments the deuterated compounds used were commercially available at highly pure levels (∼99%); this was done in reaction to one of the many counter-points to a previous experimental evaluation of the VTO. Though, commercially pure extremely minute concentrations of any impurity involved in the synthesis of either isotopomer—which could not be removed through the performed GC purification—would be present. In the light provided by the complexity provided by olfactory coding, the spatial mapping of olfactory lobes, the building of olfaction spaces and the developing picture of dynamic protein activation (coupling dynamics with VDW/ΔG/volume sensitive receptor and low reorganization energies), the question pertaining to the VTO which must be immediately addressed is: Is it needed?

5. THEORY

Before the present iteration of the VTO gained attention, Quantitative Structure-Activity Relations (QSARs) were developed to determine novel drug molecules from known batches of molecules and their known experimental activities by developing statistical relationships and machine learning algorithms to find correlation between particular protein activations by ligands and specific characteristics of those ligands. A particular descriptor used within QSAR is the EigenVAlue (EVA), developed at Shell Research Ltd., [109, 110] which attempts to correlate activities to vibrational eigenvalues as opposed to characteristics that more logically allude to binding (e.g., size, polarity, functional groups, hydrogen bond forming groups, etc.). An early implementation of the EVA descriptor to predict odor relationships was performed by Takane and Mitchell [111]. Within this work, 47 structurally diverse molecules were sampled and dendrograms were formed by considering the region of the IR spectra where each molecule possessed vibrational modes. They found that the EVA descriptor was an excellent zero-order approximation, and determined into which of 7 categories (ambergris, bitter almond, camphoraceous, jasmine, rose, mugeut, and musk) an odorant fits. The authors of this work note that although the vibrational frequencies of the molecules naturally placed the odorants into their appropriate categories, this was merely likely due to the vibrations reflecting structural aspects of the molecules; making the EVA a "once-removed" structural analysis tool. This conclusion is in direct relation to why Wright's theory originally failed (and the clear problem with the Haffenden et al. experimental conclusions); a common cause likely exists between the particularities of odorant perception and the existence of particular absorption bands, yet that does not mean the bands cause the perception.

The first attempt at building a model to determine the viability of Turin's VTO re-constructed a Marcus-type expression for the time-scales of electron transfer in a biological environment and determined parameter ranges reasonable to physiological conditions [112]. Within the context of the Marcus theory formulation, a Coulombic interaction was introduced between the tunneling electron and an introduced intermediate set of oscillating partial charges representing the odorant molecule. Important biological factors determined by Brookes et al. include: the Huang-Rhys factors, the importance of limiting D→A electron transfers in the absence of an odorant (likely due to either distance between D and A or a non-Ohmic junction), and the possibility that the electron/hole source may likely be a biological oxidizing agent. It was determined that the charge transfer rate was adequately feasible for use in neurological detection and signaling. Additionally, bounds for a reasonable reorganization energy were formulated by considering a hydrated system to display an upper bound (∼1eV) and resonance condition to define the lower bound. They determined that if the reorganization energy was only slightly larger than k_BT a large signal to noise ratio was obtainable. Brookes et al. conclude that the overall non-mechanical mechanism suggested by Turin was feasible within the system, and incorporate it as a possible mechanism in a general Swipe Card model of olfaction (where selective docking plays a role, but activation of the OR protein is based on a non-mechanical actuation) [113].

The question as to the relative rates between the elastic and inelastic processes with respect to both the donor-acceptor energy difference and the reorganization energies associated with real molecules was addressed by Solovyov [114]. They

devised a model Hamiltonian coupling the olfactory receptor and odorant via a harmonic approximation, simulated an environment through a collection of harmonic oscillators and a tunneling term built around the hopping integral. The odorant molecule was optimized and vibrational frequencies and IR activities were determined through a B3LYP-DFT approach. They approximate the electric field of the receptor to be equal to a Zn^{+2} dication at a distance of 15.4Å, as histidine and zinc ions have been previously discussed to be a probable acceptor/donor pair [41]. Several protio and dueterio variants of acetophenone, citronellyl nitrile, and octanol were examined; it was determined that energy regions of highly IR active vibrations were also parametric regions where there were large enhancements to the inelastic/elastic tunneling ratio; additionally, some less active modes were able to make contributions. Additionally, Solov'yov et al. propose a scenario by which deuterated analogs of similarly-sized (or functionalized) molecules may accidentally activate novel (non-endogenous, non-intended) receptors. The authors conclude that it is possible to determine molecules based on tunneling rate ratio enhancement because they correspond to characteristic vibrations under physiological conditions (as the analogous non-physiological statement has generally been known for decades).

Turin then provides several insights as to the molecular and physiological factors concerning his theory, and revises the underlying theory [115]. The insights concerning his theory are threefold: (1) The discriminatory factor of ORs on odorants cannot be merely electronic as isotopomers are detected (even only sometimes) as distinct odors. (2) The basis for discrimination cannot be mass alone, as a fully deuterated acetophenone differs only 3% from the protio isotopomer. (3) Under physiological conditions, the C-H/C-D modes do not drastically alter the heat capacity. A revision of the VTO is undertaken as it is argued that the standard IET spectroscopy theory is not valid because all orbitals within the biophysical system are localized; this lack of direct overlap requires some slight alteration in the theory. A new simulation model is developed based on a donor-bridge-acceptor model Hamiltonian. This new approach predicts the probable discrimination between acetophenone and d_8-acetophenone, while predicting that deuterated isotopomers of ethylene cannot be discriminated. The paper continues by presenting the results of a T-maze experiment testing and validating the predicted hypothesis concerning acetophenone and d_8-acetophenone, yet no evidence was provided to support the claims concerning ethylene.

A spin-boson model was developed to describe the importance of dissipation in electron transfer processes under a polar master equation by Chęcińska [116]. Within the model, the environment is again described by a collection of harmonic oscillators, the physical parameters being determined by physiological arguments similar to previous works [112, 114], and the odorant molecule is modeled as a single oscillator in an expandable manner. They determined that under resonant conditions reverse transfer (A→D) is a likely event without preventative mediation from the surrounding protein environment, likely in the form of reorganization. They also found that reduced dissipation limits the frequency detection and discrimination of the system. Operating under a similar model, Tirandaz et al. [117] examined the system's ability to discriminate enantiomers based on an asymmetric double well potential. They found that such a system was able to discriminate enantiomers based on the ratio of the tunneling frequency to the localization frequency, used as an overall measure of chiral interactions.

Block et al. [92] had previously made three claims to be answered by those supporting the VTO. These claims are: (1) The suggested mechanism by which electrons are delivered to the system is too unreliable to support such a vital system as olfaction. (2) Electron transfer mechanisms are highly sensitive to both bonding and average environmental fields that are not adequately considered in present models. (3) Assumptions concerning environmental fluctuations are not realistic. To answer claims 2 and 3, Solov'yov et al. determined acetophenone to be a viable odorant molecule to examine, selected based on experimental utility and docking into a homology model of an OR based on rhodopsin apoprotein [49]. The vibrational properties of the odorant were calculated under the influence of the OR while the newly perturbed Huang-Rhys factors were determined. Finally, alterations in binding due to post-ET reorganization are considered and comments on this are provided. Within the homology model, particular candidate amino acid residues—favorable to the binding of acetophenone—were selected as putative donor and acceptor sites; interestingly, methionine was selected as a possibly active residue as it was previously suggested to be involved in electron relays [118]. It was determined that the electron transfer has only a minor impact on the potential energy of the OR, and that the changes in vibrational character of the odorant will likely not affect electron transfer in the system. Furthermore, chemical fluctuations (including proton and methyl radical transfers) and dynamic fluctuations were considered and shown to have no appreciable impact on the average IR spectra of the odorant. Finally, it was reiterated that the reorganization energies of membrane proteins can be so low as to be negligible, e.g., a reorganization energy of 0.03 eV is observed for the photosynthetic protein of *Rhodobacter capulatus* at room temperature [119].

Apart from directly modeling the electrostatics and dynamics of the system, there have been several studies attempting to divine other testable aspects of the odorant-receptor system to validate/invalidate the VTO. A possible test for the VTO was designed based on the use of a ^{13}C isotope instead of the more commonly employed ^{2}H isotope [120]. Therein, it was suggested that committing a number of $^{12}C \rightarrow {}^{13}C$ exchanges to match the mass shift in a deuterated isotopomer of the same molecule you are capable of generating odorants with (roughly) the same molecule, differing vibrational spectra, and roughly the same Gibb's free energy. That allows one to probe the on/off rate of—let's say $^{13}C_8$-acetophenone and d_8-acetophenone—and determine whether any change in this quantity is due to a free energy difference or possibly due to a difference in vibrational spectra. It should be here noted that no perceived effect was seen in the behavioral study by Haffenden et al. that included ^{13}C isotopic exchange, possibly giving credence to the VTO within

the context of this test [82]. Additionally, Maia et al. completed MM/MD calculations to obtain geometries of 23 molecules (16 musks and the remainder being structurally similar to the musks, yet without musk odor character) and employed B3LYP-DFT calculations to obtain the vibrational spectra. Considering central frequency bands centered at intense peaks $\pm 200\,cm^{-1}$ at $700\,cm^{-1}$, $1{,}000\,cm^{-1}$, $1{,}500\,cm^{-1}$ and $1{,}750\,cm^{-1}$; it was determined that no single frequency or band could be responsible for the activation of a musk receptor (otherwise musks would not activate or non-musks would activate). The response was likely—if at all related—due to a collection of modes sitting roughly between 700 and $1{,}700\,cm^{-1}$; the authors further disputed Turin's assessment that a carbonyl stretch at 2,000–2,400 cm^{-1} was responsible for the musk odor because this band appears at 1,680–1,810 cm^{-1} in the present work and is not present in several of the studied musk odorants.

Saberi and Seyed-allaei [121] examined the molecular volume (considering both size and flexibility of the binding pocket, characteristics featured in other works, such as [122, 123]) and attempted to correlate it to olfactory sensitivity for the olfactory receptors of *D. melanogaster*. They cite neural measurements that allude to the use of a combinatorial coding in olfaction, yet wished to determine the vital discriminatory properties of the olfactory system. They, logically, assumed that any mismatch in the volume/receptor relationship will affect the physiological response. An initial assumption was that the total activity was a separable function of volume effects and all remaining considerations; where molecular volumes are determined by a Gaussian distribution built on tuning curves constructed by neural responses of individual neurons. It was thought that if all receptors had the same preference for molecular volume/flexibility, then changing the volume of an odorant would affect the intensity of odor and not the character. Molecular volume was found to be a factor, but not the sole one involved in olfactory discrimination; yet there did seem to be a non-linear volume dependence that may be capable of masking other factors involved in olfaction. This study was explicitly concerned with *D. melanogaster*, yet could be repeated for other species.

Finally, it is prescient to consider the more overt ways by which isotopic exchange may affect enzymatic processes. Krzan et al. [107] examined the effects of ^2H isotope exchange via saturation in deuterated media. They—of course—found contributions to the enzymatic rates and binding affinities due to the Ubbelohde effect as $^1H \rightarrow {}^2H$ exchange within the protein effects intramolecular bonds and thereby alters the energy balance between the active and inactive states of the protein. This is—the authors claim—the first attempt at examining isotopic effects within the context of the protein's atoms; yet there are decades of work examining the effects of isotopic specific endogenous and synthetic ligands. Within these previous studies the binding isotope effect, alterations in zero-point energy, and changes in vibrations effecting hydrogen bonding have all been discussed [124–126].

Recently, Tirandaz et al. [127] reexamined their chiral-odorant polaron Hamiltonian model—expanding it to determine a non-planar vibrational state—and determined several aspects of the model that could provide new tests of the vibrational theory, while also displaying the versatility of a system behaving within the model. Therein they constructed a rate expression describing the IET frequency based on an odorant capable of undergoing a tunneling interconversion between two chiral states, similar to the classical ammonia tunneling problem. Using this model, the authors determined a lower thermal limit to the possible detection of an odorant within the VTO context, and limiting relationships and trends with respect to odorant concentration (thermodynamic pressure) and isotopic mass substitutions. Importantly, they determined that the substitution of higher isotopic masses increases the system's sensitivity under the VTO. Finally, though very narrowly, they find that the VTO is capable of chiral recognition under biological conditions. In a series of papers, Kraft et al. examined—through both *in vivo* calcium ion imagining and computational methods—the validity of the "shape-based" theory of olfaction by examining the response to several Group 14-for-carbon substitution of the t-butyl functional group in the lilal and Bourgeonal odorants [128–130]. As these authors state, the benefit of this substitution series is that it maintains the molecular geometry while increasing the hydrophobic bulk of the molecule. Within the series of papers, their focus was to examine the molecular mechanism responsible for odor detection and perception through a three pronged approach: (1) conduct *in vivo* detection threshold experiments, (2) *in vitro* calcium ion imaging of activation, and (3) computational support. They determined that the human OR17-4 receptor was activated—and likely solely activated—by the odorants above through both structure-odor-relationships and *in vivo* analysis. Afterward, a homology model was constructed for the receptor based on the rhodopsin protein and docking simulations of the various substituted odorants were made, noting their change in free energy. They then compared the requirements for breaking of the disulfide bond, which binds the intracellular G-protein to the transmembrane GPCR. They take that the energy required to directly break the disulfide bond to be a bound for the energy harvested from the vibrational quantum; using this bound they find that the energy ranges defined by these criteria do not match the activation patterns seen in their (both *in vivo* and *in vintro*) works. The free energy changes seen in the docking calculations with respect to the increasing hydrophobic bulk do match those results. It was finally determined that olfaction was largely based on van der Waals (VDW) surface and electrostatic surface properties, finding no evidence that the VTO played any role in olfaction [130].

6. GCPR/EVOLUTION-BIOLOGICAL-GENETIC

Dating back to the unicellular stages of evolution, chemoreception was the earliest form of communication between cells and their environments (including other cells) [131]. Similar chemoreception systems solve similar problems between those early unicellular life forms and the individual cells of today's multicellular life. It should not be surprising

that many metazoan signaling systems are constructed from components already found in their unicellular ancestors [132], while other systems were coopted entirely from pre-existent systems [133–135]. Note that in the case of GPCRs, the unicellular precursors of metazoans already possessed most of the cytoplasmic components of GPCRs, including all of the G_α subunits. Nature seemed to grab the right (or closest-to-right) tool for a job and set it to a new task.

One of these novel receptor classes developed by metazoans was the GPCR system, where most GPCRs families have their ancient origins in the last common eukaryotic ancestor [136]. Generally speaking, GPCRs' transmembrane signaling proteins are comprised of seven helical domains crossing from the extra- to the intra- cellular environments. Each receptor possesses a ligand binding pocket near the extraceullular surface and an intracellular heterotrimeric G-protein complex, which dissociates after the GPCR is activated. Members of the family mediate extracellular chemical signals and share homologous structure [137]. Speaking generally once more, GPCRs are divided into 5 major categories by the most used classification system: Glutamate, Rhodopsin, Adhesion, Secretin, and Frizzled. Although this system is designed specifically for GPCRs, it has been suggested to extend a similar system to include non-GPCRs, including insect ORs [138].

GPCRs populate batteries of receptors in the mammalian olfactory system (including: ORs, vomeronasal receptors, olfactory TAAR, Formyl peptide receptors, GC-D receptors) and neurotransmitter receptors (NRs) in many species, e.g., vertebrates and terrestrial varieties of both *Nemertea* and *Annelida*, use GPCRs as ORs [139, 140]. At a fundamental system level these jobs are similar, as both accept a chemical species traveling through space to interact with a binding protein whose signal is eventually detected by an ionotropic receptor (IR) after having undergone several intermediate processes [141]. NRs typically have lower sensitivity (nano- to mili- molar range) and deal with a smaller, controlled number of chemical compounds, many of which are highly specific ligand/receptor relationships [141]. By contrast, in olfaction, individual odorants activate subsets of receptors instead of single receptors and activation/inhibition/antagonism all play a role and possibly generate temporal dynamics that are important to the overall odorant code and possibly novel odorant perceptions [142]. Slight changes in either structure or concentration of an odorant are capable of affecting the activation pattern, leading to a different odorant code [139]. This odorant code permits mammals, including humans, to perceive a larger variety of odors than ORs expressed, as humans are capable of perceiving over 10,000 odorants with a trillion being an extremely liberal estimate under contention [131, 143–145].

The architecture of terrestrial vertebrate olfactory systems is fairly conserved. Air is up-taken through a stereo arrangement of nostrils, an arrangement important to odor tracking. This air, laden with odorant molecules, passes along the epidermis of the nasal cavity where receptor lined neurons project into the cavity; each olfactory receptor neuron (ORN) expresses one receptor type [139]. Within this span of receptors and neurons, some pairs are considered generalists (those that are typically involved in the activation of odors) and some pairs are specialists (those involved in the detection of pheromones) [139]. After the receptor is activated, it's neuron conducts the signal to a glomerulus, an organ that acts as a encoding pre-process site before the signal reaches the olfactory lobe of the brain [146–148].

Similar to the terrestrial vertebrate system, the overall system-level olfactory procedure is well conserved in insects. Air passes through a porous cuticular wall—typically along the antennae—where the sensillium contains dendrites for ∼5 ORNs. The axons of these ORNs project into glomeruli within the antennal lobes of the insect brain. This physical pathway is utilized by neurons transferring mechanosensory, thermosensory, hygrosensory, and gustatory information as well [141, 149]. The zonal organization of the glomeruli is not precisely understood [149], but important electrophysiological studies are being done to understand these patterns and to build representations of odorant spaces [4, 98, 99, 150]. Importantly, these glomeruli patterns show similarity between individuals within a species [151]. Generally, different ORNs respond to different odors, and these responses are varied in type (excitatory or inhibitory) and dynamics [149]. The importance of this glomeruli pattern-based code is supported by cisgenic monoexpression of an OR in its non-wildtype neuron, which changes the overall innate behavioral response to an odorant [152].

Insect olfaction utilizes three types of chemosensory protein (CSP) receptors: insect ORs, IRs, and gustatory receptors (GRs) [139, 141]. An insect OR is a transmembrane protein of roughly 44 kilodaltons showing no homology to GPCRs, yet having similar topologies and functionalities. Of note, insect ORs possess inverted topology to GPCRs, as they have an extracellular C-terminus and an intracellular N-terminus [153, 154]. It is generally suggested that insect ORs act as ligand-gated ion channels [155], yet may also—through odorant sensing complexes—activate a G-protein pathway [156]. This dual channel mechanism is capable of providing both a rapid (ionotropic) and sensitive (metabotropic) detector [156]. This dual channel construction comes from a heteromultimer composition of one ligand-specific receptor acting as a ligand-gated ion channel coupled with a (highly conserved) ORco-type receptor [141, 157]. Whereas most ORs vary widely in sequence [158, 159], the ORco receptors show good sequence identity; these coreceptors have been identified in *Lepidoptera*, *Diptera*, *Coleopteran*, *Hymenoptera*, *Hemipteran* and *Orthopteran* [154, 157].

Insects typically express two types of olfactory protein on a single ORN (or sometimes four IRs, see [139]); this is different from their vertebrate counterparts. It is vital to note that the secondary protein expressed on the ORN is typically the ORco receptor for that species; this is to say, an ORN contains a single OR and the species' ORco [151, 158]. As ORs very widely in their sequence identity—suggesting that species developed their present repertoire of ORs individually—the ORco receptors show amazing similarity across species [151, 158]; a study of several species have shown a 65-87% sequence similarity for their ORco analogs, including: *D. Melanogaster*, *A. Gambaie*, *H. Zea*, and *C. Captitata* [158]. It has been thought that the expression of multiple olfactory proteins per ORN was an adaptation to

expand the number of odorants perceived while maintaining a low number of neurons and ORs [151]; it is more likely that the glomeruli pattern holds the sensory diversity, and the OR-ORco pairing is designed to exploit multiple signaling pathways. That is evidenced by the fact that OR83b (the ORco analog of *D. Melanogaster*) is not directly involved in odorant recognition [139]. Suppression of the expression of the ORco analog has been shown to deplete the overall activity of the olfactory system [158, 160]. Additionally, these ORco analogs are capable of fulfilling the role of their interspecies counterparts; an anosmic mutant *D. Melanogaster*—without expressed OR83b—regains its electrophysiological response to odorant stimuli when transgenic Or83b orthologs were inserted and expressed in the fly's ORN [158].

7. FUTURE OUTLOOK/CONTEXTUALIZATION

Some studies have attempted to relate the vibrational theory to GCPRs within the CNS. Oh et al. [161] have completed studies attempting to find relationships between the molecular vibrations and activity of compounds at the histamine and adenosine receptors. A selection of several agonists for the candidate receptor were optimized at the BLYP-DFT level of theory and their molecular vibration frequencies were calculated. Analysis within a Corralled Intensity of Molecular Vibrational Frequency (CIMVF) framework suggested that the 0–5,000 cm^{-1} energy range of molecular vibrations is divided into 1,000 partitions of 5 cm^{-1}, and the value of each partition is the sum of the intensities within the partition. Upon completing a hierarchical clustering of the CIMFV data, it was determined that this method above others was capable of clustering the agonists of both the histidine and adenosine receptors within a tree. Dendrographic analysis of ligand activity correlated with vibrational frequencies [161–163]. Oh does not attribute that directly to the mechanism by which these CNS GPCRs are activated, yet describes it as a possible useful tool in divining novel ligands for these receptors.

In a similar vein to the discussion of Barwich [17], Hoehn et al. attempted to expand Turin's IET-based VTO by applying it to predict possible effects of deuterated ligands for non-olfactory GPCRs in the CNS [164]. They initially examined several well-known psychedelic 5-HT receptor agonists and algorithmically determined shared spectral features that could be responsible for their collective activation properties through a spectral indexing method. This putative active peak was similar in frequency to those previously reported for the histamine and adenosine receptors [161–163]; that is not entirely unreasonable as a steric/docking consideration providing additional discriminatory facilities to the receptor, as it is known that receptors interact with several ligands and a ligand is capable of interacting with several receptors [165]. After ascertaining a putative peak, their focus shifted to validation by comparing the peak volume—proportional to the tunneling probability associated with this vibrational mode—to the activities of known ligands at the receptors. The selected ligands were DOX and 2C-X (X = Br, I, trifluoromethyl, and an ethyl silyl ether). The tunneling probability did roughly scale with the efficacies of the selected substances. Based on these findings, the relative efficacies of several deuterated analogs of the LSD molecule were predicted and proposed as a test of the vibrational theory for general GPCRs. In a follow-up paper, the authors performed the prescribed test on DAM-57, a less legally controlled variant of the LSD molecule [166]. The findings conclusively showed that the predicted pattern of efficacy for isotopologues of DAM-57 did not match the experimental findings. Thus the VTO is unlikely to participate in non-olfactory GPCRs; and as the lineage of GPCR maintains many similarities in both form and function, it makes it unlikely that the VTO participates in olfaction, as well.

A great deal of recent work has been directed toward determining the nature and the cipher of the odorant olfactory code [167, 168]. Olfactory lobe maps have begun to be made for both insect [169–172] and vertebrate species [146, 147, 173, 174]. The coding has proven to be sufficiently complex as to have evaded deciphering and provides an ample enough vector space to encode all perceivable odors [143, 144, 175]. It was suggested, though likely hyperbolic, that the total number of individual odors perceivable by the human olfactory system was upwards of 1 trillion [143], but that has been contested [144, 145]. The dimensionality of the odorant space has been examined to determine the minimal number of relevant olfactory classes for characterization [145, 176, 177]. Recent evidence has also shown—through inserted electrical probes in live mice—that the encoding of the olfactory lobe appears in the piriform cortex and posterolateral cortical amygdala, brain regions responsible for olfactory learning and innate behavioral response to odorants [178]. Interestingly, it was recently determined through exploring the perception of multi-component odorant mixtures that these mixtures are better understood as unique vectors within odor space than as averages between the two component odorant vectors [168]; this possibly explains early claims of odorant mixing in the vibrational theories of Wright and Turin [38, 41, 85]. As the complexity inherent in understanding structure-odor relationships led to the VTO, it should be noted that the unexplored complexity associated with olfactory coding may justify the lack of a simple structure-odor relationship and remove the impetus behind the VTO.

The topic of artificial olfaction is growing and has been adopting the more useful aspects of the discussion of organic olfaction, such as coding, metalloprotein-based detection and IETS [142, 179–182]. It is worth stating that even if all of this work does nothing to describe the biophysical and physiological process of olfaction, we are inadvertently proposing novel methods and tools for the development of artificial olfaction. Herein alone, electron transfer mechanics have been shown to be a possible means of artificial olfaction, while multiple sensors can provide a level of detection sensitivity and versatility that single detectors cannot. In general, many articles pertaining to the VTO have appeared within highly ranked journals; it is apparent that this conflict in vision—a conflict that neither side may win in the end—is one that the greater community would like to see resolved. Such a resolution will require far better communication between disciplines and a far more fair discussion between the entrenched camps on both sides of the debate.

AUTHOR CONTRIBUTIONS

All authors conducted background research for this article. RH completed most of the writing, while other authors heavily edited the text.

ACKNOWLEDGMENTS

The authors would like to thank Dr. Shuhao Yeh both for constructive discussions and for his critical readings of the contiguously evolving drafts of this review.

REFERENCES

1. Buck L, Axel R. A novel multigene family may encode odorant receptors: a molecular basis for odor recognition. Cell (1991) **65**:175–87. doi: 10.1016/0092-8674(91)90418-X
2. Clyne PJ, Warr CG, Freeman MR, Lessing D, Kim J, Carlson JR. A novel family of divergent seven-transmembrane proteins: candidate odorant receptors in Drosophila. *Neuron* (1999) **22**:327–38. doi: 10.1016/S0896-6273(00)81093-4
3. Gao Q, Chess A. Identification of candidate drosophila olfactory receptors from genomic DNA sequence. *Genomics* (1999) **60**:31–39. doi: 10.1006/geno.1999.5894
4. Vosshall LB, Amrein H, Morozov PS, Rzhetsky A, Axel R. A spatial map of olfactory receptor expression in the Drosophila antenna. *Cell* (1999) **96**:725–36. doi: 10.1016/S0092-8674(00)80582-6
5. Rosenbaum DM, Cherezov V, Hanson MA, Rasmussen SGF, Thian FS, Kobilka TS, et al. GPCR engineering yields high-resolution structural insights into 2 adrenergic receptor function. *Science* (2007) **318**:1266–73. doi: 10.1126/science.1150609
6. Manglik A, Kim TH, Masureel M, Altenbach C, Yang Z, Hilger D, et al. Structural insights into the dynamic process of β^2-adrenergic receptor signaling. *Cell* (2015) **161**:1101–11. doi: 10.1016/j.cell.2015.04.043
7. Sounier R, Mas C, Steyaert J, Laeremans T, Manglik A, Huang W, et al. Propagation of conformational changes during *Mu*-opioid receptor activation. *Nature* (2015) **524**:375–8. doi: 10.1038/nature14680
8. Huang W, Manglik A, Venkatakrishnan AJ, Laeremans T, Feinberg EN, Sanborn AL, et al. Structural insights into *Mu*-opioid receptor activation. *Nature* (2015) **524**:315–21. doi: 10.1038/nature14886
9. Nygaard R, Zou Y, Dror RO, Mildorf TJ, Arlow DH, Manglik A, et al. The dynamic process of β^2-adrenergic receptor activation. *Cell* (2013) **152**:532–42. doi: 10.1016/j.cell.2013.01.008
10. Dror RO, Pan AC, Arlow DH, Borhani DW, Maragakis P, Shan Y, et al. Pathway and mechanism of drug binding to G-protein-coupled receptors. *Proc Natal Acad Sci USA* (2011) **108**:13118–23. doi: 10.1073/pnas.1104614108
11. Davies PCW. Does quantum mechanics play a non-trivial role in life? *Biosystems* (2004) **78**:69–79. doi: 10.1016/j.biosystems.2004.07.001
12. Lloyd S. Quantum coherence in biological systems. *J Phys.* (2011) **302**:012037. doi: 10.1088/1742-6596/302/1/012037
13. Fleming GR, Scholes GD, Cheng YC. Quantum effects in biology. *Proc Chem.* (2011) **3**:38–57. doi: 10.1016/j.proche.2011.08.011
14. Lambert N, Chen YN, Cheng YC, Li CM, Chen GY, Nori F. Quantum biology. *Nat Phys.* (2013) **9**:10–8. doi: 10.1038/nphys2474
15. Brookes JC. Quantum effects in biology: golden rule in enzymes, olfaction, photosynthesis and magnetodetection. *Proc R Soc Lond A Math Phys Eng Sci.* (2017) **473**:20160822. doi: 10.1098/rspa.2016.0822
16. Wiseman H, Eisert J. *Nontrivial Quantum Effects in Biology: A Skeptical Physicists' View. 1st Edn.* Singapore: World Scientific Publishing CO. (2012).
17. Barwich AS. What is so special about smell? Olfaction as a model system in neurobiology. *Postgrad Med J.* (2015) **92**:27–33. doi: 10.1136/postgradmedj-2015-133249
18. Malcolm Dyson G. Raman effect and the concept of odour. *Perfum Essent Oil Rec.* (1937) **28**:13–9.
19. Malcolm Dyson G. The scientific basis of odour. *J Soc Chem Indust.* (1938) **57**:647–51. doi: 10.1002/jctb.5000572802
20. Wright RH. Odour and molecular vibration. I. Quantum and thermodynamic considerations. *J Appl Chem.* (1954) **4**:611–5. doi: 10.1002/jctb.5010041104
21. Wright RH, Serenius RSE. Odour and molecular vibration. II. Raman spectra of substances with the nitrobenzene odour. *J Appl Chem.* (1954) **4**:615–21. doi: 10.1002/jctb.5010041105
22. Amoore JE. Stereochemical specificities of human olfactory receptors. *Perfum Essent Oil Rec.* (1952) **43**:321–3.
23. Amoore JE. Stereochemical theory of olfaction. *Nature* (1963) **198**:271–2. doi: 10.1038/198271a0
24. Amoore JE. Current status of the steric theory of odor. *Ann NY Acad Sci.* (1964) **116**:457–76. doi: 10.1111/j.1749-6632.1964.tb45075.x
25. Moncrieff RW. The characterization of odours. *J Physiol.* (1954) **125**:453–65. doi: 10.1113/jphysiol.1954.sp005172
26. Moncrieff RW. The odorants. *Ann NY Acad Sci.* (1954) **58**:73–82. doi: 10.1111/j.1749-6632.1954.tb54846.x
27. Wright RH, Michels KM. Evaluation of far infrared relations to odor by a standards similarity method*. *Ann NY Acad Sci.* (1964) **116**:535–51. doi: 10.1111/j.1749-6632.1964.tb45083.x
28. Doolittle RE, Beroza M, Keiser I, Schneider EL. Deuteration of the melon fly attractant, cue-lure, and its effect on olfactory response and infra-red absorption. *J Insect Physiol.* (1968) **14**:1697–712. doi: 10.1016/0022-1910(68)90202-3
29. Blum MS, Doolittle RE, Beroza M. Alarm pheromones: utilization in evaluation of olfactory theories. *J Insect Physiol.* (1971) **17**:2351–2361. doi: 10.1016/0022-1910(71)90083-7
30. Barker RJ, Berdel RL, Waller GD. The molecular basis for scent discrimination: response to nitrobenzene-d5 of honey bees (*Apis mellifera* L.) conditioned with nitrobenzene. *Experientia* (1973) **29**:418–9. doi: 10.1007/BF01926754
31. Wright RH. Odor and molecular vibration: neural coding of olfactory information. *J Theor Biol.* (1977) **64**:473–502. doi: 10.1016/0022-5193(77)90283-1
32. Sugawara R, Tominaga Y, Iida Y. A deuterium effect in insect attraction. *Agricult Biol Chem.* (1978) **42**:1289–90.
33. Havens BR, Meloan CE. The application of deuterated sex pheromone mimics of the american cockroach (*Periplaneta americana*, L.), to the study of wright's vibrational theory of olfaction. In: Charalambous G, editor. *Food Flavors: Generation, Analysis and Process InfluenceProceedings of the 8th International Flavor Conference. vol. 37 of Developments in Food Science*. New York, NY: Elsevier (1995). p. 497–524.
34. Hara J. Olfactory discrimination between glycine and deuterated glycine by fish. *Experientia* (1977) **33**:618–9. doi: 10.1007/BF01946534
35. Wright RH. The perception of odor intensity: physics or psychophysics? *Chem Sens.* (1978) **3**:73–9. doi: 10.1093/chemse/3.1.73
36. Wright RH. Odor and molecular vibration: optical isomers. *Chem Sens.* (1978) **3**:35–7. doi: 10.1093/chemse/3.1.35
37. Eriksson A, Lindner P, Mrtensson O. Molecular properties and odour. Effects of substituents on pyridine and pyridine odour. *J Theor Biol.* (1981) **90**:477–86. doi: 10.1016/0022-5193(81)90300-3
38. Wright RH. Molecular vibration and odour blending. *Chem Sens.* (1983) **8**:103–6. doi: 10.1093/chemse/8.1.103
39. Pfaffmann C. Taste and smell. *Annu Rev Psychol.* (1956) **7**:391–408. doi: 10.1146/annurev.ps.07.020156.002135
40. Klopping HL. Olfactory theories and the odors of small molecules. *J Agricult Food Chem.* (1971) **19**:999–1004. doi: 10.1021/jf60177a002

41. Turin L. A spectroscopic mechanism for primary olfactory reception. *Chem Sens*. (1996) **21**:773–91. doi: 10.1093/chemse/21.6.773
42. Turin L. A method for the calculation of odor character from molecular structure. *J Theor Biol*. (2002) **216**:367–85. doi: 10.1006/jtbi.2001.2504
43. Lambe J, Jaklevic RC. Molecular vibration spectra by inelastic electron tunneling. *Phys Rev*. (1968) **165**:821–32. doi: 10.1103/PhysRev.165.821
44. Kirtley J, Scalapino DJ, Hansma PK. Theory of vibrational mode intensities in inelastic electron tunneling spectroscopy. *Phys Rev B* (1976) **14**:3177–84. doi: 10.1103/PhysRevB.14.3177
45. Lambe J, McCarthy SL. Light emission from inelastic electron tunneling. *Phys Rev Lett*. (1976) **37**:923–5. doi: 10.1103/PhysRevLett.37.923
46. Khanna SK, Lambe J. Inelastic electron tunneling spectroscopy. *Science* (1983) **220**:1345–51. doi: 10.1126/science.220.4604.1345
47. Phillips WA, Adkins CJ. A theory for the intensities of inelastic electron-tunnelling spectra. *Philos Mag B* (1985) **52**:739–50. doi: 10.1080/13642818508240633
48. Reed MA. Inelastic electron tunneling spectroscopy. *Mater Today* (2008) **11**:46–50. doi: 10.1016/S1369-7021(08)70238-4
49. Reese A, List NH, Kongsted J, Solovyov IA. How far does a receptor influence vibrational properties of an odorant? *PLoS ONE* (2016) **11**:e0152345. doi: 10.1371/journal.pone.0152345
50. Farid RS, Moser CC, Dutton PL. Electron transfer in proteins. *Curr Opin Struct Biol*. (1993) **3**:225–33. doi: 10.1016/S0959-440X(05)80157-5
51. Ichiye T. Electron transfer through proteins: overview. In: Roberts GCK, editor *Encyclopedia of Biophysics*. Berlin; Heidelberg: Springer-Verlag (2013). p. 614–21.
52. Beratan DN, and Skourtis SS. Electron transfer through proteins. In Roberts GCK, editor *Encyclopedia of Biophysics*. Berlin; Heidelberg: Springer-Verlag (2013). p. 625–30. doi: 10.1007/978-3-642-16712-6_13
53. Saen-Oon S, Lucas MF, Guallar V. Electron transfer in proteins: theory, applications and future perspectives. *Phys Chem Chem Phys*. (2013) **15**:15271–85. doi: 10.1039/c3cp50484k
54. Marcus RA. Electron transfer reactions in chemistry: theory and experiment (nobel lecture). *Angew Chem Int Edn English*. (1993) **32**:1111–21. doi: 10.1002/anie.199311113
55. Siddarth P, Marcus RA. Correlation between theory and experiment in electron-transfer reactions in proteins: electronic couplings in modified cytochrome c and myoglobin derivatives. *J Phys Chem*. (1993) **97**:13078–82. doi: 10.1021/j100152a008
56. Ananthanarayanan VS, Kerman A. Role of metal ions in ligand receptor interaction: insights from structural studies. *Mol Cell Endocrinol*. (2006) **246**:53–9. doi: 10.1016/j.mce.2005.11.023
57. Kinouchi K, Standifer KM, Pasternak GW. Modulation of μ1, 2, and opioid binding by divalent cations. *Biochem Pharmacol*. (1990) **40**:382–4. doi: 10.1016/0006-2952(90)90704-O
58. Standifer KM, Clark JA, Pasternak GW. Modulation of Mu1 opioid binding by magnesium: evidence for multiple receptor conformations. *J Pharmacol Exp Therapeut*. (1993) **266**:106–13.
59. Holst B, Elling CE, Schwartz TW. Metal ion-mediated agonism and agonist enhancement in melanocortin MC1 and MC4 receptors. *J Biol Chem*. (2002) **277**:47662–670. doi: 10.1074/jbc.M202103200
60. Gerlach LO, Jakobsen JS, Jensen KP, Rosenkilde MR, Skerlj RT, Ryde U, et al. Metal ion enhanced binding of AMD3100 to Asp262 in the CXCR4 receptor. *Biochemistry* (2003) **42**:710–7. doi: 10.1021/bi0264770
61. Wang S, Wacker D, Levit A, Che T, Betz RM, McCorvy JD, et al. D4 dopamine receptor high-resolution structures enable the discovery of selective agonists. *Science* (2017) **358**:381–6. doi: 10.1126/science.aan5468
62. Viswaprakash N, Dennis JC, Globa L, Pustovyy O, Josephson EM, Kanju P, et al. Enhancement of odorant-induced responses in olfactory receptor neurons by Zinc nanoparticles. *Chem Sens*. (2009) **34**:547. doi: 10.1093/chemse/bjp031
63. Vodyanoy V. Zinc nanoparticles interact with olfactory receptor neurons. *BioMetals* (2010) **23**:1097. doi: 10.1007/s10534-010-9355-8
64. Moore CH, Pustovyy O, Dennis JC, Moore T, Morrison EE, Vodyanoy VJ. Olfactory responses to explosives associated odorants are enhanced by zinc nanoparticles. *Talanta* (2012) **88**:730–3. doi: 10.1016/j.talanta.2011.11.024
65. Hagerty S, Daniels Y, Singletary M, Pustovyy O, Globa L, MacCrehan WA, et al. After oxidation, zinc nanoparticles lose their ability to enhance responses to odorants. *BioMetals* (2016) **29**:1005–18. doi: 10.1007/s10534-016-9972-y
66. Jia H, Pustovyy OM, Wang Y, Waggoner P, Beyers RJ, Schumacher J, et al. Enhancement of odor-induced activity in the canine brain by zinc nanoparticles: a functional MRI study in fully unrestrained conscious dogs. *Chem Sens*. (2016) **41**:53. doi: 10.1093/chemse/bjv054
67. Seebungkert B, Lynch JW. A common inhibitory binding site for zinc and odorants at the voltage-gated K^+ channel of rat olfactory receptor neurons. *Eur J Neurosci*. (2001) **14**:353–62. doi: 10.1046/j.0953-816x.2001.01646.x
68. Horning MS, Trombley PQ. Zinc and copper influence excitability of rat olfactory bulb neurons by multiple mechanisms. *J Neurophysiol*. (2001) **86**:1652–60. doi: 10.1152/jn.2001.86.4.1652
69. Takeda A. Zinc homeostasis and functions of zinc in the brain. *Biometals* (2001) **14**:343–51. doi: 10.1023/A:1012982123386
70. Persson E, Henriksson J, Tallkvist J, Rouleau C, Tjlve H. Transport and subcellular distribution of intranasally administered zinc in the olfactory system of rats and pikes. *Toxicology* (2003) **191**:97–108. doi: 10.1016/S0300-483X(03)00208-7
71. Frederickson CJ, Giblin LJ, Krężèl A, McAdoo DJ, Muelle RN, Zeng Y, et al. Concentrations of extracellular free zinc (pZn)e in the central nervous system during simple anesthetization, ischemia and reperfusion. *Exp Neurol*. (2006) **198**:285–93. doi: 10.1016/j.expneurol.2005.08.030
72. Duan X, Block E, Li Z, Connelly T, Zhang J, Huang Z, et al. Crucial role of copper in detection of metal-coordinating odorants. *Proc Natl Acad Sci USA* (2012) **109**:3492–7. doi: 10.1073/pnas.1111297109
73. Li S, Ahmed L, Zhang R, Pan Y, Matsunami H, Burger JL, et al. Smelling Sulfur: copper and silver regulate the response of human odorant receptor OR2T11 to low-molecular-weight thiols. *J Amer Chem Soc*. (2016) **138**:13281–8. doi: 10.1021/jacs.6b06983
74. Block E. Fifty years of smelling sulfur: from the chemistry of garlic to the molecular basis for olfaction. *Phosphorus Sulf Silicon Relat Elements* (2017) **192**:141–4. doi: 10.1080/10426507.2016.1247091
75. Rodrguez FI, Esch JJ, Hall AE, Binder BM, Schaller GE, Bleecker AB. A copper cofactor for the ethylene receptor ETR1 from Arabidopsis. *Science* (1999) **283**:996–8. doi: 10.1126/science.283.5404.996
76. Frazier JL, Hetiz JR. Inhibition of olfaction in the moth heliothis virescens by the sulfhydryl reagent fluorescein mercuric acetate. *Chem Sens*. (1975) **1**:271. doi: 10.1093/chemse/1.3.271
77. Persson E, Henriksson J, Tjlve H. Uptake of cobalt from the nasal mucosa into the brain via olfactory pathways in rats. *Toxicol Lett*. (2003) **145**:19–27. doi: 10.1016/S0378-4274(03)00266-2
78. Frederickson CJ, Koh JY, Bush AI. The neurobiology of zinc in health and disease. *Nat Rev Neurosci*. (2005) **6**:449–62. doi: 10.1038/nrn1671
79. Takeda A, Ohnuma M, Sawashita J, Okada S. Zinc transport in the rat olfactory system. *Neurosci Lett*. (1997) **225**:69–71. doi: 10.1016/S0304-3940(97)00181-X
80. Henriksson J, Tallkvist J, Tjlve H. Uptake of nickel into the brain via olfactory neurons in rats. *Toxicol Lett*. (1997) **91**:153–62. doi: 10.1016/S0378-4274(97)03885-X
81. Henriksson J, Tjlve H. Uptake of inorganic mercury in the olfactory bulbs via olfactory pathways in rats. *Environ Res*. (1998) **77**:130–40. doi: 10.1006/enrs.1997.3817
82. Haffenden LJW, Yaylayan VA, Fortin J. Investigation of vibrational theory of olfaction with variously labelled benzaldehydes. *Food Chem*. (2001) **73**:67–72. doi: 10.1016/S0308-8146(00)00287-9
83. Peryam DR, Swartz VW. Measurement of sensory differences. *Food Technol*. (1950) **4**:390–5.
84. 04 ASE. *Standard Test Method for Sensory Analysis Duo-Trio Test*. Conshohocken, PA: ASTM International (2011).
85. Keller A, Vosshall LB. A psychophysical test of the vibration theory of olfaction. *Nat Neurosci*. (2004) **7**:337–8. doi: 10.1038/nn1215
86. Franco MI, Turin L, Mershin A, Skoulakis EMC. Molecular vibration-sensing component in *Drosophila melanogaster* olfaction. *Proc Natl Acad Sci USA* (2011) **108**:3797–802. doi: 10.1073/pnas.1012293108

87. Olton DS. Mazes, maps and memory. *Amer Psychol*. (1979) **34**:583–96. doi: 10.1037/0003-066X.34.7.583
88. Gane S, Georganakis D, Maniati K, Vamvakias M, Ragoussis N, Skoulakis EMC, et al. Molecular vibration-sensing component in human olfaction. *PLoS ONE* (2013) **8**:e55780. doi: 10.1371/journal.pone.0055780
89. Gane S, Georganakis D, Maniati K, Vamvakias M, Ragoussis N, Skoulakis EMC, et al. Correction: molecular vibration-sensing component in human olfaction. *PLoS ONE* (2013) **8**. doi: 10.1371/annotation/2f278ed8-d5e7-440a-9e49-c8d1df20d1f1
90. Büttner MW, Penka M, Doszczak L, Kraft P, Tacke R. Silicon analogues of the musk odorant versalide. *Organometallics* (2007) **26**:1295–8. doi: 10.1021/om060934h
91. Gronenberg W, Raikhelkar A, Abshire E, Stevens J, Epstein E, Loyola K, et al. Honeybees (*Apis mellifera*) learn to discriminate the smell of organic compounds from their respective deuterated isotopomers. *Proc R Soc Lond B Biol Sci.* (2014) **281**:20133089. doi: 10.1098/rspb.2013.3089
92. Block E, Jang S, Matsunami H, Sekharan S, Dethier B, Ertem MZ, et al. Implausibility of the vibrational theory of olfaction. *Proc Natl Acad Sci USA* (2015) **112**:E2766–74. doi: 10.1073/pnas.1503054112
93. Turin L, Gane S, Georganakis D, Maniati K, Skoulakis EMC. Plausibility of the vibrational theory of olfaction. *Proc Natl Acad Sci USA* (2015) **112**:E3154. doi: 10.1073/pnas.1508035112
94. Nagashima A, Touhara K. Enzymatic conversion of odorants in nasal mucus affects olfactory glomerular activation patterns and odor perception. *J Neurosci*. (2010) **30**:16391–8. doi: 10.1523/JNEUROSCI.2527-10.2010
95. Seok WK, Meyer TJ. Mechanism of oxidation of benzaldehyde by polypyridyl oxo complexes of Ru(IV). *Inorgan Chem*. (2005) **44**:3931–41. doi: 10.1021/ic040119z
96. Hahn I, Scherer PW, Mozell MM. A mass transport model of olfaction. *J Theor Biol*. (1994) **167**:115–28. doi: 10.1006/jtbi.1994.1057
97. Wilkes FJ, Laing DG, Hutchinson I, Jinks AL, Monteleone E. Temporal processing of olfactory stimuli during retronasal perception. *Behav Brain Res*. (2009) **200**:68–75. doi: 10.1016/j.bbr.2008.12.031
98. Paoli M, Anesi A, Antolini R, Guella G, Vallortigara G, Haase A. Differential odour coding of isotopomers in the honeybee brain. *Sci Rep*. (2016) **6**:21893. doi: 10.1038/srep21893
99. Drimyli E, Gaitanidis A, Maniati K, Turin L, Skoulakis EMC. Differential electrophysiological responses to odorant isotopologues in drosophilid antennae. *eNeuro* (2016) **3**:e0152–15. doi: 10.1523/ENEURO.0152-15.2016
100. Alcorta E. Characterization of the electroantennogram in *Drosophila melanogaster* and its use for identifying olfactory capture and transduction mutants. *J Neurophysiol*. (1991) **65**:702–14. doi: 10.1152/jn.1991.65.3.702
101. Wade D. Deuterium isotope effects on noncovalent interactions between molecules. *Chem Biol Interact*. (1999) **117**:191–217. doi: 10.1016/S0009-2797(98)00097-0
102. Block E, Jang S, Matsunami H, Batista VS, Zhuang H. Reply to Turin et al.: vibrational theory of olfaction is implausible. *Proc Natl Acad Sci USA* (2015) **112**:E3155. doi: 10.1073/pnas.1508443112
103. Vosshall LB. Laying a controversial smell theory to rest. *Proc Natl Acad Sci USA* (2015) **112**:6525–6. doi: 10.1073/pnas.1507103112
104. Pevsner J, Hou V, Snowman AM, Snyder SH. Odorant-binding protein. Characterization of ligand binding. *J Biol Chem*. (1990) **265**:6118–25.
105. Vogt RG, Prestwich GD, Lerner MR. Odorant-binding-protein subfamilies associate with distinct classes of olfactory receptor neurons in insects. *J Neurobiol*. (1991) **22**:74–84. doi: 10.1002/neu.480220108
106. Pelosi P. Odorant-binding proteins. *Crit Rev Biochem Mol Biol*. (1994) **29**:199–228. doi: 10.3109/10409239409086801
107. Krzan M, Vianello R, Marsavelski A, Repic M, Zaksek M, Kotnik K, et al. The quantum nature of drug-receptor interactions: deuteration changes binding affinities for histamine receptor ligands. *PLoS ONE* (2016) **11**:e0154002. doi: 10.1371/journal.pone.0154002
108. Paoli M, Münch D, Haase A, Skoulakis E, Turin L, Galizia CG. Minute impurities contribute significantly to olfactory receptor ligand studies: tales from testing the vibration theory. *eNeuro* (2017) **4**:ENEURO.0070-17.2017. doi: 10.1523/ENEURO.0070-17.2017
109. Jonathan P, McCarthy WVM, Roberts AMI. Discriminant analysis with singular covariance matrices. A method incorporating cross-validation and efficient randomized permutation tests. *J Chemometr*. (1996) **10**:189–213. doi: 10.1002/(SICI)1099-128X(199605)10:3<189::AID-CEM410>3.0.CO;2-I
110. Ferguson AM, Heritage T, Jonathon P, Pack SE, Phillips L, Rogan J, et al. EVA: a new theoretically based molecular descriptor for use in QSAR/QSPR analysis. *J Comput Aided Mol Design* (1997) **11**:143–52. doi: 10.1023/A:1008026308790
111. Takane Sy, Mitchell JBO. A structure-odour relationship study using EVA descriptors and hierarchical clustering. *Org Biomol Chem*. (2004) **2**:3250–5. doi: 10.1039/B409802A
112. Brookes JC, Hartoutsiou F, Horsfield AP, Stoneham AM. Could humans recognize odor by phonon assisted tunneling? *Phys Rev Lett*. (2007) **98**:038101. doi: 10.1103/PhysRevLett.98.038101
113. Brookes JC, Horsfield AP, Stoneham AM. The swipe card model of odorant recognition. *Sensors* (2012) **12**:15709–49. doi: 10.3390/s121115709
114. Solov'yov IA, Chang PY, Schulten K. Vibrationally assisted electron transfer mechanism of olfaction: myth or reality? *Phys Chem Chem Phys*. (2012) **14**:13861–71. doi: 10.1039/c2cp41436h
115. Bittner ER, Madalan A, Czader A, Roman G. Quantum origins of molecular recognition and olfaction in drosophila. *J Chem Phys*. (2012) **137**:22A551. doi: 10.1063/1.4767067
116. Chęcińska A, Pollock FA, Heaney L, Nazir A. Dissipation enhanced vibrational sensing in an olfactory molecular switch. *J Chem Phys*. (2015) **142**:025102. doi: 10.1063/1.4905377
117. Tirandaz A, Taher Ghahramani F, Shafiee A. Dissipative vibrational model for chiral recognition in olfaction. *Phys Rev E* (2015) **92**:032724. doi: 10.1103/PhysRevE.92.032724
118. Wang M, Gao J, Mller P, Giese B. Electron transfer in peptides with cysteine and methionine as relay amino acids. *Angew Chem Int Edn*. (2009) **48**:4232–4. doi: 10.1002/anie.200900827
119. Jia Y, DiMagno TJ, Chan CK, Wang Z, Popov MS, Du M, et al. Primary charge separation in mutant reaction centers of *Rhodobacter capsulatus*. *J Phys Chem*. (1993) **97**:13180–91. doi: 10.1021/j10052a024
120. Klika KD. The potential of 13C isotopomers as a test for the vibrational theory of olfactory sense recognition. *ISRN Org Chem*. (2013) **2013**:515810. doi: 10.1155/2013/515810
121. Saberi M, Seyed-allaei H. Odorant receptors of Drosophila are sensitive to the molecular volume of odorants. *Sci Rep*. (2016) **6**:25103. doi: 10.1038/srep25103
122. Boesveldt S, Olsson MJ, Lundstrm JN. Carbon chain length and the stimulus problem in olfaction. *Behav Brain Res*. (2010) **215**:110–3. doi: 10.1016/j.bbr.2010.07.007
123. Brookes JC, Horsfield AP, Stoneham AM. Odour character differences for enantiomers correlate with molecular flexibility. *J R Soc Interf*. (2009) **6**:75–86. doi: 10.1098/rsif.2008.0165
124. Rakowski K, Paneth P. Isotope effects on binding. *J Mol Struct*. (1996) **378**:35–43. doi: 10.1016/0022-2860(95)09146-7
125. Dybala-Defratyka A, Rostkowski M, Paneth P. Enzyme mechanisms from molecular modeling and isotope effects. *Arch Biochem Biophys*. (2008) **474**:274–82. doi: 10.1016/j.abb.2008.01.012
126. Świderek K, Paneth P. Binding isotope effects. *Chem Rev*. (2013) **113**:7851–79. doi: 10.1021/cr300515x
127. Tirandaz A, Taher Ghahramani F, Salari V. Validity examination of the dissipative quantum model of olfaction. *Sci Rep*. (2017) **7**:4432. doi: 10.1038/s41598-017-04846-8
128. Doszczak L, Kraft P, Weber HP, Bertermann R, Triller A, Hatt H, et al. Prediction of perception: probing the hOR17-4 olfactory receptor model with silicon analogues of bourgeonal and lilial. *Angew Chem Int Edn*. (2007) **46**:3367–71. doi: 10.1002/anie.200605002
129. Drrich S, Gelis L, Wolf S, Sunderktter A, Mahler C, Guschina E, et al. Comparative analysis of the olfactory properties of silicon/germanium/tin analogues of the lily-of-the-valley odorants lilial and bourgeonal. *ChemPlusChem* (2014) **79**:1747–52. doi: 10.1002/cplu.201402160
130. Wolf S, Gelis L, Drrich S, Hatt H, Kraft P. Evidence for a shape-based recognition of odorants *in vivo* in the human nose from an analysis of the molecular mechanism of lily-of-the-valley odorants detection in the Lilial

and Bourgeonal family using the C/Si/Ge/Sn switch strategy. *PLoS ONE* (2017) **12**:e0182147. doi: 10.1371/journal.pone.0182147
131. Hoover KC. Smell with inspiration: the evolutionary significance of olfaction. *Amer J Phys Anthropol*. (2010) **143**:63–74. doi: 10.1002/ajpa.21441
132. Gazave E, Lapébie P, Richards GS, Brunet F, Ereskovsky AV, Degnan BM, et al. Origin and evolution of the Notch signalling pathway: an overview from eukaryotic genomes. *BMC Evol Biol*. (2009) **9**:249. doi: 10.1186/1471-2148-9-249
133. King N, Westbrook MJ, Young SL, Kuo A, Abedin M, Chapman J, et al. The genome of the choanoflagellate *Monosiga brevicollis* and the origin of metazoans. *Nature* (2008) **451**:783–8. doi: 10.1038/nature06617
134. Manning G, Young SL, Miller WT, Zhai Y. The protist, Monosiga brevicollis, has a tyrosine kinase signaling network more elaborate and diverse than found in any known metazoan. *Proc Natl Acad Sci USA* (2008) **105**:9674–9. doi: 10.1073/pnas.0801314105
135. Suga H, Dacre M, de Mendoza A, Shalchian-Tabrizi K, Manning G, Ruiz-Trillo I. Genomic survey of premetazoans shows deep conservation of cytoplasmic tyrosine kinases and multiple radiations of receptor tyrosine kinases. *Sci Signal*. (2012) **5**:ra35. doi: 10.1126/scisignal.2002733
136. de Mendoza A, Sebé-Pedrós A, Ruiz-Trillo I. The evolution of the GPCR signaling system in eukaryotes: modularity, conservation, and the transition to metazoan multicellularity. *Genome Biol Evol*. (2014) **6**:606–19. doi: 10.1093/gbe/evu038
137. Zhang Z, Wu J, Yu J, Xiao J. A brief review on the evolution of GPCR: conservation and diversification. *Open J Genet*. (2012) **2**:11–7. doi: 10.4236/ojgen.2012.24B003
138. Nordström KJV, Lagerström MC, Wallér LMJ, Fredriksson R, Schiöth HB. The secretin GPCRs descended from the family of adhesion GPCRs. *Mol Biol Evol*. (2009) **26**:71–84. doi: 10.1093/molbev/msn228
139. Kaupp UB. Olfactory signalling in vertebrates and insects: differences and commonalities. *Nat Rev Neurosci*. (2010) **11**:188–200. doi: 10.1038/nrn2789
140. Fleischer J, Breer H, Strotmann J. Mammalian olfactory receptors. *Front Cell Neurosci*. (2009) **3**:9. doi: 10.3389/neuro.03.009.2009
141. Bohbot JD, Pitts RJ. The narrowing olfactory landscape of insect odorant receptors. *Front Ecol Evol*. (2015) **3**:39. doi: 10.3389/fevo.2015.00039
142. Su CY, Menuz K, Carlson JR. Olfactory perception: receptors, cells, and circuits. *Cell* (2009) **139**:45–9. doi: 10.1016/j.cell.2009.09.015
143. Bushdid C, Magnasco MO, Vosshall LB, Keller A. Humans can discriminate more than 1 trillion olfactory stimuli. *Science* (2014) **343**:1370–2. doi: 10.1126/science.1249168
144. Gerkin RC, Castro JB. The number of olfactory stimuli that humans can discriminate is still unknown. *eLife* (2015) **4**:e08127. doi: 10.7554/eLife.08127
145. Meister M. On the dimensionality of odor space. *eLife* (2015) **4**:e07865. doi: 10.7554/eLife.07865
146. Vassar R, Chao SK, Sitcheran R, Nunez JM, Vosshall LB, Axel R. Topographic organization of sensory projections to the olfactory bulb. *Cell* (1994) **79**:981–91. doi: 10.1016/0092-8674(94)90029-9
147. Ressler KJ, Sullivan SL, Buck LB. A zonal organization of odorant receptor gene expression in the olfactory epithelium. *Cell* (1993) **73**:597–609. doi: 10.1016/0092-8674(93)90145-G
148. Belluscio L, Lodovichi C, Feinstein P, Mombaerts P, Katz LC. Odorant receptors instruct functional circuitry in the mouse olfactory bulb. *Nature* (2002) **419**:296–300. doi: 10.1038/nature01001
149. Hallem EA, Dahanukar A, Carlson JR. Insect odor and taste receptors. *Annu Rev Entomol*. (2006) **51**:113–35. doi: 10.1146/annurev.ento.51.051705.113646
150. Liu F, Chen Z, Liu N. Molecular basis of olfactory chemoreception in the common bed bug, cimex lectularius. (2017) **7**:45531. doi: 10.1038/srep45531
151. Krieger J, Breer H. Olfactory reception in invertebrates. *Science* (1999) **286**:720–3. doi: 10.1126/science.286.5440.720
152. Troemel ER, Kimmel BE, Bargmann CI. Reprogramming chemotaxis responses: sensory neurons define olfactory preferences in *C. elegans*. *Cell* (1997) **91**:161–9. doi: 10.1016/S0092-8674(00)80399-2
153. Sanchez-Gracia A, Vieira FG, Rozas J. Molecular evolution of the major chemosensory gene families in insects. *Heredity* (2009) **103**:208–16. doi: 10.1038/hdy.2009.55
154. Hill CA, Fox AN, Pitts RJ, Kent LB, Tan PL, Chrystal MA, et al. G protein-coupled receptors in *Anopheles gambiae*. *Science* (2002) **298**:176–8. doi: 10.1126/science.1076196
155. Sato K, Pellegrino M, Nakagawa T, Nakagawa T, Vosshall LB, Touhara K. Insect olfactory receptors are heteromeric ligand-gated ion channels. *Nature* (2008) **452**:1002–6. doi: 10.1038/nature06850
156. Wicher D, Schafer R, Bauernfeind R, Stensmyr MC, Heller R, Heinemann SH, et al. Drosophila odorant receptors are both ligand-gated and cyclic-nucleotide-activated cation channels. *Nature* (2008) **452**:1007–11. doi: 10.1038/nature06861
157. Missbach C, Dweck HK, Vogel H, Vilcinskas A, Stensmyr MC, Hansson BS, et al. Evolution of insect olfactory receptors. *eLife* (2014) **3**:e02115. doi: 10.7554/eLife.02115
158. Jones WD, Nguyen TAT, Kloss B, Lee KJ, Vosshall LB. Functional conservation of an insect odorant receptor gene across 250 million years of evolution. *Curr Biol*. (2005) **15**:R119–21. doi: 10.1016/j.cub.2005.02.007
159. Swaney WT, Keverne EB. The evolution of pheromonal communication. *Behav Brain Res*. (2009) **200**:239–47. doi: 10.1016/j.bbr.2008.09.039
160. Zhang R, Gao G, Chen H. Silencing of the olfactory co-receptor gene in Dendroctonus armandi leads to EAG response declining to major host volatiles. *Sci Rep*. (2016) **6**:23136. doi: 10.1038/srep23136
161. Oh SJ. Characteristics in molecular vibrational frequency patterns between agonists and antagonists of histamine receptors. *Genomics Inform*. (2012) **10**:128–32. doi: 10.5808/GI.2012.10.2.128
162. Chee HK, Oh SJ. Molecular vibration-activity relationship in the agonism of adenosine receptors. *Genom Inform*. (2013) **11**:282–8. doi: 10.5808/GI.2013.11.4.282
163. Chee HK, Yang JS, Joung JG, Zhang BT, Oh SJ. Characteristic molecular vibrations of adenosine receptor ligands. *FEBS Lett*. (2015) **589**:548–52. doi: 10.1016/j.febslet.2015.01.024
164. Hoehn RD, Nichols D, Neven H, Kais S. Neuroreceptor activation by vibration-assisted tunneling. *Sci Rep*. (2015) **5**:9990. doi: 10.1038/srep09990
165. Buck LB. Olfactory receptors and odor coding in mammals. *Nutr Rev*. (2004) **62**:S184–8. doi: 10.1111/j.1753-4887.2004.tb00097.x
166. Hoehn RD, Nichols DE, McCorvy JD, Neven H, Kais S. Experimental evaluation of the generalized vibrational theory of G protein-coupled receptor activation. *Proc Natl Acad Sci USA* (2017) **114**:5595–600. doi: 10.1073/pnas.1618422114
167. Malnic B, Hirono J, Sato T, Buck LB. Combinatorial receptor codes for odors. *Cell* (1999) **96**:713–23. doi: 10.1016/S0092-8674(00)80581-4
168. Snitz K, Yablonka A, Weiss T, Frumin I, Khan RM, Sobel N. Predicting odor perceptual similarity from odor structure. *PLoS Comput Biol*. (2013) **9**:e1003184. doi: 10.1371/journal.pcbi.1003184
169. Sachse S, Rappert A, Galizia CG. The spatial representation of chemical structures in the antennal lobe of honeybees: steps towards the olfactory code. *Eur J Neurosci*. (1999) **11**:3970–82. doi: 10.1046/j.1460-9568.1999.00826.x
170. Hallem EA, Carlson JR. The odor coding system of *Drosophila*. *Trends Genet*. (2004) **20**:453–9. doi: 10.1016/j.tig.2004.06.015
171. Silbering AF, Okada R, Ito K, Galizia CG. Olfactory information processing in the Drosophila antennal lobe: Anything goes? *J Neurosci*. (2008) **28**:13075–87. doi: 10.1523/JNEUROSCI.2973-08.2008
172. Grabe V, Strutz A, Baschwitz A, Hansson BS, Sachse S. Digital *in vivo* 3D atlas of the antennal lobe of *Drosophila melanogaster*. *J Compar Neurol*. (2015) **523**:530–44. doi: 10.1002/cne.23697
173. Takahashi YK, Kurosaki M, Hirono S, Mori K. Topographic representation of odorant molecular features in the rat olfactory bulb. *J Neurophysiol*. (2004) **92**:2413–27. doi: 10.1152/jn.00236.2004
174. Mori K, Takahashi YK, Igarashi KM, Yamaguchi M. Maps of odorant molecular features in the mammalian olfactory bulb. *Physiol Rev*. (2006) **86**:409–33. doi: 10.1152/physrev.00021.2005
175. Sell CS. On the unpredictability of odor. *Angew Chem Int Edn*. (2006) **45**:6254–61. doi: 10.1002/anie.200600782
176. Haddad R, Khan R, Takahashi YK, Mori K, Harel D, Sobel N. A metric for odorant comparison. *Nat Meth*. (2008) **5**:425–9. doi: 10.1038/nmeth.1197

177. Khan RM, Luk CH, Flinker A, Aggarwal A, Lapid H, Haddad R, et al. Predicting odor pleasantness from odorant structure: pleasantness as a reflection of the physical world. *J Neurosci*. (2007) **27**:10015–23. doi: 10.1523/JNEUROSCI.1158-07.2007
178. Iurilli G, Datta SR. Population coding in an innately relevant olfactory area. *Neuron* (2017) **93**:1180–1197.e7. doi: 10.1016/j.neuron.2017.02.010
179. Raman B, Stopfer M, Semancik S. Mimicking biological design and computing principles in artificial olfaction. *ACS Chem Neurosci*. (2011) **2**:487–99. doi: 10.1021/cn200027r
180. Sen A, Suslick KS. Shape-selective discrimination of small organic molecules. *J Am Chem Soc*. (2000) **122**:11565–6. doi: 10.1021/ja000002j
181. Rivera JF, Arce JC, Velasco-Medina J. Specific single-molecule detection based on orbital mediated tunneling in nanotube double-barrier heterostructures. *IEEE Trans Nanotechnol*. (2012) **11**:1174–82. doi: 10.1109/TNANO.2012.2219553
182. Saito H, Chi Q, Zhuang H, Matsunami H, Mainland JD. Odor coding by a mammalian receptor repertoire. *Sci Signal*. (2009) **2**:ra9. doi: 10.1126/scisignal.2000016

Conflict of Interest Statement: The authors declare that the research was conducted in the absence of any commercial or financial relationships that could be construed as a potential conflict of interest.

frontiers in Physics

ORIGINAL RESEARCH
published: 26 January 2017
doi: 10.3389/fphy.2017.00002

RFEA Measurements of High-Energy Electrons in a Helicon Plasma Device with Expanding Magnetic Field

*Njål Gulbrandsen * and Åshild Fredriksen*

Department of Physics and Technology, University of Tromsø-The Arctic University of Norway, Tromsø, Norway

In the inductively coupled plasma of the Njord helicon device we have, for the same parameters as for which an ion beam exists, measured a downstream population of high-energy electrons emerging from the source. Separated measurements of energetic tail electrons was carried out by Retarding Field Energy Analyzer (RFEA) with a grounded entrance grid, operated in an electron collection mode. In a radial scan with the RFEA pointed toward the source, we found a significant population of high-energy electrons just inside the magnetic field line mapping to the edge of the source. A second peak in high-energy electrons density was observed in a radial position corresponding to the radius of the source. Also, throughout the main column a small contribution of high-energy electrons was observed. In a radial scan with a RFEA biased to collect ions a localized increase in the plasma ion density near the magnetic field line emerging from the plasma near the wall of the source was observed. This is interpreted as a signature of high-energy electrons ionizing the neutral gas. Also, a dip in the floating potential of a Langmuir probe is evident in this region where high-energy electrons is observed.

Keywords: low-temperature plasmas, plasma expansion, electron energy distribution function, retarding field energy analyzer, high-energy electrons, ion beam, helicon plasma device

OPEN ACCESS

Edited by:
Roderick William Boswell,
Australian National University, Australia

Reviewed by:
Bill Amatucci,
United States Naval Research Laboratory, USA
Kazunori Takahashi,
Tohoku University, Japan
Alan A. Howling,
École Polytechnique Fédérale de Lausanne, Switzerland
J. P. Sheehan,
University of Michigan, USA

****Correspondence:***
Njål Gulbrandsen
njal.gulbrandsen@uit.no

Specialty section:
This article was submitted to Plasma Physics, a section of the journal Frontiers in Physics

Received: *24 October 2016*
Accepted: *11 January 2017*
Published: *26 January 2017*

Citation:
Gulbrandsen N and Fredriksen Å (2017) RFEA Measurements of High-Energy Electrons in a Helicon Plasma Device with Expanding Magnetic Field. Front. Phys. 5:2. doi: 10.3389/fphy.2017.00002

1. INTRODUCTION

An electric double-layer forming spontaneously in a helicon plasma source with an expanding magnetic field was first measured by Charles and Boswell [1]. It was named current-free double layer (CFDL), as it formed self-consistently without external current forcing. The CFDLs formed in these experiments have later been repeated in a number of helicon devices [2–9]. As a result of a potential the drop set up between the source and the diffusion chamber an ion beam is formed. As no external current is necessary to form this ion beam, the free electrons in the CFDL in the downstream plasma, play an important role in balancing the ion current in the beam.

To understand the underlying physics of characteristic parameters of CFDLs it is thus important to obtain information about the electrons and their energy distribution. Previously, Takahashi et al. [10] observed, in a similar experiment, high-energy electrons at a magnetic field line mapping to the edge of the source by measuring the electron energy distribution function (EEDF) with a RF compensated Langmuir probe.

Some theoretical models and numerical simulations have been carried out [11] and may indicate the role of electrons in the formation of the CFDL. The first one-dimensional modeling [12] and 1D PIC simulations [13] were able to reproduce the potential drops and an ion beam was produced in the simulations. However, these models are only one-dimetional and do not include the full effect of the expanding magnetic field.

Later, others [14–17] have pointed out the 2D nature of the CFDL, in that the electrons follow the magnetic field lines and escape toward the side walls, while the non-magnetized ions follow a straight path from the source into the expansion chamber [18]. A curved 2D CFDL potential structure [19, 20] and the conics of enhanced plasma density along the outermost magnetic fields emerging from the source region [21] has been observed. Takahashi et al. [10] and Charles [21] has proposed that the enhanced plasma density along the last field line is produced by an additional ionization from the high-energy electrons transported from the source along the field line. On the other hand Saha et al. [22] has argued that the electric field set up between the positively charged ion beam region and the electrons following the field lines will accelerate the ion beam also radially giving rise to an oscillation that is responsible for the higher densities at the edges.

Still, more complete measurements of the high-energy electrons remain to be carried out. In this paper, we report the first measurements of energetic electrons in the downstream region of the CFDL in the Njord device, applying a Retarding Field Energy Analyzer (RFEA). By inverting the grids of an RFEA, the probe can be applied to measure the flux of the high-energy tail of electrons [23–26]. In Section 2, the experimental setup and diagnostics is explained, and the measured distributions of energetic electrons are reported and discussed in Section 3.

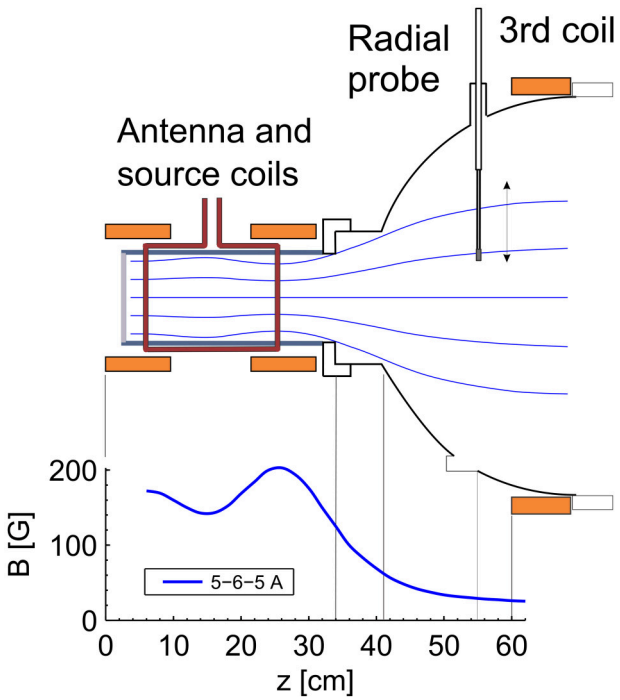

FIGURE 1 | The experimental setup and magnetic field configuration in Njord.

2. EXPERIMENTAL SETUP

The Njord device (**Figure 1**) at the University of Tromsø (UiT) is an inductively coupled helicon plasma device [9, 27]. The source consists of a 30 cm long, 13 cm diameter Pyrex tube with a Boswell type [28] saddle antenna wrapped around it, coupling up to 1000 W of RF-power at 13.56 MHz to the argon gas. Two magnetic field coils are placed around the source tube. In this study we used 5 A in the first coil and 6 A in the second coil to produce a maximum magnetic field of 200 G in the source. The plasma expands through a 20 cm diameter and 8 cm long port into a 120 cm long and 60 cm diameter expansion chamber. A turbomolecular pump connected to the expansion chamber keeps the base pressure at 10^{-6} Torr. The outer edge of the first source coil defines $z = 0$ and positive z is in the direction of the gas flow, from the source to the expansion chamber. The source itself starts at $z = 4$ cm.

A third field coil placed at $z = 60$ cm is used with a current of 5 A to provides a downstream magnetic field of about 30G. This field prevents electrons from the near wall region of the source from being lost at the walls of the large port.

Argon gas is fed to the source through an inlet in a grounded aluminum end plate of the source at $z = 4$ cm in **Figure 1**. The gas flow is controlled by an Omega flow controller and was kept at 2.0 sccm in this study, giving rise to pressures of 0.34 mTorr in the expansion chamber.

A radial probe feedthrough, at $z = 55$ cm, indicated in **Figure 1**, can be fitted with either an RFEA, an RF-compensated Langmuir probe or an emissive probe.

TABLE 1 | Typical parameters for the Njord device.

	Source	Expansion chamber
Pressure, P		0.34 mTorr (46 mPa)
Magnetic field, B	200 G	29 G
RF power (13.56 MHz)	1000 W	
Plasma density, n_i	$2 \cdot 10^{11}$ cm^{-3}	$3 \cdot 10^{10}$ cm^{-3}
Electron temperature, T_e	8 eV	6 eV
Ion temperature, T_i[a]		0.2 eV
Plasma potential, V_p	64 V	46 V

[a] *From LIF [29].*

The control parameters and some typical plasma parameters for the Njord device are given in **Table 1**.

The RFEA had a grounded brass housing with a cylindrical shape, a diameter of 16 mm and a thickness of 10 mm. The probe had four grids, three made from stainless steel mesh with a transmission factor of 44%, wire diameter of 0.050 mm and mesh openings of 0.100 mm while a fourth, the second from the aperture, was made of a nickel mesh with transmission of 67%, wire diameter of 0.024 mm and mesh openings of 0.100 mm. The distance between the grids was 0.7 mm, the front aperture was 2 mm and the diameter of the collector area was 3 mm.

Figure 2A shows the grid configuration for ion measurements. The repeller, R, was biased to −80 V and the discriminator, D, was scanned from 0 to 100 V. S is the secondary electron repeller and was kept at −18 V. The collector

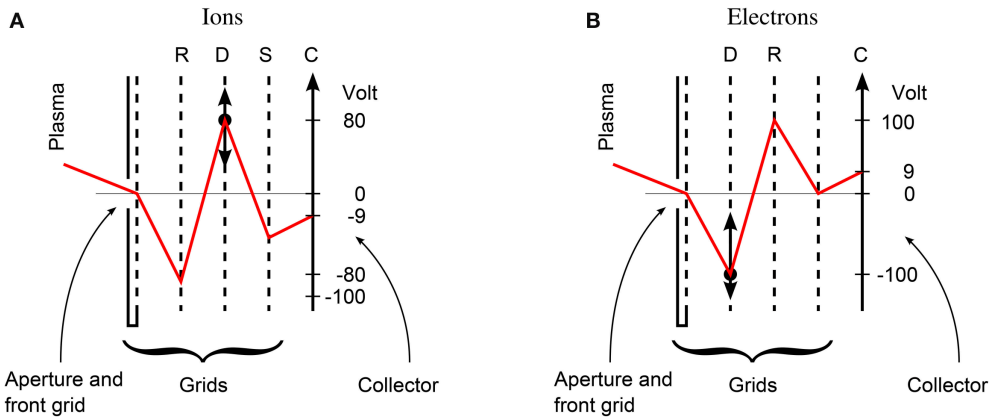

FIGURE 2 | RFEA grid configurations for (A) ion measurements and **(B)** electron measurements.

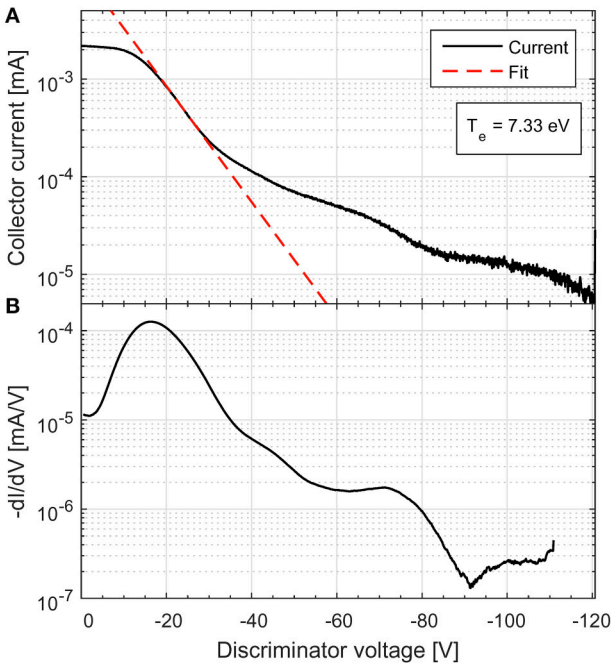

FIGURE 3 | An electron-RFEA measurement form $r = -7$ in Njord. (A) The collector current, **(B)** the derivative of the collector current.

was kept at −9 V. The ion RFEA measurements is further described in Gulbrandsen et al. [29].

Figure 2B shows the grid configuration for electron measurements. D is the discriminator grid and was scanned from 0 to −120 V, R is the repeller grid biased at +100 V and C is the collector kept at +9 V. The innermost grid was not needed in this configuration and was therefore grounded. This grid configuration with the discriminator in front of the repeller is similar to the one used by Gahan et al. [24, 30]. Only the electrons with energies high enough to overcome the sheath potential in front of the probe will be recorded, so that the RFEA detects only the high-energy tail of the EEDF [30]. The high-energy electron-tail temperature can be extracted from a linear fit to a plot of the logarithm of collector current [31]:

$$\frac{\mathrm{d}}{\mathrm{d}V}\left(\ln(I)\right) = \frac{e}{kT} \tag{1}$$

The derivative of the collector current is proportional to the EEDF for energies high enough to enter the probe [24].

An RF-compensated Langmuir probe [32] and a floating emissive probe were used to measure some of the background parameters of the plasma. For the emissive probe, we used the floating potential method where the floating potential at saturation is taken as the plasma potential [33, 34]. When the emission current exceeds the electron saturation current, the emissive probe will float close to the plasma potential. We used a filament current of 2.9 A. This method is expected to give a potential slightly lower than the plasma potential with an accuracy of the order of T_e/e [35, 36].

3. RESULTS AND DISCUSSION

Figure 3A shows an example of a logarithmic plot of collector current vs. discriminator voltage from the electron-RFEA in Njord at $r = -7$ cm. As only electrons overcoming the plasma potential barrier are collected, no saturation current is expected at the most positive voltage bias. The voltage axis runs from positive toward negative values, such that the electrons with lowest energy appears at the left. For the first 15 V a plateau where the collector current is changing very little is observed. From −15 to −30 V the collector current drops exponentially and a linear fit to the logarithm of the current using equation (1), reveals a tail-temperature of about 7.3 eV. For voltages lower than −30 V the collector current is higher than expected from the temperature fit. This high-energy tail indicates an electron population with even higher energies.

Figure 3B shows a logarithmic plot of the derivative of the collector current as a function of discriminator voltage. The

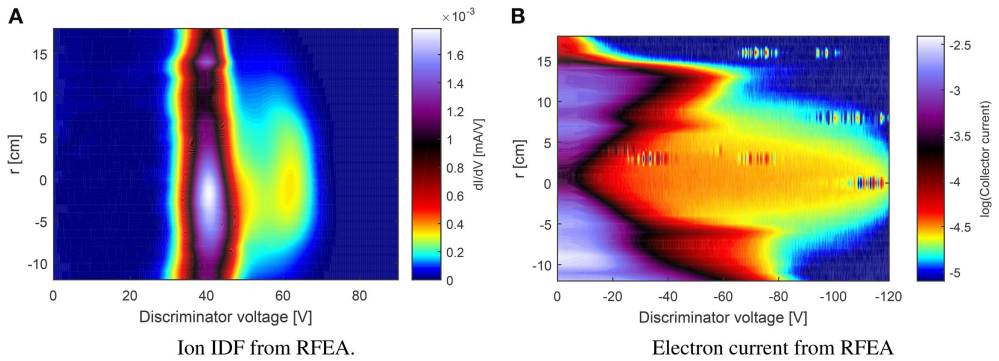

FIGURE 4 | RFEA measurements of (A) ions and **(B)** electrons in Njord at 2.0 sccm flow and 5-6-5 A magnetic field.

derivative was found by applying a 151 point, 4 degree Savitzky-Golay filter [37] to the collector current. This derivative should be proportional to the EEDF for energies high enough to enter the probe [24]. In this case the plasma potential was around 40 V, so that the electron energies in the plasma would be about 40 eV higher than what the discriminator voltage shows.

Figure 4A shows radial profiles of RFEA Ion Distribution Functions (IDF) [29] measured at $z = 55$ cm. A beam can be seen at around 60 V. The beam flux decreases with radius and disappear around $r = 12$ cm. The background distribution (around $V_b = 40$ V) has a maximum in the center ($r = 0$ cm) and another peak at $r = 14$ cm. The ion beam RFEA measurements are further discussed in Gulbrandsen et al. [29].

In **Figure 4B** the logarithm of the collector current of the RFEA in electron measurement configuration is plotted vs. discriminator voltage and radial position. The high-energy electrons seen at ± 7 cm correspond to the width of the source and the width of the ion beam, while the high-energy electrons at $r = 14$ cm corresponds well with a magnetic field line emerging from the edge of the source [29]. We have already seen increased ion densities in this position (**Figure 4A**), possibly due to ionization from the high-energy electrons. The yellow plateau in the figure indicates a small density of electrons with energies larger than 100 eV near the center of the plasma column. Saha et al. [22] has earlier measured electrons with energies more than 100 eV in the center of the plasma in a similar experiment using a RFEA with a floating front grid and a fixed voltage electron repeller. The radial profile they obtained looks similar to the one we have for energies higher than 100 ev (less than -100 V).

Some selected profiles of the electron currents from **Figure 4B** along with their derivatives are shown in **Figure 5**. **Figure 5A** shows an electron measurement from the background plasma of the outer parts of the expansion chamber ($r = 18$ cm), shielded from the source. We observe what appears to be a part of a low density single Maxwellian electron population with a temperature around 6 eV. A small plateau of the collector current is observed for the first 5 V of the scan.

Figure 5B is from $r = 14$ cm and shows a higher density. A larger plateau is visible in the beginning of the scan. The main population observed seems to have an apparent temperature of 9.6 eV, but there is an indication of an even higher energy tail from -80 V to -100 V.

Figure 5C from $r = 7$ cm shows several populations of electrons. Between -20 and -40 V a Maxwellian electron distribution is found with an apparent temperature of 6.5 eV. Then there is indications of an other population between -40 and -80 V, and then a high-energy tail below -80 V.

Figure 5D is near from the center of the expansion chamber. Here we see parts of a single Maxwellian electron distribution with temperature of 5.3 eV. In addition there is a long plateau in the collector current going from -20 V and to the end of the scan which indicates the existence of a few electrons with an even higher energy.

Next we compared parameters derived from the RFEA with equivalent parameters obtained with Langmuir and emissive probes. **Figure 6A** shows the plasma potential from an RF-compensated Langmuir probe [32] (dots), floating emissive probe (circles), ion RFEA facing the source (crosses) and ion RFEA pointing 90° away from the source (triangles). The plasma potential from the RFEA measurements corresponds well with the Langmuir probe within a couple of volt, while the plasma potential from the emissive probe was about 7–8 V higher. Earlyer simulations have shown that the plasma potential measured with an RFEA could be as much as 5 V lower than the real plasma potential [38, 39]. It is also of interest to notice that the potential from the emissive probe has peaks near $r = \pm 10$ cm while the Langmuir probe and the RFEA has minima at the same place, which indicates that the emissive probe responds differently to energetic electrons. These measurements are not carried out at the same time so it might be that the Langmuir probe and the RFEA was affecting the plasma and reducing the plasma potential. Normally the potential from a floating emissive probe is expected to be slightly lower than the plasma potential with about $2T_e/e$ [36].

In **Figure 6B** the floating potential from the Langmuir probe shows distinct minima around $r = \pm 8$ cm, which can be expected from the fact that the higher electron flux from the energetic electrons will contribute to a reduced the floating potential. This behavior of the floating potential is similar to the one observed by Takahashi et al. [16].

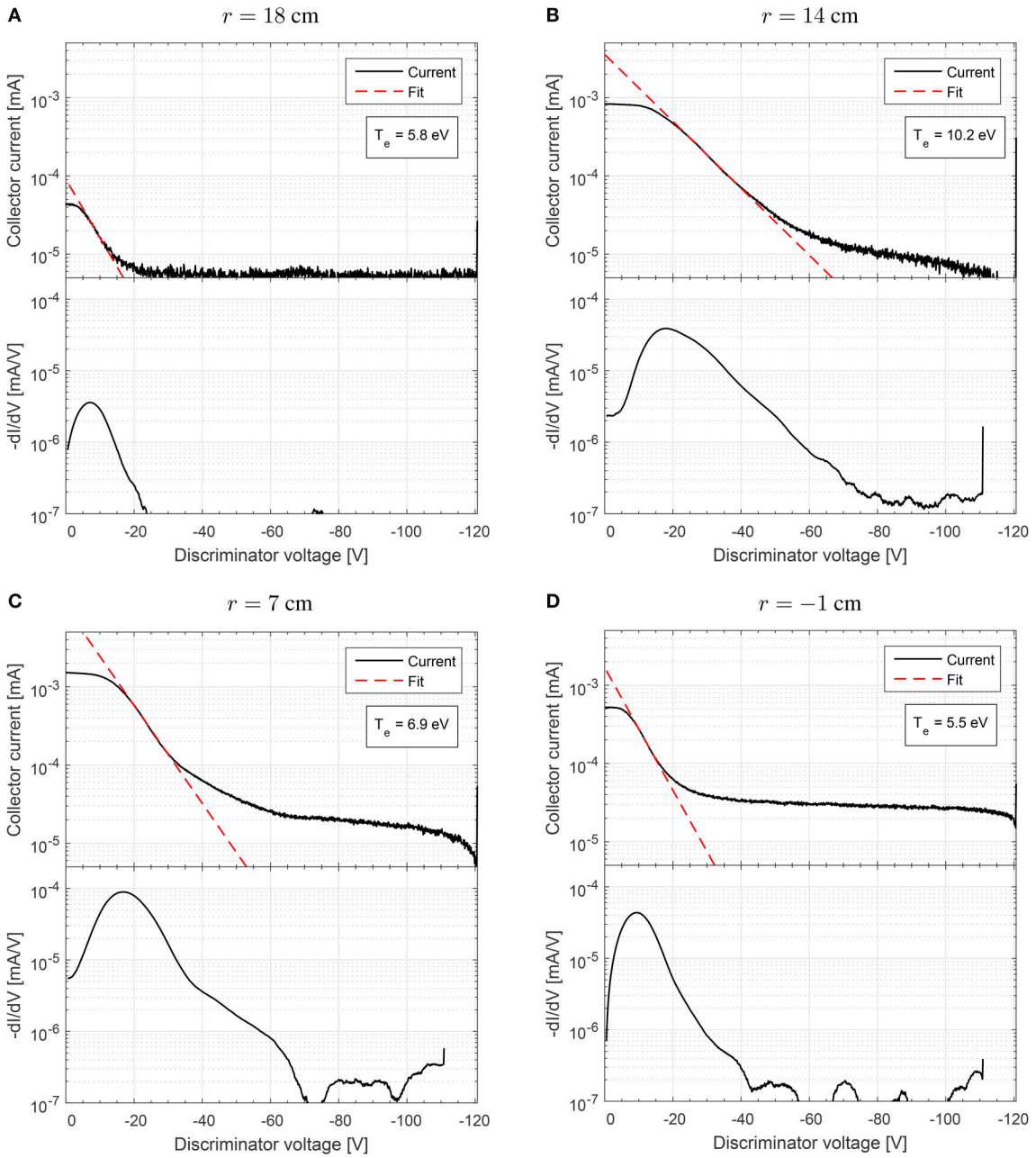

FIGURE 5 | Electron-RFEA measurement from Njord from four different positions, (A) in the background plasma, **(B)** at the other most magnetic field line coming from the source, **(C)** at the edge of the ion beam and **(D)** in the middle of the ion beam.

Figure 6C shows electron temperature from Langmuir probe (dots) and electron-RFEA (crosses). The electron temperature was extracted from the current-voltage characteristic of the RFEA as shown in **Figure 5**. Only the the high-energy tail of the EEDF is detected [24]. In the center the RFEA and Langmuir probe corresponds well, but at the edges the RFEA detected a higher temperature indicating a high-energy population of electrons. This resembles the two-temperature distributions Takahashi et al. [6] found in a similar device measuring electron energy probability functions (EEPF) using a RF-compensated Langmuir probe.

Figure 6D shows the ion density from the Langmuir probe and the ion flux to the RFEA facing the source, 0°, and 90° away from the source. Both the density and the ion flux had a peak in the center corresponding to the region where the beam was detected. The density also had a peak around $r = +10$ cm that was not observed for $r = -10$, and it is also not observed in the ion flux. Instead, we observe a small peak in the ion flux at $r = 14$

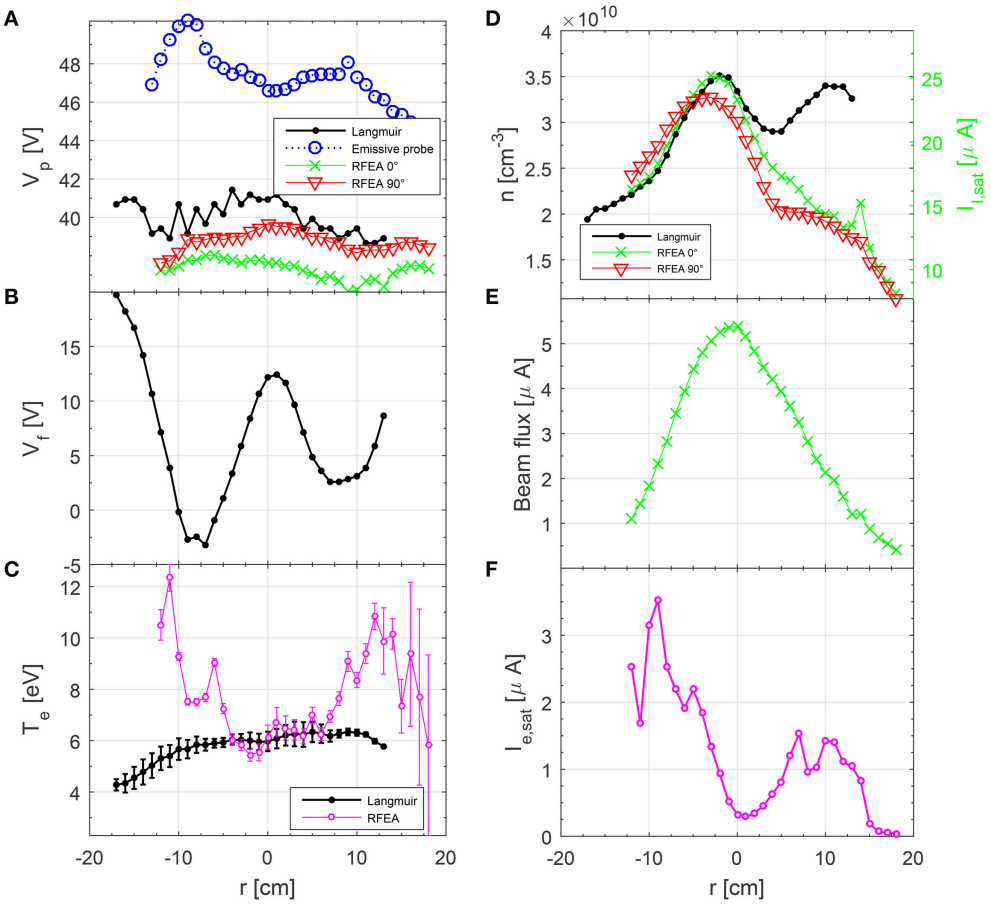

FIGURE 6 | 2.0 sccm 5-6-5A 1000W. (A) Plasma potential from Langmuir probe (dots), emissive probe (circles) and RFEA facing the source (crosses) and 90° away from the source (triangles). **(B)** Floating potential form Langmuir probe. **(C)** Electron temperature form Langmuir probe (dots) and tail-temperature from electron-RFEA (crosses). The error bars represents the estimated uncertanty. **(D)** Ion density from Langmuir probe (dots), ion saturation current from the RFEA facing the source (crosses) and ion saturation current from the RFEA facing 90° away from the source (triangles). **(E)** Beam flux (in units of current) from ion-RFEA. **(F)** Electron saturation current from electron-RFEA.

cm when the RFEA is facing the source that is not observed when the probe is turned 90° away from the source. The asymmetry in the density profile might be explained at least in part by the fact that for negative r the probe shaft is crossing the center of plasma and this might affect the plasma somewhat. It might also be that a slight asymmetry in the source antenna or the power deposition can create an asymmetry in the plasma density.

In **Figure 6E** the total integrated ion beam flux has a peak in the center and then decreases toward the edges. Using the half-value width the beam radius is around $r_{1/2} = 7$ cm.

Figure 6F shows the electron saturation current from the electron-RFEA, wich is proportional to the energetic electron flux to the RFEA. The profile is "hollow" and has a minimum in the center and peaks at $r = 7$, 10, -5 and -9 cm.

At a first look the plateau observed in the first few volts of electron RFEA-measurements (**Figures 3**, **4B**, **5**) resembles an electron beam. But as we have seen from **Figures 4B**, **5** it is to a larger or smaller degree found on all the electron RFEA-measurments, also the ones of the background plasma ($r = 18$ cm) where we expect no high-energy electrons, because it was shielded from the source by the walls of the port. As can be seen in **Figure 5** the size of this plateau seems to vary fairly systematic with the total electron current to the RFEA-probe. When we compare the derived temperatures from the electron-RFEA with RF-compensated Langmuir probe in **Figure 6C** we find that the electron-RFEA temperatures matches well with the Langmuir probe temperatures in the center ($r = -4$ to 6 cm) and at the end ($r = 18$) indicating that the RFEA sees the high-energy part of the same Maxwellian electron distribution as the Langmuir probe. We conclude that this plateau seen for the first 5 to 20 V of each scan is not a feature of the electron distribution in the plasma, but rather an effect of the probe. It might be related to the RF-oscillations in the sheath in front of the probe since the probe surface was grounded or it might be some kind of saturation effect in the probe due to a high electron flux. If we neglect this plateau, the rest of the measurements make good sense and we manage to match the temperature with the Langmuir probe in the areas where we see less high-energy electrons.

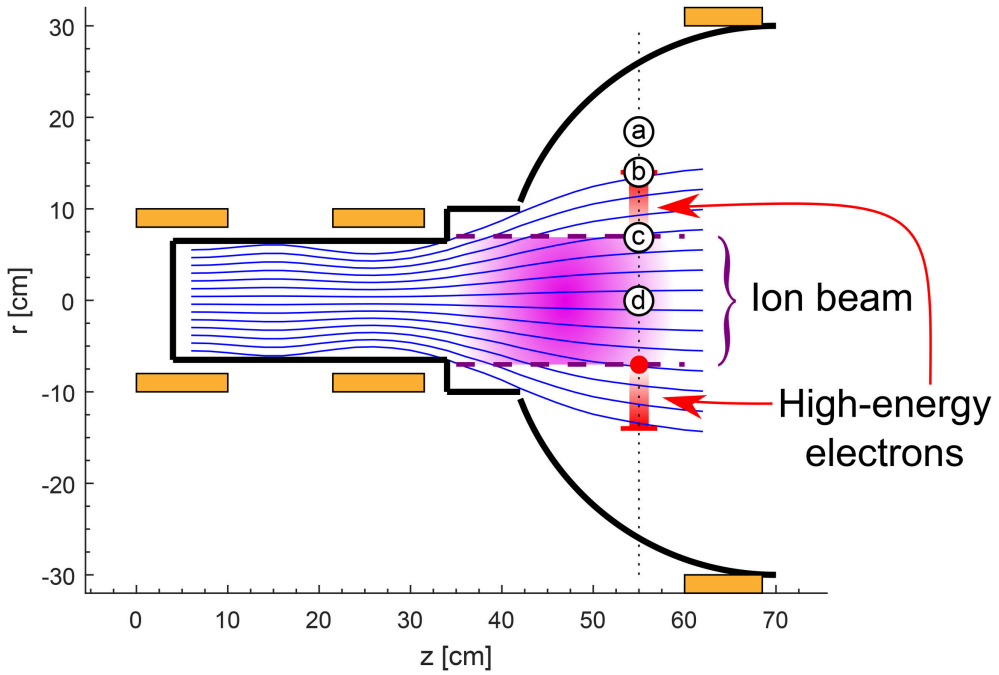

FIGURE 7 | Positions of observed features with respect to the magnetic field. The letters "a,b,c,d" refers to the different profiles in **Figure 5**.

To summarize we take a closer look at the positions of the shown features with respect to the magnetic field and source geometry. **Figure 7** shows the magnetic field lines originating in the source of Njord as calculated from the axial magnetic field. The three magnetic coils are marked as orange boxes. The vertical dotted line at $z = 55$ cm marks the axial position of the probes. The horizontal dashed lines at $r = \pm 7$ cm represent the observed width of the beam [29]. This type of ion detachment from magnetic field lines has earlier also been observed by Takahashi et al. [18] and Cox et al. [20].

With the electron-RFEA we see peaks in the electron current at the outer edges of the beam (marked with a red dot). The red marks crossing the line at $z = 55$ cm and $r = \pm 14$ cm are the locations of the small maximum seen in the ion RFEA measurements (**Figure 4A**). These marks fits well with the calculated outermost magnetic field line coming from the source and they are in the same area where we observe high electron temperatures and high electron currents with the RFEA. The letters "a,b,c,d" refers to the different profiles in **Figure 5**. Where (a) is in the background plasma, (b) is at the outermost magnetic field line from the source, (c) is at the edge of the ion beam and (d) is in the middle of the beam.

4. CONCLUSION

Direct measurements of high-energy electrons have been performed with a RFEA set up for detection of energetic electrons. We found significant maxima in energetic electron densities, positioned just inside the magnetic field emerging from the edge of the source. In addition we observe a second maxima corresponding to the width of the source, indicating that some electrons might detach from the magnetic field line and continue strait forward along the edges of the ion beam. Electron temperatures deduced from the electron IV-characteristic show T_e maxima about 10 eV from the energetic electron population at the magnetic field line emerging from the edge of the source. In the center of the plasma column the deduced T_e agrees with that of the Langmuir probe. These findings corresponds well with the "two-temperature" distributions seen by Takahashi et al. [10] in EEPFs from Langmuir probe.

In support of the direct measurements, signatures of high-energy electrons downstream of the DL have been observed as a small peak in the ion saturation current at a magnetic field line emerging from the edge of the source. This indicates additional ionization by high-energy electrons. A dip in the floating potential just inside this magnetic field line, but outside the radius of the source also indicate a high-energy electron flux.

In total our findings supports the idea that high-energy electrons are transported from the source along the magnetic field emerging from the edge of the source and contribute to the ionization of the neutral gas downstream.

AUTHOR CONTRIBUTIONS

All authors contributed as a team effort. The measurements where conducted and analyzed by NG under the supervision of ÅF.

FUNDING

This study was entirely funded by UiT.

REFERENCES

1. Charles C, Boswell R. Current-free double-layer formation in a high-density helicon discharge. *Appl Phys Lett.* (2003) **82**:1356–8. doi: 10.1063/1.1557319
2. Cohen SA, Siefert NS, Stange S, Boivin RF, Scime EE, Levinton FM. Ion acceleration in plasmas emerging from a helicon-heated magnetic-mirror device. *Phys Plasmas* (2003) **10**:2593–8. doi: 10.1063/1.1568342
3. Sun X, Cohen SA, Scime EE, Miah M. On-axis parallel ion speeds near mechanical and magnetic apertures in a helicon plasma device. *Phys Plasmas* (2005) **12**:103509. doi: 10.1063/1.2121347
4. Plihon N, Corr CS, Chabert P. Double layer formation in the expanding region of an inductively coupled electronegative plasma. *Appl Phys Lett.* (2005) **86**:091501. doi: 10.1063/1.1869533
5. Sutherland O, Charles C, Plihon N, Boswell RW. Experimental evidence of a double layer in a large volume Helicon reactor. *Phys Rev Lett.* (2005) **95**:205002. doi: 10.1103/PhysRevLett.95.205002
6. Takahashi K, Shida Y, Fujiwara T, Oguni K. Supersonic ion beam driven by permanent-magnets-induced double layer in an expanding plasma. *Plasma Sci IEEE Trans.* (2009) **37**:1532–6. doi: 10.1109/TPS.2009.2024342
7. Scime EE, Biloiu IA, Carr J, Thakur SC, Galante M, Hansen A, et al. Time-resolved measurements of double layer evolution in expanding plasmaa). *Phys Plasmas* (2010) **17**:055701. doi: 10.1063/1.3276773
8. Popescu S, Ohtsu Y, Fujita H. Current-free double-layer formation in inductively coupled plasma in a uniform magnetic field. *Phys Rev E* (2006) **73**:066405. doi: 10.1103/PhysRevE.73.066405
9. Byhring HS, Charles C, Fredriksen Å, Boswell RW. Double layer in an expanding plasma: simultaneous upstream and downstream measurements. *Phys Plasmas* (2008) **15**:102113. doi: 10.1063/1.3002396
10. Takahashi K, Charles C, Boswell R, Cox W, Hatakeyama R. Transport of energetic electrons in a magnetically expanding helicon double layer plasma. *Appl Phys Lett.* (2009) **94**:191503. doi: 10.1063/1.3136721
11. Baalrud SD, Lafleur T, Boswell RW, Charles C. Particle-in-cell simulations of a current-free double layer. *Phys Plasmas* (2011) **18**:063502. doi: 10.1063/1.3594565
12. Lieberman MA, Charles C. Theory for formation of a low-pressure, current-free double layer. *Phys Rev Lett.* (2006) **97**:045003. doi: 10.1103/PhysRevLett.97.045003
13. Meige A, Boswell RW, Charles C, Boeuf JP, Hagelaar G, Turner MM. One-dimensional simulation of an ion beam generated by a current-free double-Layer. *Plasma Sci IEEE Trans* (2005) **33**:334–5. doi: 10.1109/TPS.2005.844956
14. Charles C, Boswell RW, Hawkins R. Oblique double layers: a comparison between terrestrial and auroral measurements. *Phys Rev Lett.* (2009) **103**:095001. doi: 10.1103/PhysRevLett.103.095001
15. Takahashi K, Fujiwara T. Observation of weakly and strongly diverging ion beams in a magnetically expanding plasma. *Appl Phys Lett.* (2009) **94**:061502. doi: 10.1063/1.3080205
16. Takahashi K, Igarashi Y, Fujiwara T. Plane and hemispherical potential structures in magnetically expanding plasmas. *Appl Phys Lett.* (2010) **97**:041501. doi: 10.1063/1.3467857
17. Singh N. Current-free double layers: a review. *Phys Plasmas* (2011) **18**:122105. doi: 10.1063/1.3664321
18. Takahashi K, Itoh Y, Fujiwara T. Operation of a permanent-magnets-expanding plasma source connected to a large-volume diffusion chamber. *J Phys D Appl Phys.* (2011) **44**:015204. doi: 10.1088/0022-3727/44/1/015204
19. Saha SK, Raychaudhuri S, Chowdhury S, Janaki MS, Hui AK. Two-dimensional double layer in plasma in a diverging magnetic field. *Phys Plasmas* (2012) **19**:092502. doi: 10.1063/1.4752074
20. Cox W, Charles C, Boswell RW, Hawkins R. Spatial retarding field energy analyzer measurements downstream of a helicon double layer plasma. *Appl Phys Lett.* (2008) **93**(7):071505. doi: 10.1063/1.2965866
21. Charles C. High density conics in a magnetically expanding helicon plasma. *Appl Phys Lett.* (2010) **96**:051502. doi: 10.1063/1.3309668
22. Saha SK, Chowdhury S, Janaki MS, Ghosh A, Hui AK, Raychaudhuri S. Plasma density accumulation on a conical surface for diffusion along a diverging magnetic field. *Phys Plasmas* (2014) **21**:043502. doi: 10.1063/1.4870758
23. Gahan D, Daniels S, Hayden C, Sullivan DO, Hopkins MB. Characterization of an asymmetric parallel plate radio-frequency discharge using a retarding field energy analyzer. *Plasma Sour Sci Technol.* (2012) **21**:015002. doi: 10.1088/0963-0252/21/1/015002
24. Gahan D, Dolinaj B, Hopkins MB. Comparison of plasma parameters determined with a Langmuir probe and with a retarding field energy analyzer. *Plasma Sour Sci Technol.* (2008) **17**:035026. doi: 10.1088/0963-0252/17/3/035026
25. Conway GD, Perry AJ, Boswell RW. Evolution of ion and electron energy distributions in pulsed helicon plasma discharges. *Plasma Sour Sci Technol.* (1998) **7**:337. doi: 10.1088/0963-0252/7/3/012
26. Lafleur T, Charles C, Boswell RW. Electron temperature characterization and power balance in a low magnetic field helicon mode. *J Phys D Appl Phys.* (2011) **44**:185204. doi: 10.1088/0022-3727/44/18/185204
27. Fredriksen Å, Mishra LN, Gulbrandsen N, Miloch WJ. On the measurement of subsonic flow in a capacitively coupled helicon plasma source. *J Phys.* (2010) **257**:012019. doi: 10.1088/1742-6596/257/1/012019
28. Boswell RW. Very efficient plasma generation by whistler waves near the lower hybrid frequency. *Plasma Phys Control Fusion* (1984) **26**:1147. doi: 10.1088/0741-3335/26/10/001
29. Gulbrandsen N, Fredriksen Å, Carr J, Scime E. A comparison of ion beam measurements by retarding field energy analyzer and laser induced fluorescence in helicon plasma devices. *Phys Plasmas* (2015) **22**:033505. doi: 10.1063/1.4913990
30. Gahan D, Daniels S, Hayden C, Scullin P, O'Sullivan D, Pei YT, et al. Ion energy distribution measurements in rf and pulsed dc plasma discharges. *Plasma Sour Sci Technol.* (2012) **21**:024004. doi: 10.1088/0963-0252/21/2/024004
31. Ingram SG, Braithwaite NSJ. Ion and electron energy analysis at a surface in an RF discharge. *J Phys Appl Phys.* (1988) **21**:1496. doi: 10.1088/0022-3727/21/10/005
32. Sudit ID, Chen FF. RF compensated probes for high-density discharges. *Plasma Sour Sci Technol.* (1994) **3**:162. doi: 10.1088/0963-0252/3/2/006
33. Kemp RF, Sellen JM. Plasma potential measurements by electron emissive probes. *Rev Sci Instr.* (1966) **37**:455–61. doi: 10.1063/1.1720213
34. Wang EY, Hershkowitz N, Intrator T, Forest C. Techniques for using emitting probes for potential measurement in rf plasmas. *Rev Sci Instr.* (1986) **57**:2425–31. doi: 10.1063/1.1139088
35. Ye MY, Takamura S. Effect of space-charge limited emission on measurements of plasma potential using emissive probes. *Phys Plasmas* (2000) **7**:3457–63. doi: 10.1063/1.874210
36. Sheehan JP, Raitses Y, Hershkowitz N, Kaganovich I, Fisch NJ. A comparison of emissive probe techniques for electric potential measurements in a complex plasma. *Phys Plasmas* (2011) **18**:073501. doi: 10.1063/1.3601354
37. Magnus F, Gudmundsson JT. Digital smoothing of the Langmuir probe I-V characteristic. *Rev Sci Instr.* (2008) **79**:073503. doi: 10.1063/1.2956970
38. Miloch WJ, Gulbrandsen N, Mishra LN, Fredriksen Å. Ion velocity distributions in the sheath and presheath of a biased object in plasma. *Phys Plasmas* (2011) **18**:083502. doi: 10.1063/1.3614520
39. Gulbrandsen N, Miloch WJ, Fredriksen Å. Interpretation of ion velocity distributions measured with a grounded retarding field energy analyzer (RFEA) in an inductively coupled helicon plasma. *Contr Plasma Phys.* (2013) **53**:27–32. doi: 10.1002/ctpp.201310005

Conflict of Interest Statement: The authors declare that the research was conducted in the absence of any commercial or financial relationships that could be construed as a potential conflict of interest.

The handling Editor declared a past co-authorship with one of the authors ÅF and states that the process nevertheless met the standards of a fair and objective review.

frontiers in Physics

ORIGINAL RESEARCH
published: 06 December 2018
doi: 10.3389/fphy.2018.00139

Social Learning of Prescribing Behavior Can Promote Population Optimum of Antibiotic Use

Xingru Chen[1] *and Feng Fu*[1,2]*

[1] Department of Mathematics, Dartmouth College, Hanover, NH, United States, [2] Department of Biomedical Data Science, Geisel School of Medicine at Dartmouth, Lebanon, NH, United States

The rise and spread of antibiotic resistance causes worsening medical cost and mortality especially for life-threatening bacteria infections, thereby posing a major threat to global health. Prescribing behavior of physicians is one of the important factors impacting the underlying dynamics of resistance evolution. It remains unclear when individual prescribing decisions can lead to the overuse of antibiotics on the population level, and whether population optimum of antibiotic use can be reached through an adaptive social learning process that governs the evolution of prescribing norm. Here we study a behavior-disease interaction model, specifically incorporating a feedback loop between prescription behavior and resistance evolution. We identify the conditions under which antibiotic resistance can evolve as a result of the tragedy of the commons in antibiotic overuse. Furthermore, we show that fast social learning that adjusts prescribing behavior in prompt response to resistance evolution can steer out cyclic oscillations of antibiotic usage quickly toward the stable population optimum of prescribing. Our work demonstrates that provision of prompt feedback to prescribing behavior with the collective consequences of treatment decisions and costs that are associated with resistance helps curb the overuse of antibiotics.

Keywords: evolutionary dynamics, game theory, antibiotic resistance, public health, cooperation

OPEN ACCESS

Edited by:
Matjaž Perc,
University of Maribor, Slovenia

Reviewed by:
Xiaojie Chen,
University of Electronic Science and Technology of China, China
Chengyi Xia,
Tianjin University of Technology, China

***Correspondence:**
Feng Fu
fufeng@gmail.com

Specialty section:
This article was submitted to Social Physics, a section of the journal Frontiers in Physics

Received: *18 October 2018*
Accepted: *21 November 2018*
Published: *06 December 2018*

Citation:
Chen X and Fu F (2018) Social Learning of Prescribing Behavior Can Promote Population Optimum of Antibiotic Use. Front. Phys. 6:139. doi: 10.3389/fphy.2018.00139

1. INTRODUCTION

Antibiotics have been used primarily as human medicine for the treatment and prevention of bacterial infections for about 80 years; later as a growth promoter applied in animal feeds, for about 65 years [1, 2]. In this period, it has proved itself incredibly powerful to benefit individual patients, to suppress the overall epidemic of diseases and also to expand livestock production [3–5]. However, the wide use of antibiotics in our society is tagged along by the development of resistance, first identified in the 1940's [3, 6–19].

In recent years, the number of new antibiotics approved by the U.S. Food and Drug Administration (FDA) has been dramatically reduced, suggesting an "EROOM" law (a phenomenon in contrast to the Moore's law) [11, 20, 21]. Even worse, the time period of an antibiotic's effectiveness from its introduction to first resistance identified becomes increasingly short (**Figure 1A**; see data sources in section 1 of the *SI*, **Data Sheet 1**). Moreover, superbugs (multi-drug resistant bacteria) such as Methicillin-resistant *S. aureus* (MRSA) seem to outsmart our efforts to treat infectious diseases [6–8, 12, 13, 16, 22–25]. Antibiotic resistance is associated with worsening mortality and medical costs [26]. As a consequence, we are confronted with antibiotic resistance crisis, at the risk of running out of effective antibiotics for infection treatments [19].

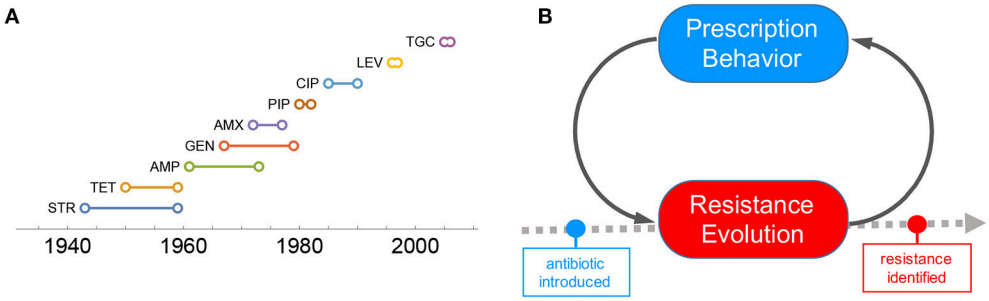

FIGURE 1 | Problem of antibiotic resistance. **(A)** Timeline plot of resistance emergence for common antibiotics. The time period of an antibiotic's effectiveness from its introduction to first resistance identified becomes increasingly short. **(B)** Prescribing behavior is one of the driving factors contributing to the fast emergence of resistance. The interaction between resistance evolution and prescripting behavior plays an important role in determining the timeline of resistance emergence.

One of the important factors contributing to the the fast emergence of resistance is overprescribing [27–30]. High demand for antibiotics driven by individual self-interest is not necessarily aligned with the social optimum of antibiotic consumption. Under certain conditions, the overuse of antibiotics can lead to the tragedy of the commons [24, 31–34]. Therefore, it is of significant public health interest to understand and manage antibiotic resistance from this behavioral perspective.

Here, we focus on the interaction of prescription behavior and resistance evolution through a feedback loop (**Figure 1B**): collective outcomes of prescribing decisions affect the underlying resistance evolution, which in turn influences prescription behavior. The behavior-disease interaction model of this kind is simple yet proof of concept [35–38], and sheds light on how social learning of prescription behavior in response to the underlying evolutionary dynamics of resistance can render population optimum of antibiotic use.

2. MODEL

Previous work demonstrates that social learning promotes the emergence of institutions for governing the commons [39, 40]. Inspired by this, we will explore how social learning of prescription behavior in response to the underlying evolutionary dynamics of resistance can promote population optimum of antibiotics usage. We will study a behavior-disease interaction model that incorporates a feedback loop between prescription behavior and resistance evolution:

Here, b denotes the birth rate per capita, which is set equal to the death rate d; β_s and β_m are the transmission rates of the two strains; γ_s^0, γ_s^t, γ_m^0, and γ_m^t are the respective recovery rates of different infection cases (infected with sensitive or resistant strain; untreated or treated); ϵ_s and ϵ_m are the effectivenesses of the antibiotics for treating sensitive and resistant infections, respectively. S, I and R are the fractions of susceptible, infected and recovered individuals in the population with I_s^0, I_s^t, I_m^0, and I_m^t denoting the four infection cases (infected with sensitive or resistant strains, and untreated or treated); R_s and R_m the two recovery cases, respectively. The two parameters μ_s and μ_m indicates the mutation rates between the two strains.

As given in the last equation (Equation 1), prescription norm changes in response to the actual payoffs of individual prescribing vs. non-prescribing behavior (f_A vs. f_B), which are determined by disease prevalence and resistance evolution on the population level [41]. This feedback loop between prescription behavior and resistance evolution constitutes an adaptive social learning process in which the society adjusts antibiotic use in response to the underlying resistance evolution.

We focus on quantifying the extent to which the (over)use of antibiotics would cause the emergence of resistance in the long run (see section 4). To do so, we introduce the parameter θ to denote the presentation rate of infected individuals who bring their condition to a physician's attention and seek antibiotic treatment for their illness (In this regard, the θ value is determined by individual disease awareness and health-seeking behavior). To account for prescribing norm of physicians, we use p to denote the likelihood that each patient at presentation

$$
\begin{cases}
\frac{dS}{dt} = b - \beta_s S[I_s^0 + (1-\epsilon_s)I_s^t] - \beta_m S[I_m^0 + (1-\epsilon_m)I_m^t] - dS, \\
\frac{dI_s^0}{dt} = \beta_s(1-\mu_s)S[I_s^0 + (1-\epsilon_s)I_s^t] + \beta_m\mu_m S[I_m^0 + (1-\epsilon_m)I_m^t] - p\theta I_s^0 - \gamma_s^0 I_s^0 - dI_s^0, \\
\frac{dI_s^t}{dt} = p\theta I_s^0 - \gamma_s^t I_s^t - dI_s^t, \\
\frac{dI_m^0}{dt} = \beta_s\mu_s S[I_s^0 + (1-\epsilon_s)I_s^t] + \beta_m(1-\mu_m)S[I_m^0 + (1-\epsilon_m)I_m^t] - p\theta I_m^0 - \gamma_m^0 I_m^0 - dI_m^0, \\
\frac{dI_m^t}{dt} = p\theta I_m^0 - \gamma_m^t I_m^t - dI_m^t, \\
\frac{dR_s}{dt} = \gamma_s^0 I_s^0 + \gamma_s^t I_s^t - dR_s, \\
\frac{dR_m}{dt} = \gamma_m^0 I_m^0 + \gamma_m^t I_m^t - dR_m, \\
\frac{dp}{dt} = \omega p(1-p)(f_A - f_B).
\end{cases}
\tag{1}
$$

is prescribed antibiotic treatment, $0 \leq p \leq 1$. Thus, the overall prescribing rate, $p\theta$, mediates the selection pressure on resistance that is attributed to collective consequence of prescription behavior.

3. RESULTS AND DISCUSSION

We use the next-generation approach to calculate basic reproductive ratios for both strains, $\mathcal{R}_s$ and $\mathcal{R}_m$ in closed-form (see section 2 of the *SI* for details, **Data Sheet 1**). We assume that resistance is costly in the absence of treatment, but confers an advantage in the presence of treatment; that is, resistance compromises the efficacy of treatment, $0 \leq \epsilon_m < 1$. Comparing $\mathcal{R}_s$ and $\mathcal{R}_m$ allows us to answer questions of interest, such as predicting whether resistance can evolve in the long run.

For simplicity, we first consider resistance evolution under full treatment ($p = 1$), in which infected individuals, once seen by medical professionals at their presentation, unvaryingly receive antibiotic treatment. As shown in **Figure 2A**, we characterize the conditions for resistance evolution in the parameter space (θ, ϵ_m). For small θ values below a threshold (blue region in **Figure 2A**), neither can the disease be eradicated, nor can resistance evolve. Disease can be eradicated for high θ and ϵ_m (yellow region in **Figure 2A**). However, for combinations of intermediate θ and low ϵ_m (red region in **Figure 2A**), resistance evolves and leads to disease escape despite full treatment.

To further gain intuitive understanding of how resistance evolution depends on antibiotic use, we plot the disease prevalence with respect to treatment probability p, corresponding to the three scenarios as colored in **Figure 2A**. The sensitive strain is predominant for all $0 \leq p \leq 1$, whereas the resistant strain is maintained at low frequency purely by the mutation-selection equilibrium (**Figure 2B**). Disease can be eradicated for sufficiently high treatment rate and resistance has no chance to evolve (**Figure 2C**). In **Figure 2D**, disease eradication is impossible due to the emergence of resistance that greatly comprises the efficacy of treatment; resistance can be selected for p above a critical threshold $p > p_h$ (see section 3 of the *SI*, **Data Sheet 1**), and as a consequence, the predominant incidence of infections switches from sensitive to resistant strains.

Let us now turn our attention to this last scenario where resistance evolution is inevitable for $p > p_h$. Empirical evidence shows that there exists a threshold in prescription rate above which sustained resistance can cause huge public health crisis [42]. To determine the population optimum of antibiotic use, we need to take into account the impact of resistance on the cost-benefit analysis of antibiotic treatment (**Figure 3**). The cost of sensitive infection, if treated, can be mitigated. In contrast, resistant infections may greatly exacerbate the overall cost for both treated and untreated cases [43]. Under these conditions, the overall social burden of the disease can be minimized at $p = p_h$ (i.e., population optimum). Although the disease prevalence and thus the risk of infection for susceptible individuals can be lowered by overprescribing beyond p_h (**Figure 3A**), the cost associated with resistance is much greater than the benefit, if any, that full treatment could provide (**Figure 3B**).

Despite these population-level considerations, individual self-interest can cause antibiotic overuse, thereby leading to a tragedy of the commons. This is largely due to the disconnect between individual behavior and population-level resistance in prescribing decision-makings. Therefore, curbing antibiotic overuse requires provision of feedback to individual prescribing behavior with the social costs and consequences of their collective action. In light of this, we investigate whether population optimum of antibiotic use can be reached if the society learns from the collective consequences of treatment decisions and costs that are associated with resistance and accordingly adjusts prescription behavior.

We assume disease dynamics coevolves with a social norm that governs prescription behavior (see section 4 of the *SI*, **Data Sheet 1**). We use evolutionary game theory to study the evolution of prescription norm [39, 41]. Prescription norm changes in response to the actual payoffs of individual prescribing vs. non-prescribing behavior, which are determined by disease prevalence and resistance evolution on the population level. This feedback loop between prescription behavior and resistance evolution constitutes an adaptive social learning process in which the society adjusts antibiotic use in response to the underlying resistance evolution.

We find that how swiftly the society responds to the underlying resistance evolution has an impact on the coevolutionary dynamics (**Figure 4**). Slow social learning leads to prolonged oscillatory dynamics of overprescribing and underprescribing, and thus gives chance for resistance to accumulate and build up in the population, causing resurgences of marked resistance prevalence alternated with sensitive infections (**Figure 4A**). In stark contrast, fast social learning can help the population steer out cyclic oscillations of antibiotic use due to overcorrection. In this latter case, the society adapts prescription norm so quickly that resistance has no chance to grow into pronounced prevalence as it is outpaced by the change in prescribing behavior. Besides, fast social learning helps the society settle on a social norm that reaches the population optimum of antibiotic use (**Figure 4B**).

We demonstrate that social learning without centralized institutions can maneuver the population toward a socially optimal policy of prescribing, therefore helping curb the overuse of antibiotics. Our theoretical results are in line with recent trial findings that highlight the importance of provision of social norm feedback in reducing antibiotic overuse [29]. Taken together, in order to reach sustainable use of antibiotics, it is important to promote awareness of the population problem of resistance by providing prompt feedback to prescribing behavior with the social cost of resistance.

Owing to the drastic slowdown of new drug discoveries [21, 44], managing resistance evolution with an emphasis on human factors, as we demonstrate here, seems to be necessary and feasible [45]. Prior studies suggest that the consumption of antibiotics and the patterns in which different agents are deployed directly impact the frequency of resistance and the number of ineffective antibiotics [42, 46, 47]. To inform rational

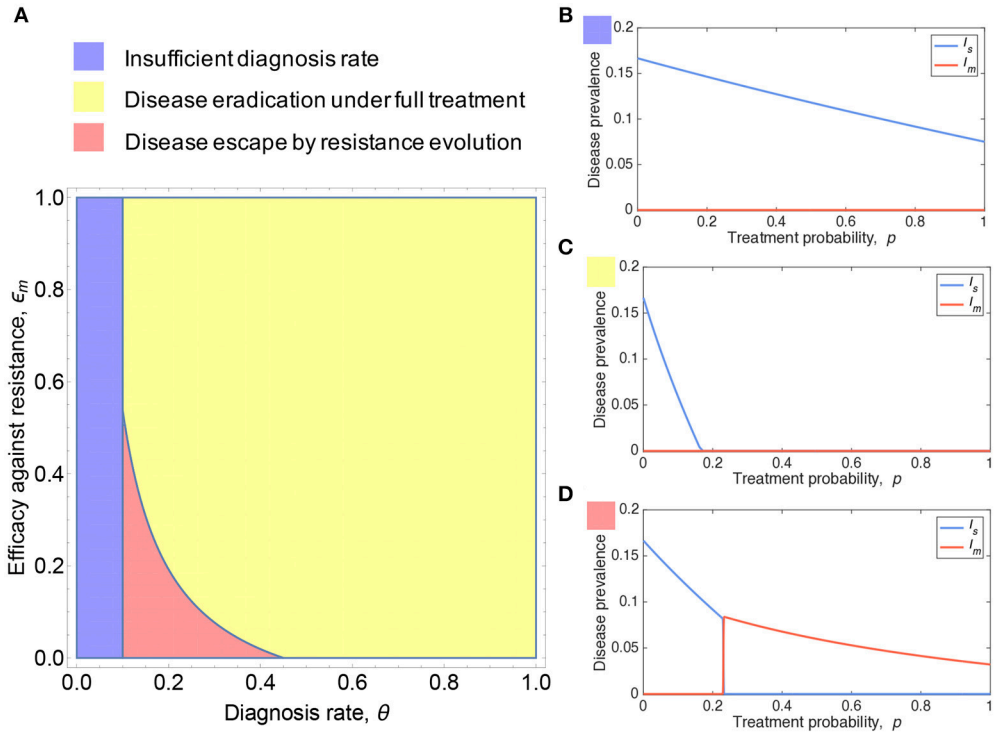

FIGURE 2 | Resistance evolution and antibiotic usage. **(A)** Shown is the parameter region of presentation rate θ and efficacy against resistance ϵ_m under which antibiotic resistance can emerge. **(B–D)** plot the prevalence of sensitive and resistant strains as a function of treatment probability p. Resistance can be favored under sufficiently high treatment coverage and as a consequence, the tragedy of the commons in antibiotic overuse can occur. Parameters: $b = 0.1$, $\beta_S = 0.3$, $\beta_m = 0.26$, $\gamma_s^0 = \gamma_m^0 = 0.1$, $\gamma_s^t = 0.3$, $\gamma_m^t = 0.2$, $\epsilon_S = 1$, **(A)** $\epsilon_m = 0$, **(B)** $\epsilon_m = 0.6$, $\theta = 0.05$, **(C)** $\epsilon_m = 0.8$, $\theta = 0.6$, **(D)** $\epsilon_m = 0$, $\theta = 0.2$, **(B–D)** $\mu_S = \mu_m = 10^{-6}$.

use of antibiotics, efforts should be focused on developing new diagnostic technologies and strategies for reducing the inappropriate use of antibiotics [48], determining the optimal timing of deployment sequence for existing drugs [49, 50], and optimizing combination therapies [51, 52]. Moreover, promoting and enforcing infection control procedures in hospitals can prevent the spread of resistance and mitigate the impact of resistance on society [9, 15, 16, 27, 45, 48, 50, 53, 54]. Along these lines, it is worthwhile for future study to incorporate population structure [55, 56] and multiple drugs [57–59] in the coevolutionary dynamics of prescribing behavior and multi-drug resistance.

The socially optimum use of antibiotics implies a second order of dilemma—not every sickness should be treated, but who on earth deserves the treatment and who would have to forgo? This consideration leads to the ethics dilemma of accessibility of antibiotics, an important topic worthy of further investigation. Reducing antibiotics usage via national guidelines has been found to lead to significant decreases in resistance [46, 47], yet denials or approvals of antibiotic treatment seem to be determined by an arbitrary trade-off between preventing resistance and treating infected patients [20]. With multiple interest groups such as pharmaceutical industry, public institutions as well as patients themselves involved in the problem, it is of fundamental interest to look into the issues of supervising the common pool resources [60–62] and enhancing collaborative efforts through the behavioral perspective [18, 24].

4. METHODS AND ANALYSIS

We begin our analysis with characterizing the conditions for resistance evolution for given levels of antibiotic use p in the long run.

4.1. Basic Reproductive Ratios

The competition dynamics of sensitive vs. resistant strains is described by the evolutionary epidemiological model, as given in Equation (1). The basic reproductive ratios $\mathcal{R}_s$ and $\mathcal{R}_m$ of the two strains can be determined by the spectral radius of the next-generation operator FV^{-1}, where F is the reproduction matrix and V the state transition matrix [63–65]. We obtain that

$$\mathcal{R}_s = \frac{\beta_s(\gamma_s^t + b) + \beta_s(1-\epsilon_s)p\theta}{(\gamma_s^t + b)(p\theta + \gamma_s^0 + b)}, \tag{2}$$

$$\mathcal{R}_m = \frac{\beta_m(\gamma_m^t + b) + \beta_m(1-\epsilon_m)p\theta}{(\gamma_m^t + b)(p\theta + \gamma_m^0 + b)}. \tag{3}$$

We assume that resistance incurs a fitness penalty, so that the transmission rates $\beta_s > \beta_m$. Despite the fact that laboratory studies revealed a scenario where compensatory

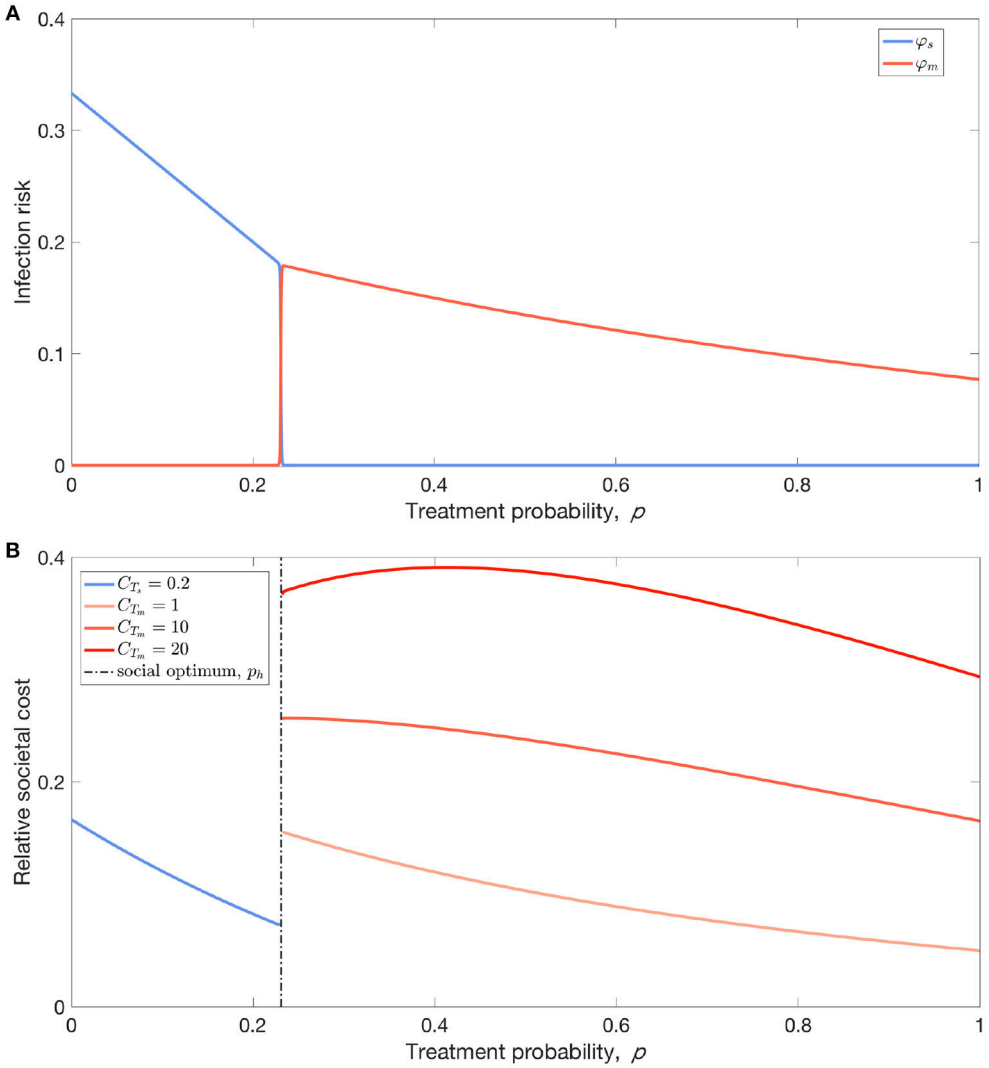

FIGURE 3 | Cost-benefit analysis of antibiotic usage. **(A)** From the perspective of susceptible individuals, their infection risk reduces with increasing treatment probability (coverage) p, but there exists a threshold of treatment coverage, p_h, above which the risk of infection almost exclusively comes from resistant strain instead of sensitive stain. **(B)** Accounting for the differing costs of treating patients infected with sensitive and resistant strains, the threshold p_h corresponds to the social optimum of antibiotic usage: the total societal disease burden is decreasing with p for $p < p_h$, but followed by a surge in the total cost of infection due to resistance. Parameters: **(A,B)** $b = 0.1$, $\beta_S = 0.3$, $\beta_m = 0.26$, $\gamma_s^0 = \gamma_m^0 = 0.1$, $\gamma_s^t = 0.3$, $\gamma_m^t = 0.2$, $\epsilon_s = 1$, $\epsilon_m = 0$, $\theta = 0.2$, $\mu_s = \mu_m = 10^{-6}$, **(B)** relative social burden of the disease: $C_{I_s} = 1$, $C_{T_s} = 0.2$, $B_{T_s} = 0.3$, $C_{I_m} = 2$, $B_{T_m} = 0.1$.

evolution (resistant bacteria ameliorating the costs by acquiring fitness-compensatory mutations) and cost-free resistances can slow down the primary driver for reversibility and that co-selection between the resistance mechanism and other selected markers can delay any latent reversibility driven by fitness costs *in vitro* [66], clinical studies have found that the compensatory adaptation is not effective *in vivo*, which is in line with our assumption [67]. Theoretical arguments and experimental results, in addition, provide basis for that the fitness costs of resistance is critical to the displacement of resistant strains with sensitive ones [66, 67].

Both $\mathcal{R}_s(p)$ and $\mathcal{R}_m(p)$ are decreasing functions of p under our model assumptions (see *SI*, **Data Sheet 1**). We demonstrate that the graphs of the two basic reproductive numbers will vary with values of their endpoints $\mathcal{R}_s(1)$ and $\mathcal{R}_m(1)$ (see the *SI* for details). Without loss of generality, we scrutinize the following three cases: (I) $R_s > 1$; (II-a) $R_s(1) < 1$ and $R_m(1) < 1$; (II-b) $R_s(1) < 1 < R_m(1)$. The case noteworthy in practice is the last one, in which resistant strains predominate and even full treatment can not eradicate the disease.

For a better understanding of the disease dynamics in case (II-b), we perform a further investigation of the relations among

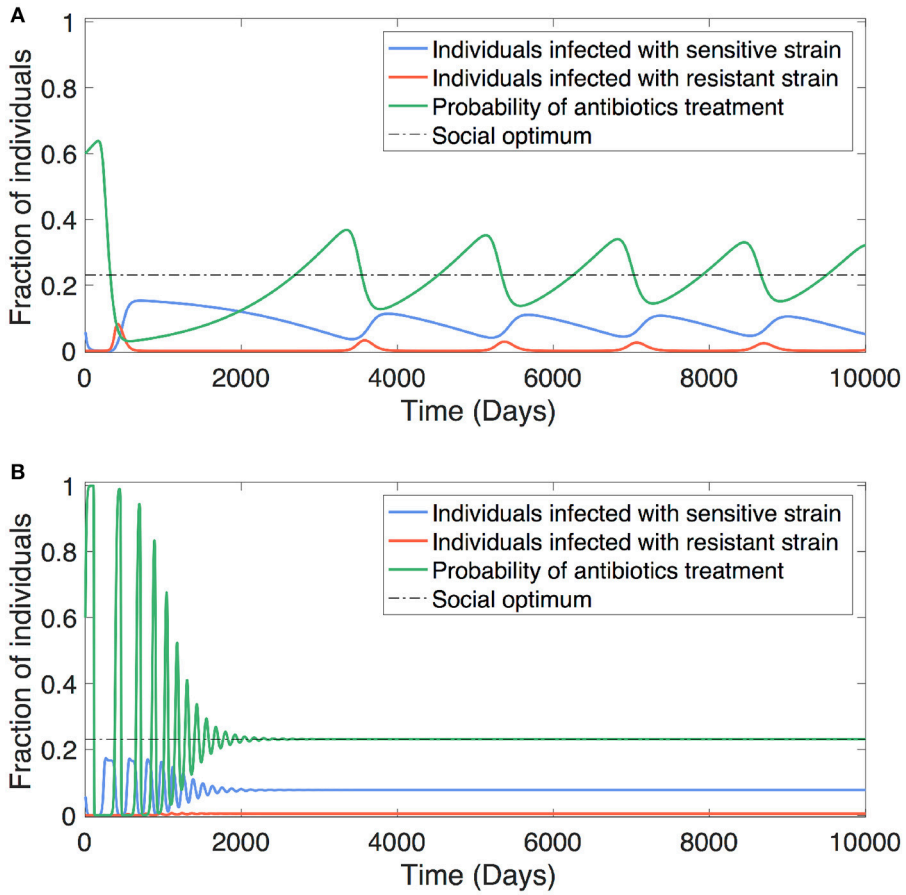

FIGURE 4 | Social learning impacts antibiotic usage. The antibiotic usage behavior can be adjusted in response to the underlying dynamics of resistance evolution. The convergence of optimum antibiotic usage is determined by how promptly the society learns from the collective consequences of treatment decisions and costs that are associated with resistance. **(A)** Slow learning leads to oscillatory dynamics of antibiotic usage (between overuse and lesser use) together with alternating dominance of resistant and sensitive strains. **(B)** Fast learning can steer out cyclic oscillations of antibiotic usage due to overcorrection, and therefore helps the society quickly reach socially optimal usage. Parameters: $b = 0.1$, $\beta_S = 0.3$, $\beta_m = 0.26$, $\gamma_S^0 = \gamma_m^0 = 0.1$, $\gamma_S^t = 0.3$, $\gamma_m^t = 0.2$, $\epsilon_S = 1$, $\epsilon_m = 0$, $\theta = 0.2$, $\mu_S = \mu_m = 10^{-6}$, relative social burden of the disease: $C_{I_S} = 1$, $C_{T_S} = 0.2$, $B_{T_S} = 0.3$, $C_{I_m} = 2$, $C_{T_m} = 20$, $B_{T_m} = 0.1$, **(A)** $\omega = 0.001$, **(B)** $\omega = 0.1$.

those parameters, where the presentation rates θ_s and θ_m for the two infected cases are seen as independent. Substituting $p = 1$ into (2) and (3) and combining with the inequality $R_s(1) < 1 < R_m(1)$, we derive an equivalent condition for case (II-b) to occur:

$$\begin{cases} 0 \le \epsilon_s \le 1, & \text{if } \theta_s > \theta_s^*, \\ \epsilon_s^* < \epsilon_s \le 1, & \text{if } \theta_s < \theta_s^*. \end{cases} \quad \text{and} \quad \begin{cases} 0 \le \epsilon_m \le 1, & \text{if } \theta_m < \theta_r^*, \\ 0 \le \epsilon_m < \epsilon_r^*, & \text{if } \theta_m > \theta_r^*. \end{cases} \tag{4}$$

The values of θ_s^*, ϵ_s^*, θ_r^* and ϵ_r^* are given in the *SI*. Therefore, to get the basic reproductive ratio below 1 and thus control the disease, we need θ_m to be greater than θ_m^* or ϵ_m greater than ϵ_m^*. The two solvents correspond to either patients presenting promptly after infection or introducing potent antibiotics in treatment.

Moreover, let p_h be the critical prescribing probability (which can be translated into treatment coverage, namely, the proportion of patients that are prescribed antibiotic treatment) at which the dominance of the two strains switches in case (II-b). For $\gamma_s^0 = \gamma_m^0$, we derive a simplified form

$$p_h = \frac{\beta_s - \beta_m}{\theta[\frac{\beta_m(1-\epsilon_m)}{\gamma_m^t + b} - \frac{\beta_s(1-\epsilon_s)}{\gamma_s^t + b}]}, \tag{5}$$

where p_h is referred to as the social optimum of antibiotic use (see details in section 3 of the *SI*, **Data Sheet 1**).

4.2. Cost-Benefit Analysis

When $p < p_h$, the sensitive strain dominates and the system converges to an equilibrium, of which we derive a closed form approximation $(\hat{S}, \hat{I_s^0}, \hat{I_s^t}, \hat{R_s})$; when $p > p_h$, the resistant strain dominates, with the system converging to another equilibrium, approximated by $(\hat{S}, \hat{I_m^0}, \hat{I_m^t}, \hat{R_m})$. We prove in the *SI* (**Data Sheet 1**) that S is increasing while I^0 and $I^0 + I^t$ are decreasing with respect to p for both equilibria.

For susceptible individuals, if the sensitive strain dominates, the infection probability at equilibrium is approximately

$$\varphi_s = \frac{\beta_s[\hat{I}_s^0 + (1-\epsilon_s)\hat{I}_s^t]}{\beta_s[\hat{I}_s^0 + (1-\epsilon_s)\hat{I}_s^t] + b}, \tag{6}$$

which can be simplified as $1 - \hat{S} = 1 - \frac{1}{\mathcal{R}_s}$. Analogously, if the resistant strain prevails, the infection probability at equilibrium is approximately

$$\varphi_m = \frac{\beta_m[\hat{I}_m^0 + (1-\epsilon_m)\hat{I}_m^t]}{\beta_m[\hat{I}_m^0 + (1-\epsilon_m)\hat{I}_m^t] + b} = 1 - \frac{1}{\mathcal{R}_m}. \tag{7}$$

Although the actual treatment cost can be determined only after treatment outcomes, it is expected that (1) sensitive strain claims lower sickness and treatment costs while it redounds to greater treatment benefit ($C_{I_s} < C_{I_m}$, $B_{T_s} > B_{T_m}$ and $C_{T_s} < C_{T_m}$), (2) treatment of patients with sensitive strains can mitigate the overall cost of infection ($C_{T_s} - C_{I_s} < B_{T_s}$), and in contrast (3) treatment of patients with resistant strains may exacerbate the overall cost of infection ($C_{T_m} - C_{I_m} > B_{T_m}$) [43].

When it comes to the population, the total social cost is a piecewise function

$$C_{\text{social}} = \begin{cases} (C_{T_s} - B_{T_s})(\hat{I}_s^0 + \hat{I}_s^t) + (C_{I_s} + B_{T_s} - C_{T_s})\hat{I}_s^0, & \text{when } p < p_h \\ (C_{T_m} - B_{T_m})(\hat{I}_m^0 + \hat{I}_m^t) - (C_{T_m} - C_{I_m} - B_{T_m})\hat{I}_m^t. & \text{when } p > p_h. \end{cases} \tag{8}$$

Invoking the monotonicity of $\hat{I}_s^0$ and $\hat{I}_s^0 + \hat{I}_s^t$, it is easy to verify that the total social cost C_{social} is decreasing when $p < p_h$. However, C_{social} may not be monotonic when $p > p_h$ (see detailed analysis in section 3 of the *SI*, **Data Sheet 1**).

4.3. Social Learning

We consider that prescription behavior coevolves with disease dynamics. We regard the problem as a two strategy game, prescribing (denoted as A) vs nonprescribing (B). The evolution of prescribing behavior can be described by:

$$\dot{p} = \omega p(1-p)(f_A - f_B), \tag{9}$$

where p is the frequency of prescribing A and $\dot{p}$ is referred to as the rate of prescription norm evolution, driven by the time scale parameter of social learning, ω.

The expected payoffs f_A and f_B are

$$f_A = \lambda_s(B_{T_s} - C_{T_s}) + \lambda_m(B_{T_m} - C_{T_m}), \tag{10}$$

$$f_B = \lambda_s(-C_{I_s}) + \lambda_m(-C_{I_m}), \tag{11}$$

with

$$\lambda_s = \frac{\beta_s[I_s^0 + (1-\epsilon_s)I_s^t]}{\beta_s[I_s^0 + (1-\epsilon_s)I_s^t] + \beta_m[I_m^0 + (1-\epsilon_m)I_m^t]}, \tag{12}$$

$$\lambda_m = \frac{\beta_m[I_m^0 + (1-\epsilon_m)I_m^t]}{\beta_s[I_s^0 + (1-\epsilon_s)I_s^t] + \beta_m[I_m^0 + (1-\epsilon_m)I_m^t]}. \tag{13}$$

Here λ_s and λ_m are the conditional probabilities of individuals being infected with sensitive or resistant strains, respectively.

Denote the fractions of individuals infected with sensitive and resistant strains by I_s and I_m, respectively ($I_s = I_s^0 + I_s^t$ and $I_m = I_m^0 + I_m^t$). The behavior of the disease dynamics are described by I_s and I_m while the prescribing norm is presented by p, all as functions of the time t.

AUTHOR CONTRIBUTIONS

XC and FF conceived the model, performed analyses, and wrote the manuscript.

ACKNOWLEDGMENTS

We are grateful for support from the G. Norman Albree Trust Fund, Dartmouth Faculty Startup Fund, Walter & Constance Burke Research Initiation Award and NIH Roybal Center Pilot Grant.

SUPPLEMENTARY MATERIAL

The Supplementary Material for this article can be found online at: https://www.frontiersin.org/articles/10.3389/fphy.2018.00139/full#supplementary-material

REFERENCES

1. Jones F, Ricke S. Observations on the history of the development of antimicrobials and their use in poultry feeds. *Poultry Sci.* (2003) **82**:613–17. doi: 10.1093/ps/82.4.613
2. Castanon J. History of the use of antibiotic as growth promoters in European poultry feeds. *Poultry Sci.* (2007) **86**:2466–71. doi: 10.3382/ps.2007-00249
3. Aminov RI. A brief history of the antibiotic era: lessons learned and challenges for the future. *Front Microbiol.* (2010) **1**:134. doi: 10.3389/fmicb.2010.00134
4. Zaffiri L, Gardner J, Toledo-Pereyra LH. History of antibiotics. From salvarsan to cephalosporins. *J Investigat Surg.* (2012) **25**:67–77. doi: 10.3109/08941939.2012.664099
5. Van Boeckel TP, Glennon EE, Chen D, Gilbert M, Robinson TP, Grenfell BT, et al. Reducing antimicrobial use in food animals. *Science* (2017) **357**:1350–2. doi: 10.1126/science.aao1495
6. Garrett L. *The Coming Plague: Newly Emerging Diseases in a World Out of Balance*. London: Penguin (1994).
7. Levy SB. The challenge of antibiotic resistance. *Sci Am.* (1998) **278**:46–53.
8. Walsh C. Molecular mechanisms that confer antibacterial drug resistance. *Nature* (2000) **406**:775. doi: 10.1038/35021219
9. Palumbi SR. Humans as the world's greatest evolutionary force. *Science* (2001) **293**:1786–90. doi: 10.1126/science.293.5536.1786
10. Levy SB. *The Antibiotic Paradox: How the Misuse of Antibiotics Destroys Their Curative Power*. Cambridge, MA: Da Capo Press (2002).
11. Norrby SR, Nord CE, Finch R, European Society of Clinical Microbiology and Infectious Diseases. Lack of development of new antimicrobial drugs: a potential serious threat to public health. *Lancet Infect Dis.* (2005) **5**:115–9. doi: 10.1016/S1473-3099(05)01283-1
12. Spellberg B, Guidos R, Gilbert D, Bradley J, Boucher HW, Scheld WM, et al. The epidemic of antibiotic-resistant infections: A call to action for the medical

community from the Infectious Diseases Society of America. *Clin Infect Dis.* (2008) **46**:155–64. doi: 10.1086/524891
13. Arias CA, Murray BE. Antibiotic-resistant bugs in the 21st century? a clinical super-challenge. *N Engl J Med.* (2009) **360**:439–43. doi: 10.1056/NEJMp0804651
14. Davies J, Davies D. Origins and evolution of antibiotic resistance. *Microbiol Mol Biol Rev.* (2010) **74**:417–33. doi: 10.1128/MMBR.00016-10
15. zur Wiesch PA, Kouyos R, Engelstädter J, Regoes RR, Bonhoeffer S. Population biological principles of drug-resistance evolution in infectious diseases. *Lancet Infect Dis.* (2011) **11**:236–47. doi: 10.1016/S1473-3099(10)70264-4
16. Rossolini GM, Arena F, Pecile P, Pollini S. Update on the antibiotic resistance crisis. *Curr Opin Pharmacol.* (2014) **18**:56–60. doi: 10.1016/j.coph.2014.09.006
17. Cully M. The politics of antibiotics. *Nature* (2014) **509**:S16. doi: 10.1038/509S16a
18. World Bank Group *Drug-resistant Infections: a Threat to Our Economic Future.* Discussion Draft Published online (2016).
19. Reardon S. Resistance to last-ditch antibiotic has spread farther than anticipated. *Nat News* (2017). doi: 10.1038/nature.2017.22140
20. Projan SJ. Why is big Pharma getting out of antibacterial drug discovery? *Curr Opin Microbiol.* (2003) **6**:427–30. doi: 10.1016/j.mib.2003.08.003
21. Scannell JW, Blanckley A, Boldon H, Warrington B. Diagnosing the decline in pharmaceutical R&D efficiency. *Nat Rev Drug Discov.* (2012) **11**(3):191–200. doi: 10.1038/nrd3681
22. Flores PA, Gordon SM. Vancomycin-resistant Staphylococcus aureus: an emerging public health threat. *Cleveland Clin J Med.* (1997) **64**:527–32.
23. Woodford N, Livermore DM. Infections caused by Gram-positive bacteria: a review of the global challenge. *J Infect.* (2009) **59**:S4–S16. doi: 10.1016/S0163-4453(09)60003-7
24. Conly J. Antimicrobial resistance: revisiting the tragedy of the commons. *Bull World Health Organ.* (2010) **88**:797–876. doi: 10.2471/BLT.10.031110
25. Magiorakos AP, Srinivasan A, Carey R, Carmeli Y, Falagas M, Giske C, et al. Multidrug-resistant, extensively drug-resistant and pandrug-resistant bacteria: an international expert proposal for interim standard definitions for acquired resistance. *Clin Microbiol Infect.* (2012) **18**:268–81. doi: 10.1111/j.1469-0691.2011.03570.x
26. Vaughan L, Wise K, Holmes-Maybank K, Charity P. *Antibiotic Resistant Threats in the United States.* Prevention for Disease Control (2013). Available online at: https://www.cdc.gov/drugresistance/pdf/ar-threats-2013-508.pdf
27. Nyquist AC, Gonzales R, Steiner JF, Sande MA. Antibiotic prescribing for children with colds, upper respiratory tract infections, and bronchitis. *JAMA* (1998) **279**:875–77.
28. Christakis NA, Fowler JH. Commentary–Contagion in prescribing behavior among networks of doctors. *Market Sci.* (2011) **30**:213–16. doi: 10.1287/mksc.1100.0595
29. Hallsworth M, Chadborn T, Sallis A, Sanders M, Berry D, Greaves F, et al. Provision of social norm feedback to high prescribers of antibiotics in general practice: a pragmatic national randomised controlled trial. *Lancet* (2016) **387**:1743–52. doi: 10.1016/S0140-6736(16)00215-4
30. Murshid MA, Mohaidin Z. Models and theories of prescribing decisions: a review and suggested a new model. *Pharm Pract (Granada)* (2017) **15**:990. doi: 10.18549/PharmPract.2017.02.990
31. Hardin G. The tragedy of the commons. *J Natl Resour Policy Res.* (2009) **1**:243–53. doi: 10.1126/science.162.3859.1243
32. Baquero F, Campos J. The tragedy of the commons in antimicrobial chemotherapy. *Rev Esp Quimioter.* (2003) **16**:11–3. Available online at: http://www.seq.es/seq/0214-3429/16/1/11.pdf
33. Foster KR, Grundmann H. Do we need to put society first? The potential for tragedy in antimicrobial resistance. *PLoS Med.* (2006) **3**:e29. doi: 10.1371/journal.pmed.0030029
34. Porco TC, Gao D, Scott JC, Shim E, Enanoria WT, Galvani AP, et al. When does overuse of antibiotics become a tragedy of the commons? *PLoS ONE* (2012) **7**:e46505.
35. Bauch CT. Imitation dynamics predict vaccinating behaviour. *Proc R Soc Lond B Biol Sci.* (2005) **272**:1669–75. doi: 10.1098/rspb.2005.3153
36. Fu F, Rosenbloom DI, Wang L, Nowak MA. Imitation dynamics of vaccination behaviour on social networks. *Proc R Soc Lond B Biol Sci.* (2011) **278**:42–9. doi: 10.1098/rspb.2010.1107
37. Zheng C, Xia C, Guo Q, Dehmer M. Interplay between SIR-based disease spreading and awareness diffusion on multiplex networks. *J Parall Distrib Comput.* (2018) **115**:20–8. doi: 10.1016/j.jpdc.2018.01.001
38. Sanz J, Xia CY, Meloni S, Moreno Y. Dynamics of interacting diseases. *Phys Rev X* (2014) **4**:41005. doi: 10.1103/PhysRevX.4.041005
39. Sigmund K, De Silva H, Traulsen A, Hauert C. Social learning promotes institutions for governing the commons. *Nature* (2010) **466**:861. doi: 10.1038/nature09203
40. Chen X, Szolnoki A. Punishment and inspection for governing the commons in a feedback-evolving game. *PLoS Computat Biol.* (2018) **14**:e1006347. doi: 10.1371/journal.pcbi.1006347
41. Nowak MA. *Evolutionary Dynamics*. Cambridge, MA: Harvard University Press (2006).
42. Baquero F. Trends in antibiotic resistance of respiratory pathogens: an analysis and commentary on a collaborative surveillance study. *J Antimicrob Chemother.* (1996) **38**(Suppl A):117–32.
43. Roberts RR, Hota B, Ahmad I, Scott RD, Foster SD, Abbasi F, et al. Hospital and societal costs of antimicrobial-resistant infections in a Chicago teaching hospital: implications for antibiotic stewardship. *Clin Infect Dis.* (2009) **49**:1175–84. doi: 10.1086/605630
44. Verhoef TI, Morris S. Cost-effectiveness and pricing of antibacterial drugs. *Chem Biol Drug Design.* (2015) **85**:4–13. doi: 10.1111/cbdd.12417
45. Levin BR. Minimizing potential resistance: a population dynamics view. *Clin Infect Dis.* (2001) **33**(Suppl 3):S161–9. doi: 10.1086/321843
46. Seppala H, Klaukka T, Vuopio-varkila J, Muotiala A, Helenius H, Lager K, et al. The effect of changes in the consumption of macrolide antibiotics on erythromycin resistance in group A streptococci in Finland. *N Engl J Med.* (1997) **337**:441–6.
47. Kristinsson KG. Effect of antimicrobial use and other risk factors on antimicrobial resistance in pneumococci. *Microb Drug Resist.* (1997) **3**:117–23.
48. Kanthor R. Detection drives defence. *Nature* (2014) **509**:S14. doi: 10.1038/509S14a
49. Wang YC, Lipsitch M. Upgrading antibiotic use within a class: tradeoff between resistance and treatment success. *Proc Natl Acad Sci USA.* (2006) **103**:9655–60. doi: 10.1073/pnas.0600636103
50. McClure NS, Day T. A theoretical examination of the relative importance of evolution management and drug development for managing resistance. *Proc R Soc Lond B Biol Sci.* (2014) **281**:20141861. doi: 10.1098/rspb.2014.1861
51. Bonhoeffer S, Lipsitch M, Levin BR. Evaluating treatment protocols to prevent antibiotic resistance. *Proc Natl Acad Sci USA.* (1997) **94**:12106–11.
52. Cottarel G, Wierzbowski J. Combination drugs, an emerging option for antibacterial therapy. *Trends Biotechnol.* (2007) **25**:547–55. doi: 10.1016/j.tibtech.2007.09.004
53. Smith DL, Levin SA, Laxminarayan R. Strategic interactions in multi-institutional epidemics of antibiotic resistance. *Proc Natl Acad Sci USA.* (2005) **102**:3153–8. doi: 10.1073/pnas.0409523102
54. World Health Organization. *Guidelines for the Reatment of Malaria.* World Health Organization (2015). Available online at: https://www.who.int/malaria/publications/atoz/9789241549127/en/
55. Leventhal GE, Hill AL, Nowak MA, Bonhoeffer S. Evolution and emergence of infectious diseases in theoretical and real-world networks. *Nat Commun.* (2015) **6**:6101. doi: 10.1038/ncomms7101
56. Chen X, Fu F, Wang L. Influence of different initial distributions on robust cooperation in scale-free networks: a comparative study. *Phys Lett A.* (2008) **372**:1161–7. doi: 10.1371/journal.pone.0171680
57. Lipsitch M, Samore MH. Antimicrobial use and antimicrobial resistance: a population perspective. *Emerging Infect Dis.* (2002) **8**:347. doi: 10.3201/eid0804.010312
58. Donskey CJ, Chowdhry TK, Hecker MT, Hoyen CK, Hanrahan JA, Hujer AM, et al. Effect of antibiotic therapy on the density of vancomycin-resistant enterococci in the stool of colonized patients. *N Engl J Med.* (2000) **343**:1925–32. doi: 10.1056/NEJM200012283432604
59. Enne VI, Livermore DM, Stephens P, Hall LM. Persistence of sulphonamide resistance in *Escherichia coli* in the UK despite national prescribing restriction. *Lancet* (2001) **357**:1325–8. doi: 10.1016/S0140-6736(00)04519-0

60. Wu T, Fu F, Zhang Y, Wang L. Adaptive role switching promotes fairness in networked ultimatum game. *Sci Reports* (2013) **3**:1550. doi: 10.1038/srep01550
61. Wu T, Fu F, Dou P, Wang L. Social influence promotes cooperation in the public goods game. *Phys A Statist Mechan Applic.* (2014) **413**:86–93. doi: 10.1016/j.physa.2014.06.040
62. Perc M, Jordan JJ, Rand DG, Wang Z, Boccaletti S, Szolnoki A. Statistical physics of human cooperation. *Phys Reports* (2017) **2**:281–93. doi: 10.1016/j.physrep.2017.05.004
63. Heffernan JM, Smith RJ, Wahl LM. Perspectives on the basic reproductive ratio. *J R Soc Interf.* (2005) **2**:281–93. doi: 10.1098/rsif.2005.0042
64. Diekmann O, Heesterbeek J, Roberts M. The Construction of Next-Generation Matrices for Compartmental Epidemic Models. *J R Soc Interface* (2009) **7**:873–85. doi: 10.1098/rsif.2009.0386
65. Hurford A, Cownden D, Day T. Next-generation tools for evolutionary invasion analyses. *J R Soc Interface*. (2010) **7**:561–71. doi: 10.1098/rsif.2009.0448
66. Andersson DI, Hughes D. Antibiotic resistance and its cost: is it possible to reverse resistance? *Nat Rev Microbiol.* (2010) **8**:260. doi: 10.1038/nrmicro2319
67. MacLean RC, Vogwill T. Limits to compensatory adaptation and the persistence of antibiotic resistance in pathogenic bacteria. *Evol Med Public Health.* (2014) **2015**:4–12. doi: 10.1093/emph/eou032

Conflict of Interest Statement: The authors declare that the research was conducted in the absence of any commercial or financial relationships that could be construed as a potential conflict of interest.

frontiers in Physics

ORIGINAL RESEARCH
published: 28 May 2018
doi: 10.3389/fphy.2018.00050

Determination of Polar Cap Boundary for the Substorm Event of 8 March 2008

Chi Wang[1,2]*, *Jiangyan Wang*[1,2], *Ramon Lopez*[3], *Hui Li*[1], *Jiaojiao Zhang*[1] and *Binbin Tang*[1]

[1] State Key Laboratory of Space Weather, National Space Science Center, Chinese Academy of Sciences, Beijing, China, [2] College of Earth and Planetary Science, University of Chinese Academy of Sciences, Beijing, China, [3] Department of Physics, The University of Texas at Arlington, Arlington, TX, United States

The polar cap boundary (PCB) is a fundamental indicator of magnetospheric activities especially during a substorm cycle. Taking a period on 8 March 2008 as an example, we investigate the location of PCB and its dynamics during a substorm event. The PCB location is determined from the Piecewise Parabolic Method with a Lagrangian Remap (PPMLR) -Magnetohydrodynamic (MHD) simulation data and Defense Meteorological Satellite Program (DMSP) observations, respectively. Model-observation comparison indicates that the PPMLR-MHD model gives a reliable estimate of PCB location during a complex substorm sequence. We further analyze the evolution of PCB in that period. The polar cap expands under southward interplanetary magnetic field (IMF), since the low-latitude dayside reconnection produces new open magnetic flux. Meanwhile, more solar wind energy enters and stores in the magnetosphere with the decreasing SML (SuperMAG Auroral Lower) index. After the substorm expansion onset, the polar cap contracts for a while due to the explosive increase of nightside reconnection. When the IMF direction turns northward, the polar cap contracts continuously, since the dayside reconnection ceases and no more open magnetic flux are supplied, and the storage energy in the magnetosphere releases with the increasing SML index. The model results are in good accord with the features from observations.

Keywords: polar cap boundary, MHD simulation, substorm, DMSP observations, magnetic reconnection, open magnetic flux

OPEN ACCESS

Edited by:
Hermann Lühr,
Helmholtz-Zentrum Potsdam Deutsches Geoforschungszentrum (GFZ), Germany

Reviewed by:
Alexei V. Dmitriev,
National Central University, Taiwan
Arnaud Masson,
European Space Astronomy Centre (ESAC), Spain

***Correspondence:**
Chi Wang
cw@spaceweather.ac.cn

Specialty section:
This article was submitted to Space Physics, a section of the journal Frontiers in Physics

Received: *25 February 2018*
Accepted: *09 May 2018*
Published: *28 May 2018*

Citation:
Wang C, Wang J, Lopez R, Li H, Zhang J and Tang B (2018) Determination of Polar Cap Boundary for the Substorm Event of 8 March 2008. Front. Phys. 6:50. doi: 10.3389/fphy.2018.00050

INTRODUCTION

The high-latitude polar ionosphere has two characterized regions, namely the polar cap and the auroral oval. In the auroral oval, the geomagnetic field lines are closed and map to the plasma sheet and the plasma sheet boundary layer in the magnetosphere, whereas the field lines in the polar cap are open and connect to the solar wind. The separatrix boundary which separates these two basically different magnetic and plasma domains is named as polar cap boundary (PCB).

The polar cap region connects the interplanetary space with geospace. The variations of PCB location and polar cap area reflect the balance between the dayside merging and nightside reconnection [1, 2]. The dayside reconnection opens the original closed geomagnetic field lines, thus the polar cap area will increase and PCB will move to lower latitude with the increasing

dayside reconnection rate. On the other hand, the nightside reconnection closes the open field lines. The polar cap area will decrease, and PCB will move to higher latitude with the increasing nightside reconnection rate. Since the upstream solar wind conditions have a major influence on the reconnection of magnetopause/magnetotail, its variations may lead to the dynamics of PCB. Especially, the Y component of IMF can cause an asymmetry of the two-cell plasma convection pattern at the high-latitude ionosphere (e.g., [3, 4]), thereby the dawn-dusk asymmetry of cutoff latitudes for protons and electrons [5], and polar cap boundary (e.g., [6, 7]). In many studies, the polar cap boundary and area were used as a diagnostic of magnetospheric activities specifically during a substorm cycle (e.g., [8–13]).

The magnetospheric substorm is a brief disturbance in the Earth's magnetosphere. Its main disturbance regions include the entire magnetotail, plasma sheet and ionosphere near the auroral zone. In general, the duration of a substorm case ranges from half hour to several hours. A typical substorm loading-unloading cycle includes the growth, expansion and recovery phase (e.g., [14]). During the growth phase solar wind energy is added to the magnetosphere and its configuration evolves toward an unstable state. This unstable situation is followed by a transient explosive unloading with a very high tail reconnection rate. The beginning time of this explosive unloading is named as substorm expansion onset. During the expansion phase the magnetosphere releases stored energy through a variety of processes. In recovery phase these die away and the magnetosphere becomes quiet [15]. Therefore, the magnetospheric substorm is closely related to the energy store and release in the solar wind-magnetosphere coupling.

In situ observation has the inevitable disadvantage of monitoring the entire coupling solar wind-magnetosphere system and its temporal evolution because of the poor data coverage of satellite. In comparison, the three-dimensional global magnetohydrodynamic (MHD) models which aim to model the fundamental physical processes in the coupling solar wind-magnetosphere system are powerful tools for simulating and analyzing the entire process of a real substorm event. Many studies have already employed global MHD models to simulate a real substorm event and checked the reliability of their results by comparing with observations. Using the Lyon-Fedder-Mobarry (LFM)—MHD model, Fedder et al. [16] reported the first global MHD simulation of an actual substorm event observed by Viking spacecraft on 19 October 1986. They compared model-derived synthetic auroral emissions to Viking images, and also compared synthetic AU (Auroral Upper) and AL (Auroral Lower) indices to geomagnetic measurements. Their simulation results are in reasonable agreement with the observations throughout the growth phase and expansion onset. Wiltberger et al. [11] presented LFM simulated results of a substorm that occurred on 10 December 1996, and obtained excellent agreement between the simulation results and the magnetotail observations during the growth and expansion phases including lobe field increasing, dipolarizations, and fast flows. Raeder et al. [17] has simulated a substorm event of 24 November 1996 using their Geospace General Circulation Model (GGCM)—MHD model. They compared the simulated results with ground magnetometers, Assimilative Mapping of Ionospheric Electrodynamics (AMIE) polar cap potential and field aligned current, open magnetic flux estimated by Polar Visible Imaging System, Geostationary Operational Environmental Satellite (GOES)-8 magnetometer data, International Monitoring Platform (IMP)-8 magnetic field data, and Geotail plasma and field data. The comparison showed their model reproduced the prominent substorm features of this event. Wang et al. [18] has simulated a substorm event of 28 September 2004 for the first time using Space Weather Modeling Framework (SWMF)-MHD model, and validated their results using Geotail and Cluster satellite observations. It was showed that the SWMF model can predict well the large-scale variations of the magnetospheric magnetic field and ionospheric currents during this substorm event. Using the Piecewise Parabolic Method with a Lagrangian Remap (PPMLR)-MHD model, Wang et al. [19] simulated the substorm event of 8 March 2008 and compared the equivalent current systems (ECS) in the ionosphere derived from the MHD model and geomagnetic observations using the KRM inversion algorithm. The magnetic latitude and

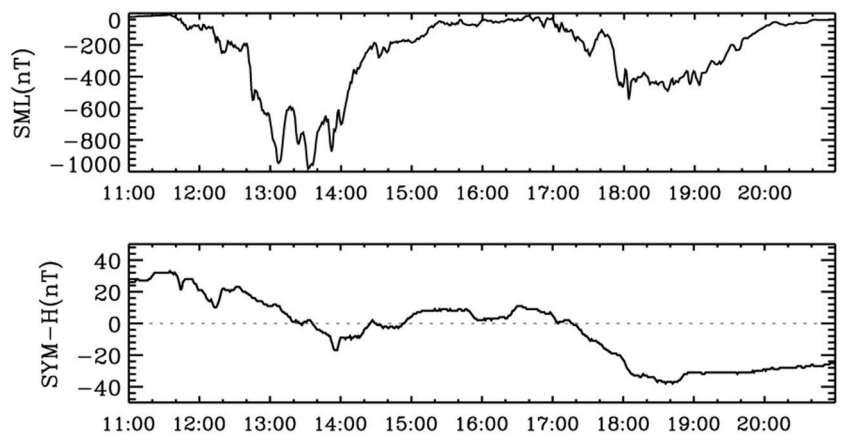

FIGURE 1 | SML index and SYM-H index of the 8 March 2008 event.

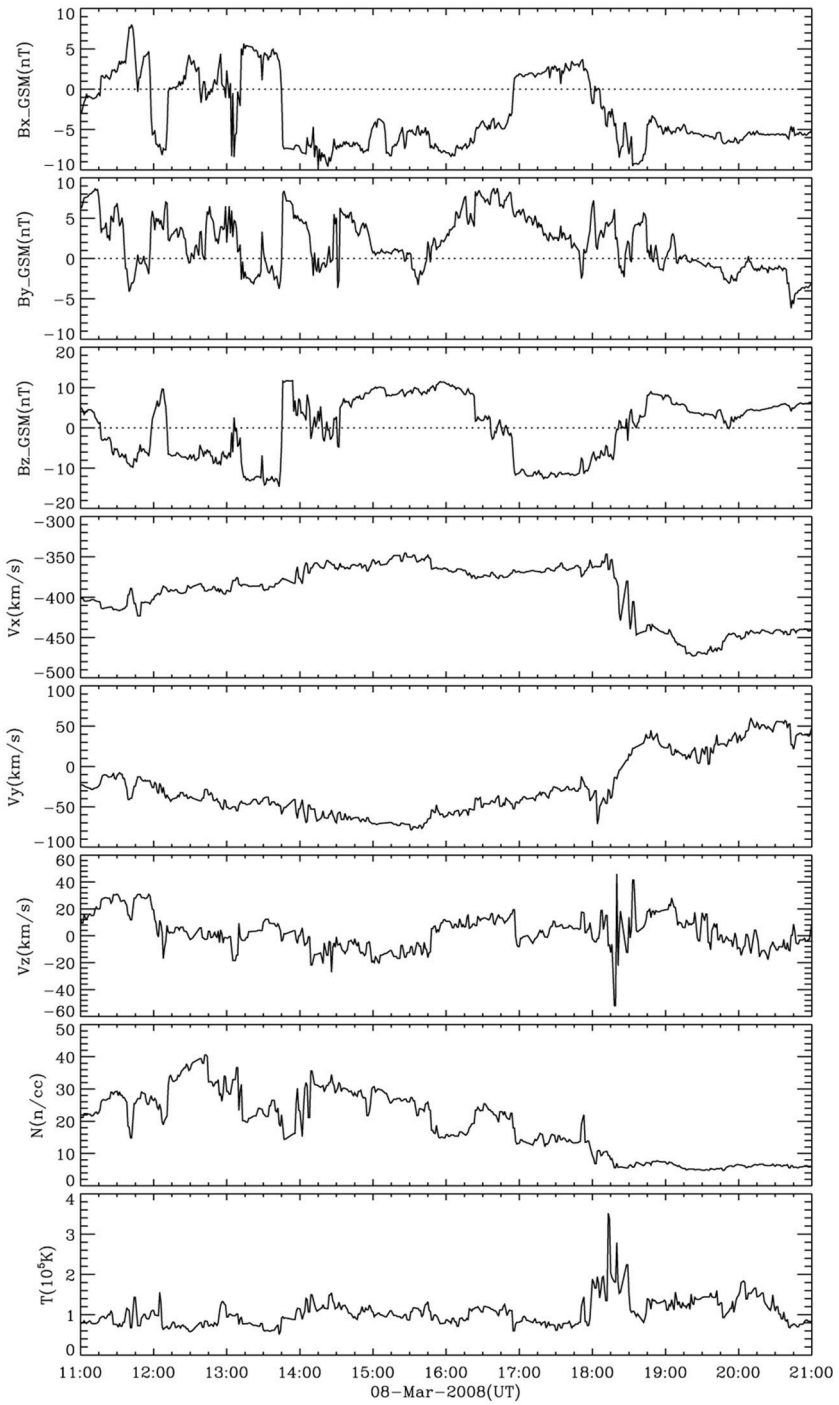

FIGURE 2 | Solar wind properties of the 8 March 2008 event from the OMNI data; From the top to the bottom, the three components of interplanetary magnetic field (IMF) and solar wind velocity, the solar wind plasma number density and temperature, respectively.

local time distributions of the ECS from MHD simulation are in good agreement with the inversion results.

Recently, Wang et al. [20] showed the PPMLR-MHD model can present a reliable PCB location under steady magnetospheric conditions. However, the reliability of PPMLR simulated PCB and its dynamics under magnetospheric substorm activities are still unknown. Taking advantage of the simulation data used previously by Wang et al. [19], we will validate in this study the PPMLR simulated PCB by comparing with Defense Meteorological Satellite Program (DMSP) observations, and analyze further the dynamics of PCB during the substorm event on 8 March 2008.

THE 8 MARCH 2008 EVENT OUTLINE

Figure 1 presents the SML (SuperMAG Auroral Lower) and SYM-H (Symmetric disturbance—Horizontal component) index during the 8 March 2008 event. The minimum SYM-H index is about −35 nT, implying there are no major magnetic storms. Indicated by the SML index, two isolated substorms occurred during this time period. The first one started at about 1,130 UT, reached its peak round 1,340 UT, then started to recover till 1,530 UT. The second one started at 1,650 UT and lasted more than 3 h before returning to the quiet level. The first substorm seems more intense than the second one, with the minimum SML value of about 950 nT compared with 550 nT for the second one.

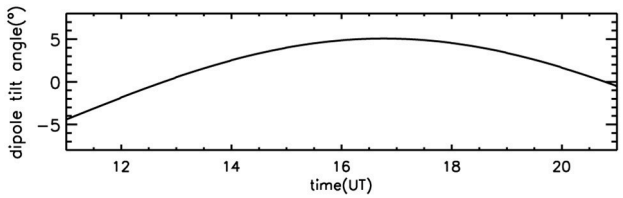

FIGURE 3 | The dipole tilt angle changes with the universal time during 8 March 2008 event.

The upstream solar wind observations of this event which are obtained from NASA OMNI data (http://cdaweb.gsfc.nasa.gov/) are plotted in **Figure 2**. It is noted that the simulation of 8 March 2008 event in Wang et al. [19] adopted three assumptions when they used these OMNI data as the input parameters of PPMLR-MHD model. (1) The OMNI data were used for the inflow boundary of MHD model without the correction of the time difference for the solar wind propagation from 30 Re to the bow shock nose (∼5 min). (2) The IMF Bx was fixed as zero for keeping the divergence-free condition in the PPMLR-MHD simulation. (3) The Earth's dipole moment was assumed to be due southward. **Figure 3** shows that the dipole tilt angle changes within the range from −5° to 5° during the 8 March 2008 event. Since a dipole tilt angle with the magnitude of 35° just brings 1–2° deviation degree to the PCB latitudes [21], we do not think that the assumption of zero dipole tilt angle will significantly affect the PCB determination.

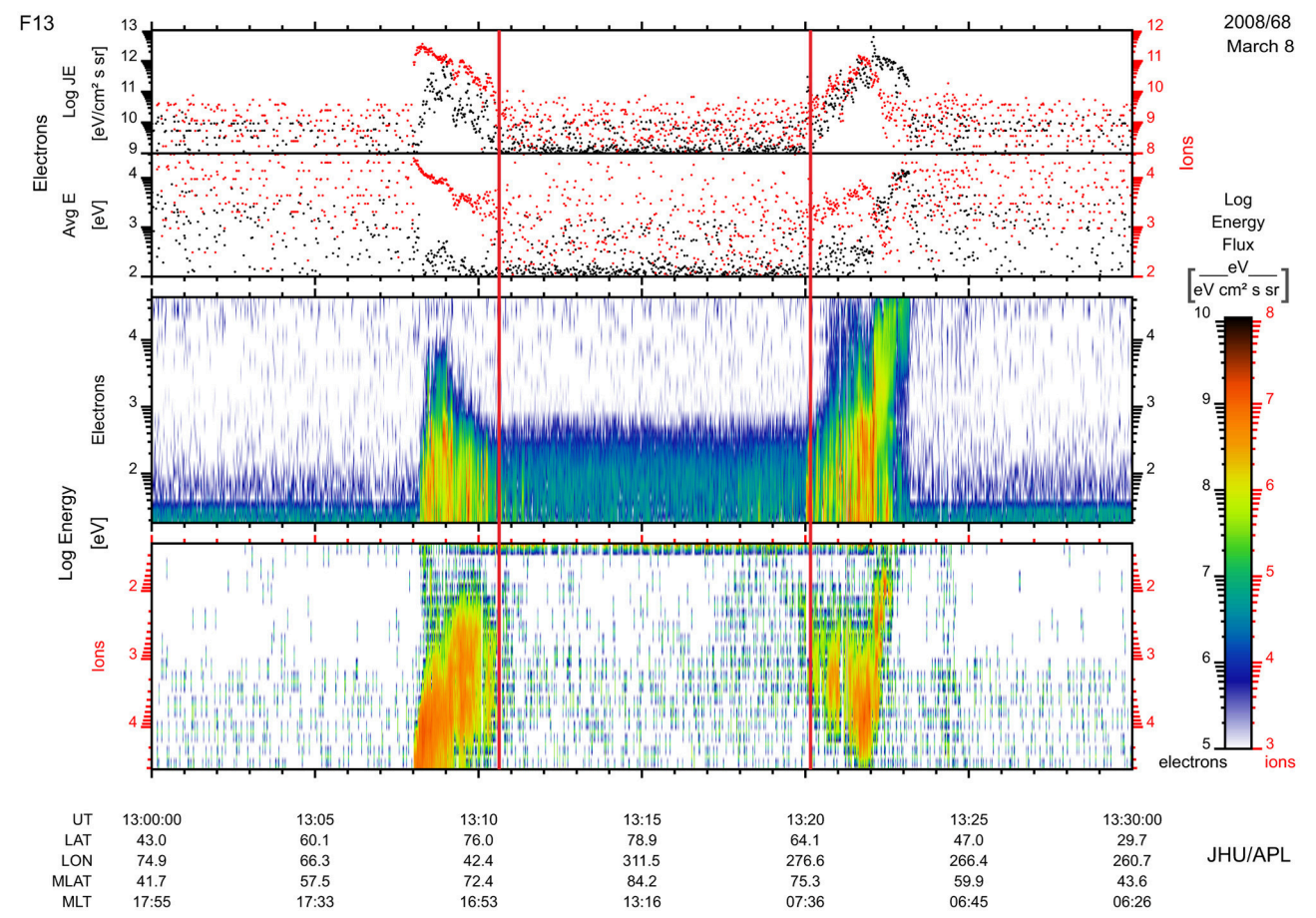

FIGURE 4 | Electron and ion precipitation fluxes measured from DMSP F13 during the northern hemisphere pass on 8 March 2008. The first panel plots total energy flux in $eVcm^{-2}s^{-1}sr^{-1}$, and the second panel shows average energy in eV; Black refers to electron, red to ion. The spectrogram itself shows differential energy flux in $cm^{-2}s^{-1}sr^{-1}$. The actual PCB locations are marked by the vertical red lines.

TABLE 1 | A list of DMSP PCB crossings at the northern hemisphere during the 8 March 2008 event.

Satellite	UT	Φ_{DMSP} (°)	θ_{DMSP} (°)	θ_{MHD} (°)	$d\theta$ (°)
F17	11:44	65.96	79.55	78.25	1.3
F17	11:50	270.68	76.39	74.37	2.02
F16	12:40	91.61	69.57	67.69	1.88
F15	12:50	86.17	70.48	70.09	0.4
F15	12:59	309.32	75.23	72.35	2.88
F13	13:11	79.38	72.06	69.72	2.34
F13	13:20	290.42	72.43	71.57	0.86
F17	13:22	72.4	69.34	69.02	0.32
F17	13:33	269.48	72.74	70.08	2.66
F16	14:20	97.87	67.11	67.37	−0.26
F16	14:31	320.22	72.73	71.57	1.16
F15	14:32	86.6	72.53	68.67	3.86
F15	14:41	302.19	71.87	73.14	−1.27
F17	15:05	65.33	76.55	77.8	−1.25
F17	15:12	277.31	78	80.5	−2.5
F16	16:05	84.78	79.25	80.97	−1.72
F16	16:10	325.46	78.59	80.06	−1.47
F15	16:16	41.63	84.88	86.15	−1.27
F15	16:18	333.55	83.89	80.97	2.92
F13	16:35	61.57	82.21	87.59	−5.38
F13	16:40	295.09	77.32	78.24	−0.92
F17	16:47	55.59	80	84.72	−4.72
F17	16:53	281.24	78.06	76.06	2
F16	17:44	101.02	76.33	71.57	4.76
F15	17:53	94	72.77	68.01	4.76
F16	17:54	305.64	68.03	68.33	−0.3
F15	18:03	294.03	68.23	69.36	−1.13
F17	18:25	66.52	70.74	68.01	2.73
F17	18:37	273.31	67.77	70.07	−2.3
F16	19:24	110.01	73.78	70.81	2.97
F16	19:33	303.61	74.4	77.8	−3.4
F15	19:42	294.47	74.66	78.7	−4.04
F13	19:56	74.5	80.23	83.77	−3.54
F13	20:02	290.74	76.14	80.05	−3.91

DETERMINATION OF PCB FROM SIMULATION DATA

We diagnose the PCB location from the PPMLR-MHD simulation data used previously by Wang et al. [19]. For the details of the PPMLR-MHD model and the simulation of 8 March 2008 event, please refer to Wang et al. [19].

PCB is considered to be the separatrix line between the open and closed magnetic field lines. To obtain the whole PCB from the global MHD simulation data, we trace magnetic field lines from the foot-points at the inner boundary using the Runge-Kutta method (e.g., [22, 23]). The grid resolution of foot-points is one degree in both magnetic latitude and longitude with the latitude changing from 90° to 0° and the longitude from 0° to 360°. Every tracing completes when the field line returns to the inner boundary, or it reaches the boundary of computational domain, or its length exceeds 1,000 Re. If the field line finally reaches the inner boundary, it is assumed to be a closed field line; otherwise, it is an open one. We map all foot-points of those field lines from the inner boundary to the ionosphere along the dipole field lines. The ionospheric grids connected to the open and closed field lines are marked with 1 and −1, respectively. The zero contour of these grids is our expected PCB.

RESULTS

In this section, we employ DMSP satellite particle observations to determine the PCB location, and make comparison between the MHD results and DMSP crossings. Based on the simulation and observation results, we also go further to analyze the evolution of PCB during the 8 March 2008 event.

The DMSP satellites orbit the Earth in a Sun-synchronous 98° inclination orbit near 840 km altitude. Each satellite carries the SSJ/4 sensor that measures the flux of precipitating ions or electrons between 30 eV to 30 keV once per second. There are four DMSP satellites (F13, F15, F16, F17) which overpass the northern polar region on March 2008.

Since the high energy (>few keV) particles are generally considered to be trapped on closed field lines only, and cannot persist for long on open field lines, the boundary between energetic particles (1∼10 s keV) at lower latitudes and softer precipitation at higher latitudes can be identified with the PCB (e.g., [24–26]). **Figure 4** shows an example of the boundary location identification procedures applied to a northern hemisphere pass of F13. In this overpass the PCB crossings as the F13 satellite passes into and then out of the polar cap are marked by the vertical red lines.

Using the above-mentioned method, we determine 34 PCB crossings at the northern hemisphere during this event. The specific details of crossings are listed in **Table 1**, which includes No. of satellite, universal time, longitude (Φ_{DMSP}) and latitude (θ_{DMSP}) of DMSP crossings in the Solar Magnetospheric (GSM) coordinate system, the corresponding PCB latitudes from PPMLR simulation (θ_{MHD}), the deviations between DMSP determined and PPMLR simulated PCB latitudes ($d\theta = \theta_{DMSP}$-θ_{MHD}).

The model-data comparison has been conducted to test whether the simulations follow general trends of the observations. The results in **Table 1** indicate that the average deviation of PCB latitudes between the MHD simulations and the DMSP observations is about 2.33°, and the correlation coefficient between them is 0.89. **Figure 5** shows the pattern of PCB latitudes changing with the universal time. Here, the dawn-side crossings correspond to $180° < \Phi_{DMSP} < 360°$, the dusk-side crossings correspond to $0° < \Phi_{DMSP} < 180°$, the blue dots refer to the PCB latitudes from DMSP observations, and the red dots denote the results from PPMLR simulations. As shown in **Figure 5**, we obtain a good agreement of the simulation results with key DMSP observations. Nevertheless, there are still some small disagreements between the simulation results and observations; for instance, the PPMLR-MHD model overestimates the dawn

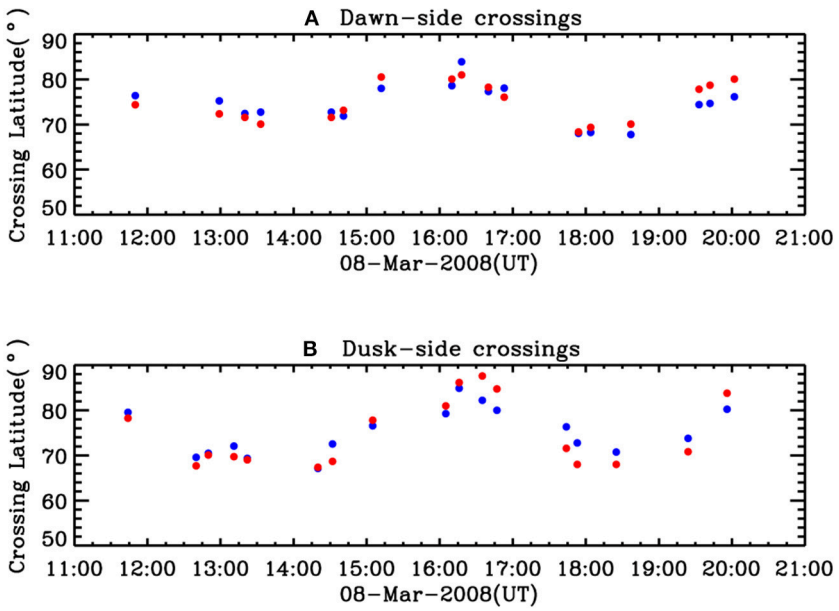

FIGURE 5 | The pattern of comparison of PCB latitudes between DMSP observations and PPMLR simulations.

side sector of PCB and underestimate the dusk side sector of PCB during the second substorm case to some extent. The reasons that cause the deviation between the PCB location derived from DMSP measurements and PPMLR-MHD simulations could be as follows. (1) Based on the PPMLR-MHD simulations, Hu et al. [27] found that even under quiet interplanetary conditions, the Earth's magnetosphere is never exactly steady, but keep oscillating. Therefore, the MHD simulation has the systematic error which may cause errors to the PCB determined from MHD simulations. (2) The PPMLR-MHD simulation adopts the assumptions of zero IMF Bx and zero tilt angle. While the IMF Bx and tilt angle are not the main influencing factor of PCB location, these simple assumptions may bring errors to the results of MHD simulations. (3) The ionospheric conductances of PPMLR-MHD model are determined based on two empirical models shown in Moen and Brekke [28] and Ahn et al. [29] respectively. The differences between the empirical model and the real situation should cause errors to the results of MHD simulations to a certain extent as well.

Furthermore, we analyze the evolution of PCB based on the **Figure 5** and the corresponding SML index and solar wind conditions as well. At the start of this event, the IMF is oriented southward except for the time around 1,200 UT when the IMF has a northward turning briefly, suggesting that the low-latitude dayside reconnection should be creating new open magnetic flux [1, 30], and indeed the PCB tends to lower latitude between 1,120 and 1,240 UT. The decreasing SML index means more solar wind energy flow into and store in the magnetosphere. Following the expansion onset of the first substorm (1,240 UT, it is consistent with the results determined by the methods in [31, 32]), the dusk-side PCB latitude begins to increase until around 1,315 UT. Due to the limited number of DMSP crossings, we are not able to obtain the changing tendency of dawn-side PCB during this time. However, this is still enough to indicate that the reconnection increases sharply and destroys more open magnetic flux in the tail after the expansion onset. When IMF Bz turns northward at 1,345 UT, dawn- and dusk-side PCB persistently tend to much higher latitude until 1,635 UT since the low-latitude dayside reconnection ceases and no more open magnetic flux are produced. Meanwhile, the storage energy in the magnetosphere releases with the increasing SML index. After 1,640 UT, the turning southward of IMF Bz opens the low-latitude dayside reconnection again, and causes the PCB latitude decreases and the polar cap expands. The energy loads in the magnetosphere with the decreasing SML index. The IMF Bz once again turns northward at 1,824 UT. After that, the PCB latitude begins to increase, and the storage energy releases with the increasing SML index again. Although the DMSP satellite has a very limited number of crossings, we can still identify the typical changing features of PCB during this substorm event. The simulation results reproduce the observations quite well.

CONCLUSIONS

Taking the 8 March 2008 Event as an example, we investigate the PCB and its dynamics during substorm events. The PCB locations are directly determined from the simulation data used previously by Wang et al. [19]. We take advantage of DMSP particle observations to determine the PCB satellite crossings, and then present the comparison of PCB locations between the PPMLR-MHD results and DMSP measurements. During this event, we find good agreements between the MHD modeling results and observations.

Based on the MHD simulations and DMSP observations, we analyze the evolution of PCB during this event as well. The polar cap is found to expand when the IMF becomes southward since the low-latitude dayside reconnection creates new open magnetic flux. Meanwhile, more solar wind energy flow into and store in the magnetosphere with the decreasing SML index. After the substorm expansion onset, the polar cap contracts for a while due to the explosive increase of nightside reconnection. When the IMF turns northward, the polar cap contracts continuously because the low-latitude dayside reconnection ceases and no more open magnetic flux are produced, and the storage energy in the magnetosphere releases with the increasing SML index.

Although the DMSP satellite has a very limited number of crossings, we can still identify the typical changing features of PCB during this substorm event. The MHD simulation reproduces the features from observations quite well. Results shown in this study illustrate the accuracy with which an MHD simulation can be used to model the magnetosphere-ionosphere system and present the evolution of PCB even during complex substorm sequences.

DATA AVAILABILITY STATEMENT

All the simulation data used in this study are available by emailing the authors (CW:cw@spaceweather.ac.cn JW:jywang@spaceweather.ac.cn). The SML index was obtained from the website at http://supermag.jhuapl.edu/indices/. The OMNI data were generated by J. H. King and N. Papitashivilli and obtained from http://cdaweb.gsfc.nasa.gov/. The DMSP particle detectors were designed and calibrated by Dave Hardy, Fred Rich, and colleagues of AFRL, and data were provided via Applied Physics Laboratory at the Johns Hopkins University (JHU/APL) (http://sd-www.jhuapl.edu/Aurora/spectrogram/index.html).

AUTHOR CONTRIBUTIONS

CW analyzing results and writing the whole paper; JW, HL, JZ, BT simulating the substorm case and analyzing the simulation results; RL analyzing the DMSP data.

FUNDING

This work was supported by the NNSFC grants 41731070, 41574159, 41404123, 41774155, CAS grants QYZDJ-SSW-JSC028, XDA15052500, and in part by the Specialized Research Fund for State Key Laboratories of China.

ACKNOWLEDGMENTS

The authors would like to acknowledge Prof. Youqiu Hu for his information on the PPMLR-MHD simulation code, by which the simulation data used in this study were calculated.

REFERENCES

1. Dungey JW. Interplanetary magnetic field and the auroral zones. *Phys Rev Lett* (1961) **6**:47–8. doi: 10.1103/PhysRevLett.6.47
2. Milan SE, Provan G, Hubert B. Magnetic flux transport in the Dungey cycle: a survey of dayside and nightside reconnection rates. *J Geophys Res.* (2007) **112**:A01209. doi: 10.1029/2006JA011642
3. Reiff PH, Burch JL. IMF By-dependent plasma flow and Birkeland currents in the dayside magnetosphere: 2. A global model for northward and southward IMF. *J Geophys Res*. (1985) **90**:1595–609. doi: 10.1029/JA090iA02p01595
4. Heppner JP, Maynard NC. Empirical high-latitude electric field models. *J Geophys Res*. (1987) **92**:4467–89. doi: 10.1029/JA092iA05p04467
5. Dmitriev AV, Jayachandran PT, Tsai LC. Elliptical model of cutoff boundaries for the solar energetic particles measured by POES satellites in December 2006. *J Geophys Res*. (2010) **115**:A12244. doi: 10.1029/2010JA015380
6. Lee DY, Ohtani S, Lee JH. On the poleward boundary of the nightside auroral oval under northward interplanetary magnetic field conditions. *J Geophys Res*. (2010) **115**:A08204. doi: 10.1029/2009JA014906
7. Lukianova R, Kozlovsky A. IMF By effects in the plasma flow at the polar cap boundary. *Ann Geophys*. (2011) **29**:1305–15. doi: 10.5194/angeo-29-1305-2011
8. Newell PT, Feldstein YI, Galperin YI, Meng CI. Morphology of nightside precipitation. *J Geophys Res*. (1996) **101**:10737–48. doi: 10.1029/95JA03516
9. Lyon JG, Lopez RE, Goodrich CC, Wiltberger M, Papadopoulos K. Simulation of the March 9, 1995, substorm: auroral brightening and the onset of lobe reconnection. *Geophys Res Lett*. (1998) **25**:3039–42. doi: 10.1029/98GL00662
10. Lopez RE, Wiltberger M, Lyon JG, Goodrich CC, Papadopoulos K. MHD simulations of the response of high-latitude potential patterns and polar cap boundaries to sudden southward turnings of the interplanetary magnetic field. *Geophys Res Lett*. (1999) **26**:967–70. doi: 10.1029/1999GL900113
11. Wiltberger M, Pulkkinen TI, Lyon JG, Goodrich CC. MHD simulation of the magnetotail during the December 10, 1996, substorm. *J Geophys Res*. (2000) **105**:27649–663. doi: 10.1029/1999JA000251
12. Milan SE. Dayside and nightside contributions to the cross polar cap potential: placing an upper limit on a viscous-like interaction. *Ann Geophys*. (2004) **22**:3771–7. doi: 10.5194/angeo-22-3771-2004
13. Milan SE, Cowley SWH, Lester M, Wright DM, Slavin JA, Fillingim M, et al. Response of the magnetotail to changes in the open flux content of the magnetosphere. *J Geophys Res*. (2004) **109**:A04220. doi: 10.1029/2003JA010350
14. Rostoker G, Akasofu SI, Baumjohann W, Kamide Y, Mcpherron RL. The roles of direct input of energy from the solar wind and unloading of stored magnetotail energy in driving magnetospheric substorms. *Space Sci Rev*. (1988) **46**:93–111. doi: 10.1007/BF00173876
15. Pulkkinen TI, Baker DN, Toivanen PK, Pellinen RJ, Friedel RHW, Korth A. Magnetospheric field and current distributions during the substorm recovery phase. *J Geophys Res*. (1994) **99**:10955–66. doi: 10.1029/93JA02718
16. Fedder JA, Slinker SP, Lyon JG, Elphinstone RD. Global numerical simulation of the growth phase and the expansion onset for a substorm observed by Viking. *J Geophys Res*. (1995) **100**:19083–93. doi: 10.1029/95JA01524
17. Raeder J, McPherron RL, Frank LA, Kokubun S, Lu G, Mukai T, et al. Global simulation of the Geospace Environment Modeling substorm challenge event. *J Geophys Res*. (2001) **106**:381–95. doi: 10.1029/2000JA000605
18. Wang H, Ma S, Ridley AJ. Comparative study of a substorm event by satellite observation and model simulation. *Chinese Sci Bull*. (2010) **9**:859–866. doi: 10.1007/s11434-009-0282-4
19. Wang C, Zhang JJ, Tang BB, Fu SY. Comparison of equivalent current systems for the substorm event of 8 March 2008 derived from the global PPMLR-MHD model and the KRM algorithm. *J Geophys Res*. (2011) **116**:A07207. doi: 10.1029/2011JA016497
20. Wang C, Wang JY, Lopez RE, Zhang LQ, Tang BB, Sun TR, et al. Effects of the interplanetary magnetic field on the location of the open-closed field line boundary. *J Geophys Res Space Phys*. (2016) **121**:6341–52. doi: 10.1002/2016JA022784
21. Kabin K, Rankin R, Rostoker G, Marchand R, Rae IJ, Ridley AJ, et al. Open-closed field line boundary position: a parametric study using an

MHD model. *J Geophys Res*. (2004) **109**:A05222. doi: 10.1029/2003JA010168
22. Atkinson KE. *An Introduction to Numerical Analysis, 2nd ed*. New York, NY: John Wiley & Sons (1989).
23. Butcher JC. *Numerical Methods for Ordinary Differential Equations*. New York, NY: John Wiley & Sons (2008).
24. Hardy DA. Precipitating Electron And Ion Detectors (SSJ/4) for the Block 5D/flights 6-10 DMSP Satellites: Calibration and Data Presentation. Rep. AFGL-TR-84-0317. Bedford, MA: Air Force Geophysics Lab (1984).
25. Sotirelis T, Newell PT, Meng CI. Shape of the open closed boundary of the polar cap as determined from observations of precipitating particles by up to four DMSP satellites. *J Geophys Res Space Phys*. (1998) **103**:399–406. doi: 10.1029/97JA02437
26. Milan SE, Lester M, Cowley SWH, Oksavik K, Brittnacher M, Greenwald RA, et al. Variations in the polar cap area during two substorm cycles. *Ann Geophys*. (2003) **21**:1121–40. doi: 10.5194/angeo-21-1121-2003
27. Hu YQ, Guo XC, Li GQ, Wang C, Huang ZH. Oscillation of quasi-steady Earth's magnetosphere. *Chin Phys Lett*. (2005) **22**:2723–6.
28. Moen J, Brekke A. The solar flux influence on quiet time conductances in the auroral ionosphere. *Geophys Res Lett*. (1993) **20**:971–4. doi: 10.1029/92GL02109
29. Ahn BH, Richmond AD, Kamide Y, Kroehl HW, Emery BA, de laBeaujardiére O, et al. An ionospheric conductance model based on ground magnetic disturbance data. *J Geophys Res*. (1998) **103**:14769–80. doi: 10.1029/97JA03088
30. Dungey JW. The structure of the exosphere or adventures in velocity space. In: De Witt C, Hieblot J, LeBeau L, editors. Geophysics: The Earth's Environment. New York, NY: Gordon and Breach (1963). p. 503–50.
31. Li H, Wang C, Peng Z. Solar wind impacts on growth phase duration and substorm intensity: a statistical approach. *J Geophys Res Space Phys*. (2013) **118**:4270–8. doi: 10.1002/jgra.50399
32. Newell PT, Gjerloev JW. Evaluation of SuperMAG auroral electrojet indices as indicators of substorms and auroral power. *J Geophys Res*. (2011) **116**:A12211. doi: 10.1029/2011JA016779

Conflict of Interest Statement: The authors declare that the research was conducted in the absence of any commercial or financial relationships that could be construed as a potential conflict of interest.

frontiers in Physics

ORIGINAL RESEARCH
published: 29 August 2018
doi: 10.3389/fphy.2018.00081

Time, the Arrow of Time, and Quantum Mechanics

*Gerard 't Hooft**

Institute for Theoretical Physics, Utrecht University, Utrecht, Netherlands

It is brought forward that viable theories of the physical world that have no variable at all that can play the role of time, do not exist; some notion of time is one of the very first ingredients a candidate theory should possess. Almost by definition, time has an arrow. In contrast, time *reversibility*, or even the possibility to run the equations of motion backwards in time, is not at all a primary requirement. This means that the direction of the arrow of time may well be uniquely defined in the theory, even locally. It is explained that a rigorous definition of time, as well as a formulation of the causality and locality concepts, can only be given when one has a model for the physical phenomena described. The only viable causality condition is one that is symmetric under time reversal. We explain these statements in terms of the author's favored deterministic cellular automaton interpretation of quantum mechanics, also to be referred to as "vector space analysis," and expand on these ideas. It is also summarized how our more rigorous causality condition affects Bell's theorems. What distinguishes quantum systems from classical ones is our fundamental inability to control the microscopic details of the initial state when phenomena are studied in the light of some theoretical model.

Keywords: arrow of time, quantum mechanics, time, 6-bit universe, information loss, GZH paradox

OPEN ACCESS

Edited by:
George Jaroszkiewicz, Independent researcher, Walton on the Wolds, United Kingdom

Reviewed by:
Yutaka Shikano, Institute for Molecular Science (NINS), Japan
Sisir Roy, National Institute of Advanced Studies, India
Hans-Thomas Elze, Università degli Studi di Pisa, Italy

***Correspondence:**
Gerard 't Hooft
g.thooft@uu.nl

Specialty section:
This article was submitted to Mathematical Physics, a section of the journal Frontiers in Physics

Received: *20 April 2018*
Accepted: *17 July 2018*
Published: *29 August 2018*

Citation:
't Hooft G (2018) Time, the Arrow of Time, and Quantum Mechanics. Front. Phys. 6:81. doi: 10.3389/fphy.2018.00081

1. INTRODUCTION; DEFINING TIME

The universe as we know it is characterized by a framework called *space-time*, in which *events* take place. The events are characterized first of all by their *locations* in space, and *moments* in time, all together indicated in terms of coordinates. The number of coordinates needed, usually real numbers, is called the dimension of space-time. The coordinate that indicates time, is a very special one. It is the only coordinate in which it is meaningful to define an ordering in the values given, the order of time. This ordering defines an orientation, called the arrow of time. It allows us to define an ordering (or at least a partial ordering) of all events.

Whenever we build *models* that explain the existence and nature of the events, it is of extreme importance to have such an ordering of events; it allows us to explain them sequentially: one event can be the cause of a subsequent event if its time variable is lower, or it could be the consequence of an event if its time coordinate is higher. It is difficult, probably impossible, to devise a model of our universe, if no ordering is defined for the model to describe the events.

This in fact will bring us to provide a definition of time that is more primary, more basic than all other ingredients of our model, including the notion of space. Our universe is known to carry a memory of things that happened in the past. Whenever we build a model of our universe, one that is controlled by "laws of physics," it should come with a completely unambiguous prescription of *the order in which the laws of Nature should be imposed on all events that take place*. Regard the laws of physics as a computer program to calculate the next sequence of events. The data that we have to

enter into the program may come from events calculated earlier. They may not come from events that still have to be specified, because in that case conflicts may arise: if event A affects the features of event B then event B should not react back to modify event A, otherwise the rules cease to be unique; they will literally be circular, making them either self-contradictory or ambiguous, and for that reason they would not be suitable to explain observed phenomena.

Notice that this is the extreme opposite of Newton's action principle: if event A acts on event B with some force, event B should *not* react back onto A. Newton's action principle, action = reaction, is different because it is in space-like directions, and because it often neglects some minute time delays that are involved: the (re-) action cannot spread faster than the speed of light.

The ordering caused by the rule "A affects B but B cannot affect A," is one we cannot do without. Assuming indeed that the universe allows for the existence of such an elementary action $\neq$ reaction principle, we obtain a unique *definition* of time:

Time is the order in which our models for nature predict, prescribe or explain events.

Notice that this definition of time supposes that we construct models to explain our universe. If one *only* would collect data, without attempting to explain them, we would not need any notion of time. After all, the data could have been presented to us in "non chronological" order. It is our model that definitely requires an order. Any parameter, any coordinate that increases monotonically in that order, will be a useful time coordinate.

Notice also that quantum mechanics provides no exception to our rule; it also requires a definition of an ordered time coordinate. We can say this because the Schrödinger equation[1] involves exclusively a first order derivative in time. Therefore only one boundary condition is needed, taken to be the situation in some distant past, to determine the situation in the future.

The primary definition of time given above, only defines the time ordering, but does not attach real numbers to time. In fact, the use of integers, so as to count the events that we calculated, would have been more appropriate. Considering the humongous size of our universe, and the extremely short time sequences expected to be relevant at the Planck scale, one may expect these integers, if they exist at all, to be extremely large, larger than $\sim 10^{60}$. Scaling these numbers down for practical use, probably suffices to explain why, at present, real numbers seem to be more useful than integers to indicate time.

According to special relativity, one can have events that are *space-like* separated. This means that there may be events A and B such that our model allows us to calculate what happens in A and in B without the need to specify their order. The importance of this is that the definition of time given above is not unique; it is a feature of the notion of time that will have to be taken into consideration when building more advanced models, but it seems to be less basic as far as first principles is concerned.

Among the questions asked to the author was one concerning the theory of special relativity. Issues concerning special relativity in relation to the question of time and its arrow, are discussed in **Appendix B**.

2. QUANTUM MECHANICS

The theory of quantum mechanics is arguably one of the greatest discoveries of physics; it revolutionized our understanding of molecules, atoms, radiation, and the world of the sub-atomic particles. Yet even now, almost 100 years later, there is still no complete consensus as to what the theory tells us about *reality*, or even whether "reality" exists at all. Some authors adhere to the idea that *all* "realities" exist somewhere in some alternative universes, and that these universes evolve together as a "multiverse[2]."

The present author does not go along with such ideas. Quantum mechanics is a superb description of the world of tiny things, but, on the face of it, quantum mechanics seems merely to reflect humanity's ignorance. *We do not know* which reality it describes, and as long as this is the case, we should not be surprised that, in a sense, all possible realities play a role whenever we try to make the best possible prediction of the outcome of an experiment. The fact that many of us have technical difficulties implementing such a thought in the equations known to work best today, may well be due to lack of imagination as to how eventually the correct view will be found to emerge.

The author has made his own analysis of the known facts, and came to the conclusion that the Copenhagen doctrine, that is, the consensus reached by many of the world experts at the beginning of the twentieth century, partly during their numerous gatherings in the Danish capital, has it almost right: there is a wave function, or rather, something we call a quantum state, being a vector in Hilbert space, which obeys a Schrödinger equation.[3] The absolute squares of the vector components may be used to describe probabilities whenever we wish to predict or explain something. Powerful techniques were developed, enabling one to guess the right Schrödinger equation if one knows how things evolve classically, that is, in the old theories where quantum mechanics had not yet been incorporated. It all works magnificently well. According to Copenhagen, however, there is one question one should *not* ask: "What does *reality* look like of whatever moves around in our experimental settings?" or: what is really going on?

According to Copenhagen, Such a question can never be addressed by means of any experiment, so it has no answer within the set of logical statements we can make of the world. Period, schluss, fini. Those questions are senseless.

It is this answer that we dispute. Even if this kind of questions cannot be answered by *experiments,* we can still *in theory* try to build credible models of reality. Imagine the famous detective Sherlock Holmes entering a room, with a dead body lying on the

[1]Here, and in what follows later, all equations of the form $\frac{\mathrm{d}}{\mathrm{d}t}|\psi\rangle = -iH|\psi\rangle$, where H is a hermitian operator, are referred to as Schrödinger equation, regardless whether they act on wave functions or more general vectors in Hilbert space.

[2]'Multiverse' can mean different things. In cosmology, it means that there may be different regions of our universe where the inflation rates and perhaps also the effective laws of nature, vary. In quantum mechanics, one might view the 'many worlds' together as a multiverse.

[3]See footnote 1.

floor. The door is open, and so is the window. A crime has been committed. Did the perpetrator come through the window or through the door? Or did something altogether different happen? Sherlock Holmes ponders about all possibilities, but he will *not* say: the perpetrator came through the window *and* through the door, using a wave function, etc. etc. Clearly such answers are not accepted in the ordinary world. Sherlock Holmes may well conclude that he cannot derive the answer with certainty, but what he can try to find out is what *could have* happened. Have we been brainwashed to accept wave functions in the world of the atoms? Should we not, here also, ask what it really was, or what it could have been, that has been going on?

Perhaps we are using the wrong language. Maybe atoms and molecules do not exist in the form we imagine them. Maybe Nature's true degrees of freedom are very different, and only when we consider the statistics of many atoms, our language that assumes these to be particles obeying quantum equations may be seen to work out correctly.

When early attempts to construct such models failed, investigators tried another path: maybe one can *prove* that there exists no reality at all whose probabilities can be caught in terms of a Schrödinger equation? Suppose that we impose conditions on such models such as *locality* and *causality*. Can one prove or disprove that realistic models exist?

What then happened is well-known. The first to consider such an option was Einstein, together with his co-authors Podolsky and Rosen [1] and Jammer [2]. They conceived of a *Gedanken* experiment to show that quantum mechanics cannot exactly provide a local description of what is going on. This conclusion is in fact somewhat contradictory, because quantum mechanics *was* used to describe as accurately as possible what predictions can be made, and that result was rarely disputed by anyone; indeed it was confirmed later by real experiments.

The setup was revised by a somewhat more realistic scenario using particle spins, by Bell, and he gave the apparent contradiction in a more precise wording: Bell's theorem:

> *No physical theory of local hidden variables can ever reproduce all of the predictions of quantum mechanics;*

the outcome of a quantum mechanical calculations of some non-local correlations contradicts any acceptable "classical" explanation by at least a factor $\sqrt{2}$. The inequality, called *Bell inequality*, was subsequently generalized and made more precise [3].

3. CAUSALITY, CORRELATIONS AND QUANTUM MECHANICS

This finding did not go undisputed. Many authors attempted to locate the flaw in Einstein's and Bell's argument, but logically it seemed to be impeccable. Bell assumed that determinism means that one can build a model, any model, in which classical equations control the behavior of dynamical variables, and where, at the tiniest scales where these variables describe the data, the evolution laws do not leave the slightest ambiguity; there are no wave functions, no statistical considerations, as everything that happens is controlled by certainties. Moreover, there is some sense of locality: the laws control all processes using only the data that are situated at given localities, while action at a distance, or backwards in time, are forbidden. The classical degrees of freedom that "really" exist were called "beables."

Here, the first topic for discussion arises: *what does "action backwards in time" mean?* In "La Nouvelle Cuisine," Bell [4, 5] formulated as precisely as he could what "causality forward in time" means:

> A theory is said to be locally causal if the probabilities attached to values of local beables in a space-time region 1 are unaltered by specification of values of local beables in a space-like separated region 2, when what happens in the backward light cone of 1 is already sufficiently specified [...]

Region 2 is assumed to be completely outside the past light cone of 1, so what happens there, must be immaterial. It sounds fine, and many researchers agree with it, but there is a problem:

> Region 2 also has a past light cone, and if we consider some modification of the events in 2, these may disagree with what we postulated to have in region 1, since the two past light cones overlap.

Consequently, *correlations* between the data in region 1 and region 2 *cannot* be excluded. In fact, such correlations are known to occur ubiquitously in the physical world, so what does "Bell-causality" really mean?

What Bell needed to have said is that, *in any model* describing the laws of nature, only the data in the past light cone of 1, should determine what happens in 1, while he should not have referred to correlations. *Yet Bell's inequalities are about correlations*, and these are assumed to be absent outside the light cone.

In the same vein, "backwards causality" is rejected: the past should not depend on the future. This is true in the following sense: *our model* should not require knowledge of the data in the future, to prescribe the data at present (it should only require data in the past light cone). Correlations do occur. In fact, if our model reflects reversibility in time—which most models do—then the data inside the future light cone *can be used* to determine, that is, to reconstruct, the present or the past, back from the future.

In the above, the words *our model* were emphasized. What is important here is that causality cannot be a feature or property of the physical data themselves, but rather a property of the equations of motion with which we try to mimic these data. If two different theories can be used to describe the same set of data, then one of these theories might have causality and the other not. This is an element of the Bell "paradox" that may not have been emphasized sufficiently.

Most models of nature are reversible in time; we can run the basic equations backwards in time as easily as forwards in time[4].

[4]We refer here to the equations at small time intervals and accordingly acting at small distance scales. Thermodynamics on the other hand, valid for large time intervals cannot be easily inverted in time.

This implies that theories with causality forwards in time must also have causality backwards in time; this was ignored by Bell.

There is nevertheless a good reason why Bell's profound result is considered irrefutable by most researchers today. The actions of observers in quantum experiments, are considered to be completely classical, and they reflect the observers' *free will*. To overrule Bell's theorem, the observers' free will must be correlated with quantum data in the past. This is considered "absurd" by most researchers. In the next section, and in **Appendices A** and **C**, this author's response, as to why these correlations may be not so absurd after all, is further illuminated.

The theory used by the author was called "Cellular Automaton (CA) Interpretation" [6], but perhaps a preferable denomination is "vector space analysis[5]." It is the idea that a classical system may be analyzed by associating any state of the system by a vector, such that all states together form an orthonormal basis of a vector space called Hilbert space. "vector space analysis" consists of the mathematical procedures made possible by performing any kind of transformations in this vector space. One ends up with a Schrödinger equation exactly as in quantum mechanics. Thus, vector space analysis contradicts Bell's theorem. Our theory consists of the assertion that what we call quantum mechanics today can be the result of a vector space analysis of some classical system. The "CA Interpretation" of quantum mechanics consists of the assumption that this is true, while we refrain from further attempts to identify the classical system underlying it. The author hopes however that the search for appropriate classical models will continue, and that it will bear fruit.

We end this section with the remark that a restriction exists called "causality," that can be imposed on any model for elementary particles. It is not disputed, but in fact used a lot in quantized field theories. This condition considers operators $\phi(x)$ in quantum field theories, describing (elementary or composite) fields ϕ at 4-space-time coordinates x. Let x_1 and x_2 be space-like separated. Then we have for the commutator,

$$(x_1 - x_2)^2 > 0 \quad \rightarrow \quad [\phi(x_1), \phi(x_2)] = 0\,. \tag{3.1}$$

This says that any operation $\phi(x_1)$ acting on any quantum state at space-time point x_1, cannot affect the result of any dynamical effect of $\phi(x_2)$ occurring at x_2. In the Standard Model for the elementary particles, this condition, "no Bell telephone," is found to hold true, and it has important applications in calculations. However, this condition does not distinguish causal relations in the forward time direction from ones in the backwards time direction, so that it could not be used to derive inequalities such as Bell's. The "no Bell telephone" condition does not depend on the arrow of time.

4. THE BELL AND CHSH INEQUALITIES

Bell's Gedanken experiment is in essence much the same as the Einstein Rosen Podolsky set-up. A local device is constructed that can emit two entangled particles, α and β, which leave the machine in opposite directions. Alice (A) and Bob (B), both choose whether to measure property X or property Y of the particles they can see. Alice chooses setting a to measure α and Bob setting b to measure β.

The correlations needed to explain the quantum mechanical result require that the settings a and b chosen by Alice and bob, must be correlated with one another as well as the (classical) spins of the two entangled particles. The author calculated the minimal amount of correlation that is needed to produce the quantum result. We found the following distribution [6]:

$$W(a, b, \lambda) = C|\sin(2a + 2b - 4\lambda)|\,, \tag{4.1}$$

where a is the angle chosen by Alice for her measurement, b is Bob's angle, and λ a parameter describing the polarization of the entangled photons produced by the source—and detected by Alice and Bob. W is the probability distribution, and C is a normalization constant. It features a *3 body correlation*: whenever we integrate over all values of a, or all values of b, or all values of λ, we get a flat distribution.

To show rigorously that such correlation features are unacceptable for any theory that generates quantum mechanics from classical mechanical laws, Bell had to formulate his definition of causality. We indicated above that his definition does not apply for physical systems, so one could terminate the discussion here and now, since correlation functions are not bounded by light cones. Yet the correlation function (4.1) is considered unacceptable by most investigators. How can it be that decisions by Alice and Bob, made out of free will, can yet be correlated with something that happened earlier–the polarization chosen by the entangled photons emitted by the source? Did these photons "know" what settings Alice and Bob would later choose, or is this a case of "conspiracy?" How can a single photon guide the classical dynamical variables a and b?

To explain this, we now summarize how vector space analysis works. Suppose we have a classical theory at, for instance, the Planck scale, 10^{-33} cm. This would be typically a cellular automaton. It can be in $2^{10^{99}}$ states in every cm^3, typically. Every one of these states is called "ontological," which means it is realized or it is not realized, but superpositions do not exist. It is precisely the thing that Einstein, Bell and others wanted to disprove. Just in order to do mathematics, we now attach a basis vector to every one of these ontological states. They are set up such that they form an orthonormal basis of a $2^{10^{99}}$ - dimensional vector space, at each cm^3. At the beat of a clock, typically with the Planck frequency of some 10^{44} Hertz, these states evolve into other states. This we write using the evolution matrix, which consists of one 1 in each row and in each column, and zeros everywhere else.

The math we use consists of diagonalizing this matrix. This gives us the eigen states of the energy, i.e., the Hamiltonian. One finds that the states of this model obey the Schrödinger equation. Now all energy eigen states are superpositions of the ontological states, and if we limit ourselves to states with energies below 1 TeV for every excitation, then this corresponds to a very tiny subspace of the entire Hilbert space, while every state we can use is a superposition of ontological states. Without loss of generality, we can interpret the coefficients of these superpositions by

[5]The phrase "vector space analysis" is used in information technology; it is the same mathematics that is used there. We add to that procedures involving unitary transformations.

taking their absolute squares to indicate probabilities. This is further elucidated in **Appendix A**. Here it is important to observe that "reality" is always described as one of te original ontological states, and never a superposition, yet we may use the Schrödinger equation to describe both the ontological states and the superpositions. The elements of the ontological basis always evolve into other elements of this basis, and superpositions into superpositions. We call this the *law of conservation of ontology*.

There is a good reason why many attempts at making realistic models explaining the violation of Bell's inequalities failed, which is that, in these models, it was attempted to mimic superpositions of particular modes in terms of other valid modes of an automaton. It is much better to keep superpositions as what they are, superpositions of valid automaton modes which, for that reason cannot by themselves act as ontological states. What happens instead is that, if one considers some superposition of physical states, one is actually considering a probabilistic mixture, but what exactly the true, unmixed, physical states are differs from one experiment to the next, in such a way that the final state can never be in a superposition. Because this feature is of tremendous importance, we explain some technical details of this point in **Appendix A**.

Now we can see that, in deriving their inequalities, Bell and CHSH had to make assumptions that we cannot agree with. Their main assumption is that Alice and Bob may choose what to measure, and that this should not be correlated with the ontological state of the entangled particles emitted by the source. However, when, in choosing their settings, either Alice or Bob change their minds ever so slightly, their classical settings represent a different ontological state than before. The photon they look at now, will be a superposition of the old photons that they wanted to detect, but the entire state, photon plus settings, will be orthogonal to the previous one. In particular, because of the ontological conservation law, the new photon they look at must be an ontological one. Alice and Bob do *not have the free will* to look at photons that are not ontological. So, while changing their minds, Alice and/or Bob had to put the universe in a different ontological state than the previous state, and this modification goes back billions of years, all the way to the origin of the universe. One could call this retro-causality, but it is merely due to the fact that the (classical as well as quantum) equations can, in principle, be solved backwards in time.

As a consequence, Alice's and Bob's settings can and will be correlated with the state of the particles emitted by the source, simply because these three variables do have variables in their past light cones in common. The change needed to realize a universe with the new settings, must also imply changes in the overlapping regions of these three past light cones. This is because the universe forces itself to stay ontological at all times.

The restriction that the universe must be in an ontological state at all times, is the only restriction. This implies that Alice and Bob still have free will in the classical sense; they can choose any of the ontological states of the universe, no matter what kind of random number generator or lotto machine they were using. But they cannot put the universe in a superposition of states, which is only something we can do in our mathematical models when studying probability distributions, wishing to bring these in a form such that we can apply Schrödinger equations.

So let us emphasize and summarize this essential point:

> *Whenever observers seem to be using their "free will" to choose the settings of the detectors they use, they cannot 'change their minds' unless microscopic data at all times in the past are modified as well. Among others, the (entangled) photons in Bell's experiment will be re-arranged into some other quantum state in such a way that the photons eventually measured will always be in an ontological state: they cause a detector either to click or not to click, but they can never cause detectors to go into a superposition of states.*

In particular, if we assume that the universe started with a given, fixed state at $t = 0$ (the Big Bang), then there is no option anymore for any observer to change his mind; his actions are fixed, even if he thought to have free will. The settings a and b are correlated with the photon polarizations λ, which should not be confused with "causation backwards in time."

A related quantum paradox that has been put forward as another illustration of quantum weirdness, is the so-called GHZ paradox. This paradox is of interest because its resolution can be phrased in terms of an over simplified model of the universe, illustrating the important role of the *observer* as being part of the system. In **Appendix C**, we explain what happens in the cellular automaton theory when this Gedanken experiment is performed.

5. INFORMATION LOSS AND THE ARROW OF TIME

Most well-known physical theories that explain the apparent absence of time reversal symmetry contain elements of thermodynamics and entropy. Actually, in these descriptions of nature, one can explain the absence of this symmetry elegantly by blaming it to an asymmetry in the *boundary conditions*. When writing differential equations for the laws of nature, one always has to add what we know about the boundaries. As for the boundaries in the space-like directions, little is known, since the universe looks very homogeneous, and no boundary effects have ever been detected. The universe is either strictly infinite in the space-like directions, or we live on a spatially compact manifold such as a 3-sphere or a torus. These boundary conditions show much symmetry.

In the time-like direction, however, there cannot be complete symmetry. The universe appears to have started extremely small, conceivably it all started in a single point. That point must have been highly ordered, having total entropy very small or possibly zero. This is a reasonable boundary condition at the origin of time.

Yet at the other end, when time grows to be very large, we see no need of any boundary condition; the universe may simply continue to expand forever, undergoing perpetual increase of entropy. Thus we have equations that are symmetric under time reversal but asymmetric in their boundary conditions. This suffices to explain the time asymmetry we see today.

However, there are examples of mathematical systems where features exist that can be attributed either to the bulk of the

system or to the boundary[6], so that relegating all time symmetry violating effects to the boundary may conceivably not always work.

As long as we adhere to the quantum mechanical description of all microscopical dynamical laws, we find the CPT theorem on our way, which implies that if we combine time reversal T with parity reversal P and particle-antiparticle interchange C, then this symmetry is perfect. We could well stick to our verdict that Nature's boundary conditions in the time direction suffice to explain the arrow of time.

One may observe however that another source of time reversal asymmetry can be contemplated. As explained in previous sections, this author does not believe that "quantum mechanics" will be the last and permanent framework for the ultimate laws of nature. If we drop it, to be replaced by some classical ideas, the need for time reversal symmetry also subsides. We could opt for an underlying theory where information, in the classical sense, can disappear. Considering cellular automata, systems where information does get lost are much more general than the ones where information is conserved, so that switching the direction of time brings about much more dramatic changes.

How can such models lead to effective quantum theories? Does local time reversal symmetry re-emerge? We claim that, for an automaton, the possibility to generate statistical correlations that are solely based on vector space analysis, that is, vectors evolving in Hilbert space, which lead to quantum mechanics, may be quite generic, and include models featuring information loss.

The way to deal with information loss in this context is very straightforward in principle, while extremely difficult in practice. The way to handle this in principle is by the introduction of *information classes*: we identify the elements of an orthonormal basis of Hilbert space not with single states of the automaton, but with information classes. An information class is defined to be a class of states in an automaton that have the property that, after a finite amount of time, they all evolve to become the same state in the automaton. In principle, such classes may become extremely large, but in practice the odds of two states that resemble one another at one moment in time, to evolve into exactly the same state in the near future, might rapidly go to zero as time proceeds, so that the information classes may continue to be manageable. Formally, they might become big enough to form states that can be distinguished by only inspecting the data living on a boundary surface rather than specifying what happens in the bulk. This is what we see in the physical equations for black holes, called *holography*, so that this may be seen as an indirect piece of evidence favoring underlying models with information loss.

In underlying models with information loss, the act of time reversal takes a very interesting shape: the time reverse of ontological states in Hilbert space (beables) tend to form quantum superpositions of beables in the time-reversed Hilbert space. This may perhaps explain why superpositions follow the same laws of nature as ontological states, but for the time being we just regard these generic observations to be something to keep in mind when, much like Sherlock Holmes, we attempt to figure out, in terms of models, what it might have been that actually took place, when all information we have been able to acquire, takes the shape of quantum superpositions.

[6]The θ angle in QCD is a case in point. One can describe that as a lack of invariance under topological gauge transformations, which can be entirely attributed to the boundary. Equivalently, one can regard this effect as a PC violating term in the action, which is local.

AUTHOR CONTRIBUTIONS

The author confirms being the sole contributor of this work and approved it for publication.

ACKNOWLEDGMENTS

The author thanks T. Maudlin, P. W. Morgan, T. Myers, T. Norsen, and many others, for extensive discussion on these and related issues on weblogs. I also thank the editors and referees who insisted upon further clarifications to improve the original manuscript.

REFERENCES

1. Einstein A, Podolsky B, Rosen N. Can Quantum mechanical description of physical reality be considered complete? *Phys Rev.* (1935) **47**:777.
2. Jammer M. *The Conceptual Development of Quantum Mechanics*. New York, NY: McGraw-Hill (1966).
3. Clauser JF, Horne MA, Shimony A, Holt RA. Proposed experiment to test local hidden-variable theories. *Phys Rev Lett.* (1969) **23**:880–4. doi: 10.1103/PhysRevLett.23.880
4. Bell JS. On the Einstein Podolsky rosen paradox. *Physics* (1964) **1**:195.
5. Bell JS. La nouvelle cuisine. In: Bell M, Gottfried K, Veltman M, editors. *On the Foundations of Quantum Mechanics. Speakable and Unspeakable in Quantum Mechanics*. Ann Arbor, MI: University of Michigan (2001). p. 216–34.
6. 't Hooft G. The cellular automaton interpretation of quantum mechanics. In: *Fundamental Theories of Physics*, 1st Edn., Vol. 185. Cham: Springer International Publishing (2016). p. 298.
7. Mermin ND. Quantum mysteries revisited. *Am J Phys.* **58**:731 (1990). doi: 10.1119/1.16503
8. Greenberger D, Horne M, Zeilinger A. Going beyond Bell's theorem. In: Kafatos M, editor. *Bell's Theorem, Quantum Theory, and Conceptions of the Universe*. Dordrecht: Kluwer Academic (1989), p. 69–72.
9. Kaufman B. Crystal statistics. II. Partition function evaluated by spinor analysis. *Phys Rev.* (1949) **76**:1232.

Conflict of Interest Statement: The author declares that the research was conducted in the absence of any commercial or financial relationships that could be construed as a potential conflict of interest.

APPENDIX

A. Superpositions and Born's Probabilities

Whenever theories with classical logic are proposed to explain quantum phenomena, the following questions are often raised:
Question 1: *In Bell's experiment, a pair of particles—call them photons—is in an entangled state. In an ontological theory, it seems as if this pair of particles "knows ahead of time" which superposition of states will later be chosen by Alice and by Bob for their measurements. Why does this not violate causality?*
Question 2: *How come that the squares of amplitudes exactly represent the probabilities for the outcomes of measurements?* (Born's rule)
And question 3: *What happens when a wave function collapses?* And what happens when a measurement or observation is made?

These questions are all strongly related, and they can be answered together in what was advertised earlier as the Cellular Automaton Interpretation of Quantum Mechanics [6].

The basic idea is that, at the tiniest distance scale that is meaningful in physics, presumably the Planck scale, around 10^{-33} cm, there are laws of physics which are most efficiently formulated by not giving any reference to Hilbert space, quantum superpositions, qubits, or even action-at-a-distance. We have a *cellular automaton* there, or something that resembles this very much. A cellular automaton can best be regarded as a basic computer program, where, in a massive venture of parallel computing, digital data that are localized on some sort of grid, are being updated at the beat of an extremely fast clock. The speed of the clock may vary at some points, but these are details that we do not want to go into. Most importantly, information spreads with a limited velocity, basically the speed of light, and all this information is classical. Temporarily, for simplicity, we assume the system to be reversible in time, although, as was explained earlier, this might not be necessary.

This is clearly the kind of theory that Einstein, Bell, and many others thought they could disprove, but as we shall explain now in more detail, this is not quite the end of the story. There are various aspects of the system that need much more scrutiny, in particular the ubiquitous presence of very strong correlations at the micro-scale, which permeates to macroscopic distances, and the fact that it is fundamentally impossible to compress (to "zip") the system into a more course-grained model that reproduces all details. As soon as one tries to compress anything, uncertainties emerge that manifest themselves by looking like quantum superpositions. But I am running ahead of my arguments, let us consider the situation in a meaningful order. The more complete story is presented in 't Hooft [6].

In principle, the automaton can be in a huge number of distinct states, roughly $2^{10^{99}}$ states in every cubic cm (a number obtained by assuming one boolean degree of freedom in a cubic Planck length). Only if we consider all of these states, the system can be seen to be deterministic. Every single one of these states is important, but, because of strong correlations, we perceive our world as if there are much fewer states possible, typically $2^{10^{50}}$ in a cm^3 (one boolean degree of freedom in 1 TeV^{-3}). Yet compressing the system cannot be done without losing information; a more powerful technique is required.

It so happens that a more powerful technique does exist; we call it "vector space analysis." In mathematics, this is not new[7]. For instance, in group theory, it turned out to be useful to give matrix representations of elements of a group. Consider a subset of a permutation group. The elements of the set in which the permutations take place are represented as orthonormal vectors in our vector space. The dimensionality of this vector space equals the dimension (number of elements) of the set. It can be finite or infinite. This vector space is our Hilbert space. One now can use all mathematical tricks available for vectors to investigate the properties of the group. For instance, one can diagonalize the matrices. This involves orthogonal (unitary) transformations of all sorts for the vectors.

It is now assumed that we can do the same in the set of states of the automaton. After a number of transformations, we get matrices representing the evolution that are diagonal or almost diagonal. The effective dimensionality of our Hilbert space can now be considerably reduced because large parts of it factorize. However, they do not factorize along the original dividing lines of our orthonormal set. We get different kinds of vectors, all of which are now superpositions of vectors of the original set. All of this is just mathematical manipulation; the physics is kept as it was.

In particular, the evolution law is an ontological matrix in terms of the original ontological states; an ontological unitary matrix is a matrix containing only one and for the rest zeros in all its rows and all its columns (arbitrary phase factors are allowed, as long as each row and each column only contains one element with absolute value one, while all other matrix elements vanish). After some combination of extensive linear superpositions, our matrices will look much more generic than before.

While every one of our $2^{10^{99}}$ states evolves into another state within time units as small as the Planck time, being of the order of 10^{-44} seconds, we will find superpositions of states that evolve much slower. The effective time unit will now be the inverse of the energies of the most energetic particles in our particle accelerators. These energies are many orders of magnitude lower than the Planck energy, so indeed, we have a much smaller Hilbert space than the original one. What is known about physics today is the evolution laws of this tiny subspace of Hilbert space. Since the time dependence is much slower here, we can write the evolution law in terms of a hermitian hamiltonian: the Schrödinger equation. We only postulate determinism in the original cellular automaton model with its humongous number of states, not in the effective, reduced model that is called physics today. Can this system violate the Bell/CSHS inequalities?

First we need to specify how an observation is made, in terms of the states of the original automaton. Suppose we want to establish the presence of a planet. In the interior of the planet, atoms and molecules are densely packed, so that the world in there looks quite different from the vacuum state. We now assume that the vacuum state is represented by states in the automaton that show different statistical abundances and

[7] In physics, the most spectacular application is the solution of the 2-dimensional Ising Model, by Onsager and Kaufman [9]. They turn the classical model into a quantum field theory that happens to be integrable.

correlations than the states that represent densely packed atoms and molecules. Locally, the statistical differences between these states may be minute; our ability to distinguish the vacuum state from the rocky material may be far from perfect; say that, inside a small volume of a mm^3, a given state has a likelihood of $(1-\varepsilon)/(1+\varepsilon)$ of being a vacuum rather than a rock. For the whole planet, we have to raise this number to a power equal to the volume of the planet measured in mm^3. Thus one finds almost with certainty that there is a planet rather than a vacuum in that neighborhood.

The planet is a classical object. What we just found is that such classical objects are bound to be sufficiently well identified and characterized in terms of the original states of the automaton. Let us assume that this holds for all objects that we normally call "classical," not necessarily as large as planets. When we do a measurement or make an observation, we must be looking at a large subset of the classical states of the automaton.

Now consider a quantum experiment. We can't use the entire Hilbert space, because it contains far too many states. So we use the strongly reduced subspace of Hilbert space that represents only low-energy particles. All these states are superpositions of cellular automaton states. Specifying our initial state $|\psi\rangle_{\rm init}$ as well as we can, we still represent it as a superposition of ontological states $|\mathrm{ont}\rangle_i$:

$$|\psi\rangle_{\rm init}=\sum_i \alpha_i|\mathrm{ont},\ \mathrm{init}\rangle_i\ ;\qquad \sum_i|\alpha_i|^2=1. \tag{A1}$$

At this point we merely need to *define* that $|\alpha_i|^2$ represents the probability that the ontological state $|\mathrm{ont}\rangle_i$ is our initial state. From the mathematics of linear representation theory, it would be hard to deduce any other link between probabilities and amplitudes than that one. In any case, in what follows, we shall see that what holds for the initial state will continue to hold for all states arrived at in later times.

So let us consider the evolution of this state. Our mathematical procedures for the decompositions of our state vectors never affected the physical evolution law for the ontological states. This means that, *as long as we use linear Schrödinger equations*, also at later times, relation (A1) continues to hold, up to the final state:

$$|\psi\rangle_{\rm final}=\sum_i \alpha_i|\mathrm{ont},\ \mathrm{final}\rangle_i\ ;\qquad \sum_i|\alpha_i|^2=1. \tag{A2}$$

Note that the basis of states will have changed, but the superposition coefficients α_i have stayed exactly the same, and hence also the probabilities stayed the same[8]. And now consider the measurement. We compare the final superimposed state with the ontological states the system should end up in. They are again the ontological states $|\mathrm{ont},\ \mathrm{final}\rangle_i$ of Equation (A2). Now the α_i are finally recognized as representing the probabilities for the final state. Born's probability rule is the simple consequence of the mathematical representation theory. The answer to the question where Born's probability rule comes from is that, if we put it in for the initial state, Born's rule stays the same during the entire evolution.

Note now that, if we started with one single ontological state $|\mathrm{ont},\mathrm{init}\rangle_1$, then the final state will *automatically* also be a single ontological state $|\mathrm{ont},\mathrm{final}\rangle_1$. This continues to be true if we use the Schrödinger equation to describe the evolution. Consequently, the Schrödinger equation will *automatically* cause the final state to collapse into a single ontological state, if the initial state was a single ontological state. The reason why this appears not to happen in ordinary quantum mechanics is that we do not use the full Schrödinger equation for all states, but only for the lower energy states where the equation is known, and we idealized the initial state, involuntarily replacing the ontological initial state by a superposition, hence a probabilistic distribution of initial ontological states.

It is often claimed that quantum probabilities should be seen as fundamentally different from the classical uncertainties that are due to lack of knowledge of the initial state; in our approach however, the quantum probabilities are there for exactly the same reasons as in classical theories.

Now consider the EPR/Bell experiment. We do not explicitly construct a microscopic, classical model for all Standard Model interactions. Although general strategies for such a construction have been proposed, it is still too difficult to reproduce all symmetries of Nature. We do however claim that any contradiction with the Bell/CHSH inequalities has disappeared.

When Alice and Bob perform their observation, they cannot select a superposition of photon states, but only one ontological photon. The outcome of Alice's measurement is always an ontological state of the form $|a,\ A\rangle_{\rm ont}$, where a is the setting chosen, given by an angle, and $A=\pm1$ is her finding. Together with Bob's finding, the final, classical state is $|a,\ A,\ b,\ B\rangle_{\rm ont}$. In our model, the calculation gives a superposition,

$$\psi\rangle_{\rm final}\ =\alpha_1|a,+,\ b,+\rangle_{\rm ont}+\ \alpha_2|a,+,\ b,-\rangle_{\rm ont} \tag{A3}$$

$$+\alpha_3|a,-,\ b,+\rangle_{\rm ont}+\ \alpha_4|a,-,\ b,-\rangle_{\rm ont}, \tag{A4}$$

The observed outcome is never a final state of the form (A2) or (A3), but *always* one specific ontological state, $|\mathrm{ont},\ \mathrm{final}\rangle_1$. The *model calculation* gives an entangled superposition of the ontological state $|a,b\rangle$ combined (multiplied) with a superposition of the four states $|+,+\rangle$, $|+,-\rangle$, $|-,+\rangle$, and $|-,-\rangle$.

If we modify the initial state, the calculated final state will be a different entangled superposition, but the ontological state will be in the basis of the angles a,b and the measurements A and B. Modifying the initial ontological state will always lead to a single final ontological state, *never* a superposition, since the coefficients α_i never change.

What was misleading in Bell's exposition of the experiment is that he thought that a modification of the settings a and b would lead to a different superposition of the measurements $A=\pm$ and $B=\pm$. In our vector representation, any modification of a and b, regardless how tiny, requires a modification of the initial ontological state. The new ontological state will be orthogonal, hence totally unrelated to the previous one, so that

[8]We often get the question whether taking the absolute squares of α_i as being the probabilities, doesn't change everything. The answer is no, because the coefficients do not change at all during the entire evolution, as long as we stay in the ontological basis.

the two photons emitted by the source cannot be related to the photons emitted previously. Thus, the idea that one can modify the settings (a, b) without modifying the polarization of the entangled photons emitted by the source, is an illusion.

One can also say that the settings a and b emerge to be *entangled* with the polarized photons. As soon as the settings are fixed, the photons will only be in a single ontological state. I won't push this description too much, because at the end we should have just a single setting and a single ontological photon state.

The most important difference between our presentation and the usual treatment of Bell's observations is that the observers Alice and Bob, together with the settings a and b chosen by them, *are parts of the physical system*. Any modification of the settings (a, b), whether done out of "free will" or otherwise, will require a different initial ontological state.

B. Causality and the Arrow of Time in Special Relativity

Within the CA interpretation of quantum mechanics, special relativity is difficult to handle in this procedure, since the Lorentz group, or the Poincaré group, are notoriously difficult to implement, as these groups are not compact. It is quite conceivable that Poincaré transformations link ontological states not to other ontological states, but to superpositions of ontological states. Yet the presence or absence of symmetries should not be our immediate concern. We may for instance assume that only the homogeneous part of the Lorentz group is a genuine symmetry at the ontological level, or possibly an approximate symmetry.

The more important feature of special relativity is the fact that it gives a limit to the propagation speed of signals. Now this is quite easy to impose on CA models or theories. We just assume that, at the beat of our clock, the contents of a given cell of our automaton can only be passed on to a neighboring cell. Signals then can never propagate faster than the speed of this process. Outside the associated light cone, the validity of "No Bell Telephone," Equation (3.1), is then guaranteed.

As we stated in section 3, this is the only acceptable causality condition for physical models, classical as well as quantum. It implies that the time ordering is only a partial ordering – for space-like separated events the time ordering is irrelevant. The *arrow* of time is defined as the order in which the equations for our models (classical, quantum, cellular automaton of continuum field theories) are to be applied in our model simulations. Thus, relativistic theories will have an arrow of time as much as non-relativistic ones. As we emphasized in section 1. the fundamental definition of time, as well as its arrow, can only be applied to our *models* of Nature, not the physical data themselves. This also holds for the concept of causality.

The difficulty of imposing Lorentz- and Poincaré symmetry for CA models continues when time reversibility is broken at the ontological level, but models where the propagation speed of information is limited can easily be extended to being non-reversible in time as well. This happens almost automatically.

C. The GHZ Paradox and the 6-bit Universe

There are many newer versions, generalizations and refinements of the original Gedanken experiments considered by EPR and Bell. Sometimes, the paradoxes concern not only probabilities, but even certainties where clashes with "classical" physics are seen to occur, but they all have in common that one or more observers choose between two or more different settings that measure properties of quantum objects, whose operators do not commute.

An interesting case, where the magic mystery seems to reach new heights, is the GHZ paradox. We briefly recapitulate the setup, which is explained in more detail in the literature [7, 8].

A source is constructed such that it emits three entangled particles, each having two possible spin states, ± 1. The quantum state produced is

$$\psi = \tfrac{1}{\sqrt{2}}\big(|+,+,+\rangle - |-,-,-\rangle\big). \tag{C1}$$

The operators to be considered are $\sigma^{a,b,c}_{x,y}$ where a, b and c refer to the three particles a, b and c, and

$$\sigma^a_x|\pm,\cdots\rangle = |\mp,\cdots\rangle \quad \sigma^a_y|\pm,\cdots\rangle = \pm i|\mp,\cdots\rangle \tag{C2}$$

while $\sigma^b_{x,y}$ and $\sigma^c_{x,y}$ act similarly on particle b, and on c, respectively. It is not difficult to derive that these operators obey

$$\begin{aligned} XXX &\equiv \sigma^a_x\sigma^b_x\sigma^c_x = -1\\ XYY &\equiv \sigma^a_x\sigma^b_y\sigma^c_y = 1\\ YXY &\equiv \sigma^a_y\sigma^b_x\sigma^c_y = 1\\ YYX &\equiv \sigma^a_y\sigma^b_y\sigma^c_x = 1. \end{aligned} \tag{C3}$$

The three Pauli matrices σ_i acting on the same particle, anti-commute, σ^a_x, $\sigma^a_y = -\sigma^a_y\,\sigma^a_x$, while two Pauli matrices acting on different particles commute. Thus one derives that if we permute two pairs of σ operators in Equation (C3), two minus signs emerge, which enables us to derive easily that all four operators in Equation (C3) commute with one another. Therefore, all operators in Equation (C3) can be measured simultaneously, and the result always obeys (C3).

Now, the three particles are sent to three different observers, who sit in three different, sealed rooms. Each observer decides, "at his free will," to choose to measure either $X = \sigma_x$ or $Y = \sigma_y$. The observers cannot communicate with each other, so they do not know what the others choose. They just meticulously write down whether they measure X or Y, and what their outcome is, $+1$ or -1. After having done a long series of measurements, they come out of their rooms, and compare notes.

All observers, on average, found as many pluses as minuses, because the expectation values of $X = \sigma_x$ and $Y = \sigma_y$ are zero. Also, there is no pair correlation, since for every pair, the expectation values for XX, XY, YX and YY are also zero. But the three observations are correlated: the three-point correlations, given in Equation (C3), are very strong.

Moreover, they seem to contradict classical logic. The list of observations will obey (C3). But at every run, one might

have asked: what would this observer have found if (s)he chose the other setting, or more generally, given a particle entering his room, and (s)he measures either X or Y, what would the outcome in either case have been? So we add to the list of observations, at each run, all possible answers: XXX, $XXY, \cdots, YYY$. Now take the last three equations of (C3). Take their product. Since every Y occurs exactly twice in the product, the Ys together always contribute $+1$ in the product. What is left is the three Xs. So we get $XXX = +1$. But this is wrong, it violates the first equation of Equation (C3). One must conclude that the three entangled particles know, ahead of time, whether their observers will have chosen X or Y. Apparently, the observations that were not actually made, do not have well-defined values for X or Y at all. These are called *counter factual*. Quantum mechanics forbids counter factual observations. How can this happen in a cellular automaton?

In this case, vector space analysis suggests that a simple model can be constructed of the entire universe. There are just 6 binary dynamical variables in this universe. A priori, this universe could have started choosing any of $2^6 = 64$ distinct initial states.

Like our real universe, this model universe may have started out with a big bang. At that moment, not all possible states have been realized. Only 48 of the 64 initial states were allowed. During a period of chaos, the 48 states may have been scrambled many times, but there are 16 states that cannot be realized at any time. This is how the laws of nature for the model universe are programmed.

At the beginning of the experiment, three particles are selected. These are three of the 6 bits. All of them can be $+1$ or -1. Now we have the three observers, A, B, and C. Each of them has to decide whether to choose X or Y. They each grab the one bit they can find in their rooms. That bit represents their free will. It can be anything, but its properties are determined by laws of nature. Each observer knows that the probability for this bit to be $+1$ or -1 will be equal, so the observers will be convinced they are acting out of free will. There are $2^3 = 8$ possible terms in the sequence XXX, $YXX, \cdots, YYY$. In 4 of these (where the number of Ys is even), there is a constraint: only 4 of the $2^3 = 8$ possible answers are allowed. Therefore, $4 \times 4 = 16$ outcomes are forbidden. This is what the laws of nature tell you here: of all ontological states, 16 are forbidden.

Thus, we claim that classical laws of nature in the 6 bit universe can perfectly well reproduce the GHZ "miracle," but we must accept that the observer's free will is controlled by laws of nature as much as all other phenomena.

Of course, quantum physicists object that this is unfair: "you have used 'retro-causality' to establish your laws of nature." Well, the view presented in the main body of this paper is, that the laws of nature are usually time-reversal invariant, and this means that if a complete state of the universe is known at present, it also causes limitations to the allowed states in the past, and that is where our constraints come from. We simply cannot expect "perfect" free will in our universe. Maybe you think this is "conspiracy." So be it, but the laws of nature in our approach are foremost classical.

Advantages of publishing in Frontiers

OPEN ACCESS
Articles are free to read for greatest visibility and readership

FAST PUBLICATION
Around 90 days from submission to decision

HIGH QUALITY PEER-REVIEW
Rigorous, collaborative, and constructive peer-review

TRANSPARENT PEER-REVIEW
Editors and reviewers acknowledged by name on published articles

Frontiers
Avenue du Tribunal-Fédéral 34
1005 Lausanne | Switzerland

Visit us: www.frontiersin.org
Contact us: info@frontiersin.org | +41 21 510 17 00

REPRODUCIBILITY OF RESEARCH
Support open data and methods to enhance research reproducibility

DIGITAL PUBLISHING
Articles designed for optimal readership across devices

FOLLOW US
@frontiersin

IMPACT METRICS
Advanced article metrics track visibility across digital media

EXTENSIVE PROMOTION
Marketing and promotion of impactful research

LOOP RESEARCH NETWORK
Our network increases your article's readership